CIVIL ENGINEERING JOURNAL

číslo 1/2021

Obsah:

JAN SOKOL'S APPROACH TO THE RENEWAL OF MONUMENTS WITH AN EMPHASIS ON HIS ACTIVITIES AT PRAGUE CASTLE

Martin Šnorbert

Czech Technical University in Prague, Faculty of Civil Engineering, Department of Architecture, Thákurova 7, 166 29 Prague 6 - Dejvice, Czech Republic; martin.snorbert@fsv.cvut.cz

ABSTRACT

This contribution deals with the approach of the architect Jan Sokol to the renovation of monuments within his architectural work. Close attention is paid to the biographical part, as it describes the development of the architect's relation to the history of art and cultural heritage of previous generations. Personalities who influenced him during his studies, but also during architectural practice, are mentioned. It also captures the period when Sokol worked as an employee in a state studio which was focused on the preservation and restoration of monuments. Subsequently, selected buildings and projects designed by this architect in the field of historic preservation are discussed. Of these, the most emphasized are the projects which were created for the area of Prague Castle. To understand these projects, the preserved texts, plans and ideas of the author are used. Unfortunately, many of the discussed projects were not implemented, but they are very valuable in their thought form. And this is one of the reasons why this article iss written, it tries to show the quality of Sokol's projects. Furthermore, the purpose is to point out the personality of the architect, who has not been fully appreciated yet, nevertheless he has inspired several of his students and other architects. In conclusion, it is pointed out that the Sokol's discussed approach was based on a deep knowledge of the construction of the historical buildings and history of art, and that led him to approach to these buildings with a certain humbleness. It is further stated that the architect Jan Sokol was a generally gifted author with an overlap into fields areas.

KEYWORDS

Architect Jan Sokol, Historic preservation, Town planning, Prague Castle, Romanesque Palace in Olomouc, St. Vitus Cathedral, Pinkas Synagogue

INTRODUCTION

As a part of my doctoral dissertation, I deal with the topic of architectural interventions in the area of Prague Castle in the second half of the 20th century. While studying the materials, I was interested in the name and the work of Jan Sokol, who I wanted to find out more about. About the projects of a man who did not adapt to the taste of his period but kept his distinctive approach. About an architect, whose significance for the Czech architecture after World War II has not been fully appreciated yet by the non-professional public, but also by some experts.

Sokol's personal memories, texts and plans, which were arranged and published in book form, helped me understand the researched topic. His son Václav had the main credit for publishing the book. Doctoral dissertation by Karin Urbanová Kasanová was used as another source of information. Several articles in professional periodicals were also dedicated to Sokol.

LIFE AND STUDIES

Jan Sokol was born on May 24, 1904 in Roudnice nad Labem, but his family moved relatively soon to Náchod, where Jan lived out his youth and adolescence. He spent most of the time during the holidays in Jablonné v Podještědí, where his uncle worked as a chaplain. He graduated from the grammar school in Náchod and then he decided to study architecture at the Czech Technical University in Prague.

He was not completely satisfied with the style of teaching (the core of architecture - design was not introduced until the third year of study). During last two years, he studied and prepared the final work under the guidance of architect Antonín Engel. Although he lectured poorly, according to Sokol, he acknowledged him and very gratefully thought back to a month-long study stay in Italy, for which he was selected together with 19 other students. Not only this, but also the fact that Engel wrote him a recommendation after graduation, shows the fact that Sokol was a good and careful student, whom Engel liked. However, Sokol did not want to continue in this kind of classicism, which he adhered to in his last works due to his teacher.

Fig. 1 – Working environment in the studio of Le Corbusier in Paris [1]

A one-year scholarship in France was very important and instructive. He studied at the École des Beaux-Arts and even he got into the studio of Le Corbusier. He worked here, for example, on the project of Villa Savoy or on the palace Tsentrosoyuz. He later wrote this down: *"Le Corbusier was a great artist, which is why his buildings were so impressive. (…) August Perret was in this activity* (in searching of the impulse for a new architecture - author's note) *further than Le Corbusier, nevertheless he did not abandon the classical tradition, still did not achieve the impressive modernity of Le Corbusier. At one time it seemed to me that he was right and that I should have worked with him, but in the end I saw that all I should do was to try to find myself and look for advice, not an example of others."*[2] In Paris he established contacts with many Czech

personalities, for example, the philosopher Jan Patočka, the painter František Kupka or the composer Bohuslav Martinů. Professor Vojtěch Birnbaum[1] also arrived in France to see Sokol. And when Gočár arrived in Paris, he invited Sokol to be his guide, because he heard that Sokol had worked for Le Corbusier. After returning home, he was offered the opportunity to spend another year in France, but he decided to go to England (after consulting with Prof. Wirth[2]), because he wanted to get acquainted with urbanism in theory and practice. He visited London, Edinburgh, Birmingham. He returned to Czechoslovakia via Rotterdam, Amsterdam, Frankfurt, Dessau, Berlin and Dresden.

He returned to Prague, but unfortunately during the financial crisis, so the promise of a job in Gočár's studio did not come off, nevertheless Gočár became an important person during this period, as Sokol was able to study at his school (which did not contribute to Sokol's popularity at CTU). In cooperation with Emanuel Hruška, they made a good name for themselves in several town planning competitions, in which they placed in award-winning places. In order to ensure himself a permanent salary, he was employed at the Ministry of Public Works as a contract architect. From the beginning this work did not satisfied him, because he was more of a clerk than the architect. Eventually, he found an interesting content of work, which consisted in finding land for state buildings, assigning projects. Some of them he could even draw in advance. In 1939 he became a professor of style at the Academy of Arts, Architecture and Design in Prague (he had previously worked there as an associate professor) and from 1941 to 1945 he worked as a rector there. He took over the leadership of the school after Otakar Novotný, because in the mentioned year 1941, a large part of the original professors was retired in order to make positions for teachers who were coming from the resigned border. The attempt to return these professors after the war then brought considerable problems and difficulties. They were joined by an investigation because he served under a relatively high position during the Protectorate. In connection with the rise of the communists to power, Sokol as Catholic began to be unpopular, became undesirable at school, which led to the dissolution of his school (studio) at the Academy of Arts, Architecture and Design in 1951, but until the final end at 1959 he had lectures about style. After these events, he began working in the historic preservation and in SÚRPMO[3], which enabled him to work again at Prague Castle. Especially before the war, it was true that whoever wanted to participate in competitions had to belong to some association. Sokol joined the two - the Club of Architects, which was associated with the magazine Stavba and from the beginning with the chairman Oldřich Starý. The second was the Mánes art association and he valued it more. He met many important architects there and other artists. Sokol died, after a long and interesting life with many vicissitudes, on September 27, 1987.

SOKOL AND HISTORIC PRESERVATION

Sokol was already interested in monuments, and especially in the history of art, while he studied at university. He enrolled at Charles University for an art history course as an extraordinary student. The following year he attended lectures and seminars in a small group of future art

---

[1] Vojtěch Birnbaum (7.1.1877 - 30.5.1934) was a Czech historian and art theorist, university teacher, he also devoted himself to historic preservation.

[2] Zdeněk Wirth (August 11, 1878 - February 26, 1961) was a Czech art historian, one of the founders of historic preservation, a university teacher, an academic of the Czechoslovak Academy of Sciences and a founding member of the Club for Old Prague.

[3] The State Institute for the Reconstruction of Historic Towns and Buildings (SÚRPMO) was a state institute, which was established in 1954 as a centralized workplace for a comprehensive solution for the reconstruction of historic city centres in Czechoslovakia (following the R - studio at Stavoprojekt existing since 1949). After 1989, there was a gradual decline in activity.

historians. He was very pleased that Josef Cibulka[4], a professor at the Faculty of Theology, began lecturing art history at Czech Technical University. Sokol had known him from earlier times thanks to his uncle, who worked as a priest in Jablonné nad Orlicí and asked Cibulka for advice about painting the church (in addition, Cibulka was a native of nearby Ústí nad Orlicí). This teacher had a great influence on Sokol and recommended him to join the Club for Old Prague and to the seminars of Professor Birnbaum. Birnbaum did not accept beginners, but Sokol succeeded through an intercession from Cibulka. From 1924 to 1926, Sokol and Cibulka prepared an inventory of Lanškroun monuments for the Czech Academy.

Sokol also dealt with these topics during his pedagogical work at the Academy of Arts, Architecture and Design in Prague. After a not very pleasant ending at school, he received an offer for a position at SÚPPOP[5]. Sokol took a long time to think, because he was always close to the monuments (see described above), but he was afraid that the work in the historic preservation was filled mainly with clerical tasks but scientific work with semi-creative practice was disappearing. The staffing was not ideal either, because young and inexperienced historians came to the fore. Sokol would rather have joined one of the design institutes - he was thinking especially of the Institute of Reconstruction, which was led by Vilém Lorenc.[6] Unfortunately, he did not get there due to the inability of the ministry and the Union of Architects to stand up for Sokol. Eventually, Sokol decided to accept the offer. The work in the historic preservation was considered as a quiet office, but it will be shown from the following examples of Sokol's works and projects that this consideration was not true. In the words of the professor Sokol: "*He* (Preservationist - author's note) *must defend an idea that is rarely understood and even less ever shared against the attack of the ignorant and unconscious majority, which has always been here, but now had all the power in its hands. Most of this majority often included own monument authorities on national committees, whose persuasion and even swearing had to be considered."* [3]

In the 1960s, Sokol took part in the adaptation of the Old Palace of Prague Castle, he was asked to create a relatively extensive study, and therefore Gočár suggested him that he should enter a design institute due to the scope of this task. Sokol agreed but told Gočár that he had recently applied for a position at SÚRPMO. However, the director had rejected him because of the personnel reference. Gočár decided to intercede for Sokol and thus began Sokol's work in SÚRPMO. He ended his work at this institute in the first half of the 1970s, after that he designed only smaller contracts under his own name.

Modifications of the Strahov Monastery for the Monument of National Literature

Even before joining SÚPPOP, Sokol received an assignment from the Ministry of Education for the reconstruction of the Strahov Monastery in Prague, which was empty due to the dissolution of religious orders (including Strahov Premonstratensian Order), internment and imprisonment of many ecclesiastic representatives. The previous amateur experiment reached a deadlock, and therefore professional guidance was required, which was provided by Professor Sokol. He came into conflict with employees of the communist ecclesiastical office. For example, the capitular hall was rebuilt into a vestibule, but during this event, some underground canals were destroyed.

---

[4] Josef Cibulka (July 1, 1886 - April 2, 1968) was a Czech art historian and archaeologist focused on the history of religious art and medieval archeology, a university teacher and a Roman Catholic priest.

[5] The State Institute of Monument Care and Nature Protection (SÚPPOP) was a Czechoslovak institute under the Ministry of Education (respectively culture), established in 1958 and based on the Act on Cultural Monuments (No. 22/1958 Coll.). It ran until 1990.

[6] Vilém Lorenc (March 21, 1905 - April 1, 1978) was a Czech architect, preservationist and town planner, one of the initiators of the establishment of the State Institute for the Reconstruction of Historic Towns and Buildings (SÚRPMO).

These canals drained water from underground springs, which Sokol pointed out. As a result of this destruction, soil movements took place and groundwater had to be captured again and drinking water had to be drained into the sewer at vast expense. On the other hand, Sokol appreciated that he could create a working group composed of his students at the Academy of Arts, Architecture and Design in Prague. The teaching therefore took place in situ, directly in connection with the implementation and students could involve in all aspects of the architect's work (supervision of craftsmen, administrative tasks, solving construction details and problems on the construction site).

Reconstruction of the Town Cheb

Very soon after taking office, he was entrusted with the management of the monumental reconstruction of the town Cheb. It was a government task with an extremely short completion date. Josef Pošmourný[7] was originally entrusted with this task. He tried to meet the deadline, probably not entirely in legal ways, for which he was removed and even imprisoned (in the end it turned out that it was caused by his "building enthusiasm"). Every month, during the inspection day, Sokol fought battles with representatives of the company that carried out the reconstruction, but at the same time this company did not have adequate qualifications to carry it out. In addition, they were mainly interested in the financial side of the whole thing and to accomplish the reconstruction as soon as possible. Except for his experience as an architect, Sokol was also able to use his historical knowledge - he was concerned with the development of a complex urban plan of the entire town and Cheb Castle.

Fig. 2 – Architect Sokol (on the right) at work in SÚPPOP [4]

---

[7] Josef Pošmourný (March 8, 1910 - February 21, 1974) was a Czech architect, preservationist, administrative officer, art historian and university teacher.

Renovation of a Romanesque Palace in Olomouc

One of the other tasks was to renovate and adapt the remains of the Přemyslid Palace in Olomouc, but according to Sokol, it was a bishop's palace built in the Romanesque period. It was difficult to define the extent of what belongs to the palace in this taskn. He also tried to ensure that the visitor's flow of this monument did not limit the operation and function of the adjacent church. The following spaces were finally declared as a national monument: The Gothic gallery with decorative Romanesque windows, the chapel of St. Anna and St. John and the round tower. Quite surprisingly, there was also a clash with the local chapter. This ecclesiastical office did not have much understanding for Sokol's efforts to seek a compromise in operational matters, and unfortunately even the canons did not fully understand the artistic value of this palace. Making the windows accessible required a relatively large intervention in the valuable Gothic complex, as it was necessary to raise the roof frame above the north and west wings. Sokol figured out a very ingenious and effective solution, supported by a footbridge, which allowed movement around the entire perimeter of the Gothic gallery, while people could see the Romanesque remains at a certain distance. There were delays and changes caused by historical and construction research, and Sokol had to complete detailed plans in his new work at SÚRPMO. The construction slowed down further, and work was eventually halted for several years due to archaeological research, after which the necessary activity was no longer carried out and a lack of funding meant that the modification was not completely finished. Sokol gained a negative but valuable experience from this project.
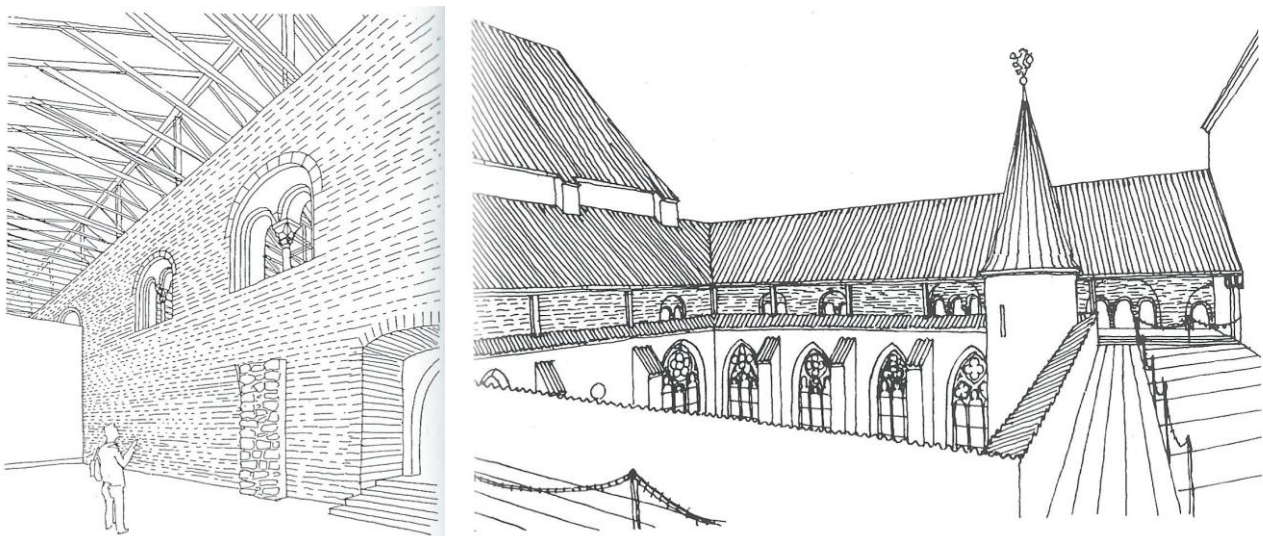
Fig. 3 and 4 – Plans for the modification of the bishop's palace in Olomouc [5]

Pinkas Synagogue

In 1951, a new challenge appeared. It concerned the modification of the Pinkas Synagogue and the modification of its immediate surroundings. This synagogue was built in the late Gothic period (more precisely in 1535) and had gone through several modifications over the centuries. The task was to design the conversion of the synagogue into a memorial to the Jewish victims of the Holocaust. The difficulty was that this important building was the last remnant and evidence of older buildings. It was therefore necessary to integrate the synagogue into a broader context with the surroundings. He could have proved his urban skills here. He tried to connect the building itself as much as possible with the neighbouring cemetery and the buildings on it. He wanted to create a coherent complex of the Jewish ghetto. He intended to reduce traffic in Josefovská Street to one lane and move the other to Kaprova Street, which is wider. This solution would allow a small zone

----

with the level of the original street to be preserved around the synagogue. His intension was to create a dignified space between the synagogue and the cemetery wall, from which a new main entrance to the synagogue would lead. In the second phase, he focused on interior design. Remains of the original glazed plaster have been preserved in the synagogue hall, which had to be cleaned and completed. The names of the dead Jews should be written in red on the walls and arches. In the end, this idea was realized quite differently - the text was not written as a human hand, but in a neat artistic font and was written in new wet plaster, so the durability of the inscriptions was very low. As with the previous project, the implementation of the adaptations was delayed, mainly due to the international political relations of the Soviet republics with the state of Israel. Work on revitalization did not begin until the 1960s, and the resulting (current) state underwent many changes compared to Sokol's design. There were more author teams, and today it is difficult to recognize which modifications are at least the mental work of the professor.

SOKOL AND PRAGUE CASTLE

Sokol gained his first knowledge about the area of Prague Castle while he was studying with future art historians as part of his studies at Charles University. Together with other students, they often visited the Castle and observed from the outside the progress of work on the reconstruction of this area. Through his uncle, he met the castle builder Fiala[8] and even helped the architect with drawing of plans on weekends.

Even on a personal family level, Sokol has always been close to the Castle, and therefore close to the presidents of the First Republic. His great-aunt Anna Černá, who originally ran the kitchen in Vienna by Professor Albert and was acquainted with the family of President Masaryk. The first President appointed her shortly as a housekeeper at Prague Castle and later at Lány Castle. Sokol's aunt also had contact with Mrs. Masaryk and her daughter Alice. All this resulted in two visits of Sokol in Lány - once he spent a weekend there with his brother and the second opportunity was in 1934, when he had lunch with his future wife and with the president. Masaryk left a great impression on him. As a part of his work at the Castle in 1936–1939, he often met President Beneš. During this period, Pavel Janák became the official castle architect. He decided to create a larger design group, which would consist of an architect (Janák), a town planner (Sokol) and a landscape architect (Fierlinger[9]). Janák realized that it was necessary not only to solve the modifications of the Castle itself, but also the wider surroundings, especially the northern area which was formed mainly by gardens. After the communist coup, Sokol was ignored due to the Catholic faith and did not continue the work on the Castle until the second half of the 1960s and in the 1970s.

First Activities at Prague Castle (1936 – 1939)

Sokol was a part of the design team, led by architect Janák. Any disagreements were resolved by a commission of experts led by President Beneš. First, they dealt with the renovation of Queen Anne's Summer Palace and the adjacent garden, on the occasion of the PEN International's congress, which should take place here in 1938. The first clashes occurred very early, mainly because Fierlinger had no sense for history and wanted to modify the garden in the

---

[8] Karel Fiala (November 29, 1862 - April 3, 1939) was a Czech architect, conservator, who significantly contributed to the construction - historical research, modifications and completion of Prague Castle and some other monuments.

[9] Otakar Fierlinger (May 21, 1888 - September 8, 1941) was a Czech landscape architect and town planner. His brother was the politician Zdeněk Fierlinger who was the Prime Minister of Czechoslovakia in the years 1945 - 1946.

park style of the 18th century using floral embroidery and buksus edging. On the other hand, Sokol, but also Janák, promoted a flower garden that would better correspond to the time of formation of the Belvedere. Fierlinger was joined by gardeners because they found the architects' solution more laborious and expensive. The architects enforced their version, but only briefly. After all the ups and downs, the gardeners eventually overcame the resistance and implemented their project. At this time, the castle property also included the Hvězda Summer House and the surrounding area. The considered adjustments were another source of disagreement. Janák wanted the surroundings of the Renaissance summer house to have the form of a game preserve, while Fierlinger promoted the park and the star pool in front of the summer house with a fountain. Janák won this dispute. Sometimes disagreements were discussed at the construction committee, where Janák and Sokol were defended by Zdeněk Wirth, and Fierlinger and Beneš's advisers - Strimpl and Stretti-Zamponi - stood in opposition to them. In most cases, Beneš preferred the solution of architects. Another project in this period was the extension of the road on the Marian walls to the west along the castle and Lumbe's gardens, while the road led to Pohořelec.

Sokol had relatively good memories of Beneš, and since he could have known Masaryk before, he mentioned in his memoirs a comparison of these first Czechoslovak presidents in relation to art: *"Both presidents were not very interested in art, especially fine arts. Masaryk chose a man he trusted, and then he didnnot care about anything anymore, he gave him a free hand. Beneš had similar attitude, but he did not give up his participation. He went to exhibitions diligently."*[6]

Pre-war tasks in churches in the area of Prague Castle

Sokol collaborated in this field mainly with the sculptor Josef Wagner[10]. In 1935, canon Švec, who worked in the Basilica of St. George asked Sokol to create a project for a new main altar, because until then the existing one was assembled from various parts and was therefore not perceived as definitive. The task was to design an altar that would not be too heavy, but at the same time to be concise and monumental. He solved a mensa without an altar extension, a Renaissance sanctuary in the wall should be used as a tabernacle. This required that the altar must be high enough so that it would not be lost when it would be viewed from the nave. Sokol designed four steps leading to the mensa, then tall candlesticks and a cross to make the whole table stand out. In the first design, metal candlesticks and a cross, a stone altar plate and other elements of wood were considered. Wood was not popular by preservationists (they were afraid that it would rot soon), so the second design included a table made of bronze sheet metal and a wrought relief of an altarpiece. There were some problems - the stairs needed iron reinforcement, which did not correspond to Sokol's idea of technical purity, Wagner preferred the modelled relief to the wrought iron. A snag also appeared during the construction, as it was not possible to get a bronze sheet of the appropriate thickness to make the tablecloth of the altar self-supporting, so the iron reinforcement had to be used again as for the stairs. The shape of the altar was thus preserved, but with certain concessions, in addition, Wagner's modelled relief then contrasted even more with the construction. That is why Sokol did not feel a lot of regret when the altar was removed by the Germans at the beginning of the protectorate.

The second important common project was the competition for the tomb of St. Adalbert. The place for this tomb was determined because of the historical situation, it was not considered that the cathedral also serves as a place of worship, which would be greatly devalued by a large tombstone in the middle. Sokol tried to create a certain sacredness of the tomb, although in the competition assignment he felt that a monument to a historical figure was expected rather than the

---

[10] Josef Wagner (March 2, 1901 - February 10, 1957) was a Czech sculptor and draughtsman, a disciple of Jan Štursa and Josef Mařatka, and a professor at the School of Arts and Crafts in Prague.

----

tomb of a Catholic saint. Wagner understood his idea and they worked together intensively for several months. Nevertheless, they did not win the competition, because the chairman of the jury was Professor Matějček[11]. Although he claimed to be a follower of modern art, he actually supported the art of the 19th century. In the end, he pushed through the design of the sculptor Vobišová and the work was immediately assigned to her, but it was not implemented in this period.[12] During the Second Republic, another competition was announced for the silver tomb of St. Wenceslas. Sokol and Wagner participated again, although the character of this competition was different, because it was the completion of a tomb, which was started by the architect Kamil Hilbert. Again, both authors emphasized the sanctity of the tomb. The grave looked like a flat coffin carried by a group of angels modelled by Wagner. Unfortunately, they failed again, Matějček preferred a banal tomb of historical shape which was covered with reliefs.

Fig. 5 and 6 – Altar in the Basilica of St. George [7] and model of the tomb of St. Adalbert [8]
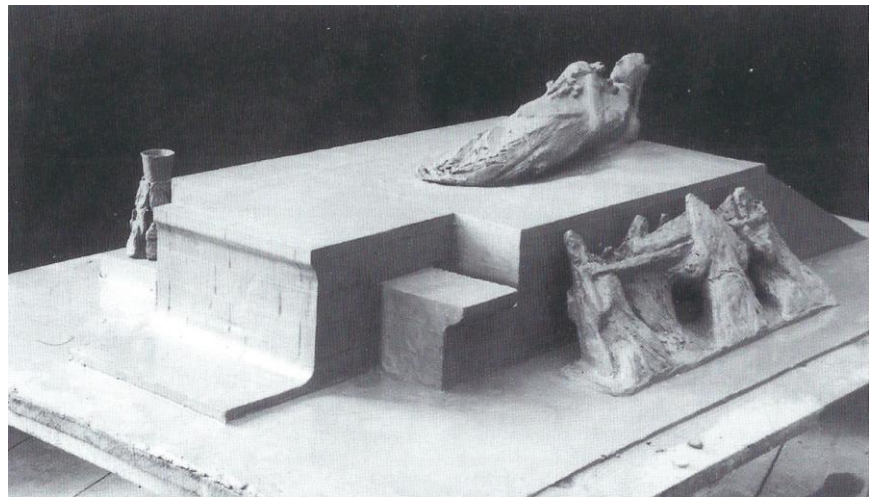
Door and Vestibule of the Golden Gate

After WWII in 1946, another competition was announced within the Cathedral of St. Vitus, Wenceslas and Adalbert. Sokol and Wagner finally won this competition. It was about the door of the Golden Gate. The solution soon turned into a challenging architectural task. It was not specified in which of the openings the door should be hung, whether in the double outer or inner. Practical reasons then required the creation of a vestibule, which could form a disruptive element from the inside. Originally, the competition was announced for a narrower group of several sculptors, to which Wagner was invited. He accepted it on the condition that he would work with an architect (Sokol), because he considered this task primarily as an architectural task. The first

---

[11] Antonín Matějček (January 31, 1889 - August 17, 1950) was a Czech art historian, professor at Charles University, and lectured at the Academy of Arts, Architecture and Design in Prague and at the Academy of Fine Arts. He dealt mainly with Czech art of the Gothic period and the 19th century.

[12] The implementation finally happened in 2017, when the plaster casts of the sculptor Karla Vobišová - Žáková were restored at the Academy of Fine Arts in the studio of Professor Petr Siegl. These models were taken to the HVH metalworking studio in Horní Kalná, led by brothers Pavel and Petr Horák. Wax models were made and divided into individual parts and cast from silver. Finally, the sculptural group was installed on a stone pedestal in the cathedral in 2018. Currently, there is a legal dispute for copyright to this statue, as one of the relatives of the mentioned author is trying to register for them. The lawyers of the Prague archbishopric stand against her.

design supposed wooden doors, mainly due to their low weight. Flat bronze reliefs would be placed on them. The vestibule was composed of a large barred box at the head of the transept, in the corner there was designed a pillar with the archangel Michael, who created a support for the vestibule. The design won first place, although there were some objections to Wagner's sculptures, and therefore a new competition was announced. This time already architectural. And with the fact that Professor Sokol was invited, he demanded the participation of the sculptor (Wagner) and the common work could begin again.
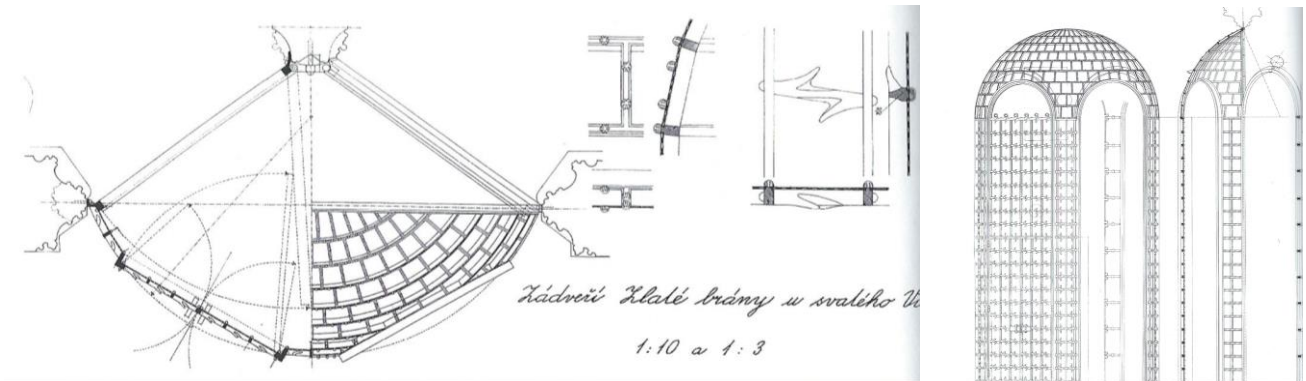

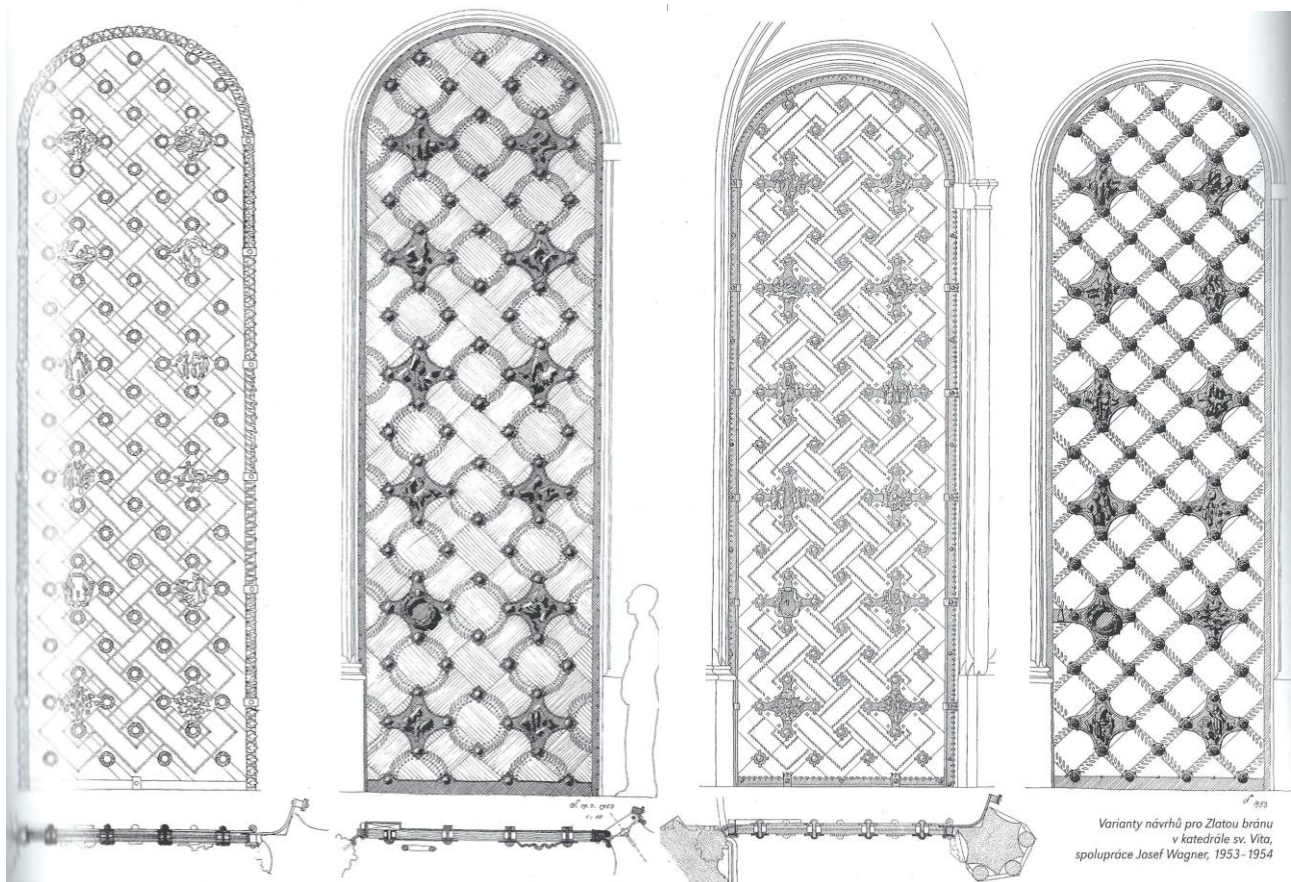*Fig. 7 and 8 – The final solution of the Golden Gate vestibule [9]*

Fig. 9 – Options of plastic decoration of the Golden Gate door [10]

The vestibule was necessary, but also a weakness of the first design. Therefore, Sokol decided to hang the door on a stone pillar between the outer openings, so that when it opens, the

----

wings fold in the middle. The vestibule will then be able to be flat, concave inwards and finished at the top by a small flat dome. The difficulty was that the stone pillar was very slight, but Sokol masterfully handled it by inserting a self-supporting metal cage into the stone frame. The cage inwards forms the glazed wall of the vestibule, on the other side the first door frame. After solving the vestibule, attention was focused on the door leaves. It should be wooden, and the sculptures would be attached to them like plaques. The construction of such large doors caused problems, and there were growing worries about the torsion of long woods, which were not sufficiently dry and would be exposed to different temperatures and humidity on each side. In the end, Sokol came up with the idea of constructing a door panel from short diagonal planks in a double layer, interleaved and connected by screw bolts. The most difficult task from Sokol's point of view was the plastic decoration. The choice of topic was not easy, because at this time the Union for the Completion of the Prague Cathedral had already been abolished and the project was paid by the President's Office, so the themes should not be too religious. The artists finally agreed to work on a New Testament parable. Wagner set about modelling with great zeal and enthusiasm, Sokol was still deciding how to place the reliefs on the smooth surface of the door. This activity was suspended by Wagner's death in 1957, and other sculptors told Sokol that they would like to continue working on it, but the professor decided to reject them all. One of the reasons was a certain pieta to a deceased friend. He decided to finish the door without the sculptures. The final and today's form is a smooth surface of wood, which is studded with variously shaped and gilded screw heads.

Sokol appreciated that this door looked naturally, as if it was from past periods. His attitude was beautifully expressed by the architect Karin Urbanová Kasanová in her doctoral dissertation: *"Sokol's deep knowledge of history led him to a certain humbleness. His work becomes part of the complex, like small stones that make up a mosaic. The eye focuses on the complex and does not watch the small stones of the mosaic, until one is missing, people realize the loss. It is an approach that certainly does not lead to a star celebration of the architect's personality."* [11]

Working at the Castle in the 1960s and 1970s

After the accession of President Antonín Novotný in 1957, a new concept of adaptation was made at Prague Castle. The architectural and construction aspect was reserved for the Association of Architects under the leadership of Jiří Gočár[13], while the program and thought aspect was under the responsibility of the newly established Idea Council for the Modification of Prague Castle. It was decided that the architects would draw up an overall plan for the construction maintenance of the Castle, as it is called General. That is why, after many years, Sokol was asked to help with solving of the problems of Prague Castle. A new use was sought for unused buildings - the Burgrave's Office should be rebuilt into the House of Czechoslovak Children, the monastery of St. George to the Memorial of the Czechoslovak State and Lobkowitz Palace to the Palace of Labour. A multi-stage competition was announced for the mentioned General, in which various authors (Czech and Slovak) were invited, and therefore many unusable proposals appeared. One of the results was the initiative to build a new bridge from the Riding Hall to Hradčanské náměstí, which would create a new main entrance to the Castle. Smaller competition tasks were also announced and Sokol was invited to one of them. It was about building and colour modification of the southern facade of the Castle associated with the solution of utility and ceremonial lighting. Sokol did it dutifully and got this job. Based on this, Jiří Gočár offered him membership in the renewed committee of the Association of Architects for the renovation of the Castle. Sokol accepted and met

---

[13] Jiří Gočár (June 12, 1913 - July 20, 1979) was a Czech architect, a graduate of Czech Technical University, the son of a famous architect, from 1949 to 1953 he was the head of the Stavoprojekt studio. He was later chairman of the Union of Architects.

here with architects Jaroslav Fragner and Oldřich Starý, Professor Fuchs[14] and historian Poch.[15] The committee was chaired by Jiří Gočár. The idea council no longer met at this time. The modifications were discussed in the mentioned committee, and the architects were given a hearing, especially from Chancellor Novák. The above-mentioned large ideological projects were abandoned, only the House of Czechoslovak Children was realized. More specific intentions began to be preferred.

Modifications of the Old Palace were solved by a group consisting of Kotrba[16], Poche and Studený.[17] According to their data, a study was prepared within SÚRPMO, namely by architects Hlavatý[18] and Matašovský.[19] Professor Sokol received this study for assessment. He used this for an extensive tour of the whole building, he pointed out to the historical and artistic value of the building and warned that the proposed modifications are insufficient. Gočár therefore asked Sokol to draw up a new, larger study. Sokol was accepted into SÚRPMO because of this task. In this study, Sokol considered that it was necessary to distinguish and introduce four units that are above each other and together create the whole building - the Romanesque, early Gothic, high Gothic and late Gothic part. The visitors would then go through the individual restored layouts in chronological order. Everything should be graded by modifications of the Vladislav's building, which was used on ceremonial occasions at that time. The study, with the help of Burian[20] and other experts, was completed within a year. It was soon approved, the implementation should happen gradually in several stages, but unfortunately nothing was implemented at all.

---

[14] Bohuslav Fuchs (March 24, 1895 - September 18, 1972) was a Czech architect, town planner and theorist of considerable influence and European significance. One of the first pioneers of modern international style.

[15] Emanuel Poche (October 8, 1903 - March 14, 1987) was a Czech art historian, assistant of Prof. Birnbaum, author of many professional and popular publications, member and one period chairman of the Club for Old Prague.

[16] Viktor Kotrba (March 7, 1906 - September 3, 1973) was a Czech architect, historian of architecture, worker of historic preservation and art theorist.

[17] Vladimír Studený (March 11, 1904 - February 19, 2005) was a Czech architect, painter. A conscientious archivist, thanks to whom many building drawings from the renovation of Prague Castle have been preserved.

[18] Josef Hlavatý (March 19, 1923 - April 24, 2012) was a Czech architect, a student of Jan Sokol at the Academy of Arts, Architecture and Design in Prague. He collaborated long with architect Rothmayer and he was a member of the studio SÚRPMO 05.

[19] Miloslav Matašovský (December 15, 1922 - 2004) was a Czech architect, author of theoretical studies and realizations of the regeneration of historic town cores (Prague, Teplice).

[20] Jiří Burian (* February 1, 1935) is a Czech art historian, author of art publications and museological and exhibition realizations.
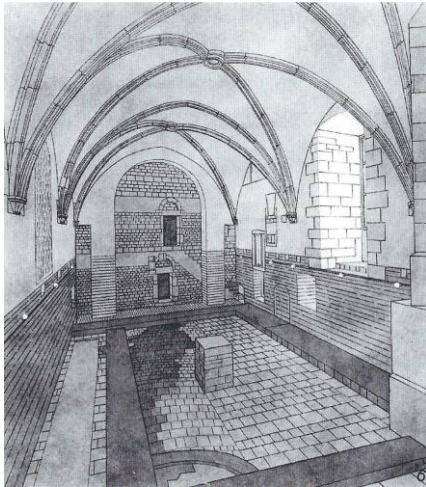
Fig. 10 and 11 – Design of modifications of the Old Palace [12] and perspectives of the General of Prague Castle [13]

The biggest task for Sokol was a plan for the modification of the entire area of Prague Castle, based on an urban solution through architectural details, design of lighting and greenery after solving technical requirements (heating, sewerage, low current, high current, etc.). It was a difficult task, as the castle is a large area with an important location, it was necessary to solve the traffic difficulties related to the Lesser Town and Petřín tunnel and the connection to the new transport solution in the surroundings. It was decided to withdraw from the plan to build a bridge between the Riding Hall and Hradcany square, even though an implementation project had already been prepared. Therefore, Sokol had to create a new concept of access ways to the Castle. There was also a creative task that corresponded with Sokol's town planning interest. It was about the consolidation and completion of castle parks and gardens. He worked hard on it, and he did most of it himself. Unfortunately, even in this case, the project was not implemented.

The General had three components. In the first of them – architectural part, Professor Sokol had prime position, in the second devoted to town planning he collaborated with Martin Krise[21] and in the last technical part he left the management to his colleague Bašta, he retained only control authority. In the end, the whole General expanded in scope, it was developed from the originally architectural – town planning solution to a realization project with all the necessities, for example the schedule of implementation of works and costs associated with the implementation. It turned out that it would cost a lot of money, and Sokol soon realized that there would be no implementation again, and that was one of the reasons why he finally retired in 1976.

Modifications to the interior of the cathedral

One of the Sokol's last work was related to the Cathedral of St. Vitus, Wenceslas and Adalbert. Sokol held the idea that the cathedral is primarily the first church in the country, a sacred building. However, this did not correspond to the ideas of the then ruling regime, it preferred the concept of the cathedral as a museum of the dead periods, dead art, dead religion. The professor Sokol had long pointed out to the need for modifications caused mainly by liturgical reforms. The opportunity for a shift in this matter was the approaching millennial anniversary of the founding of the Prague bishopric in 1973. The appointment of a new archbishop Tomášek also contributed to the shift.

---

[21] Martin Krise (* 1942) is a Czech architect, town planner and preservationist, a member of the Club for Old Prague

----

In his earlier (soon after the war) design, Sokol had considered moving the royal mausoleum to the northern arm of the cross nave, in front of the organ loft. A new main altar would be built in its place with the tomb of St. Adalbert. Therefore, a new nave would be released for ordinary but large masses. An older nave could be used for smaller gatherings. In the new plan, he followed up on the previous one, but gave up the idea of moving the mausoleum, instead he designed to use it as a divide between the new and older part and to serve as a backdrop for the new altar (according to liturgical reforms the altar should have the form of a table and ensure that the priest could celebrate the mass turned towards people). The new mensa should create the spiritual centre of the cathedral and within it would be located the tomb of St. Adalbert. A space for celebrants would be delimited around it. He had also devised visitor's flow during visitor's hours, when tourists should concentrate on the side naves and the centre of the cathedral would be closed to them. Sokol wrote an article about this, created a plan and perspective with an altar in the middle. All this was discussed with the Prague Archbishopric and general permission was given to the modifications.

Sokol imagined that the plan would be further developed and would be financed only from the resources of the archbishopric. However, this was not realistic in the that political situation, so Sokol's plan was forwarded to the President's Office by the Archbishop. There the plan was received very positively with regard to the fact that various temporary solutions would be cancelled, but it depended very much on the opinion of the preservation commission, headed by academician Filip.[22] However, he did not have the prime position in similar matters, so Sokol went to see other members - Poch and Kotrba, whom he had known from earlier times. At an informal meeting, they agreed with Sokol, liked his plan and promised him support, but when the official meeting of the preservation commission took place, everything turned around. At least Poche was silent, but Kotrba suddenly disagreed with the placement of the mensa in front of the mausoleum (which was the main idea of the design). So that meant stopping this project.

Fortunately, it did not take long period and Sokol was commissioned to design a new altar according to regulations of the Second Vatican Council (i.e. the altar should be turned towards people). For this purpose, the extension of the choir platform was fitting, the new altar could be placed on a new part of the platform together with the rood screen and the cross. In front of the platform, new staircases leading to the side naves were created, and thus the original relation between the choir of St. Vitus and the mentioned naves and the royal oratory. He decided to use the extended grade of Mocker's altar for the bishop's throne. Sokol tried to extend this task to the reconstruction of the entire choir, which clearly shows the effort to save something from his earlier study. He did not like Mocker's altar, but he was forced to keep it, so he wanted to use it at least as a backdrop for the cathedra. Behind this altar there was a stone spiral staircase leading to the little upper tower, where the monstrance was previously exhibited (but at that time the little towers were no longer used). Between the altar and the saint's tomb, a church back area was formerly established, there were brooms, candlesticks, carpets and ladders. Sokol tried to restore the dignity of this place and therefore proposed to remove Mocker's staircase, the cabinets for church equipment behind the grave, Max's statue of St. Vitus, which stood on the tomb like on a pedestal. In terms of restoring the original architectural idea, he decided to relocate the altar of St. Vitus from the gallery to the original place in the high choir. This would loosen the end of the cathedral that the decorative Parléř's consoles would be noticeable, even from the cathedral gallery. This was presented to the preservationists at the Castle and initially accepted positively again, but Poche did not take part in the meeting and he unfortunately persuaded the commission to adjust its positive opinion and Sokol was again defeated.

---

[22] Jan Filip (December 25, 1900 - April 30, 1981) was a Czech archaeologist and historian, professor at Charles University, in 1963–74 he was the director of the Archaeological Institute of the Czechoslovak Academy of Sciences.
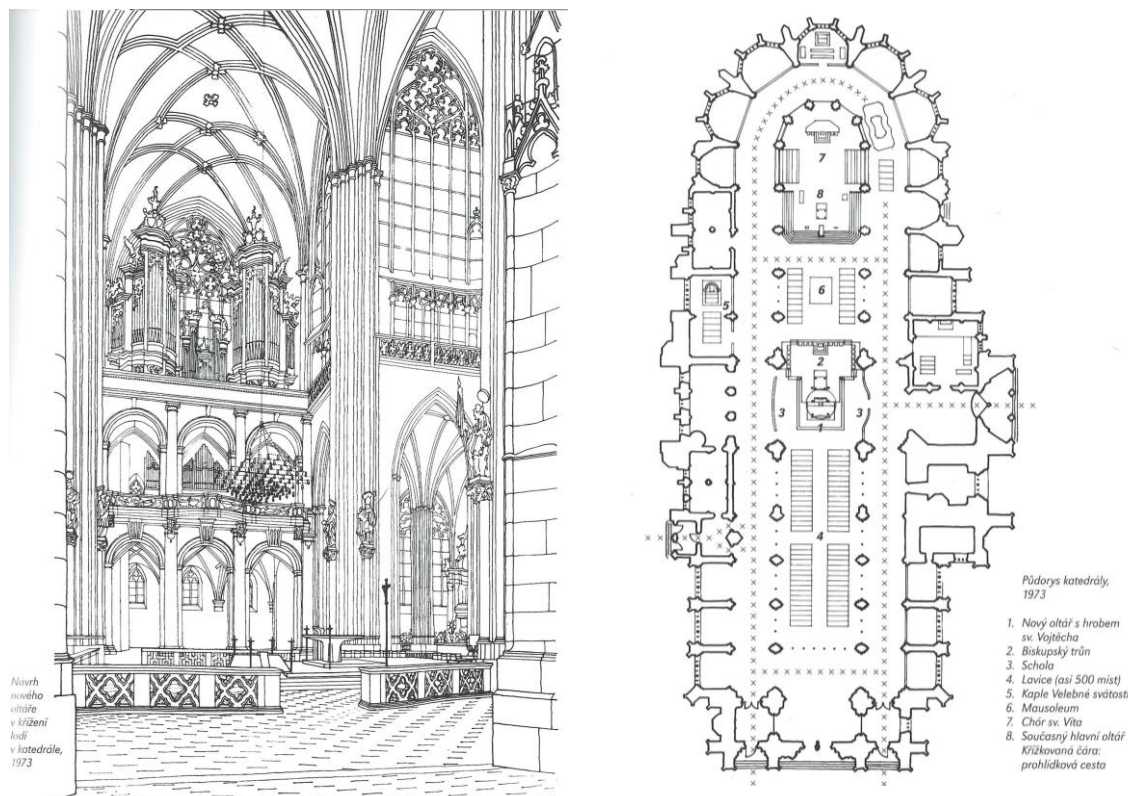
Fig. 12 and 13 – Perspective of the new altar at the crossing of naves [14] and designed floor plan of the cathedral [15]

In the end, he was only allowed to prepare a new mensa. The altar slab was designed from marble which was supported by six legs made of gilded steel I profiles. The altar was made, but instead of a marble slab, a Romanian limestone slab was used.

CONCLUSION

Architect Sokol was and still is an inspiring person who was active in the field of historic preservation. Although the number of his realizations is not considerable, thanks to his written memories and documents it is possible to deal with the whole breadth of his projects.

His work showed a deep knowledge of the construction of the historical buildings and history of art, which resulted in his humble approach to projects related to the restoration of monuments. Although he did not originally want to pursue the career of a preservationist, because it was more of a clerical position, over time he came to like this work, because he could apply his creativity, spiritual foundation and town planning principles, which interested him from a young age. In his work, he tried to find new ways and approaches (in which he tried to get closer to Le Corbusier, August Perret and others). He emphasized the emotional and spiritual side of human perception and experience of architecture. He took it as a success, if his interventions in historical architecture were perceived as a natural part of the complex, he did not want to exhibit unnecessarily.

Professor Sokol was a generally gifted architect with an overlap to various fields. He has influenced (not only during his school activity at the Academy of Arts, Architecture and Design in Prague) many other architects, and above all the ideological and intellectual basis of his designs is comprehensive and precise. Therefore, it is clearly a loss that many of his ideas did not realize for various reasons.

ACKNOWLEDGEMENTS

REFERENCES

[1]   Sokol J., Sokol V., 2004. Moje plány: paměti architekta, 113 (Triáda) 344 pp.
[2]   Sokol J., Sokol V., 2004. Moje plány: paměti architekta, 133 (Triáda) 344 pp.
[3]   Sokol J., Sokol V., 2004. Moje plány: paměti architekta, 206 (Triáda) 344 pp.
[4]   Sokol J., Sokol V., 2004. Moje plány: paměti architekta, 207 (Triáda) 344 pp.
[5]   Sokol J., Sokol V., 2004. Moje plány: paměti architekta, 272-273 (Triáda) 344 pp.
[6]   Sokol J., Sokol V., 2004. Moje plány: paměti architekta, 164 (Triáda) 344 pp.
[7]   Sokol J., Sokol V., 2004. Moje plány: paměti architekta, 235 (Triáda) 344 pp.
[8]   Sokol J., Sokol V., 2004. Moje plány: paměti architekta, 238 (Triáda) 344 pp.
[9]   Sokol J., Sokol V., 2004. Moje plány: paměti architekta, 242 (Triáda) 344 pp.
[10]   Sokol J., Sokol V., 2004. Moje plány: paměti architekta, 239-240 (Triáda) 344 pp.
[11]   Urbanová Kasanová K., 2010. Tvůrčí proces architekta Jana Sokola, 76 (ČVUT v Praze, Fakulta architektury) 344 pp.
[12]   Sokol J., Sokol V., 2004. Moje plány: paměti architekta, 211 (Triáda) 344 pp.
[13]   Sokol J., Sokol V., 2004. Moje plány: paměti architekta, 212 (Triáda) 344 pp.
[14]   Sokol J., Sokol V., 2004. Moje plány: paměti architekta, 251 (Triáda) 344 pp.
[15]   Sokol J., Sokol V., 2004. Moje plány: paměti architekta, 252 (Triáda) 344 pp.

SEISMIC MITIGATION EFFICIENCY STUDY OF THE COUPLING BEAM DAMPER IN THE SHEAR WALL STRUCTURE

Xin Huang

College of Airport, Civil Aviation University of China, Tianjin, China;
huangxin1395602 @163.com

ABSTRACT

Coupling beam damper can be easily repaired in the post-earthquake, which can dissipate the seismic energy of the structure in the earthquake action. In this paper, the seismic mitigation efficiency of the coupling beam damper in the shear wall structure is analysed by using the fast nonlinear analysis method. Meanwhile, the effect of the layout location and number of the coupling beam dampers on the seismic mitigation efficiency of the structure are studied. Finally, the effect of the performance parameter of the coupling beam damper on the seismic mitigation efficiency is also analysed. The results indicate that: the story shear force and the drift angle of the shear wall structure can be effectively decreased because of the coupling beam damper, and the maximum decreased amplification of the story drift angle and base shear force can reach up to 16.7% and 8.8% respectively. Relating to the decreased amplification of the base shear force, the decreased amplification of the story drift angle of the structure with coupling beam damper is obvious. The coupling beam damper installed in the upper part of the structure is more economical, because the deformation of the structural coupling beam is mainly concentrated in the upper part of the structure. To ensure economic of the structure with damper, the reasonable coupling damper performance parameter should be determinate according to the dynamic response of the shear wall structure in the earthquake action. The above research work can provide guidance for the seismic design of the shear wall structure.

KEY WORDS

Shear wall structure, Coupling beam damper, Earthquake action, Seismic mitigation efficiency, Damper optimal layout, Performance parameter of the damper

INTRODUCTION

To ensure the safety of buildings in the earthquake region, dampers are installed to dissipate the energy of the earthquake action in the building structure. The principle and design method of the structure with damper are studied by many scholars. According to the difference of the structural systems, the different dampers are used in the structure including soft steel dampers, viscoelastic dampers and friction pendulum dampers [1-4]. To improve the energy-dissipating capacity and deflection of the damper, the optimal design and test study of the damper were carried out [1], and the novel damper was also developed [2]. Meanwhile, the effect of the viscoelastic damper on the structural dynamic response was studied [3], and the shaking table test of the structure with damper was developed to analyse the seismic mitigation efficiency of the damper [4]. For the high-rise structure with the outrigger, the viscoelastic damper was installed in the outrigger floor, and the earthquake response of structure had been effectively decreased because of the damper action [5-6]. The calculation method of additional damping ratio of structure with damper based on linear equivalent method was studied, and the result showed that linear

----

equivalent method can be adopt in structure energy dissipation design [7]. Meanwhile, the damper was also installed in the non-structural components to improve the seismic performance of the structure, the steel bar and U-shaped damper connection methods were adopted for the RC frame with the precast concrete cladding panels [8]. To improve the seismic mitigation efficiency of the structure, the effect of the location and number of the viscous dampers were also studied [9], and the economy of the structure with damper were analysed [10].

The shear wall is the basic lateral-resistance structural component of the high-rise structure. To ensure the anti-seismic safety of the shear wall, dampers can be set on the coupling beam to reduce the vibration, and the coupling beam damper is easy to replace in the post-earthquake. At present, to improve the energy dissipation capacity of the damper in the coupling beam, the optimize design of the viscoelastic damper and the friction pendulum damper of the coupling beam were developed [11-12], and the influence of the coupling beam damping on the structural displacement and acceleration were analysed [13]. The current analysis put emphasis on the component design of the coupling beam damper, and the effect of the coupling beam damper on the high-rise structure with the frame- tube core system is mainly analysed. However, systematic studies on the seismic mitigation efficiency of the coupling beam damper on the shear wall structure rarely have been reported now. Moreover, the optimization of the location and quantity of the coupling beam damper are often ignored, but those analyses are very important to control the cost and the seismic mitigation efficiency of the high-rise structure. To provide seismic design guidance for coupling beam damper in shear wall structure, the seismic mitigation and layout method of coupling beam damper in shear wall structure should be systematic studied.

In this paper, the seismic mitigation efficiency of the shear wall structure with the coupling beam damper is systematic studied by using the fast nonlinear analysis method. Meanwhile, the effect of the layout location and number of the coupling beam dampers on the seismic mitigation efficiency of the structure are also analysed. Finally, the effect of the performance parameter of the coupling beam damper on the seismic mitigation efficiency of the structure is studied.

ANALYSIS METHOD AND MODEL OF COUPLING BEAM DAMPER

Seismic mitigation analysis method

The coupling beam damper can dissipate the structural energy by the plastic deform in the earthquake action. To analysis seismic mitigation efficiency of the shear wall structure with the coupling beam damper, the nonlinear property of the coupling beam damper can be simulated as the external nonlinear force by using the fast nonlinear analysis method [14]. Structural equilibrium equation can be expressed as:

$$M\ddot{u}(t) + C\dot{u}(t) + Ku(t) + R_{NL}(t) = R(t) \tag{1}$$

Where M is the mass matrix, C is the damper matrix, K is the stiffness matrix without damper stiffness; $\ddot{u}(t)$, $\dot{u}(t)$, $u(t)$ are the node acceleration, velocity and displacement, respectively; $R(t)$ and $R_{NL}(t)$ are the external load and nonlinear force of the damper, respectively.

To consider the linear load action of the nonlinear element, the elastic force is applied to Equation 1. Therefore, equilibrium equation 1 can be expressed as:

$$M\ddot{u}(t) + C\dot{u}(t) + K'u(t) = \bar{R}(t) \tag{2}$$

Where $\bar{R}(t) = R(t) - R_{NL}(t) + K_e u(t)$ is the external load, $K' = K + K_e$, K_e is the stiffness matrix of the damper.

Equation 2 can be transferred to the motion equation in the mode state coordinate system by using the Ritz vector, and the internal force of the nonlinear element can be solved by the iterative calculation.

Model of the coupling beam damper

The coupling beam damper is a mild steel damper, which dissipates the earthquake energy by the shear force deformation of the coupling beam in the earthquake action. The relationship of the force and displacement of the coupling beam damper is listed in Equation 3.

$$f = \alpha k d_k + (1-\alpha) f_\beta \qquad (3)$$

Where d_k is the deflection of the damper, k is the stiffness of the damper, α is the yielding stiffness ratio, f_β is the yielding strengthen, z is the internal parameter of the resilience model.

SEISMIC MITIGATION EFFICIENCY OF THE COUPLING BEAM DAMPER

To analyse the seismic mitigation efficiency of the coupling beam damper in the shear wall structure, the dynamic responses of the shear wall structure with and without the coupling beam damper are analysed.

Analysis model of the shear wall structure

The height of the building is 34.1m, and the typical floor height is 4.5 m. Shear wall structural system is adopted for the building [15], and the thickness of shear wall is 200mm. The heights of the coupling beam are 2550 mm and 2650 mm. The strength grade of C40 is adopted for the concrete, and the HRB grade reinforcement is adopted. Dynamic responses of the shear wall structure are analysed by using ETABS v9.7 software based on the fast nonlinear analysis method [14].

Initial stiffness of the coupling beam damper is 100 kN/mm, the yield load is 150 kN, the yield displacement is 1.5mm, and the post-yield stiffness ratio is 0.05. The layout of the shear wall and the coupling beam damper are described in Figure 1. The four dampers are installed in the X-direction and the three dampers are installed in the Y-direction in every story of the shear wall structure.

(a)

(b)
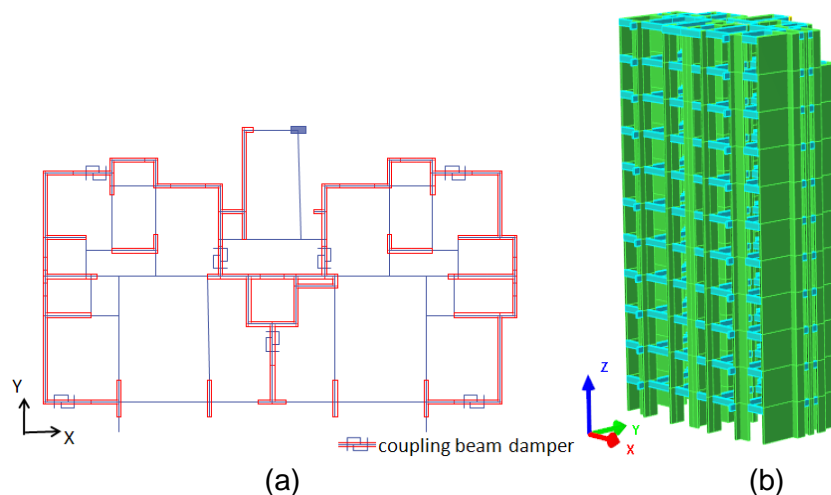
Fig.1–The layout of the shear wall and the coupling beam damper: (a) damper layout, (b) 3-D model

Dynamic history analysis of shear wall structure is developed by using the El-Centro wave (1940,EW) and the Loma-Prieta wave (1989,EW). The duration of the earthquake wave is 20 s, and the maximum amplitude of the acceleration is 0.55m/s². The time history curve and acceleration spectra of the earthquake waves are shown in Figure 2.
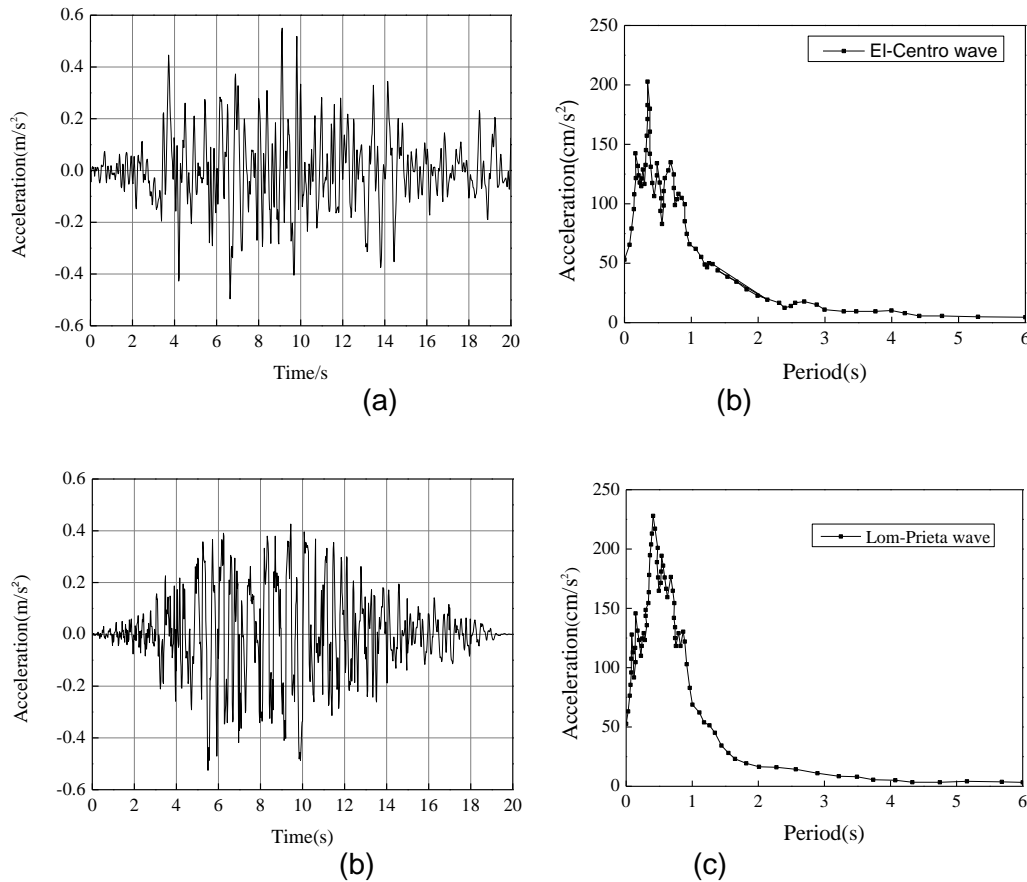
Fig. 2– The time history curve and acceleration spectra of the earthquake waves : (a) the El-Centro history curve, (b) the El-Centro Spectra, (c) the Lom-Prieta history curve, (d) the Lom-Prieta Spectra

Seismic mitigation efficiency

To analysis seismic mitigation efficiency of the coupling beam damper, story drift angel and base shear force of shear wall structure with and without damper are compared. Considering the space of the building, the coupling beam dampers are installed from the 3th story to the 10th story of the structure.

The shear force and drift angel of the structural story in frequent earthquake action are listed in Table1, Figure 3 to Figure 6.

Tab. 1 - Drift angle and base shear force of the structure with and without damper

Condition		Structure without damper		Structure with damper		
Earthquake wave		Drift angel	Base shear force (kN)	Drift angel	Base shear force (kN)	Additional damping ratio
El-Centro wave	X	1/1484	3255	1/1663	3343	1.7%
	Y	1/2107	3385	1/2274	3280	1.0%
Loma-Prieta wave	X	1/1049	4904	1/1259	4472	2.0%
	Y	1/1632	4638	1/1687	4449	0.5%

(a)   (b)
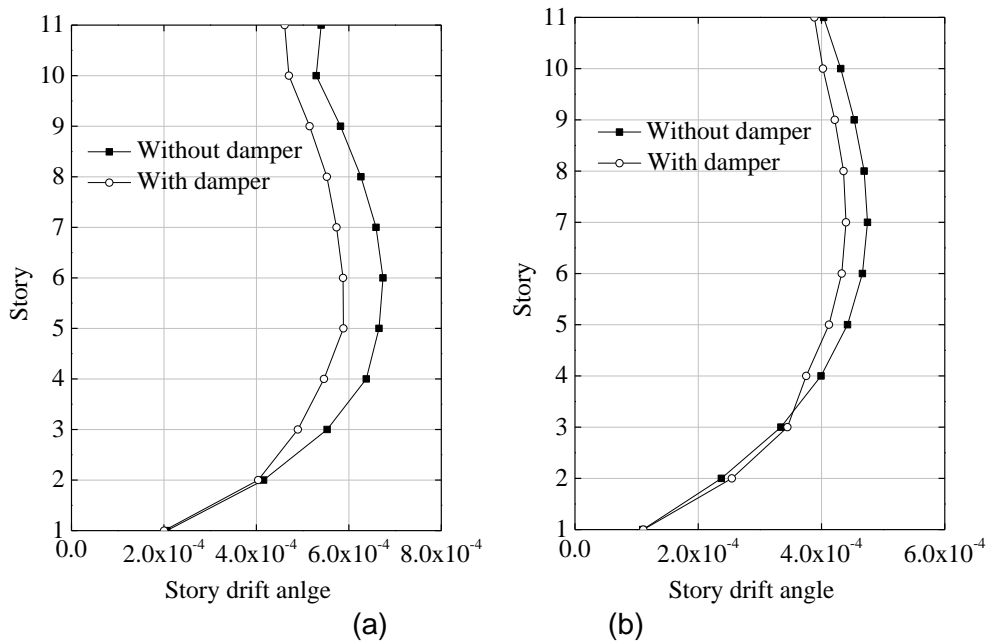
Fig. 3 – Story drift angle of the structure with and without damper in the El-Centro earthquake action: (a) X-direction; (b) Y-direction

----
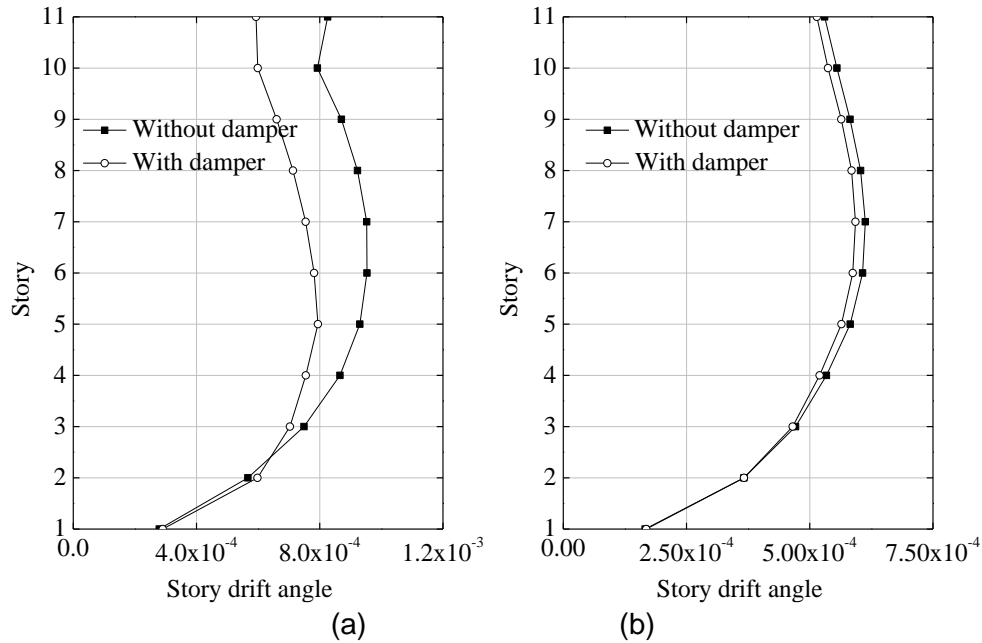
Fig. 4 – Story drift angle of the structure with and without damper in the Loma-Prieta earthquake action: (a)X-direction story, (b) Y-direction
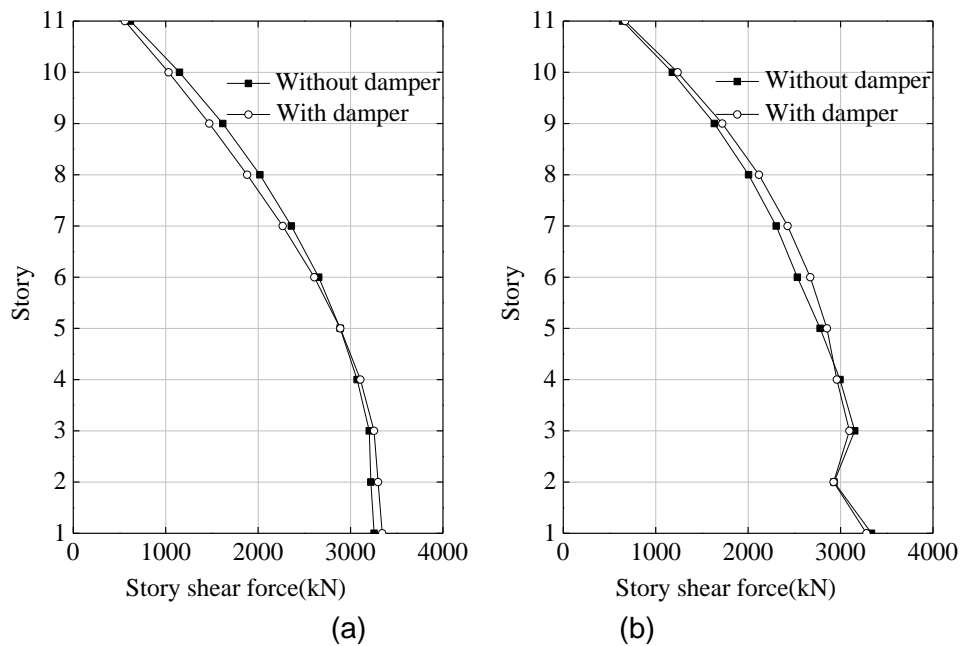
Fig. 5 – Story shear force of the structure with and without damper in the El-Centro earthquake action: (a)X-direction, (b) Y-direction
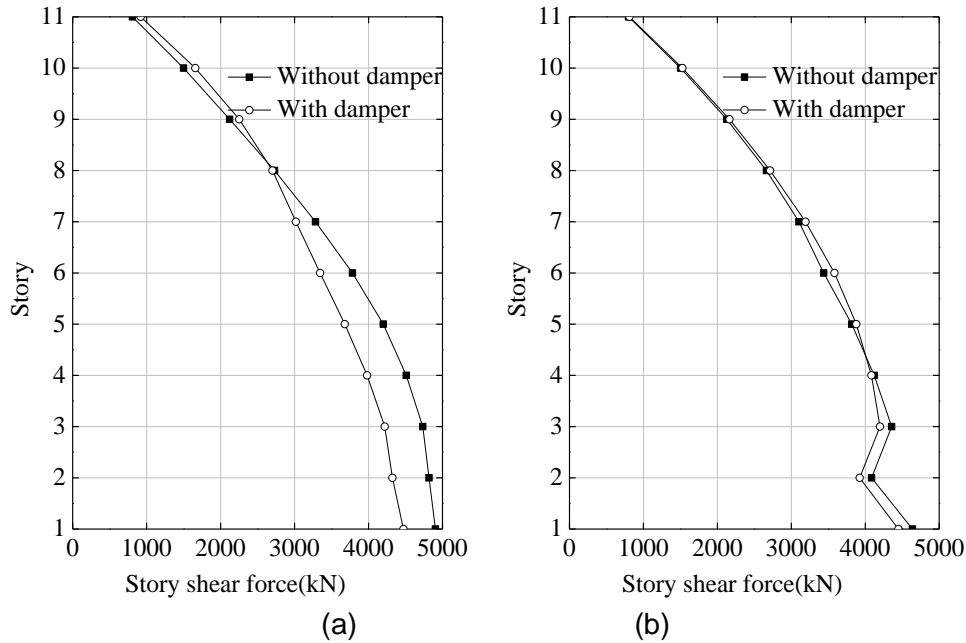
Fig. 6 – Story shear force of the structure with and without damper in the Loma-Prieta earthquake action: (a)X-direction, (b) Y-direction

From the Table1 and Figure 3 to Figure 6, relating to the structure without damper, the story drift angle can be decreased from 1/2017 to 1/2274 and the base shear force can be decreased from 3385kN to 3280N of the structure with damper in the Y-direction in the El-Centro earthquake action. The similar conclusions can be obtained for the Loma-Prieta wave action, for example, the story drift angle can be decreased from 1/1632 to 1/1687 and the base shear force can be decreased from 4638kN to 4449N of the structure with damper in the Y-direction. The additional damping ratio of the structure with coupling beam damper can reach up to 1.7% and 2.0% in the El-Centro earthquake action in the X-direction and Y-direction respectively.

The results indicate that story shear force and drift angle of structure can be effectively decreased because of the energy dissipation action of the coupling beam damper, which can ensure safety of the major structure.

To measure the seismic mitigation efficiency of coupling beam damper on the shear wall structure, the dimensionless parameters are used to represent the reduced amplification of structural dynamic responses. The reduced amplification of structural story drifty angle and base shear force are calculated respectively by using Equation 4 and Equation 5. The seismic mitigation efficiency of coupling beam damper is shown in Figure 7.

$$D_d = (D_1 - D_2) / D_1 \qquad (4)$$

$$D_V = (V_1 - V_2) / V_1 \qquad (5)$$

Where, D_d and D_V are the maximum reduced amplification of the structural story drift angle and base shear force respectively, D_1 is the structural story drift angle without considering damper action, D_2 is the structural story drift angle considering damper action, V_1 is the structural base shear force without considering damper action, V_2 is the structural base shear force considering damper action.
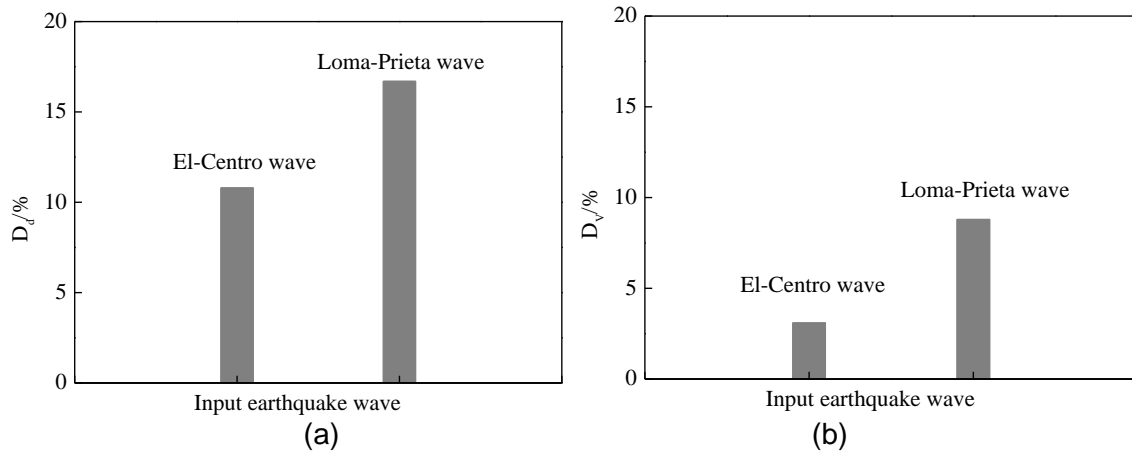
Fig. 7 – Seismic mitigation efficiency of shear wall structure by using the coupling beam damper: (a) reduced amplification of story drift angle, (b) reduced amplification of story shear force

From the Figure 7, the decreased amplification of the story drift angle is obvious relating to that of the base shear force, for example, the decreased amplitude of the story drift angle is 16.7%, and the decrease amplitude of the base shear force is 8.8% in the Loma-Prieta earthquake wave action. Coupling beam damper can be adopted to improve the seismic performance of shear wall structure when the story drift angle of structure can't satisfy seismic design code requirement.

THE EFFECT FACTOR ANALYSIS OF COUPLIN BEAM DAMPER

Optimal layout location and number of coupling beam damper

To analyse the influence of the layout location and number of the dampers, two kinds of the layout schemes of the coupling beam dampers of the structure are considered. The coupling beam dampers are installed from the 3th story to the 10th story for the Scheme A, and the coupling beam dampers are only installed in the 7th to the 10th story for the Scheme B. Relating to the Scheme A, the number of dampers in the Scheme B are reduced by half.

The story shear force and drift angel of the Scheme A and B in the frequent earthquake action are listed in Table 2 and Figure 8 to Figure 11.

Tab. 2 - Drift angle and base shear force of the Scheme A and Scheme B

| Condition Earthquake wave		Scheme A			Scheme B		
		Drift angel	Base shear force (kN)	Additional damping ratio	Drift angel	Base shear force (kN)	Additional damping ratio
El-Centro wave	X	1/1663	3064	1.7%	1/1643	3081	1.5%
	Y	1/2274	3449	1.0%	1/2216	3422	0.6%
Loma-Prieta wave	X	1/1259	4472	2.0%	1/1206	4595	1.6%
	Y	1/1687	4449	0.5%	1/1645	4545	0.3%
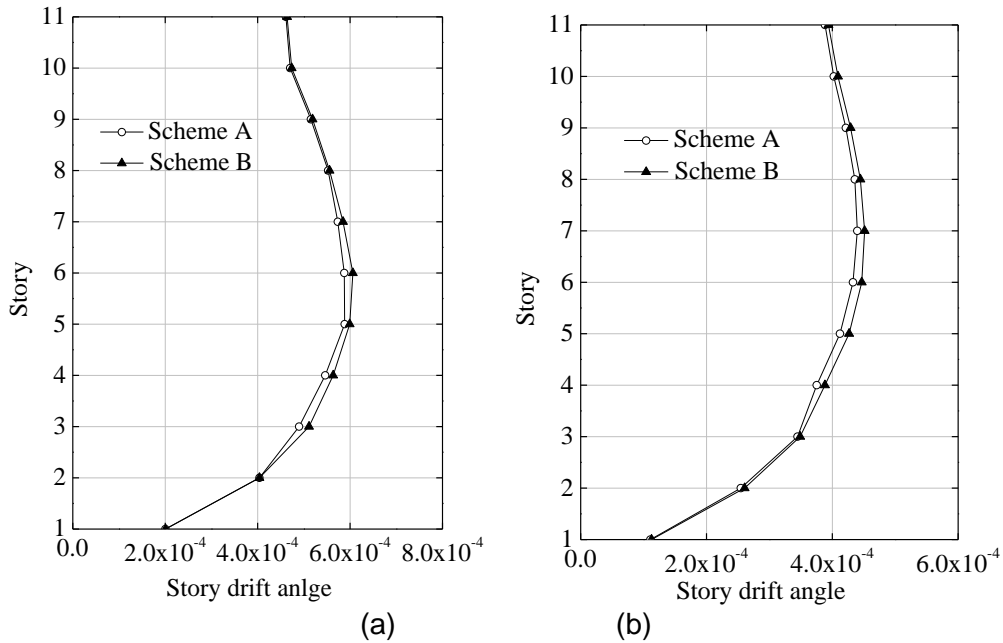
Fig. 8 – Story drift angle of the Scheme A and Scheme B in the El-Centro earthquake action: (a) X-direction; (b) Y-direction
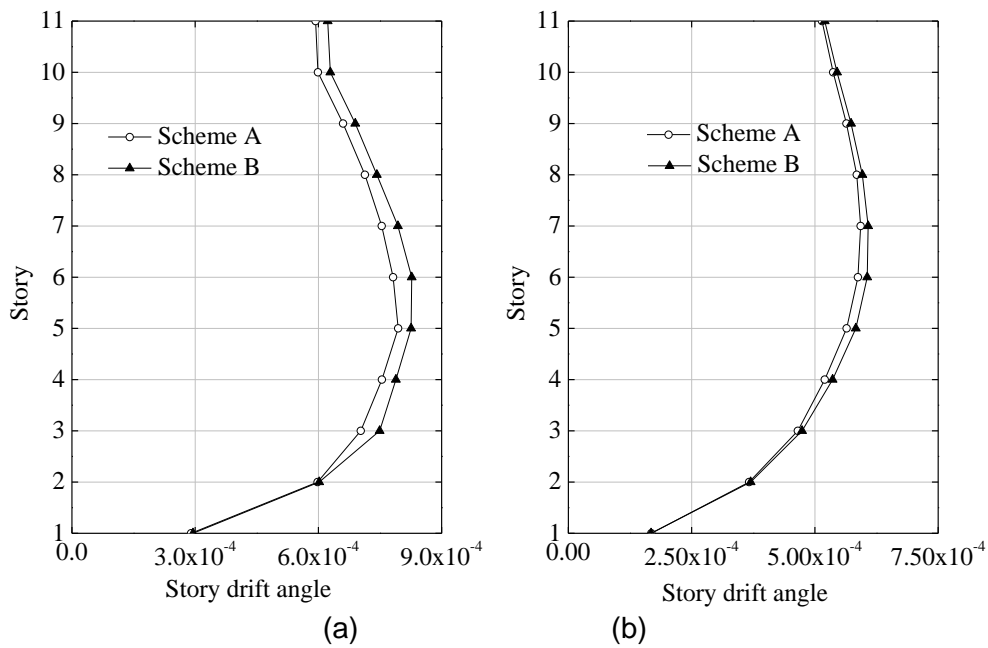
Fig. 9 – Story drift angle of the Scheme A and Scheme B in the Loma-Prieta earthquake action: (a) X-direction; (b) Y-direction

----
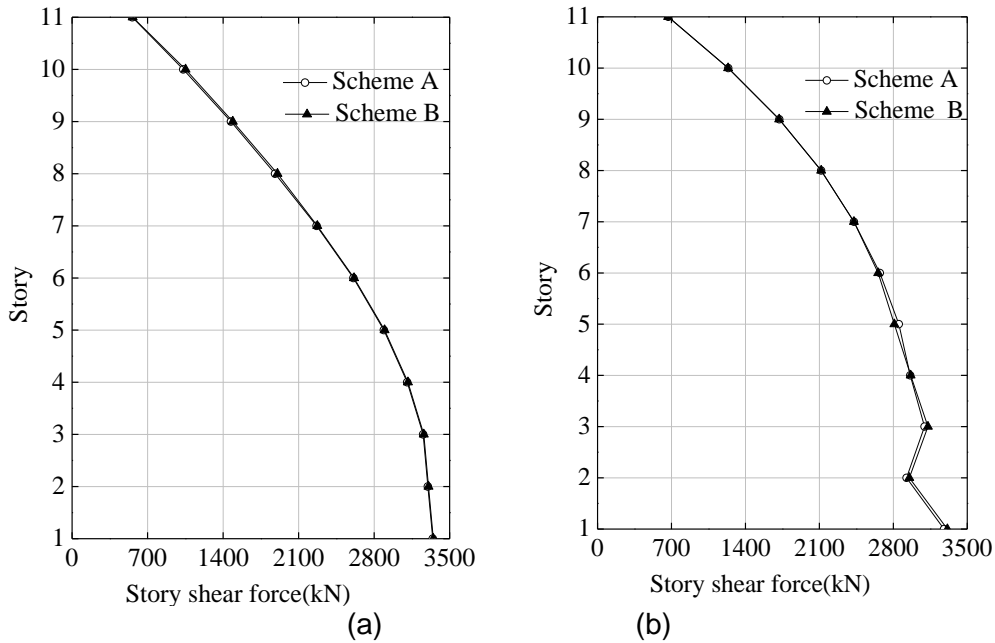
Fig. 10 – Story shear force of the Scheme A and Scheme B in the El-Centro earthquake action: (a)X-direction, (b) Y-direction
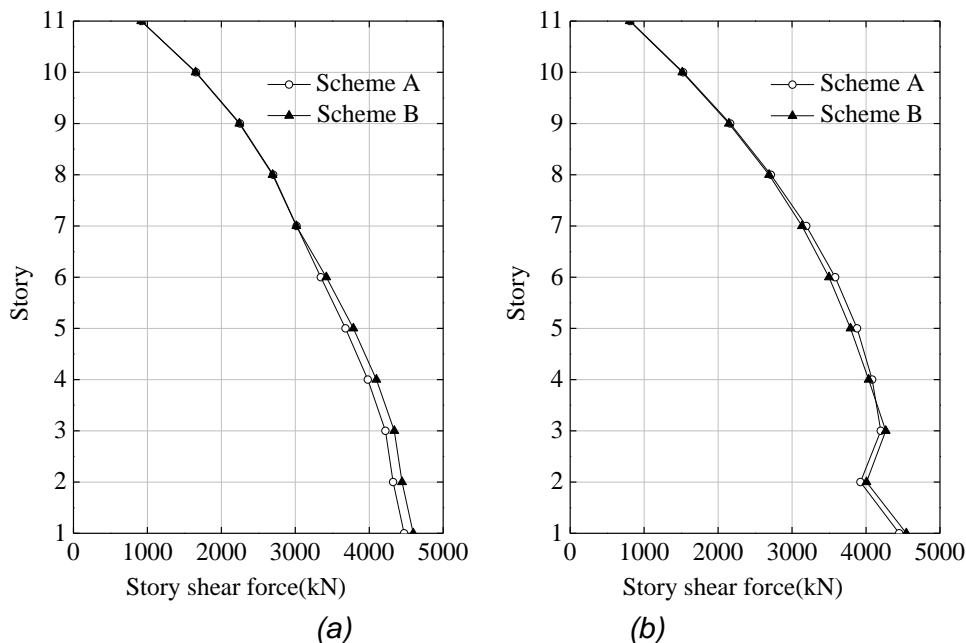
Fig. 11 – Story shear force of the Scheme A and Scheme B in the Loma-Prieta earthquake action: (a)X-direction, (b) Y-direction

From the Table 2 and Figure 8 to Figure 11, the story drift angle of the Scheme A and Scheme B are 1/1663 and 1/1643 respectively, and the story shear force of the Scheme A and Scheme B are 3449kN and 3422kN in the X-direction in the El-Centro earthquake action. Meanwhile, the additional damper ratio of the Scheme A and Scheme B is 1.7% and 1.5% respectively. The similar conclusions can be obtained for the Loma-Prieta wave action.

It shows that the seismic mitigation efficiency of the Scheme B is not obviously lower than that of the Scheme A. The reason is that the deformation of the structural coupling beam is mainly

concentrated in the upper part of the structure because the deformation of the shear wall structure belongs to the bending deformation, so it is more economical when the coupling beam dampers are installed in the upper part of the structure.

Performance parameter of coupling beam damper

To analyse the effect of the performance parameter of the coupling beam damper, dynamic responses of the shear wall with different performance parameter are analysed, and the Parameter one and the Parameter two of the coupling beam damper are listed in Table 3. The energy dissipation capacity of Parameter two is large than that of the Parameter one. The story shear force and drift angel of the structure are listed in Table 4.

Tab. 3 - The performance parameter of the coupling beam damper

Performance parameter	Initial stiffness (kN/mm)	Yield load (kN)	Yield displacement/mm	Post-yield stiffness ratio
Parameter one	100	150	1.50	0.05
Parameter two	150	250	1.67	0.05

Tab. 4 - Drift angel and base shear force of the structure with the Parameter one and the Parameter two

Condition Earthquake wave		Parameter one		Parameter two	
		Drift angel	Base shear force (kN)	Drift angel	Base shear force (kN)
El-Centro wave	X	1/1663	3064	1/1667	2974
	Y	1/2274	3449	1/2291	3430
Loma-Prieta wave	X	1/1259	4472	1/1269	4444
	Y	1/1687	4449	1/1689	4417

From Table 4, relating to the structure with the Parameter one, the story drift angle of the structure is 1/1667 and base shear force is 2974kN, y direction story drift angle is 1/2291 and base shear force is 3455kN in the X-direction in El-Centro wave action of the structure with the parameter two. The biggest reduced amplification of story shear force is 3% in the El-Centro earthquake action because of the performance parameter change of the coupling beam damper. The results indicate that the drift angle and the base shear force of the shear wall structure has not obviously difference for the performance parameter one and two of the coupling damper, and the reason is that the damper with the high performance parameter cannot play obvious effect because of shear wall structure deflection limit in the earthquake action. To ensure economic of the structure with damper, the reasonable performance parameter of the coupling damper should be determinate according to the dynamic response of the shear wall structure in the earthquake action.

CONCLUSIONS

The seismic mitigation efficiency of coupling beam damper in the shear wall structure was analysed, and the effect of the layout location, number and performance parameter of the coupling beam dampers were also studied in this paper. The following conclusions were obtained:

(1) The story shear force and drift angle of shear wall structure can be effectively decreased because of coupling beam damper action, for example, the story drift angle can be decreased from 1/2017 to 1/2274 and the base shear force can be decreased from 3385kN to 3280N of the structure with damper in the Y-direction in the El-Centro earthquake action.

(2) The decreased amplification of the story drift angle is obvious relating to that of the base shear force, for example, the maximum decreased amplitude of the story drift angle is 16.7%, and the decrease amplitude of the base shear is 8.8% in the Loma-Prieta earthquake wave action.

(3) The coupling beam damper installed in the upper part of the structure is more economical, because the deformation of the shear wall structure belongs to the bending deformation, for example, the additional damper ratio of the Scheme A and Scheme B is 1.7% and 1.5% respectively.

(4) The seismic mitigation efficiency has not obviously difference for the Parameter one and Parameter two of the coupling damper. To ensure economic of the structure with damper, the reasonable performance parameter of the coupling damper should be determinate according to the dynamic response of the shear wall structure in the earthquake action.

ACKNOWLEDGEMENTS

REFERENCES:

[1] Jarrahi H, Asadi A, Khatibinia M, Etedali S. Optimal design of the rotational friction dampers for improving seismic performance of inelastic structures. Journal of Building Engineering, 2020, 27: 100960.

[2] Xu L H, Xie X S, Li Z X. Development and experimental study of a self-centering variable damping energy dissipation brace. Engineering Structures, 2018;160:270-280.

[3] Gong S M, Zhou Y, Ge P. Seismic analysis for tall and irregular temple buildings: A case study of strong nonlinear viscoelastic dampers. Structural design of tall and special building, 2017;26:e1352.

[4] Cai WH, Yu B J, Kaewunruen S. Shaking Table Tests of Suspended Structures Equipped with Viscous Dampers. Applied Sciences, 2019,9, 2616; doi:10.3390/app9132616.

[5] Kim H S, Kang J W. Smart outrigger damper system for response reduction of tall building subjected to wind and seismic excitations. International journal of steel structures, 2017;17(4):1263-1272.

[6] Lin P C, Takeuchi T, Matsui R. Seismic performance evaluation of single damped-outrigger system incorporating buckling-restrained braces. Earthquake engineering and structural dynamics, 2018;47:2343-2365.

[7] Wang Qi，Gan Gang. Calculation of effective additional damping ratio of energy dissipation structure based on linear equivalent method. Journal of Building Structures, 2012, 33(11): 46-52(in chinese).

[8] Jiang Q, Wang H Q, Feng Y L et.al. Seismic performance analysis of a damage-controlling RC frame with damping cladding panels. Engineering mechanics, 2019, 36(10): 144-151(in chinese).

[9] De Domenicoa D, Ricciardia G, Takewakib I. Design strategies of viscous dampers for seismic protection of building structures: A review. Soil dynamics and earthquake engineering, 2019, 118: 144-165.

[10] Shi S, Du D S, Wang S G et.al. Assessment of reinforcement scheme for a high-rise steel structure based on seismic resilience and reinforcement benefit ratio. China civil engineering journal, 2019, 52(11): 1-11(in chinese).

[11]   Zhang Z, Ou J P, Li D S, Zhang S F. Optimization Design of Coupling Beam Metal Damper in Shear Wall Structures. Applied Sciences, 2017,7, 137; doi:10.3390/app7020137.

[12]   Wang T, Yang F L, Wang X, Cui Y. Experimental Study on a Hybrid Coupling Beam With a Friction Damper Using Semi-steel Material. Frontiers in Materials, 2019, 6, doi:10.3389/frmats.2019.00135.

[13]   Renee M L, Constantin C, Michael M. Viscoelastic coupling dampers for the enhanced multiple seismic hazard level performance of high-rise buildings. Earthquake Spectra, 2018, 34(4): 1847-1867.

[14]   Chinese version of the ETABS.2004. Beijing Golden civil software technology company and China architecture standard design and Research, China Architecture and Building Press: Beijing, China (in Chinese).

[15]   Code for seismic design of buildings (GB50011-2016). 2016. China Ministry of Construction, China Architecture and Building Press: Beijing, China (in Chinese).

STUDY ON SURFACE STABILITY AND RESIDUAL DEFORMATION OF OLD GOAF IN DONGJIAGOU MINE，CHINA

Zechuang Li [1], Peifeng Cheng[1], Zhibin Liu[1] and Junjie Zheng[2]

1. *School of Civil Engineering, Northeast Forestry University, Harbin 150040, Heilongjiang, China; lzc@nefu.edu.cn, chengpeifeng@126.com (corresponding author), lzb_nefu@163.com*

2. *School of Civil Engineering and Mechanics, Huazhong University of Science and Technology, Wuhan 4300074, Hubei, China; zhengjj@hust.edu.cn*

ABSTRACT

Old goaf under the overpass becomes serious hidden trouble of subgrade-pavement and bridge engineering. Based on geological survey, geophysical survey and theoretical analysis, this paper studies on formation mechanism and distribution characteristics of the surface residual deformation in old goaf in No.9 Line Overpass across Rapid Rail Transit Line No.3 in Dalian city. A comprehensive analysis and evaluation has been made on the stability of old goaf. Based on the calculation principle of the probability integration method, the conception of ground residual subsidence coefficient and the predicted model of residual deformation are proposed, ground residual deformation of old goaf under the overpass is predicted. According to the zonal principles of ground stability, the stabilities of areas are divided. The results indicated that, new overpass has an important effect on the old goaf overburden rock activation in study area that the surface will be instability uneven settlement and the ground residual deformation values will exceed allowable values. Some treatment should be done to the old goaf because of the poor stability of goaf and non-goaf within influence zone in study area.

KEYWORDS

INTRODUCTION

According to the Standard for Building, water, railway, regulations of compressed coal mining and leaving coal pillar of main well lane (revised in 2017)[1], the surface subsidence of 10 mm caused by mining was taken as the beginning of the surface movement period, which ends when the surface subsidence remains less than 30 mm for 6 consecutive months. The duration of surface movement in the mining process is 2.5 H_0 (unit: day, H_0 is the average mining depth (m)), usually 3 to 5 years. It is generally believed that at the end of the surface movement period, the surface deformation of the coal mining subsidence area tends to be stable, and the residual deformation of the surface is small, which is harmless to the ground buildings. However, land utilization in old coal mining subsidence areas in recent years [2-3] shows that there are some serious problems in land exploration in coal mining subsidence areas. In 1990, the Handan-Changzhi railway line, China passed through the coal mined-out area, and the surface above the mined-out area subsided, resulting in partial line collapse. In 1997, the railway passing through the mined-out area in Huichun, Jilin province, China was severely distorted and subsided. The vertical deformation of the railway subgrade was 197 mm; the cracking and deformation of buildings

----

caused by surface residual deformation are more common. Therefore, the residual deformation of the old goaf can cause huge economic losses [4-6].

After the surface movement period of old goaf is over, the collapsed rock blocks near the old goaf are subjected to greater rock pressure and compression, but the remaining voids and the delamination and cracks in overburden of the old goaf will not be fully compacted due to the existence of rock structure[7]. When affected by external forces (such as the load of new building on the surface, seismic force, etc.), the relatively stable state in the overlying rock layer will break, activating the old mined-out area[8] and producing new deformation in the overlying rock and the ground surface, which will affect buildings on the ground [9-10]. The stability of the old mined-out area and the prediction of residual deformation have attracted extensive attention from researchers. Wang and Deng [11] studied and established a grey Markov prediction model (GM-Markov) for residual settlement in old goafs. Zhang et al [12] proposed a new method for the analysis and prediction of the stability of surface structures above old goafs based on multi-scale empirical mode decomposition (EMD). Mi et al [13] studied and established an aggregate Kalman filter prediction model for residual settlement in the old goaf and compared the aggregate Kalman filter predicted value with the original measured data sequence through examples. Ma et al [14] applied the probability integral method to calculate the remaining surface movement and deformation in the study area, and analyzed the influence of the remaining surface deformation on the stability of the line. Zhu et al [15] used the principle of probability integration to construct the function of surface residual movement deformation influenced by mining. The calculation results show that the maximum value of the surface residual movement deformation appears on both sides of the old goaf, which is consistent with the conclusions that the old mined-out area has large boundary void and activation potential. Chen [16] predicted and analyzed the surface subsidence along the railway via the surface subsidence prediction program, combined with the goaf movement time and surface analysis. There are few researches about the calculation of surface deformation during surface residual deformation at home and abroad has not yet been conducted.

This article proved the range of goaf in study area and its spatial distributions characteristics, analyzed the stability of old goaf, studied the law of ground residual deformation, proposed the prediction model of residual deformation and zoned the study area based on ground stability combined with the feature data, drilling data and geophysical data based on survey from old coal mine goaf in No.9 Line Overpass across Rapid Rail Transit Line No.3 in Dalian Economic and Technological Development Zone.

OLD GOAF IN DONGJIAGOU MINE

The No.9 Line Overpass is located in Dalian Economic and Technological Development Zone, Dongjiagou Sub-district, Dalian City, Liaoning Province, China. It goes through the original mining area of Dongjiagou Coal Mine and passes through north of Rapid Rail Transit Line No.3, as shown in Figure 1. The No.9 Line Overpass is of butterfly-shaped interconnecting design. Its main bridge is 1091.282m long totally.
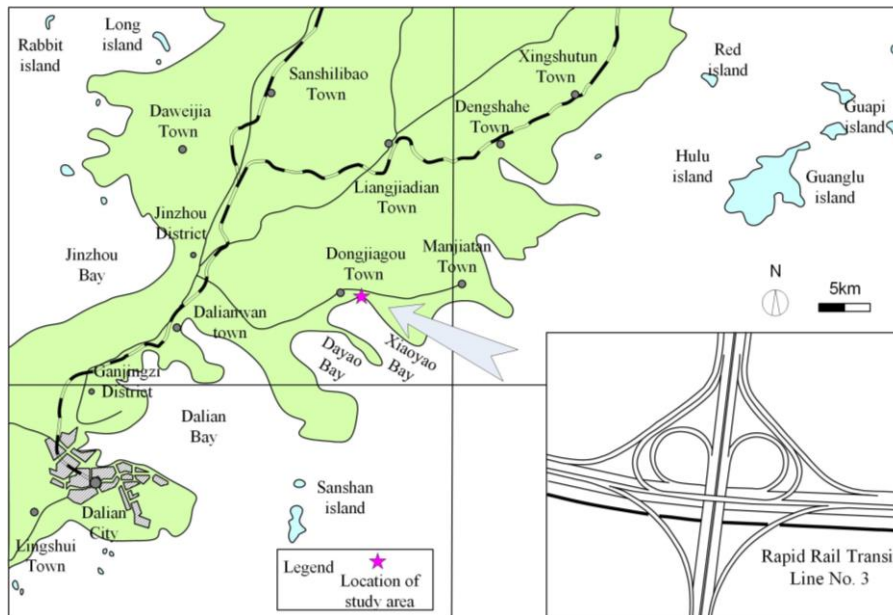
Fig.1- Location of study area and schematic diagram of the overpass

Geological overview

The study area covers two geomorphic types, namely, slope diluvial inclined plain and alluvial marine depositional plain. To be specific, it is the slope diluvial inclined plain in the north of the study area, with flat and open terrain. And it is the alluvial marine depositional plain in the south of the study area, slightly tilting toward the sea. In conclusion, the study area lies higher in its northeast while lower in its southwest and features minor topographic relief with topographic slope generally less than 10° and ground elevation of 0.12-11.54m.

The thin quaternary strata in the study area have burial depth of 5.2-19m, whose eastern part is shallower than western part. And the lithology mainly involves backfill, clay and silty clay. Roof surrounding rocks in the old goaf are mainly composed of limestone, sandstone and shale. Among them, limestone enjoys better physical and mechanical properties. The upper and lower strata are mainly made up of contain limestone, including sandstone interlayer. The medium stratum features disordered deposition sequence and thus highly unstable position. The coal measure stratum crosses southwest of the study area in banded shape, with its occurrence tendency of 200° and dip angle of 20°. The position containing coal is of honeycomb and generally turns shallower from the west to the east.

Mining history

Dongjiagou Coal Mine had been put into operation since 1966 and came to an end due to resource depletion in 1995. The exploitation method of tunnelling laneway along coal bed tendency was adopted. And the mining methods included wall full-collapse mining and heading-and-stall mining. By these two ways, goafs were formed after coal was mined and were just put aside. Some sections were temporarily supported by timbers which taken back after mining, while some other sections that could not be supported, especially those with thicker coal beds, were left in caved manner. The recovery ratio was about 60%-70% [17].

Due to different height of destroying overlying rock mass, collapse pits were formed on the surface in areas with shallow mining depth and uneven mining thickness. As surveyed and

Article no. 3

THE CIVIL ENGINEERING JOURNAL 1-2021
----

recorded, the study area and its adjacent areas have developed 4 collapse pits during surface movement period in the goaf in Dongjiagou Mine. One of them is shown in Figure 2 and its specific location is shown in Figure 5.

Fig.2- Surface collapse pit in the east of the study area

EVALUATION METHOD

Stability analysis for Surface of Old goaf

As shown in Figure 3, roof rocks ABCD sink under the action of gravity W together with horizontal pressure P applied by wedges ABM and CDN on both sides after ore bed is mined out. Therefore, AB and CD faces resist against friction arising from P. Unit length of the goaf (laneway) is taken as the calculation unit. When a building is constructed above the goaf (it is assumed that the unit pressure of the building base is P_0), pressure applied in the laneway roof is shown as follows on the basis of force balance analysis:
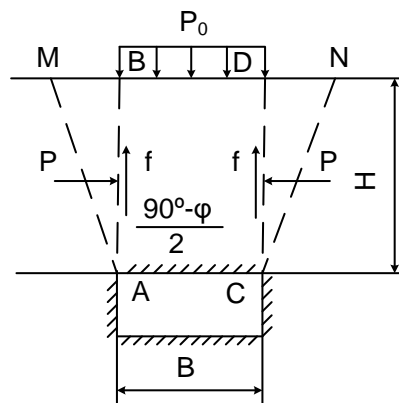

Fig.3- Schematic diagram for roof stability of Goaf

$$Q = \gamma H \left[B - H \tan \varphi \tan^2 (45° - \frac{\varphi}{2}) \right] + BP_0 \tag{1}$$

Where: Q -- pressure borne by roof per unit length of laneway, kN/m;

H -- burial depth of laneway roof, m;

B -- laneway width, m;

Y -- rock stratum unit weight, kN/m³;

φ -- internal friction angle of rock stratum, (°).

When H reaches a specific value, the roof rock stratum just stays natural balance (namely, Q = 0) and H is just critical safety depth H_0 for the building constructed above the goaf. The critical depth is calculated by the following formula.

$$H_0 = \frac{B\gamma + \sqrt{B^2\gamma^2 + 4B\gamma P_0 \tan \varphi \tan^2 (45° - \frac{\varphi}{2})}}{2\gamma \tan \varphi \tan^2 (45° - \frac{\varphi}{2})} \tag{2}$$

When $H < H_0$, the foundation is unstable. When $H_0 \le H \le 1.5 H_0$, the foundation is unsatisfactorily stable. When $H \ge 1.5 H_0$, the foundation is stable.

Prediction model of residual deformation of old Goaf

Closed rectangle sectioning integral model

As the residual deformation in the mining subsidence area is deemed as an extension of the conventional subsidence, it is assumed that its distribution law keeps consistent with movement law of the conventional mining subsidence. Therefore, calculation of residual deformation on the surface of the mining subsidence area is still based on the conventional probability integral method, but it is required to correct the surface movement calculation parameters. Considering that the study area falls into the old goaf in the abandoned coal mine and has insufficient data concerning coal mining and overlying strata deformation observation, the surface residual calculation parameters are determined according to empirical equation and method of specific geological conditions [18].

The method is based on random medium theory. With overlying stratum as loose medium, a surface residual deformation function is established on the basis of statistical law, as shown in Figure 4. Influence of the whole mining area on the surface is equal to sum of influence of numerous infinitesimal mining units on the surface. Mining thickness, length and width refer to dimension of an infinitesimal mining unit. A basin formed after mining of a mining unit is defined as a unit basin. The subsidence in a unit basin is defined as a unit subsidence (w_e). If the Mining Area o1CDE is marked as D; width o1C of its working face D_1; length CD of its working face D_3, residual deformation W (x, y) of an arbitrary point B (x, y) arising from the whole mining process is defined as:

$$W(x, y) = mq' \cos \alpha \iint_D w_e(x - s, y - t) dt ds$$

$$= mq' \cos \alpha \int_0^{D_3} \int_0^{D_1} \frac{1}{r^2} \exp[-\pi \frac{(x - s)^2 + (y - t)^2}{r^2}] dt ds \tag{3}$$

Where, m -- mining thickness;

     q' -- residual subsidence coefficient;

     α -- coal bed dip angle;

     r -- main influence radius.
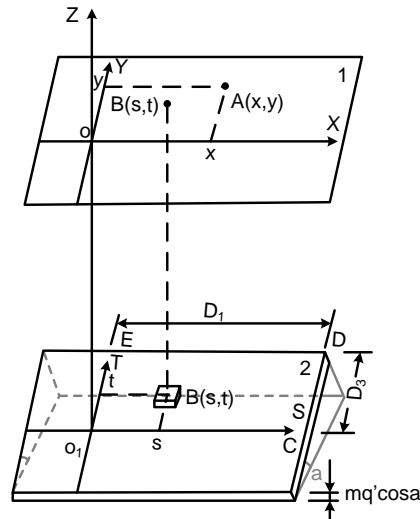
Fig.4- Coordinate system of coal mining space (1 for Surface; 2 for Mined Coal Bed)

For subsidence caused by mining of multiple working faces considers, it is expected to consider sum for influence of all working faces on surface points.

Determination of surface residual calculation parameters

In accordance with the random medium theory, it is assumed that all mining gaps are filled and compacted fully after rock strata movement; the subsidence coefficient is 1 [18]; the residual subsidence coefficient is defined as q', the calculation formula for residual subsidence coefficient is shown as follows:

$$q' = 1 - q \tag{4}$$

Where, q -- conventional ground surface subsidence coefficient, which is figured out according to actual observed results of surface movement-caused deformation for general mining areas, and is selected from attached Tables 3-1 in the Standard[1] for mining areas without actual observed data.

Calculation formula of the main influence radius r is shown as follows:

$$r = \frac{H}{\tan \beta} \tag{5}$$

Where, H -- mining depth;

     β -- main influence angle.

DISTRIBUTION CHARACTERISTICS OF OLD GOAF

The geophysical methods adopted were high-density resistivity method and shallow seismic reflection method to survey and analyze the old goaf space distribution characteristics. 10 measuring profiles in the high-density resistivity method were arranged, with each 150-600m long and exploratory point interval of 10m. 4 measuring profiles in the shallow seismic reflection method were arranged, with shot point offset of 8m. And 24 receiving channels are allocated for cymoscopes at intervals of 2m. 5 drilling exploration measuring profiles were arranged, with 56 boreholes at intervals of 20-45m, as shown in Figure 5. The light grey coloured "ZK0+420" and other characters in Figure 5 are the mark numbers of the overpass, namely the numbers used to locate the main bridge, ramps and other specific positions of the overpass. Taking "ZK0+420" as an example, the letter "Z" means the main bridge, the ramp can be marked with letters such as "F", which can be set artificially; "K" is the abbreviation of "kilometer", and the 0 behind K has kilometer as its unit, and the last three digits behind the plus sign means the number of meters, then "ZK0+420" means the position which is 420 meters from the 0th kilometer from the starting point of the main bridge.
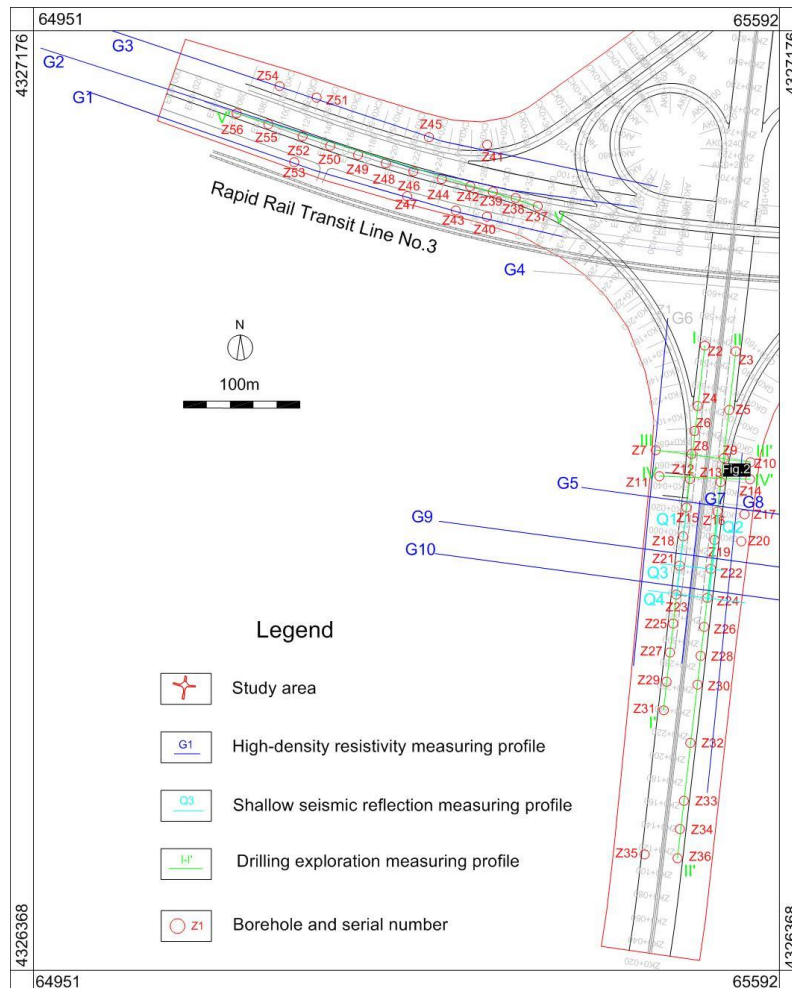
Fig.5 - Map of an engineering geological exploration

3 high-density resistivity section lines were arranged north of Rapid Rail Transit Line 3, with G2 high-density resistivity measuring profile shown in Figure 6(a); 7 high-density resistivity measuring profiles south of Rapid Rail Transit Line No.3, including 3 north-to-south profiles and 4 east-to-west profiles, with G8 high-density resistivity measuring profile shown in Figure 6(b). In

high-density resistivity diagram, the warm-toned area reflected high resistivity of rock mass, indicating underground goaf or fracture zone, while the cool-toned area reflected low resistivity of rock mass, indicating limestone and sandstone area.
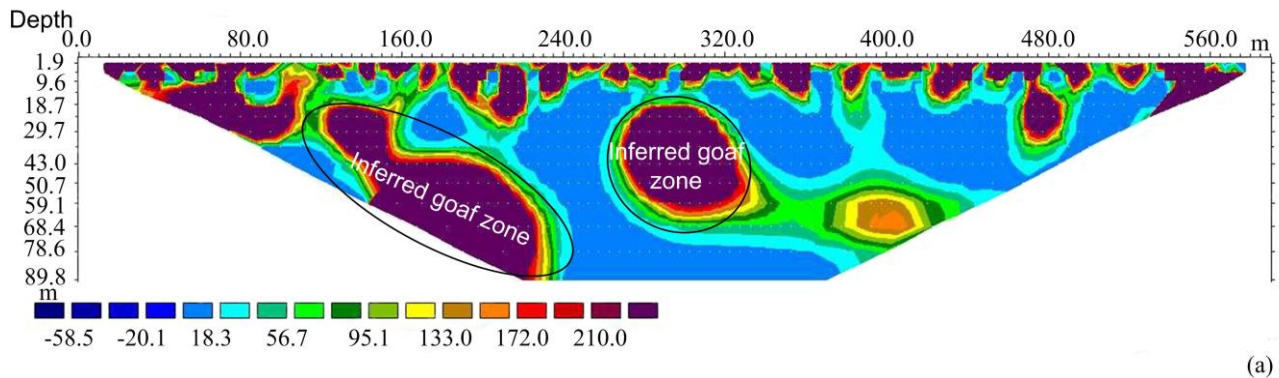
(a)- For G2 measuring profile
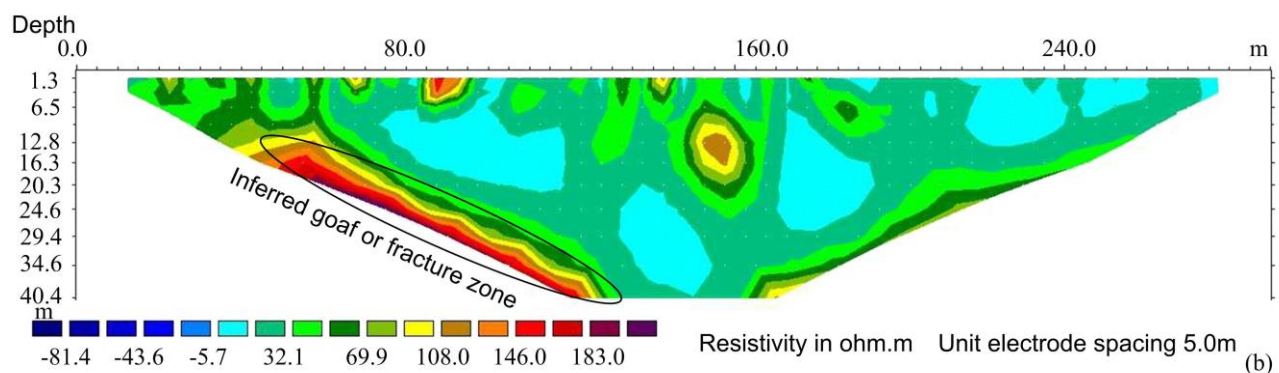
(b)- For G8 measuring profile

Fig.6- Surveying inversion result diagram of high-density resistivity method

As shown in Figure 6(a), closed high-resistance abnormal areas were formed in such places as were limited to measuring profile 120-230m long and 19-88m deep, as well as 265-330m long and 18.7-59m deep. Therefore, it is deduced that such areas were goaf zones. As shown in Figure 6(b), closed high-resistance abnormal areas were formed in such place as was limited to measuring profile 45-120m long and 16.3-40.4m deep. Therefore, it is inferred that such area was goaf or fracture zone.

4 shallow seismic reflection measuring profiles were arranged south of Rapid Rail Transit No. Line, including 2 north-to-south profiles and 2 east-to-west profiles. In such area, there was a low-velocity layer that was composed of plain fill and features greatly different thickness. The weathering zoning of the rock-soil layer under the low-velocity layer was an obvious characteristic. Elastic wave velocity of the near-surface stratum was 170 -700m/s; that of the moderately weathered rock stratum 1,000-1,500m/s; that of the lower minor-stratified rock stratum 1,600m/s. Figure 7 shows Q2 profile interpretation result diagram. The wave velocity at the point of Q2 survey profile which is 35-75m long and 30-40m deep measures 600~850m/s, and it is significantly lower than the 900-1200 m/s wave velocity at the point which is 30-40m deep and 0-35m long. At the regions around the points under the ground which is 30-40m below the intersection of Q3 and Q2 and that of Q4 and Q2, the wave velocity is also low, and the wave velocity is also in the range of 600~850m/s. These observations indicate that the point of the Q2 profile line which is 35-75m long

----

and 30-40m deep is characterized by poor integrity and low strength, and thus it is presumed to be a goaf zone.
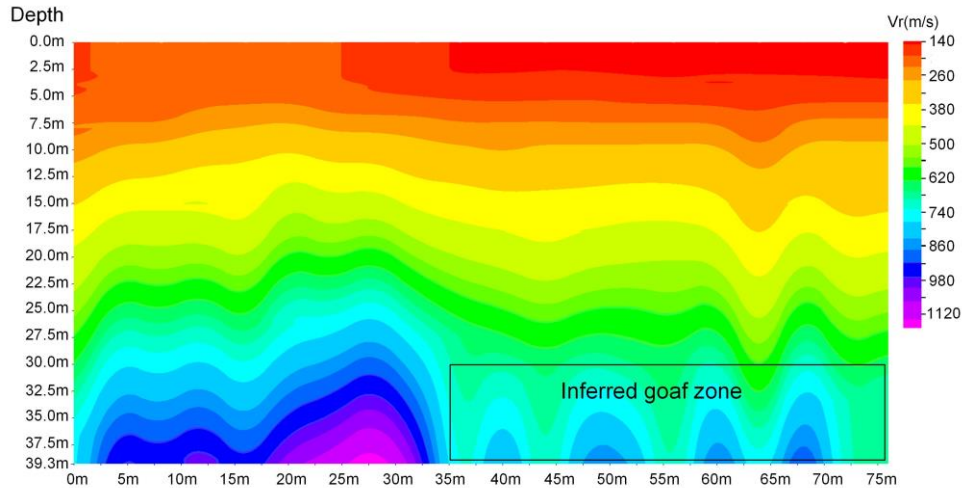
Fig.7- Inversion result diagram of Q2 shallow seismic reflection measuring profile

1 drilling exploration profile was arranged north of Rapid Rail Transit Line No.3; 4 profiles south of Rapid Rail Transit Line No.3. In general, the drilling exploration results show that the roof of the goaf in Dongjiagou Coal Mine was supported by timbers in some parts, while the other parts were not supported, leaving caving. Upon drilling exploration, it is indicated that most boreholes have developed fracture and cave, especially those in the roof composed of sandstone and shale as sandstone and shale feature poor integrity and low strength and the roof was subject to cave when support structures failed to work. Roof made up of limestone had small caving area while large fracture, indicating that limestone features high strength while slow caving speed. In caved places, the maximum depth of borehole was 49.8m. Caving happens in coal bed and shale stratum mostly. III-III' engineering geological profile diagram is shown in Figure 8.
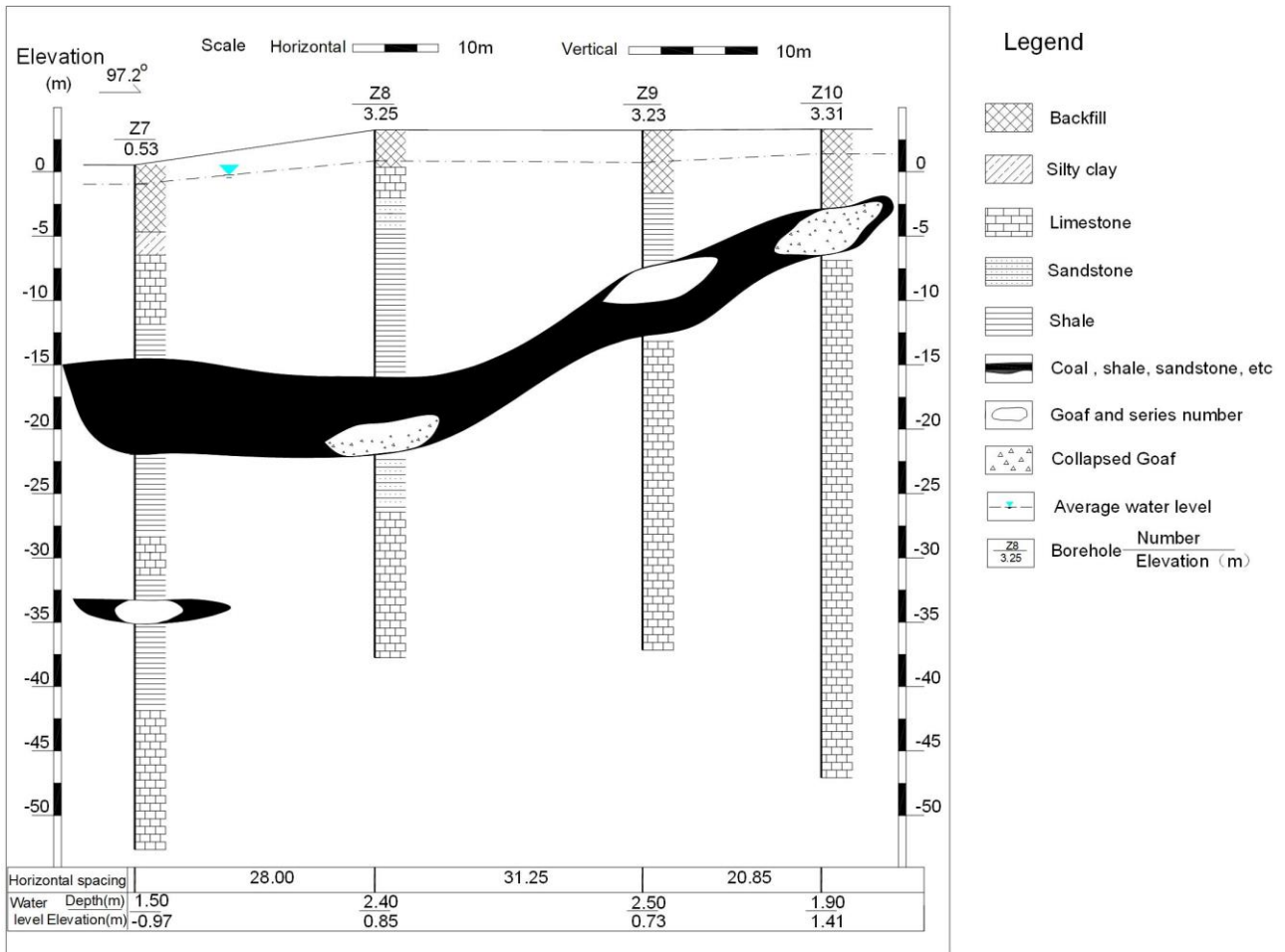
Fig.8- III-III' engineering geological profile

According to the survey results and previous data, it is analyzed that all goafs are under the underground water level. To be specific, goafs north of Rapid Rail Transit Line No.3 are distributed within EK0+024 - EK0+214 of the No.9 Line Overpass to be constructed, with width of 66m, and those south of Rapid Rail Transit Line No.3 within ZK0+299 - ZK0+489 of the overpass said, with width of 90m. Distribution of goafs is detailed in Table 1:

Tab. 1- Distribution characteristics of goaf (laneway)

Goaf (laneway)	Mining depth (m)	Length of working face (m)	Width of working face (m)	Height of working face (m)	Mileage	Location
Goaf C1	29.1-49.8	190	66	3	EK0+024—EK0+214	North of Line No.3
Laneway H1	29.1-34.8	59	3	3.5	EK0+195	
Laneway H2	43.4-49.8	75	3	2	EK0+112	
Goaf C2	16.2-46.9	70	45	2.2	ZK0+420—ZK0+490	South of Line No.3
Goaf C3	6.2-43.4	172	45	2.5	ZK0+298—ZK0+470	
Laneway H3	16.2—46.9	60	3	2	FK0+040—ZK0+480	
Laneway H4	6.2—43.4	133	3	3	ZK0+335—GK0+080	

STABILITY ANALYSIS AND PREDICTION OF OLD GOAF

Surface stability evaluation of Old Goaf

According to survey results and geotechnical test data, stability evaluation parameters were selected as follows: laneway width B - 3m; internal friction angle of rock stratum φ - 36°; unit weight of rock stratum γ - 26kN/m³; unit pressure of building base P_0 - 2,500kN/m².

Before the No.9 Line Overpass was constructed, it is only needed to consider self-supporting effect of roof rocks in goafs. As calculated by Equation 2, critical depth H_0 = 15.9m, $1.5H_0$ = 23.9mm. As depth H_1 of Goaf C1 = 29.1 - 49.8m, namely, $H_1 > 1.5H_0$, the goaf kept stable. As depth H_2 of Goaf C2 = 16.2 - 46.9m, namely, $H_2 > H_0$, and the average burial depth $\bar{H}_2$ = 33m, namely, $\bar{H}_2 > 1.5H_0$, the goaf kept stable basically. As depth H_3 of Goaf C3 = 6.2 - 43.4m, namely, burial depth $< H_0$ partially, and the average burial depth $\bar{H}_3$ = 33m, namely, $\bar{H}_3 > 1.5H_0$, the goaf kept unstable partially.

When the No.9 Line Overpass was constructed above goafs, it is also needed to consider influence of additional foundation stress incurred. As calculated by Equation 2, critical depth $H_0^{'}$ = 47.9m, $1.5H_0^{'}$ = 71.8m. As depths H_1, H_2 and H_3 of Goafs C1, C2 and C3 are all less than $1.5H_0^{'}$, and average burial depth of these three goafs is less than $H_0^{'}$, the No.9 Line Overpass to be constructed may result in insufficient safety thickness of roof in old goafs and it is likely to result in surface collapse due to roof collapse.

To sum up, most overlying rock strata in old goafs were under stable state. Some unstable overlying rock strata stay relatively stable after years of creep compression, with little residual deformation influence, and hence the surface was relatively stable. Under disturbance of the overpass to be constructed, the relative mechanical equilibrium state of overlying rock strata was broken, exciting old goafs, and the surface continues residual deformation. In such case, stability of the study area was assessed as follows:

a)	Goafs north of Rapid Rail Transit Line No.3 were distributed within EK0+024 - EK0+214, with burial depth of 29.1-49.8m. Considering poor surface stability, there was great risk of surface collapse in goafs.

b)	Goafs south of Rapid Rail Transit Line No.3 were distributed within ZK0+299 - ZK0+489, with burial depth of 6.2-46.9m. Considering poor surface stability, there was great risk of surface collapse in goafs.

c)	There was no surface collapse of goafs found in the southern and northeastern parts of the overpass and such parts keep far away from goafs. Therefore, there is no risk of surface collapse.

These stability analysis results keep consistent with surface deformation monitoring results as worked out by Chen et al [18].

PREDICATION FOR RESIDUAL DEFORMATION OF OLD GOAFS

According to locations, mining scopes and characteristics of old goafs, the study area was divided into 3 portions for calculation, namely Goafs C1, C2 and C3. Ranges of integration for s and t are determined by Equation 3 according to mining scope, namely, working face width D_1 and working face length D_3. Residual deformation coefficient q' and influence radius r were determined by Equation 4 and 5. For rock movement parameters of goafs, see Table 2.

Tab.2- Coal burial characteristics and rock movement parameter of portions

Goafs	Mining thickness m（m）	Mining depth H （m）	Coal dip angle α （°）	Working face width D_1 （m）	Working face length D_3 （m）	Residual deformation coefficient q'	Influence radius r（m）
C1	3	40	20	66	190	0.15	20.30
C2	2.2	33	20	45	70	0.1	15.57
C3	2.5	27	20	45	172	0.11	12.86

Calculation for these goafs was made referring to prediction model of residual deformation for old goafs. For residual deformation influence functions after reactivation of goafs, see Equations 6-8, it is considered that deformation effects of all working faces resulting from mining operations are equal to sum of influence on surface points. That is, calculated results of goafs are summed to figure out residual deformation of any surface point. For distribution of deformation contour lines, see Figure 9.

Goaf C1:

$$W(x,y) = -0.106[erf(0.087x) - erf(0.087x - 16.590)][erf(0.087y) - erf(0.087y - 5.763)] \quad (6)$$

Goaf C2：

$$W(x,y) = 0.052[erf(0.114x - 7.969) - erf(0.114x)][erf(0.114y) - erf(0.114y - 5.123)] \quad (7)$$

Goaf C3：

$$W(x,y) = -0.065[erf(0.131y) - erf(0.131y - 5.908)][erf(0.131x) - erf(0.131x - 22.580)] \quad (8)$$

Where, erf - probability integral function.
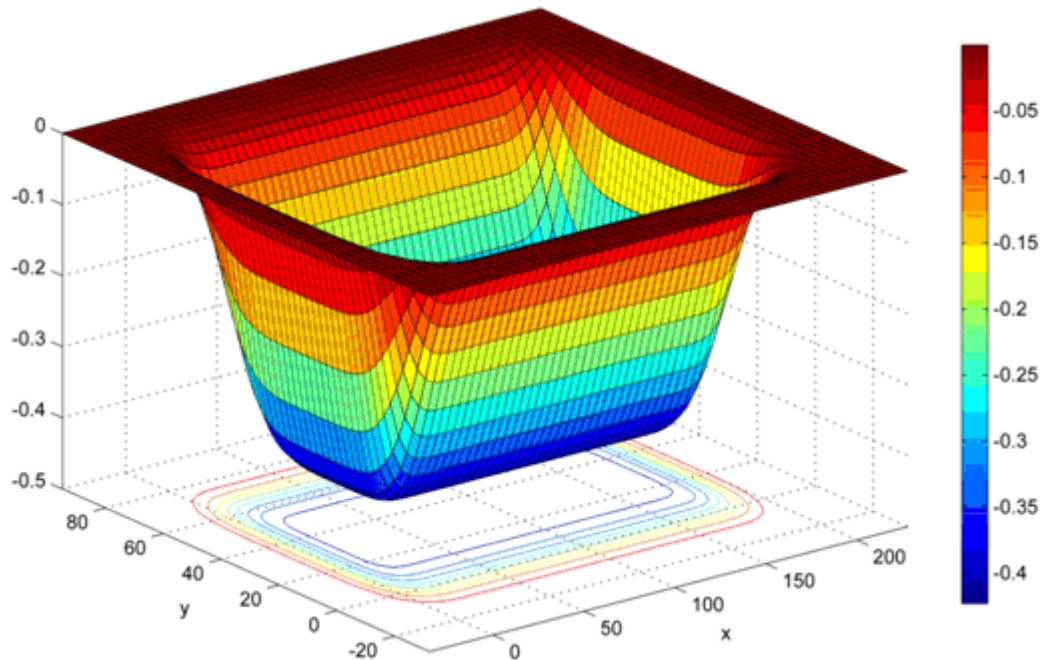
Fig.9- Residual deformation contour lines influencing function prediction after reactivation of goaf C1 (unit: m)

Taking Goaf C1 as an example. 3D residual deformation contour diagram is of peviform (shaped like a basin) and residual deformation contour lines are distributed in approximately rectangular manner. It is indicated that the surface may be prone to uneven subsidence; that the maximum subsidence is located in the center of rectangle; that the subsidence decreases along with farther distance from the center in the same direction. Within goaf, there exists larger surface deformation. The residual deformation in Goaf C1 reaches 422.8mm at maximum, exceeding deformation control limit (allowable value: 300mm). The residual deformation values in Goaf C2 and C3 are 206.7mm and 258.4mm at maximum, respectively, approaching allowable deformation. It is indicated that the residual deformation resulting from reactivation of old goafs exerts great impact on stability of the No.9 Line Overpass.

SURFACE STABILITY ZONING

Surface stability zoning principle: Geological disasters in the study area were controlled by formation lithology, geological structure and space distribution of goafs and were also closely related to human engineering activities in terms of their formation and development. Therefore, in surface stability zoning of goafs, it is needed to mainly consider general consistency in geological structure, formation lithology, space distribution of goafs and human engineering activities. In addition, such factors as current development conditions and tendency, hazard extent, stability and residual subsidence distribution law shall be taken into consideration.

According to the zoning principle, the study area was divided into 2 engineering geological sub-areas, namely, engineering geological sub-area with unstability (I) and engineering geological sub-area with stability (II). Characteristics of engineering geological sub-areas and hazard extent of geological disasters are summarized according to distribution and area of engineering geological sub-areas, space distribution of goafs, disaster features and conditions, as shown in Table 3. Distribution conditions in goafs are detailed in Figure 10.
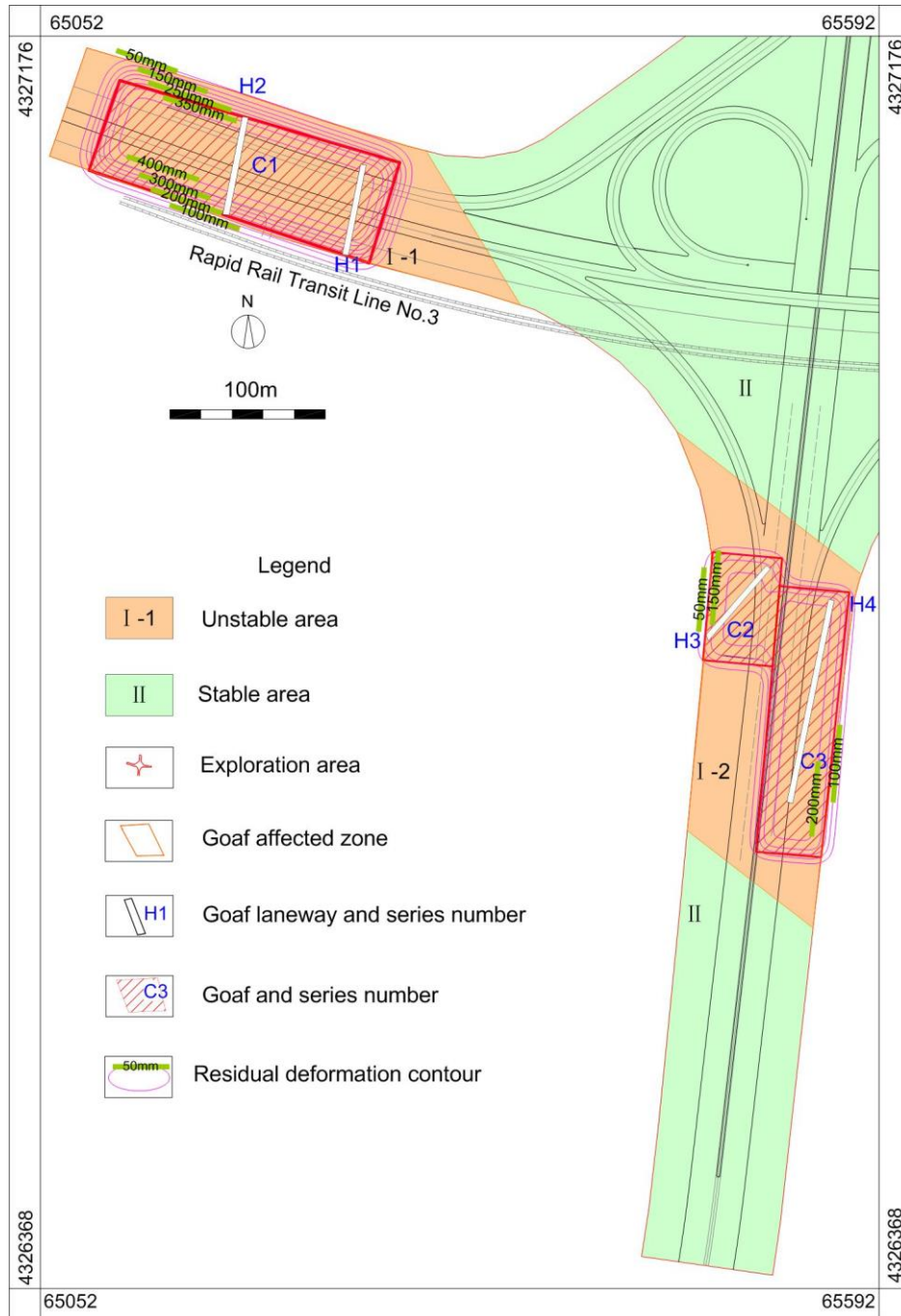
Fig.10- Distribution of Goafs for the No.9 Line Overpass across Rapid Rail Transit Line No.3 and zoning of surface stability

Tab.3- Engineering Geological Zoning

Engineering geological sub-area	Code	Area (m^2)	Distribution range
Area with surface instability	I-1	21484.8	The area is located westward of Rapid Rail Transit Line No.3 within EK0+000 - EK0+310 of the overpass. There are 2 goaf laneways and 1 goaf in this area, with goaf burial depth of 29.1-49.8m. Considering instability, there is great risk of surface collapse in goafs.
	I-2	21990.1	The area is located south of Rapid Rail Transit Line No.3 within ZK0+260 - ZK0+560 of the overpass. There are 2 laneways and 2 goafs in this area, with goaf burial depth of 6.2-46.9m. Considering instability, there is a great risk of surface collapse in goafs.
Area with surface stability	Ⅱ	80484.3	The area is located out of influence scope of goafs. There is no surface collapse of goafs found in the southern and northeastern parts of the overpass and such parts keep far away from goafs. Therefore, there is no risk of surface collapse.

CONCLUSION

The following conclusions are made upon above research:

Through stability evaluation, it is worked out that a majority of overlying rock strata in old goafs of Dongjiagou Coal Mine were under stable state. Some unstable overlying rock strata stayed relatively stable after years of creep compression, with little residual deformation influence, and hence the surface is relatively stable. Under disturbance of the No.9 Line Overpass to be constructed, the relative mechanical equilibrium state of overlying rock strata is broken, reactivating old goafs, and the surface continues residual deformation.

A closed rectangle integral model is established according to calculation principle of probability integral method and a prediction model of surface residual deformation for old goafs is proposed. Thanks to these efforts, the influence of inclined coal bed on surface deformation is predicted according to changes of coordinates for calculation units. As a result, it is available to predict the deformation of any surface point resulting from reactivation of old goafs. Furthermore, due to infinitesimal of units relative to goafs, the engineering precision requirement is completely met.

As predicted by the residual deformation prediction model, the surface residual deformation contour lines resulting from the rectangle-shaped goafs are distributed in approximately rectangular manner. The maximum subsidence is located in the center of rectangle.

The residual deformation in Goaf C1 is 422.8mm that exceeds deformation control limit (allowable value: 300mm). The residual deformation values in Goafs C2 and C3 are 206.7mm and 258.4mm at maximum respectively, approaching the allowable deformation limit as well. According to the surface stability zoning principle, the study area is divided into 2 engineering geological sub-areas. Goafs and their surrounding non-goafs within the study area have poor stability, thus requiring improvement to ensure safety of the overpass.

ACKNOWLEDGEMENTS

REFERENCES

[1]   State Administration of Work Safety et al., 2017. Building, water, railway, regulations of compressed coal mining and leaving coal pillar of main well lane. China Standard Press

[2]   Yao X.L., Reddish D.J., 1994. Analysis of residual subsidence movements in the UK coalfields. Quarterly Journal of Engineering Geology & Hydrogeology, Vol. 27, No. 1: 15-23.

[3]   Marwan A.L.H, M. Nicolas, J.F. Noirel, et al, 2005. Residual subsidence analysis after the end of coalmine work. Example from Lorraine colliery, France. symposium post mining, 16-18.

[4]   Cui X, Gao Y, Yuan D, 2014. Sudden surface collapse disasters caused by shallow partial mining in Datong coalfield, China. Natural Hazards, Vol. 74, No. 2: 911-929.

[5]   Donnelly L.J., Cruz H.D.L., Asmar I, et al., 2001. The monitoring and prediction of mining subsidence in the Amaga, Angelopolis, Venecia and Bolombolo Regions, Antioquia, Colombia. Engineering Geology, Vol. 59, No. 1: 103-114.

[6]   Zhou D, Wu K, Chen R, et al., 2014. GPS/terrestrial 3D laser scanner combined monitoring technology for coal mining subsidence: a case study of a coal mining area in Hebei, China. Natural Hazards, Vol. 70, No. 2: 1197-1208.

[7]   Xuan D, Xu J, 2014. Grout injection into bed separation to control surface subsidence during longwall mining under villages: case study of Liudian coal mine, China. Natural Hazards, Vol. 73, No. 2: 883-906.

[8]   Palchik V, 2005. Localization of mining-induced horizontal fractures along rock layer interfaces in overburden: field measurements and prediction. Environmental Geology, Vol. 48, No. 1: 68-80.

[9]   Guo G.L., Wei K.L., Mu B.S., et al., 2005. Mechanism and control of ground residual deformation over longwall goaf. Transactions of Nonferrous Metals Society of China, Vol. 15, No. 3: 76-79.

[10]   Swift G, Reddish D, 2002. Stability problems associated with an abandoned ironstone mine. Bulletin of Engineering Geology & the Environment, Vol. 61, No. 3:227-239.

[11]   Wang Z.S., Deng K.Z, 2010. Study on grey markov prediction model for old goaf residual subsidence. Journal of geodesy and geodynamics, Vol. 30, No. 6: 126-130.

[12]   Zhang A.B., Gao J.X., Zhang Z.J., 2011. Deformation analysis and prediction of building above old mine goaf based on multiscale method. Rock and Soil Mechanics, Vol. 32, No. 8: 187-192.

[13]   Mi L.Q., Zha J.F., Wang X, 2012. Ensemble Kalman filter prediction model of old goaf residual subsidence. Metal Mine, No. 8: 138-141.

[14]   Ma L.X., Wu C.Y, Gao Y.W., Evaluation of the influence of residual deformation above mined-out area on the stability of urban rail transit. Coal geology and exploration, Vol. 41, No. 1: 40-49.

[15]   Zhu G.Y., Xu Z.H, Xie C, et al., 2014. Study of influence functions of surface residual movement and deformation above old goaf. Chinese Journal of Rock Mechanics and Engineering, Vol. 33, No. 10: 1962-1970.

[16]   Chen M.X., 2018. Research on the surface subsidence status and residual settlement prediction of the goaf. Journal of railway engineering society, Vol. 35, No. 6: 16-20, 76.

[17]   Guo G.L., 2001. Deformation mechanism and control of building foundation above the old goaf. (China Mining University Press) 2-140.

[18]   Chen L.Y., Chen S.X, Wu X.H., 2010. Study on surface deformation monitoring in Dongjiagou coal mine, No. 14: 17.

EFFECT OF BLASTING ON THE STABILITY OF LINING DURING EXCAVATION OF NEW TUNNEL NEAR THE EXISTING TUNNEL

Tran Tuan Minh[1], Nguyen Quang Huy[2]

1. *Hanoi University of Mining and Geology, Underground and mining construction department, Ha Noi city, Vietnam; tuanminhhumg@yahoo.com*
2. *Institute of transport science and technology, Bridge and Tunnel design department, Ha Noi city, Vietnam; quanghuy170687@gmail.com*

ABSTRACT

In recent years, experimental and numerical researches on the effect of blasting pressure on the stability of existing tunnels was widely obtained. However, the effect of the blasting pressure during excavation a new tunnel or expansion old tunnels on an existing tunnel has disadvantages and still unclear. Some researches were carried out to study the relationship of the observed Peak Particle Velocity (PPV) on the lining areas along the existing tunnel direction, due to either the lack of in situ test data or the difficulty in conducting field tests, particularly for tunnels that are usually old and vulnerable after several decades of service. This paper introduces using numerical methods with the field data investigations on the effect of the blasting in a new tunnel on the surrounding rock mass and on the existing tunnel. The research results show that not only predicting the tunnel lining damage zone under the impact of blast loads but also determination peak maximum of explosion at the same time at the surface of tunnel working.

KEYWORDS

Blasting vibration, Tunnels, Drilling and blasting method, Existing tunnels

INTRODUCTION

The effects of drilling and blasting in case of excavation of new tunnels or expansion old tunnels near the existing tunnels along of the express way from North to South of Vietnam such as tunnels in the Hai Van pass tunnel project, Cu Mong tunnel, Deo Ca tunnel, etc are obtained. Traditional excavation method was widely used during excavation tunnels through the mountains in Vietnam in [1], this method has advantages for economy conditions, workers and engineers in Vietnam. In the past the researches for the stability of rock mass around transported tunnels and the assessments of the effects of tunnel blasting on the existing tunnels and buildings were carried out by not only authors in Vietnam such as in [2], [3], [4], [5], [6-7], [8-9] but also other authors in the world in [10], [11], [12], [13], and [14]. Researches in Vietnam are obtained for the stability of buildings on the surface of the ground, the assessment standard only for buildings during blasting on the open pit mining [3].

In the recent years some researches were carried out using physical models to study the effect of blasting vibration on an existing tunnel in [6-7], [8], and [9]. Smith et al presented the results of experimental studies carried out at small scale into the propagation of blast waves along straight tunnels roughened by means of different-sized roughness elements fixed along the two model tunnels sides. The results indicated that the use of rough-walled tunnels could provide an efficient protective solution to a sensitive structure. Previous publications have indicated that the

----

strongest vibrations of the existing tunnel lining occur on the side closest to the blasting centre and are proportional to the maximum segmental explosive charge instead of the total charge. Rock masses with harder rock and fewer discontinuities seem to contribute to stronger tunnel vibrations than softer rock and more discontinuities. However, a few researches were carried out to study the relationship of the blasting pressure values on the displacements and internal forces in lining of existing tunnels. It is therefore necessary to find appropriated solutions for drilling and blasting to avoid damage to the lining of existing tunnels also normal operation of old tunnels. In this paper there is introduced the research on the changing of internal forces in lining of old tunnels with other the values of blasting pressures in geological conditions of Co Ma, Deo Ca and Hai Van Pass projects.

NUMERICAL MODELING OF DEO CA TUNNEL PROJECT BASED ON THE SEISMIC COEFICIENTS (K_c)

Introduction of the project

Deo Ca project consists of total length 13.4 km, twin tunnels with each tunnel 3.9 km, the distance between two tunnels is 30 m. According to the investor, Deo Ca Investment Joint Stock Company, it will take vehicles just over 10 minutes to pass through the tunnel, instead of travelling around 60 minutes through the pass. Vehicles using the tunnel can avoid rockslides, which often occur in the rainy season. With a total length of 13.19 km, the Deo Ca Tunnel consists of the 4.12 km Deo Ca Tunnel and the existing 500 m Co Ma Tunnel. The two-lane tunnel is said to be installed with most modern equipment in Vietnam so far and vehicles can travel at 80 km/h. Bridges and roads leading to the two tunnels have a combined length of over nine kilometres. The project costs over VND11 trillion (USD485.2 million).

Deo Ca Tunnel will help boost trade and tourism in the central region in addition to creating a link between Phu Yen's Nam Phu Yen and Khanh Hoa's Van Phong. The Deo Ca Tunnel, which was put into operation in August 2017, is the second longest mountain road tunnel in the country, after the Hai Van Tunnel, which is 6.28 kilometres long and runs between Thua Thien in Hue Province and Da Nang City.

Geological conditions

The tunnels were excavated in the granite and gneiss layers with uniaxial compressive strengths higher than 100 MPa, using drilling and blasting method. Because of the changing of the level of top mountains along the direction of tunnel, hence in this study using numerical modelling for typical sections in case of R2B rock mass, the granite layers with RMR > 60. The geological conditions can be seen as in Table 1. Planning profile and geological conditions of Deo Ca tunnel are seen as in the (Figures1-3).

Tab. 1 - *Properties of rock mass*

Parameters	Siltstone
Unit weight of rock γ, MN/m^3	0.026
Uniaxial compressive strength of intact rock σ_{ci}, MPa	80
Tensile strength σ_t, MPa	0.5
Cohesion c, MPa	2
Friction angle φ	40
Young modulus E, MPa	2500
Poisson ratio v	0.3
Dilation angle ψ, degree	0
Residual friction angle c_{re}, degree	30
Span of roadways B, m	13.2
Height of tunnels H, m	9.5

Fig. 1 - *Planning profile of Deo Ca tunnel*

Fig. 2 - *Geological profile of Deo Ca tunnel*

Fig. 3 - Profile of two tunnels

Numerical modelling

In this section, the simulation results obtained from Phase 2 (i.e. Rock and Soil 2-dimensional analysis program) are presented due to it is believed to be an effective method for support design which has been widely used in mining engineering, especially in terms of the deformation mechanics of surrounding rock mass. The length of the numeric model is 113.2 m and the height 66.5 m respectively. The all boundaries of the model are applied to the fixed conditions to simulate the real application.

The supports used by rock bolts with diameter of bolts d = 22 mm; Young modulus of steel in rock bolts E = 200000 MPa; tensile capacity of bolts - 0.15 MN; out of plane spacing of bolts - 1.5 m; in plane spacing of bolts 1.5 m. The length of bolts can be defined based on the radius of plastic zone around tunnels, here length of bolts L = 3500 mm. Existing tunnels supported by concrete liner with the thickness 350 mm, rebar of steel d = 22 mm; spacing of rebar 250 mm.

Blasting pressures are applied in the model by using seismic loading coefficient by formula:

$$P = K_c.\gamma \tag{1}$$

Here K_c - seismic coefficient; γ - body forces of rock mass.

The Seismic coefficients are dimensionless coefficients which represent the (maximum) earthquake acceleration as a fraction of the acceleration due to gravity. Typical values are in the range of 0.1 to 0.3. In this study we used the range values of K_c = 0.1; 0.2; 0.3; 0.4; 0.5; 0.6 respectively.

Based on numerical method with using Phase 2 and seismic coefficient can be received model (Figure 4) and the result of displacement vectors of rock mass around tunnel as in the (Figure 5). Using results of numerical method can be established the relationship between the stress and displacements of rock mass on the boundary of existing tunnels and the changing of seismic coefficient, bending moment of concrete lining with other values of seismic coefficients. The results can be seen as in the (Figures 6-8).

The research results indicate that the values on the vertical axis which located in the left corner of existing tunnels, the minimum displacements located in the rightwall of the old tunnel respectively, besides the maximum values of displacements are investigated on the floor near the left corner of existing tunnels. Basing the assessment standards for the stability of tunnels can show that if the values of displacements of rock mass around tunnels and concrete lining are bigger than limited values, the concrete lining will be cracked. The results of research also show that it is necessary to use some solutions for blasting technologies to reduce blasting vibration on the existing tunnel.

(a) The initial model *(b) Model using seismic loading coefficients*
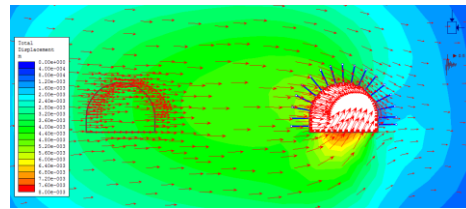
Fig.4 - Blasting model new tunnel near the existing tunnels

(a) Displacement vector in case of seismic coefficient $K_c = 0.1$ *(b) Displacement vector with the seismic coefficient $K_c = 0.5$*

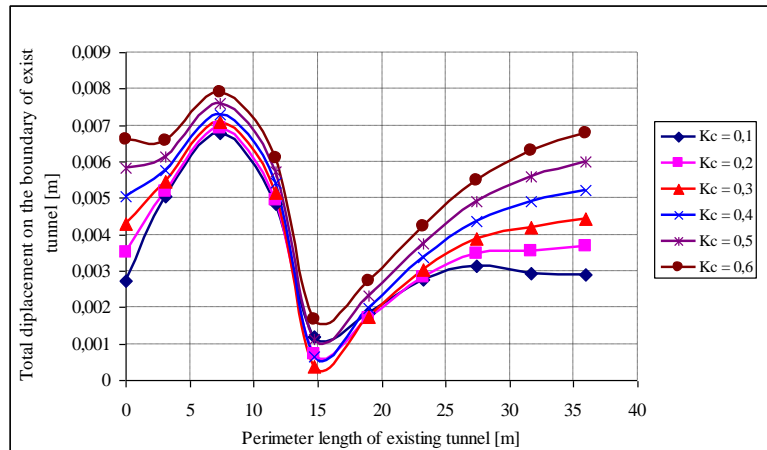*Fig. 5 - Displacement vector of rock mass around tunnels*

Fig. 6 - The changing of displacements of rock mass around existing tunnel
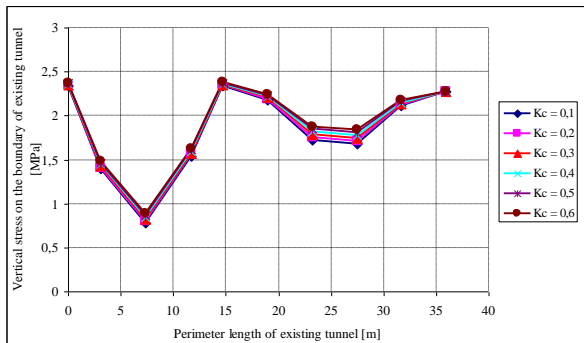
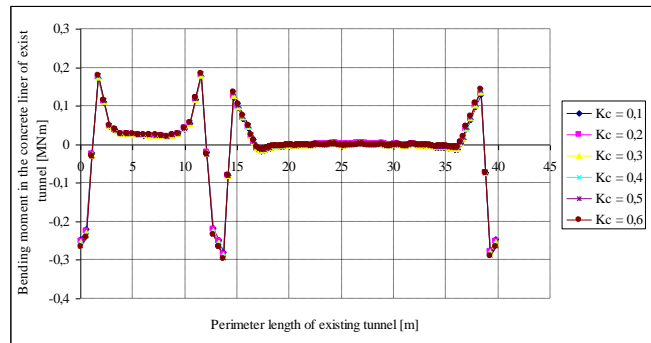*Fig. 7 - The relationship between stress around existing tunnels and K_c*

Fig. 8 - Bending moment in concrete lining of existing tunnel with other values of K_c

NUMERICAL MODELING USING EQUIVALENT BLASTING PRESSURE FOR COMA TUNNEL PASS PROJECT

The Co Ma Tunnel is a 2 tube tunnel that was built as a part of the Ca pass tunnel and road project to reduce the travel distance for commuters by 8 km between the Khanh Hoa and Phu Yen provinces and to help them avoid landslides during the rainy season.

Opened in September 2015, vehicles can travel at a maximum speed of 80 km per hour through this 500 m long tunnel. The tunnel operators wanted an energy-efficient lighting solution that would ensure the safety and comfort for all users at all times.

The supports used by rock bolts with diameter of bolt d = 22 mm; Young modulus of steel in rock bolts E = 200000 MPa; tensile capacity of bolts - 0.15 MN; out of plane spacing of bolts - 1.5 m; in plane spacing of bolts 1.5 m. The length of bolts can be defined based on radius of plastic zone around tunnels, here length of bolts L = 3500 mm. Existing tunnels supported by concrete liner with the thickness 350 mm, rebar of steel d = 22 mm; spacing of rebar 250 mm. The length of the numerical model is 113.2 m and the height 66.5 m respectively (Figure 9). The all boundaries of the model are applied to the fixed conditions to simulate the real application. Here, the values of equivalent blasting pressures are applied in the model by distributed loads (P) in new tunnels from 1 MPa; 2 MPa to 12 MPa, the weight of explosion at the same time Q = 50 - 150 kg respectively.
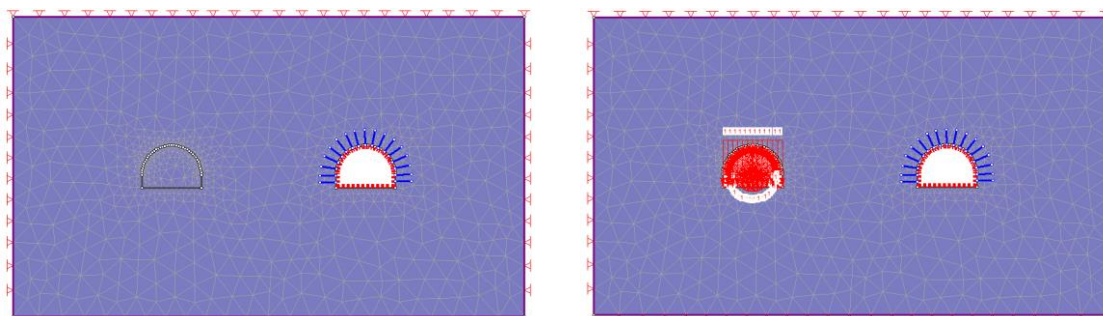
(a) Initial model without new tunnel

b) After excavation blasting new tunnel

Fig. 9 - Numerical modeling for excavation new tunnel using equivalent blasting pressure and existing tunnels in Co Ma pass project in Viet Nam

The research results (Figures.10-14) indicate that the values on the vertical axis which located in the left corner of existing tunnels, the minimum displacements located in the rightwall of old tunnel respectively, the maximum values of displacements are investigated on the floor near the left corner of existing tunnels. Basing the assessment standards for the stability of tunnels, if the values of displacements of rock mass around tunnels and concrete lining are bigger than

----

limited values, the concrete lining will be cracked. The results of research also show that in case of using equivalent blasting pressure 7 MPa the internal forces in the concrete liner of existing tunnel are negligibly changed. It is necessary to use some solutions for blasting technologies to reduce blasting vibration on the existing tunnel and the weight of explosion in new tunnel will be less than 50 kg respectively.
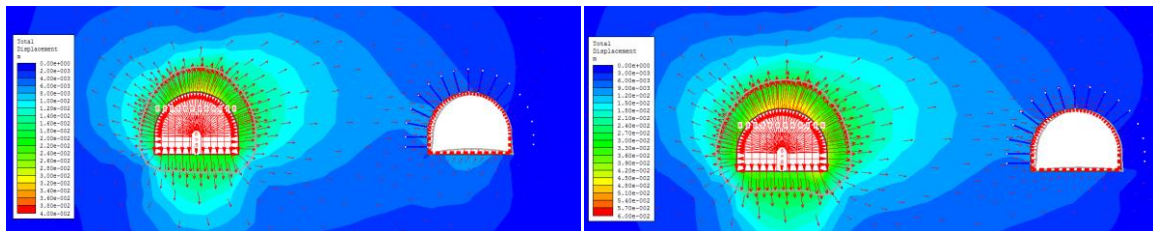
(a) Displacement vector in case of equivalent blasting pressure P = 6 MPa

(b) Displacement vector incase of equivalent blasting pressure P = 8 MPa

Fig. 10 The distribution of displacement vector in rock mas around two tunnels
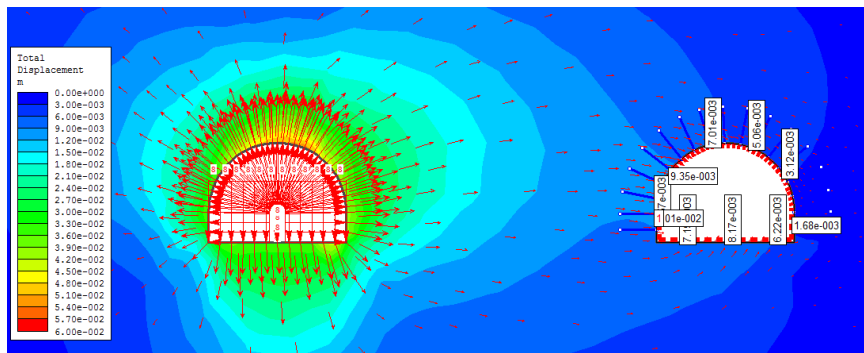
Fig. 11 - The values of displacement on the boundary of existing tunnel in case of P = 6 MPa
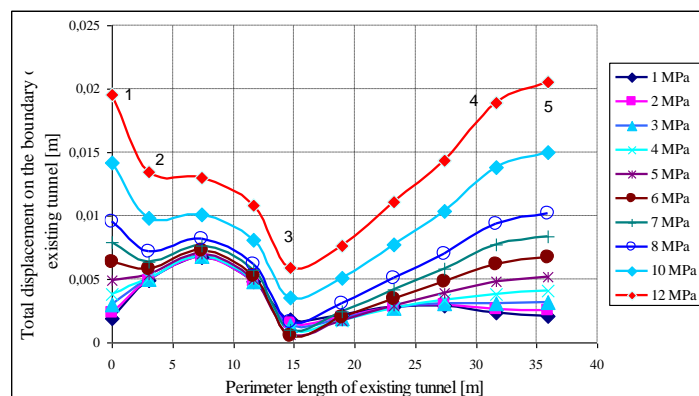
Fig. 12 - The changing of displacements of rock mass on the boundary of existing tunnel
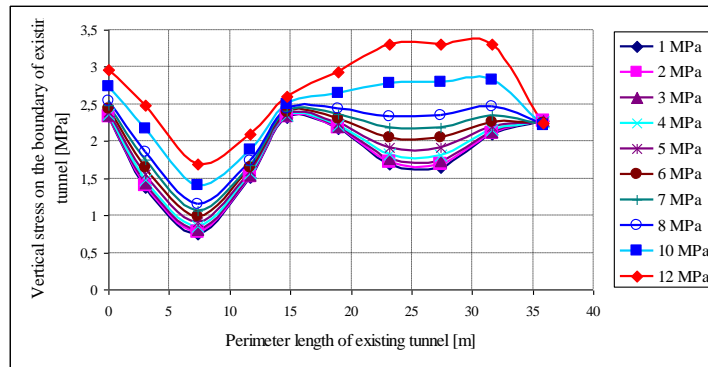
Fig. 13 - The relationship between vertical stress in rock mass around existing tunnel
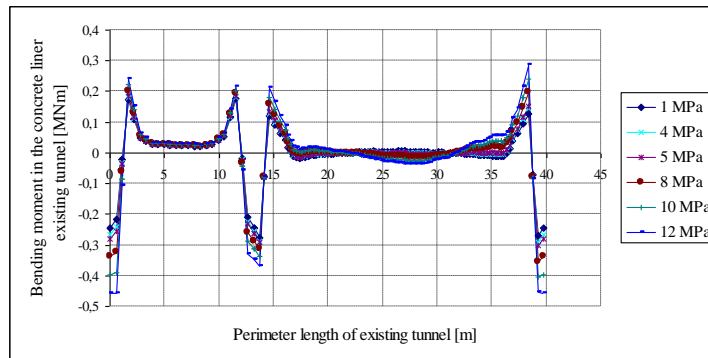
Fig. 14 - The changing bending moments in the concrete lining of existing tunnel

NUMERICAL MODEL IN CASE OF EXPANSION BLASTING THE AUXILIARY TUNNEL NEAR THE OLD TUNNELS IN HAI VAN PASS PROJECT OF VIETNAM

Hai Van pass project located between Thua Thien Hue and Da Nang provinces of Vietnam, main tunnel was finished in 2005 with the total length of tunnel 6280 m with twin parallel tunnels, 4 lanes in each tunnel, and two ventilation shafts. Main tunnel has total length 6280 m, span of tunnel 13 m, the distance between main tunnel and auxiliary tunnel is 30 m, area of auxiliary tunnel before expansion is 15,5 m^2, the height of auxiliary tunnel 4.5 m, span 5.3 respectively, View 3D for Hai Van tunnel project can be seen as in (Figure 15).
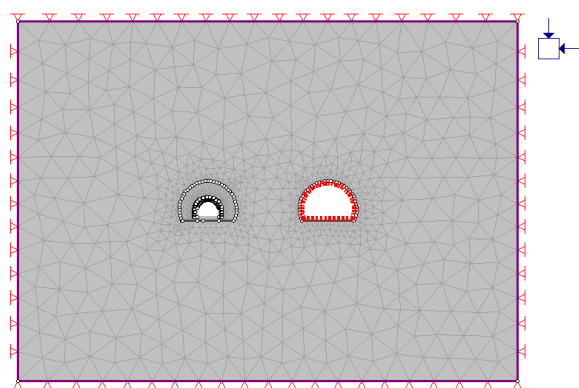
Fig. 15 - View 3D for Hai Van tunnel in Viet Nam

Fig. 16 - Numerical modeling by Phase 2

In this study numerical a method will be used for analysis. Because of the difference of the geological conditions along tunnels to model for research is chosen the range of quality of rock mass with RMR ratio in the catalogues of Bieniawski RMR = 60 - 80. Base on the results of investigation for rock mass conditions and profile of the auxiliary tunnel with span 5.3 m and height 4.5 m. In the main tunnel concrete lining has the thickness 35cm, rebar with diameter d = 22 cm, and space of rebar reinforcement a = 20 cm. Using numerical method PHASE 2 can be received model in this case as in the (Figure16**)**. In the case study using the dimension of external boundary of model is 125 m and height 90 m, number of nodes and elements in model 14438, 24710 respectively, equivalent blasting pressure in this model can be defined by formula:

$$P = 0{,}00337\rho v^2 \qquad\qquad (2)$$

Where:

P - Blasting pressure, psi; ρ - Density of explosion; v - Velocity of explosion, fps.

Its assumption that the blasting pressure in the holes of drilling pattern in the auxiliary tunnel before expansion from existing profile to the design profile of tunnel are replaced from 7 to 20 MPa as in the (Figure 17).
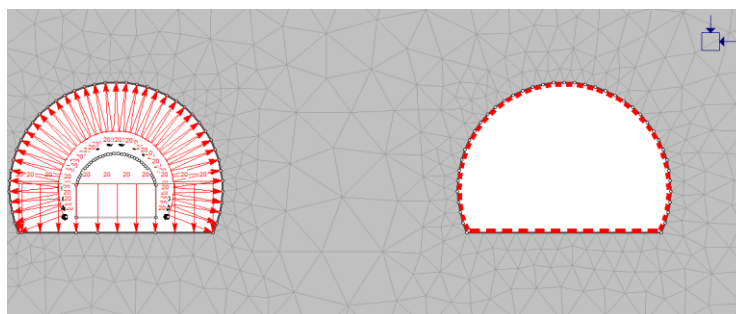
Fig. 17 - Numerical simulation for expansion the auxiliary tunnel of Hai Van in case of P = 20 MPa

Based on the values of internal forces in concrete lining of main tunnel when changing the values of blasting pressure during excavation expansion the auxiliary tunnel are calculated the minimum values of blasting pressure effecting on the linings of existing support in the main tunnel of Hai Van pass project. The results of the distribution of displacement vector and zone damage of explosion around the auxiliary tunnel and main tunnel when changing the values of equivalent blasting pressure can be shown as in (Figure18).

(a) The distribution of displacement vector   (b) zone damage of explosion
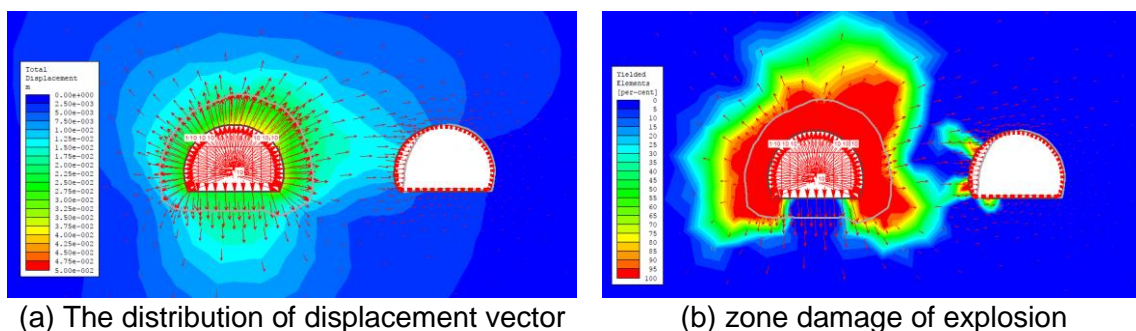
Fig. 18 -The results of displacement vector and zone damage of explosion around the auxiliary tunnel in case of blasting pressure 10MPa in Hai Van pass

To assessment the changing internal forces in the concrete lining of existing tunnel of Hai Van pass project, established the relationship between the values of blasting pressure in the

----

auxiliary tunnel and the internal forces of concrete lining in the existing tunnel. Research results can be seen as in the (Figures.19-21).
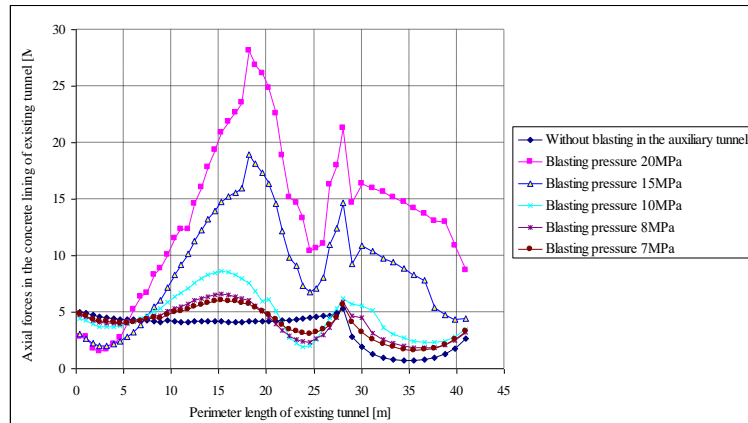
*Fig. 19 - Alternation of axial force in the concrete lining of existing tunnel before and after expansion blasting the auxiliary tunnel*
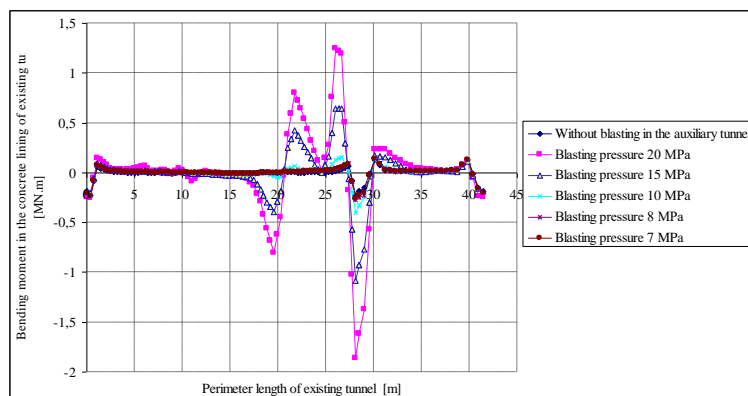
Fig. 20 - Changing bending moment in the concrete lining of existing tunnel before and after expansion blasting the auxiliary tunnel
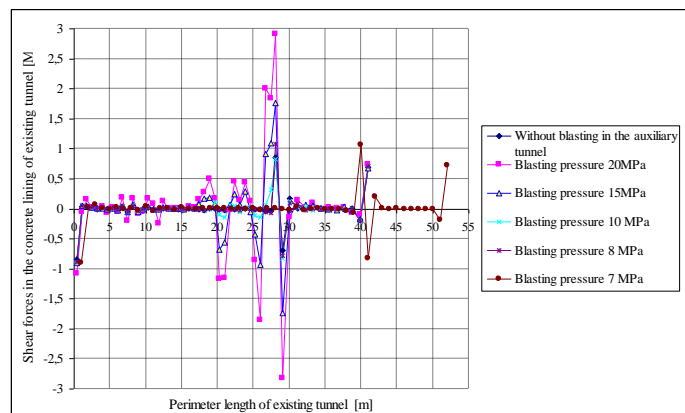
Fig. 21 - Variation of shear forces in the concrete lining of existing tunnel before and after expansion blasting the auxiliary tunnel

Results in the (Figures19-21) show that, if the values of internal forces in the concrete lining in old tunnel are equal these values in the lining before expansion blasting the auxiliary tunnel, can

be received optimal blasting pressure during blasting in the auxiliary tunnel. Results can also show that, in case study the values of blasting pressure 7 MPa is optimal. Base on this value should have to control blasting solution to reduce blasting pressure on the boundary of auxiliary tunnel will be less than 7 MPa.

NUMERICAL MODELING THE STABILITY OF CONCRETE LINER IN THE EXISTING RAILWAY IN CO MA PASS PROJECT

In this section present the effects of blasting vibration on the stability of concrete liner of railway tunnel in the geological conditions of Co Ma pass project. Railway tunnel was built 100 years ago by France, tunnel located Km 1234+464 in Dai Lanh commune, Van Ninh district, Khanh Hoa province. Height of railway tunnel 4.0 m, span of tunnel 4.33 m respectively. Site plan of railway tunnel $N^0 24$, Co Ma transported tunnel and profiles of them can be seen as in the (Figures 22-24). Railway tunnel was supported by concrete liner, the properties of rock mass around railway tunnel and support liner can be seen such as [9]:

Properties of back fill around concrete liner (Silstone - 1): Poisson ratio $v = 0.331$; Unit weight of back fill material $\gamma = 0.0255$ MN/m³; Friction angle $\varphi = 18$ Degree; Young modulus $E = 1583$ MPa; Cohesion $c = 0.36$ MPa.

Properties of rock mass around railway tunnel (2): Uniaxial compressive strength of intact rock $\sigma_{ci} = 80$ MPa; Unit weight of rock mass $\gamma = 0.0255$ MN/m³; Tensile strength $\sigma_t = 0.3$ MPa; Cohesion $c = 1.0$ MPa; Friction angle $\varphi = 25$ Degree; Young modulus $E = 5000$ MPa; Poisson ratio $v = 0.293$; Residual friction angle $c_{re} = 22$ Degree; Span of roadways $B = 13.2$ m; Height of tunnels $H = 9.5$ m; Depth of tunnels, 70m; Lateral earth pressure coefficient $K_0 = 1.0$.

Properties of old concrete liner in railway tunnel (3): Poisson ratio $v = 0.3$; Unit weight of concrete liner $\gamma = 0.022$ MN/m³; Young modulus $E = 3000$ MPa.
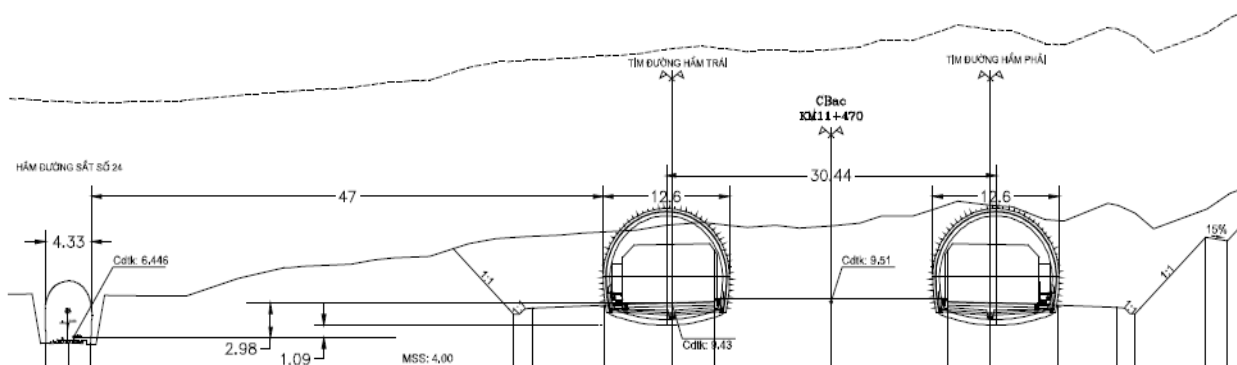
Fig. 22 - Profile of railway tunnel $N^0 24$ and transported tunnel under Ca pass [9].
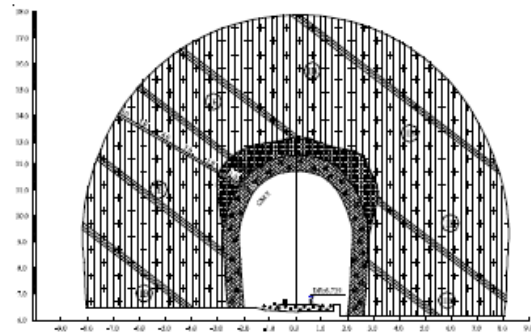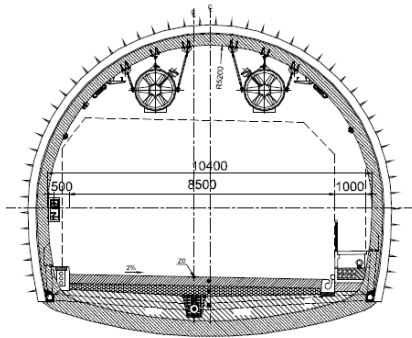
Fig. 23 - Profile of new transported tunnel

Fig. 24 - Profile of existing railway tunnels N⁰24

Using numerical method in Phase 2 can be received model in this case as in (Figure 25). In the case study using the dimension of external boundary of model is 113.2 m and height 66.5 m, number of nodes and elements in model 2092, and 4020 in case of without new transported tunnel, and 1974 nodes and 3720 elements respectively when creating a new transported tunnel in the model as in the Figures 25 and 26. The conditions of external boundary of model are chosen fixed strain such as in the rock mass far from boundary of new tunnel the stress will be initial values.
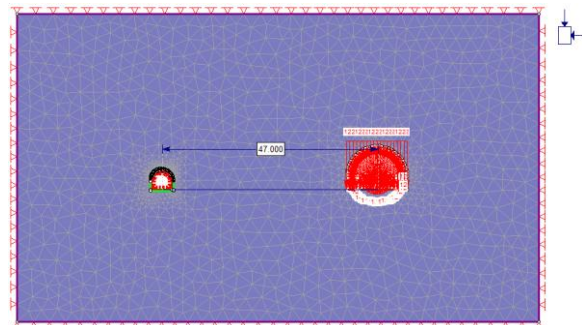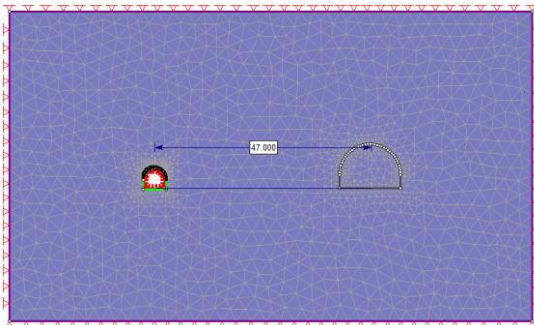
Fig. 25 - Model of railway tunnel without new Co Ma transported tunnel

Fig. 26 - Equivalent blasting pressure in new tunnel and existing railway tunnel N⁰24
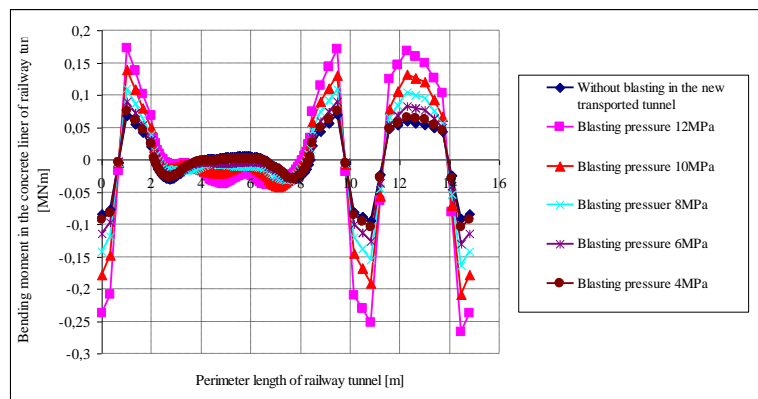
Fig. 27 - The changing of bending moment in the concrete liner of existing railway N⁰24 with other values of equivalent blasting pressure in new transported tunnel Co Ma.
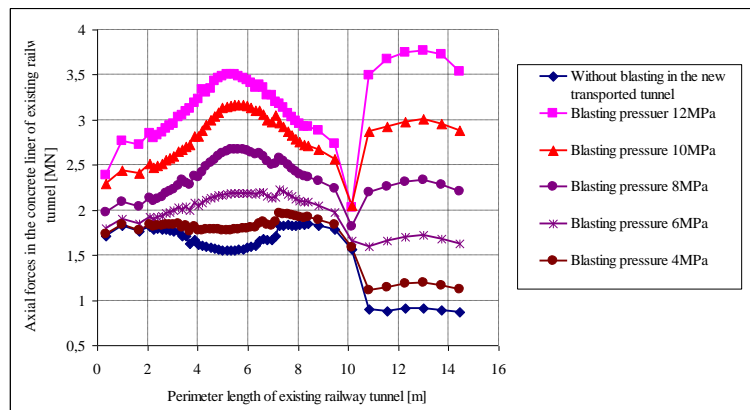
Fig. 28 - Axial forces in concrete liner of existing railway tunnel
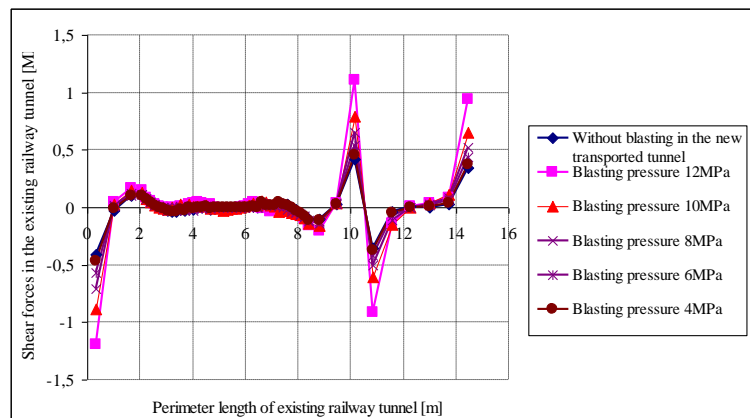
Fig. 29 - Shear forces in concrete liner of existing railway tunnel

Results in (Figures 27-29) can show that, the values of internal forces in the concrete liner of existing railway tunnel are the same as these values of this concrete liner in case of without new transported tunnel, the values of blasting pressures will be optimal. By research results can be received the optimal blasting pressure in this case 4 MPa, the equivalent weight of explosion at the same time during excavation new tunnel approximately 42 kgs explosion of P3151.

EXPERIMENTAL INVESTIGATION OF THE RESULTS

In the experiences excavation tunnels contour and smooth blasting methods can be used to reduce effects vibration of blasting during expansion the auxiliary tunnel on the stability of concrete lining in the existing tunnel in Hai Van pass project in Vietnam. In this project recommended using characteristics of drilling and blasting parameters of drilling pattern such as in (Tables.2-3).

Experimental blasting in Hai Van pass project shows that, when using optimal blasting pressure 7 MPa on the contour of the auxiliary tunnel, the values of internal forces in concrete lining of existing tunnel in Hai Van are not change. In the case study the density of explosion in each hole is less than 1kg, total density of explosion at the surface of tunnel less than 45 kgs. The results of explosion of project can be shown as in figs.30-32.

Tab. 2 - Parameters of drilling and blasting pattern recommended during expansion the auxiliary tunnel in Hai Van Pass project of Viet Nam

N^0	Parameters	Symbol	Values	Units
1	Length of holes	L_k	1.	m
2	Spacing holes	W	0.8	m
3	Specific charging of explosion	q	kg/m^3	0.8
4	Total density of explosion	Q	kg	42.75
5	Total number of blast holes in the surface	N	98	holes
6	The length of explosive in the holes	L_e	0.6	m
7	The uncharged length in the cut holes	L_u	0.7	m
8	The length of explosive in the holes in the contuor holes	L_3	0.3	m
9	The uncharged length in the contuor holes	L_c	1.0	m

Fig. 30 - Drilling and blasting works when expansion the auxiliary tunnel in Hai Van project
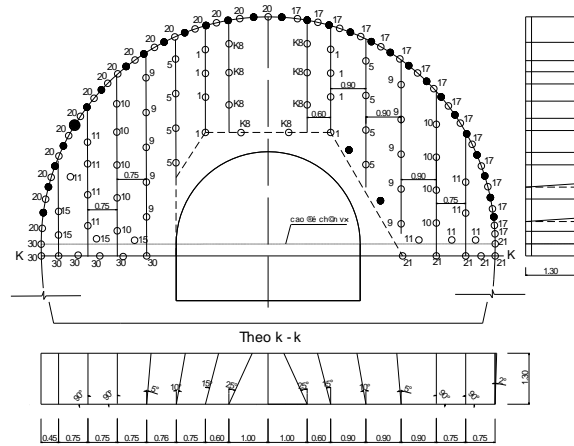
Fig. 31 - Holes pattern in the surface of the auxiliary tunnel

Tab. 3 - Characteristics of holes in the face of auxiliary tunnel

N^0	Number of blast holes	Holes	Electrical detonator	Time delay	holes	length of holes	Total density of explosion, kg			The uncharged length, m	Length of holes	Angle of holes, degree	
							one hole	total density	total holes			Vertical	Horizontal
1	fire hole 1	1-8	1	25	2	1.3	0.6	4.8	8	0.7	5.6	90	115
2	fire hole 2	9-16	5	125	2	1.3	0.6	4.8	8	0.7	5.6	105	105
3	fire hole 3	17-24	9	250	1.5	1.3	0.45	3.6	8	0.85	6.8	90	100
4	fire hole 4	25-34	11	350	1.5	1.3	0.45	4.5	10	0.85	8.5	90	95
5	fire hole 5	34-41	13	450	1	1.3	0.3	2.4	8	1	8	90	90
6	fire hole 6	42-51	15	600	1	1.3	0.3	3.3	11	1	11	90	90
7	contour holes	52-66	17	800	1	1.3	0.3	4.8	16	1	16	90	92
8	lifter holes 1	67-75	20	1125	1	1.3	0.3	4.8	16	1	16	90	92
9	lifter holes 2	76-80	21	1225	2.5	1.3	0.75	4.5	6	0.55	3.3	90	92
10	lifter holes 2	81-98	30	4350	2.5	1.3	0.75	5.25	7	0.55	3.85	90	92
	Total							**42.75**	**98**				
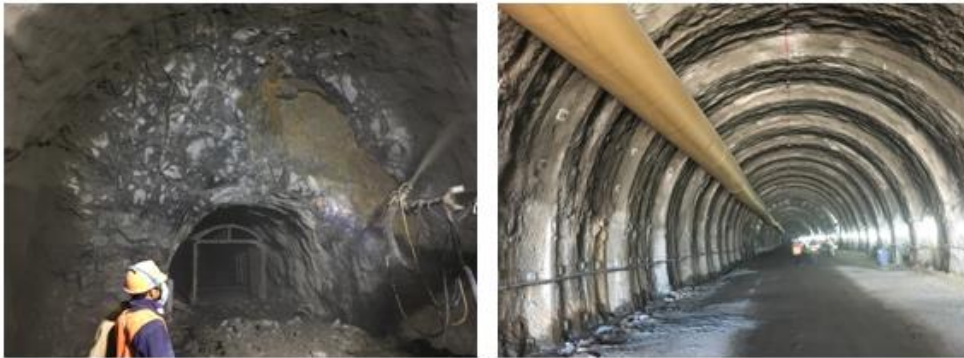
Fig. 32 - Investigation blasting results after expansion the auxiliary tunnel in Hai Van pass project

CONCLUSION AND DISCUSSION

The above research results can show that, blasting vibration during excavation new tunnels has influence on the stability of rock mass around existing tunnel such as the stability of support lining of existing tunnel. Blasting vibration can be replaced by equivalent blasting pressure in the numerical modelling which impact on the stability such as displacements, stress on the boundary of old tunnel, and the values of internal forces in the support liner of existing tunnel.

Based on the determination of the optimal values of equivalent blasting pressures can be explained that the existing tunnel will be stable in case of drilling and blasting in the new tunnel has not influence on the values of internal forces in support liner of existing tunnel.

Experimental blasting in Hai Van pass project shows that, when using optimal blasting pressure 7 MPa on the contour of the auxiliary tunnel, the values of internal forces in concrete lining of existing tunnel in Hai Van are not change. In case study the density of explosion in each hole is less than 1kg, total density of explosion for surface less than 45 kgs and using 10 delay times for other holes group. The vibration of process blasting and drilling in the auxiliary tunnel have not influence on the stability of old linings.

The results of experimental blasting in Co Ma pass project in case of excavation new transported tunnel near the railway tunnel can indicate that, using optimal blasting pressure 4 MPa on the contour of new tunnel, the drilling and blasting in new tunnel has not influence on the stability of old railway tunnel. The weight of explosion at the same time in new tunnel over 40 kgs.

Received results also show that in the practice when building new tunnels near the existing tunnel to reduce effects of vibration of blasting can be used other blasting solutions such as using many delay times between holes, types of electrical detonators, direction controls of vibration ways, arrangement of cut holes in the surface, using empty holes etc. In other words, appropriated drilling and blasting parameters must be controlled and used, both models for smooth and contour blasting are recommended in the contour of the auxiliary tunnels.

REFERENCES

[1]   Vo Trong Hung, Le Dinh Tan, Nguyen Tien Khiem., 1999. Research on dynamic behaviors of rock mass and supports of tunnel under blasting wave. Journal of geotechnics, N01, Ha Noi. pp15-20.

[2]   Le Dinh Tan (2000). The dynamic calculation of underground structures under impacting of blasting wave. Doctor thesis. Military Technical Academy, Ha Noi.

[3]   Regulation of safety, maintain, using and transportation of industrial explosions. QCVN 02:2008/BCT.

[4]   Nguyen Xuan Man et al (2010). Determination of failure zone diameter of single explosions in rock mass. Proceeding of the 19th conference Ha Noi University of mining and geology. Ha Noi.

[5]   Nguyen Hai Hung et al (2014). The effects of delay time on the military structures. Proceeding of the 19th conference Ha Noi university of mining and geology. Ha Noi.

[6]   Dang Van Kien (2014). Investigation blasting vibration during excavation tunnel by drilling and blasting method in the urban conditions by two-dimension model. Journal of mining industrial. N06, Ha Noi. pp7-12.

[7]   Dang V.K., Dias D., Do N.A., Vo T.H. (2018), Impact of Blasting at TunnelFace on an Existing Adjacent Tunnel. International Journal of GEOMATE, July, 2018 Vol.15, Issue 47, pp.22-31, 2018.

[8]   Dam Trong Thang, Bui Xuan Nam, Tran Quang Hieu. Blasting in mining and structures. Publishing house of natural and technology science. Ha Noi 2014. 454p.

[9]   Nguyen Hieu Nghia, Nguyen Duc Thuan (2016). Some problems for safety during excavation transported tunnels through the mountain by NATM using blasting near the operated buildings, Centre TVTK KCCT-TEDI. Designastion and consultion information - N0III/2016, pp34-45.

[10]   Martin stolárik (2008). Modeling of vibration effect within small distances, Acta Geodyn. GEOMATE, Vol.5, No.2 (150), 137-146.

[11]   Jens Anders Brenne Volden Engineering (2015). Geological evaluation of the applicability of Drill & Split in tunnels at the Follo line project. Norwegian University of Science and Technology. June 2015.

[12]   Jinxing Lai,[1,2] Haobo Fan,[2] Jianxun Chen,[1,2] Junling Qiu,[2] and KeWang[2]. [1]Shaanxi Provincial Major Laboratory for Highway Bridge & Tunnel, Chang'an University, Xi'an 710064, China; [2]School of Highway, Chang'an University, Xi'an 710064, China. Blasting Vibration Monitoring of Undercrossing Railway Tunnel Using Wireless Sensor Network. 10 March 2015.

[13]   Qingguo Liang· Jie Li· Dewu Li· Erfeng Ou. Effect of Blast-Induced Vibration from New Railway Tunnel on Existing Adjacent Railway Tunnel in Xinjiang, China. Rock mechanics and rock engineering. January 2012.

[14]   Мангуш С.К, Крюков Г.М, Фисун А.П (2000). Взрывные работы при подземной разработке полезных ископаемых, Москва 2000.

TRAFFIC VOLUMES TEST OF AIRPORT RUNWAY

Xingang Shi, Liangcai Cai and Guanhu Wang

University of Air Force Engineering, Department of Airport Construction Engineering, Xi'an, China; kgdwxsxg @163 .com, 994174763 @163.com, 794599756 @qq.com

ABSTRACT

Currently, airport pavement design only considers the different horizontal standard deviation at the end and the middle of the runway, which had ignored the longitudinal distribution of airport runway traffic volume (ARTV). Especially for short take-off and landing aircraft, the take-off and landing distribution are not full of the whole runway. In allusion to the characteristics of ARTV, this paper developed a test system for the wheel track distribution and conducted a test of a short take-off and landing aircraft. Based on the statistics and analysis of test results, the horizontal and longitudinal distribution statistical laws of ARTV were obtained. At last, the longitudinal passage factor was proposed, and the planar distribution model was established to evaluate the ARTV at each point of the runway. By comparison with current design specifications, it is indicated that the pavement thickness will be designed more conservative without considering the planar distribution of traffic volumes.

KEYWORDS

Airport, Pavement design, Traffic volume, Planar distribution, Influence factors

INTRODUCTION

The design of a new runway requires information on many parameters: including airport runway traffic volume (ARTV), coverage and pass-to-coverage ratio, mixed traffic analysis if there is more than one significant aircraft and design life. Among all the parameters, ARTV was defined as number of aircraft wheel passes the pavement [1]. In the beginning, the ARTV model was simplified as the uniform distribution [2]. As early as the late 1950s, the USA Air Force had carried out tests on ARTV. Based on the test data, it was suggested that the airplane wheel tracks were uniformly distributed in the 1/3 width range of the middle runway [3]. In 1960, Vedros, professor of USA Army Engineering Laboratory, put forward the Pass-to-coverage ratio to build the uniform distribution model, which was widely recognized and concerned [4]. The field survey results of aircraft distribution in Buffalo International Airport and Atlanta International Airport [5][6] shown that the APTV model was better fitted by a normal distribution.

Review of the pavement design methods in various countries, different considerations were given to the lateral distribution of ARTV. Airport Pavement Structural Design System in Australia suggested that the transverse distribution standard deviations of wheel track were 1.8m to 3.4m, 0.8m to 1.8m and 2.4m to 3.2m in runway, taxiway and connection lane, respectively [7]. In 2003 Boeing, in conjunction with FAA, conducted the B747 aircraft wheel track lateral offset tests using laser testing technology at New York's Kennedy International Airport and Anchorage International Airport [8][9]. According to the results of previous tests, the standard deviation of transverse distribution was determined as 30.435 inch (773 mm) in FAA consultation bulletin (150/5320-6E) [10]. The specification revised in 2016 (AC 150/5320-6F) also adopted the same distribution model [11] [12]. It is assumed that the lateral distribution of wheel tracks is standard Beta distribution in

----

the Guideline on PCN Assignment of Netherlands [13]. The wheel tracks standard deviations of take-off and landing are recommended as 2.4 m and 2.6 m for 45 m runway width, 2.4 m and 3 m for 60 m runway width. In the pavement design guidelines for Japanese airports, the distribution of front landing gear in the cross direction of runway is classified according to the design load. The range of runway standard deviations for take-off and landing are 0.42 m to 0.91 m and 1.31 m to 1.74 m [14] [15].

In China, Multiple aircraft wheel tracks had been recorded by Lu and Wang, suggesting the normal distribution of APTV [16] - [18]. The newly revised asphalt pavement design in China (MH/T 5010-2017) [19] also adopted the same distribution model as FAA. Normal distribution of APTV was more suitable in coverage calculation than uniform distribution based on the research of Li and Lin [20][21]. Lei [22][23] conducted a comprehensive comparison of the lateral distribution test systems including infrared, video, piezoelectric and laser. Finally, laser testing technology was determined to carry out the lateral offset tests in Hongqiao Airport. The measured results showed that the wheel track distribution obeys a negative skew distribution with a mean value of 0.17m and a standard deviation of 0.99. Furthermore, Shi et al. [24][25] used the used the test statistical results for the pavement response study. It can be seen from the above reviews that in the field of pavement thickness design [26], runway width design [27] and pavement remaining life prediction [28], the lateral distribution of APRV had been widely used.

The distribution of ARTV evolved from uniform to normal, which declared the method progressed from "point" to "line". However, it is quite clear that ARTV could not bestrew the whole runway especially for military aircraft using both sides and whose taking off distance was less half of the runway. There is not only lateral distribution in the ARTV, but also longitudinal distribution due to different take-off and departure spots, landing locations and aircraft sideslips, especially for short take-off and landing aircraft. There is limited information in literatures describing the longitudinal distribution of APRV. This paper developed a test system for the wheel track distribution and conducted a test of a short take-off and landing aircraft. Then based on the statistics and analysis of test results, the horizontal and longitudinal distribution statistical laws of ARTV were obtained. The planar distribution model was established to evaluate the ARTV at each point of the runway, which provided a new method for the description of APTV.

CHARACTERISTICS OF ARTV

Compared with the traffic volume of highway, the ARTV has the following characteristics: First, ignoring the influence of short-distance acceleration, it is approximated that speed and load of the vehicle are constant when driving in the lane. That is, the motion states of vehicles in different cross-sections are unchanged. However, the lift of an aircraft is subject to changes in speed, resulting in loads variation acting on different cross-sections. Second, the road traffic volume is calculated by the direction coefficient, the lane coefficient and the vehicle type distribution coefficient. The distribution coefficient is constant, that is, the vehicle wheel track is assumed to be evenly distributed in the lane. The ARTV is calculated by multiplying the traffic coverage rate and the number of traffic passes. The traffic coverage rate reflects that the statistical law of the wheel track in the cross section, which obeys the normal distribution. Besides, same state of motion and same distribution of traffic volume is assumed when the vehicle is driving in the lane, while the lateral standard deviation of ARTV has changed because of the aircraft taking off offset the runway centerline, and landing alignment the runway centerline. Last but not least, the road traffic volume is constant in the longitudinal direction, while the ARTV in longitudinal direction is different due to diversification in aircraft take-off starting position, take-off running distance, landing grounding point position, and landing slip. However, the traffic volume distribution is similar to the highway traffic volume distribution in the taxiway, connecting lane, towing lane and tarmac, etc.

From above analysis, there are different traffic volumes in every point of the runway. In fact, the characteristics of ARTV consist of lateral and longitudinal distributions. The current specification only considered the lateral variance. Longitudinal distribution had been simplified as the different offset standard deviations at the edge of the runway and the middle of the runway. It is necessary to consider the longitudinal traffic distribution in pavement design.

ARTV TEST

Test methods and principles

Distance measuring techniques including infrared, video, piezoelectric and laser had been used to capture the wheel-track of the aircraft [22][23]. Infrared ranging method is that the transmitter sent infrared beam and when the wheels pass through cutting the beam, receivers cannot receive the infrared signal to trigger the event and record the wheel track position. It is clear that the infrared ranging method has the advantages of high propagation speed and low cost. However, the receiving and transmitting devices of the system are arranged at a long distance, and the system has poor anti-interference ability. Besides it is difficult to measure the offset of the complex axial type, and the test accuracy is greatly affected by the environment. The video test technology arranges high-speed cameras at the end of the runway to capture the position of the landing point. And the distribution of the wheel trace was obtained by analyzing the video images. Thus, the system is easy to install, simple to maintain, and intuitive to process the test results, while there are also high requirements for the camera, high cost, and heavy data processing task. What more, it is hard to extract of the landing point accurately. Pressure sensors or distributed optical fiber sensors were deployed under the pavement to measure the pavement response by Piezoelectric testing technology. The use of piezoelectric testing technology to test aircraft wheel tracks has low cost and high precision. But there are also defects such as large pre-distribution of the sensor and difficulty in repairing once damaged. Laser testing technology use laser transmitter to transmit laser beam. When the wheel passes by, the laser reflects, and the receiving device receives the echo signal. The distance between the wheel and the rangefinder is calculated by the product of wave velocity and time difference. This method has stable performance, strong anti-interference, simple adjustment, high precision and moderate cost. The paper intends to use laser testing technology to measure the APTV.

Laser test system

As shown in Figure 1, the laser test system consists of five parts: laser ranging sensor, data storage unit, visible laser calibration device, instrument stents and power supply unit. The system adopts FSA-ITS02 laser sensor, produced by Shenzhen Lanshi Laser Radar Co., Ltd. The test accuracy of the system can reach 5cm and the measuring frequency is 2 kHz to 4 kHz. It can trigger the measurement of high-speed moving objects within 120m range. In order to meet the requirements of high-frequency acquisition and recording, industrial-grade serial data recorder produced by Shenzhen Jingmei Technology Co., Ltd was employed. The data transmission rate can reach 921600bps. After power-on, the trigger data will be stored in an SD card. The calibration system is a DANGER laser pointer which emits visible laser light before measurement to ensure perpendicularity between the test system and the runway. The power supply unit is a 12V/60A lithium battery, which can work continuously for 48 hours. The instrument bracket is made of aluminium alloy, which can provide sufficient support strength and reduce the weight of the equipment to facilitate equipment transportation and installation. The height of the sensor can be 75-100cm. The pitch angle of the device can be adjusted from -45°-45°.
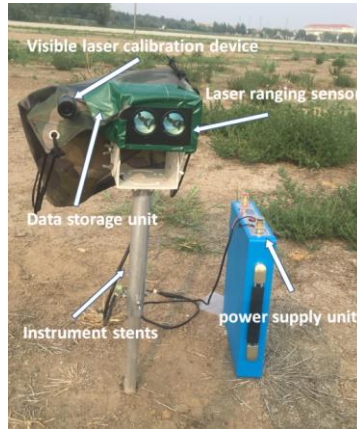
Fig. 1 - Field installation of test equipment

Test scheme

Test Profile and device arrangement

The test site was selected at an airport in Tianjin, whose runway length is 2800m×60m. The wheel track test of aircraft A was carried out according to the flight plan. A total of 436 flights were recorded. During the test period, more southerly winds were observed at the test site, so the north end of the runway was the main take-off and landing direction. The equipment was arranged at the north end of the runway according to the following principles:

The laser ranging device was arranged in the flat area on one side of the runway. The distance from the instrument to the center line of runway meet the flight safety requirements, which is generally not less than 60m. In order to avoid the bird-riding vehicle passage and the other inconvenient installation area, the distance from the equipment to the runway center line ranged from 63.2m to 93.3m. Layout distances of all test equipment are shown in Table 1. The longitudinal layout distance was arranged according to the principle that half of the runway should be covered, the landing site at the end of the runway and the take-off site in the middle of the runway should be densely arranged, and the taxiing region should be appropriately sparse. the test area of 1285m was divided into three parts:

(1) Landing region: the initial position was 191m away from the end of the runway, and 6 instruments were installed in total, covering the landing area. (2) Middle taxiing region: a total of 5 sets of equipment were installed in the high-speed taxiing area; (3) Take-off region: a total of 6 instruments were installed to cover the take-off position of the test aircraft.

Tab. 1 - Layout distances of all test equipment

Device number	1	2	3	4	5	6	7	8	9
Distance from the centerline of the runway (m)	72.2	73.5	78.2	78.6	82.7	82.9	83.1	87.8	63.2
Distance from the end of the runway (m)	191	239	277	368	430	483	562	652	740
Device number	10	11	12	13	14	15	16	17	
Distance from the centerline of the runway (m)	87.8	88.8	88.5	89.01	90.9	91.3	92.2	93.3	
Distance from the end of the runway (m)	814	881	972	1036	1101	1165	1222	1285	

Article no. 5

THE CIVIL ENGINEERING JOURNAL 1-2021

Installation Steps

(1)   Hammer the bracket and wedge it into the soil foundation in the flat area. Install the fixed laser ranging sensor, ensure the sensor slope is 0 (Figure 2 (a)).

(2)   The tester holds the self-made equipment debugging board (Figure 2(b)), stands near the centerline of the runway, and debugs the vertical line of the runway. The other tester turns on the calibration laser pointer and adjusts the height of the device so that the visible laser projection point is 25 ± 5 mm above the center of the runway (Figure 2(c)).

(3)   Adjust the angle of the sensor from left to right to make laser projection move around the debugging board. When the sensor reading is at the minimum, the device is perpendicular to the middle line of the runway (Figure 2(d)).

(4)   Install the memory card after power off and then restart to conduct the test (Figure 2(d)).

(a)   (b)   (c)

(d)   (e)
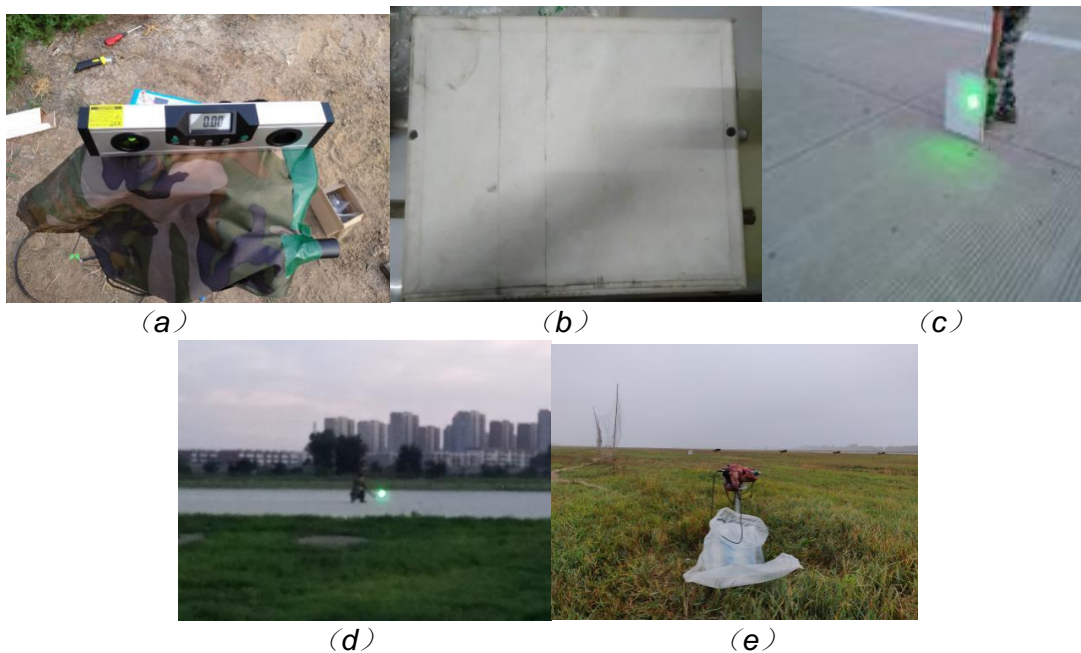
Fig. 2 - Installation step

LATERAL STATISTICAL REGULATION OF APTV

The Cartesian coordinate system was setup at the mid-point of the runway edge. x-direction is along the lateral edge of the runway, and y- direction is along the center line of the pavement. Figure 3 illustrates the coordinate system.
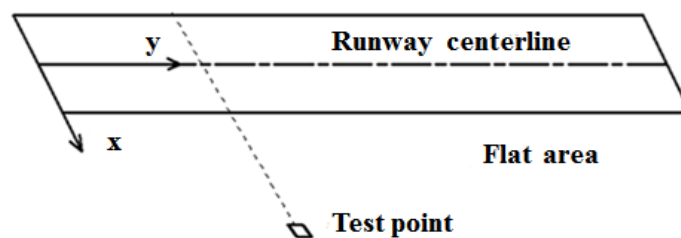
Fig. 3 - Coordinate system of the planar distribution model

The runway was divided into groups along x direction with the interval of 2 m length. And the coverage of each group was counted divided into the states including landing, single-aircraft take-off and double-aircrafts take-off (two fighter jets taking off at the same time, side by side).

Figures below show the horizontal distribution of APTV during landing recorded by equipment No.7 and No.14.
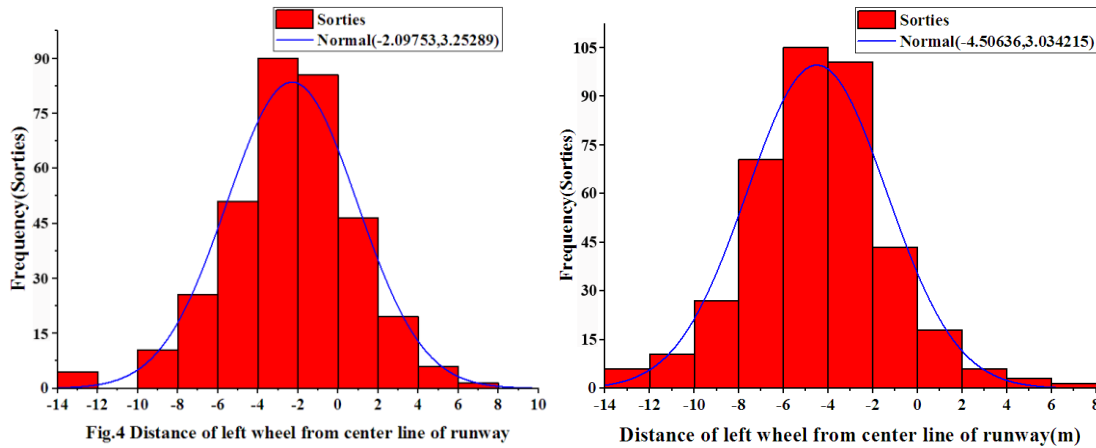
Fig. 5 - Lateral distribution histograms and fitting curves of landing wheel track by equipment No.7 and equipment No.14, respectively

As can be seen from the Figure 5, 333 aircraft passes through equipment No. 7. The test results have an average value of -2.290m and a standard deviation of 3.253m. Equipment no. 14 tested 357 sets of data, with an average value of -4.506m and a standard deviation of 3.034m. The frequency distribution histograms of the two groups were found to have good normality fitting. What is more the k-s test showed that the wheel offset of all the two sections follow the normal distribution.

Track volume for landing

The landing track volumes of the 17 groups were analyzed by the same statistical and hypothesis-test method. The equation and curve shown in Figure 5 were obtained by fitting the variation of the mean and standard deviation in y direction.
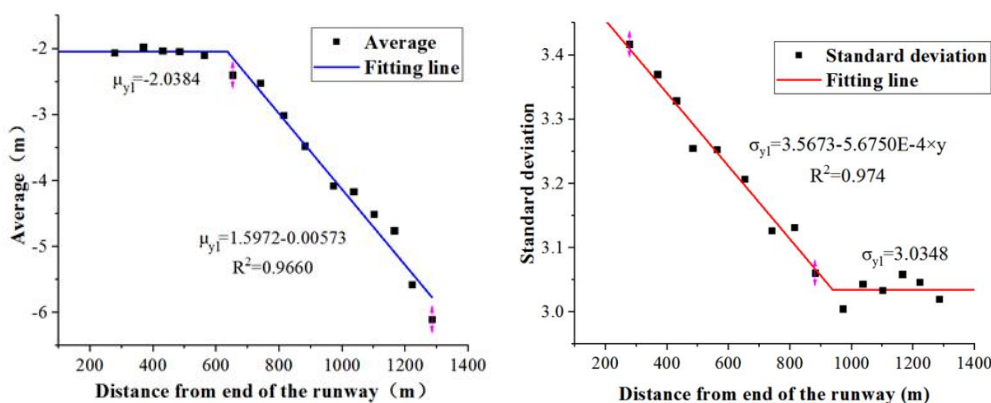
Fig. 5 - Mean value and standard deviation in y direction for landing track volume

The landing wheel coverage recorded by equipment No. 1 was only 49 times. There are insufficient data to acquire the statistics regulation of the cross section. From Figure 5, the average values of equipment from No. 2 to No. 7, -2.0385 was used to illustrate the beginning average. Average value from No. 8 to No. 17 decreased as the aircraft slowed down and deviated from the

----

runway centerline. It can also be seen from Figure 5 that the standard deviation decreased constantly after landing, as the aircraft aligned with the runway centerline. Besides, when the aircraft pass through equipment No. 12, the standard deviation maintained a constant. The variation mean value μ_{yl} and standard deviation σ_{yl} were represented by the following piecewise functions.

$$\mu_{yl} = \begin{cases} -2.0385 & , \quad 0 \le y \le 634.5 \\ 1.5972 - 0.00573y, & 634.5 < y \le 2500 \end{cases} \tag{1}$$

$$\sigma_{yl} = \begin{cases} 3.5673 - 5.6750 \times 10^{-4} \times y, & 0 \le y \le 938.3 \\ 3.0348 & , \quad 938.3 < y \le 2500 \end{cases} \tag{2}$$

The above track value of landing refers to the outside edge of the main landing gear wheel. The average track value at the center of a wheel needs to add half of the width of the wheel, while the standard deviation remains unchanged.

$$f_{Xl}(x,y) = \frac{1}{\sigma_{yl}\sqrt{2\pi}} e^{-\frac{(x-\mu_{yl}+w/2)^2}{2\sigma_{yl}^2}} \tag{3}$$

Where, W is the width of the wheel.

Track volume of single-aircraft take-off

The same Analysis was used to process the horizontal deviation statistical data of single take-off wheel track. The fitting equation and curve shown in Figure 6 were obtained by statistical analysis of mean value and standard deviation of single take-off wheel track.
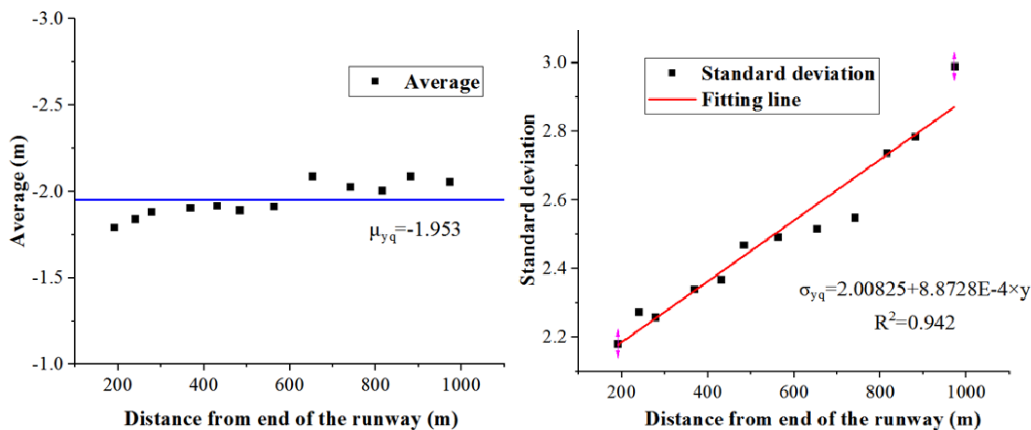
Fig.6 - Mean value and standard deviation in y direction for single-aircraft take-off track volume

The single take-off wheel coverage recorded by equipment No. 13 to No.14 was not more than 50 times. There are not enough data to acquire the statistics regulation of these cross sections. As shown in Figure 6, the average values of equipment No. 2 to No. 7 float around -1.9 m. Mean value of the average, -1.953 was used to illustrate the average. Besides, with the increase of the flight distance, the standard deviation of the take-off wheel-track increases gradually. Following formula (6) exhibited good linear fit between standard deviation and y-coordinate.

$$\mu_{yq} = -1.953 \tag{4}$$

$$\sigma_{yq} = 2.00825 + 8.8728 \times 10^{-4} \times y \tag{5}$$

The wheel-track distribution of the middle point of the main landing gear on one side near the flat area can be expressed as

$$f_{Xq}(x,y) = \frac{1}{\sigma_{yq}\sqrt{2\pi}} e^{-\frac{(x-\mu_{yq}+0.106)^2}{2\sigma_{yq}^2}} \tag{6}$$

Track volume for dual-aircrafts take-off

Same methods were used to analysis the take-off track volumes of two aircrafts. Figure 7 displays the fitting equation and fitting curve.

(a) Fitting equation and curve of mean values for left and right take-off tracks
(b)
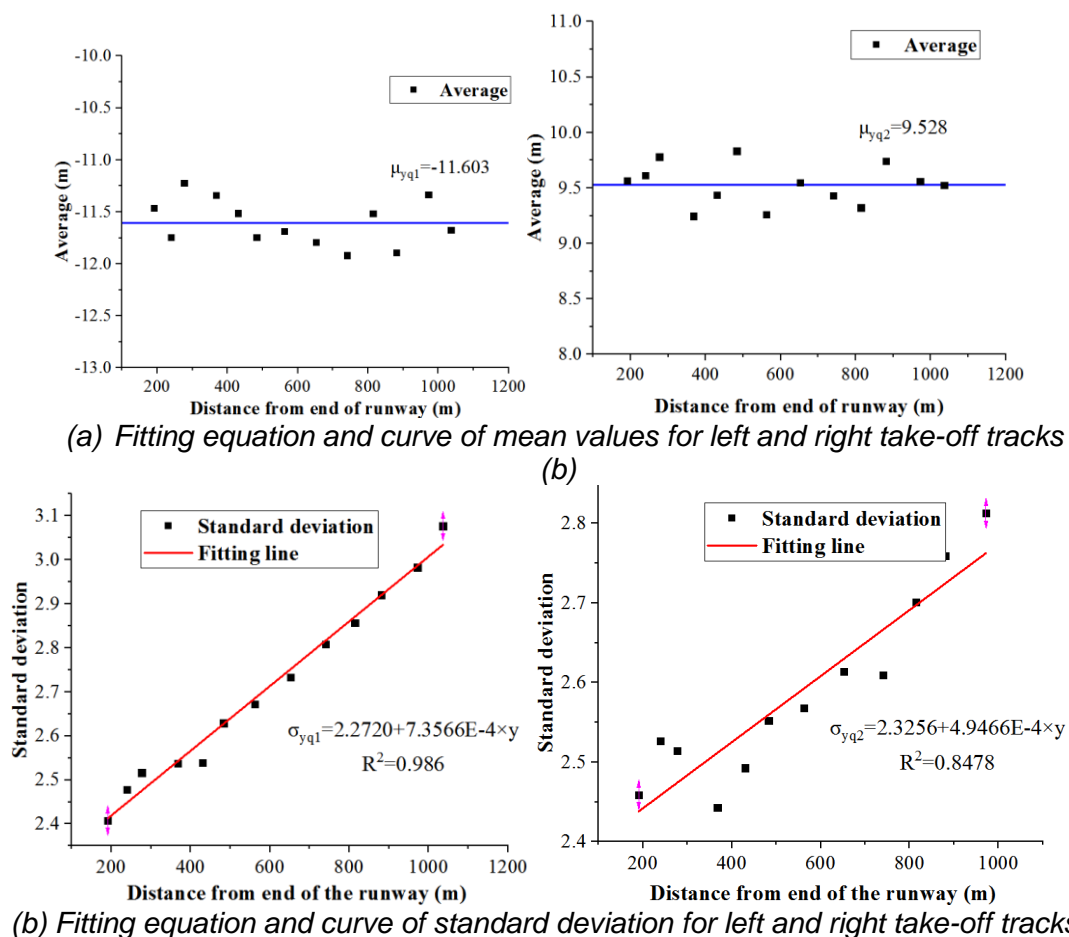
(b) Fitting equation and curve of standard deviation for left and right take-off tracks
Fig. 7 - Fitting equation and curve of standard deviation for take-off track volume of two aircrafts

The take-off wheel coverage of two aircrafts recorded by equipment No. 14 to No.17 was not more than 50 times. There are not enough data to acquire the statistics regulation of these cross sections. As shown in Figure 7, Mean value of the average, -11.603m and 9.528m were used to illustrate the traffic volume of close to the flat area and away from the flat area. What is more, similar to the single aircraft, the standard deviation increases gradually with the increase of the flight distance. It is interesting that the deviation which close to flat area had good linear fitting with high R-square of 0.986, while the deviation which away from the flat area had poor linear

----

fitting with R-square of 0.8478. The interference between aircraft skidding may led to the fluctuations.

$$\mu_{yq1} = -11.603 \tag{7}$$

$$\mu_{yq2} = 9.528 \tag{8}$$

$$\sigma_{yq1} = 2.2720 + 7.3566 \times 10^{-4} \times y \tag{9}$$

$$\sigma_{yq2} = 2.3256 + 4.9466 \times 10^{-4} \times y \tag{10}$$

The wheel-track distribution of the middle point of the main landing gear for two aircrafts can be expressed as:

$$f_{Xq1}(x, y) = \frac{1}{\sigma_{yq1}\sqrt{2\pi}} e^{-\frac{(x-\mu_{yq1}+0.106)^2}{2\sigma_{yq1}^2}} \tag{11}$$

$$f_{Xq2}(x, y) = \frac{1}{\sigma_{yq2}\sqrt{2\pi}} e^{-\frac{(x-\mu_{yq2}+0.106)^2}{2\sigma_{yq2}^2}} \tag{12}$$

LONGITUDINAL STATISTICAL REGULATION OF ARTV

The design of a runway length is determined by the accelerate-stop distance associated with an aborted take-off under the most adverse environmental conditions. For the majority of the airports, the runway length is surplus, which will result in that ARTV cannot cover the entire pavement. Longitudinal passage factor is the ratio of flight sorties passing through a certain cross-section to the total flight sorties and can be calculated by the following formula:

$$f_Y(y) = \frac{N_y}{N} \tag{13}$$

Where N_y is the flight sorties passing through a certain cross-section, N is the total flight sorties.

Longitudinal traffic volume of landing

The tire marks in the middle of the runway reflect that the landing point of the aircraft is basically within the test range of the first 7 equipment. Remove the days of occasional damage, the longitudinal passage factor of landing in each cross-section is calculated as shown in Table 5.

It can be seen from the Figure 8 that all aircrafts have landed and skidded after the 7th cross-section. That is to say, the longitudinal passage factor identically equal to 1 before the aircraft leaves the runway at the linking taxiway. Polynomial fitting of longitudinal passage factor along y direction can be obtained as shown in Figure 8.
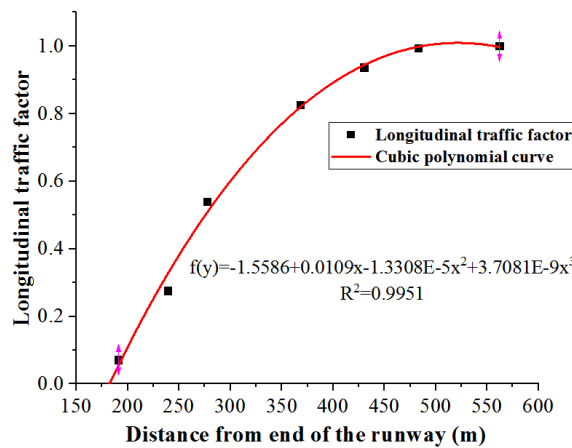
Fig. 8 - Fitting equation and curve of landing longitudinal passage factor

The Piecewise function (14) is adopted to represent the longitudinal passage factor of the whole runway

$$f_{Yl}(y) = \begin{cases} 0 & , \quad y < 180.95 \\ -1.5586 + 0.0109y - 1.3308E - 5y^2 + 3.7081E - 9y^3 & , \quad 180.95 < y \leq 459.65 \\ 1 & , \quad y > 459.65 \end{cases} \tag{14}$$

Longitudinal traffic volume of single-aircraft take-off

When a single aircraft takes off, the beginning positions are basically at the runway take-off line, and the longitudinal distribution of the take-off point can be ignored. Through observation and statistics, it is found that there are little aircraft take off before the 10th cross-section. In other words, the departure point of the aircraft is basically located at the equipment No. 10 to No. 17.

Figure 9 shows good linear fitting of the longitudinal passage factors along the runway, which can be express by the following piecewise function (15).
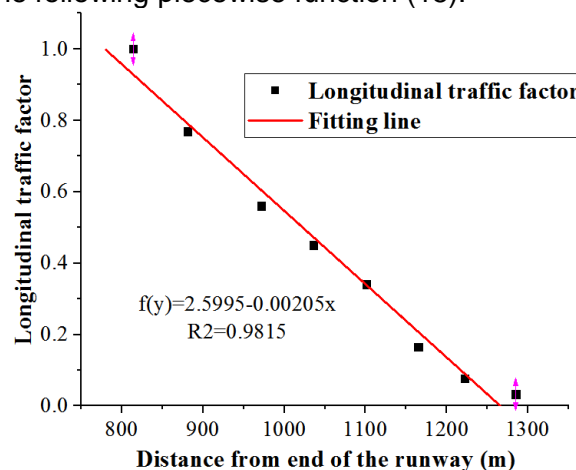
Fig. 9 - Fitting equation and curve of longitudinal passage factor for single aircraft take-off

----

$$f_{Y_{q\text{单}}}(y) = \begin{cases} 1 & , & 150 < y \le 780.24 \\ 2.5995 - 0.00205y & , & 780.24 < y \le 1268.05 \\ 0 & , & y > 1268.05 \end{cases} \quad (15)$$

Longitudinal traffic volume of dual-aircrafts take-off

It has been known that the take-off point is also basically at the runway take-off line, similar to single-aircraft take-off. The longitudinal distribution of the beginning point can be ignored. Through observation and statistics, it was found that the dual-aircrafts left the ground successively after the cross-section of equipment No. 10.

Figure 10 shows the polynomial fitting of dual-aircraft longitudinal passage factor along y direction.
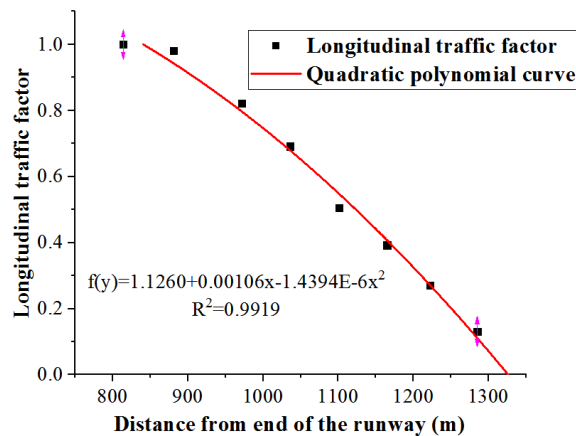
Fig. 10 - Fitting equation and curve of longitudinal passage factor for dual-aircraft take-off

Adopt the following piecewise function (15) to represent the longitudinal passage factor of the whole runway:

$$f_{Y_{q\text{双}}}(y) = \begin{cases} 1 & , & 150 < y \le 840.56 \\ 1.126 + 0.00106y - 1.4394E - 6y^2 & , & 840.56 < y \le 1326.25 \\ 0 & , & y > 1326.25 \end{cases} \quad (16)$$

PLANE DISTRIBUTION MODEL OF ARTV

Previous sections have studied the lateral and longitudinal traffic volume of landing, single-aircraft take-off and dual-aircraft take-off. Normal fitting curves of ARTV were obtained, which reflect the probability of wheel-track migration on each cross-section. Longitudinal passage factor is defined as the probabilistic representation of the total flight sorties passing through a cross-section. The joint distribution of lateral and longitudinal directions represented the traffic volume probability at a certain point of the pavement surface.

The total number of flights operated by the airport in its design life is assumed to be N times, including N_s times of single-aircraft take-off and N_d times of dual-aircraft take-off, where $N = N_s + 2N_d$. Take-off and landing ratio of flight sorties at one side to the other is $a:b$ ($a+b=1$). The ARTV of landing, single-aircraft take-off and dual-aircraft take-off can be represented by Eq. (17), Eq. (18), Eq. (19) and Eq. (20) respectively.

$$N_{x,yl} = aN \cdot f_{Xl}(x,y) \cdot f_{Yl}(y) + bN f_{Xl}(x, L-y) f_{Yl}(L-y) \tag{17}$$

$$N_{x,yqs} = aN_s \cdot f_{Xqs}(x,y) \cdot f_{Yqs}(y) + bN f_{Xqs}(x, L-y) f_{Yqs}(L-y) \tag{18}$$

$$N_{x,yqd1} = aN_d \cdot f_{Xq1}(x,y) \cdot f_{Yqd}(y) + bN_d f_{Xq1}(x, L-y) f_{Yqd}(L-y) \tag{19}$$

$$N_{x,yqd2} = aN_d \cdot f_{Xq2}(x,y) \cdot f_{Yqd}(y) + bN_d f_{Xq2}(x, L-y) f_{Yqd}(L-y) \tag{20}$$

The traffic volumes of main landing gear left wheel were calculated by the upper planar distribution model. It is necessary to add right wheel traffic volume to the formulas to get the whole coverage. Neglect the effect of aircraft drift and wheel roll, the normal distribution mean at the center of right wheel needs to add the width of the two main landing gears, while the standard deviation remains unchanged.

It is known that the take-off and landing sorties of this airport support aircraft in the design life are 100,000 times. The probability of taking off and landing at one side to the other is 7:3 and the take-off ratio of single-aircraft to dual-aircraft is 1:3. The airport had a runway length of 2800m, and width of 60m. Assumed that all aircrafts leave the runway from the contact channel (the longitudinal coordinates at both ends are 300m and 2500m respectively). Based on the wheel track test statistical regulation and the planar distribution model, the coverage of the main landing gear wheels under three states of landing, single-aircraft take-off and dual-aircraft take-off can be obtained, as shown in Figure11, Figure12 and Figure 13 respectively.
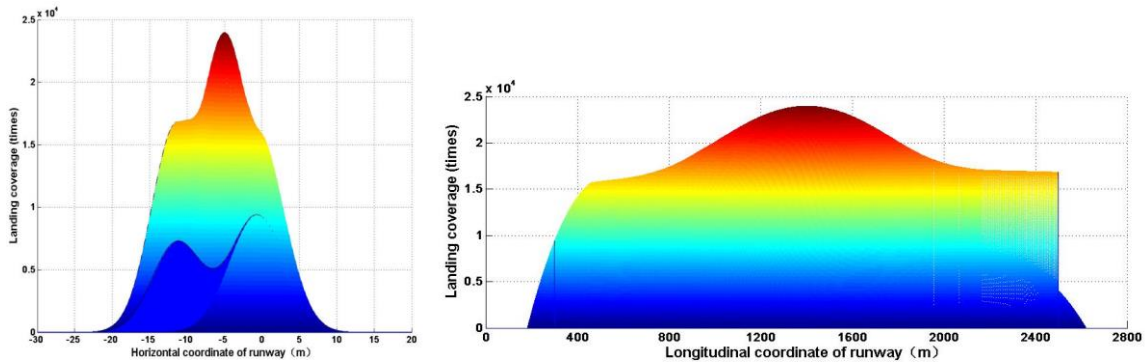
Fig. 11 - Traffic distribution surface of landing
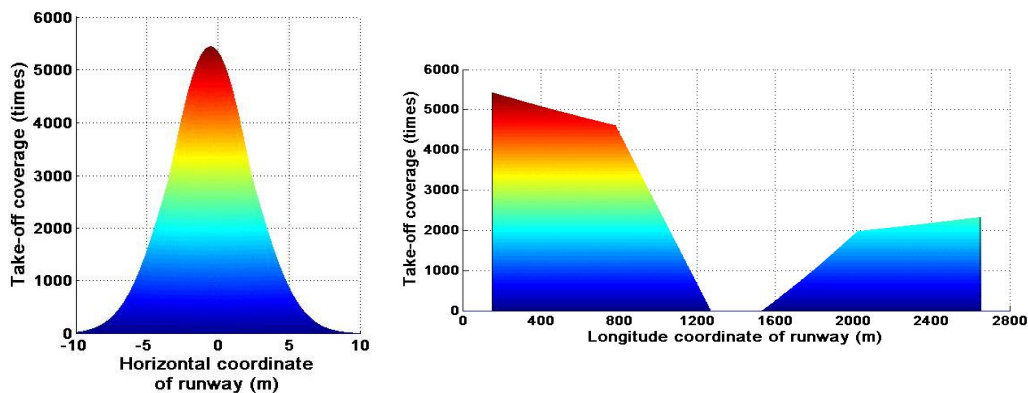
Fig. 12 - Traffic distribution surface of single-aircraft take-off

----
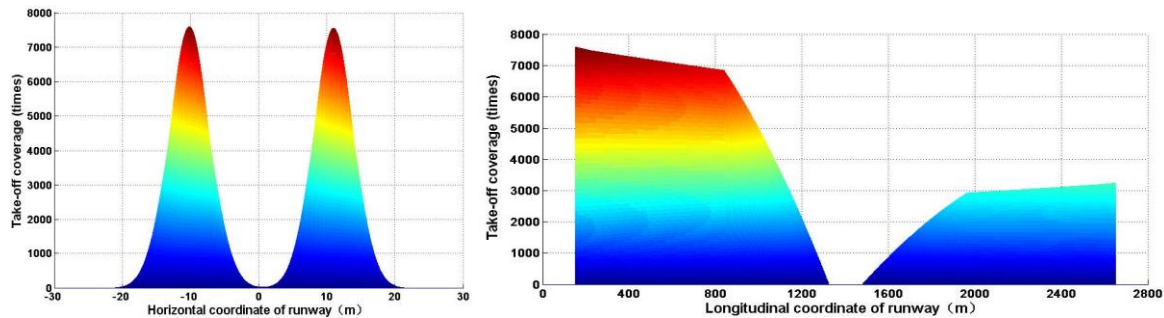
Fig. 13 Traffic distribution surface of dual-aircraft take-off

As seen in Figure 11 to Figure13, it is shown that the wheel tracks distributed throughout the runway. Coverage times at every point of the pavement can be clearly calculated using the above model, with maximum value of 23986 times for landing, 5423 times for single-aircraft take-off, 7575 times and 7535 times for dual-aircraft take-off near the flat area and for away from the flat area. If the lateral distribution of the wheel track is calculated according to the specification, with an average value of 0.02m and a standard deviation of 2.83m, neglecting the longitudinal distribution, the ARTV is shown in following Figure 14.
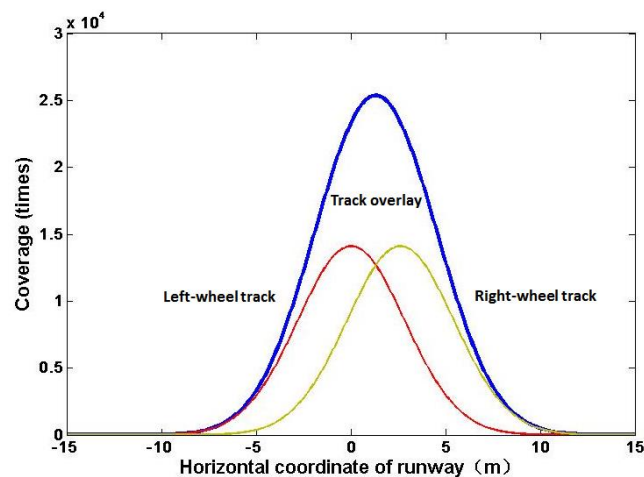
Fig. 14 - Traffic volume curve of lateral distribution

As can be seen from the figure above, the traffic volume curve only considering the transverse distribution is one case of the planar distribution model, which has not considered the aircraft's take-off and landing point, taxiing offset and longitudinal passage probability of each cross-section. It can be calculated that the maximum coverage times of the traffic volume distribution curve are 25,370 times. Compared with the above planar model, it is found that without considering the longitudinal distribution of APTV will make an excessive estimate of the traffic volume and more conservative for the pavement thickness design. What is more, the planar model can also be used to determine the width of airport runway based on runway risk probability. These are also our future research directions.

CONCLUSIONS

This paper pointed out that there are not only lateral distributions, but also longitudinal distributions of ARTV based on the analysis of its characteristics. An airport runway traffic

measurement system was developed, which adopted laser testing technology to test the wheel track distribution in landing, single-aircraft take-off and dual-aircraft take-off. The regulation of lateral distribution of wheel tracks was analyzed statistically. The longitudinal passage factor was proposed to illustrate the longitudinal distribution of ARTV. Then, the planar distribution model of ARTV was established. The example showed that the planar distribution model could evaluate the coverage times of every point on the pavement. In addition, by comparing with traffic volume calculation method in current design specification, it was found that only considering the lateral distribution of traffic volume will make the pavement design more conservative.

The model proposed in this paper developed the traffic volume calculation method from transverse distribution curve to planar distribution surface, without considering the load of different aircraft weight. Combined with the planar distribution of load, it can provide the traffic volume basis for pavement segmentation design and establish the pavement design method based on the cumulative damage surface.

ACKNOWLEDGMENTS

REFERENCES

[1]   Richard G. Ahlvin Origin of Developments for Structural Design of Pavements Report No. GL-91-26 U.S.Army Corps of Engineers, Waterways Experiment Station, Vickburg, MS.1991.

[2]   Zhang Yaohua. Study on Evaluation System of cement concrete pavement of airport. Tianjin: Tianjin University, 2007 (in Chinese).

[3]   Paul Stephen Dempsey. Airport Planning & Development Handbook—a Global Survey. USA　New York: McGraw-Hill，1999.

[4]   Vedros, P. J. "Study of Lateral Distribution of Aircraft Traffic on Runways," Miscellaneous Paper No. 4-369, Jan 1960, U. S. Army Engineer Waterways Experiment Station, CE, Vicksburg, Miss.

[5]   Brown,D.N.and Thompson,O.O. Lateral Distribution of Aircraft Traffic, Miscesllaneous Paper S-73-56,U.S.Army Corps of Engineers, Waterways Experiment Station, Vickburg, MS.1973

[6]   Hosang V. A.　Field survey and analysis of aircraft distribution on airport pavements[R]. Washington，D．C．，USA: FAA，1975．

[7]   MINCAD Systems Pty. Ltd. APSDS 4 User Manual Airport Pavement Structural Design System. Australia, September 2000.

[8]   FAA, the Boeing Company. Statistical Extreme Value Analysis of JFK Taxiway Centerline Deviations for 747 Aircraft. FAA/Boeing Cooperative Research and Development Agreement 01-CRDA-0164，2003.11.

[9]   FAA, the Boeing Company. Statistical Extreme Value Analysis of ANC Taxiway Centerline Deviations for 747 Aircraft. FAA/Boeing Cooperative Research and Development Agreement 01-CRDA-0164，2003.11.

[10]   U.S. Department of Transportation, Federal Aviation Administration. Airport Pavement Design and Evaluation, AC No: 150/5320-6E. U.S. Department of Transportation，Federal Aviation Administration，2009.9.

[11]   U.S. Department of Transportation, Federal Aviation Administration. Airport Pavement Design and Evaluation, AC No: 150/5320-6F. U.S. Department of Transportation，Federal Aviation Administration，2016.

[12]   U.S. Department of Transportation, Federal Aviation Administration. Standardized Method of Reporting Airport Pavement Strength – PCN (DRAFT), AC No: 150/5335-5A. U.S. Department of Transportation，Federal Aviation Administration.

[13]   CROW.Guideline on PCN Assignment in the Netherlands. CROW-report 05-06，Netherlands: Galvanistraat，2005.8.

[14]   Japanese Transport Ministry. Essentials and Design Examples of Airport Pavement Design. Port Airport Construction and Design Technical Service Center, 2008

[15]   Airport Pavement Design and Maintenance, Bagu Haogao, Tianbo Translation, China Communications Press, 2015.

[16]   G.P. Cen, S. Lu, G. Hong. Research on reliability design method of airport runway width. Science and Technology Guide, 2014, 32 (22): 47-51

[17]   H. Fang, L.C. Cai, L.L. Zhang, Z. Liu, Z.H. Wang, Traffic volume analysis of airport pavement based on traffic coverage, Sichuan Architectural Science Research, 2013;39(1)(2013): 60-63.

[18]   Z.H. Wang, L.C. Cai, Q.K. Gu. The cumulative damage optimization model of airport rigid pavement considering load stress distribution. Journal of civil engineering, 2011 (11): 151-158.

[19]   Chinese specifications for asphalt pavement design of civil airports: MH/T 5010-2017, PR China (Beijing): Civil Aviation Administration: 2017.

[20]   Q. Li, H.D. Zhao, Z.K. Yao. Calculation Method of the plane load frequency based on channel response, Journal of Tongji University (NATURAL SCIENCE EDITION), 2008;36 (12): 1637- 1641.

[21]   X.P. Lin. Theory and design method of airport runway overlay under complex conditions. Ph. D. Thesis, Tongji University, China, 2007.

[22]   L. Lei, H.D. Zhao, C. Wu. Comparative analysis of horizontal distribution test system of aircraft wheel track. Traffic engineering, 2012, 10:63-68.

[23]   L. Lei, research on the lateral distribution rule of runway wheel track of civil airport [D]. Master's thesis of tongji university,2013.05.

[24]   E.H. Shi, spatial structure response of asphalt pavement surface under non-uniform contact stress [D]. Master's thesis of tongji university, March 2015

[25]   J. Yuan, E.H. Shi, L. Lei, X.P. Shao, Lateral Deviation Pattern and Method of Aircraft Wheel Path on Shanghai Hongqiao International Airport，Journal of Civil Aviation University of China, 2015,33(2):1-6

[26]   L.K. Ma，H. D. Zhao，Z. M. Du，Z. A. Chen. Cumulative damage calculation of flexible pavement considering aircraft operation characteristics, Journal of Chongqing Jiaotong University (Natural Science), 2017;36 (9): 38-43.

[27]   Cen Guoping，Lu Song，Hong Gang，Lin Kexin，Xu Feng. Research on Reliability Design Method of Airport Runway Width, Science & Technology Review, 2014,32(22):47-51.

[28]   L.C. Cai, H.F. Wang, L.L. Zhang, P.F. Wang. A residual life prediction model for airport pavement based on cumulative damage, Journal of Traffic and Transportation Engineering, 2014;14 (4) : 1-6.

GENERATION OF CRACKS IN HIGHWAY EMBANKMENT ON BLACK COTTON SOIL

Yongzhen Cheng, Yun Dong, Jingke Wu, Baoliang Li and Jihua Zhang

Huaiyin Institute of Technology, Faculty of Architecture and Civil Engineering, Huai'an, No.89 Beijing North Road, China; e-mail: dyun@hyit.edu.cn

ABSTRACT

This research revealed the crack generation of the highway embankment from the water losing shrinkage of the wet black cotton soil (BCS), which is a type of soil with high swell-shrink potential. The road seepage meter was used to test the permeability of filling materials, which was used to replace BCS. The moisture content and embankment deflection of BCS foundation were measured after the rainy season. Based on the coupled consolidation theory for unsaturated soil, the change in additional tension stress of the embankment induced by water loss shrinkage of BCS was simulated by Abaqus. The results indicated that the rainfall seeped into the foundation through highly permeable refill materials to result in BCS expansion and decrease the embankment strength. After the rainy season, the additional tensile stress caused by water loss shrinkage of BCS induces cracking of highway embankment, and the maximum cracking depth often appears at the shoulder of highway. The deep and wide cracks are easy to appear in the low embankment constructed on a thick BCS foundation under strong evaporation.

KEYWORDS

Embankment crack, Black cotton soil, Moisture change, Shrinkage, Tension stress

INTRODUCTION

Black cotton soil (BCS) is discovered in abundance in Ethiopia [1]. BCS is a type of soil with a high expansion when the moisture content in soil changes [2,3]. The swell/shrink behaviour gives rise to serious engineering problems in highway embankment on BCS. A case in point was found in the existing highway connecting the capital Addis Ababa with Adama, where the subgrade strength decreased in the heave rainy season, and the embankment cracks developed in the following dry season. It is to determine out the influence of spatial and boundary conditions on the crack generation to overcome those subgrade diseases.

Replacement of BCS with nonexpansive materials is the main method to overcome the water swelling of BCS in Ethiopia. It is recommended in the design features of the highway to remove the existing BCS up to a depth of 0.6-1.8 m and replace it with selected suitable materials up to the bottom of the sub-base layer. The depth of the excavation is determined in accordance with the plasticity index and the volume of traffic. In some researches, the active zone of BCS was measured as an evaluation index to determine the depth of the excavation. As the moisture content remains stable, BCS below the active zone has a small influence on the upper highway embankment. The depth of the excavation can be determined with the help of the classification of BCS [4-6]. Unfortunately, the subgrade cracks occurred in the highway connecting the capital Addis Ababa with Adama, where the BCS was excavated and replaced by gravel soil or the mixes of clay and scoria [7].

Addis Ababa - Adama highway in Ethiopia, which was implemented by a design and research institute in China, developed many cracks in the embankment after a heavy rainy season. This research reveals the causation of crack in highway embankment, using the field experiment and numerical simulation. The moisture change of BCS at the different depth was measured by drilling and sampling. The permeability test was performed on the replacement materials. The deflection was also measured on the highway embankment with and without cracks. The increase in moisture content was determined in the BCS after the rainy season. Nevertheless, the cracks were generally found in the highway embankment with a height of less than 1.75 m. The slope instability due to rainfall infiltration rarely happens in such a low embankment. Hence, subgrade cracks should occur in the process of soil surface evaporation after a heavy rain. On the basis of the coupled consolidation theory for unsaturated soil, BCS shrinkage due to water loss was simulated by Abaqus/Standard to obtain the stress distribution in highway embankment, starting with the wet status of subgrade after a heavy rainy season.

THE STUDY SITE

Rainfall and evaporation at Ethiopia

Ethiopia is situated in the tropics, but most regions of the country are milder due to the high terrain. The heavy rainy season starts in June with the coming of the southwest monsoons and continues till September. The dry season lasts from October to January of the next year. The months from February to May constitute the light rainy season. The region of plateau gets about 1,000-1,500 mm rainfall per year, but it reduces to 250-500 mm in the lowland. Evaporation intensity can be modelled for soil–atmosphere interaction problems by the meteorological data [8]. Here FAO 56 PM model was employed to calculate the evaporation intensity in Ethiopia, using the air temperature, dew point temperature and wind speed [9,10]. The evaporation intensity ranges from 3.11×10^{-8} m/s to 7.25×10^{-8} m/s in the most region of Ethiopia.

Soil stratification

A total of twelve boreholes were drilled along the existing motorway route connecting the capital Addis Ababa with Adama. The thickness of BCS ranges from 0.5 m to 3.2 m. The properties of BCS obtained according the Chinese standards [11] are presented in Table 1. The grain analysis was performed on BCS samples by the transfer pipette. The clay content in the BCS is between 45% and 51%, and the silt content is between 49% and 55%. The liquid limit of BCS ranges from 68.5% to 73.8%, and the plasticity index ranges from 31.6% to 37.2%. All soil samples plot on the right of 'B' line, and locate above the 'A' line in the plasticity chart. Hence, The UCSC classification of BCS is CH (clay with high plasticity). In addition, BCSs are characterized by the high liquid limit and free swell index. The California bearing ratio (CBR) is measured at only 1.6%, and far from the requirement of the roadbed fillings [12]. Below BCS layer, the soil is silty clay with a handful of decomposed rock. Standard penetration tests (SPTs) were performed on this soil layer, and the average SPT blow count for this layer was between 10 and 15.

Tab. 1 - Properties of BCS

Parameters	Values
Silt ($>$2μm) (%)	45-51
Clay ($<$2μm) (%)	49-55
Liquid limit (%)	68.5-73.8
Plastic limit (%)	34.2-42.7
Plasticity index (%)	31.6-37.2
Free swell index (%)	136-182
California bearing ratio (%)	1.3-2.1

Formation of crack in highway embankment

The highway embankment was constructed on BCS in numerous sections of the researched motorway. The top 80 cm of the foundation BCS was excavated and then back filled with gravel soil or the mixes of the scoria and clay. The fillings of the embankment are the nonexpansive clays with stiff consistency. The side slope of the highway embankment is 1.75(H):1(V). The thin BCS layer closes the slope surface to resist the rainfall penetration. Unfortunately, the embankment in various sections cracked after a heavy rainy season. The cracks usually occurred on the low embankment located at areas with flat terrain, where the mixes of clay and scoria replaced BCSs in foundation. The cracks included lengthways cracks, transverse cracks and other linear cracks, and were characterized by the extreme breadth of about 3 cm, and some of them even penetrate through the roadbed [7].

EXPERIMENT AND SIMULATION

Sampling and testing

BCSs were sampled from km26+180 in the existing highway connecting the capital Addis Ababa with Adama, where the embankment cracked after a heavy rainy season. The laboratory tests were performed on soil samples and highway embankment in Ethiopia. Those tests included moisture content of BCS, water permeability coefficient of fillings and deflection of the highway embankment. The moisture content of the disturbed soil samples at the different depth was measured in the laboratory. This investigation was to determine the moisture change in BCS below the replacement layer, which was a key reason for the embankment cracks. According to Chinese standards [13], the permeability tests were performed on the replacement materials by road seepage meter. The structural diagram of the road seepage meter is presented in Figure 1. Granular soil samples (300×300×200 mm) were compacted under a compactness of 93%. The seepage meter was first fixed on the sample. Then the water was poured into the measuring cylinder. When the water dropped to the scale of 100 ml, the timer started. Every 60 seconds, water level was noted down till the scale of 500 ml. The water permeability coefficient is the quotient of water seepage divided by the needed time. Moreover, the deflection tests were performed on the top of the highway embankment near cracks using the Benkelman beam.
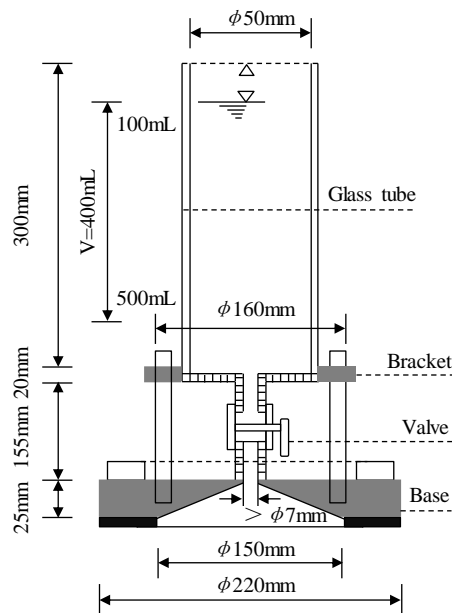
Fig. 1 - The structural diagram of road seepage meter

Numerical analysis

Coupled consolidation theory for unsaturated soil

The rainfall will cause the reduction in soil suction and result in the expansion of the clays. However, the following the drought events lead to the soil desiccation, the expansion of clays disappears and the shrinkage occurs [14]. The soil desiccation after a heavy rain may lead to shrinkage crack of the soil. Here BCS shrinkage due to water loss was simulated by Abaqus/Standard based on the coupled consolidation theory for unsaturated soil. The change in volume of clay as exposure to water is described by double-variables theory as follows [15].

$$d\varepsilon_v = m_1^s d(\sigma_m - u_a) + m_2^s d(u_a - u_w) \tag{1}$$

$$d\theta = m_1^w d(\sigma_m - u_a) + m_2^w d(u_a - u_w) \tag{2}$$

where $d\varepsilon_v$ is the volumetric strain of the clays, $d\theta$ is the change in volumetric moisture content, σ_m is the mean net normal stress, u_a is the pore air pressure, u_w is the pore water pressure, $(\sigma_m - u_a)$ is the mean normal stress, $(u_a - u_w)$ is the matric suction, m_1^s is the compression coefficient related to the normal stress, m_2^s is the compression coefficient related to the matric suction, m_1^w is the coefficient of water change related to the normal stress, m_2^w is the coefficient of water change related to the matric suction.

The void ratio and moisture content can be defined as follows, using the mean normal stress and matric suction.

$$e = f(\sigma_m - u_a, u_a - u_w) \tag{3}$$

$$wG_s = g(\sigma_m - u_a, u_a - u_w) \tag{4}$$

where e is the void ratio of the clay, w is the moisture content, G_s is the specific gravity of the clay, f and g are arbitrary functions.

The volumetric strain and change in moisture content of the unsaturated soils can be written as:

$$d\varepsilon_v = \frac{\partial e}{(1+e_0)\partial(\sigma_m - u_a)}\Delta(\sigma_m - u_a) + \frac{\partial e}{(1+e_0)\partial(u_a - u_w)}\Delta(u_a - u_w) \tag{5}$$

$$d\theta = \frac{\partial wG_s}{(1+e_0)\partial(\sigma_m - u_a)}\Delta(\sigma_m - u_a) + \frac{\partial wG_s}{(1+e_0)\partial(u_a - u_w)}\Delta(u_a - u_w) \tag{6}$$

The compression coefficient can be calculated by Eqs. (1), (2), (5) and (6).

$$m_1^s = \frac{1}{1+e_0}\frac{\partial e}{\partial(\sigma_m - u_a)} \tag{7}$$

$$m_2^s = \frac{1}{1+e_0}\frac{\partial e}{\partial(u_a - u_w)} \tag{8}$$

$$m_1^w = \frac{G_s}{1+e_0}\frac{\partial w}{\partial(\sigma_m - u_a)} \tag{9}$$

$$m_2^w = \frac{G_s}{1+e_0}\frac{\partial w}{\partial(u_a - u_w)} \tag{10}$$

The water continuity equation of an unsaturated soil can be obtained by soil-water mass conversation if the water is assumed to be incompressible.

$$\frac{1}{\rho_w g}\left(\frac{\partial}{\partial x}\left(k\frac{\partial(u_a - u_w)}{\partial x}\right) + \frac{\partial}{\partial y}\left(k\frac{\partial(u_a - u_w)}{\partial y}\right) + \frac{\partial}{\partial z}\left(k(\frac{\partial(u_a - u_w)}{\partial z} + 1)\right)\right)$$
$$= \rho_d C_w \frac{\partial(u_a - u_w)}{\partial t} + m_1^w \frac{\partial(\sigma_m - u_a)}{\partial t} \tag{11}$$

where ρ_w is the density of water, ρ_d is the dry density of the soil, g is the acceleration of gravity, k is the hydraulic conductivity, C_w is the specific water capacity of the soil.

The laboratory tests were performed to construct the constitutive relation for unsaturated soil of BCS. Those tests include the specific gravity test, free shrink test, suction test and swell-consolidation test, which are determined by following standard methods[11]. Previous research listed the constitutive surface for unsaturated soil of BCS [16].

Falling head permeability tests were performed to obtain the saturated hydraulic conductivity of the subgrade soil. The soil-water characteristic curve (SWCC) describes the relationship between the suction and water content in soil and can be obtained by suction tests. With the help of SWCC, the unsaturated hydraulic conductivity versus matric suction was described by Van Genuchten, M model [17].

$$k(u_a - u_w) = k_s \frac{\left\{1 - |a(u_a - u_w)|^{n-1}\left[1 + |a(u_a - u_w)|^n\right]^{-m}\right\}^2}{\left[1 + |a(u_a - u_w)|^n\right]^{m/2}} \tag{12}$$

where $k(u_a - u_w)$ is the hydraulic conductivity; k_s is the saturated hydraulic conductivity; $(u_a - u_w)$ is the matric suction; a, n and m are the fitting parameters, $m=1-1/n$. The variation of hydraulic conductivity with matric suction for BCS is shown in Figure 2.
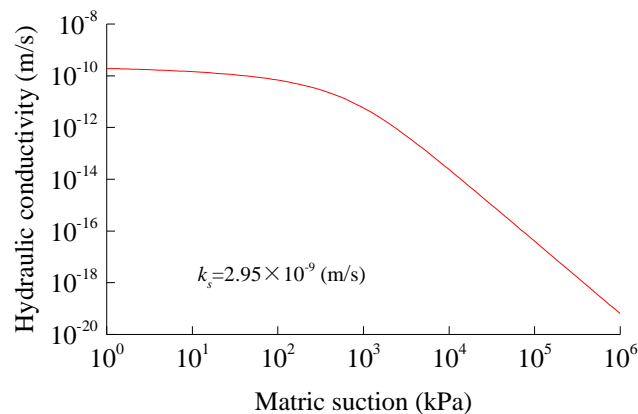
Fig. 2 - Variation of hydraulic conductivity with matric suction for BCS

Numerical model

The thermal mechanical coupling has the analogous differential equations with the hydro-mechanical coupling. In addition, Abaqus/standard provides the "coupled thermal stress analysis" option. Hence, coupled thermal stress analysis was performed to solve the coupled consolidation problem for unsaturated soil by Abaqus codes. The simulation performed a main program and four user subroutines such as USDFLD, UMAT, UMTHT and UEXPAN. The main program defines the mesh, initial conditions, boundary conditions and step. With the help of the FORTRAN, USDFLD read the net normal stress and matric suction of every nodes from the main program, and calculated the material parameters of the subgrade soils based on the constitutive relation for unsaturated soil, those material parameters included the elasticity modulus (E), expansion coefficient (a), compression coefficients (m_1^s , m_2^s , m_1^w , m_2^w) and unsaturated hydraulic conductivity ($K(u_a-u_w)$). The parameters $K(u_a-u_w)$, m_2^w and the change in mean normal stress were inputted into UMTHT to calculate the unsaturated seepage. Elasticity modulus E was inputted into UMAT to update the stiffness matrix. Expansion coefficient a was inputted into UEXPAN to calculate the change in the thermal stress.
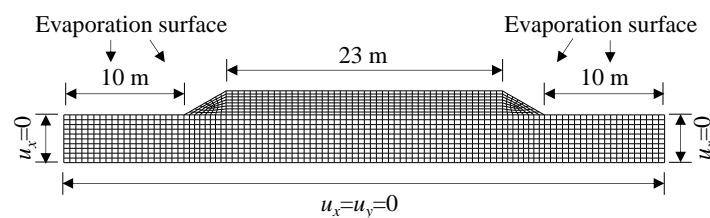
Fig. 3 - 2-D views of highway embankment section

The FEM of the highway embankment on BCS is presented in Figure 3. The width of the crest was 23 m. The side slope of the highway embankment was 1.75(H):1(V). The element types CPE4T used in the simulation were continuum stress/displacement element with heat flux being allowed. The bottom nodes were restricted to move in all directions. The lateral nodes were restricted to move in x direction. The slope and outside foundation constituted the evaporation surface. Moreover, unsaturated properties of the subgrade soil were not an option. The embankment weight was the only load in the simulation. The simulation started after a long-term rainy season, hence the initial suction of the subgrade is assumed to be 10 kPa, which is corresponding to the field capacity for most soil.

RESULT AND DISCUSSION

Moisture changes in foundation BCS

BCSs below replacement base were excavated and air-dried during construction. Hence the moisture content in the soil sample for testing the degree of compaction was only 18.4%. The moisture content in the BCS after a heavy rainy season is shown in Table 2. The moisture content in BCS below replacement base increased in the rainy season until closed to the plastic limit and was in the range of 36-40%. It was very close to the moisture content in BCS of beside farmland, which was in the range of 25.8-40.9%. The findings indicated that the backfill soil was a material with a large permeability and allowed rainwater to permeate into BCS below replacement base.

Tab. 2 - Moisture content distributions in BCS located at K26+180

Foundation BCS depth (cm)[a]	10	20	30	40	50	60	70	80
Measured moisture content (%)	38.3	40.0	39.8	36.0	37.6	38.2	38.1	37.6
Plastic limit (%)	38.2	39.9	38.9	38.4	38.9	38.4	39.7	39.0
Farmland BCS depth (cm)	25	50	75	100	125	150	175	200
Measured moisture content (%)	25.8	38.2	40.1	38.8	40.2	40.0	40.9	40.9
Plastic limit (%)	38.9	38.4	39.3	38.6	39.1	38.6	38.7	39.1

[a] The bottom of the backfill foundation was the starting sample surface.

The materials backfilled the foundation trench included the gravel soil and the mixes of the clay and scoria. The particle distribution of those materials is presented in Figure 4. The scoria has the superiority of good gradation and high strength, is a high quality subgrade material. However, its high permeability allows the rainwater to permeate into BCS below replacement base. Hence the scoria was mixed with clays to backfill the foundation trench. Both materials should give play to their respective advantages in high strength and low permeability.

Fig. 4 - Particle distribution of materials to backfill foundation
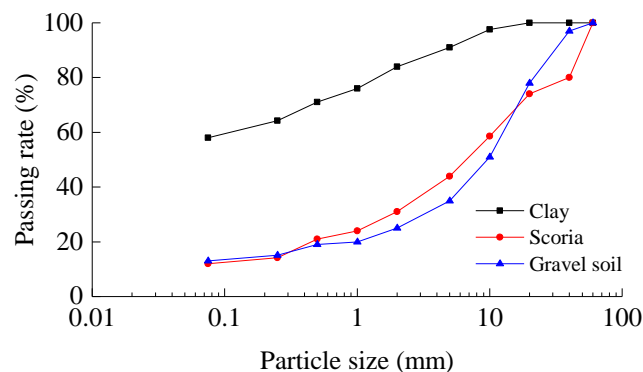
Tab. 3 - Water permeability coefficient of fillings

Clay: scoria	Permeability
3:1	8
2:1	10
3:2	15
1:1	17
1:2	100
1:3	200
Gravel soil	7

Unfortunately, the mixes of scoria with clay are still a material with the high permeability. The water permeability coefficient of the replacement materials is presented in Table 3. The water permeability coefficient of the mixes decreased with the increase in the clay content. When the ratio of clay content to scoria content was 1:3, the water permeability coefficient of the mixes was 200 mL/min. Even if this ratio increased to 3:1, the water permeability coefficient of the mixes only decreased to 8 mL/min, which was close to the permeability of the gravel soil.

Tab. 4 - Measured deflection of highway embankment [a]

ID	Deflection [b] (0.01 mm)	Deflection [c] (0.01 mm)
km 19.500-19.900	—	173
km 25.980-26.180	129	178
km 40.000-40.550	139	146
km 40.550-41.000	123	140
km 41.200-42.000	109	179

[a] The design deflection was 160/0.01 mm.
Deflection of embankment (**b**) before rain and (**c**) after rain.

BCS Over-excavation and replacement with the scoria developed a catchment area below the subgrade base in the areas with flat terrain. When rainwater seeped into BCS through the replacement layer, BCS would expand and weaken the integral strength of the highway embankment. The measured deflections of highway embankment in some section are presented in Table 4. The mixes of clay and scoria replaced BCSs in the section of km 40-41, but subgrade drainage was smooth due to the large longitudinal gradient. The integral strength of highway embankment decreased little. The measured deflections also met the design requirement. Sections of km 25.98-26.18 and km 41.2-42 were characterized with minor gradient. The deflections of the highway embankment increased tremendously due to the smooth drainage and cannot meet the requirement of the subgrade strength.

Embankment crack due to BCS shrinkage

The cracks were generally found on the highway embankment with a height of less than 1.75 m. Hence, the embankment cracks are probably caused by BCS shrinkage linked to the evaporation and not the rainfall infiltration. The BCSs below replacement base swell as exposure to water in the rainy season, and undergo the water losing shrinkage in the following dry season, which causes the additional tensile stress within the highway embankment. When the tensile stress exceeds the ultimate tensile strength of the soil, the embankment cracks occur in the different style. Thus, our analysis focuses on the contribution of major principal stress and refers to the criterion provided by literature [18], in which the major principal stress for creation of subgrade crack is 10 kPa.

Figure 5 presents the deformation and stress distribution of highway embankment after BCS evaporation of 30 days. The evaporation intensity, embankment height and BCS thickness were fixed at 5×10^{-8} m/s, 2 m and 4 m, respectively. The maximum soil movement took place at the slope and decreased gradually along the embankment width, and its value approximates to zero at the center of the road. The differential deformation developed the additional tensile stress in the highway embankment. The minimum crack depth took place at the center of the road and increased gradually along embankment width, and the cracks near the slope even penetrated through the highway embankment.
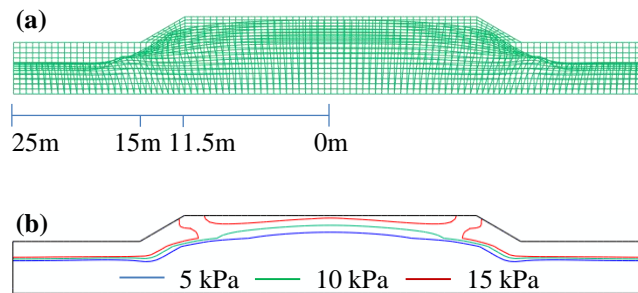
Fig. 5 - Deformation (a) and stress distribution (b) of highway embankment after BCS evaporation of 30 days
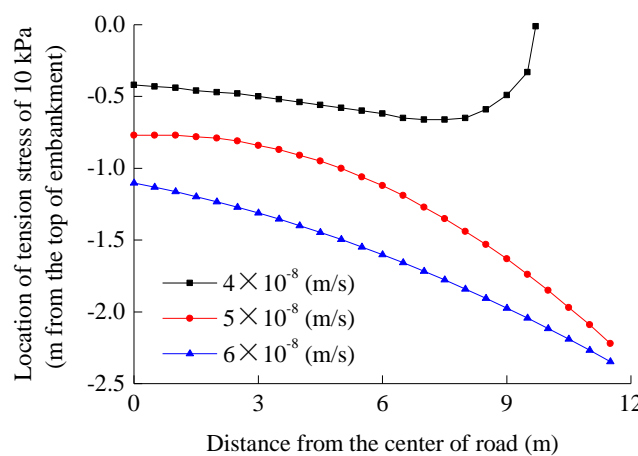
Fig. 6 - Influence of evaporation intensity on crack depth of highway embankment

The influence of evaporation intensity on crack depth of highway embankment is presented in Figure 6. Embankment height and BCS thickness were fixed at 2 m and 4 m, respectively. The possible crack area and depth increased with the increase in evaporation intensity. After 30 days of soil evaporation, the cracks may occur at any location of the highway embankment under the evaporation intensity of 6×10^{-8} m/s. The cracks even penetrated through the highway embankment at the sites near the road shoulder. When the evaporation intensity decreased to 4×10^{-8} m/s, the cracks took place in the range of 0-9.7 m, and the maximum depth was only about 0.5 m.
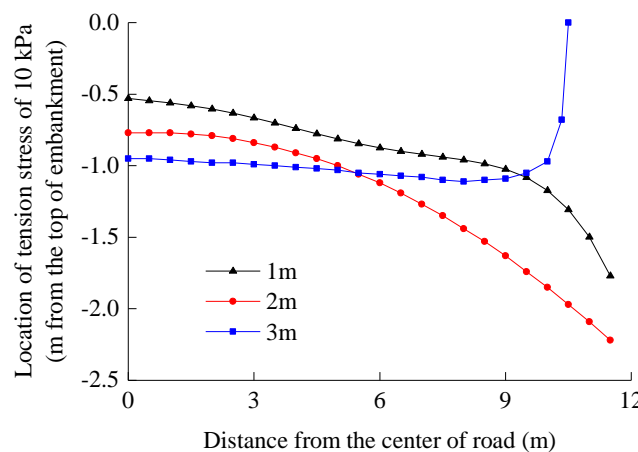
Fig. 7 - Influence of embankment height on crack depth of highway embankment

----

The influence of embankment height on crack depth of highway embankment is presented in Figure 7. Evaporation intensity and BCS thickness were fixed at $5×10^{-8}$ m/s and 4 m, respectively. The location of the tension stress at a value of 10 kPa was closer to the bottom in the lower embankment. After 30 days of soil evaporation, the maximum crack of 1 m and 2 m high embankment penetrated through the highway embankment into the foundation, but the maximum crack depth of 3 m high embankment was only about 1.1 m. The embankment weight will restrain the expansion of the foundation BCS as exposure to water. Hence the foundation BCS under the higher embankment has a relatively small shrinkage in the dry season. So the higher highway embankment developed the cracks with the smaller depth.
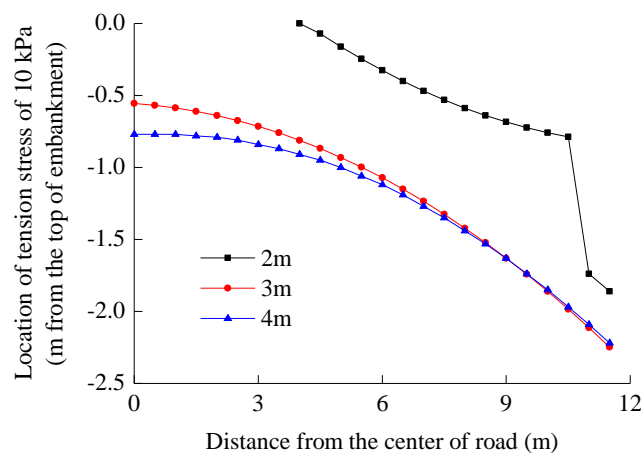
Fig. 8 - Influence of BCS depth on initial cracking of highway embankment

The influence of BCS thickness on crack depth of highway embankment is presented in Figure 8. The evaporation intensity and embankment height were fixed at $5×10^{-8}$ m/s and 2 m, respectively. After 30 days of soil evaporation, the cracks were not found within the highway embankment on 1 m thick of BCS. When the thickness of BCS increased to 3 m, cracks penetrated through the highway embankment. However, crack behaviour of highway embankment on 3 m and 4 m thick BCS had no obvious difference. This is attributed to the active zone of BCS, which is in the range of 1.8-2.6 m [6]. As the moisture content remains stable, BCS below the active zone has a minor influence on the upper highway embankment.

CONCLUSIONS

In this research, the crack generation within highway embankment was investigated. The water permeability coefficient of the replacement materials was tested in the laboratory to explain the change in moisture content of foundation BCS. The simulation was performed to investigate the tension stress of the embankment induced by the BCS shrinkage. The simulation took the wet status of subgrade after a heavy rainy season as a starting point. The following conclusions are drawn:

(1)　The high permeability of the replacement base allowed rainwater to permeate into BCSs, and their water swelling leaded to the decrease in the subgrade strength.

(2)　Water losing shrinkage of wet BCS induced the additional tension stress within highway embankment.

(3)　The maximum crack depth took place at the position near the shoulder and decreased gradually along embankment width. Greater evaporation intensity, lower highway embankment and thicker layer of BCS induced the deeper cracks within highway embankment.

ACKNOWLEDGEMENTS

REFERENCES

[1]   Yitagesu, F.A., van der Werff, H., van der Meer, F., Hecker, C., 2012. On the relationship between plasticity and spectral characteristics of swelling soils: The 3–5 µm wavelength region. Applied clay science, 69: 67-78.

[2]   Ola, S.A., 1978. The geology and geotechnical properties of the black cotton soils of northeastern Nigeria. Eng. Geol, 12: 375-391.

[3]   Ackroyd, L.W., 1986. Husain, R. Residual and lacustrine black cotton soils of northeast Nigeria. Geotechnique, 36(1): 13-18.

[4]   Zhao, P., Xu, Z.X., Tang, L., Zeng, D.L., 2014. Research on the black cotton soil swell-shrink characteristics and the depth of black cotton soil influenced by the atmosphere in Ethiopia. Journal of Railway Engineering Society, 4: 46-50.

[5]   Xu, Z.X., Tang, L., Zhang, K., He, X.J., Hou, W.L., 2014. Research on survey methods and engineering properties of black cotton soil of Ethiopian railway. Journal of Railway Engineering Society, 2: 15-18.

[6]   Wang, X.Y., Yu, X.L., Song, H., Zhou, Y.D., 2017. Research on the replacement depth and treatment method of black cotton soil in Ethiopian. Highway, 3: 7-12.

[7]   Wang, X.F., Wang, Y., Zhang, Y.H., 2012. Design for treatment of subgrade on black cotton soil (BCS). Highway, 9: 46-53.

[8]   Gerard, P., Mpawenayo, R., Douzane, M., Debaste, F., 2016. Influence of climatic conditions on evaporation in soil samples. Environmental Geotechnics, 6(6): 323-333.

[9]   Irmak, S., Irmak, A., Allen, R.G., Jones, J.W., 2003. Solar and net radiation-based equations to estimate reference evapotranspiration in humid climates. J Irrig Drain Eng, 129: 336-347.

[10]   Cheng, Y.Z., Huang, X.M., Li, C., Shen Z.P., 2017. Field and numerical investigation of soil–atmosphere interaction at Nairobi, Kenya. European Journal of Environmental and Civil Engineering, 21(11): 1326-1340.

[11]   Research institute of highway ministry of transport., 2007. JTG E40—2007 Test Methods of Soils for Highway Engineering (China Communications Press) 415 PP.

[12]   CCC first highway consultants co., LTD., 2015. JTG D30—2015 Specification for design of highway subgrades (China Communications Press), 220 PP.

[13]   Research institute of highway ministry of transport., 2008. JTG E60—2008 Field test methods of subgrade and pavement for highway engineering (China Communications Press), 136 PP.

[14]   Vardon, P.J., 2015. Climatic influence on geotechnical infrastructure: a review. Environmental Geotechnics, 2(3): 166–174.

[15]   Fredlund, D.G., Morgenstern, N.R., 1976. Constitutive relations for volume change in unsaturated soils. Canadian Geotechnical Journal, 13(3): 261-276.

[16]   Cheng, Y.Z., Huang, X.M., Li, C., Li, L.Y., 2017. Numerical analysis of crack generation within embankment built on expansive soil foundation. Journal of Southeast University (English Edition), 33(2): 224-229.

[17]   Van Genuchten, M.T., 1980. A closed form equation for predicting the hydraulic conductivity of unsaturated soils. Soil Sci Soc Am J, 44: 892–898.

[18]   Zheng, J.L., Yang, H.P., 2009. Expansive soil engineering of highway, 170-171 (China communications press) 268 PP.

THE SEISMIC BEHAVIOR OF BURIED SEABED WALLS IN LIQUEFACTION SOIL

Javad Royaei and Kabir Sadeghi

Department of Civil and Environmental Engineering, Near East University, Boulevard, Turkey; mahaniranian1@gmail.com

ABSTRACT

The present study aimed to investigate the seismic behavior of enclosed seawater walls, the buried site of which lies in liquefaction soil. An experimental specimen was manufactured and tested on the seismic table, and a numerical study was also modeled in the ABAQUS software based on the experimental outcomes. In both the experimental and numerical studies, a susceptible liquefaction layer around the root of the wall was considered due to the root lean soil leakage and large lateral pressure, and the soil behind the root caused the failure of the buried section. According to the results, the lateral movement significantly decreased due to the backing effect of this layer on the buried section of the wall. Furthermore, an active wedge was formed from the buried side to the back of the containment, and the braces were overwhelming due to the presence of the locks in the wedge and their movement along with the wedge. The displacement of the crown and foot of the wall decreased with the increased base acceleration and higher frequency of the entrance movement.

KEYWORDS

Coastal wall, Liquefaction, Improvement, Seismic behavior

INTRODUCTION

Given the strategic role of coastal structures in the economy of every country and the geographical location of Iran in the earthquake zone, the seismic study of coastal walls is of paramount importance. The damages observed in recent earthquakes (e.g., 1995 Japan Kobe earthquake and 1999 Taiwan Chichi) indicate the great displacements of coastal walls, while further damages have also occurred due to the deformation of a soft layer or layers of soil/pier walls. In the cases where landfill and soil have not been leak-proof, the walls have been reported to exhibit safety behaviors during an earthquake [1]. As coastal soils and sea sediments, the density is often low to moderate, while there is a high likelihood of susceptible layers to liquefaction in soil. Therefore, the effects of these layers on the prediction of the seismic behavior of coastal walls must be properly examined.

Curtain walls are a common type of coastal walls, which are supported by the lateral pressure of soil and water through various components (e.g., shield, harness, and bar), as well as the inactive passive soil pressure in front of the buried wall. The static behavior of these structures is assessed based on the conventional estimation methods of soil lateral pressure in extreme states and establishing the equilibrium force and anchor ratios using a joint foot or the foot method [2]. However, the dynamic behavior of restored walls is more complicated, which is mainly due to the multiplicity of the influential factors in their behavior and influence. Restored walls are mutually supportive. In addition to the performance of the components, the response of these structures strongly affects the dynamic behavior of the soil relative to the input motion [3]. The seismic performance of these walls is defined based on their ability to operate and the amount of the damage caused by tension (e.g., displacement). The relevant parameters in this regard include the displacements of important areas (e.g., displacement of the shield and deck) and containment or the cracking of the surrounding soil,

and the tensions of the component instruments, such as the shield tensions in the upper and buried areas, stresses of the inhibitory cable, and barrier stress.

In performance-based design, it is essential to define the injury criteria by selecting the appropriate factors. In addition, the desirable process of failure with increased earthquake load should be defined for restored walls. For instance, if shield repair is difficult, the containment must be surrendered before shield submission. Since it is often more difficult to repair the buried section of a wall, this section has a higher seismic resistance and should be avoided by breaking the shield, interlock cable, and rupture. In addition to the features of the instrument parts (shield, bar, and inhibition), the stability of these structures depends on the geotechnical conditions of the bedding and landing.

In general, three friction modes could be considered for these structures. If a failure occurs in an inhibition rod or shield, the failure of the set is classified as shift/shaft shaping/shift. The change in the location of a set is due to the deformation or rupture of the containment or the rupture of a set known as shape/break in restraint. If the soil around the buried length cannot prevent the wall from rising, the failure will be referred to as a 'bursting section failure'. According to the field studies in this regard, the presence of a liquefaction layer in sections of the soot or lower soil leads to significantly larger shape variations. In addition to the existing walls that have been constructed without any liquefaction hazard in susceptible liquefied soils, several cases of the appearance of such layers have been reported in the sector where there are sensitive coastal walls. Considering that walls often have a considerable length, inevitable changes in the type of the layers may lead to the placement of a lubricating layer in one or more structural parts of the structure. Figure 1 shows the possible states of liquefaction layering.
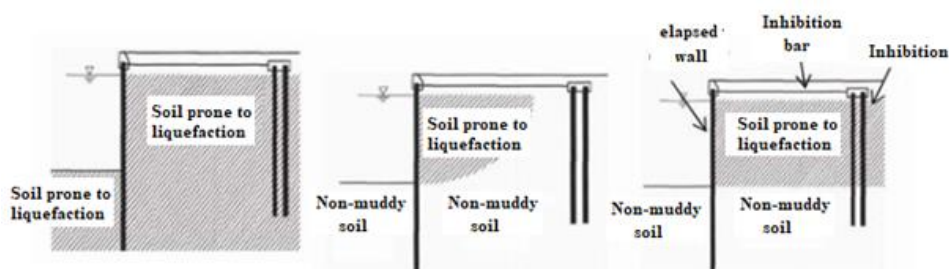
Fig. 1 – Possible States of Rangeland Soil on Site [4]

Table 1 shows the historical data regarding the displacement of the displaced walls of a passage (d) relative to their height from the level of desiccation (H) in the rangeland sites for the earthquakes that are equivalent to the seismicity of the design.

Tab. 1 - Relative Displacement of Septum Walls for Earthquakes Equivalent to Seismic Design Coefficient

Soil Data	No Dimensional Displacement (d/H)%			
	0-5	5-15	15-25	25-50
Un-liquefaction	■			
Shell Sand on Surface Only		■		
Shell Sand in Ash and Adjacent Inhibition			■	
Shell Sand on Slopes with Bottom Soil				■

RESEARCH SIGNIFICANCE

Due to the limitations of the quasi-static analysis method in the regions susceptible to liquefaction, recent studies in this regard have been primarily focused on the dynamic behavior of shield walls. The main objective of these studies has been to identify the mechanism of breaking the

----

walls of the shingles on site. Research in this field has been carried out using laboratory and numerical methods. Laboratory studies have been based on the physical scale simulations of the small scale in the gravimetric field (1 g) of the seismic table (gravity field) in the form of centrifuge experiments [5-7] and occasionally actual-scale tests [8], while numerical studies have mainly aimed to behave, simulate, and predict these components numerically.

The Japanese NIED Research Institute has conducted experiments using a large seismic table with the size of 3.6×12.6×3 meters to investigate the seismic behavior of shield walls. These experiments have been modeled using two-dimensional nonlinear dynamical analysis and an effective stress-strain method based on the Tohata-Yay behavioral model. Based on the results the mentioned experiments, the behavior of the set (especially before failure) could be simulated with acceptable accuracy [5]. In addition, the displacement of a damaged shield wall during the 1983 earthquake in the Akita port of Japan was analyzed by Yayy and Kamauka using the same model during the earthquake, and the wall (height: 16 m) was displaced 1.1-1.8 meters to the sea due to its soaking liquefaction and cracked at the depth of six meters from the sea level due to the sinking of the steel shield. The analysis also modeled the only behavior before the sinking of the metal wall, and the displacement of the wall crown was estimated with the acceptable accuracy of 1.3 meters [9]. Shuah-Owishi also performed the displacement approximately five meters to the river during the 1964 earthquake due to the soiling and burial section. The numerical modeling of the wall indicated the displacement rate of the horizon by using the mentioned model at 35.3 meters [10]. The obtained results were considered considering the close proximity of the numerical model after the failure of the observation and proper prediction of the variation of water pressure and displacements. Similar studies could contribute to the recognition of the dynamic behavior of shields.

The present study aimed to investigate the effects of the placement of a mating layer on the buried side of an enclosed seabed wall based on laboratory tests and numerical analysis. After introducing the rupture process, the effects of the doping upgrade on the reduction of the shrink displacement were evaluated. The total height of the wall was 35 meters, and the buried length was 14 meters. After the formation of the T-shaped concrete, its placement was restrained by a trickling peg to a candle-buried depth in the soil. Furthermore, sub-surface studies after construction showed that a layer with liquefying potential was part of the wall length of the buried section. For this purpose, a T-model of the failure of a small model of the wall was identified using the seismic table and confirmed for use in various for improvement based on numerical analysis. Dynamic analysis was also performed using the ABAQUS software.

Physical model

To identify the behavior of the buried seabed walls on a susceptible site to liquefaction, a small sample of the APM Terminals' port wall was constructed based on similarity laws [11] and tested by the seismic equipment. For this purpose, a box composed of transparent Plexiglas was used with the length, width, and height of 180, 50, and 75 centimeters, respectively. The constructive structures (walls, harnesses, and inhibitory cables) were embedded in the middle section of the box, and Plexiglas was used to construct a T-shaped coastal wall and containment. In addition, different layers of soil were poured through silica. The sand had a homogeneous grain size and resembled the standard sandwiches of the Tuyur and Langunaman in terms of the physical properties and granularity curves [12].

To achieve variable degrees of accumulation in the soil layers, we used the wet towering method. For this purpose, 5% of water was added to the sand, and the soil was meticulously poured into the box in five-centimeter layers to reach the desired percentage. At appropriate stages, the walls, containment, inhibitory cables, and sensors were placed at the predetermined locations. After filling the box, the front side of the wall was partly drilled to apply the pre-stress phase, and after stopping the bar, the front side of the wall was removed to the damp level. To observe the changes in the shape formed during the seismic eruption, a grid of sandstone with the thickness of one and 10 centimeters was prepared to face the box. Upon the completion of the model, it was saturated with

----

carbon dioxide gas to remove the air from the open air and accelerate the water saturation process. Model saturation was accomplished by gradually passing the water from the box under constant speed. Figure 2 depicts the geometry of the physical sample. In the non-upgrading model, the loose layer (Dr=25%) contained the entire buried wall surface, while the lower layer and bottom layer had extremely high density (Dr=85%).
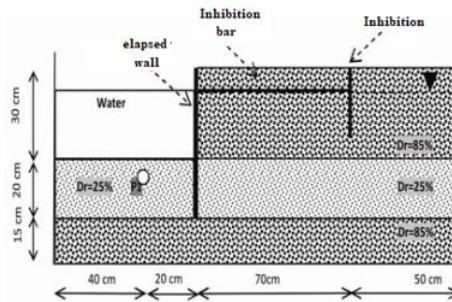
Fig. 2 – Geometry and Layout of Physical Medal without Improvement

An important challenge in this regard is the numerical simulation of a liquefaction phenomenon in which large strains occur in soil and introducing proper behavioral laws for susceptible liquefied soils. Such rules should be able to track the stress near the line of failure during periodic loading, generate a stress-strain loop, calculate the increment of the shear strain, and analyze non-isotropic soil behavior.

One of the models that provides these requirements is based on the multiple shear mechanisms [1], which was introduced by Yai et al. [14, 13] in the FLIP [1] and DIANA software [15]. Dynamic analysis and parametric reference studies [1] have employed this model. Tohata-yay model is a non-linear plastic model, which is based on the large-scale laboratory observation of the behavior of sand in unlade conditions. The main features of the present study are considering the effects of the main stress axis on the effective stress, non-isotropic consolidation, and loading history of soil behavior. The effects of these factors were expressed using two specific concepts known as simple shear virtual mechanism and liquefaction front. Considering the two-dimensional behavior under smooth strain conditions, the effective stress-strain and strain components are as follows [13]:

$$\sigma'_Z = \frac{\sigma'_x + \sigma'_y}{2} \tag{1}$$

$$\varepsilon^T = (\varepsilon_x . \varepsilon_y . \gamma_{xy}) \tag{2}$$

$$\sigma'^T = (\sigma'_x . \sigma'_y . \tau_{xy}) \tag{3}$$

Considering the fundamental equation of the model, relation (4) divides the mechanism of the rotational motion into two parts. In the first part, the volume-change mechanism is considered, and in the second part (right sentence) the shear modification of the soil is applied without the change of volume [13].

$$\begin{Bmatrix} \sigma'_{xx} \\ \sigma'_{yy} \\ \sigma'_{xy} \end{Bmatrix} = -B \left(\varepsilon_P - (\varepsilon_{xx} + \varepsilon_{yy}) \right)^2 \begin{Bmatrix} 1 \\ 1 \\ 1 \end{Bmatrix} + \sum_{i=1}^{I} Q_i(\gamma_i) \Delta\theta_i \begin{Bmatrix} \cos\theta_i \\ -\cos\theta_i \\ \sin\theta_i \end{Bmatrix} \tag{4}$$

In these relations, σ' is the effective stress, ε shows the total strain, and εp represents the plastic strain. In addition, coefficient B is as follows:

$$B = \left(\frac{0.5 k_{ma}}{-\sigma'^{0.5}_{ma}} \right)^2 \tag{5}$$

----

where σ'_{ma} and k_{ma} are respectively the mean effective reference stress and volume modulus of the soil in the predetermined stress. The second sentence of Equation 4 shows the shear deformation of the soil, which was equal to the total shear deformation (I, i=1, I) of the shear mechanism. These one-dimensional hypothetical mechanisms or shear modifications are only affected by change, and their vector is considered to be the effect of the main axis of the stress. Scalar Q_i (γ_i) is defined as the expression $\frac{dQ^{(i)}}{d\gamma^{(i)}}$, which represents the tangential shear modulus relative to, $\Delta\theta$ in the form of $R^{(i)}_{L/U}$, as follows [13]:

$$\Delta\theta = \pi/I \qquad (6)$$

$$R^{(i)}_{L/U} = \frac{dQ^{(i)}}{d\gamma^{(i)}}\Delta\theta \qquad (7)$$

In the current research, the volumetric change volume showed the correlations of the effective transformation of the volumetric strains, in which water absorption was considered in addition to the volume change in the soil. The effective stress was also obtained from the tension path calculated by the liquefaction front. Moreover, the lamellar fringes were affected by the same cumulative shear work, which was plotted as a contour in the stress space. Cumulative shear worked up to each step of loading, and the area below the shear strain graph was regarded as the shear stress from the origin of the graph to the step, which partly occurred during the elastic behavior, and the other part occurred during the plastic behavior.

$$B = \left(\frac{0.5k_{ma}}{-\sigma'_{ma}{}^{0.5}}\right)^2$$

According to the laboratory observations, the correlations between the cumulative shear work and ductile water overpressure was unique and independent with the stress, shear stress, and axial stress axis of the main stresses up to a certain amount of shear work. In addition, the correlation was transmitted to the tension space without further use, and the concept of the phase change line was applied to divide the tensile space into two expandable and compressible sections. As is shown in Figure 3, a bilinear function of the liquefaction appeared as a variable known as liquefaction frontend (S_0), which is a function of the cumulative shear bonding of the plastic factor without completing each step in the calculation as a function of the modulus soil shear at the medium effective stress level of the same stage.

In summary, the computational process is in the Taha-Yaa model should be described in detail. In each step, the process of transformation, the liquefaction section parameter S_0 is calculated after calculating the cumulative shear sheathing work. With this parameter and deviation stress ratio, *r* as the average effective stress ratio of the intermediate model could be determined, and after the multiplication of *S* to the mean effective initial stress, *σ0 'm* volumetric strain plastic *ε p* could be obtained from another middle ground. With the calculation of the shear mechanism (4), the effective stresses at the end steps are calculated. Notably, S_0 shows that the state of liquefaction is the soil and changes over time. $S_0 = 1$ represents the initial conditions (small shear stresses), and $S_0 = 0$ indicates failure due to liquefaction [13].

The parameters required for this model are described in Table 2. In the present study, the specific parameters of the model (P1, P2, S1, C1, and W1) were used to calculate the stepwise changes in the soil behavior under the shear load. These parameters were based on trial-and-error and fit the optimal diagram regarding the results of the soil cycling experiments from Qabil three-axis or simple-period cutting [5, 9, 10, 13, 14]. To determine the parameters, we needed the resistance curve of liquefaction (periodic shear stress as the number of the cycles to reach), 5% shear strain, and the growth curve of the overpressure of drilling water during the loading cycles.
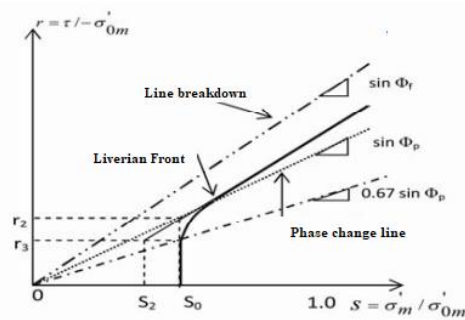

Fig. 3 – Liquefaction Front

Tab. 2 - Introducing Parameters of Tohata-Yay Model

Parameters	Description	Performance
P_{sat}	Mass Volumetric Saturation	-
P_{ref}	Effective Medium Reference of Tension	-
K_{ma}	Volumetric Modulus Change Shape	Volumetric
G_{ma}	Modulus Shear	Shear
φ_f	Internal Angle Friction	Shear
φ_p	Angle Phase Change	Dilation
W1	Control Effect of Cumulative Shearing Work	Dilation
C1	Threshold of Shearing Work	Dilation
P1	Control of First-phase Increase in Pressure Hole	Dilation
P2	Control of Second-phase Increase in Pressure Hole	Dilation
S1	Control of Lower-limit of Front Liquefaction	Dilation
Hv	Hysteric Coefficient	Shear

After modeling the conditions of the soil samples in periodic testing using software, the following steps were performed, and errors occurred in estimating the model parameters.

- For the initial estimation and prevention of the infinity strains (S_1), take a small positive amount of about 0.005 until S_0 does not exactly equal zero.

- The normal shear rate is in the lower values, and the water supply produces no pressure. As the initial guess, C_1 is taken to be one since this parameter is effective. However, no significant increase is observed in the strain (P1, W1, and P2) for the large strains that are determined by the initial guess (C1=1).

- W1 and P1 were determined by comparing the analytical hole pressure overpressure curve and laboratory based on section r_u <0.6. Since W1 does not dominate P1, W1 starts with a good assumption and is determined from P1. The prime premise for P1 is a value within the range of 0.4-0.7, and after determining P1, W1 is precise. The larger W1 and P1 show the slower growth of water pressure. Notably, the ratio of the excess water pressure to hole $r_u = \frac{\Delta u}{\sigma_{v0}}$ in which the hole pressure is added with Δu and the effective initial verbal stress, σ_{v0} is shown by comparing the growth curves of the excess water pressure of the cavity calculated, while based on section, r_u>0.6 is estimated. In the case of calculating the shape deformation, the soil and pew structures are required, and this parameter is more acceptable by comparing the computational and experimental curves of the shear strain that has been estimated by the loading cycle. In this regard, the higher P2 indicates that the increased slice strain amplitude is faster. After estimating the mentioned parameters for the large strains, their suitability is assessed in the small strains. With a model for software analysis, these

values are not considered suitable for the laboratory values of the lower strains, and the C1 changes [14] are higher for the loose soils (C1) [16].

NUMERICAL SIMULATION

To maintain the correlation of the numerical model with the actual project, the geometric properties of the sections were considered similar to Shahid Rajaee port coastal wall. Figure 4 illustrates the general scheme of the numerical models in the current research. In the selected areas, four sections were observed with a backfill as the first layer, and the second layer was divided. In the first layer, two areas were adjacent to the burial side of the bumper, which were the region behind the root and the front of the root. In all the analyses, the landing and second layer were modeled with dense aggregates, and the first sub-sets varied. Therefore, the naming of the models was due to the material disparity carried around the buried section, and the model without refurbishing a set and no front behind the root of the wall was not condensed.
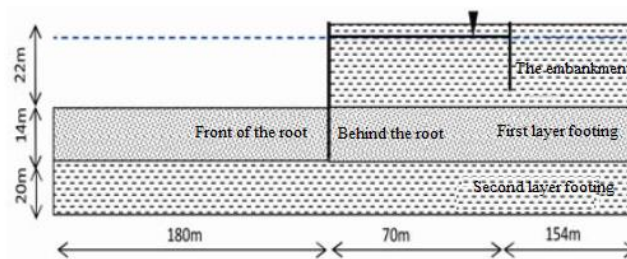

Fig. 4 – Public Plan of Numerical Models

The main constituent of the limited components of this model has the size of 404×56 meters, and the meter is located in the central part of the building. Soil compositions with the eight-component tetrahedral elements of strain flat, anchor bar with two-point springs, shields, and harnesses unbound the shell elements and could be networked [15]. To prevent numerical problems, dimensional elements are required depending on the input wavelength to the environment [17], and the dimensions of the largest element in terms of the base acceleration frequency and wavelength could be selected. The weakest material is selected to obtain more accurate responses, and the elements in the backfill and in the vicinity of the shield to the front smaller restraint are also considered. Due to the executive process, construction of the exterior walls, and calculation of the initial stresses, a step-by-step analysis method was used in the current research. Initially, the flat ground was analyzed under the load weight, followed by the activation of the shield and shield elements, and the set was balanced. At the third stage, the front side of the wall was removed to the barrier level after establishing the balance condition, the bar was activated as well.

In the fourth step, the bar was applied by an axial force equivalent to the flattened strain condition to its end node. By defining a similar force in the opposite direction to the corresponding node of the bar on the shield and the 'matched motion' condition for the two knots, an obstacle rod was attached to the wall during the fifth stage and the front side of the wall, reaching the dripping line of -22 meters. These stages were analyzed in the static state. The static analysis was performed using Moher-Kolumb model, and drainage conditions and tension were also employed.

At the fifth stage, the initial tension was transferred to the dynamic analysis stage. At the outset of the dynamic analysis stage, there was no drainage, and the behavioral model was changed into the Tohata-yay model. In total, 10 seconds of ground motion acceleration was performed at two-second steps for the seismic analysis of the samples. The maximum and minimum automatic time of the calculations was one and 0.0001 seconds, respectively, and these stages were performed by controlling the integral time error. The dependence of the controller was obtained as the time step, and in the case of dependency, the time step was corrected.

The Runge-Kutta time-integral method consists of two steps. With integration in every step of the procedure, the Newton-Raphson and convergence criterion as a ratio increase the unbalanced force selected for the external forces. To assess the effects of frequency and base acceleration in the present study, the models were accelerated with the maximum range of 0.25 and 0.50 gram. Per acceleration of the harmonic input, the frequencies of 1, 2, and 3 Hz were applied. These specifications were selected so that in addition to the occurrence of liquefaction in a set without improvement, the effect of continuity could be determined by using the rotational load before and after leakage [17]. Therefore, the dimensions of the largest element were selected based on the base acceleration frequency and wavelength in the weakest materials.

Smaller containment responses were considered, and to implement the construction of the shield walls and calculate the initial stresses, the step-by-step analysis method was used. For this purpose, flat ground was initially analyzed under the load weight, and with the activation of the shield and control elements, the set was more accurately balanced. In addition, the elements in the region of the earth and vicinity of the shield to the front in the third stage and the front wall were removed to the level of the barrier. After activating the balance condition, the barrier element was also activated. In the fourth step, the bar was subjected to an axial force equal to the strain condition of the flat end its end node. By defining a similar force in the opposite direction to the corresponding node, an obstacle rod on the shield and a 'matched motion' condition for the two knots were attached to the wall with an obstacle rod.

At the fifth stage, the soil from the front of the wall that reached the line (22 m) was removed, and the analysis of the steps was static. The static analysis of the Mohar-Coulomb model and drainage conditions were also performed, and the tensions and initial stresses of the fifth stage were transferred to the dynamic analysis stage. At the outset of the dynamic analysis stage, the conditions were not drained, and the behavioral model was changed into the Tohata model. The base acceleration was applied for 10 seconds in steps of 0.01 second. The automatic time steps were determined with the maximum of one second and minimum of 0.0001 second using the ground fault controller, and the integration was performed. The dependency controller examined the response as far as the time step, and corrected the time step in the case of dependency.

To control the two steps, the Runge-Kutta integral method was used in this method. Integration in each step of the time was performed by the Newton-Raphson method, and the convergence criterion was selected as increased ratio of the unbalanced force to the external force [18]. To investigate the effects of frequency and base acceleration, the models were exposed to base acceleration with the maximum range of 0.25-0.50 gram. In the acceleration steps, the harmonic input moved at the frequencies of 1, 2, and 3 Hz. These specifications were selected so that in addition to the occurrence of liquefaction in an unsorted set, the effect of the continuity of the load application would be assessed before and after liquefaction.

Tab. 3 - Specimen Properties

Member	Section	P (kg/m^3)	Dimension	Ball length	Thickness
Wall	T-shape	2500	4*4	4	0.8
Inhibition	Circular	2500	1	-	-

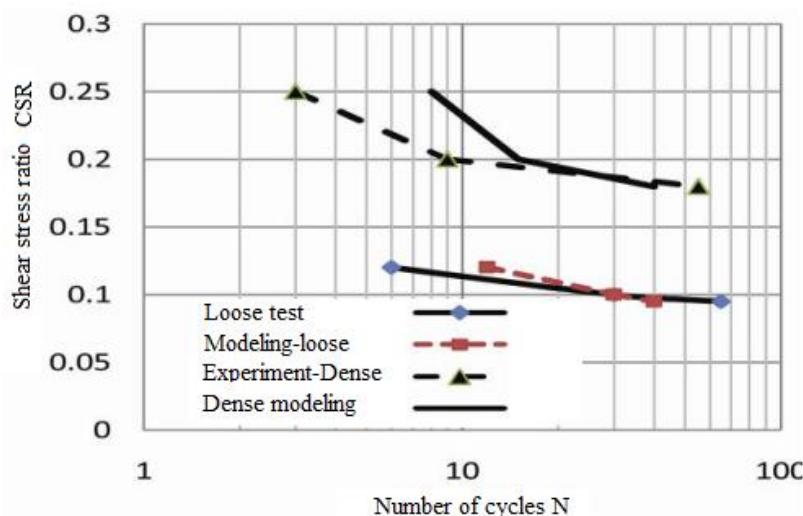---

Fig. 5 – Modeling of Sand Resistance against Liquefaction

Tab. 3 - Characteristics of Soil Materials

Situation	$P_{sat}(kg/m^3)$	K_{ma} MPa	G_{ma} MPa	φ_f	φ_p	W1	C1	P1	P2	S1	Hv
Weak	1900	223	86	34	28	4	1.5	0.3	3.8	0.005	0.24
Dense	1980	300	115	40	28	40	1	0.1	1.0	0.005	0.24
Very Dense	2000	324	125	42	28	42	1	0.1	0.8	0.005	0.24

To determine the soil parameters in loose and dense compaction conditions for use in the Taha-Yaah model, cyclic experiments were performed on the sand specimens with the density of 35% and 75% [19]. After the numerical modeling, the specimen conditions were determined in the cyclic and by the simultaneous comparison of the percolation water pressure and shear strain with the measured values using the Taha-yea model parameters in the form of trial-and-error. Given the importance of shear strain over excess water pressure, the lubrication criterion reached the strain amplitude of DA=5% in determining the parameters. In addition, the soil areas were modeled with extremely dense soil parameters (95%). Figure 5 shows the comparison of the results of the numerical model in these samples with the experimental values. The parameters used for the analysis are presented in Table 4. Considering the similarity of the selected mass to the standard Taureau [12], the maximum shear modulus and GMA of the proposed correlations with the Taoyu sand were also determined [20].

RESULTS AND DISCUSSION

In the current research, the unshaped physical model was located at 0.25 gram and the frequency of 3 Hz after saturation and subjected to sinusoidal acceleration. Figures 6-a and 6-b respectively depict the initial and final state of the unmodified model and SPM1. By applying the base acceleration, the foot of the wall that was immersed in the soil susceptible to liquefaction was displaced more than the crown of the wall. This type of failure is referred to as 'burst section failure'. Due to the wide affected areas, including all the components of the buffer structure, the repair of the structure after the occurrence of this mode might be very costly and even impossible.

According to section B, the path of the color lines indicated that most of the deformations were concentrated in the loose soil near the root of the wall. In addition to the significant elevation of the bottom of the sea, the movement of the sidewall also significantly reduced the backing effect of this layer to the buried wall section, thereby leading to the large period, followed by an active wedge from the buried side to the back of the containment. Due to the fact that the barrels were located in this wedge and the movement alongside, the braces also suffered considerable periods.

The shaped areas in front of the root and the sea, along with the horizon, compressed and extended along the vertical axis, while behind the root, the deformation portion was compressed along the horizon and extended along the vertex. With this type of deformation on both sides of the root, a combination of flattening and cutting would be possible with different marks. Due to its low weight and low wall density, no significant changes occurred in the soil under the root in the current research. On the other hand, the embankment summit increased to the wall and decreased in depth, which could be attributed to density, the lateral movement of the wedge, and the combination of these factors.

(a)   *(b)*
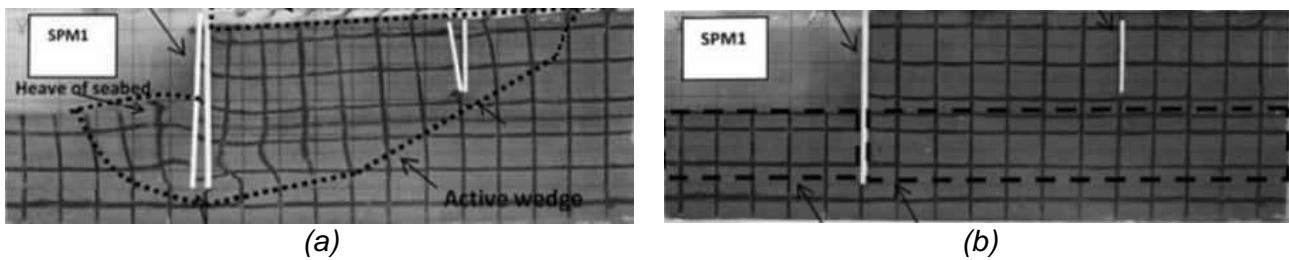
Fig. 6 – a) Original Form, b) Final Shape of Ungraded Model

As can be seen in Figure 7, the wall crown shifted to the sea during a shake of 97.4 centimeters, which was equivalent to the wall height of 16%. Given the final shape of the model, the displacement of the foot of the wall was clearly greater than this ratio. As is shown in Figure 8, the displacement occurred simultaneously with the significant increase in the ratio of the excess water pressure and the soil liquefaction in the front of the root of the wall at the distance of 20 centimteres (Figure 2) (points P1).
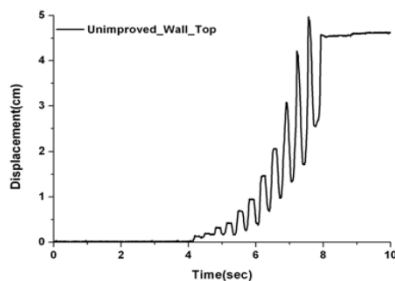
Fig. 7 – Movement History of Crown of Wall   *Fig. 8 – History of Water Drainage Ratio Simulation*
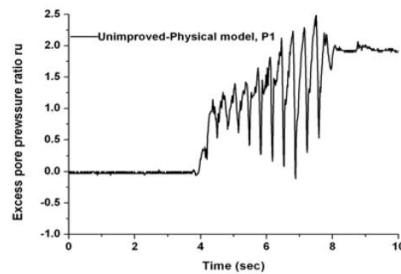
The introduced set in the numerical model underwent significant changes after applying the base acceleration. Regardless of the amount of these deformations, which depended on the features of the base motion, the overall geometry of the set was similar to (9), indicating the reversal of the restraint and the wall toward the sea. In addition to lateral movement, a considerable amount of seating was observed at the crown and foot of the wall.

(a)   *(b)*
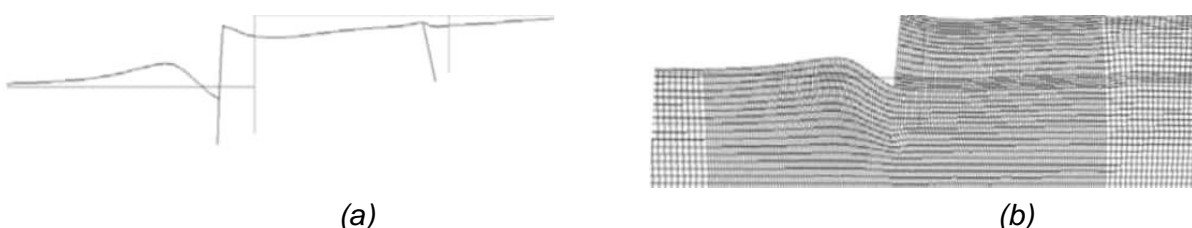
Fig. 9 – Uniform Geometry of Numerical Model (a=0.25 g, f=3 Hz); a) External Boundaries, b) Elements

----

In the current research, soil sedimentation, its lateral displacement, and the elevation of the bottom of the sea were also considered as the most important changes in the soil layers. According to section B, most of the deformations were concentrated in a clear range, which started from the bottom of the wall and extended along one or two straight lines to the back of the containment. The other part was the level of the rupture in front of the root of the wall, and the sea was formed on the side. In contrast to the shape deformation of the structure, the deformation of the other parts of the complex was negligible. Furthermore, the final geometry of the collection was observed to be close to the laboratory sample. Therefore, it could be concluded that assessing the effectiveness of the upgrading soil around the root is of particular importance. Figure 10 indicates that the displacement slope of the foot of the bot was higher than the top of the tower due to the fact that the foot of the wall was loose in the loop, thereby causing the change of the failure mode to 'bursting section failure' based on the acceleration period during which the change of the foot of the wall became larger than the crown. In addition, the increased frequency of the input motion caused the displacement values to significantly decrease, and the change in the failure mode occurred later on. For instance, while displacing the foot of the wall during the inertia movement with the frequency of 1 Hz at the angle of 4.8 seconds from the crown displacement, it occurred during the base acceleration, which was similar to the frequency of 3 Hz at 6.8 seconds.

The final displacement of the wall crown was observed at the frequency of 4/00, 1 Hz m (18%), and the height of the wall of the dripping code (frequency: 62.2 and 2 Hz) was estimated at 12%. In addition, the wall height of the dripping code (frequency: 14.2 and 3 Hz m) was 9.72%. as is shown in Figures 10 and 11, the history of the change of wall location with the increased acceleration of the system caused the wall foot fracture to become faster, and a larger wall than the accelerator had larger displacements at all the moments. For instance, the final displacement of the wall crown during the acceleration of 0.50 gram and frequency of 20.5 1 Hz m (23%) of the wall height of the dripping code (frequency: 97.3 and 2 Hz m), 18% of the wall height of the dripping code (frequency: 19.3 and 3 Hz m) was estimated at 14%. On the other hand, the height of the wall was of a desiccant code, and the doubled base acceleration rate could not increase the displacement doubles.

As is depicted in Figure 12, the endless displacement of the bezel of the wall crown decreased in terms of height due to the simulation in the studied accelerations, with an almost equal slope due to the higher frequency. Figure 13 shows the strong dependence of the displacement on the input frequency, the importance of this parameter in the analysis of the seismic behavior of the set, and the results of the wall arrangement. Correspondingly, a significant meeting occurred under the wall during the baseline vibration with the accelerated velocities, and this arrangement increased with higher acceleration, while decreasing at the higher frequency of the inertial movement.
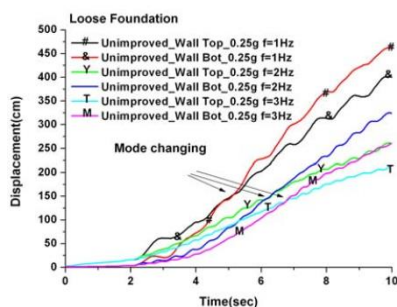

Fig. 10 – Comparison of Failure of Wall in Ungraded Site during Base Acceleration of 0.25 g and Frequency of 1, 2, and 3 Hz
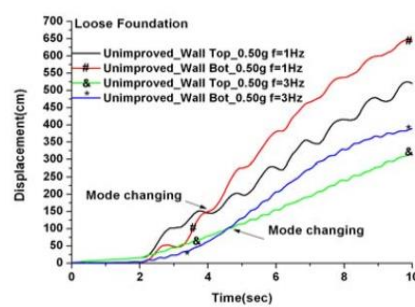
Fig. 11 – Comparison of Failure of Wall in Ungraded Site during Base Acceleration of 0.25 g and Frequency of 1, 2, and 3 Hz

----
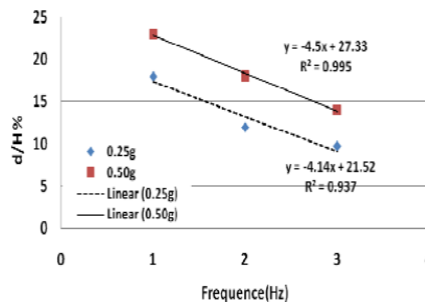
Fig. 12 – Dependence of Displacement between Crown Dimension of Wall and Input Frequency in Unshared Site

According to the findings of the current research, the loose-layer liquefaction was denser compared to the layers that were prone to increased water pressure, which could lead to less leakage in the areas with lower primary stress. Figure 16 shows the position of several elements examined in the loose layer. The horizontal distance of the P2, P1, and P3 elements from the root of the wall was estimated at 20, 10, and 30 meters, respectively, and the horizontal distance of the P4 components was 10 meters. Furthermore, the elements examined from the second element of the loose layers had higher initial tensile stress compared to the upper elements without a common knot with the elements in the dense aggregates.

As is depicted in Figure 14, the monotonic component of the cavity water pressure ratio (run) in the front and near the root of the wall grew more significantly than the particle elements, while this ratio decreased significantly with the increased distance of the element from the root of the wall at a considerable rate. This is because the elements were close to the fringe and had static shear stress, which increased the shear strain and liquefaction potential of the soil [17]. The presence of smaller effective overhead and initial shear stress also caused these areas to behave as the weakest part of the complex in the event of soil loosening and accelerate in the strongholds.
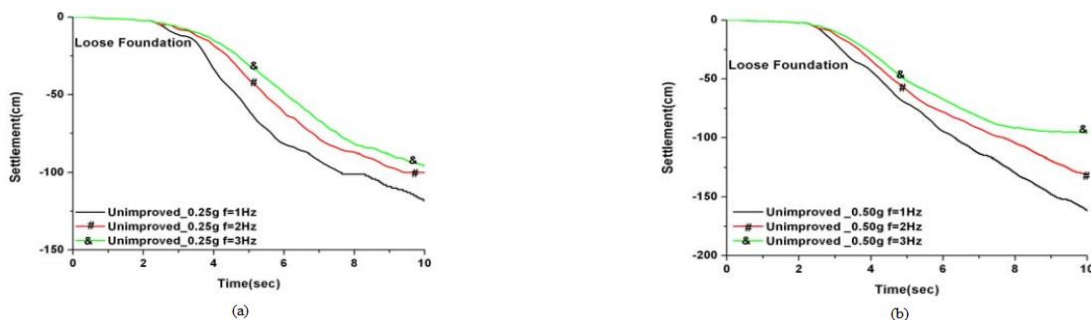
Fig. 13 – Seating of Wall in Unmodified Site at Frequencies of 1, 2, and 3 Hz with Base Acceleration of a) 0.25 g and b) 0.50 g

Based on this form, while the elements were located at 10 meters in front of the wall during the acceleration of 0.25 gram and liquefied, the soil was located at 30 meters (approximately twice the depth of the buried section), tolerating a small load of 25% of the initial stress. It was also observed during this loading in the soil, the elements were loose behind the wall due to the larger overhead, and the excess water pressure could not be produced, thereby leading to no risk of liquefaction in these areas.
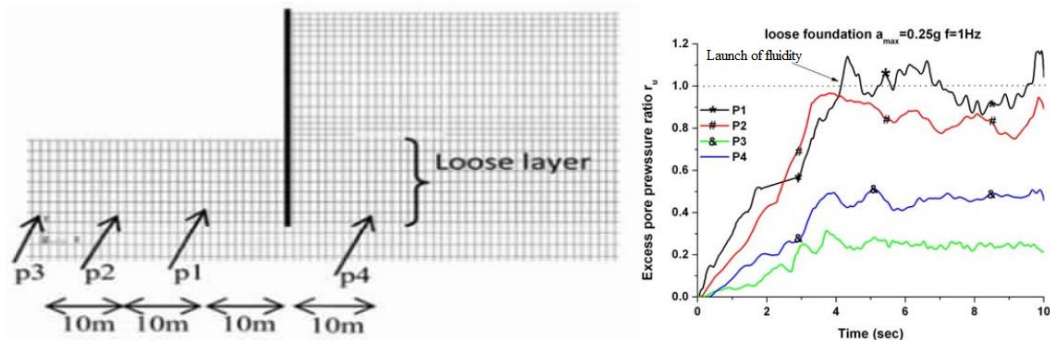
Fig. 14 – Liquefaction of Front and Back Elements of Wall with Base Acceleration of 0.25 g and Frequency of 1 H

Considering the design of the shield walls based on the assumption of the joint foot or groove operation, the monotonic component of the flexural anchor of the foot of the wall was extracted in order to recognize the changes in the ankle of the wall in this situation. During the dynamic loading, if the anchor was applied to the wall contrary to the anchor's direction, the median part of the free wall length could be obtained. Therefore, it could be concluded that the soil around the root of the wall acts as a support and behaves at the foot of the wall. Figure 15 shows the comparison of the curvature of the bending anchor curves of the wall at 1, 0, 0.1, and 5 seconds, gravity of 0.25 gram, and frequency of 1 Hz. It was also observed that at the outset of the loading, an anchor resistant to the buried section (distance from the wall foot: 14-0.0 m) was in the opposite direction to the anchor, affecting the mid-section of the free-wall length. Over time, not only the anchor was destroyed, but it extended the free length into the buried section. The time history of the monotonic component of the bending anchor of the foot of the wall (Figure 16) indicates that the growth of the anchor began from the initial moments of the base acceleration due to the lack of a change in the monotonic anchorage entering the middle section of the wall at different accelerations in terms of the signs. The presence of this anchor with an anchor on the wall and a loose layer around the buried section not only produced a rigid anchor in this section, but another anchor entered the middle section with a stimulus state and unstable in the wall.

Fig. 15 – Variation of Bending Anchor of Wall at Reconstruction Site (second PH6 503) (5) and PH3 (303) 3, (PH6 4) 0/01 Not Found during Base Acceleration of 0.25 g and 1 H Frequency

Fig. 16 – History of Bending Anchor in Middle and Foot of Wall in Non-Upgraded Site

----

The presence of an anchor actuator at the foot of the wall suggested that even assuming a joint foot in the susceptible site to liquefaction would be hypothesized to be a loss if the entire buried section was in such a layer.

IMPROVEMENT AROUND THE ROOT

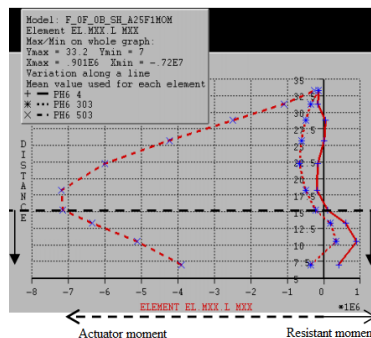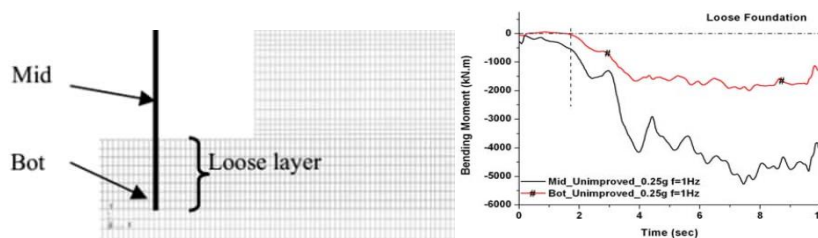As mentioned earlier, density was used as the method of improvement in the present study. In this section, the effects of the bulk density of the sides of the section have been described with an emphasis on the wall displacement and bending anchor variations. The basis for selecting the front side of the wall was to improve the liquefaction, which started from the soil of this area. It seemed that the improvement of this section would reduce the displacement of the set or change the failure mode. Due to the fact that the lateral pressure of the loose soil was denser than the soil, it seemed that the improvement of the soil behind the wall would reduce the pressure on the wall given the importance of identifying the effects of the improvement length on the set performance. Furthermore, the behavior of the models in the I-2.5-B-2.5 and I-5-B-5 designs were evaluated at 1 Hz, where I and B represented the equivalent soil height in the front and behind of the wall (Figure 19).

In these designs, the front and back sides of the wall were about five and 12 times the length of the buried wall with very dense material. The improvement of the two sides of the roots in the studied lengths significantly decreased the displacements, and Figure 17 shows that during the base acceleration of 0.5 gram and 1 Hz frequency in the model I-2.5-B-2.5,the displacement of the wall crown decreases from 25% of the wall height relative to the dredging level to 18% and the displacement of the wall foot from 30% to 15%. The design also prevented the foot of the wall from the wall crown, making it easier to repair the operations in the absence of shield bomber damage.

Figure 18 shows a posture without the crown and foot of the wall compared to the height of the dairy code at the base acceleration of 0.25 and 0.5 gram. With the execution of the I-2.5-B-2.5 design in both moves, the footprint of the foot of the wall was corrected from its crown. By the five-fold increase of the repair length on each side, the displacement of the crown and foot of the wall decreased more effectively. Due to the small difference in the results of the I-5.0-B-5.0 model, the optimal optimization time for the provided specification was less than five times the buried depth on the sides of the root.
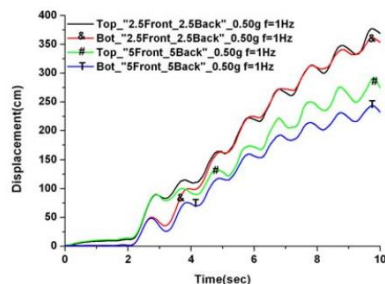
Fig. 17 – History of Displacement of Peak and Foot of Wall in Models I-2.5-B-2.5 and I-5.0-B-5.0 at Acceleration of 0.5 and 1 g
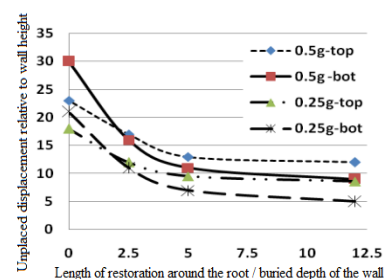
Fig. 18 – Effect of Length of Recovery on Displacement

To justify the effects of the proposed designs, attention should be paid to the changes in the bending anchor on the middle section and foot of the wall. For this purpose, in the form (19), the variation of the monotonic curvature anchor was denoted in the middle and foot of the wall at the acceleration of 0.5 g and 1 Hz frequency for the unmodified model. Unlike the ungraded model in which there were the joint foot conditions with an anchor zero at the foot of the wall (only lasted two seconds), improvement was observed in the sides and maintained the behavior to the end of the vibration. In addition, median wall anchor significantly decreased, and the same trend was observed in the other improvement projects.
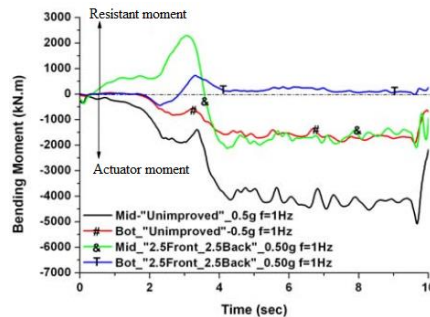
Fig. 19 – Wall Bending Anchorage Model I-2.5-B-2.5 at Acceleration of 0.5 g and 1 Hz Frequency

CONCLUSION

In the current research, the effects of a lubricant susceptible layer around the buried section of an enclosed seabed wall using physical and numerical modeling were investigated in terms of the base acceleration and intake frequency, and the efficiency of the back and front portions of the buried section in the reduction of the wall displacement and variation was also assessed. Furthermore, the failure mode was evaluated, and the obtained results indicated that if there is susceptible layer liquefaction around the root of the wall, the front of the root on the seafloor increases the cavity water pressure excess ratio due to the lower initial effective stress and presence of the initial static shear stress. Leakage in the front of the root and the large lateral pressure on the root of the root also significantly increased the likelihood of the bursting fracture failure, and the failure could primarily be attributed to the formation of the soil recessive effect around the buried section, as well as the use of an anchor actuator in this section.

According to the results, the dependency of the sharp change of the locations on the base acceleration and frequency of the entrance motion highlighted the importance of these factors in the seismic behavior of the set. As a result, the application of a larger base acceleration led to large displacements, while the displacement increased at the higher frequencies of the inertia movement. By improving the soil on both sides of the root and preventing the bursting fracture, the displacement of the crown and foot of the wall significantly decreased. In addition, the effects of improving the sides of the root on the reduction of the displacement of the foot of the wall were considered more significant compared to the reduced displacement of the crown of the wall. Finally, the minimum required length of the root grooves for the studied designs was observed to be 2.5 times the length of the root of the wall to prevent the failure of the buried section, while the reverse process did not show a significant increase after the five-fold upgrade to the root length.

REFERENCES

 [1]   International Navigation Association, "Seismic Design Guidelines for Port Structures", Balkema, Tokyo, 2001.

[2]   Ramos, M.C. & Mart´nez-Casasnovas, J.A., " The cost of soil erosion in vineyard fields in the Penedes–Anoia Region (NE Spain)", Catena 68 194 – 199. 2006.

[3]   Psarropoulos, P. N., Klonaris, G., Gazetas, G., "Seismic Earth Pressures on Rigid and Flexible Retaining Walls", Soil Dynamics and Earthquake Engineering, 2005, 25, 795- 809.

[4]   Mondal, G.C. & Rai, D. (2008), " Performance of harbor structures in the Andaman Islands during the 2004 Sumatra earthquake", Engineering Structures 30 174–182.

[5]   Mohajeri, M., Kobayshi, Y., Kawaguchi, K., Sato, M., "Numerical Study on Lateral Spreading of Liquefied Ground Behind a Sheet Pile Model in Large-Scale Shake Table Test, " The 13th World Conference on Earthquake Engineering, Vancouver, Canada, 1-6 August 2004.

[6]   Motamed, R., Towhata, I. "Shaking Table Model Tests on Pile Groups Behind Quay Walls Subjected to Lateral Spreading", Geotechnical and Geoenvironmental Engineering, 2010, 136, 477-489.

[7]   Ueda, K. Tobita, T., Iai, S. "A Numerical Study of Dynamic Behaviour of a self-supported Sheet Pile Wall", The 14th World Conference on Earthquake Engineering, Beijing, China, 12-17 October 2008.

[8]   Kohama, E., Sugano, T, Shiozaki, Y., Mutoh, M., "Dynamic Behaviour of a Steel Sheet Pile Quay Wall in the Full-Scale Experiment with Regard to Liquefaction", The 13th World Conference on Earthquake Engineering, Vancouver, Canada, 1-6 August 2004.

[9]   Nozu, A., Ichii, K., Sugano, T., "Seismic Design of Port Structures", Journal of Japan Association for Earthquake Engineering, 2004, 4 (3).

[10]   Sawada, S., Ozutsumi, O., Iai, S., "Analysis of Liquefaction-Induced Residual Deformation for Two Types of Quay Walls: Analysis by FLIP", The 12th World Conference on Earthquake Engineering, Auckland, New Zealand, 30 January-4 February 2000.

[11]   Iai, S., "Similitude for Shaking Table Test on Soil-Structure-Fluid Model in 1g Gravitational Field", The Port & Harbour Research Institute, Japan, 1988.

[12]   Ghalandarzadeh, A., Akbari-Paydar, N., "Shaking Table Tests of Flexible Quay Walls Subjected to Backfill Liquefaction", Asian Regional Conference on Soil Mechanics and Geotechnical Engineering, New Delhi, India, 2007, pp 690-693.

[13] I   ai S., Matsunaga, Y., Kameoka, T., "Strain Space Plasticity Model for Cyclic Mobility", Report of the Port and Harbour Research Institute of Japan, 1990.

[14]   Iai, S., Matsunaga, Y., Kameoka, T., "Parameter Identification for a Cyclic Mobility Model", Report of The Port and Harbour Research Institute of Japan, 1990.

[15]   Manie, J., Kikstra, W. P., "DIANA User's Manual: Matlab", 1st Edition, TNO DIANA BV, Netherlands, 2009, pp 475-479.

[16] I   chii K., S. Iai, Y. Sato H. Liu, "Seismic Performance Evaluation Chart for Gravity Type Quay Walls", Journal of Structural Engineering / Earthquake Engineering, JSCE, 2002, 19, 21-31.

[17]   Kramer, S. L., "Geotechnical Earthquake Engineering", Prentice Hall, 1996.

[18]   Manie, J., Kikstra, W. P., " DIANA User's Manual: Analysis", 1st Edition., TNO DIANA BV, Netherlands, 2009, pp 497-499.

[19] A   hmadi, M., Shirasb, A.," Liquefaction Resistance of Firozpur Sand using Cyclic Simple Shear Test", The 6th National Conference on Civil Engineering, Semnan, Iran, 26-27 April 2011.

[20]   Arable, A., Ghalandarzadeh, A., Mostafagharabaghi, A. R., Abedi, K., "A Numerical Study of Liquefaction-Induced Deformation on Caisson-Type Quay Wall Using a Partially Coupled Solution", Journal of Offshore Mechanics and Arctic Engineering, 2010, 133 (2).

RESEARCH ON THE INFLUENCE OF MILD STEEL DAMPERS ON SEISMIC PERFORMANCE OF SELF-RESETTING PIER

Mengqiang Guo and Yanli Shen

*University of Hebei Engineering, Faculty of Civil Engineering, Handan, Hebei, China;
guo1933619417@163.com, shenyanli@hebeu.edu.cn*

ABSTRACT

In order to improve the energy consumption capacity of the assembled self-resetting pier, the mild steel damper is added to the prefabricated self-resetting pier to form a prefabricated self-resetting pier with an external mild steel damper. Two sets of pier models were established by numerical simulation. On the basis of verifying the correctness of the traditional prefabricated self-resetting pier model, the two sets of pier models were subjected to low-cycle reciprocating loading to study the influence of the mild steel damper yield strength parameters and the pier axial compression ratio parameters on the seismic performance of the pier structure. The results show that compared with traditional prefabricated self-resetting piers, the hysteresis curve of self-resetting piers with mild steel dampers is fuller, and energy consumption and bearing capacity are greatly improved. With the increase of the yield strength of the mild steel damper, the energy consumption capacity will decrease when the loading displacement is less than 25mm, but the overall energy consumption capacity will increase. As the axial compression ratio of the pier column increases, the bearing capacity and energy consumption capacity of the structure increase significantly, but the impact is not obvious when the axial compression ratio exceeds 0.052.

KEYWORDS

Self-resetting pier, Mild steel damper, Axial compression ratio, Seismic performance

INTRODUCTION

Compared with cast-in-place concrete piers, fabricated self-resetting piers have the advantages of good seismic performance, high post-earthquake repairability, and low damage. In particular, the combination of damping technology and self-resetting pier design forms a layered protection. The bridge system that can eliminate the plastic hinge and quickly restore its function after an earthquake has important research value. Mander et al [1] first introduced the idea of self-resetting structure in the design of bridge piers, using unbonded prestressed steel bars to improve the seismic performance of the bridge piers. The pseudo-static test results showed that the prefabricated self-resetting bridge piers have small residual displacements, but weak energy consumption. In order to improve the energy dissipation capacity of bridge piers, Solberg et al [2] proposed to install energy dissipation steel bars to improve the seismic performance of bridge piers. The pseudo-static test results showed that energy dissipation steel bars increased the energy dissipation capacity of bridge piers. Marriott et al [3-4] proposed to install an external energy dissipation device to improve the post-earthquake recovery of the self-resetting pier. The pseudo-static and pseudo-dynamic test results show that the new prefabricated self-resetting pier has higher bearing capacity and energy consumption, and easy to repair after an earthquake. Trono et al [5] confirmed that self-resetting piers have obvious advantages in damage and residual displacement through shaking table tests. Guo Jia, Xin Kegui et al [6-7] expounded the working principle of prefabricated self-reset bridge pier test. Haitham [8] performed a numerical simulation on the performance of the fabricated bridge pier under reciprocating load and verified the influence of the

----

concrete constitutive model on the simulation results. Bu et al [9] conducted pseudo-static tests on 5 circular cross-section piers. The test results showed that compared with bonded prestressed tendons, unbonded prestressed tendons have less prestress loss and more sustainable and effective prestress. Wang Junwen et al [10] conducted a pseudo-static test on a hollow concrete pier and 3 precast and assembled hollow piers with prestressed sections. The test results showed that the unbonded prestressed tendons reduced the residual displacement of the structure, but the energy dissipation capacity decline. Ge Jiping [11] conducted a pseudo-static test study on prefabricated self-resetting bridge piers. The study showed that the bottom of the pier and the cap were separated and swayed. Although the bottom damage of the pier column was reduced, the overall energy consumption was reduced. Guo et al [12] tried to set up replaceable external energy-consuming devices. Research shows that different energy-consuming device parameters have a certain impact on the seismic performance of bridge pier structures. In summary, the traditional prefabricated self-resetting piers have good self-reset capability and small residual displacement, but they have poor energy consumption and they are not easy to repair after an earthquake. Fabricated self-resetting piers with external mild steel dampers have the advantages of good energy consumption and easy repair after earthquakes. It is necessary to conduct more in-depth research on fabricated self-resetting piers with additional mild steel dampers.

This research proposes a fabricated self-resetting pier structure with mild steel dampers. The establishment of a refined numerical model and the validation of the validity of the numerical simulation are carried out to study the seismic performance of fabricated self-resetting piers with mild steel dampers, and the influence of different yield strength parameters and different axial compression ratio parameters on the seismic performance of the structure.

METHODS

Fabricated Self-resetting Pier Structure with Mild Steel Damper

An external mild steel damper is added to the foundation of the traditional prefabricated self-resetting pier. The pier and the cap are separated. The mild steel dampers are symmetrically arranged at the centre of the two sides of the pier at a 45-degree angle along the transverse direction. The damper can effectively transfer stress and avoid slippage of the structure. The structure diagram of the assembled self-resetting pier with external mild steel damper as shown in Figure 1.
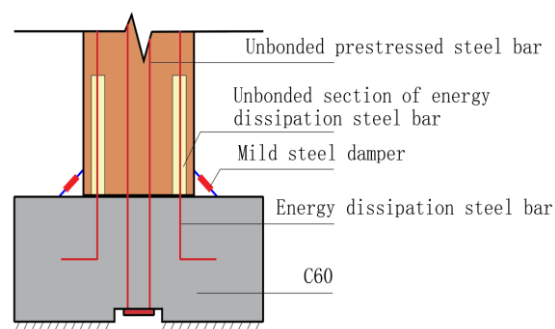
*Fig. 1 - Structure Drawing of Prefabricated Self-Resetting
Pier with External Mild Steel Damper*

Basic Structure and Working Principle of Mild Steel Damper

The structure diagram of the mild steel damper is shown in Figure 2 and the main component size diagram is shown in Figure 3. The mild steel damper is mainly composed of 1. shaft sleeve hinge support, 2. shaft hinge support, 3. high-strength bolts, 4. mild steel rod, 5. shaft sleeve, and 6. shaft.

（a）Assembly Drawing　　　　（b）Sectional Drawing
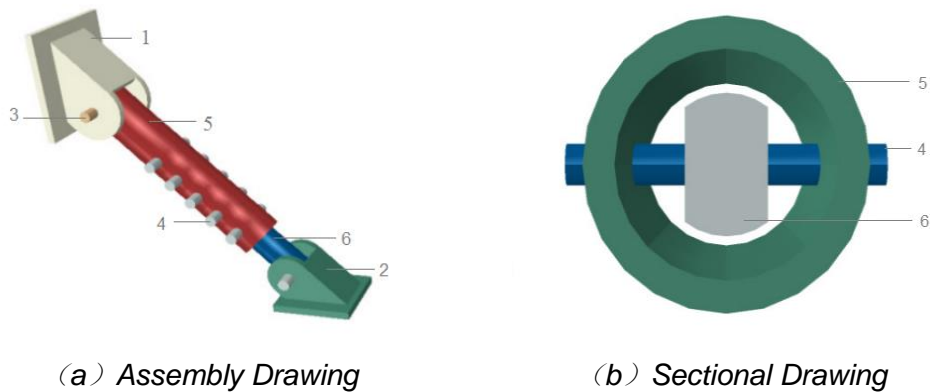
Fig. 2 - Structural Diagram of Mild Steel Damper
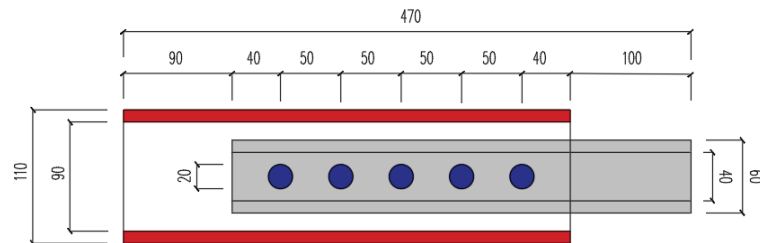
Fig. 3 - The Main Component Dimension Diagram of Mild Steel Damper

The shaft hinge support 2 and the shaft sleeve hinge support 1 are consolidated with the bridge pier structure through high-strength bolts. The shaft 6 and the shaft sleeve 5 are respectively hinged with the shaft hinge support 2 and the shaft sleeve hinge support 1 through the high-strength bolt 3, so that the damper only receives axial force. The shaft 6 is arranged inside the shaft sleeve 5, the shaft and the shaft sleeve are provided with five one-to-one corresponding circular holes along the axial direction, and a soft steel rod 4 penetrates between each corresponding shaft sleeve circular hole and the shaft circular hole. Except for mild steel bars, other parts are made of Q345 high-strength steel. When the mild steel damper is deformed, the sleeve and the shaft move to squeeze the mild steel rod to yield and consume energy.

Yield Mechanism of Mild Steel Damper Prior to Energy Dissipation Steel Bar

Under the condition of ignoring the second-order effect of the bridge pier, the schematic diagram of the corner between the bottom of the bridge pier and the cap under the action of earthquake as shown in Figure 4.
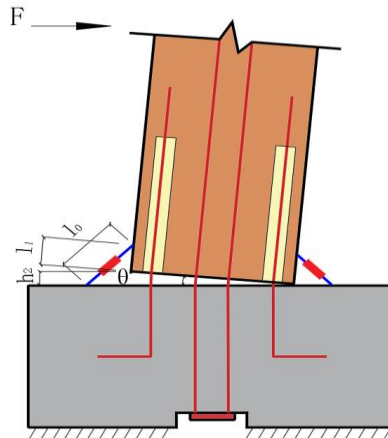
Fig. 4 - Schematic Diagram of Assembled Self-Resetting Pier with External Mild Steel Damper

When an angle of θ occurs between the bottom of the pier and the cap under the action of an earthquake load, ε_0 is the deformation of the energy dissipating steel bar, as Equation (1).

$$\varepsilon_0 = (b-c)\sin\theta \tag{1}$$

h_2 is the rising height of the left edge of the bottom of the pier, as Equation (2)

$$h_2 = b\sin\theta \tag{2}$$

l_2 is the deformed length of the damper, as Equation (3)

$$\left(l_1\cos\theta + h_2\right)^2 + \left(l_1\sin\theta + b - b\cos\theta + l_1\right)^2 = l_2{}^2 \tag{3}$$

ε_1 is the deformation of the damper, as Equation (4)

$$\varepsilon_1 = l_2 - l_0 \tag{4}$$

In the above Equation, l_0 is the initial length of the damper, b is the transverse dimension of the pier, and c is the distance between the energy dissipating steel bar and the edge of the pier. Generally, $\varepsilon_1 > \varepsilon_0$, because the greater the radius, the greater the arc length under the same corner. When satisfied: (ε_1-Yield displacement of damper > ε_0-Yield displacement of energy dissipation steel bars), it shows that the damper yielded before the energy dissipation steel bar, this research is based on it. Mild steel dampers are used as the first line of defence against energy dissipation, and energy-consuming steel bars are used as the second line of defence against energy dissipation. Mild steel dampers act earlier than energy-consuming steel bars. The steel bars play a protective role to avoid premature yielding of energy-consuming steel bars, which is conducive to the continuous performance of the structure's seismic performance under aftershocks, which improves the safety performance of the structure, and the external mild steel dampers are easy to replace after earthquakes.

Shear Capacity Analysis

The shear force in the horizontal direction of the pier is mainly borne by the pier column itself, the horizontal component of the prestressed tendons, the friction between the bottom of the pier and the cap, and the horizontal component of the mild steel damper. The shear resistance mechanism as shown in Figure 5.

Fig. 5 - Shear Mechanism

When the angle between the pier bottom and the cap is θ under the horizontal force of the pier top, the compressed concrete of the pier column forms a compression rod, and the prestressed tendons form a tension rod. The shear capacity of the pier column is mainly divided into five parts, as Equation (5).

$$V_k = V_y + V_l + V_f + V_1 + V_2 \tag{5}$$
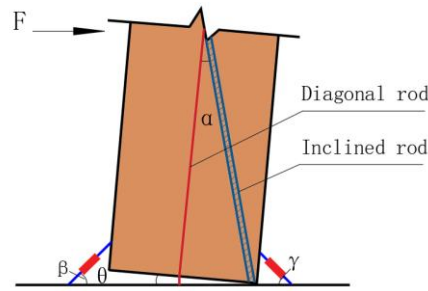
In Equation (5), V_k is the shear bearing capacity of the pier column; V_y is the horizontal component of the inclined rod; V_l is the horizontal component of the diagonal rod; V_f is the horizontal friction between the pier bottom and the cap; V_1 and V_2 are the horizontal components respectively force of the left and right mild steel dampers. Therefore, the above equation is referred to as Equation (6).

$$V_k = 0.8 f_c b_2 b_3 \cos(\frac{\pi}{2} - \alpha + \theta) + F_p \sin\theta + 0.8\mu f_c b_2 b_3 \sin(\frac{\pi}{2} - \alpha + \theta) + F_1 \cos\beta + F_2 \cos\gamma \tag{6}$$

b_3 is evaluated empirically as

$$0.2\sqrt{h^2 + (\frac{b_1}{2})^2} \tag{7}$$

In the above Equation, 0. 8 is the concrete strength reduction factor; 0. 2 is the constant coefficient; f_c is the compressive strength of the concrete; b_1 and b_2 are the width of the bridge pier in the transverse and forward directions respectively; b_3 is the equivalent width of the diagonal strut; F_p is the prestressed tendon Tensile force value; μ is the friction coefficient between the bottom of the pier and the cap, taking 0. 5; F_1 and F_2 are the axial tension and pressure values of the left and right mild steel dampers respectively; α is the angle between the line connecting the top of the column to the edge of the compressed concrete at the bottom of the column and the centre line of the pier column; β and γ are the angles between the left and right mild steel damper axis and the horizontal direction; h is the height of the pier column. In general, θ is small, and the above equation is simplified as Equation (8).

$$V_k \approx 0.8 f_c b_2 b_3 \sin\alpha + 0.8\mu f_c b_2 b_3 \cos\alpha + F_1 \cos\frac{\pi}{4} + F_2 \cos\frac{\pi}{4} \tag{8}$$

Generally $b_1/h \leq 1$, therefore, $V_y \leq V_f$. Compared with the friction between the bottom of the pier and the cap, the shear capacity of the pier is mainly determined by the pier itself, as Equation (9).

$$V_k \approx 0.8 f_c b_2 b_3 \sin\alpha + F_1 \cos\frac{\pi}{4} + F_2 \cos\frac{\pi}{4} \tag{9}$$

The prefabricated self-resetting pier model with mild steel dampers designed by this research can get: V_k =472kN. The shear bearing capacity is much greater than the maximum horizontal force of 292kN in the simulation, so the designed pier shear capacity meets the requirements.

Model Parameters and Unit Selection

In this paper, two sets of numerical models of bridge piers are established. The first group is M1, M2, M3 and M4. It mainly studies the influence of three mild steels with different yield strength parameters: BLY100, BLY160 and BLY225 [13-15] dampers on the seismic performance of the structure. The second group is M3, M5 and M6. Taking M3 pier as an example, the influence of axial compression ratio parameters of pier column on the seismic performance of the structure is mainly studied. The pier columns, caps, reinforcement, cross-sectional area of reinforcement, and prestressing tendons of the two groups of piers are the same, and the reinforcement ratio, energy dissipation steel, and prestressing tendons of the pier model are all based on the data in reference [7].

This paper used finite element software ABAQUS. The mild steel damper adopts hexahedral solid element and an ideal elastoplastic model. The main parameters of the model and the corresponding model numbers as shown in Table 1. M1 is a traditional assembled self-resetting pier. The concrete grade of each specimen is C60, the plastic damage model is adopted, the elastic modulus is 3.8×10^4 MPa, the Poisson's ratio is 0.3, and the hexahedral solid element is adopted. The steel bar is HRB335, using truss elements, and an ideal elastoplastic constitutive model. The prestressed tendons are made of 1860 grade steel strands, and each prestressed tendon uses the cooling method to apply an initial prestress of 80kN, and the expansion coefficient is set to $1.2 \times 10^{-5}/°C$. The main parameters of each component of the structure as shown in Table 2 and Table 3, the mechanical properties of reinforcement as shown in Table 4, and the reinforcement drawing of the assembled self-reset bridge pier with mild steel damper as shown in Figure 6.

Tab. 1 - Parameters of Mild Steel Damper

Model number	Mild steel damper parts	Rebar model	Quantity	Axial compression ratio
M2	Mild steel rod	BLY100	10	0.026
M3	Mild steel rod	BLY160	10	0.026
M4	Mild steel rod	BLY225	10	0.026
M5	Mild steel rod	BLY160	10	0.052
M6	Mild steel rod	BLY160	10	0.078

Tab. 2 - Main Design Parameters of Specimens

Part name	Part size/ (mm)	Rebar specifications	Number of steel bars	Concrete strength
Column size	400×400× 1700	Longitudinal bar HRB335	16Φ12	C60
		Stirrup HRB335	Φ6@60	
Cap size	1400×700 ×500	HRB335	Φ6@200	C60
			Φ6@150	
Prestressed tendons	2200	1860 steel strand	4	

Tab. 3 - Main Design Parameters of Prestressed Tendons

Part name	Prestressed tendons	Quantity	Join forces/（kN）	Single tension/（kN）
All models	Steel strand Φ25	4	320	80

Tab. 4 - Mechanical Properties of Steel Bars

Reinforced	Elastic modulus/(MPa)	Yield strength/(MPa)	Ultimate strength/(MPa)	Poisson's ratio
BLY100	1.9×10^5	78	251	0.3
BLY160	1.9×10^5	123	262	0.3
BLY225	1.9×10^5	220	350	0.3
HRB335	2.02×10^5	353	493	0.3
Q345	2.1×10^5	345	550	0.3
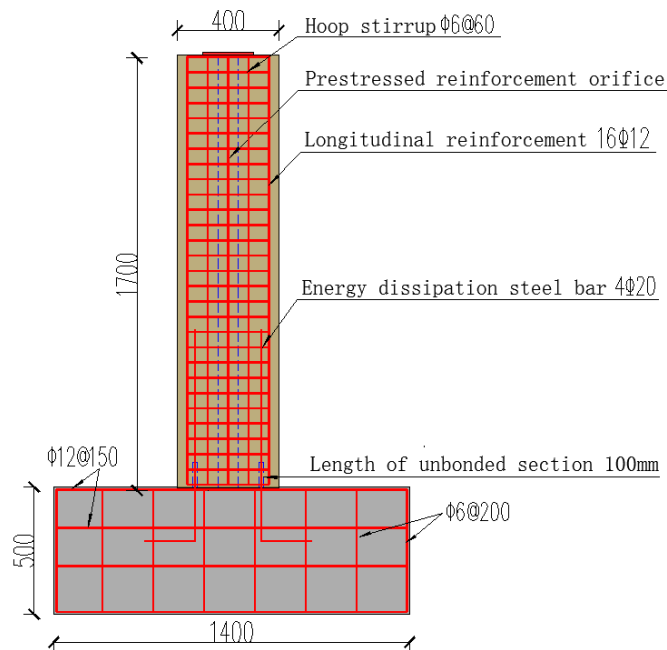
Fig. 6 - Reinforcement Diagram of Pier with Additional Mild Steel Damper

Boundary Conditions and Loading System

The bottom of the cap is fixed, and the bottom of the cap and the upper pier adopts surface-to-surface contact, and the contact characteristics of the normal direction and the tangent direction are set. The tangent direction adopts the Coulomb friction model, the friction coefficient is 0.5, and the normal direction is "hard" contact. The contact relationship between the concrete and the steel bar is assumed to ignore the bond-slip effect, and the steel bar is incorporated into the designed concrete member. The prestressed tendons are combined with the steel plate into a whole, which

binds the upper steel plate to the top of the pier, and the lower steel plate to the bottom of the cap. Rigid connection is adopted between the mild steel damper support and the bridge pier, cap and between the soft steel rod and the shaft and sleeve, which are set as binding constraints. The shaft, sleeve and support are hinged by high-strength bolts, and the contact surfaces adopt surface-to-surface contact, regardless of the Coulomb friction between the contact surfaces. Numerical experiments are used to control the horizontal displacement of the low-cycle reciprocating loading form to simulate the cyclic reciprocating motion of the bridge pier under the action of an earthquake.

Before low-cycle reciprocating loading, apply a concentrated load of 220kN, 440kN, 660kN on the top of the pier to simulate the vertical load from the superstructure, corresponding to M3, M5, M6 piers with different axial compression ratios, and add pier column structure self-respect. Couple a reference point on the top surface of the pier, and apply a reset movement to the reference point. The model loading diagram is shown in Figure 7. The maximum load displacement is 60mm, the grading load, the first level is 5mm, the second level is 10mm, the third level is 15mm, and so on, each level is increased by 5mm (0.3%), and each level is repeated 3 times. The loading method is shown in Figure 8.
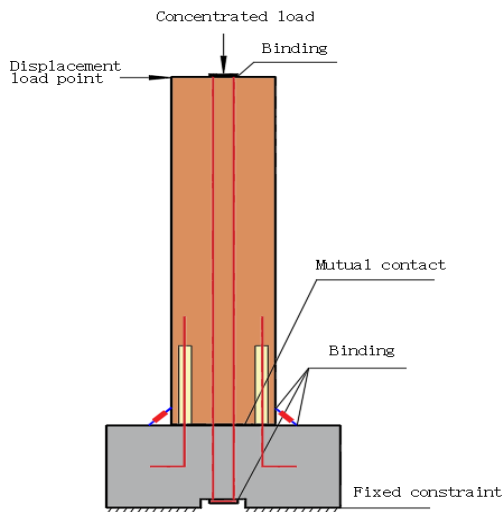
Fig. 7 - Loading diagram
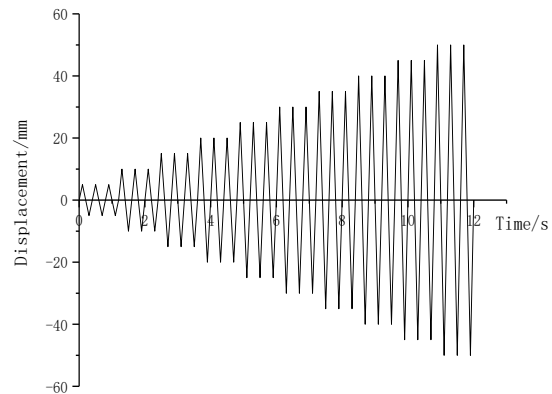
Fig. 8 - Loading method

Numerical Model Verification

The numerical model established in accordance with the traditional prefabricated self-resetting pier in the test in Reference [7] is subjected to low-cycle repeated loading, and the force-displacement curve is obtained, which is compared with the existing test results, as is shown in Figure 9. The force-displacement curve obtained based on the numerical test is basically consistent with the test result. Because the energy-dissipating steel bar in the numerical calculation adopts an ideal elastoplastic constitutive model, and does not consider the strengthening effect of the actual steel bar force, the ultimate bearing capacity is slightly lower than the results obtained from the test.
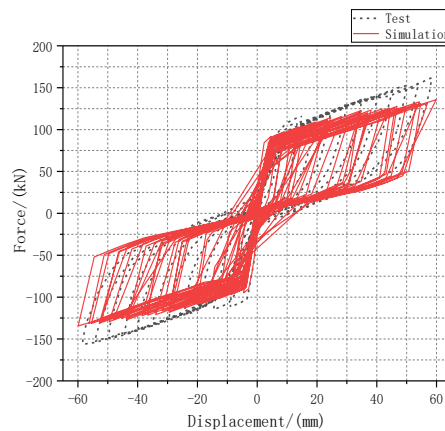
Fig. 9 - Force - Displacement Curve of M1

RESULTS AND ANALYSIS

Comparison of Hysteresis Curves of Bridge Piers with Mild Steel Dampers

The hysteresis curve is of great significance to the analysis of the seismic performance of structures or components, and comprehensively reflects its seismic performance. The comparison of hysteresis curves is shown in Figure 10.
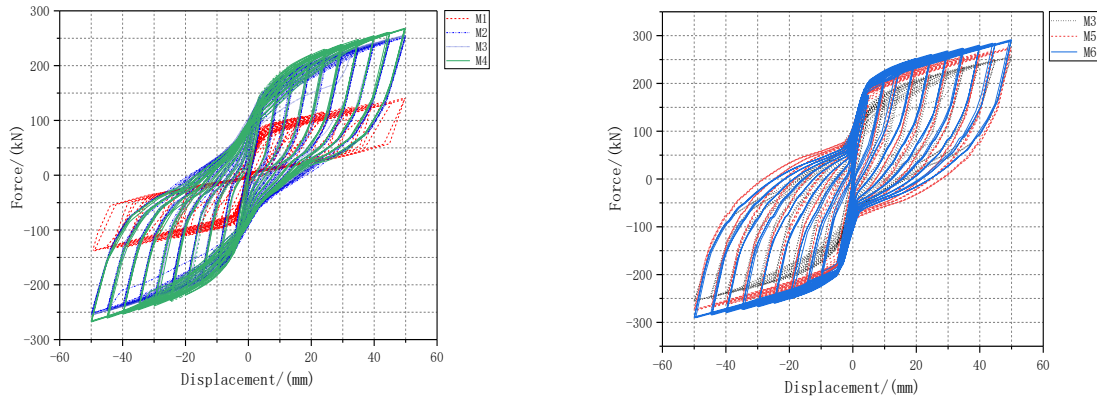
（a）Hysteresis Curve of M2,M3,M4 and M1　　（b）Hysteresis Curve of M3,M5 and M6

Fig. 10 - Hysteresis Curve

In Figure 10(a), the following conclusions can be drawn: (1) Compared with M1 piers, the force-displacement curves of M2, M3, and M4 piers are generally shuttle-shaped, with a more full shape, and the energy consumption and bearing capacity have been improved to a certain extent. The mild steel dampers have a good seismic effect. (2) The force-displacement curves of M2, M3, and M4 piers are similar, indicating that the three have similar mechanical properties. In the initial stage of loading, the structure is in the elastic stage. As the displacement loading progresses, the hysteresis loop area continues to increase and consumes energy. The stiffness of the specimen is gradually degraded. At the later stage of loading, the structural force-displacement curve is gradually full and pinch phenomenon appears, indicating that the prestressed tendons have played a good role.

In Figure 10(b), as the pier-column axial compression ratio increases, the hysteresis curve of the structure becomes fuller, the bearing capacity and energy consumption capacity are improved, and the residual displacement increases.

Analysis of Energy Dissipation Capacity of Bridge Piers with Mild Steel Dampers

Energy dissipation capacity is of great significance for measuring the seismic performance of structural members. It is generally represented by the graphic area enclosed by the load-displacement curve envelope. By analyzing the hysteresis curve of the structure, the cumulative energy consumption of the structure can be calculated quantitatively. The cumulative energy consumption of the study is the superposition of the average value of the hysteresis loop area of 3 cycles per load displacement. The energy consumption curve as shown in Figure 11.
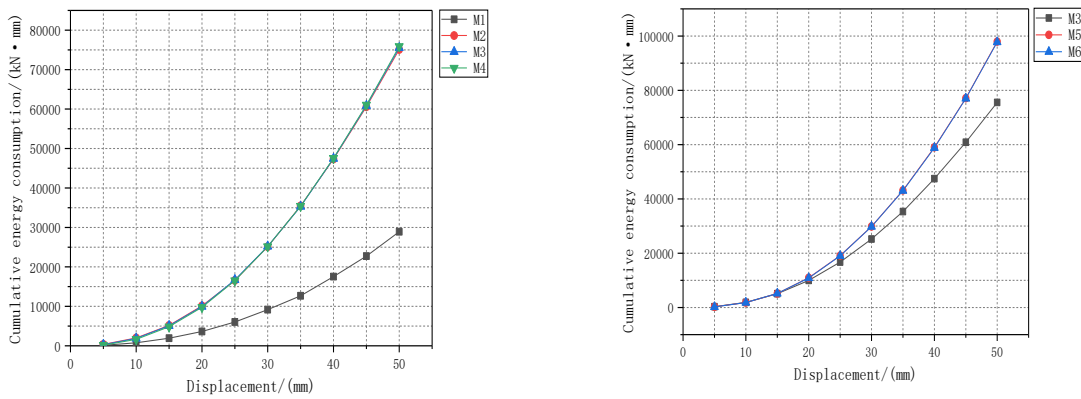
（a）Energy Dissipation Curve of M2,M3,M4 and M1

（b）Energy Dissipation Curve of M3,M5 and M6

Fig. 11 - Energy Dissipation Curve

In Figure 11(a), as the loading displacement gradually increases, the cumulative energy consumption of piers gradually increases. Compared with traditional piers M1, M3 piers, the maximum cumulative energy consumption value is increased by 2.5 times. The energy consumption capacity is better than that of traditional fabricated self-resetting piers.

In Figure 11(b), compared to M3, the cumulative energy consumption value of M5 piers has increased by 30%, while the energy consumption capacity of M5 and M6 piers is not much different, indicating that increasing the axial compression ratio of the pier column within a certain range can be improve the energy consumption capacity of the bridge pier, when the axial compression ratio exceeds 0.052, the effect is not obvious.

Figure 12 shows the ratio of the energy consumption of mild steel dampers to the total energy consumption.
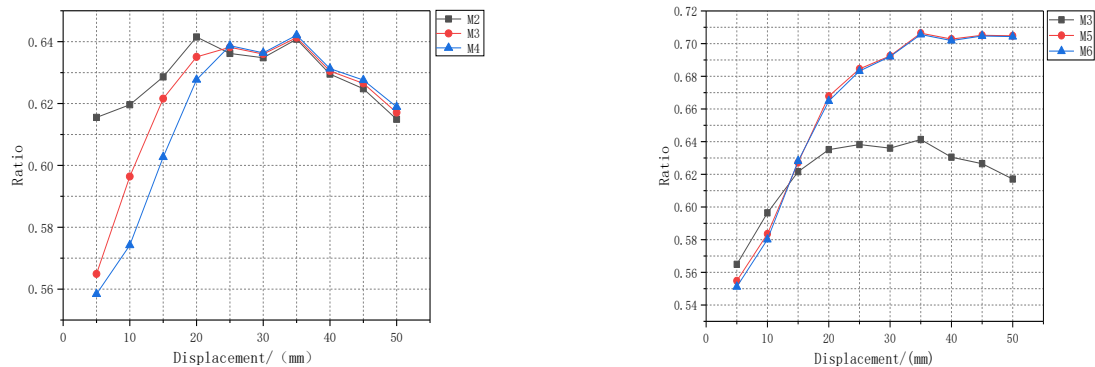
（a）*Comparison of Energy Dissipation Ratio of M2,M3 and M4 Mild Steel Dampers in Total Energy Dissipation*

（b）*Comparison of Energy Dissipation Ratio of M3,M5 and M6 Mild Steel Dampers in Total Energy Dissipation*

Fig. 12 - Proportion of Energy Dissipation of Mild Steel Dampers

In Figure 12(a), the ratio of the energy consumption of the three types of mild steel dampers with different yield strengths to their total energy consumption gradually increases with the load of displacement, and they are all greater than 0.55, indicating that the external mild steel dampers are effective improve the energy consumption capacity of bridge piers. When the horizontal displacement load is less than 25mm, the M2 pier mild steel dampers account for the largest energy consumption, and the cumulative energy consumption value is the largest, and the M4 pier has the smallest value. When the horizontal displacement load is greater than 25mm, the M4 pier mild steel dampers account for the largest energy consumption, and the cumulative energy consumption value is the largest, and the M2 pier the above value is the smallest, indicating that with the increase of the mild steel damper yield strength, when the loading displacement is small , the ratio of the energy consumption of the mild steel dampers to the total energy consumption gradually decreases, and the cumulative energy consumption value of the bridge piers decreases. When the loading displacement is large, the energy consumption of the mild steel damper gradually increases, and the cumulative energy consumption value of the pier increases. Therefore, in order to increase the overall energy consumption of the pier, the yield strength of the mild steel damper cannot be increased indefinitely, and the energy dissipation capacity of the structure under small displacement loading must also be considered. In contrast, M3 piers with BLY160 mild steel dampers have the best seismic performance. In order to make the structure have a more sustainable and stable energy dissipation capacity, the energy sharing ratio between the mild steel damper and the energy dissipation steel bar when the horizontal loading displacement limit value is 25mm is taken as the best sharing ratio, and the calculated ratio is 1.75.

In Figure 12(b), when the loading displacement is less than 13mm, as the axial compression ratio of the pier column increases, the energy consumption of the mild steel damper gradually decreases. When the loading displacement is greater than 13mm, the energy consumption of the mild steel dampers of the M5 and M6 piers gradually increases and exceeds that of the M3 pier. They are in a stable state at the later stage of the displacement loading, indicating that in the middle and late loading displacements, the pier column axis is within a certain range The larger the pressure ratio, the better the energy dissipation effect of the mild steel damper. The energy consumption ratio of the mild steel dampers of M5 and M6 piers is basically similar in the middle and later stages of displacement loading, indicating that the effect of the pier-column axial compression ratio exceeds a certain range is not obvious. Consider the energy consumption of the mild steel dampers when the loading displacement is small. The recommended value of pier column axial compression ratio is 0.052.

Comparison of Stiffness Degradation of Piers with Mild Steel Dampers

Stiffness degradation is a phenomenon that the peak point displacement increases with the increase of the number of cycles when the same peak load is maintained under cyclic loading, and the formula for stiffness degradation as Equation (10).

$$K_i = \frac{\sum\limits_{i=1}^{n} P_j^i}{\sum\limits_{i=1}^{n} \Delta_j^i} \tag{10}$$

In Equation (10), K_i is the ring stiffness of the structure; the numerator is the peak load of the i-th cycle; Δ is the deformation value at the maximum point of the i-th cycle; n is the number of times. The stiffness degradation curve as shown in Figure 13.
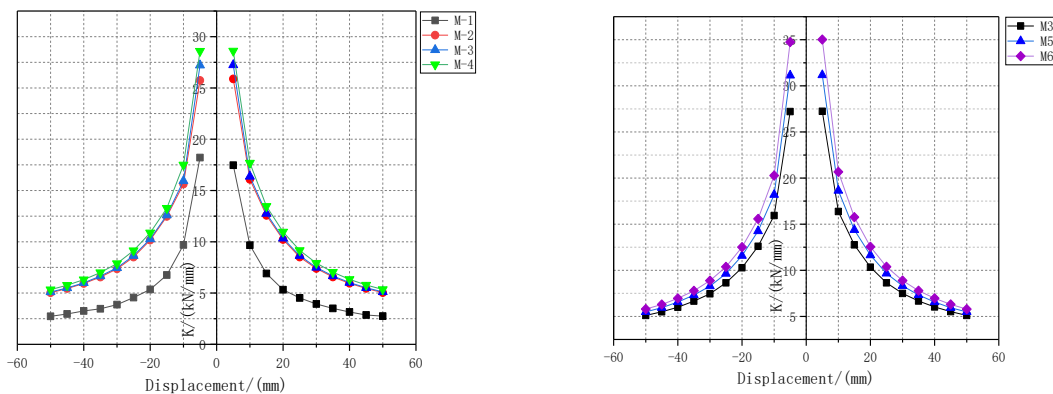
Fig. 13 - Stiffness degradation curve

The stiffness degradation is roughly symmetrical, and the stiffness degradation is more obvious and uniform. The stiffness degradation of the M2, M3, and M4 piers is relatively similar, showing similar mechanical properties. Compared with traditional prefabricated self-resetting piers, the rigidity of the prefabricated self-resetting piers with external mild steel dampers is greater, because the mild steel dampers increase the initial rigidity of the pier. The stiffness of the pier with the external mild steel damper decreases with the increase of the horizontal displacement, the descent rate is almost the same, and the slope of the stiffness curve gradually decreases. It shows that the stiffness of the assembled self-resetting pier with external mild steel dampers is obviously degraded, continuous and stable, and there is no damage to the structure due to the sudden decrease. The increase of the pier-column axial compression ratio improves the initial stiffness of the pier, but the axial compression ratio parameter has little effect on the overall stiffness degradation of the pier.

Comparison of Residual Displacement of Bridge Piers with Mild Steel Dampers

The variation of the pseudo-static residual displacement of the specimen with the load displacement level as shown in Figure 14.
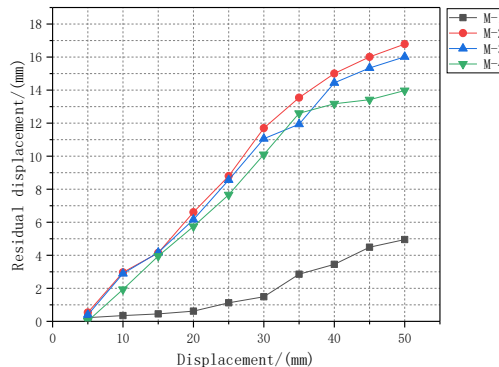
Fig. 14 - Residual Displacement Curve of M2,M3,M4 and M1

Under the action of low-cycle reciprocating load, compared with traditional prefabricated self-resetting piers, the residual displacement of self-resetting piers with additional mild steel dampers has increased. This is because the external mild steel dampers increase the unloading rigidity of the pier. Cause the residual displacement to increase. According to the reference [16], in order to make the piers repairable after the earthquake without reconstruction, it is necessary to ensure that the residual displacement angle of the pier after the earthquake does not exceed 1%. The maximum residual displacement of the M2, M3, and M4 piers is 16.7mm, which meets the requirement that the residual displacement angle is less than 1%. The residual displacement curves of M2, M3, and M4 piers have roughly the same trend. The residual displacement of M4 piers is smaller, indicating that the greater the yield strength of the mild steel dampers within a certain range, the better the self-resetting ability of the piers, but the difference is not much.

The text defines the self-resetting coefficient to measure the self-resetting ability of the structure. The larger the value, the better the self-resetting ability of the structure. Generally, $0 \leq \eta \leq 1$. The self-resetting coefficient is determined by Equation (11).

$$\eta = 1 - \frac{\Delta_i}{\Delta_j} \tag{11}$$

In Equation (11), Δ_i is the residual displacement of the structure after loading; Δ_j is the maximum displacement of the structure in the same load cycle. The comparison of self-reset coefficients under different axial compression ratios is shown in Figure 15.
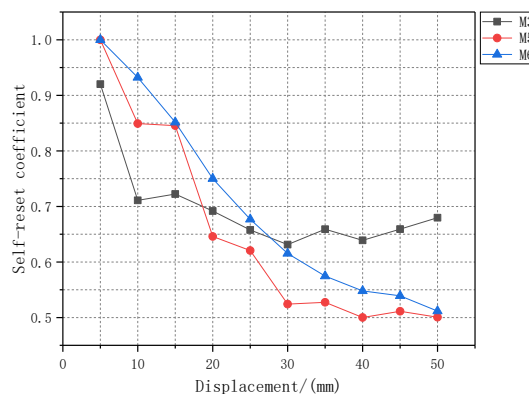
Fig. 15 - Self-Reduction Coefficient of M3,M5 and M6

In the initial stage of displacement loading, increasing the pier-column axial compression ratio within a certain range can improve the self-reset capability of the structure. In the later stage of displacement loading, the self-reset ability of the structure is reduced. It shows that the increase of the pier-column axial compression ratio makes the mild steel damper enter the fully yielding energy dissipation state earlier, resulting in greater residual deformation at the later stage of displacement loading. The self-reset coefficient curves of M5 and M6 are similar, indicating that the influence of the pier-column axial compression ratio exceeds a certain range is not obvious.

CONCLUSION

In this study, the numerical test method was used to compare the response analysis and comparison of the fabricated self-resetting piers with additional mild steel dampers and the traditional fabricated self-resetting piers under low-cycle reciprocating loads. The effects of the yield strength parameters of mild steel dampers and the axial compression ratio parameters on the seismic performance of the bridge piers are studied. Concluded as follow:

(1)   Fabricated self-resetting piers with external mild steel dampers have good self-resetting ability, high bearing capacity and energy dissipation capacity, and have good seismic performance under low-cycle repeated loads.
(2)   Within a certain range, the greater the yield strength of the mild steel damper, the greater the bearing capacity, the better the overall energy dissipation capacity, and the smaller the residual displacement. When the loading displacement is less than 25mm, the greater the yield strength of the mild steel damper, the smaller the proportion of energy consumption. In contrast, BLY160's prefabricated self-reset bridge pier has the best seismic performance, and the optimal energy dissipation ratio between the mild steel damper and the energy-dissipating reinforcement is 1.75.
(3)   The greater the axial compression ratio of the pier column in a certain range, the greater the energy consumption, bearing capacity of the structure, when the loading displacement is small, the self-reset ability of the structure is better, and when the loading displacement is large, the mild steel damper enters the full yielding energy consumption state earlier. When the axial compression ratio exceeds a certain range, the effect is not obvious. In contrast, the recommended value of pier column axial compression ratio is 0.052.
(4)   The external mild steel damper yields before the energy-dissipating steel bars to protect the energy-dissipating steel bars and avoid premature yield failure of the energy-consuming steel bars, which is conducive to the continuous development of the seismic performance of the structure under aftershocks, and its easy replacement feature is conducive to post-earthquake repair.

ACKNOWLEDGEMENTS

REFERENCES

[1]   MANDER J B, CHENG C T. Seismic resistance of bridge piers based on damage avoidance design[R]. Technical Report NCEER-97-0014. Buffalo: State University of New York at Buffalo, 1997.
[2]   SOLBERG K, MASHIKO N, MANDER J B, DHAKAL R P. Performance of a damage-protected highway bridge pier subjected to bidirectional earthquake attack [J]. Journal of Structural Engineering, ASCE, 2009, 135(5): 469-478.
[3]   MARRIOTT D, PAMPANIN S, PALERMO A. Quasi-static and pseudo-dynamic testing of unbonded post-tensioned rocking bridge piers with external replaceable dissipaters [J]. Earthquake Engineering and Structural Dynamics, 2009, 38(3): 331-354.

----

[4]   MARRIOTT D, PAMPANIN S, PALERMO A. Biaxial testing of unbonded post-tensioned rocking bridge piers with external replacable dissipaters [J]. Earthquake Engineering and Structural Dynamics, 2011, 40(15): 1723-1741.

[5]   TRONO W, JEN G, PANAGIOTOU M, SCHOETTLER M, OSTERTAG C P. Seismic response of a damage-resistant recentering posttensioned-HYFRC bridge column [J]. Journal of Bridge Engineering, ASCE, 2015, 20(7): 1-13.

[6]   HE M H, XIN K G, GUO J et al. Study on intrinsic lateral stiffness and hysteresis mechanism of self-reposition bridge piers [J]. China railway science, 2012, 33(05): 22-28. (in Chinese)

[7]   GUO J, XIN K G, HE M H et al. Experimental research and analysis on seismic performance of self-restoring bridge piers [J]. Engineering mechanics, 2012, 29(S1): 29-34+45. (in Chinese)

[8]   HAITHAM D, MOHAMED E, JOSHUA H. Behavior of segmental precast posttensioned bridge piers under lateral loads [J]. Journal of Bridge Engineering, 2012, 17(5): 735-746.

[9]   BU Z Y, OU Y C, SONG J W, et al. Cyclic Loading Test of Unbonded and Bonded Posttensioned Precast Segmental Bridge Columns with Circular Section [J]. Journal of Bridge Engineering, 2015, 21(2): 10-18.

[10]   WANG J W, ZHANG W G, AI Q H. Comparison of seismic performance tests of PC and RC Hollow Piers [J]. Journal of China highway, 2015, 28(04): 76-85. (in Chinese)

[11]   GAO J, GE J P, LIN T L. Quasi static test research on dry joint segmental assembled piers [J]. Vibration and impact, 2011, 30(04): 211-216. (in Chinese)

[12]   GUO T, CAO Z, XU Z, et al. Cyclic Load Tests on Self-centering Concrete Pier with External Dissipators and Enhanced Durability[J]. Journal of Structural En-gineering, 2015, 142(1): 10-19.

[13]   WANG M, QIAN F X, YANG W G, YANG L. Comparison study on constitutive relationship of low yield point steels, Q345B steel and Q460D steel [J]. Eengineering mechanics, 2017, 34(02): 60-68. (in Chinese)

[14]   CHEN Z Y, MAI C L, XU Z X, et al. Experimental research on seismic performance of shear plate damper made by low yield point steel [J]. J Xiamen Univ Nat Sci, 2019, 58(06): 916-921. (in Chinese)

[15]   SONG F M, WEN D H, LI Z G. Development of 225MPa low yield point steel used for earthquake resistant [J]. Thermal processing technology, 2009, 38(12):62-63+69. (in Chinese)

[16]   JAPAN ROAD ASSOCIATION (JRA). Design specifications of highway bridges: seismic design (JRA-2012)[S]. Tokyo: Japan Road Association, 2012.

ANALYSIS OF LATERAL DISPLACEMENT AND EVALUATION OF TREATMENT MEASURES OF CURVED BEAM: A CASE STUDY

Jie Li, Dongchao Liang, Junfeng Zhang, Zhaodong Shi and Huai Chen

School of Civil Engineering, Zhengzhou University, 100,Science Avenue Zhengzhou, Henan China 450001; lijie2007@zzu.edu.cn, 2428175429@qq.com, brilliantshine@163.com, 1256304513@qq.com, chenh@zzu.edu.cn

ABSTRACT

The curved beam bridge exhibits lateral displacement during construction and operation. Taking a curved beam bridge as an example, the status of lateral displacement of the bridge is investigated in detail in this paper. To understand the mechanism of the curved beam lateral displacement, further to determine the curved beam lateral displacement under temperature effect, using ANSYS software to establish solid element model of the curved beam, steady state thermal analysis method is applied to analyze temperature field. Based on the analysis, the lateral displacement under temperature effect is analyzed. Then in order to further explain the lateral displacement mechanism, to discuss the frictional force causing the residual deformation of the rubber bearing to make the lateral displacement of the curved beam, the mechanical mechanism of curved beam under temperature effect is approximately analyzed. On the basis of clarifying the mechanism of lateral displacement, the paper puts forward the reinforcement measures for the curved beam bridge. In order to verify the treatment effect, long-term displacement monitoring is performed on the bridge. Numerical studies and monitoring data show that temperature is the main factor that causes the lateral displacement. Monitoring data over the past year shows that the displacement of the bearing is less than the value of allowable displacement after the reinforcement measures are adopted, and the bridge is in a safe state.

KEYWORDS

Curved beam bridge, Lateral displacement, Numerical analysis, Reinforcement and renovation, Long-term monitoring

INTRODUCTION

Curved beam bridge is a typical "bending–torsional coupling" stress member. The mechanical characteristics of curved beam bridge is unique due to its curvature. It is different from straight beam bridge in terms of stress and deformation. The most significant difference is the lateral displacement of curved beam bridge. At present, most of the researches on the lateral displacement of curved beam bridges are mainly based on the finite element method [1-5]. A few studies on external affecting factors of displacement have analyzed dead weight, live load, and prestressed load [6]. Some studies suggest that temperature [7-8] and live load are the main reasons of beam bridge disease. The study of temperature has mainly focused on the temperature distribution of bridges [9] and the mechanism of the influence of temperature on lateral displacement [10]. In terms of measures to cope with the lateral displacement of bridges, several scholars have given reinforcement [11] and reconstruction measures for bridges with transverse displacement diseases [12] for effectively controlling the development of bridge diseases.

The above-mentioned works show that the curved beam bridge will inevitably have lateral displacement, which may lead to lateral deviation disease. The main affecting factors of lateral deviation include radius of curvature, temperature, and vehicle load and so on. At present, most studies only conduct elastic analysis of transverse displacement under the action of various factors while ignoring the essence of lateral deviation disease. However, during operation of curved beam bridge, lateral displacement occurs under the combined action of internal and external factors. The lateral displacement generated by the beam cannot be fully recovered, after the external force disappears due to the friction between the bearing and bottom of the beam and the action of its own gravity. Residual lateral displacement occurs every time when the external force acts. The lateral displacement keeps accumulating through the cycle action of the external load, and the energy inside the curved beam also accumulates. When the internal energy of the beam reaches its peak, the beam starts to release energy under the action of accidental external force. This condition may lead to the crack of the beam, the tensile crack of the expansion joint, or the outward slide of the beam. During operation of curved beam bridge, lateral displacement diseases, which are mainly manifested as transverse deflection and torsional displacement of beam, occur. Therefore, the mechanism of lateral deflection disease of curved beam bridge requires further investigation. In this study, taking a curved beam bridge as an example, on the basis of the detailed investigation of the lateral displacement disease, the numerical method is used to analyze the causes of the lateral displacement, and the reinforcement measures are proposed. Finally, the operation status of the bridge is evaluated by the measured data of a long-term health monitoring.

PROJECT OVERVIEW AND DISEASE STATUS INVESTIGATION

Brief introduction of engineering example

The engineering example is a ramp curved beam bridge. Total length of the curved beam is 1202.7m, with 12 parts, 43 spans and 42 piers. The width of the bridge is 9.5 m, with two lanes. Limited to space, the third part of the curved beam is taken as the engineering object. The third part of the curved beam is located on the curve R=400 m and the layout of the bridge span is (40 + 51.5 + 40) m. PC continuous box beam with inclined webs is used in the superstructure. The section of main beam is single box and single chamber (See Figure 1, the black spot represents the temperature measuring point.). The corbel is used to overlap the units and expansion joints are set at the corbel.
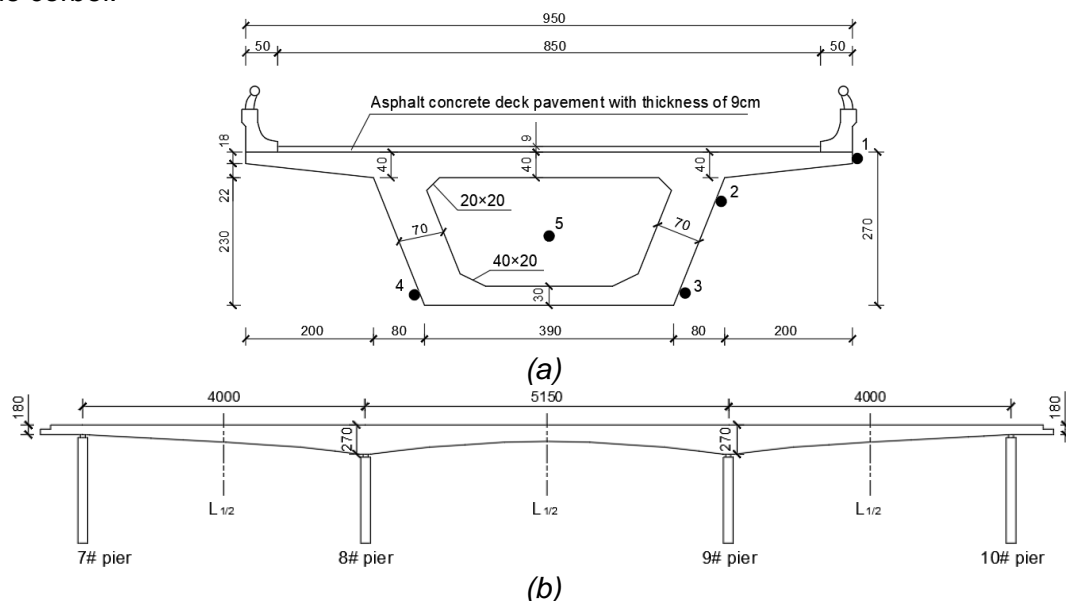

(a)

(b)

Fig. 1 – The third parts of the curved beam (cm)

The cantilever length of flange is 2.0 m. The beam height at the pier is 2.7 m and the mid span beam height is 1.8 m. The thickness of the top plate changes from 0.4 m at the pier to 0.25 m in the mid-span. The thickness of the bottom plate gradually changes from 0.3 m at the pier to 0.22 m in the mid-span. The thickness of web is 0.5-0.7 m. Longitudinal prestressed reinforcement is steel strand with high strength and low relaxation yield strength of 1860MPa, which is designed according to class A partial prestressed concrete. Rectangular single column pier is used in the substructure, and the pier top is widened horizontally to place pot type rubber double bearing. The bearing forms include one- direction bearing, two- direction bearing and fixed bearing. The transverse widening of pier column from pier top to pier body adopts straight line transition. The pier body size is 1.4 × 2.0 m. The bearing spacing of No.8 and No.9 piers is 2.0 m, and that of No.7 and No.10 side piers is 1.8 m. C50 concrete is used for main beam and C40 concrete is used for pier.

Disease status investigation

Under the influence of external loads such as temperature, concrete shrinkage and creep, as well as live load, the curved beam bridge has serious lateral displacement disease, which has led to beam cracks, bearing lateral displacement and damage.

Cracks in main beam

According to the field investigation, there are vertical cracks in the outer web of the main beam structure, transverse cracks in the wing plate, and oblique cracks in the outer web of the corbel connection. In the whole bridge, the width of the two inclined cracks which is away from the No.40 pier 4.5 m is 0.15 mm, and the other cracks are about 0.1mm. The theoretical calculation shows that [9], because the crossbeams of the curved beam bridge are all solid sections, and there are more common reinforcing bars, the crack resistance capacity of the beam can meet the structural stress requirements. The analysis also shows that the web cracks of beam body are mainly caused by concrete shrinkage and creep, but some web cracks of beam span are caused by transverse force of beam that produced by lateral displacement. Figure 2 shows a diagonal crack on the outer web of the 23rd corbel connection.

Lateral displacement deviation of curved beam

The transverse slip of the main beam and the support is concentrated in the span with small curvature radius, and no obvious disease is found in other parts. The maximum slip of the main beam bearing to the outside of the curve is 40 cm (shown in Figure 3). The numerical analysis [9] shows that the lateral displacement of the beam is mainly caused by the temperature effect, especially the transverse temperature gradient. Other factors, such as the concrete shrinkage and creep effect, the insufficient lateral limit, the large longitudinal slope of the bridge, and the lack of the limiting device for each pier of the bridge, will further worsen the disease.

Fig. 2 – Diagonal cracks in web

Fig. 3 – Lateral slip 40 cm

In the bridge span with large lateral displacement, the main problems of bearing are that the anchor bolt is sheared off, the limit steel plate is sheared off, the rubber body is ejected, and the beam concrete is damaged. The bearing damage is shown in Figure 4.

Bridge pier diseases

Due to the lateral displacement, the stress of the pier is unfavourable, which leads to cracks of the pier. The field investigation is shown in Figure 5. In addition, damages to the bridge deck and ancillary structures were also found on site, such as rubber strip breaking and mud inclusion in the expansion device, widening of some expansion joint gaps and lateral dislocation, and vertical cracks at the guardrail.

Fig. 4 – Bearing damage

Fig. 5 – Bridge pier cracks

LATERAL DISPLACEMENT MECHANISM OF CURVED BEAM BRIDGE UNDER TEMPERATURE EFFECT

A large number of studies show that temperature is the main cause of lateral displacement of curved beam bridge [9, 11]. Therefore, in view of the engineering example, the lateral displacement mechanism of curved beam bridge is discussed under the temperature effect.

Finite element modelling and temperature gradient field simulation

The finite element model of the third parts of the curved beam bridge is established by using ANSYS finite element software. The model mainly analyzes the response of the structure under the action of primary load (temperature effect) instead of long-term repeated load. In order to further simulate the physical process of residual displacement accumulation caused by bearing friction resistance, the accumulation process of residual displacement of bearing under repeated load is simulated by using combine39 element in ANSYS software.

The effect of temperature on curved beam bridge can be divided into two categories: (1) temperature gradient: including vertical temperature gradient and radial temperature gradient; (2) system temperature difference. According to the field measurement, the maximum temperature difference between the top and bottom plates of the box beam section of the bridge is about 10°C, and the vertical linear temperature difference is 10°C according to General Specification for Design of Highway Bridges and Culverts (JTG D60-2015). The transverse temperature gradient of box beam section is given in reference [9]. The trend of the bridge analyzed in this paper is from north to southeast. According to the field measurement of some bridges, the temperature difference between the inner and outer webs of the main beam can be as high as 10°C, so the transverse temperature gradient is taken as 10°C. This paper mainly analyzes the influence of three temperature gradient conditions on the displacement of curved beam bridge.

CS1: the inner temperature is 20°C and the outer temperature is 30°C;

CS2: the inner temperature is 30°C and the outer temperature is 20°C;

CS3: the temperature of top plate is 10°C.

When analyzing the influence of system temperature difference on the displacement of curved beam bridge, according to the environment of the bridge site and relevant temperature data and relevant literature, the system temperature difference of 30°C is taken, and the displacement of curved beam bridge with system temperature difference of 20°C and 40°C is compared.

Analysis without considering friction and long-term cumulative effect of bearing

According to the analysis mode of one-time load instead of long-term repeated load, the transverse displacement of main beam replaces long-term lateral cumulative displacement. That is, the temperature load is applied to the curved beam according to the temperature field distribution. The bearing reaction force and beam displacement are analysed without considering the hyper-elastic material and its friction, and the long-term cumulative effect. The number and section position are shown in Figure 1.

(1) Thermal analysis: input thermal element and heat conduction coefficient during thermal analysis. The solid element model is established. Then, the temperature boundary conditions are defined, and the steady-state thermal analysis is carried out. The temperature field of each node is calculated.

(2) Structural analysis: after entering the stage of structural analysis, the thermal element is transformed into structural element, and various parameters and reference temperature of main beam are input. The temperature of each node obtained from the thermal analysis is applied to the main beam structure for mechanical analysis.

Table 1 and Table 2 show the reaction force of support and radial displacement of beam under different temperature gradient conditions.

Tab. 1 - Reaction force of curved beam under temperature gradient (kN)

Bearing position	CS1		CS2		CS3	
	Transverse direction of bridge（FX）	Vertical direction of bridge（FY）	Transverse direction of bridge（FX）	Vertical direction of bridge（FY）	Transverse direction of bridge（FX）	Vertical direction of bridge（FY）
Pier 7# outside	10.11	457.20	16.14	-544.90	2.78	39.79
Pier 7# inside	-273.55	-440.67	284.07	548.78	20.52	63.97
Pier 8# outside	584.01	-302.35	-588.67	226.37	1.46	-59.20
Pier 8# inside	-274.15	288.53	338.32	-225.33	33.92	-39.35
Pier 9# outside	21.85	-276.86	12.77	209.53	1.42	-69.63
Pier 9# inside	271.88	257.61	-257.02	-211.55	33.50	-39.18
Pier 10# outside	9.53	426.41	19.44	-473.12	3.96	30.78
Pier 10# inside	-267.04	-409.88	271.92	470.25	18.78	72.82

Tab. 2 - Radial displacement of curved beam under temperature gradient (mm)

Position		Radial displacement		
		CS1	CS2	CS3
Pier 7#	Bottom of main beam	1.01	-1.31	-0.16
	Pier top	1.04	-1.27	-0.15
	Relative displacement	-0.03	-0.04	-0.01
	L/2	-0.66	0.52	-0.10
Pier 8#	Bottom of main beam	-0.76	0.69	-0.09
	Pier top	-0.76	0.69	-0.09
	Relative displacement	0.0	0.0	0.0
	L/2	-0.52	0.34	-0.18
Pier 9#	Bottom of main beam	-0.80	0.62	-0.10
	Pier top	-0.75	0.65	-0.10
	Relative displacement	-0.05	-0.03	0
	L/2	-0.64	0.45	-0.1
Pier 10#	Bottom of main beam	1.18	-1.41	-0.16
	Pier top	1.21	-1.36	-0.15
	Relative displacement	-0.03	- 0.05	- 0.01

It can be seen from Table 1 that under the action of temperature, the vertical bearing reaction force of curved beam bridge are relatively large. The sign of the reaction force of the inner and outer vertical supports on each pier is opposite. Under CS1 condition, the vertical bearing reaction of the inner supports at both ends of the main beam and the outer support of the middle pier is negative. The lateral torsion occurs at both ends of the beam, and the inner torsion occurs at other positions. It is the opposite under CS2. Due to the difference of arc length between inside and outside of curved beam bridge, the expansion and elongation of inner and outer arc length are not consistent under the action of temperature, which leads to radial displacement of beam. The lateral offset of curved beam bridge is restrained by the support, and the radial bearing reaction force is produced. Compared with CS1 and CS2, the transverse direction support reaction of CS3 is smaller. Under the action of vertical temperature gradient, the top plate of box beam is heated up and it is arched upward, which mainly causes the vertical deflection of the beam. Under the action of CS3, 7# and 10# bearings at both ends are compressed, and the absolute value of reaction force of inner bearing is greater than that of outer bearing. 8# and 9# internal and external supports are under tension, and the vertical reaction force of outer bearing is greater than that of inner bearing.

It can be seen from Table 2 that under CS1, both ends of the beam deviate to the inside and the middle to the outside. The maximum internal offset is 1.18 mm and the maximum lateral offset is 0.8 mm. Under CS2, the lateral offset occurs at both ends of the beam, and the inner offset occurs in the middle. The maximum lateral offset is 1.41 mm and the maximum inner offset is 0.65 mm. Compared with CS1 and CS2, under CS3, the curved beam bridge moves outward, and the maximum offset is 0.16 mm.

The displacement of main beam under the action of system temperature difference is shown in Table 3, Figure 4 and Figure 5. In Table 3, the radial displacements selected at the bottom of main beam, pier top and mid-span of each span are absolute displacement, and relative displacement is the radial displacement of main beam relative to pier top.

Tab. 3 - Radial displacement of curved beam under the action of system temperature difference

Position and temperature		Radial displacement of system temperature difference		
		20°C	30°C	40°C
Pier 7#	Bottom of main beam	-0.54	-0.84	-1.12
	Pier top	-0.37	-0.61	-0.82
	Relative displacement	-0.17	-0.23	-0.3
	L1/2	-0.31	0.52	-0.61
Pier 8#	Bottom of main beam	-0.22	-0.34	-0.45
	Pier top	-0.22	-0.34	-0.45
	Relative displacement	0	0	0
	L1/2	-0.42	0.34	-0.75
Pier 9#	Bottom of main beam	-0.38	-0.54	-0.72
	Pier top	-0.25	-0.31	-0.42
	Relative displacement	-0.13	-0.23	-0.3
	L1/2	-0.4	0.45	-0.75
Pier 10#	Bottom of main beam	-0.46	-0.67	-0.91
	Pier top	-0.31	-0.44	-0.58
	Relative displacement	-0.15	-0.23	-0.33

It can be seen from Figure 6 to Figure 7 and Table 3 that under the effect of system temperature difference, the curved beam bridge as a whole move outward. With the increase of temperature difference, the radial displacement and tangential displacement increase, and the maximum value of radial displacement increases from 0.54 mm to 1.12 mm. Due to the large longitudinal slope of the curved beam bridge, the tangential slip of the beam is serious under the action of system temperature difference, and the maximum tangential displacement increases from 12.88 mm to 26.6 mm. In addition, the vertical deflection of the inner and outer sides also increases, but the difference between the inner and outer deflections is almost the same. That is to say, the internal torsion of curved beam bridge is not affected by the system temperature difference. Compared with other loads, the radial displacement of main beam relative to pier top is larger under the action of system temperature difference. Through the above analysis, it can be seen that under the action of temperature gradient, the curved beam bridge will produce large radial displacement. And the bearing will produce large lateral reaction force and vertical negative reaction force, which will easily lead to shear failure and tensile fracture failure of the bearing. Under the effect of system temperature difference, the curved beam bridge has the greatest adverse effect, which easily leads to shear failure and tensile state of the bearing and produces large radial offset and tangential slip. However, these analyses are based on the linear elastic instantaneous loading. Due to unloading, the displacement and reaction force will inevitably recover, which cannot accurately explain the mechanical mechanism of the lateral displacement.
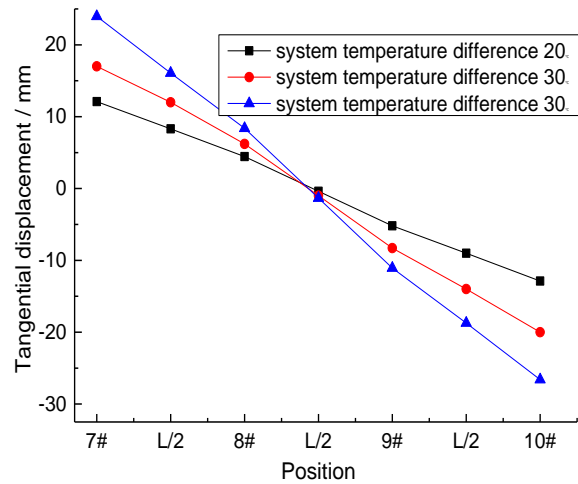

Fig. 6 – Tangential displacement under the action of system temperature difference (mm)
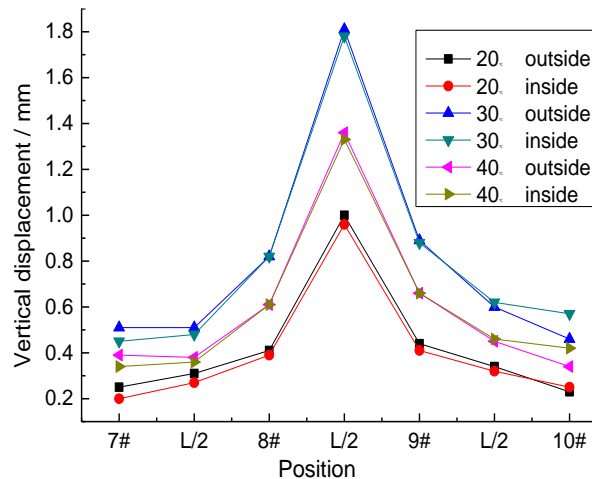

Fig. 7 – Vertical displacement under the action of system temperature difference (mm)

Lateral displacement analysis considering long term cumulative effect

Due to the friction resistance of the bearing and the bottom of the beam, the effect of gravity and other factors, the lateral offset of curved beam bridge cannot be fully recovered after the external force disappears. The residual lateral displacement exists in every external force action, and the lateral displacement is accumulated continuously under the cyclic action of external load. Therefore, the dust and garbage blocking the bearing gap, bearing material aging and bearing friction resistance are the main factors causing the lateral displacement of curved beam bridge cannot be restored. Among them, dust and garbage blocking the gap of the bearing is closely related to the bearing management and maintenance, and the bearing material aging is related to the bearing material properties and the environmental conditions, which is not easy to quantitative analysis. This paper attempts to use the Combined39 element of ANSYS software to build the bearing. The element can simulate the nonconservative system and the hysteretic effect of loading and unloading, so it can approximately simulate the cumulative displacement effect of rubber bearing which cannot be restored by friction and slip under various actions. It can also be used to calculate the residual displacement accumulation process under repeated loading.

For space limitation, taking the curved beam under the action of system temperature rise of 40°C as an example. Figure 8 shows the residual displacement of the curved beam after repeated action of the overall temperature rise and fall for 7 times. It can be seen that the maximum

----

cumulative residual displacement is 3.65 mm. Compared with Table 3, the elastic radial displacement under the action of once a load is 1.12 mm, which indicates that with the repeated action of temperature effect, the residual displacement gradually accumulates, and is greater than the radial displacement of the structure under the once a load. Figure 9 shows the cumulative process of the residual displacement of the bearing with the maximum displacement and the loading and unloading of the system temperature. It can be seen from Figure 9 that the residual displacement accumulation process of the bearing with the maximum displacement. With the cycle of temperature loading and unloading, the increment of residual displacement decreases gradually, which is basically consistent with the engineering practice. That is to say, with the aging of bearing material and the increase of friction, especially the blockage of dust and garbage, the increment of residual displacement gradually decreases.
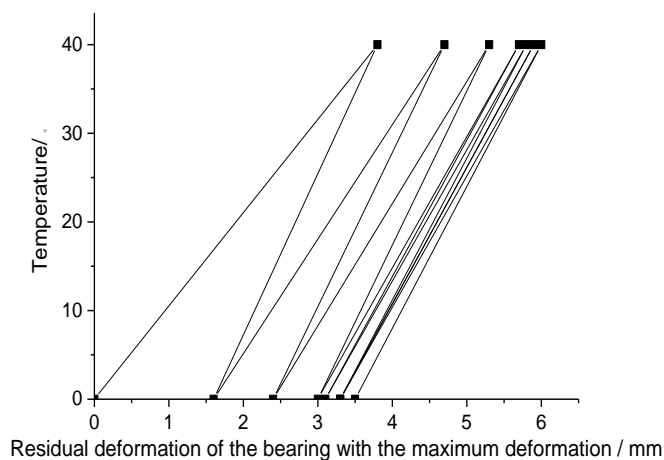
Fig.8 – Cumulative time-history of residual displacement of the largest displacement

The deviation analysis considering long-term cumulative effect can quantitatively explain the lateral displacement mechanism of curved beam bridge, which is highly consistent with the actual bridge operation. In summary, the lateral deviation of the curved beam bridge is the overall disease response caused by the radial displacement accumulated under the action of the external load combination dominated by temperature load.

REINFORCEMENT AND RENOVATION MEASURES FOR CURVED BEAM BRIDGE WITH LATERAL DEVIATION

The treatment measures of damaged bridges should be based on the actual situation, fully consider the interference and influence of traffic, and should have strong operability. The construction technology, equipment and equipment selected for reinforcement should be closely combined with the actual conditions of the construction site and have good reliability. According to the disease characteristics of the curved beam bridge, the treatment measures adopted by the bridge are firstly vertical jacking and lateral pushing to achieve the beam reset, and at the same time replace the damaged bearing. Then the pier is reinforced. Through the methods of component reinforcement, accessory component improvement and structural performance improvement, the existing diseases can be eliminated, the original function of the bridge can be restored, and the service life of the bridge can be effectively extended.

Restoration of beam

A vertical jack is installed between the beam bottom and the capping beam for vertical lifting. After jacking up, the system is converted. The control system is converted to translational system, then the horizontal translation jack is used for the reset construction.

Calculation of vertical jacking force

According to the jacking height (the jacking height of each support is 1.5 cm) designed in the reinforcement and maintenance scheme, the maximum vertical bearing reaction force on each pier of curved beam under the most unfavourable condition is calculated. Based on this, the jacks are selected and configured. The vertical reaction force of each bearing is shown in Table 4. The sum of the inner and outer vertical reaction forces of each bearing is used as the basis for setting the number of jacks.

Tab.4 - Each bearing reaction (kN)

Position	Vertical reaction forces of bearing	Sum of reaction forces
Pier 7# outer	1926.91	3502.06
Pier 7# inner	1575.15	
Pier 8# outer	4279.08	8236.63
Pier 8# inner	3957.55	
Pier 9# outer	3950.55	8266.51
Pier 9# inner	4315.86	
Pier 10# outer	1805.28	3469.43
Pier 10# inner	1664.15	

In order to ensure the smooth lifting construction of the curved beam bridge, the jacking force of jack is 1.5 ~ 2.0 times of the maximum bearing vertical reaction force.

Calculation of lateral jacking force

The lateral jacking force must consider both the friction force and the additional lateral force caused by the dead load. The calculation formula is as follows.

$$T = H_f + H_i = \mu R + H_i \tag{1}$$

Where T is the lateral jacking force of each bearing. H_f is the friction force at each bearing. H_i is the additional lateral force caused by dead load. μ is the friction coefficient of sliding block, and the value is 0.1. R is the bearing reaction. According to Equation 1, the lateral jacking force is shown in Table 5.

Tab.5 - Lateral jacking force of the pier (kN)

Position	Bearing reaction R	Friction force H_f	Lateral force H_i	Lateral jacking force T
Pier 7#	3502.06	350.21	2.65	352.86
Pier 8#	8236.63	823.66	13.02	836.68
Pier 9#	8266.51	826.65	15.76	842.41
Pier 10#	3469.43	346.93	17.26	364.19

Jack configuration and beam lifting

According to the above calculation, the hydraulic jack with the jacking force of 200t is selected. The height of the jack is 150 mm, the base diameter is 210 mm, and the stroke of the jack is 50 mm. The horizontal translation jack is a hydraulic jack with a jacking force of 200 t. The height of the jack is 375 mm, the base diameter is 300 mm, and the stroke of jack is 140 mm. The

----

vertical jack and translation jack are installed in the reaction frame, and all lifting jacks are installed in the upward direction. The axis of the jacks shall be vertical during installation. The lifting system shall be inspected before lifting. In order to observe and assess the working state of the whole jacking reset process, the jack up test was carried out before the formal lifting, with the lifting height of 5 mm. During the trial jacking, the initial loading is 80% of the theoretical jacking force, then load slowly. Until it is determined by the displacement sensor that each point has been separated, and then lift it to 5 mm. After 10 minutes of shutdown, check whether the supporting points and lifting supports of the bridge are deformed and whether the loading points are damaged by local pressure. After the lifting test is qualified, the formal lifting height is 15 mm. The jacking is divided into 5 stages. The jacking height of each stage is 3 mm, and the lifting height difference of adjacent piers is controlled within 2mm. When the jacking force approaches the dead load of the beam, the lifting speed shall be slowed down and the jacking shall be lift up slowly to the predetermined height.

Push beam body

After vertical lifting, polytetrafluoroethylene (PTFE) plate and stainless steel plate are used as lateral reset sliding plane. The sliding plane is set at the original support. According to the specific deviation of the main beam of each pier, the translation reaction frame and translation jack are installed. The offset of the main beam at pier 7#, pier 8#, pier 9# and pier 10# is 12 cm, 6.5 cm, 2 cm and 0cm respectively. The method of pushing the beam body and adjusting the bearing position is adopted for the transverse reset of the main beam. The transverse pushing of the beam body is carried out in order by stages and grades. The horizontal reset amount of curved beam is controlled at 1cm. The displacement difference of the main beam at the adjacent pier should be controlled within 1 cm. When the displacement difference is 1 cm, the maximum tensile and compressive stress of the top and bottom plate of the beam does not exceed the tensile and compressive strength of the concrete. The horizontal reset process of beam body is mainly controlled by pushing displacement and assisted by pushing force control. The numerical analysis shows that the maximum principal tensile stress of the top and bottom plate is 1.24 MPa [9], which does not exceed the design tensile strength of C50 concrete, so the lateral launching construction is safe and feasible.

Replace the bearing

The lateral displacement of curved beam bridge is accompanied by shear of bolts, rupture of bearing, and failure of stripping. Therefore, the bearing should be replaced in the restoration stage of the beam body. When the bridge is jacked and pushed to predetermined height and position according to the scheme, the old bearings that have been destroyed are removed. New bearings are also replaced and installed according to the correct position. When mounting the bearing, the bottom and top should be levelled, and the upper and lower steel plates of the bearing should be glued with epoxy resin.

Pier reconstruction and reinforcement and anti- lateral-deviation measures

For the damaged pier, the reconstruction method is to widen. The pier is widened by 30 cm on both sides of the longitudinal direction of bridge and 20 cm on both sides of the transverse direction of bridge. Pier cap, lateral limit stop and vibration isolation rubber block are added. The pier cap and stop block are not set before the pier reconstruction, so the lateral limit of curved beam is insufficient. The reconstructed pier has a good limit capacity to the lateral displacement of the beam (see Figure 9). The widening of the pier body and the addition of reinforcement in the pier can strengthen the crack resistance and bearing capacity, which can effectively prevent the pier from diseases. In addition, for the crack width d < 0.15 mm, the surface sealing treatment is

----

adopted. For the crack width d > 0.15 mm, the pressure grouting method is used to reinforce the crack. Due to the influence of beam displacement and asphalt pavement milling, all expansion joints need to be replaced, and a new type of steel comb plate expansion device is used.

Fig. 9 – Reinforcement and reconstruction of bridge piers

EVALUATION OF RECONSTRUCTION EFFECT BASED ON LONG TERM HEALTH MONITORING DATA

As mentioned above, detailed reinforcement and transformation work has been conducted for the lateral displacement disease of curved beam bridge, but the actual effect of the measures taken needs additional measured data for verification. The long-term health monitoring system of the bridge was established, and the measured data of nearly one year (October 14, 2015, September 17, 2016) of the reinforcement and reconstruction scheme were collected. The temperature load and the corresponding lateral displacement of beam which mainly affect the disease are extracted. Data at night are extracted, and data points are extracted every 15 days to avoid the influence of vehicle load on the monitoring results. According to the selected data points, the probability statistics method is applied to screen out the points that are affected by the vehicle load and considerably change.

Temperature data analysis

The temperature load selects a meaningful time in summer and winter to analyse the temperature field monitoring data of the box girder for obtaining the variation characteristics of the beam under the overall annual temperature change. According to meteorological data, the average temperature in August is the highest in a year. Figure 10(a) presents the temperature curve of August 2016, from which the temperature data of August 11–13 with the highest temperature are selected for analysis. Notably, one data point is taken every hour. Figure 10(b) shows the temperature data curve of measuring point 5 inside the beam and measuring point 2 outside the beam (the location of points is shown in Figure 1.). Figure 10(b) shows that the time of the peak temperature inside the beam (point 5) lags approximately 6 hours behind the peak temperature outside the beam (point 2). This lag is caused by the hysteresis of the heat conduction inside the concrete. The meteorological data indicate that the temperature in February 2016 is relatively low. According to the temperature distribution curve of February shown in Figure 11(a), the temperature data of February 6–8 are selected for analysis, and one data point is taken every hour. Figure 11(b) shows the distribution curve of internal and external temperatures of box girder in this period. The analysis of the measured temperature data reveals that the temperature variation rules in winter and summer are similar, and the figure is similar to the sinusoidal curve. The temperature of the top plate is higher than the external and bottom web temperatures in the same period due to the influence of solar radiation. The temperature difference between top and bottom plates is approximately 10 °C. Web temperature peak, which is the peak of the top plate temperature, appears later. The temperature of the web will be influenced by solar radiation and is mainly

----

affected by heat transfer of concrete. Heat conduction phenomenon is also evident at the bottom of the web.
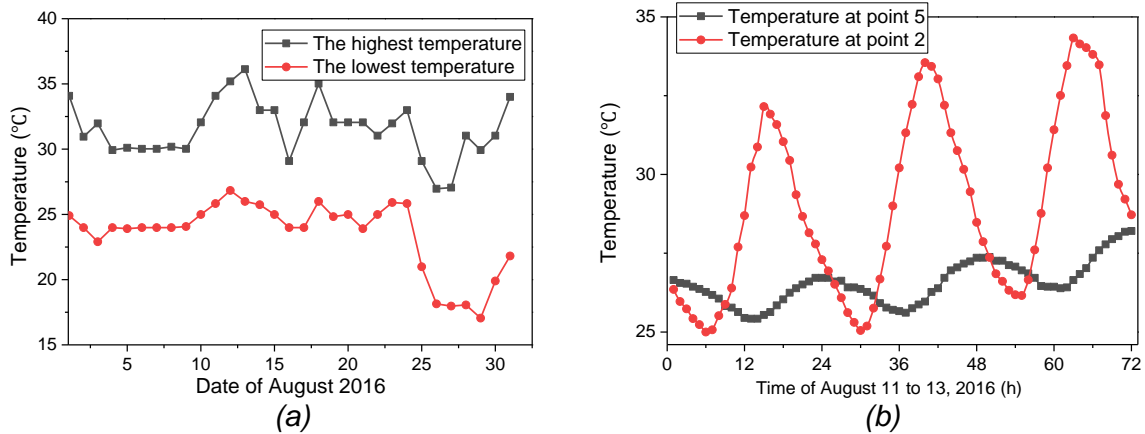

Fig. 10 – Temperature distribution curve of August 2016 and temperature history of beam
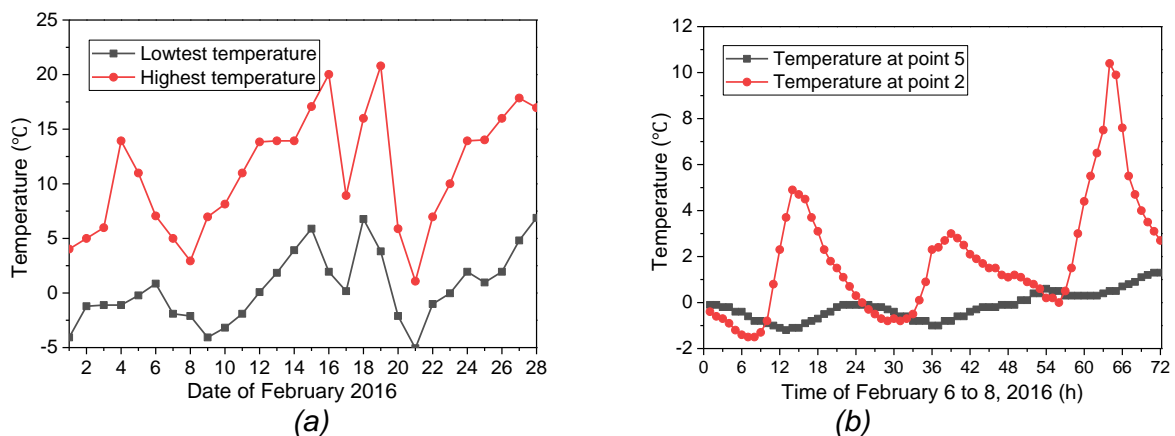

Fig. 11 – Temperature distribution curve of February 2016 and temperature history of beam

Measured lateral displacement under the influence of temperature

The lateral displacement time history curves of piers #7 and #36 are shown in Figure 12. The Figure 12 shows that only pier #7 has a horizontal displacement of 5 mm in December 2015, while pier #36 has slight change in the displacement of sensor. At the same time, the change trend of lateral displacement is the same as that of temperature. With the increase in temperature, the beam expands and exhibits deviation (pointing to the lateral) and up shift of Δ1. With the loss of the temperature, the deviation move of main girder will gradually restore (pointing to the inside). The amount is recovered as Δ2 due to the influence of gravity force component and the function of the friction between bearings, that is, Δ1<Δ2. Therefore, in the process of the cycle of heating and cooling, lateral displacement moves too late to complete the recovery of beam and gradually accumulates. Data from January 23, 2016 to June 20, 2016 are taken for analysis to intuitively study the influence of temperature on lateral displacement, and data points are taken every minute. In two days of normal traffic, the average temperatures are 7 °C and 24 °C, respectively. For urban bridges, the load distribution of vehicles in two days is roughly the same. Therefore, temperature is the influencing factor of the transverse displacement amount in two days. Figure 13 shows the transverse displacement curve of pier #36 in the two days. The transverse displacement of the main beam is low at low temperature and high at high temperature. The displacement values of the

----

remaining piers also show a similar correlation with temperature. The analysis of the 1-year monitoring data indicates that the lateral displacement is mainly caused by the deviation and torsion of structure under the influence of the system temperature difference and the temperature gradients. This deduction is consistent with the finite element analysis conclusion above.
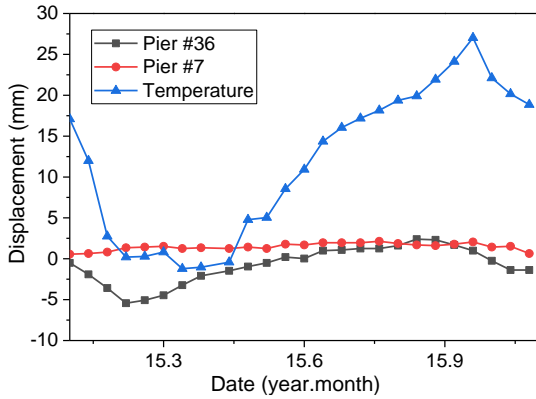

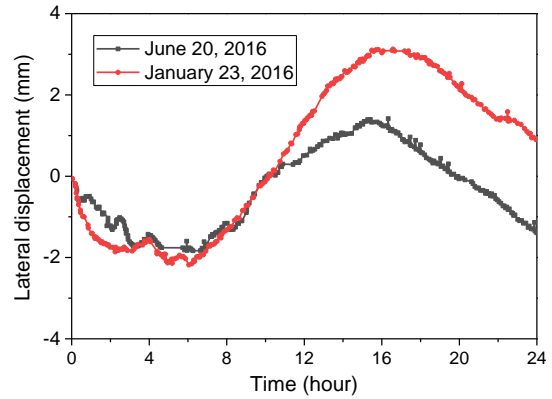Fig. 12 – Time history curve of lateral displacement

Fig. 13 – Lateral displacement of pier #36

Linear correlation coefficient R is used to further analyse the correlation between displacement and temperature. The scatter of the correlation between the lateral displacement and temperature of pier #36 is shown in Figure 14 as an example. The lateral displacement is roughly linear with the temperature. According to the linear regression method, the absolute value of the correlation coefficient between them is 0.9232, which is greater than 0.8. In other words, the lateral displacement is linear with temperature. The displacement of the remaining piers also shows a similar correlation with the temperature.
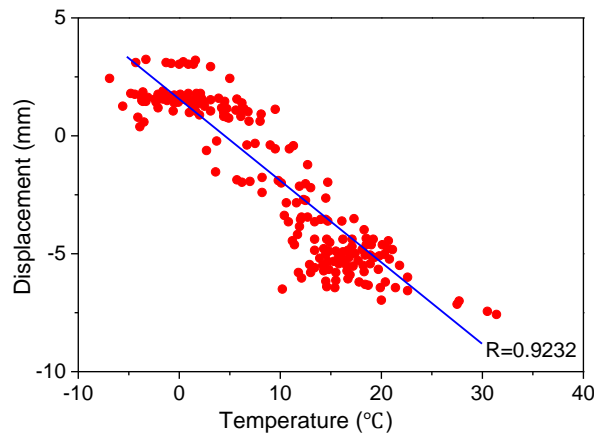
Fig. 14 – Correlation between the lateral displacement of pier #36 and temperature

Transverse creep measurement after reinforcement and transformation

According to bearing technical data, the maximum allow lateral displacement of the bearing is ±40 mm, and the maximum allow longitudinal displacement is ±100 mm. In the past year, the maximum transverse displacement was 5.6 mm, which was less than the maximum displacement of the support. This result indicates that the bearing does not break during the monitoring period. At the same time, the threshold of lateral displacement of the support is also set depending on the maximum displacement. In the monitoring system established above, the system will automatically alarm once the lateral deviation monitoring value exceeds the limit.

CONCLUSION

On the basis of the detailed investigation of the lateral displacement disease, the paper analyzes the lateral displacement mechanism of the curved beam bridge under the influence of temperature. The reinforcement and reconstruction measures after the diseases of curved beam bridge are also provided. The transformation effect is analyzed and evaluated as well on the basis of the monitoring data. The main conclusions are as follows.

(1)   Due to the structural characteristics of curved beam bridge, lateral displacement will occur under the influence of external load such as temperature, prestress, concrete shrinkage and creep effect, vehicle load and other factors. Therefore, to solve the problem of lateral displacement of curved beam, some preventive measures should be taken from the aspects of bridge design, construction and maintenance, so as to limit the lateral deflection and improve the service life of curved beam bridge.

(2)   Numerical analysis shows that under the action of temperature gradient, the curved beam bridge produces large radial displacement, the bearing produces large transverse and vertical negative reaction forces, and the bearing is prone to shear failure and tensile fracture failure. Under the action of system temperature difference, the bearing is prone to shear failure and tension state and produces large radial offset and tangential slip. Therefore, the temperature effect is the main factor causing the lateral displacement of curved beams bridge.

(3)   Without considering the long-term cumulative effect of bearing displacement, the analysis based on the assumption of one-time load instead of long-term repeated load and beam transverse displacement instead of long term cumulative displacement cannot accurately explain the mechanism of lateral displacement of curved bridge. The mechanism should be that there is residual lateral displacement in each load action under the action of internal and external factors. Under the action of repeated load, the lateral displacement is accumulated continuously, which forms the deflection of curved beam bridge.

(4)   For the curved beam bridge with lateral deflection, corresponding reconstruction and reinforcement measures can be taken to restore the normal function of the structure. At the same time, the existing diseases can be eliminated by means of component reinforcement, accessory component improvement and structural performance improvement, so as to restore the original function of the bridge and extend the service life of the bridge. For the example bridge in this paper, the long-term health monitoring data show that the bridge is in good service condition after reconstruction and reinforcement, and there is no serious lateral displacement disease.

ACKNOWLEDGEMENTS

REFERENCES

[1]   Deng T., Zhang J., Bayat M., 2018. Simplified Method and Influence Factors of Vibration Characteristics of Isolated Curved beam bridge. Structural Durability & Health Monitoring, vol. 12(3): 189-212

[2]   Granata M.F., Margiotta P., Arici M., 2013. A Parametric Study of Curved Incrementally Launched Bridges. Engineering Structures, vol. 49: 373-384

[3]   Sali J., Mohan R.P., 2017. Parametric Study of Single Cell Box Girder Bridge under Different Radii of Curvature. Applied Mechanics and Materials, vol. 857: 165-170

[4]   Samaan M., Kennedy J.B., Sennah K.,2007. Impact Factors for Curved Continuous Composite Multiple-box Girder Bridges. Journal of Bridge Engineering, vol. 12(1): 80-88

[5]   Sarode A.B., Vesmawala G.,2014. Parametric Study of Horizontally Curved Box Girders for Torsional Behavior and Stability. International Refereed Journal of Engineering and Science, vol. 3(2): 50-55

[6]   Fatemi S., Ali M.M., Sheikh A., 2016. Load Distribution for Composite Steel–concrete Horizontally Curved Box Girder Bridge. Journal of Constructional Steel Research, vol. 116(1): 19-28

[7]   Kim S., Cho K., Won J., 2009. A Study on Thermal Behaviour of Curved Steel Box Girder Bridges Considering Solar Radiation. Archives of Civil and Mechanical Engineering, vol. 9(3): 59-76

[8]   Moorty S., Roeder C.W.,1992. Temperature-dependent Bridge Movements. Journal of Structural Engineering, vol. 118(4): 1090-1105

[9]   Lin L.J., 2015. Study on Lateral Deviation of the Curved Beam Bridge, dissertation for the degree of master(Zhengzhou University): 13-78

[10]   Li J., Feng G.J., Lin L.J. Chen H., 2017. Lateral Creep Displacement Mechanism Analysis of Curved Beam Considering the Cumulative Effect of Residual Displacement under Temperature. Science Technology and Engineering, vol. 17(34): 124-129

[11]   Hossain M., Zisan M. Haque M., 2019. Analysis of Distortion-induced Stress and Retrofitting Technique of Curved Twin I-girder Composite Bridge. Arabian Journal for Science and Engineering, vol. 44(5): 4395-4404

[12]   Li J., Chen H., Lin L.J., 2017. Lateral Creep Displacement Mechanism Analysis of Curved Beam Considering the Cumulative Effect of Residual Displacement under Temperature. Construction Technology, vol. 46(16): 110-113

ENHANCEMENT OF CONCRETE PIPES THROUGH REINFORCEMENT WITH DISCRETE FIBERS

Parviz Soroushian[1] and Shervin Jahangirnejad[2]

1. *President, Metna Co., 3927 Dobie Road, Okemos, MI 48864, USA; metnaco@gmail.com*
2. *Associate, Shannin and Wilson, Inc., 3990 Collins Way, Suite100, Lake Oswego, OR 97035, USA; SHJ@shanwil.com*

ABSTRACT

An industrial-scale production and experimental investigation was conducted in order to evaluate the constructability and structural performance of different concrete pipes incorporating discrete synthetic fibers. The results indicated that synthetic fibers enable design of plain concrete pipes with a desired balance of strength and ductility. Analytical models were developed for predicting the load-carrying capacity of concrete pipes without steel reinforcement that are reinforced with discrete fibers.

KEYWORDS

Concrete pipe, Fiber reinforcement, Strength, Ductility, Damage resistance, Experimental evaluation, Analytical modeling

INTRODUCTION

Concrete pipes, manholes, pump stations, wet wells, etc. represent close to half of the investment in the infrastructure for the 20,000 sewer systems in the United States. Concrete has reached its position of prevalence in the sewer infrastructure through satisfactory performance over long periods of time [1]. The concrete-based sewer infrastructure offers a desired balance of durability, structural efficiency, and initial as well as life-cycle economy. In recent years, however, incidents of severe damage to the concrete-based sanitary sewer infrastructure have increased significantly [2]. There is a need to improve the damage resistance and service life of concrete pipes [3]. Synthetic fiber reinforcement of concrete is used in this investigation to enhance the structural performance of plain concrete pipes.

EXPERIMENTAL MATERIALS AND METHODS

Pipes were fabricated in the industrial facility of the Northern Concrete Pipe Inc. (Charlotte, MI, USA) using different concrete materials. This facility uses the dry-cast method of concrete pipe production. The effects of fiber reinforcement on the structural performance of concrete pipes were investigated. The fiber volume fraction and geometry were the key variables of the experimental program. Synthetic fibers with different lengths and diameters were used in concrete pipes as full replacement for steel reinforcement.

Materials

Fiber geometry and volume fraction were the primary variables in formulation of materials. PVA (Polyvinyl Alcohol) fibers were used in this investigation; three fiber geometries were considered (see Tab. *1*). The fiber volume fraction ranged from 0 to 2%.

Tab. 1 - Pipe fiber reinforcement conditions (no continuous steel reinforcement)

| Pipe	Fiber Vol.%	Fiber Properties			
		Type	Length, mm (in)	Diameter, mm (in)	Tensile Strength, MPa (psi)
# 6	0%	-	-	-	-
# 7	0.5%	I	6 (0.24)	0.001 (0.026)	1600 (232000)
# 8	0.5%	II	12 (0.47)	0.1 (0.0039)	1100 (159500)
# 14	0%	-	-	-	-
# 15	2%	III	15 (0.59)	0.3 (0.012)	900 (130500)

Concrete Mix Proportions and Pipe Dimensions

The base concrete mixture used for industrial-scale production of concrete pipes had an aggregate-to-binder ratio of 5.5, with fine-to-coarse aggregate ratio of 1.5, and water-to-binder ratio of 0.34. This mix provided adequate stability in fresh state for immediate demolding of the pipe. In mixtures that incorporated finer synthetic fibers, the total aggregate content was reduced by 10% in order to increase the paste content for enhancing the dispersion and interfacial bonding of fibers.

All pipes were standard class IV, wall C. This type of pipe is characterized by an internal diameter of 686 mm (27 inches), a wall thickness of 102 mm (4 inches), and a length of 2.59 m (8.5 feet) [4].

Test Method

Three-Edge Bearing Tests were performed on all pipes per ASTM C497. In this test, the pipe is supported on two parallel longitudinal strips, and the load is applied uniformly along the pipe length using an upper bearing strip (Figure 1). The lower and upper bearing strips are extended the full length of the pipe. Under increasing load levels in the tree-edge bearing test, first cracks develop along the pipe length on the top and bottom (crown and invert) interior surfaces of the pipe (Figure 2). Further increase in load generates horizontal side cracks on the outside surface of pipes. The load corresponding to 0.25 mm (0.01 in) crack width was determined through monitoring of the width of the first crack formed on the interior surface of the pipe. The peak load as well as the load-deflection behavior of the pipe were also obtained in the three-edge bearing tests. The load-deflection curves reflect upon the ductility and energy absorption capacity of pipes.
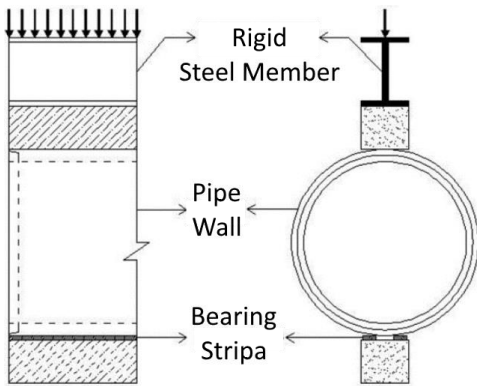
(a) Schematics

(b) Picture

Fig. 1 - Test setup.

Fig. 2 - The initial bottom crack in pipe subjected to the three-edge bearing test.

TEST RESULTS AND DISCUSSION

The loads corresponding to 0.25 mm (0.01 in) crack width as well as the first-crack and peak loads are presented in Table 2. Figure 3 shows the load-deflection responses generated in the three-edge bearing tests of concrete pipes with different fiber reinforcement conditions. It should be noted that the concrete pipe #15 with 2% volume fraction of coarse 15 mm x 0.3 mm (0.59 in x 0.012 in) PVA fibers, did not fail in a very brittle (almost explosive) manner in the three-edge bearing test; fiber pullout was prevalent in this case (Figure 4a). Reinforcement with 2% volume fraction of the coarse 15 mm x 0.3

----

mm (0.59 in x 0.012 in) fiber thus offers the promise to control damage to plain concrete pipes during handling, transportation and installation.

Tab. 2 - Measured values of different load levels in three-edge bearing tests on concrete pipe

Pipe	First Crack Load , kN (lb)	Load @ 0.25 mm (0.01 in) Crack, kN (lb)	Peak Load, kN (lb)
# 6	211 (47,500)	211 (47,500)	211 (47,500)
# 7	227 (51,000)	231 (52,000)	231 (52,000)
# 8	214 (48,000)	223 (50,000)	223 (50,000)
# 14	206(46,250)	206 (46,250)	206 (46,250)
# 15	238 (53,500)	238 (53,500)	238 (53,500)

The three-edge bearing test results for the first series of pipes presented above indicates that:

1. Pipes #6, #7 & #8 provide a basis to assess the potential of fibers to overcome the brittle mode of failure in plain concrete pipes (without continuous steel reinforcement). Many concrete pipes do not need steel reinforcement for load-bearing capacity. Steel is added to these pipes (with important implications in terms of cost and production effort) mainly to avoid damage to these brittle pipes during transportation and installation. Synthetic fibers could be a cost-effective replacement for steel as far as they ensure ductile failure mode of pipes. In the case of plain concrete pipes, with conventional hydraulic loading systems used for the performance of three-edge bearing tests, the gains in ductility with 0.5% fiber volume fraction (Pipes #7 & #8) are relatively small (compared with Pipe #6). This, however, could be a result of the load-controlled nature of the hydraulic loading system. This system, in combination with the test frame, act as a spring within which mechanical energy accumulates as the peak load is approached. Although the fiber reinforced concrete pipes (without steel reinforcement) would have some level of post-peak ductility for adequate resistance to brittle modes of failure during transportation and installation, the energy accumulated within the hydraulic loading system (and test frame) is suddenly released once the peak load is reached, causing sudden failure of pipe irrespective of the post-peak ductility provided by fiber reinforcement of plain concrete pipes. In other words, the brittle mode of failure in fiber reinforced concrete pipes (without steel reinforcement) in three-edge bearing test does not necessarily imply that these pipes are prone to damage during transportation and installation.

2. Coarser fibers 15 mm x 0.3 mm (0.59 in x 0.012 in) can be more conveniently introduced at relatively high volume fractions (2%) into the concrete mixtures used in the dry-cast method of pipe production. Finer fibers with higher specific surface areas require increased paste and plasticizer contents for uniform dispersion in concrete mixtures with adequate workability. Minor balling of fibers during production was observed (Figure 4b), which could be resolved through a slight increase in the paste content of concrete and also by pre-wetting of the hydrophilic PVA fibers.

----

3. The coarser PVA fiber exhibited a prevalent tendency towards pullout at cracks while the finer PVA fibers predominantly ruptured at cracks. The frictional pullout of coarser fiber benefits their contribution towards the ductility and energy absorption capacity of concrete pipes, which can be used to prevent brittle failure of plain concrete pipes and thus facilitate production of plain pipes which are resistant to damage during handling, shipment and installation.
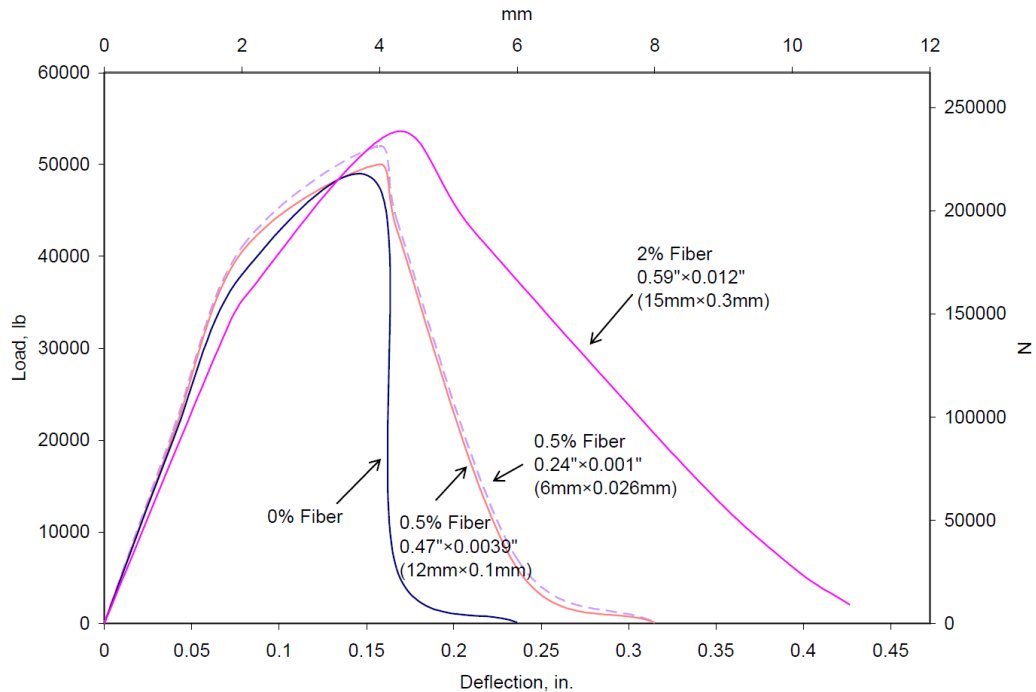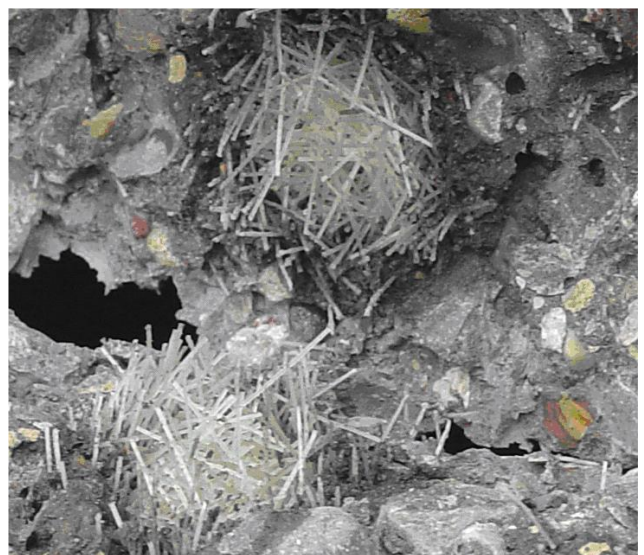

Fig. 3 - Load-deflection curves of concrete pipes with different fiber reinforcement conditions

(a) Uniform fiber dispersion

(b) Occasional fiber balling

Fig. 4 - Fiber dispersion conditions

ANALYTICAL INVESTIGATION

Pipes are subjected to earth and live loads which generate transverse bending moments in pipe walls. The transverse (circumferential) reinforcement is used in concrete pipes to resist bending moments. Under loads, pipes first develop vertical (crown and invert) cracks starting at interior surfaces, and then horizontal (springline) cracks starting at mid-height on exterior surfaces. Under the effect of bending moments, the pipe wall behaves as a rectangular reinforced concrete section.

Concrete pipes with limited demand on their load-bearing capacity may be unreinforced. Design of concrete pipes is based primarily on their flexural performance under external loads. One load criterion, that is ultimate load in three-edge bearing test, is generally used in design of concrete pipes. The analytical work presented herein seeks to establish a theoretical framework for prediction of the load levels in plain concrete pipes with synthetic fiber reinforcement.

Plain Concrete Pipes

Ultimate (D-)Load is calculated using the following equation [5, 6]:

$$f_{mr} = 0.96\, \phi_{mr}\, \frac{DL_{ut} \times D_i\,(D_i + h)}{144\, h^2} \tag{1}$$

where

DL_{ut} = the D-load that cracks the pipe (lb/ft/ft)

D_i = the internal diameter of the pipe (in), h is the wall thickness (in)

f_{mr} = the modulus of rupture (flexural strength) of concrete (psi)

Modification of Design Equations to Account for the Effects of Synthetic Fibers

Fiber reinforcement of concrete enhances its flexural load-bearing capacity at different stages of performance. This is due to the crack arrest action, tensile force resistance and frictional pullout of fibers in regions of concrete that experience tensile stresses. The simplified approach adopted here accounted for the contributions of fibers to the flexural strength of concrete.

Fibers in a cementitious matrix exhibit two types of behavior at cracks: pull-out, or rupture. The synthetic (PVA) fibers used in this investigation exhibit a stronger tendency towards rupture (especially for finer diameters and higher aspect ratios). The reason is the hydrophilic nature and strong bonding of PVA fibers to the cementitious matrix. The tendency towards fiber pull-out increases with increasing fiber diameter and decreasing fiber aspect ratio. Various methods have also been employed to promote fiber pull-out for enhancing the toughness and energy absorption capacity. These methods include use of an oiling agent and modifying the matrix to reduce the chemical and frictional bonding to PVA fibers.

Design Equations When Fiber Rupture Dominates

The fiber concrete tensile stress distribution at flexural failure is assumed to be triangular (linear) based on past experience [7]. Fibers act in tension within the tensile zone of the concrete pipe cross-section. This zone starts at neutral axis, and covers the full area towards the surface with peak tensile stress. Equilibrium of forces yield the expression for flexural strength.

The above approach together with equilibrium considerations for the flexural stress distribution of Figure 5 yield the nominal flexural strength of fiber reinforced concrete section.

$$M_n = F_{mr} + \left[\frac{\sigma_t (h-c)}{2} b \left(\frac{2(h-c)}{3} \right) \right] \tag{2}$$

where

σ_t = the tensile stress in fibrous concrete, and is calculated as follows:

σ_t = (N = number of fibers per unit area) * (U = ultimate tensile force of a single fiber)

$$\sigma_t = \left(\frac{0.5 V_f}{\pi d_f^2} \right) \left(\sigma_{fu} \frac{\pi d_f^2}{4} \right) \tag{3}$$

Therefore,

$$\sigma_t = 0.5 \, V_f \, \sigma_{fu} \tag{4}$$

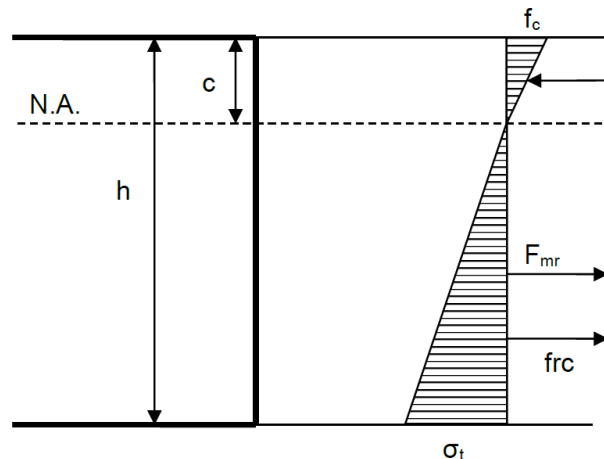In the above formula, N is the number of (3D) distributed fibers per unit cross-sectional area.

Fig. 5. - Flexural stress distribution at ultimate condition for a non-reinforced fiber concrete section.

Design Equations When Fiber Pull-Out Dominates

When fiber pull-out dominates, the fiber concrete tensile stress distribution is assumed to be the same as previous case.

$$M_n = F_{mr} + \left[\frac{\sigma_t (h-c)}{2} b \left(\frac{2(h-c)}{3} \right) \right] \tag{5}$$

The tensile stress in fibrous concrete (σ_t) is, in this case, equals to:

$$\sigma_t = N \cdot F \tag{6}$$

where

N = number of fibers per unit area

F = mean fiber frictional pullout resistance.

For randomly (3D) oriented short fibers,

$$N = \left(\frac{0.5 V_f}{\frac{\pi d_f^2}{4}} \right) \tag{7}$$

When fiber pull-out dominates (over an average length that is one-quarter of fiber length),

$$F = \left(\tau_f \, \pi d_f \, \frac{l_f}{4} \right) \tag{8}$$

Therefore,

$$\sigma_t = \left(\frac{0.5 V_f}{\frac{\pi d_f^2}{4}} \right) \left(\tau_f \, \pi d_f \, \frac{l_f}{4} \right) \tag{9}$$

which can be simplified to:

$$\sigma_t = 0.5 V_f \, \tau_f \, \frac{l_f}{d_f} \tag{10}$$

ANALYTICAL PREDICTIONS VERSUS EXPERIMENTAL RESULTS

The fiber concrete pipes tested in experimental investigations had the following properties:

f'_c = 34.5 MPa (5000 psi (34.5 MPa)

W_p = 624 kg/lin. m (420 lb/lin. ft)

$f_{mr} \cong$ 3.66 MPa (530 psi)

----

h = 102 mm (4 in)

D_i = 686 mm (27 in)

The fiber properties were presented in Table 1. Figure 6 presents the experimental results and analytical predictions of the ultimate loads for different pipes considered in the experimental program. Analytical predictions were made based on the assumptions of the predominance of either fiber rupture or pullout, as described in the following. In the case of Pipe #8, with fibers of medium aspect ratio, some fiber pull-out was observed but fiber rupture was still prevalent. For Pipe #15, which incorporated coarse fibers, fiber pull-out with a bond strength, τ, of 10 MPa (1450 psi) [8] yielded a satisfactory analytical prediction of experimental results. Fiber rupture was assumed to be prevalent in Pipe #7 with the smallest fiber diameter and highest fiber aspect ratio. The predicted value of D-load would have been higher, and closer the experimental value, for Pipe 8 (with intermediate fiber diameter and aspect ratio. The reasonable comparison of the predicted and experimental values for Pipes 7 and 15 could have resulted from the prevalence of fiber router and pullout, respectively, in these pipes.
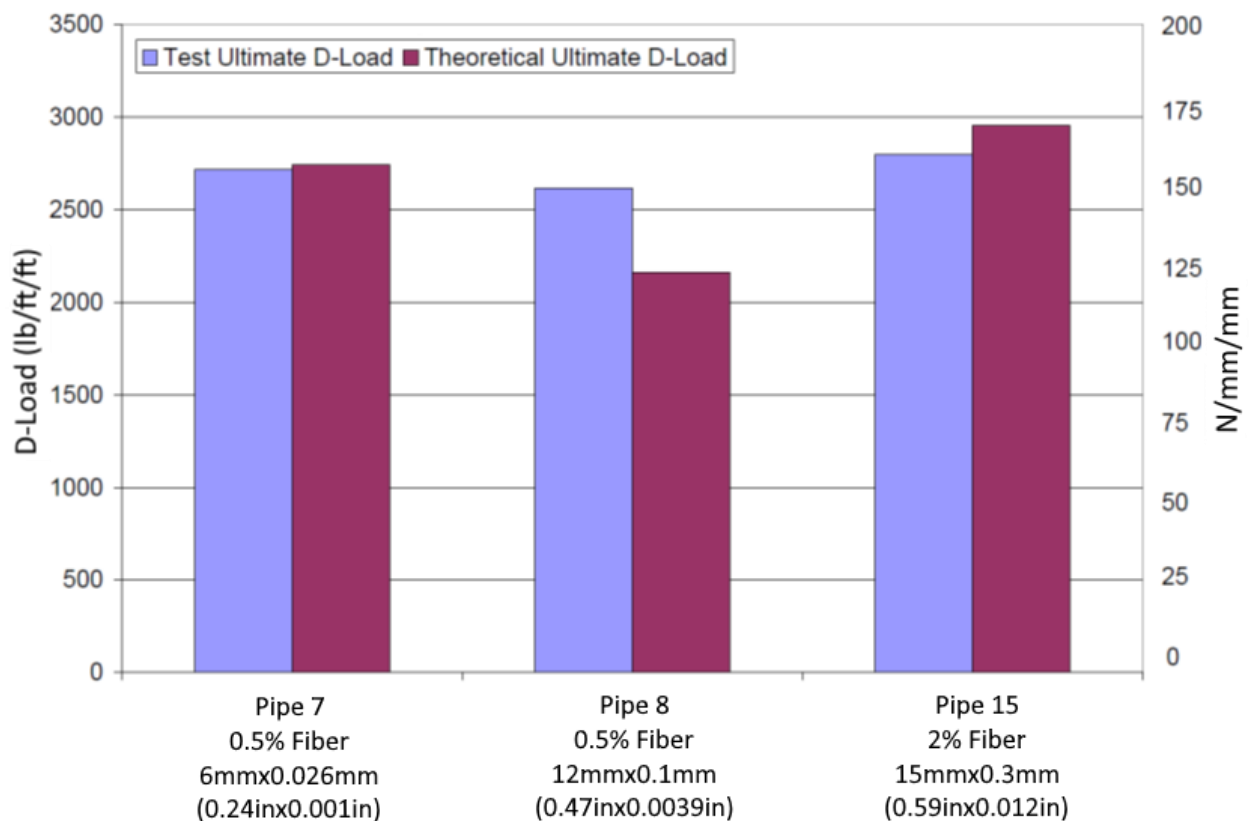

Fig. 6 - Analytical predictions of ultimate loads versus experimental results

CONCLUSION

1. Refined concrete mix formulations incorporating synthetic fibers were found to suit industrial-scale production of concrete pipes.

2. Synthetic (PVA) fiber reinforcement at about 1% volume fraction enhances the cracking and peak loads, and the post-peak ductility and damage resistance of concrete pipes.

3. Coarser (larger-diameters) PVA fibers at reasonably high aspect ratios, when compared with finer fibers, can be more conveniently dispersed in the high-performance concrete mixtures used in dry-cast method of concrete pipe production at about 1% fiber volume fraction, and exhibit a greater tendency towards fiber pull-out (versus rupture) which benefits the ductility and damage resistance of concrete pipes. PVA fibers with 15 mm (0.59 in) length and 0.3 mm (0.012 in) diameter perform satisfactorily in dry-cast concrete pipes at about 1% fiber volume fraction.

4. Concrete pipes with relatively low load-bearing requirements could be designed without steel reinforcement. The potential for damage to concrete pipes during shipment, handling and installation, however, forces the use of steel reinforcement for the purpose of damage control. Reinforcement of plain concrete pipes with coarser PVA fibers can bring about a change from brittle to ductile modes of failure at competitive cost, eliminating the need for conventional steel reinforcement of pipes with relatively low load-bearing requirements. The PVA fiber reinforced concrete pipes offer advantages over conventional steel reinforced pipes in terms of streamlined production, cost, and service life (corrosion resistance).

5. Further work for enhancing the dispersion of synthetic fibers in concrete would enable full realization of the PVA potential for improving the structural performance of concrete pipes.

ACKNOWLEDGEMENTS

NOTATION

D_i = the internal diameter of the pipe (in), h is the wall thickness (in)

DL_{ut} = the D-load that cracks the pipe (lb/ft/ft)
f_{mr} = the modulus of rupture (flexural strength) of concrete (psi)

F = mean fiber frictional pullout resistance.

N = number of fibers per unit area)

σ_t = the tensile stress in fibrous concrete,and is calculated as follows:

U = ultimate tensile force of a single fiber

REFERENCES

[1]   Alexander, M.G. and C. Fourie, 2011. Performance of swere pipe concrete mixtures with Portland and calcium auminate cements subject to mineral and biogenic acid attack. Materials and Structures, vol 44, no 313-330.

[2]   Ling, A.L., et al., 2015. *High-resolution microbial community succession of microbially induced concrete corrosion in working sanitary manholes.* PloS one, vol **10**, no 3: p. e0116400.

[3]   O'Connell, M., C. McNally and M.G. Richardson, 2010. Biochemical attack on concrete in wastewater applications: a state of the art review. Cement and Concrete Composites, vol 32, no 7: p. 479-485.

[4]   American Society for Testing and Matrials, 1999. *Standard Specification for Reinforced Concrete Culvert, Storm Drain, and Sewer Pipe*, American Society for Testing and Materials.

[5]   American Concrete Pipe Association, *Concrete pipe technology handbook*. Irving, TX, 1993.

[6]   Watkins, R.K. and L.R. Anderson, 1999*. Structural mechanics of buried pipes*, CRC press.

[7]   Herrmann, H. and J. Schnell, 2019. *Short Fiber Reinforced Cementitious Composites and Ceramics*, Springer International Publishing.

[8]   Hong, L., Y.D. Chen, T.D. Li, P. Gao and L.Z. Sun, 2020. Microstructure and bonding behavior of fiber-mortar interface in fiber-reinforced concrete, Construction and Building Materials, vol 232: p. 117235.

EXPERIMENTAL STUDY ON THE MECHANICAL AND DEFORMATION PROPERTIES OF PIPE AND SOIL IN RECTANGULAR PIPE JACKING CONSTRUCTION WITH CONTROLLABLE CEMENT GROUTING TECHNOLOGY

Jun Tang[1,2] and Shengcai Li[1]

1. *School of Civil Engineering, Huaqiao University, Xiamen 361021, China*
2. *Xiamen Xijiao Hard Science Industrial Technology Research Institute Co., Ltd, Xiamen, 361006, China;sram8888@163.com*

ABSTRACT

Based on the utility tunnel project of Chengbei Road in Suzhou, the experimental study on the mechanical and deformation properties of pipe and soil in rectangular pipe jacking construction with controllable cement grouting drag reduction technology is carried out. Based on the monitoring and analysis of pipe and soil stress and deformation of pipe joints during pipe jacking, the relevant theoretical model is established and the finite element simulation is carried out to experimentally study and compare the stress and deformation of pipe and soil in rectangular pipe jacking construction with controllable cement grouting drag reduction technology. The results show that the controllable cement grouting drag reduction technology has a significant effect on the pipe and soil stress in rectangular pipe jacking, which reduces pipe-soil interaction forces effectively, and improves the overall safety of pipe jacking construction.

KEYWORDS

Controllable cement grouting technology, Cement grouting drag reduction, Rectangular pipe jacking, Mechanical behaviour Deformation property

INTRODUCTION

Since the introduction of rectangular pipe jacking construction technology in 1990s in China, due to the limitation of economy and technical maturity, there are few theories, experiments and engineering cases based on this technology. For the rectangular pipe jacking project with large cross-section and long distance [1], accurate pipe and soil stress analysis and effective slurry drag reduction measures will be an important basis to determine whether the project can be successfully implemented and improve the economy. According to the different principles adopted, the discussion and research on pipe and soil load can be divided into simplified analysis and calculation method, field measurement and model test method, etc [2].

In the simplified analysis and calculation method, the soil pressure on the pipe can be simplified as the vertical soil pressure on the upper part of the pipe joint, the horizontal soil pressure on the side of the pipe joint, the vertical subgrade reaction at the bottom of the pipe joint, and the passive subgrade resistance caused by pipe deformation [3]. The simplified analysis and calculation

method simplify the pipe and soil load into the above four parts, and then carry out specific calculation of each part to solve the calculation question. However, this method cannot calculate the influence of different construction methods, segment stiffness and other factors on the magnitude and distribution of pipe and soil pressure and the calculated value is different from the field measured value [4].

Field measurement can reflect the comprehensive influence of various factors on soil pressure, and so many scholars attach great importance to the collection and analysis of field measurement data. The performance of lubrication for backfilling material is significant [5], and [6] conducted a field test study on a tunnel. The main beneficial mechanism of pipe jacking lubricants is the reduction of the local effective stress acting on the pipe through the generation and retention of excess pore water pressure in the soil near the interface. [7] also obtained similar research results. [8] measured the soil pressure distribution on the upper part of tunnel with gravel foundation. The research shows that the soil pressure acting on shallow tunnel can be based on the Terzaghi soil pressure and the load acting on deep tunnel is mainly the water pressure. [9] also obtained similar research results.

For the research on cement grouting drag reduction technology, [10] studied the formation process and disturbance effect of thixotropic slurry jacket during pipe jacking, showing the functions of filling, supporting, isolation and lubrication after slurry jacket injection and slurry film formation. [11] analyzed the thixotropic slurry mix proportion, and highly viscous bentonite slurry mixed with polymer was used to reduce the friction resistance. [12] carried out numerical analysis on the over excavation of deep pipe jacking construction, and the thickness and the distribution of the slurry at different pipe segments were calculated using the two‐way travel time and the radar signal propagation velocity in the slurry.

The stress of pipe jacking in the construction process is very complex, and friction drag is the main part of all kinds of drag. [13] applied a model coupling finite element method and a displacement control method to estimate the required jacking force during rectangular pipe jacking, and analyzed the factors affecting the jacking force. [14] thought that different forms of slurry jacket had great influence on the effect of cement grouting drag reduction and investigated the causes of high deflection by the finite element method. The results showed that, various stiffening ribs are used in different deflection sections with grouting to decrease friction and lower the corresponding axial jacking force. [15] analyzed several construction cases of French national micro tunnel project, and the research results show that grouting cannot only reduce the dynamic friction during the jacking process, but also effectively reduce the additional friction caused by construction interval.

ANALYSIS OF REAL-TIME MONITORING RESULTS IN THE TEST SECTION

Monitoring item and main content

In this paper, the field monitoring of soil pipe contact pressure is carried out by installing pressure sensor on the surface of pipe joint, including soil pressure monitoring and pour water (slurry) pressure, to test the influence of controllable cement grouting drag reduction technology on soil pipe jacking.

Layout of measuring point and observation method

(1)   Pipe joint design: the section size of pipe joint is 5.5m×9.1m, the wall thickness is 650mm, the inner diameter is 4.2m×7.8m, and the length and weight of single joint are 1.5m and 66.8t respectively. The pipe joint is prefabricated with reinforced concrete, with strength of C50 and impermeability grade of P8.

----

(2)   Monitored section: the total monitoring length of this pipe jacking project is 138m. Two pipe joints are selected as the monitored section. The distance between I# pipe joint and the pipe jacking machine is 20m, and the distance between II# pipe joint and I# pipe joint is 30m. The jacking distance of I# pipe joint is 118m, and the change of soil pressure in the whole pipe jacking construction can be observed. The jacking distance of II# pipe joint is 88m, which can be used as the supplementary monitoring data of the monitored section of I# pipe joint.

(3)   Layout of measuring points: 11 soil pressure gauges are arranged at the monitored section of I# pipe joint, 5 of which are located at the top of the monitored section, mainly monitoring the distribution of soil pressure at the section top and focusing on monitoring the change of soil pressure near the controllable cement grouting hole. Three soil pressure monitoring points are arranged on the right side of the section, evenly at the upper, middle and lower positions of the side wall of pipe joint, the left soil pressure monitoring points are arranged in the middle of the side wall of pipe joint, and the bottom monitoring points are evenly arranged at the bottom of the monitored section.

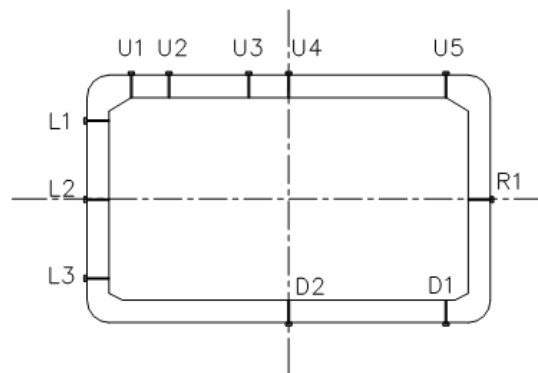The specific layout of measuring points is shown in Figure 1.

Fig.1 - Layout of measuring points for pipe joint

(4)   Embedding of monitoring sensor:

① Soil pressure gauge

According to the spatial distribution, pipe jacking construction can be divided into three main parts: starting area, jacking area and receiving area, while the pressure monitoring only needs to be carried out in the jacking area. Since the starting area is often reinforced by bored piles, mixing piles and grouting, the monitored section should be protected when passing through the starting area.

② Pour water (slurry) pressure gauge

The pore water pressure gauge can be used to measure the pressure around the controllable cement grouting port. The pressure gauge sensor should be buried as close as possible to the controllable cement grouting port.

③ Embedding of monitoring sensor:

The monitoring data of soil pressure gauge and slurry pressure sensor are recorded and stored by the acquisition module in the signal acquisition box through the signal line. The acquisition module has the ability to automatically acquire data according to the set time interval, and the acquisition time

----

mainly depends on the battery power and the capacity of storage card.

Field monitoring results and analysis

The field monitoring of the stress on I# pipe joint structure took 3 months and 4990 groups of data were collected. In the process of monitoring, all sensors on I# pipe joint worked normally, so the data of spare sensors on II# pipe joint will not be discussed. In the process of controllable slurry injection, the orifice of the osmotic water pressure gauge was blocked and the slurry pressure could not be transmitted smoothly, so the osmotic water pressure data will not be discussed.

(1)   Analysis of monitoring data of pipe and soil contact pressure during pipe jacking construction

The data of I # pipe section was monitored during the whole jacking process. According to different stages of construction, three main stages i.e. starting area, jacking area and receiving area will be discussed:

Starting area: The reinforcement thickness of the starting well is about 5m. Because the sensor is protected by a sleeve, although the data fluctuates, the pressure value is very small;

Jacking area: The jacking area is divided into jacking area with uniform geology and water rich soft soil jacking area.

① Jacking area with uniform geology

When the soil in front of the pipe jacking area was uniform and the settlement of the top soil was well controlled, the soil pressure monitoring data was relatively stable and had a certain correlation with the grouting pressure.

② Water rich soft soil jacking area

When the pipe jacking passed through the saturated soft soils area and the top may have large settlement or the ground had key protective buildings and structures, we performed high-pressure grouting around the pipe jacking. Under this condition, the monitoring data of soil pressure fluctuated greatly;

Receiving area: After the pipe jacking construction entered the receiving area, all monitoring data decreased.
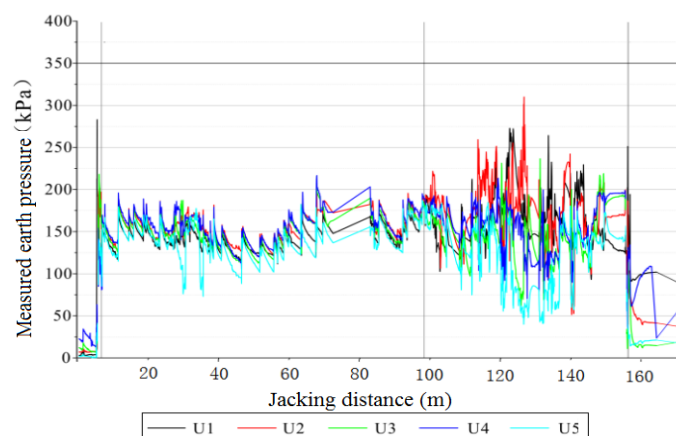

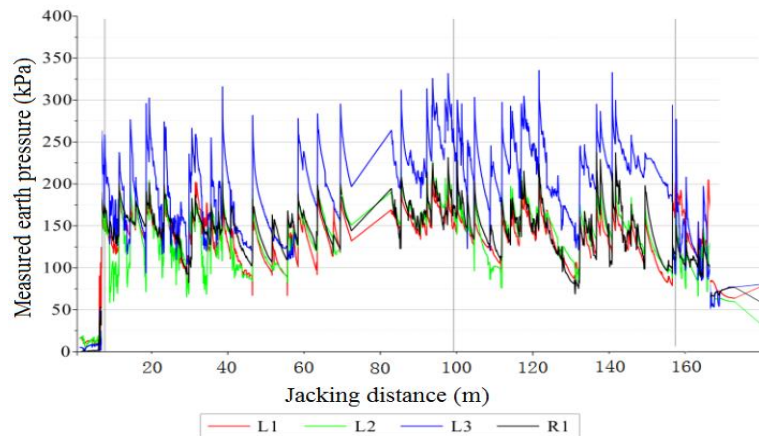*Fig. 2 - Time history curve of pressure change on top of the pipe*

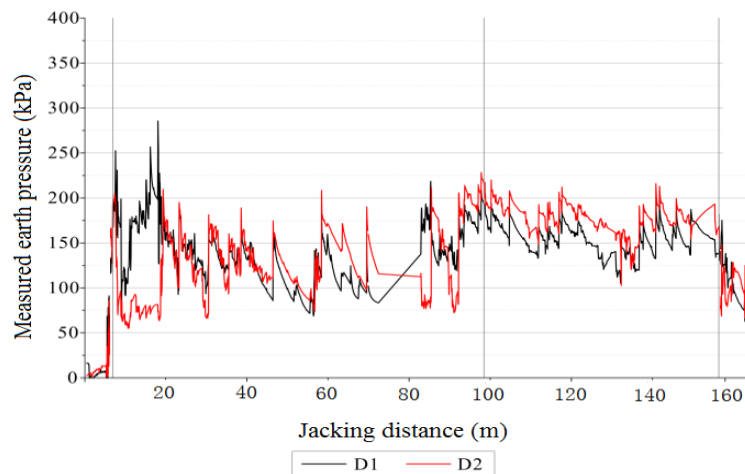*Fig.3 - Time history curve of pressure change on sidewall of the pipe*

Fig.4 - Time history curve of pressure change at the bottom of the pipe

(2)   Starting reinforcement area

Due to the sleeve protection measures adopted in the starting stage, the monitoring data of soil pressure gauge mainly reflects the pressure of the controllable slurry. In this stage, the pressure fluctuation was relatively small and the pressure value was at a relatively low level due to factors such as loose sealing and slurry loss. In order to ensure the stability of excavation surface and control the surrounding settlement, it is necessary to continuously inject controllable slurry in this stage.

(3)   Jacking area with uniform geology

When jacking under uniform geological conditions, the soil pressure on the upper part of pipe section tended to be stable with a relatively consistent attenuation law. During the controllable slurry injection, the soil pressure increased rapidly. After grouting, due to factors such as the overall loss of slurry, the loss of slurry water and the change of slurry performance, the soil pressure detection data decreased slowly. Taking the monitoring values within 5m ~ 65m interval with regular data changes as

----

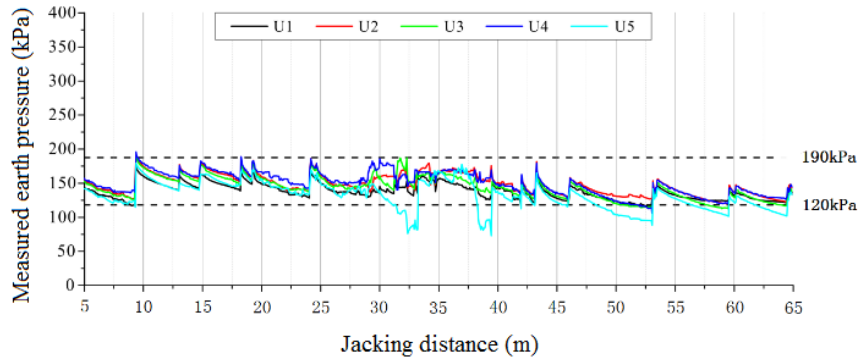an example, the analysis is as follows:

Fig.5 - Time history curve of pressure change on top of the pipe (5m~65m)

The monitoring values of soil pressure at the top of pipe joint are relatively consistent, mainly distributed between 120kPa and 190kPa. The pressure change is mainly affected by controllable slurry construction. The steep rise and fall points of soil pressure value are all at controllable slurry injection points. Through analysis, it is mainly related to the technology of grouting hole opening and pressure boosting grouting, which needs to be paid more attention in the future construction.

The soil pressure values of the upper measuring points are basically the same, and the deviation between soil pressure values of each measuring point is basically maintained between 20kPa and 50kPa, which shows that the controllable slurry performance and the selection of slurry grouting parameters in this stage are relatively reasonable.
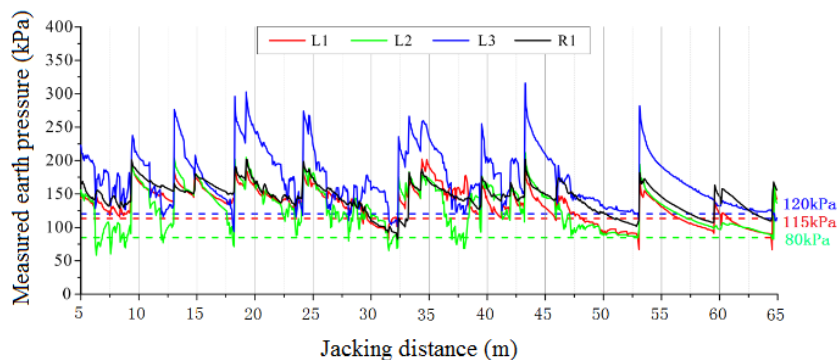

Fig.6 - Time history curve of pressure change on sidewall of the pipe (5m~65m)

The monitoring value of soil pressure on the side of pipe joint is consistent with the monitoring value on the top, but the change of L3 measuring point is more intense, and the influence of controllable slurry injection is obviously greater than other measuring points. The lower limit of the overall soil pressure of L3 measuring point is the highest, 120kPa, and the maximum is 315kPa, significantly higher than other measuring points; the lower limits of L2 and R1 are the lowest, both 80kPa, and the maximum is about 180kPa; the overall pressure of L1 is above 115kPa.
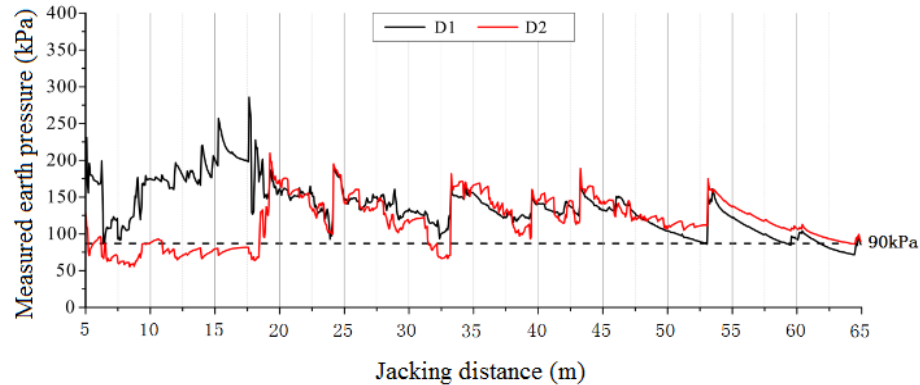

Fig.7 - Time history curve of pressure change at the bottom of the pipe (5m~65m)

The soil pressures of the lower two measuring points are between 5m and 18m, with a large difference, but after 18m, the change trend of two points is very close, which may be due to the large difference in the bottom soil pressure monitoring values caused by the insufficient slurry filling at the initial stage of slurry injection. After jacking more than 18m and three to five times of controllable cement injection, the space between D1 and D2 measuring points is gradually filled, and the pressure values of two points tend to be the same. The lower limit of the overall soil pressure values of the two points is about 90kPa, and the maximum pressure value of D1 measuring point occurs at the position of 18m jacking pipe, which is about 300kPa.

(4)   Water rich soft soil jacking area

The soil pressure value of upper monitoring point is significantly affected by controllable slurry injection, and shows irregular changes with grouting, and the overall lower limit of detection values is about 110kPa. The highest and lowest monitoring values appear at U2 and U5 measuring points respectively, about 310kPa and 45kPa.

Compared with the area with uniform geology, the variation law of the lateral soil pressure and the bottom soil pressure in the saturated soft soils area is consistent to some extent, but the influence of lateral soil pressure value is limited. The maximum value of lateral soil pressure is 330kPa at L3 measuring point and the minimum value is 50kPa at L2 measuring point; the overall lower limits of L1, L2 and L3 measuring points are about 80kPa, 100kPa and 120kPa respectively. The maximum value of bottom soil pressure appears at point D2, which is 230kPa, and the minimum value is also at point D2, which is 45kPa, and the overall lower limit value is about 100kPa.

According to the analysis of monitoring results, the injection of controllable cement for drag reduction has the greatest impact on the upper soil pressure measuring point, followed by the bottom soil pressure, while the side soil pressure of pipe joint is basically not affected. In the process of design and construction, we paid more attention to the most unfavorable working condition and stress state, so the following will focus on the uniform geology jacking area.3

ANALYSIS OF SPATIAL PRESSURE DISTRIBUTION OF PIPE AND SOIL

For rectangular pipe joint, the pipe joint can be simplified as a closed frame structure for calculation. The moment distribution of frame structure is the focus of design and construction work. In the injection of controllable cement for drag reduction, the soil pressure in the upper part of frame

----

structure is the largest, followed by the bottom soil pressure, and the soil pressure at the side is the smallest, which is most unfavourable to the frame structure.

The above-mentioned load form generally appears in the process of controllable slurry injection. According to the above analysis process, the load on the top, side and bottom of pipe joint is simplified now to establish a simplified pipe and soil model for jacking section with uniform geology, which is convenient for further computer modelling and finite element analysis.
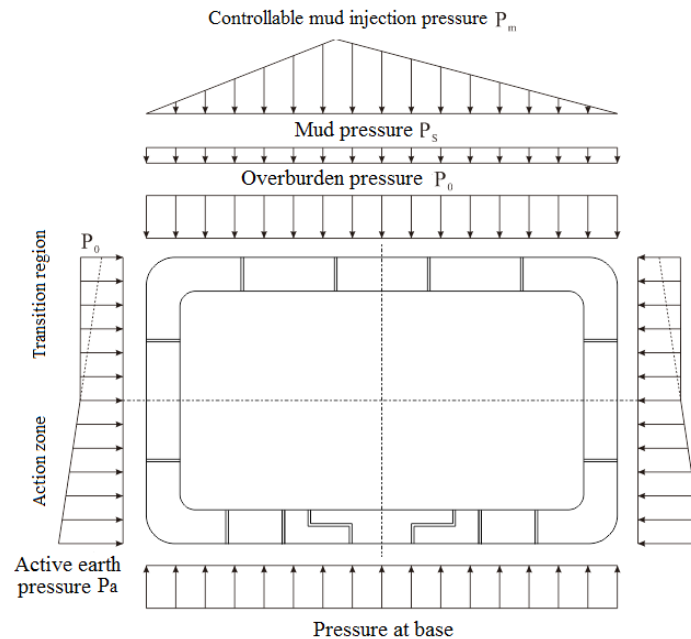

Fig.8 - Pressure model for pipe and soil

The upper soil pressure includes covering soil pressure P_0, slurry pressure P_S and controllable slurry injection pressure P_m, in which the soil pressure P_0 is the soil pressure from the top plate of pipe joint to the ground; slurry pressure P_S is the additional pressure caused by the slurry layer outside the pipe joint, which is assumed to be uniform load; slurry injection has a certain fluidity, which can be assumed to be triangle load, and the maximum value appears at the position corresponding to the pipe joint grouting hole. Here, U3 grouting hole is taken as an example.

The lateral soil pressure is divided into two regions, the upper transition region and the lower active soil pressure region. The upper transition region simplifies the linear change of soil pressure distribution form, the upper part of pipe joint is consistent with the covering soil pressure P_0, and the active soil pressure value of the middle of pipe joint is used. The lower active soil pressure region is from the middle of pipe joint to the bottom, and the active soil pressure in this region is used as Eq.1

$$p_a = [\gamma(Z - Z_w) + \gamma'(Z_w + h)]K_a + \gamma_w(Z_w + h)$$ (1)

Where: γ is the natural gravity of soil, and the saturated gravity when below the groundwater level; γ' is the effective gravity of soil (floating gravity), $\gamma' = \gamma - 10$ (kN/m³), γ_w is the gravity of water, 10kN/m³.

Tab. 1 - Main properties of the soil

Stratum	Stratum name	Stratum thickness	Natural density	Consolidated quick shear	
		h	ρ	C_q	φ_q
		(m)	(g/cm³)	kPa	°
①-5	Plain fill	3.66	1.92	--	--
④	Clay	2	1.99	47.9	15.3
⑤	Silty clay with silt	1.3	1.92	26.7	19
⑥-1	Clayey silt with sand	4.4	1.91	5.6	28.4
⑥-2	Silty sand	4	1.94	3.9	32.9
⑦	Silty clay	5.7	1.93	30	17.4

Put the data in Table 1 into the above formula to calculate the soil pressure value of each point, as shown in Figure 9.
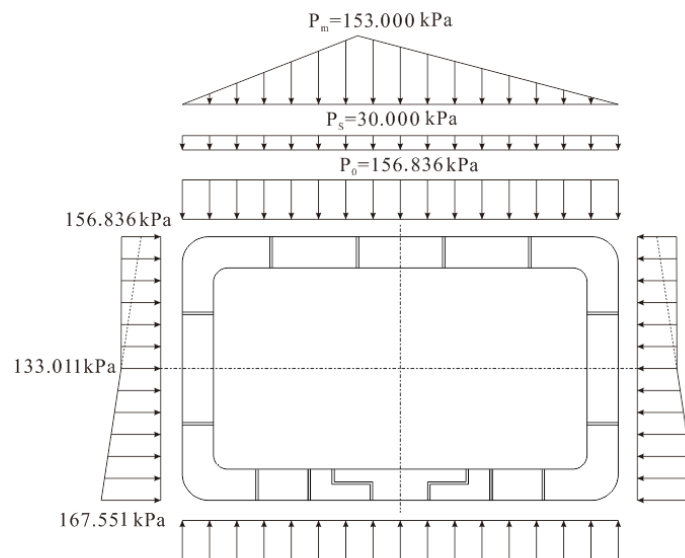

Fig.9 - Distribution hypothesis of the most unfavourable load

In this simplified model, the theoretical values of pressure at each measuring point are compared with the measured values, as shown in Table 2. It can be seen that the relative theoretical value of the model is conservative. At the same time, there is a good correlation between the measured value and the theoretical value, which can be used after appropriate reduction.

Table 2 Comparison between theoretical value and measured value of soil pressure

Location		U1	U2	U3	U4	U5	L1	L2	L3
Soil pressure (kPa)	Theoretical model	228.834	264.365	339.8783	314.643	214.873	149.012	133.034	167.625
	Measured value	188.6	201.8	275.2	239.7	107.2	111.4	78.1	124.7

FINITE ELEMENT SIMULATION

(1)   Internal force distribution modelling and calculation process

① Modelling: When building cell model, quadrilateral cell is selected for soil cell, pipe joint cell and slurry cell.

② Parameter setting: Linear elastic model is adopted for pipe joint, and physical parameters of material refer to C50 concrete parameters; classical Mohr-Coulomb elastic-plastic model with simple calculation is adopted for soil material, and measured parameters of detail geological survey are selected for physical parameters; elastic model is adopted for controllable slurry material, and laboratory test values (density 1200kg/m^3, elastic modulus 1.5m, breaking ratio 0.4) of controllable slurry are selected for material properties

③ Boundary condition: The soil cell limits the displacement in x and y directions.

④ Definition of interaction: For the contact between pipe joint and soil, controllable slurry layer and pipe joint, the tangential characteristic is calculated by penalty function, and the friction coefficient is 0.3. The normal characteristic is simulated by hard contact.

⑤ Divide the cell grid as a whole.

⑥ Loading: Use the concept of cell life and death in ABAQUS to simulate pipe jacking construction.

⑦ Calculate and obtain the corresponding pipe joint and soil stress distribution through post-processing.

When the grouting pressure is set to $0\mathrm{kPa}$, $100\mathrm{kPa}$, 130kPa, 150kPa and 180kPa respectively, the Mises stress nephogram of soil and pipe joint is shown in Fig. 10-14. With the increase of grouting pressure, Mises stress increases gradually, and the same stress distribution trend is shown in three cases. According to the stress nephogram of the soil, the maximum stress appears at the bottom corner of the excavation area, indicating that it is a weak stress area. More attention should be paid in the actual construction, and measures such as squeezing thick slurry can be taken in the dangerous area to improve the bearing capacity of pipe joint to the soil.
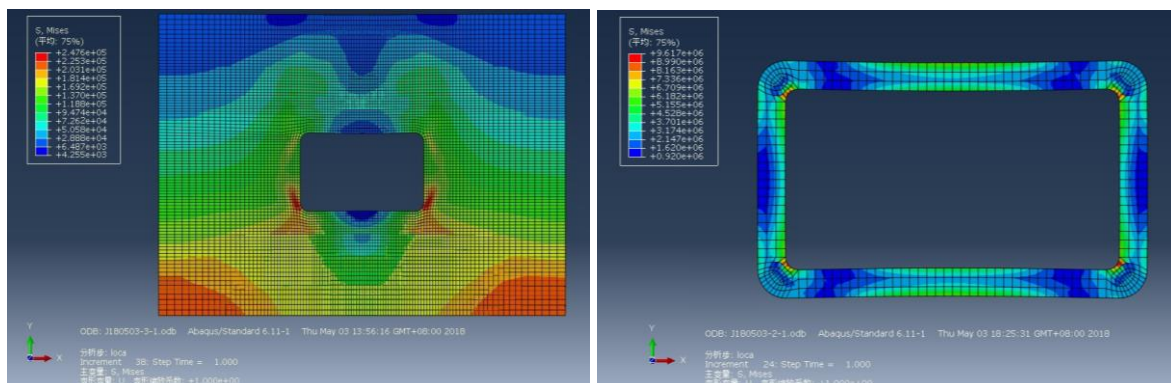

Fig. 10 - Mises stress nephogram of soil and pipe under 0kPa

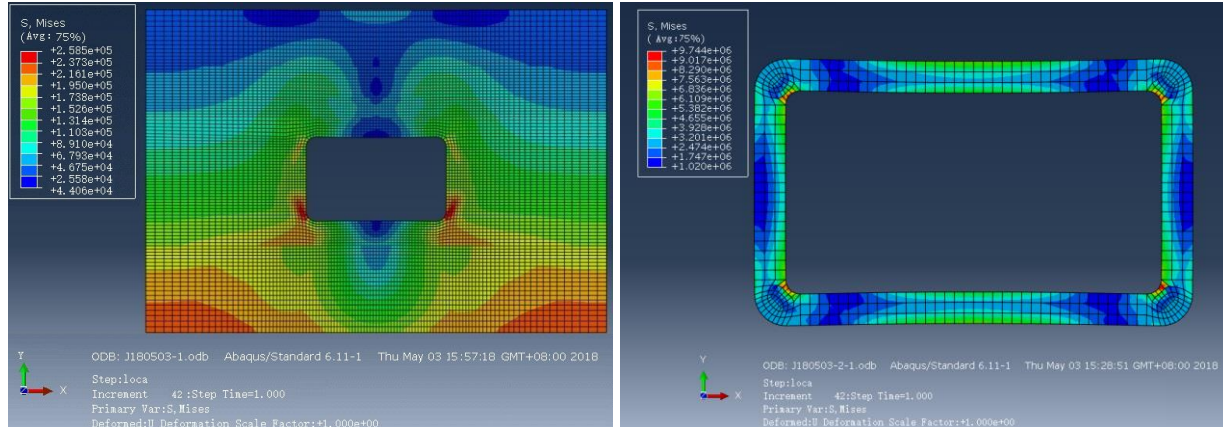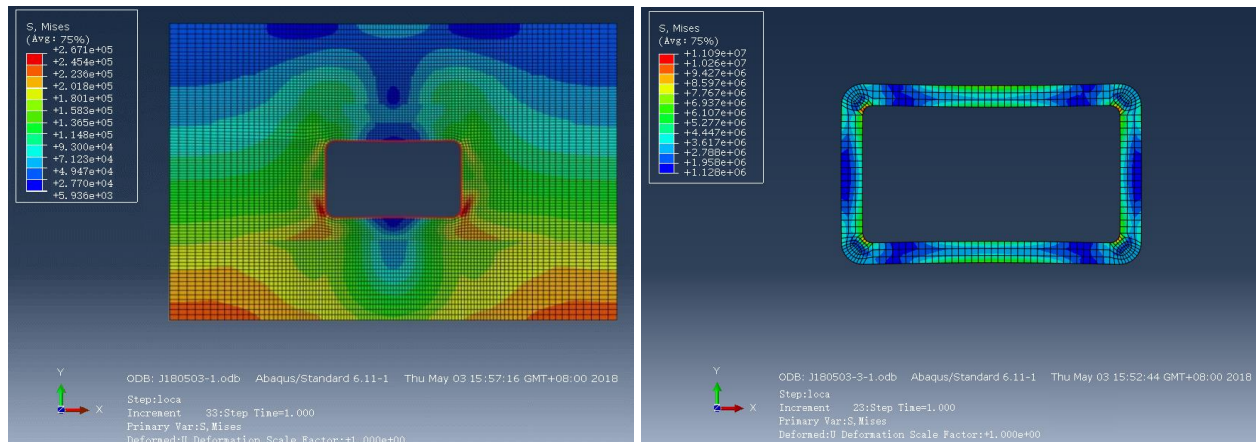

Fig.11 - Mises stress nephogram of soil and pipe under 100kPa

Fig. 12 - Mises stress nephogram of soil and pipe under 130kPa

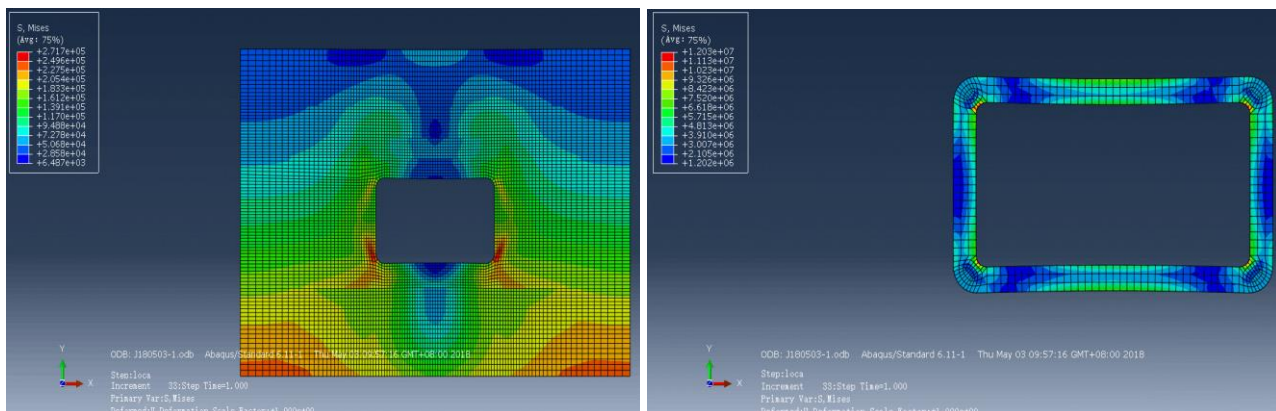*Fig. 13 - Mises stress nephogram of soil and pipe under 150kPa*

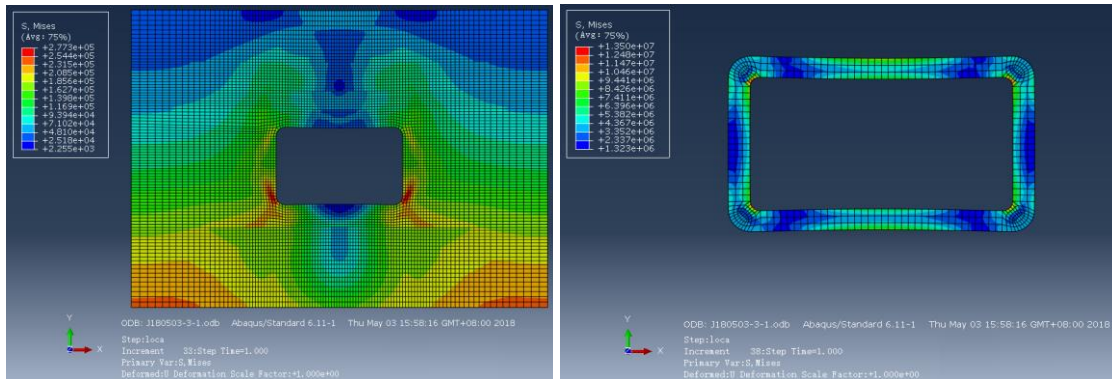

Fig. 14 - Mises stress nephogram of soil and pipe under 180kPa

(2)   Calculation results of pipe joint deformation

Figure 15 ~ Figure 18 show the pipe deformation nephogram during pipe jacking construction under different grouting pressure. It can be seen from the Figures that the soil on the side of pipe joint is highly squeezed, the compression area is basically symmetrical on both sides of the pipe centre, the soil pressure zone is circularly expanded, and the maximum horizontal displacement occurs in the centre of the pipeline. With the increase of grouting pressure, the maximum deformation of pipe joint increases nonlinearly, but the change range is small. The horizontal deformation on both sides of the pipeline indicates that the grouting layer between the pipeline and the soil is also squeezed. At the completion of pipe jacking construction, the soil pressures at the pipe top and the pipe bottom decrease. The decrease of soil pressure at the pipe top is due to the increase of lateral soil pressure under the action of soil arch, and the pipe section loses its original state and slightly deforms under the action of vertical soil pressure. There is a harmonious deformation relationship between the deformed pipe and the squeezed soil.

(3)   Analysis of finite element calculation results

In the process of pipe jacking construction, with the passing of pipe jacking machine head, due to the difference between the outer diameter of segment and machine head, it is difficult to completely recover the initial state of soil by grouting alone and easy to cause soil disturbance and ground settlement spreading from the top of pipeline axis to the ground in a ring. With the construction of pipe jacking, the disturbed soil is consolidated by drainage, and some consolidation settlement is produced until the surface settlement is stable. In a certain range, with the increase of grouting pressure, the maximum settlement of surface soil decreases nonlinearly.
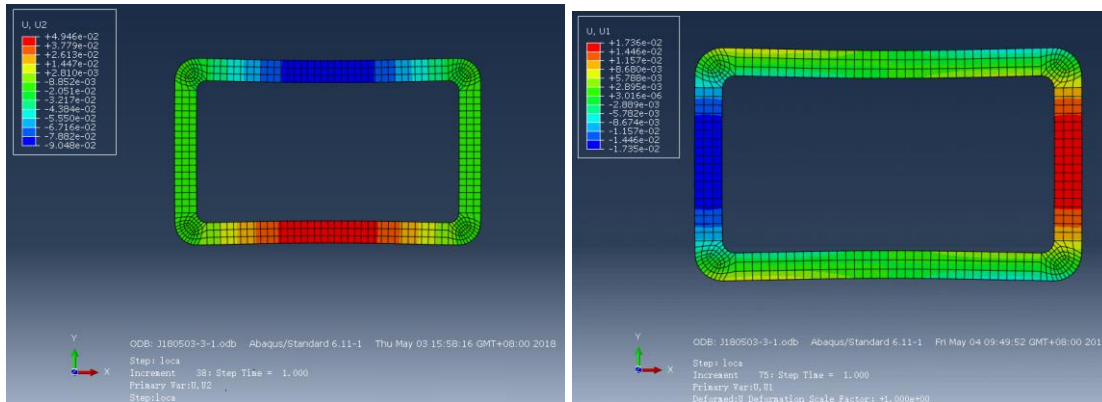
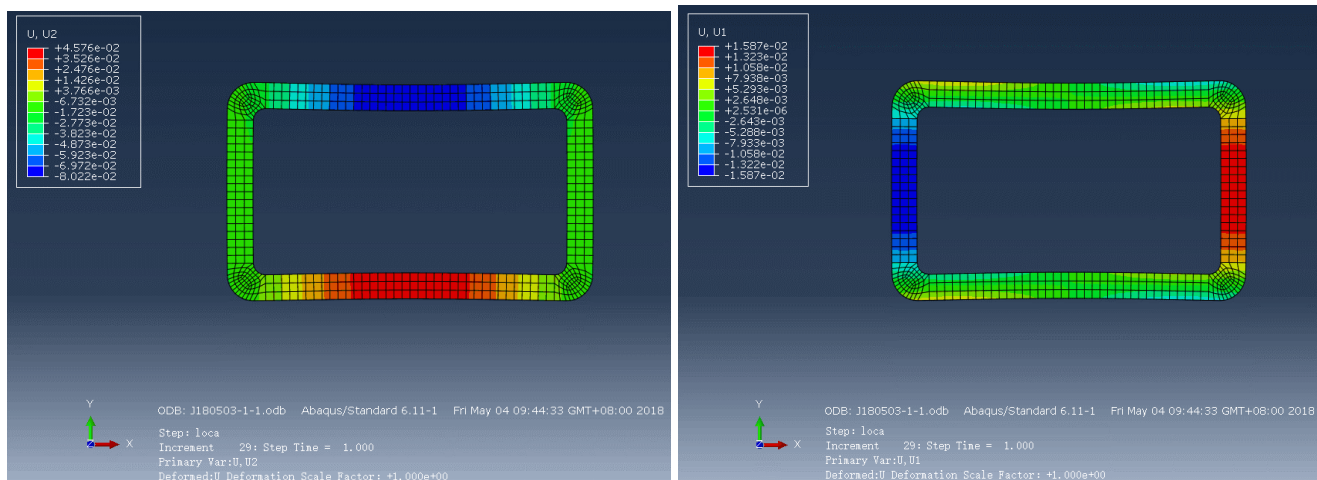*Fig. 15 - Pipe deformation under 100kPa pressure (vertical and horizontal)*

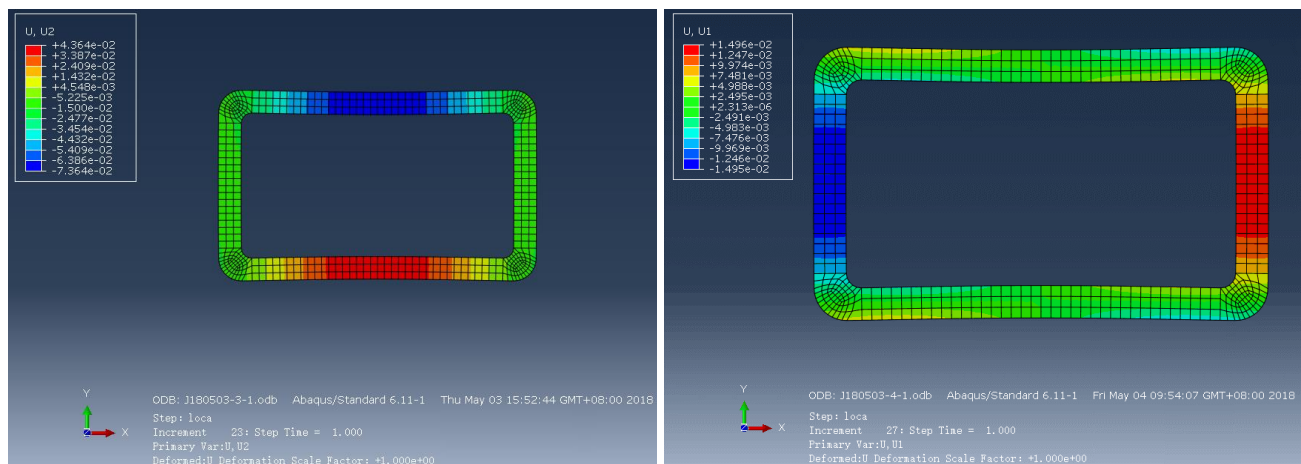*Fig. 16- Pipe deformation under 130kPa pressure (vertical and horizontal)*

Fig. 17 - Pipe deformation under 150kPa pressure (vertical and horizontal)
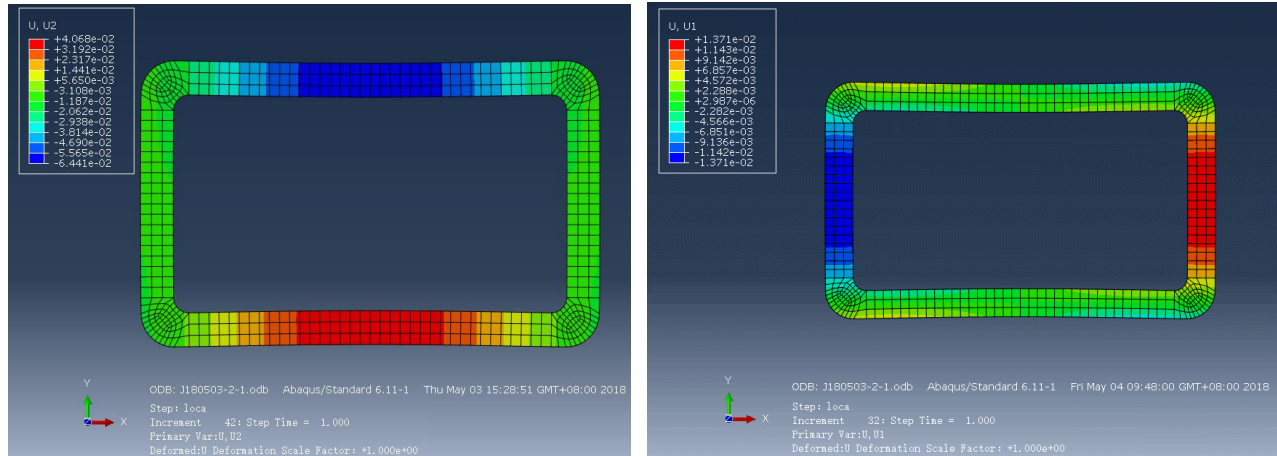

Fig.18 - Pipe deformation under 180kPa pressure (vertical and horizontal)

CONCLUSION

According to the field monitoring results, combined with theoretical analysis and numerical simulation, the variation of soil pressure and the internal force distribution of pipe joint in the construction of rectangular pipe jacking with controllable cement drag reduction technology are studied. The main conclusions are as follows:

(1)   According to the change of soil pressure, the load mode of rectangular pipe jacking can be divided into the starting area, jacking area and receiving area: it tends to be 0 when the soil pressure in the starting area is stable, because the steel sleeve protection measures are adopted; the jacking area with uniform geology is only affected by the fluctuation of grouting pressure; the water rich soft soil jacking area is partially affected by controllable cement injection for drag reduction and slurry jacket, and the maximum pressure is 345.08kPa; and the pressure in the receiving area changes irregularly.

(2)   The distribution and volume of the contact pressure of pipe and soil are significantly affected by grouting. The grouting pressure and volume in the water rich soft soil jacking area are large, which is very easy to build the pressure locally, resulting in the sudden increase of pressure at the adjacent measuring points and the abnormal decrease of pressure at the remote measuring points. Therefore, in the actual construction process, special attention should be paid to the control of grouting pressure and grouting volume, so as to avoid building the pressure and pressure mutation.

(3)   Through numerical modelling and analysis, it is difficult to completely recover the initial state of soil by grouting alone and easy to cause soil disturbance and ground settlement spreading from the top of pipeline axis to the ground in a ring. From the simulation results, it can be found that when the grouting pressure is controlled at 1.1-1.2 times of the covering soil weight, the soil displacement caused by grouting pressure can be controlled at an ideal level.

(4)   The experimental results show that the steel sleeve design can effectively protect the soil pressure gauge when the sensor passes through the reinforcement area of the tunnel portal, which provides a reference for similar engineering measurement.

REFERENCES

[1]   Wen, K. ; Shimada, H. ; Zeng, W. ; Sasaoka, T. ; Qian, D. 2020: Frictional analysis of pipe-slurry-soil interaction and jacking force prediction of rectangular pipe jacking. European Journal of Environmental and Civil Engineering, vol. 24, no. 6, pp. 814–832.

[2]   Md. Tareq Hossain Khondoker; Yaolin Yi; Alireza Bayat. 2016: Comparison of different methods for normal stress calculation during pipe jacking/microtunneling. International Journal of Geotechnical Engineering, vol. 10, no. 4, pp. 366-376.

[3]   Takeru ARIIZUMI; Masahiro YOSHIMOTO. 2000: RESULT AND ANALYSIS ON SITE MEASUREMENT OF LOAD ACTING ON SHIELD TUNNEL (3RD REPORT). Japan Society of Civil Engineers, vol. 10, pp. 275-280.

[4]   Raymond L. Sterling. 2020: Developments and research directions in pipe jacking and microtunneling. JOURNALS: Underground Space, vol. 5, no. 1, pp. 1-19.

[5]   Kazuki Maehara; Takashi Sasaoka; Akihiro Hamanaka; et al. 2019: Effect of Fatty Acids Addition into Backfilling Material in Over-cutting Area on Improvement of Lubrication Performance for Pipe Jacking;;Background:;;Methods:;;Conclusion.The Open Civil Engineering Journal, vol. 13, pp. 281-287.

[6]   Ciaran C. Reilly; Trevor L.L. Orr. 2017: Physical modelling of the effect of lubricants in pipe jacking. Tunnelling and Underground Space Technology incorporating Trenchless Technology Research, vol. 63, pp. 44-53.

[7]   K. Górski; R. L. Ignatowicz. 2016: EFFORT OF STEEL PIPE JACKING IN TERMS OF IMPERFECTION PIPES AND HETEROGENEITY OF GROUND. Nauka ta Progres Transportu, vol. 63, no. 3, pp. 171-180.

[8]   Mashimo H; Ishimura T. 2003: Evaluation of the load on shield tunnel lining in gravel. JOURNALS: Tunnelling and Underground Space Technology incorporating Trenchless Technology Research, vol. 18, no. 2-3, pp.171-180.

[9]   Sun Y; Wu F; Sun W; et al. 2019: Two Underground Pedestrian Passages Using Pipe Jacking: Case Study. Journal of Geotechnical & Geoenvironmental Engineering, vol. 145, no. 2.

[10]   Xinbo Ji; Wen Zhao; Pengpeng Ni; et al. 2019: A method to estimate the jacking force for pipe jacking in sandy soils. Tunnelling and Underground Space Technology incorporating Trenchless Technology Research, vol. 90, pp. 119-130.

[11]   Jianfeng Wang; Kang Wang; Tao Zhang; Shuai Wang. 2018: Key aspects of a DN4000 steel pipe jacking project in China: A case study of a water pipeline in the Shanghai Huangpu River. Tunnelling and Underground Space Technology incorporating Trenchless Technology Research, vol. 72, pp. 323-332.

[12]   Yonghui Zhao; Jiansheng Wu; Xiongyao Xie; Kunwei Feng; Chenchao Zeng. 2016: Ground- penetrating radar measurement of the distribution of thixotropic slurry behind large- diameter segments in long- distance pipe- jacking construction. Near Surface Geophysics, vol. 14, no. 2, pp.171-181.

[13]   J. Yen; K. Shou. 2015: Numerical simulation for the estimation the jacking force of pipe jacking. Tunnelling and Underground Space Technology incorporating Trenchless Technology Research, vol. 49, pp.218-229.

[14]   Liang Zhen; Jin-Jian Chen; Pizhong Qiao; Jian-Hua Wang. 2014: Analysis and remedial treatment of a steel pipe-jacking accident in complex underground environment. Engineering Structures, vol. 59, pp.210-219.

[15]   A.-L Pellet-Beaucour; R Kastner. 2002: Experimental and analytical study of friction forces during microtunneling operations.Tunnelling and Underground Space Technology incorporating Trenchless Technology Research, vol. 17, no. 1, pp.83-97.

RESEARCH ON MODELING AND OPTIMIZATION PROGRAM OF LONG-SPAN HYBRID GRID HANGAR BASED ON LEVERAGE PRINCIPLE

Wenbo Zhang[1], Deyou Wang[2] and Guangshun Shi[3]

1. *Beijing Municipal Engineering Consulting Corporation, Beijing, China; WenboZhang@shu.edu.cn*
2. *China Airport Planning & Design Institute Co., Ltd., Beijing, China; 2017081005@cauc.edu.cn*
3. *Shandong Provincial Architecture Design & Research Institute Co., Ltd., Shandong, China; 823704589@qq.com*

ABSTRACT

A long-span hybrid grid hangar structure and a modeling method for the long-span hybrid grid hangar structure based on the principle of leverage are proposed in this paper. Based on the SAP2000 spatial structure design software, the C# language was used to develop a plug-in to automatically create a long-span hybrid grid structure based on the principle of leverage, which realized the automatic generation by inputting parameters such as the span of the hangar structure, the number of horizontal grids, and the number of vertical grids. The optimization design method of the long-span hybrid grid structure based on particle swarm algorithm is proposed. SAP2000 software is used and the *C#* language is used to develop the optimization design program of the long-span hybrid grid structure based on the principle of leverage. The optimization design is carried out, and the optimization results show that the program can reduce the thickness of the roof and reduce the vertical displacement at the opening of the hangar roof on the basis of meeting the current specifications.

KEYWORDS

Hangar structure, Leverage, SAP2000, Optimization design

INTRODUCTION

As China continues to develop into a strong civil aviation country, more and more long aircraft are put into use [1-2]. The maintenance and storage requirements of long aircraft make the design of hangar continuously improve the requirements for span and net height. The hangar is located near the airport and the design elevation of the hangar roof structure is limited by the airport net requirements, so the hangar needs to leave as much net height as possible to meet the maintenance needs. Therefore, this requires the thickness of the hangar roof structure to be as small as possible [3]. To meet the entry and exit requirements of long aircraft, the opening side of the hangar cannot be equipped with a column, so the roof structure of the hangar has only three

----

sides support. Thus, the roof structure of the hangar should have greater rigidity, so that the vertical displacement on the side of the opening meets the requirements of the design specifications. In recent years, the space structure has developed rapidly, and various grid structures, tensile structures, and thin shell structures have been widely used in long-span structural engineering. As a result, a series of special design requirements have been developed for the hangar roof. When the long-span hangar adopts a typical spatial structure, a special design is required on the side of the door to meet the specification requirements [4]. However, such a design often affects the net height of the hangar. At the same time, as the span of the hangar increases, the design difficulty is also increasing [5]. Therefore, in order to adapt to the current long aircraft size, storage requirements and the particularity of the long opening structure, this paper puts forward a new form of aircraft hangar with better structural safety, economy and technical effect, which is of great significance to the development of civil aviation in our country. The parametric modelling of long-span hybrid grid hangar structure based on lever principle is a complex process. The grid structure is composed of joints and members, and the number of model components is usually huge. Even small-scale grid projects contain hundreds of grid joints and members [6]. The size of the joints and the type of the members in the actual project are not regular, so it is almost difficult to complete by conventional manual modelling. In the structural calculation software of space grid, the space grid model is generated automatically. Similarly, the plug-in for automatic creation of space grid can be written on SAP2000 by means of secondary development.

At present, current space grid structure design software can realize the optimization of the member section of the grid structure, but there is no mature technical support for the optimization method of the grid thickness. Only the specifications and the recommended values provided by the grid design manual [7]. For safety considerations, designers need to establish multiple groups of croupalculation models and adjust parameters to optimize design. In the whole optimization design process, some outstanding problems will inevitably appear, such as complex calculations, low work efficiency, and waste of time. Especially for the hangar structure, it is necessary to provide as much internal space as possible for the aircraft in addition to meeting the net requirements of the airport building [8]. Thus, we must optimize the design, while meeting the normal use requirements, the hangar roof structure should be as thin as possible, and the vertical displacement of the hangar structure with long opening should be as small as possible.

GEOMETRICAL CONSTRUCTION OF THE STRUCTURE

The long-span hangar structure has its particularity, which must require the boundary conditions of three sides to support and the other side to be free. In order to facilitate the freedom of aircraft entry and exit, only one column can be set at the opening, as shown in Figure 1. Due to the particularity of the hangar structure, if the opening is not specially treated, it will have greater vertical displacement, as shown in Figure 2. Therefore, reducing the vertical displacement on the side of the opening to meet the design specifications is the key to the design of the hangar roof structure.
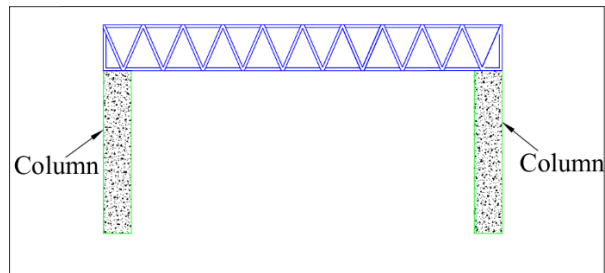

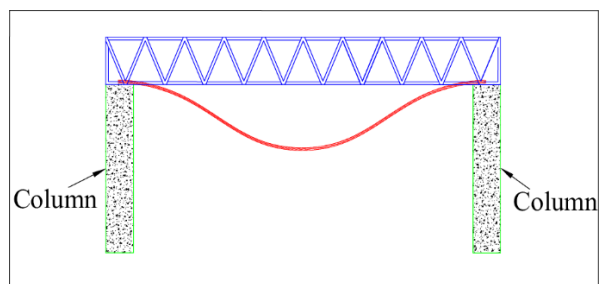*Fig. 1 – Elevation of the hangar*

Fig. 2 – Elevation of the hangar without special treatment

In order to solve the problem of vertical displacement at the opening of the hangar, considering the balance condition, the lever principle is applied to the long-span hangar structure. Move the hangar structure support inward and adopt the support as the fulcrum of the lever. After that, set cables at the left and right cantilever ends to anchor the cables vertically to the ground. As shown in Figure 3, the connection between the column and the upper grid serves as a fulcrum, and the left and right sides are equivalent to two levers. The levers can improve the bearing capacity of the hangar roof to ensure the stability and safety of the hangar structure.
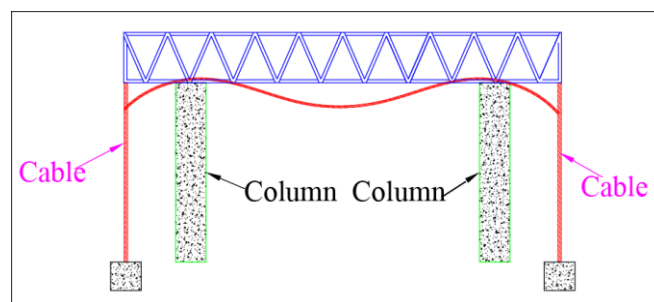

Fig. 3 – Elevation of the hangar based on the principle of leverage

Based on the above ideas, 3D3S space structure design software is used to establish a geometric model of a long-span hybrid grid hangar based on the principle of leverage, as shown in Figure 4.
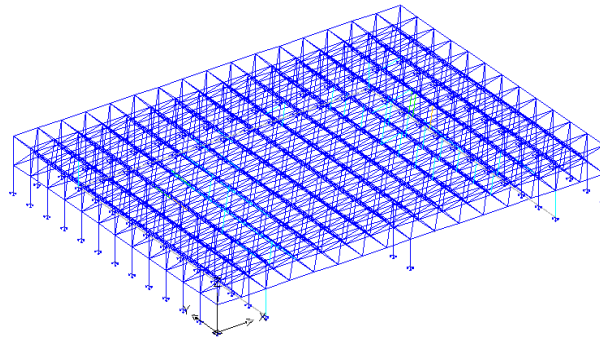

Fig. 4 – Hangar model based on the principle of leverage

STRUCTURAL MODELING PROGRAM

In this paper, the internal call method is used to write the SAP app plug-in and run it in the menu bar of SAP2000 [9-10]. The plug-in development environment uses C# VS2013, .NetFramework4.5, builds a class library project [11-12]. And add a reference to SAP2000.exe, and puts the compiled plug-in into the menu bar of SAP2000 V20 to run. The plug-in interface written in this article is shown in Figure 5.
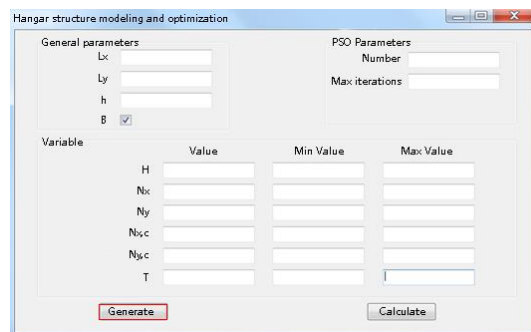

Fig. 5 – Development interface of structural modeling program

Parametric modelling process

First, the key parameters are inputted, and modelling parameters are mainly divided into general attribute parameters and grid variable parameters. In this paper, the large-span hangar spans from the centre to the left and right column as area 2 the general parameters include grid length, width, column top height h and whether the edge is cabled or not B. The grid variable parameters include grid height H, x-direction grid number, y-direction grid number, x-direction column distance to the edge position $N_{x,c}$, y-direction column distance to the edge position $N_{y,c}$, cable cooling T (simulated cable force), and the variation norm of each parameter.

The SAP2000 model generated after the input parameters is initialized, and the inverted triangular cone is selected as the basic unit of the space grid. The hangar roof adopts steel circular hollow sections, and four kinds of steel circular hollow sections of the upper, middle, lower and oblique web of the space grid are defined. The upper chord joints, the middle chord joints and the lower chord joints of the grid are established in turn, the column joints and the cable joints are

----

established, and the names of the joints are recorded respectively. Finally, the grid element model is established according to the parameters and joints, and the upper chord, middle chord, lower chord, web, column and vertical cable are established according to the grid joints.

Constraints are imposed on the hangar model generated above, and constraints are imposed on the bottom of the column and the bottom of the vertical cable to ensure that the cable and column maintain a rigid connection with the ground. Increase load conditions such as constant load, live load, temperature, etc., apply the above-mentioned load conversion joint load to the corresponding joint, use the cooling method to apply prestress to the cable, and consider increasing the limit state of normal use.

```
Sap.eCNameType tempeCNameType = Sap.eCNameType.LoadCase;
//combination
ret = SapModel.RespCombo.Add("COMB1", 1);

ret = SapModel.RespCombo.SetCaseList("COMB1", ref tempeCNameType, "dead1", 1.0);

ret = SapModel.RespCombo.SetCaseList("COMB1", ref tempeCNameType, "live2", 1.0);

ret = SapModel.RespCombo.SetCaseList("COMB1", ref tempeCNameType, "temp3", 1.0);

}
```

Example

This section uses the long-span hybrid grid hangar program plug-in developed above based on the lever principle to call the SAP2000 spatial structure design software to establish a long-span hybrid grid hangar model based on the lever principle. The input modeling parameters as shown in Table 1.

Tab. 1 - Parameters of Hangar Model

Parameter name	Parameter value
x/m	120
y/m	60
h/m	20
Grid height /m	5
N_x	40
N_y	20
$N_{x,c}$	4
$N_{y,c}$	2
T/°C	-30

Input the parameters in Table 1 into the parameter input dialog box of Figure 5 for parametric modeling of the hangar. Click [Generate], the compiled plug-in sapAPP can call the SAP2000 spatial structure design software to automatically generate the hangar mode. The hangar model initialization is shown in Figure 6, and the generated hangar model is shown in Figure 7.
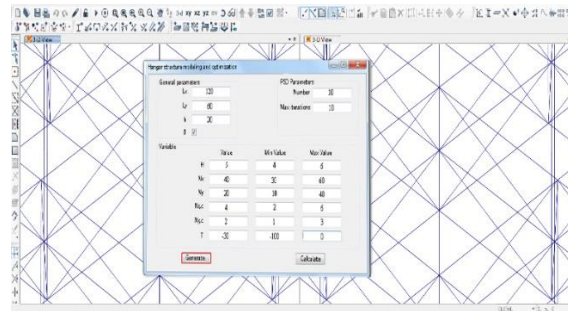
Fig. 6 – Hangar model initialization interface
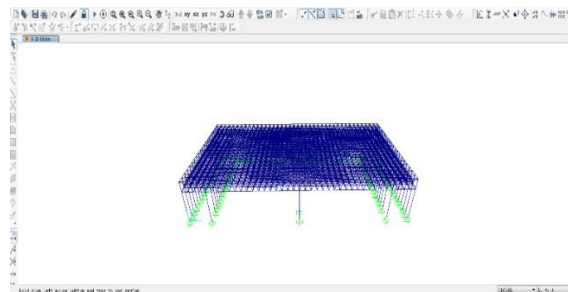
Fig. 7 – Automatic generation of hangar model

OPTIMIZATION DESIGN OF HANGAR STRUCTURE BASED ON PARTICLE SWARM OPTIMIZATION

Establishment of optimization model

Before optimizing the long-span hybrid grid hangar structure based on lever principle, it is necessary to determine the optimization model parameters, constraint conditions and objective function.

Given the length, width, height, material, section and other key parameters of the grid, the optimization model is as follows:

$$H = f\left(N_x, N_y, N_{x,c}, N_{y,c}, B, T\right) \tag{1}$$

$$U_{z1} \leq \frac{L_1}{250} \tag{2}$$

$$U_{z2} \leq \frac{L_2}{125} \tag{3}$$

$$N_x \in (10,50) \tag{4}$$

$$N_y \in (10,50) \tag{5}$$

$$N_{x,c} \in (1,10) \tag{6}$$

$$N_{y,c} \in (1,10) \tag{7}$$

$$B \in (0,1) \tag{8}$$

$$T \in (-100,0) \tag{9}$$

H—Grid thickness；

N_x—Number of grids in x direction；

N_y—Number of grids in y direction；

$N_{x,c}$—The number of grid from the edge of the column in the x direction ；

$N_{y,c}$—The number of grid from the edge of the column in the y direction ；

B—Prestressed cable；

T—Cable cooling temperature；

U_{z1}—Vertical displacement of area 1；

L_1— Area 1 span；

U_{z2}—Vertical displacement of area 2；

L_2—Area 2 span;

The objective function of the particle swarm is obtained by parametric modeling and calculation of the SAP2000 model. Under the premise of ensuring the minimum deflection of the hangar roof, the minimum thickness of the grid roof is the goal, that is, the multi-objective function is as follows:

$$Y\left(h_{\min}, U_{z1\min}, U_{z2\min}\right) = h + \frac{U_{z1}}{L_1} + \frac{U_{z2}}{L_2} \tag{10}$$

The particle in this paper refers to the key parameters of the grid, and the corresponding target value of the particle is the target value in the above optimization model.

Optimization design program development

This program is written by Microsoft Visual Studio 2013 software C # language [13-14]. According to the above parametric modeling, particle swarm optimization algorithm [15] is used to optimize the structure of long-span hybrid grid hangar. The interface of the hangar structure optimization software is shown in Figure 5. The optimization program includes 6 main modules: input the key parameters of the particle swarm, initialize the particle swarm, iterate the particle swarm, update the particle swarm, end the iteration, and output the result.

The first module inputs the key parameters of the particle swarm. The key parameters of the program are the key parameters of the grid and the number of particles, the maximum number of iterations and so on. In the PSO algorithm, the learning factors c_1 and c_2 determine the experience of the particle itself and the group. Setting smaller or longer c_1 and c_2 is not conducive to the search of particles. This section sets the learning factor $c_1=c_2=0.9$. In this paper, the long-span hybrid grid hangar structure based on the lever principle will be used to search for area 1 and 2 locally using the particle swarm algorithm, so the inertia weight w is set to 0.2.

```
public class cLiZiParam

    {

        // Whether to calculate multiple times Calculate parameters every time

        public int N = 10;// Number of particles

        public int maxIteration = 10;// Maximum iterations times

        public int keepNum = 5;// If no better solution is found for num times, exit

        // No assignment required for calculation

        public double c1 = 0.9;// c1

        public double c2 = 0.9;// c2

        public double w_max = 0.2;//w

        public double w_min = 0.2;//w
```

The second module randomly initializes each particle according to the key parameters. The particles can be initialized randomly by inputting the key parameters of grid modeling, the number of particles and the number of iterations. The third module, particle swarm iteration, is iteratively calculated by the particle swarm method to calculate the fitness value of each particle. If the fitness value is better than the current individual extreme value of the particle, set P_i to the position of the particle and update the individual extreme value in time. If the optimal particle in the individual extreme value of all particles is better than the global extreme value searched at present, the position of the particle is set to P_g ,and enter the global extreme value and sequence number update of the fourth module. The fourth module updates the particle swarm, checks the range of all parameters, and updates the speed and position of each particle. At the end of the iteration of the fifth module, check whether it meets the end basis. The sixth module outputs the results and all the parameter values of the global optimal solution. The results can also be extracted from the result.txt file under the working path, and the roof thickness and the minimum displacement of hangar roof area 1, that is, zone 1 deflection, can be extracted from the hangar optimization results.

```
    void show_Result()
        {
            string message = " Result:";
            progressBarGo.show(message);
            message = "Optimal solution：" + pg.obj.ToString("0.0000");
            progressBarGo.show(message);
            message = "H：" + pg.mHz.ToString("0.0000");
            progressBarGo.show(message);
            message = "Nx：" + pg.mGridNum_x.ToString();
            progressBarGo.show(message);
```

```
        message = "Ny：" + pg.mGridNum_y.ToString();
        progressBarGo.show(message);
        message = "Nx,c：" + pg.mSupportPosIth_x.ToString();
        progressBarGo.show(message);
        message = "Ny,c：" + pg.mSupportPosIth_y.ToString();
        progressBarGo.show(message);
        message = "T：" + pg.mTemperature.ToString("0.0000");
        progressBarGo.show(message);
        message = "Umin1：" + pg.minDis_1.ToString("0.0000");
        progressBarGo.show(message);
        message = "Umax1：" + pg.maxDis_1.ToString("0.0000");
        progressBarGo.show(message);
        message = "Umin2：" + pg.minDis_2.ToString("0.0000");
        progressBarGo.show(message);
        message = "Umax2：" + pg.maxDis_2.ToString("0.0000");
        progressBarGo.show(message);
    }
    #endregion
    }
}
```

The extraction interface is shown in Figure 8. Repeating the above 6 modules can realize the optimization design analysis of the long-span hybrid grid hangar structure based on the particle swarm optimization algorithm.
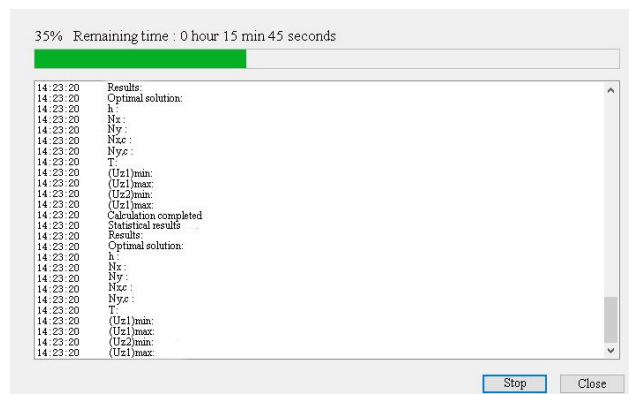

Fig. 8 – Calculation result extraction interface

The optimization program comprehensively considers the displacement of the hangar roof, the number of horizontal and longitudinal grids, the location of hangar supports, the setting of

----

vertical cables and the simulation of cable force by cooling method, which ensures the safety and economy of the optimized long-span hangar structure.

Example

The initial thickness of the grid is 5m, and the height of the column is 15m. The grid number in x direction is 40, the grid number in y direction is 20, the temperature drop of vertical cable is-30 °C, the grid number of column in x direction is 4, and the grid number of column in y direction is 2. The number of particles is set to 10, and the maximum number of iterations is set to 20 times. Taking the above basic parameters as the initial parameters of the model, the hangar structure optimization design program developed in this paper is used to optimize the automatically generated hangar structure.

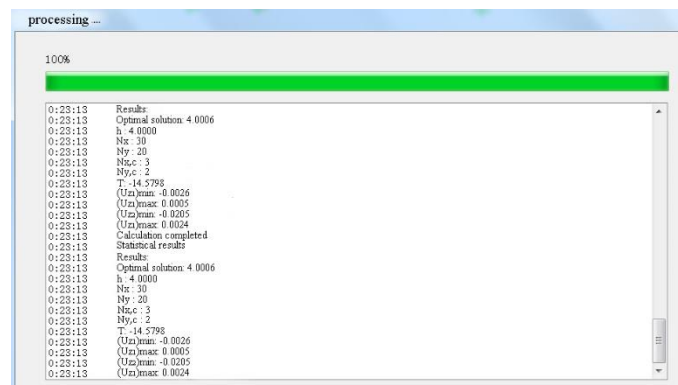The optimization result is shown in Figure 9.

Fig. 9 – Optimized the hangar structure

Sort out the results of the progress bar display in the process of optimization as shown in Table 2.

Tab. 2 - Optimization results

Iterations	1	2	3	4	5	6	7	8	9	10
H/m	4.57	4.42	4.41	4.39	4.35	4.29	4.14	4.10	4.02	4.00
U_{z1}/mm	6.70	5.60	5.30	5.10	4.60	4.50	4.50	3.40	3.10	2.60
U_{z2}/mm	13.8	17.5	18.4	18.03	19.30	19.60	20.40.	20.40	20.50	20.50
N_x	36	34	32	32	32	32	32	30	30	30
N_y	24	26	22	20	20	19	19	20	20	20
$N_{x,c}$	3	3	3	3	3	3	3	3	3	3
$N_{y,c}$	2	2	2	2	2	2	2	2	2	2
T /℃	-40.58	-36.25	-31.54	-28.47	-26.55	-26.31	-26.31	-24.14	-20.82	-20.82
Iterations	11	12	13	14	15	16	17	18	19	20
H/m	4.00	4.00	4.00	4.00	4.00	4.00	4.00	4.00	4.00	4.00
U_{z1}/mm	2.60	2.60	2.60	2.60	2.60	2.60	2.60	2.60	2.60	2.60
U_{z2}/mm	20.50	20.50	20.50	20.50	20.50	20.50	20.50	20.50	20.50	20.50
N_x	30	30	30	30	30	30	30	30	30	30
N_y	20	20	20	20	20	20	20	20	20	20
$N_{x,c}$	3	3	3	3	3	3	3	3	3	3
$N_{y,c}$	2	2	2	2	2	2	2	2	2	2
T /℃	-14.98	-14.98	-14.98	-14.98	-14.98	-14.98	-14.98	-14.98	-14.98	-14.98

The optimization design of the hangar roof in this paper is to meet the normal use requirements of the hangar, while the hangar roof structure should be as thin as possible, and the vertical displacement of the long opening of the hangar structure should be as small as possible. The thickness of the cover and the vertical displacement of area 1 of the hangar roof are the two most critical optimization indicators. According to the data obtained from the optimization results in Table 2, the variation curve is drawn with the number of iterations as the Abscissa and the roof thickness as the vertical coordinate as shown in Figure 10. The variation curve is drawn with the

----

vertical displacement of the hangar roof structure area 1 and area 2 as the vertical coordinate as shown in Figure 11.
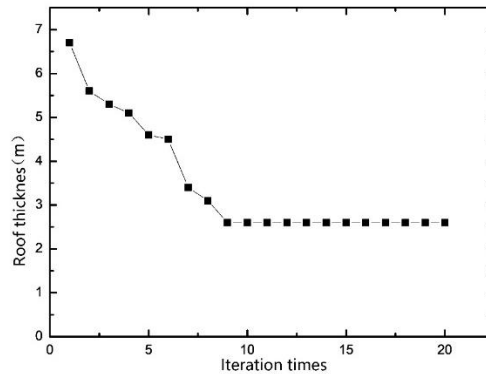

Fig. 10 – The relationship between the roof thickness and iteration times
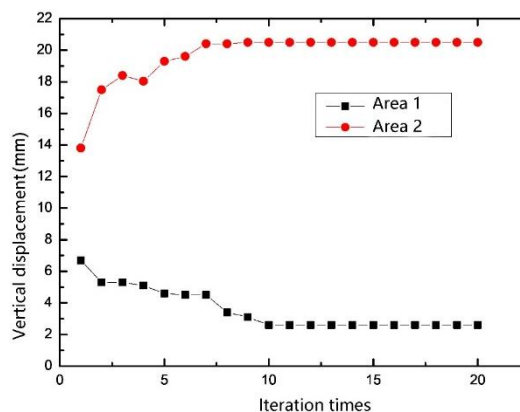

Fig. 11 – The relationship between the vertical displacement and the iteration times

It can be seen from Figures 10 and 11, that as the optimization program iteratively progresses, the hangar roof is gradually reduced, and the optimized target value is adjusted accordingly. With the optimization process of hangar roof area 1, the vertical displacement in the middle span of hangar roof is getting smaller and smaller. The results show that the developed program achieves the purpose of hangar structure optimization design. On the basis of the requirements of the current code, the thickness of the roof and the vertical displacement at the opening of the hangar roof are reduced in this program. The amount of steel used in the grid structure are reduced and the design efficiency are improved.

CONCLUSION

(1)   This paper proposes a long-span hybrid grid hangar structure based on the principle of leverage and proposes a modeling method for the long-span hybrid grid hangar structure based on the principle of leverage. This structure can better solve the current problem of vertical displacement at the opening of the hangar.

----

(2)   Based on the SAP2000 spatial structure design software, the C# language was used to develop a plug-in to automatically create hangar structure, which realized the automatic generation by inputting parameters such as the span of the hangar structure, the number of horizontal grids, and the number of vertical grids.

(3)   The optimization design method of the long-span hybrid grid structure based on particle swarm algorithm is proposed. SAP2000 software and the C# language are used to develop the optimization design program of the hangar structure. The optimization design is carried out, and the optimization results show that the program can reduce roof thickness and the vertical displacement at the opening of the hangar roof.

(4)   In this paper, the optimization program is analyzed and verified by a calculation example. The change of roof thickness and roof displacement with the number of iterations are analyzed separately. The optimization method can have a certain guiding impact for the optimization design of the future long-span space structure hangar.

REFERENCES

[1]   Lang F, 2005. Research on the selection and design of long-span aircraft maintenance warehouse [Master's thesis]. Beijing: Beijing University of Technology.
[2]   Wei X, Ma F, Li G, 2017. Research progress on the selection of aviation-type long-span maintenance hangar structure and its anti-seismic and shock-resistant performance. Journal of Ssmological Research, vol. 40:75-81.
[3]   Liu X, 1996. The development of China's grid structure in the past ten years. In: Proceedings of the 6th Space Structure Academic Conference.
[4]   Hao Y, et al., 2019. Construction technology of long-span complex space composite structure in Beijing Daxing International Airport hangar. Construction Technology, vol. 48: 115-119.
[5]   Zhu D, 2008. Research on the long-span structure design of Beijing A380 hangar. China Civil Engineering Journal, vol. 2: 10-17.
[6]   Wang X, Lu H. The development of ANSYS parametric design and optimization design program for space grid. In: Fifth National Symposium on Modern Structural Engineering.
[7]   Wang Q. Research on the overall stability of the three-story oblique quadrangular pyramid grid structure of the long-span maintenance hangar [Master's thesis]. Jinan: Jinan University.
[8]   Qin Y, 2020. A two-stage optimization approach for aircraft hangar maintenance planning and staff assignment problems under MRO outsourcing mode. Computers & Industrial Engineering, 106607.
[9]   Qiu Y, 2011. SAP2000 API and .NET technology in the rapid modeling of reticulated shell. Guangdong Civil Engineering and Architecture, vol. 1: 28-31.
[10]   Tayfur B, Can Ö, 2018. Farklı yüksekliğe sahip boşluklu perde duvarlara ait davranış eğrilerinin SAP2000 OAPI ile elde edilmesi. Akademik Platform Mühendislik ve Fen Bilimleri Dergisi, vol. 6: 84-91.
[11]   Zhou J, Lin L, Zhang J, 2013. Application of SAP2000 API and .NET technology in rapid equipment foundation modeling. Building Structure, vol. S1: 846-849.
[12]   Chen QJ, et al., 2014. Application of SAP2000 API and. NET framework for reliability assessment of RC structures. Appl Mech Mater, vol. 578: 1482-1488.
[13]   Sotiropoulos S, Lagaros ND, 2020. Topology Optimization of Framed Structures using SAP2000. Procedia Manufacturing, vol. 44: 68-75.
[14]   Lagaros ND, Vasileiou N, Kazakis G, 2019. AC# code for solving 3D topology optimization problems using SAP2000. Optimization and Engineering, vol. 20: 1-35.
[15]   Leung A, Zhang H, 2009. Particle swarm optimization of tuned mass dampers. Engineering Structures, vol. 31: 715-728

THE BOND STRENGTH OF STEEL BAR BASE ON RIB GEOMETRY BAR IN PULLOUT TEST

Anis Rosyidah[1,2], Johannes Adhijoso Tjondro[2] and I Ketut Sucita[1]

1. *Politeknik Negeri Jakarta, Department of Civil Engineering, Jl. Prof. GA. Siwabessy Kampus UI Depok,16425, Indonesia; anis.rosyidah@sipil.pnj.ac.id; i.ketutsucita@sipil.pnj.ac.id*
2. *Universitas Katolik Parahyangan Bandung, Department of Civil Engineering, Jl. Ciumbuleuit No.94, Bandung, 40141, Indonesia; jatjondro@yahoo.com*

ABSTRACT

This experiment's objective is to prove that the reinforcing rib's form contributes to its bond strength. The specimen is the concrete cubes measuring 150 × 150 × 150 mm; bar installed in the center of the concrete cube. Bars use 13, 16, and 19 mm diameters. For comparison, the experiment was also carried out on plain reinforcement diameter with 12 mm, 16 mm, and 19 mm. Concrete compression is fc' 34 MPa. The pullout test was also performed to increase the load in stages at a 200 kg/minute speed. Loading stopped if the reinforcement yielded, split concrete, or slipped bar. The experiment uses ASTM standards ASTM C234-91a. The study results are the bond strength on reinforcement with the surrounding concrete. Bond strength in the plain bar is lower than deformed. The reinforcement of steep rib compared to fishbone bond strength values incline to be the same. The ratio of the bond strength of plain compared to deformed is 15% - 18%. The bond index of the steep rib and fishbone rib between 0.11 - 0.16 so that the bond stress obtained is also relatively the same. The failure pattern that occurs is determined based on the bond stress-slip graph. There are two types of collapse in this experiment, namely pullout and splitting damage. The failure of each specimen based on the diameter and shape of the rib varies greatly. The splitting damage is seen visually only in the specimen of the D19 fishbone rib.

KEYWORDS

Bond-behavior, Relative rib area, Tensile test, Deformed bar

INTRODUCTION

Concrete is a structural material that is commonly used both for building structures and bridge structures. The nature of concrete that is resistant to fire, durable, easily formed, easy to form, and available building material; makes one reason for the use of concrete materials is still high. The type of concrete used in the structure is reinforced concrete, a composite material consisting of reinforced concrete and steel, which synergizes carrying the forces at work. Concrete can withstand the compressive force, and steel reinforcement withstands the tensile force. Steel material is straightforward to obtain, so it is still a favorite construction material.

The strength of reinforced concrete is also determined based on the interaction between reinforcement and concrete. Force transfer can work well if there is a perfect bond between the reinforcement and concrete surfaces [1]. This bond is appropriately formed when the rough reinforcement's surface so that in structural reinforced concrete using deform reinforcing.

There are currently enough factories that produce steel bars with various ribs; there are ribs that form angles, and some are perpendicular to the longitudinal groove. It is called bamboo ribs. The steep ribs are angles that form angles but the ribs' tips so that they do not converge the

----

reinforcement's longitudinal grooves. For fishbone is the ribs form an angle; the edges thick into the longitudinal grooves of reinforcement. They are commonly used as reinforced concrete material in the construction world.

It delivers a good bond between reinforcement and concrete. Guohua Xing et al. (2015) research results that the plain bar's bond strength is only 18.3% of the deform bar; thus, the deform bar's bond strength is better than the plain bar [2]. This result supports the earlier research conducted by Feldmen (2005) [3]. The contribution of bond strength values to the plain reinforcement is determined by the friction and adhesion forces. In contrast, the deform bar and the friction and adhesion forces are also determined by the interlocking force [2]. The interlocking force comes from the unevenness of the reinforcement surface.

Different shapes of deformed reinforcement steel ribs may contribute to different interlocking values, resulting in different bond stress. In SNI 2847-2019 [4], the determining factors of reinforcement development length are jointing point, coating of reinforcement steel, the diameter of reinforcement, and type of aggregate concrete used, whereas the rib shape is not included. Research on bond strength between deformed reinforcement steel and concrete by considering various rib shapes is necessary to prove that rib shape contributes to the bond stress [5], [6]. The test used to obtain bond stress is a direct pullout test. Following, in this paper, the strength of concrete reinforcement in concrete is discussed. The review's focus is the contribution of the shape of the thread reinforcement to its bond strength.

The previous research concerning the study of bond strength has been carried out, among others: et al. (2015) evaluates the bond strength of plain reinforcement in concrete compared to the deform bar [2]. Research parameters include reinforcement length embedded in concrete, reinforcement surface type, and bar diameter. The experiment behavior of plain and deform bar attachment in concrete showed only about 18.2% of reinforcing the reinforcing deform. In addition to friction and adhesion forces, the degree of the value of bond strength on the reinforcement is due to interlocking the reinforcement surface. [2]. The pullout experiment by Feldman & Bartlett (2005), plain bar embedded to concrete by reviewing various parameters including concrete compressive strength, reinforcement size, reinforcement shape, concrete blanket, and reinforcement surface roughness. The results obtained include, the maximum tensile load occurs at a minimal slip (~ 0.01 mm), the load then drops asymptotically to the residual value when the slip increases to 10 mm. The slip-load curve can be represented with a load as a linear function of the slip logarithm. The average reinforcement strength is 0.98 MPa and increased by 124% to 2.2 MPa for the deform bar [3].

The bond strength and the mechanism of collapse in the deform bar can be predicted with the bearing angle model (BAM); the failure of attachment to the deform bar can be caused by splitting. The split and shear collapse occurs to achieve ultimate strength; it needs to be restrained using stirrup bars [7]. Researched bond reinforcement whose ribs were generated using a machine to decrease the thread height, the bond stress obtained from the reinforcement bar [8].

Other research related to bond strength is Feng Xu et al. (2014) research on plain reinforcement with uniaxial and lateral biaxial loads [9]. Ultimate bond strength increases with the addition of lateral force. The size of the bar and compressive strength of concrete does not significantly influence the increase in bond strength [10]. Sungnam Hong and Sun-Kyu Park (2012) studied the relationship between bond-slip stress in reinforced concrete due to axial tensile loads [11]. Feng Lan Li et al. (2013) conducted a study of the strength of plain reinforcement with MSC (Made-Sand Concrete) [12]. Hyo-Gyoung Kwak & Jin-Kook Kim (2006) implemented the bond-slip effect on reinforced concrete portals with cyclic loads; the results obtained that the portal decreased stiffness due to failure bond-slip [13]. In 2010, Hyo-Gyoung Kwak & Jin-Wook Hwang investigated models with numerical simulations of bond-slip on reinforced concrete bridge girders. The force balance equation, the curvature distribution, and the bending moment linear distribution are influenced by slip behavior. It turned out that the results of numerical simulations with experiments obtained the same results [14].

Bond strength

Many complex factors affect bond strength. However, three factors are crucial: adhesion, friction, and interlocking force [2]. The determining factors of bond strength for plain reinforcement steel are adhesion and friction of contacting surfaces of reinforcement steel and concrete around it. During the outset loading, the reinforcement undergoes a slip, but adhesive interaction withstands it. As the load becomes heavier to withstand, friction force works [15], [16]. On deformed reinforcement steel, in addition to adhesion and friction, there is the interlocking force that occurs between the reinforcement and concrete. This force provides a greater bondability for deformed reinforcement steel than plain reinforcement steel [2].

The pattern of bond stress between reinforcement and concrete can be predicted using a direct pullout test. Furthermore, the test results are analyzed and represented in the bond stress-slip relationship graph, as presented in Figure 1 [11], [17].
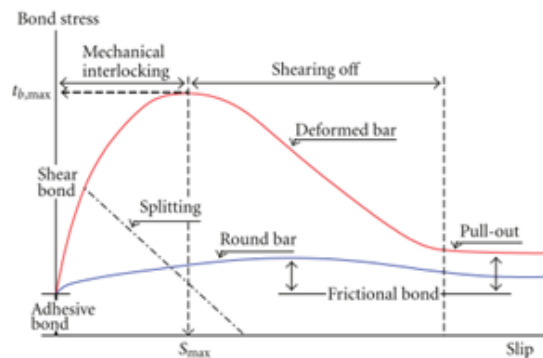

Fig. 1 - Bond Stress – Slip Relationship Graph [11], [17]

Figure 1 demonstrates the slip mechanism for bond stress of plain and deformed reinforcement steel. The bond stress value of plain reinforcement steel is lesser than deformed reinforcement steel. On plain reinforcement steel, adhesion occurs when the load is still relatively small, and the slip has not occurred, then friction withstands the more significant load [11], [17], [18]. On deformed reinforcement steel, adhesion also occurs when the load is still small, then friction and interlocking work. If the splitting failure occurs, peak stress has not been reached yet and then decreased [18]. Pullout failure occurs if the bond stress has reached a maximum value, decreases, and tends to be constant at a certain point [11], [17].

The bond stress value of the pullout test can be counted as the average bond stress value if the length of reinforcement planting is 5D (5 times the diameter of reinforcement steel) at maximum [19], [20]. 5D length is categorized in little anchorage with equal bond stress through the length of the reinforcement planted inside the concrete. The equation of average surface bond stress through the length of the reinforcement planted inside the concrete is presented in equation (1).

$$\tau = P/(\pi D L) \tag{1}$$

in which P = pullout force, D = diameter of bar, L = length of bar embedded inside the concrete.

Bond mechanism

The bond mechanism between reinforcement and concrete is affected by several parameters, such as the reinforcement surface's roughness and the reinforcement rib's shape. The geometric shape of reinforcement, especially rib, contributes significantly to its bond strength. The relationship between rib shape and bond strength is a bond index or relative rib area (fR). The

bond index is a ratio of the rib area to the area of reinforcement between ribs [11], [18], [21], [22]. There is an increase in the bond strength up to 40% with a bond index ranging from 0.04 to 0.10 that is caused by the interaction between concrete and reinforcement rib, which reduces the risk of splitting failure [21]. The equation of the bond index (fR) presented in eq. (2).

$$f_R = \pi(d_e^2 - d_i^2) / (4dS_r) \qquad (2)$$

in which f_R = bond index or relative rib area, d_e = outer diameter of reinforcement, d_i = inner diameter of reinforcement, d = nominal diameter of reinforcement, S_r = space between ribs from axis to axis.

METHODS

The test material used was deformed reinforcement steel cast monolithically with cuboid concrete with a size of 150 mm x 150 mm x 150 mm [9]. The contact area between reinforcement and concrete was as long as 5D, as shown in Figure 2 [23], [24]. The concrete quality used was fc' 34 MPa. The deformed reinforcement steel consisted of TGS (Toyogiri Iron Steel) brand, fishbone rib reinforcement steel, and KS (Krakatau Steel) brand steep rib reinforcement (Figure 3) with diameters of D13 mm, D16 mm, and D19 mm. The test results of those two types of deformed reinforcement steel were then compared with a bond strength of plain reinforcement steel with diameters approximately equal, namely D12, D16, and D19. A spiral stirrup was installed to anticipate crack and an increase of shear strength [25].
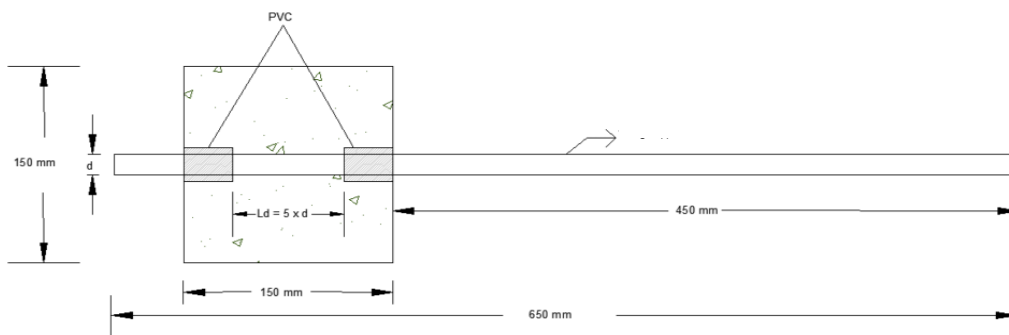

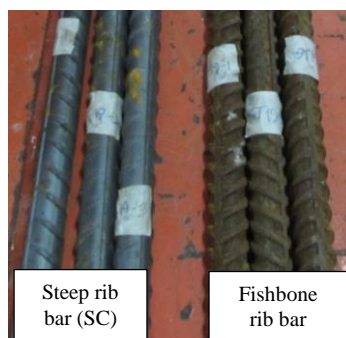*Fig. 2 - The shape of specimen for pullout test [17], [26]*

Fig. 3 - The pattern of rib bar

In this experiment, one strain gauge installed on the specimen, in this case, is the steel bar. The specimens used in this study were 27 samples, with details shown in Table 1 — each bar diameter made in 3 times. There was not 13 mm diameter plain reinforcement available in the market; thus, reinforcement with approximately equal diameter available, in this case, 12 mm, was used.

Tab. 1 - Research Samples

Steel Bar Type	Diameter (mm)	Quantity (pcs)
Steep rib bar (SC)	D13	3
	D16	3
	D19	3
Fishbone rib bar (ST)	D13	3
	D16	3
	D19	3
Plain bar (P)	D12	3
	D16	3
	D19	3
Total		**27**

The specimens are made using molds; each size 150 x 150 x 150 mm is given a partition, the molds material made from multiplex and wood. The middle of each specimen is given a hole as a reinforcement and PVC pipe, as in Figure 4. The stirrups are installed on this specimen to anticipate cracking and increase its shear strength.

The next stage is the process of casting specimens carried out in the laboratory (Figure 5). The specimen has hardened in about seven days, then opened the mold and carried out maintenance for 28 days to maintain the hydration heat reaction to achieve the concrete quality target.

Fig. 4 - Specimen moldings

Fig. 5 - Specimen casting

The bar pullout test refers to ASTM 234-91a [27]. The test equipment used was Universal Testing Machine (UTM) with concrete placed on top and reinforcement pulled, as shown in Figure 6. The specimen was tested more than 28 days old, so the concrete's compressive strength has reached 100% [28]. A dial gauge was installed on top of the steel bar to detect the total reinforcement slip. Loads added with a maximum speed of 22 kN/minute. Tests carried out until failure encountered on the test materials.

Fig. 6 - Pullout Test Set-Up Using UTM

After the pullout testing had been carried out, the test results in the form of length change and loading history were obtained. The bond index value (eq. 2) of each rib shape was calculated as well. Subsequently, the results were compared with similar research to find the tendency pattern of bond strength and each test material's failure.

RESULTS

Relative rib area (Bond Index)

The bond index value of steep type and fishbone type deformed steel bar ranges from 0.11 to 0.13 and from 0.14 to 0.16, respectively. The bond index value of steep type reinforcement steel is slightly lower than the fishbone type steel bar.

Bond stress – slip curve

The bond stress-slip curve was used to identify bond capacity between reinforcement and concrete, starting from the smallest load and gradually increasing until failure. Based on prior researches [19], [20]. The bond stress used may be average bond stress if the length of contact area between reinforcement and concrete is 5 (five) times the bar diameter at maximum. Figure 7 shows the result of the P12 plain reinforcement steel pullout test. Both specimens show differences in the shape of the bond stress-slip curve.
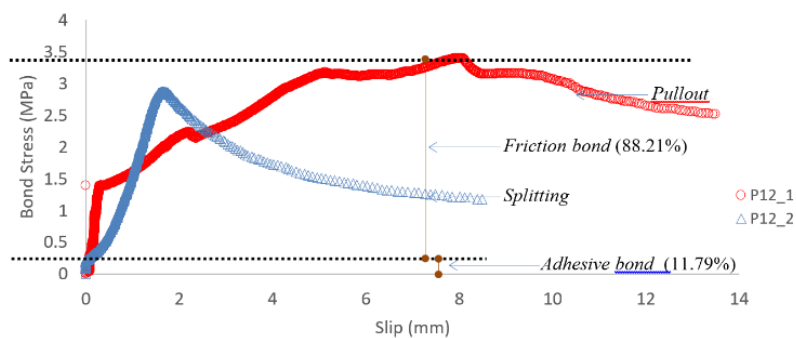

Fig. 7 - Bond Stress – Slip Graph of P12 Plain Reinforcement Steel

The curve consists of two types of bond, namely adhesive bond and friction bond. This result is identical to research conducted by Shima (1987) and Hong & Park (2012) [11], [17]. The

adhesive bond is approximately 0.4 MPa, reaching 12%, while the friction bond is 88.21% of the maximum bond stress achieved. These percentages are in line with the result of research conducted by Xing et al. [2], in which the bond strength of plain reinforcement steel is contributed by 11% adhesive bond and 89% friction bond. Figure 7 suggests that the maximum bond strain of the P12_1 specimen is 3.4 MPa because it slipped by using 8 mm. Based on the bond stress-slip curve form, the specimen of P12_1 undergoes pullout failure. P12_2 specimen shows a different pattern of the curve from the P12_1 specimen. The bond stress is also lower, less than 3 MPa, as it slipped by 1.5 mm. The P12_2 specimen undergoes splitting failure.
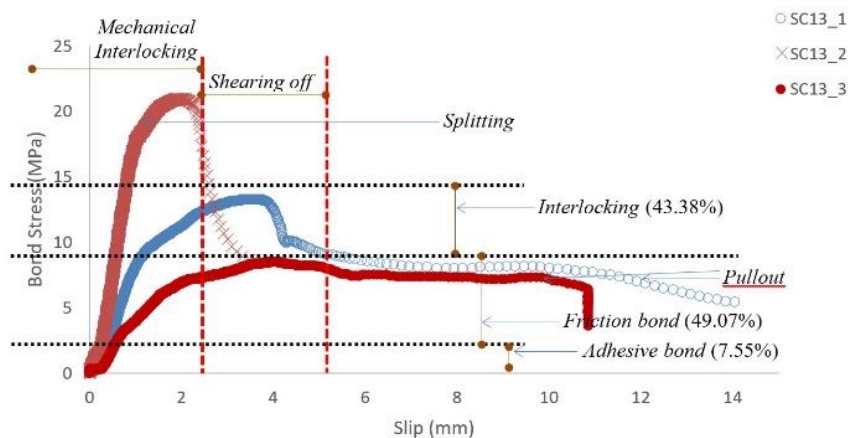

Fig. 8 - Bond Stress – Slip Graph of Steep Type Deformed Reinforcement Steel (SC13)

Figure 8 shows the pullout result; take a look at for SC13 steep type deformed reinforcement steel. Those three specimens indicate variations in the shape of the bond stress-slip curve. Specimens of SC12_1 and SC13_3 denote a similar pattern in the bond stress-slip curve with maximum bond stress reached less than 15 MPa as it slipped by approximately 4 mm. SC13_2 specimen shows more significant bond stress, nearly 20 MPa with a 2 mm slip. Bond mechanisms that occur on this specimen are an adhesive bond, friction bond, and interlocking with the contribution of 7.55%, 49.07%, and 43.38%, respectively. Failure undergone by SC13_1 and SC13_3 specimens is pullout, whereas SC13_2 undergoes splitting failure.
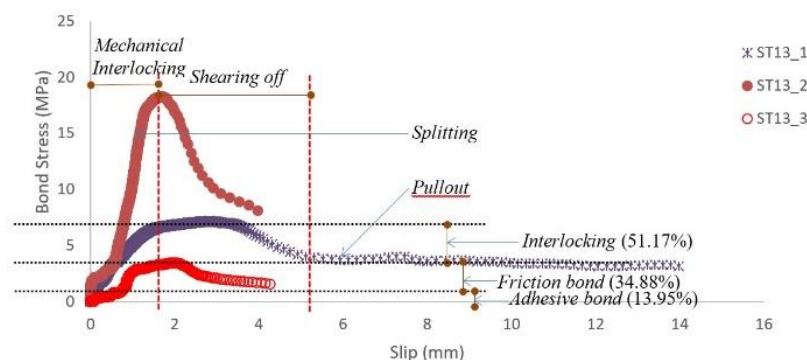

Fig. 9 - Bond Stress – Slip Graph of Fishbone Type Deformed Reinforcement (ST13)

Figure 9 illustrates the result of the pullout test for the ST13 fishbone type deformed reinforcement steel. The three specimens show the different patterns in the bond stress-slip curve. ST13_1 and ST13_3 specimens indicate a similar pattern in the bond stress-slip curve. The maximum bond stress obtained is not higher than 8 MPa with a slip of approximately 3 mm. ST13_2 denotes a higher bond strength, reaching 18 MPa with a 2 mm slip. Bond mechanisms

----

that occur on this specimen are an adhesive bond, friction bond, and interlocking with the contribution of 13.95%, 34.88%, and 51.17%, respectively. ST13_1 specimen undergoes pullout failure, whereas ST13_2 undergoes splitting failure.

Test results of 12 & 13 diameter steel bars with distinct surfaces indicate the bond stress values sequentially from the lowest to the highest: P12 plain reinforcement steel, ST13 fishbone type deformed reinforcement steel, and SC13 steep type deformed reinforcement steel.
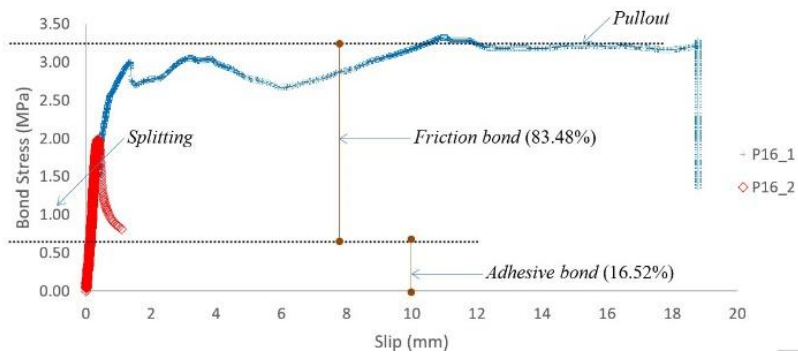

Fig. 10 - Bond Stress – Slip Graph of P16 Plain Reinforcement Steel

Figure 10 shows the result of the pullout test for P16 plain reinforcement steel. Both specimens denote different patterns in the bond stress-slip curve. It indicates that the maximum bond stress of the P16_1 specimen is 3.5 MPa as it slipped by 10 mm. Based on the pattern in the bond stress-slip curve, the P16_1 specimen undergoes pullout failure. P16_2 shows a different curve pattern from P16_1 and lower bond stress, less than 2 MPa, as it slipped by 0.5 mm. P16_2 specimen undergoes splitting failure. The bond mechanism of plain reinforcement steel only consists of the adhesive bond and friction bond with a percentage of 16.52% and 83.48%, respectively.
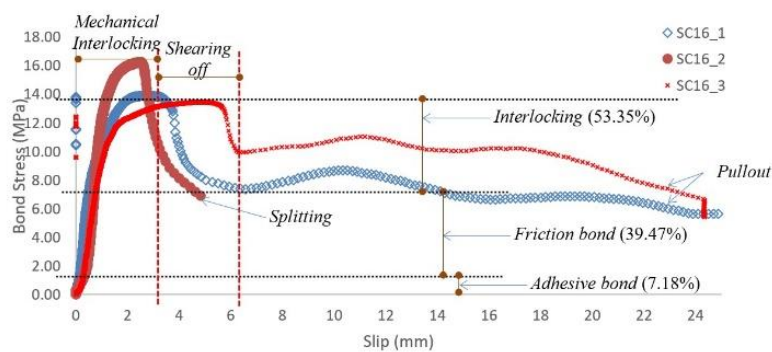

Fig. 11 - Bond Stress – Slip Graph of Steep Type Deformed Reinforcement Steel (SC16)

Figure 11 shows the result of the pullout test for SC16 steep type reinforcement steel. The three specimens indicate distinct patterns in the bond stress-slip curve. SC16_1 and SC16_3 specimens have an almost identical pattern in the bond stress-slip curve with maximum bond stress reached are 14 MPa with an approximately 4 mm slip. SC16_2 denotes higher bond stress, reaching 18 MPa with a 2 mm slip. In this specimen, bonding mechanisms are an adhesive bond, friction bond, and interlocking with a percentage of 7.18%, 39.47%, and 53.35%, respectively. Failure undergone by SC16_1 and SC16_3 is pullout, whereas SC16_2 is splitting. This stress-strain diagram has a pattern similar to the results of Wang (2018) [25].
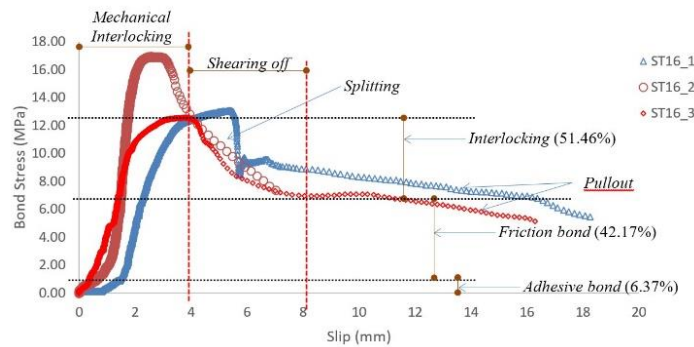

Fig. 12 - Bond Stress – Slip Graph of Fishbone Type Deformed Reinforcement Steel (ST16)

Figure 12 illustrates the result of the pullout test for ST16 fishbone type reinforcement steel. The three specimens indicate similar patterns in the bond stress-slip curve. ST16_1 and ST16_3 specimens show an almost identical pattern in the bond stress-slip curve with maximum bond stress reached is 13 MPa with a slip of approximately 4 mm. ST16_2 denotes higher bond stress, reaching 17 MPa with a slip of approximately 2 mm. In this specimen, bond mechanisms are an adhesive bond, friction bond, and interlocking with a percentage of 6.37%, 42.17%, and 51.46%, respectively. Failure undergone by ST16_1 and ST16_3 is pullout, whereas ST16_2 is splitting [25].
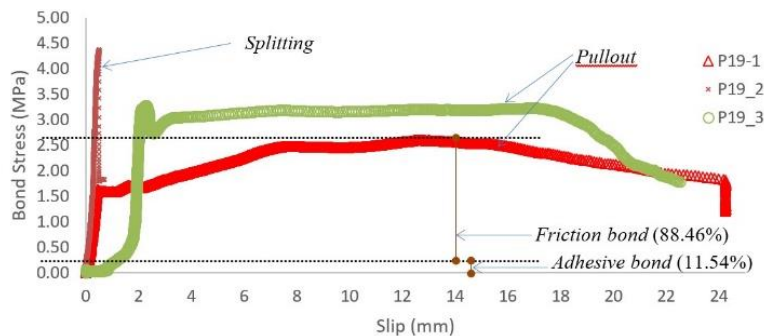

Fig. 13 - Bond Stress – Slip Graph of Plain Reinforcement Steel (P19)

Figure 13 shows that, based on the bond stress-slip curve pattern, the P19_2 specimen undergoes splitting failure. The bond stress value reaches 4.5 MPa, but the amount decreases afterward. P19_1 and P19_3 specimens indicate a similar curve pattern with bond stress lower than P19_2, which is less than 3.5 MPa. P19_1 and P19_3 specimens undergo splitting failure as well. The bond mechanism of plain reinforcement steel only consists of the adhesive bond and friction bond with a percentage of 11.54% and 88.46%, respectively.
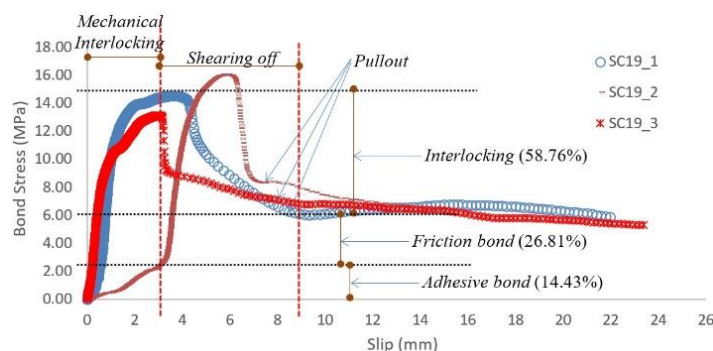

Fig. 14 - Bond Stress – Slip Graph of Steep Type Deformed Reinforcement Steel (SC19)

Figure 14 shows the result of the pullout test for SC19 steep type reinforcement steel. The three specimens indicate similar patterns in the bond stress-slip curve [23]. The maximum bond stress reached is 14 MPa with an approximately 3 mm slip. SC19_2 denotes higher bond stress, reaching 16 MPa with a 6 mm slip. Bond mechanisms that occur in this specimen are adhesive bonds (14.43%), friction bond (26.81%), and interlocking (58.76%). SC19_1, SC19_2, and SC19_3 specimens undergo pullout failure.
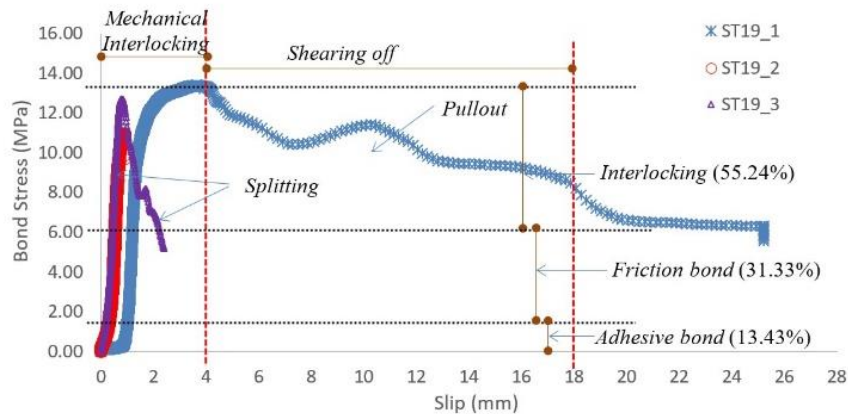

Fig. 15 - Bond Stress – Slip Graph of Fishbone Type Deformed Reinforcement Steel (ST19)

The result of the pullout test for ST16 fishbone type reinforcement steel is presented in Figure 15. The three specimens indicate different patterns in the bond stress-slip curve. ST19_2 and ST19_3 specimens show an almost identical pattern in the bond stress-slip curve, whereas ST19_1 has a different pattern with those two specimens. ST19_1 denotes the maximum bond stress, reaching more than 13 MPa with a slip of approximately 3.5 mm. ST19_2 and ST19_3 specimens indicate lower bond stress than the ST19_1 specimen. In this specimen, bond mechanisms are the adhesive bond, friction bond, and interlocking with a percentage of contribution of 13.43%, 31.33%, and 55.24%, respectively. Failure undergone by ST19_1 is pullout, whereas ST19_2 and ST19_3 are splitting.

Comparison of bond strength between plain and deformed reinforcement steel

Curves of bond stress-slip that occurs between concrete and surface of reinforcement steel, either plain or deformed, have been presented in Fig.ure7 to Figure 15. In general, the test results show that variations in diameter and reinforcement surface produce various abilities to withstand bond force. The slip that occurs shows different results in addition to the diverse magnitude of bond strength for each difference in diameter and reinforcement surface.

The bond strength of plain reinforcement steel is feeble, ranging from 2 to 4 MPa. However, the bond strength of deformed reinforcement steel is ranging from 16 to 20 MPa. This result is in line with previous research [2], [29], in which the bond strength of plain reinforcement steel is only about 18% of the bond strength of deformed reinforcement steel. The experiment result indicates that the ratio of bond strength of plain reinforcement steel compared to deformed reinforcement steel ranges between 15% and 18%. The test result showing the bond strength of all specimens is illustrated in Figure 16.
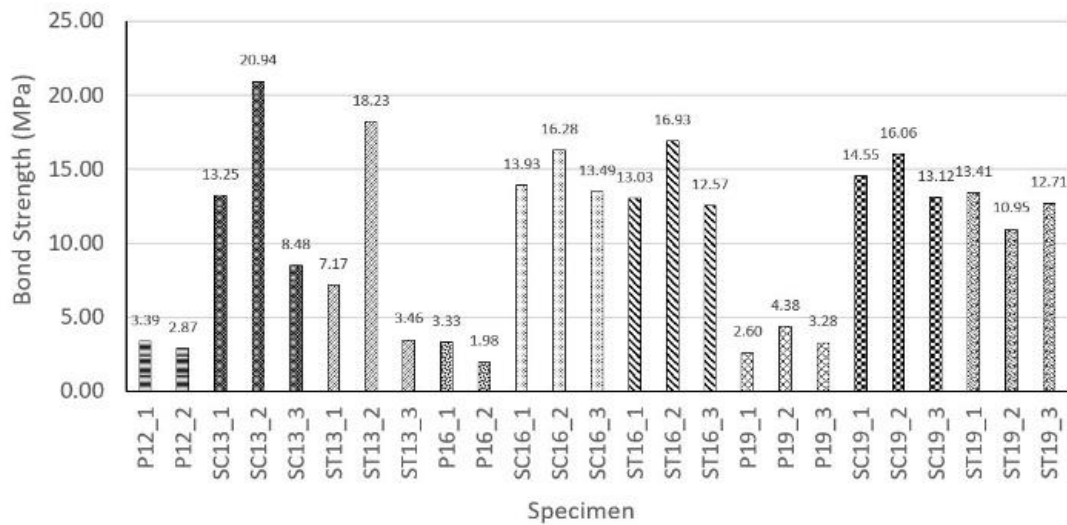
Fig. 16 - Maximum Bond Stress of Each Specimen

On the deformed bar, rib shape may affect its bond strength [5]. The parameter of the rib shape can be illustrated quantitatively in the form of the bond index. Based on research conducted by Metelli (2014) [21], a reinforcement that has a bond index ranging from 0.04 to 0.1 can increase bondability by up to 40%. The steep type deformed reinforcement steel (SC) used in this experiment has a bond index value of 0.11 – 0.13, while the fishbone type deformed reinforcement steel (ST) has a bond index value ranging between 0.14 and 0.16. Therefore, the bond index values of both types are relatively identical. The result of an experiment on these two types of deformed reinforcement steel shows that their bond strength values are relatively similar. However, steep type deformed reinforcement steel tends to have a higher bond strength than fishbone type deformed reinforcement steel.

The pattern of specimen failure

The experiment results indicate that the occurring pattern of specimen failure is splitting and pullout, as presented in Table 3. The determination of this failure pattern is based on the shape of the bond stress-slip curve and visual observation of the specimen [6], [11], [22], [30]. The failure pattern that appears visually is only the specimen failure of fishbone deformed reinforcement steel with a diameter of 19 mm (ST19_2), as illustrated in Figure 17 and 18.

Tab. 3 - The Pattern of Specimen Failure

No	Specimen	Average Bond Stress (MPa)	Adhesi	%	Friction (MPa)	%		Inter-locking	%	Pattern of Failure
1	P12_1	3.39		0.40	11.79%	2.99	88.21 %	-	-	Pullout
2	P12_2	2.87								Splitting
3	SC13_1	13.25		1.00	7.55%	7.50	49.07 %	5.75	43.38 %	Pullout
4	SC13_2	20.94								Splitting
5	SC13_3	8.48								Pullout
6	ST13_1	7.17		1.00	13.95%	3.50	34.88 %	3.67	51.17 %	Pullout
7	ST13_2	18.23								Splitting
8	ST13_3	3.46								Pullout
9	P16_1	3.33		0.55	16.52%	2.78	83.48 %	-	-	Pullout
10	P16_2	1.98								Splitting
11	SC16_1	13.93		1.00	7.18%	6.50	39.47 %	7.43	53.35 %	Pullout
12	SC16_2	16.28								Splitting
13	SC16_3	13.49								Pullout
14	ST16_1	13.03		0.80	6.37%	6.10	42.17 %	6.47	51.46 %	Pullout
15	ST16_2	16.93								Splitting
16	ST16_3	12.57								Pullout
17	P19_1	2.60		0.30	11.54%	2.30	88.46 %	-	-	Pullout
18	P19_2	4.38								Splitting
19	P19_3	3.28								Pullout
20	SC19_1	14.55		2.10	14.43%	6.00	26.81 %	8.55	58.76 %	Pullout
21	SC19_2	16.06								Pullout
22	SC19_3	13.12								Pullout
23	ST19_1	13.41		1.80	13.43%	6.00	31.33 %	7.41	55.24 %	Pullout
24	ST19_2	10.95								Splitting
25	ST19_3	12.71								Splitting

Fig. 17 - Splitting Failure of ST19_2 Specimen

Fig. 18 - Splitting Failure of ST19_3 Specimen

Figure17 and 18 show specimens that undergo splitting failure. Figure 18 does not show a crack on specimen ST19_3; however, the bond stress-slip curve indicates that the failure undergone by the specimen is splitting (Fig. 15).

CONCLUSION

Based on the results of specimen testing, conclusions can be taken as follows:

1   The steep type deformed steel bar's bond stress is relatively identical with the fishbone type deformed steel bar. The maximum bond stress reached are ranging between 13 and 20 MPa. Those bond stress values are obtained from adhesion bond by 6%-14%, friction bond by 27%-49%, and interlocking by 43% - 59%.

2   The bond stress of the plain steel bar is relatively lower than the deformed steel bar. Compared to the deformed steel bar, the bond strength ratio of plain steel bar ranges between 15% and 18%. The bond stress of plain reinforcement steel is obtained from adhesion bond by 11% - 16% and friction bond by 83% - 88%. In plain steel bar, there is not interlocking force.

3   The bond index value (relative rib area) of steep type deformed reinforcement steel is almost identical with fishbone type deformed reinforcement steel, ranging from 0.11 to 0.16. Thus, both types' bond stress values are almost similar as well because the variation is not too many different numbers.

4   The shape of the bond stress-slip graph determines the occurring failure pattern. There are two types of failure identified in this experiment, namely pullout and splitting failure. The failure of each specimen varies based on its diameter and rib shape. The splitting failure that can visually be observed is only the fishbone type deformed reinforcement steel specimen with a diameter of 19 mm.

5   To prove the rib shape contribution needs to be an investigation with a rib reinforcement specimen that has a value in the rib area index that range-wide.

ACKNOWLEDGEMENTS

REFERENCES

[1] M. Dehestani and S. S. Mousavi, "Modified steel bar model incorporating bond-slip effects for embedded element method," *Constr. Build. Mater. J.*, vol. 81, no. April, pp. 284–290, 2015.

[2] G. Xing, C. Zhou, T. Wu, and B. Liu, "Experimental Study on Bond Behavior between Plain Reinforcing Bars and Concrete," *Adv. Mater. Sci. Eng.*, vol. 2015, no. October, 2015.

[3] L. R. Feldman and F. M. Bartlett, "Bond strength variability in pullout specimens with plain reinforcement," *ACI Struct. J.*, vol. 102, no. 6, pp. 860–867, 2005.

[4] SNI 2847:2019, *Persyaratan Beton Struktural untuk Bangunan Gedung dan Penjelasan*. Bandung: Badan Standardisasi Indonesia, 2019.

[5] H. A. O. Qing-duo, W. Yan-lei, Z. Zhi-chun, and O. U. Jin-ping, "Bond strength improvement of GFRP rebars with different rib geometries," *J. Zhejiang Univ. Sci. A*, vol. 8, no. 9, pp. 1356–1365, 2007.

[6] A. Rosyidah, I. K. Sucita, and F. Hidayat, "The Bond Strength of Glass Fiber Reinforced Polymer (GFRP) Reinforcement with Monolith Concrete," *IJASEIT*, vol. 8, no. 2, pp. 495–500, 2018.

[7] O. C. Choi and H. Choi, "Bearing Angle Model for Bond of Reinforcing Bars in Concrete," *ACI Struct. J.*, vol. 114, no. 1, pp. 245–253, 2017.

[8] C. Bosco and F. Tondolo, "Bond Performance in Machined Reinforcing Bar for Reinforced Concrete," *Appl. Mech. Mater.*, vol. 166–169, pp. 828–831, 2012.

[9] F. Xu, Z. M. Wu, J. J. Zheng, Y. Hu, and Q. Bin Li, "Bond behavior of plain round bars in concrete under complex lateral pressures," *ACI Struct. J.*, vol. 111, no. 1, pp. 15–25, 2014.

[10] W.-J. Long, K. Khayat, G. Lemieux, S.-D. Hwang, and F. Xing, "Pullout Strength and Bond Behavior of Prestressing Strands in Prestressed Self-Consolidating Concrete," *Materials (Basel).*, vol. 7, no. 10, pp. 6930–6946, Oct. 2014.

[11] S. Hong and S. K. Park, "Uniaxial bond stress-slip relationship of reinforcing bars in concrete," *Adv. Mater. Sci. Eng.*, vol. 2012, no. April, 2012.

[12] F. L. Li, K. F. Yu, X. X. Ding, and C. M. Li, "Bond Properties of Plain Steel Bar in Concrete with Machine-Made Sand," *Appl. Mech. Mater.*, vol. 438–439, pp. 20–24, 2013.

[13] H. G. Kwak and J. K. Kim, "Implementation of bond-slip effect in analyses of RC frames under cyclic loads using layered section method," *Eng. Struct.*, vol. 28, no. 12, pp. 1715–1727, 2006.

[14] H. G. Kwak and J. W. Hwang, "FE model to simulate bond-slip behavior in composite concrete beam bridges," *Comput. Struct.*, vol. 88, no. 17–18, pp. 973–984, 2010.

[15] J.-Y. Lee *et al.*, "Interfacial bond strength of glass fiber reinforced polymer bars in high-strength concrete," *Composites Part B: Engineering*, vol. 39, no. 2. pp. 258–270, 2008.

[16] L. R. Feldman and F. M. Bartlett, "Bond stresses along plain steel reinforcing bars in pullout specimens," *ACI Struct. J.*, vol. 104, no. 6, pp. 685–692, 2007.

[17] H. Shima, L. L. Chou, and H. Okamura, "Micro and macro models for bond in reinforced concrete," *Journal of the Faculty of Engineering, The Uinversity of Tokyo*, vol. XXXIX, no. 2. pp. 133–194, 1987.

[18] M. Teresa, G. Barbosa, E. De Souza, and S. Filho, "Analysis of the Relative Rib Area of Reinforcing Bars Pull Out Tests 4 . Experimental Results and Discussion," *Mater. Res.*, vol. 11, no. 4, pp. 453–457, 2008.

[19] A. A. R. M.H.Harajli, B.S.Hamad, "Effect of Cofinement of Bond Strength between Steel Bars and Concrete," *ACI Struct. J.*, vol. 101, no. September-October, pp. 595–603, 2004.

[20] M. H. Harajli, B. S. Hamad, and A. A. Rteil, "Effect of Confinement on Bond Strength between Steel Bars and Concrete," *ACI Struct. J.*, vol. 101, no. 5, pp. 595–603, 2004.

[21] G. Metelli and G. A. Plizzari, "Influence of the relative rib area on bond behaviour," *Mag. Concr. Res.*, vol. 66, no. 6, pp. 277–294, 2014.

[22] J. Zuo and D. Darwin, "Splice strength of conventional and high relative rib area bars in normal and high-strength concrete," *ACI Struct. J.*, vol. 97, no. 4, pp. 630–641, 2000.

[23] C. W. Tang, "Uniaxial bond stress-slip behavior of reinforcing bars embedded in lightweight aggregate concrete," *Struct. Eng. Mech.*, vol. 62, no. 5, pp. 651–661, 2017.

[24] M. Zhao, X. Zhang, K. Yan, T. Fei, and S. Zhao, "Bond Performance of Deformed Rebar in Steel Fiber Reinforced Lightweight-Aggregate Concrete Affected by Multi-Factors," *Civ. Eng. J.*, vol. 18, no. 3, pp. 276–290, 2018.

[25] F. Wang, X. Wu, C. Guo, and W. Song, "Experimental Study on Bond Strength of Deformed Steel Bars in Recycled Glass Aggregate Concrete," *KSCE J. Civ. Eng.*, vol. 24, no. 144, pp. 1–10, 2018.

[26] E. S. Dewi, *Pengaruh Diameter Tulangan terhadap Kuat Lekat (Bond Strength) Beton Geopolimer*. 2017.

[27]   ASTM C234-91a (2000), *Standard Test for Comparing Concrete on the Basis of Bond Developed with Reinforcing Steel*. 2000.

[28]   O. Leibovich, A. N. Dancygier, and D. Z. Yankelevsky, "An Innovative Experimental Procedure to Study Local Rebar-Concrete Bond by Direct Observations and Measurements," *Exp. Mech.*, vol. 56, no. 12, pp. 673–682, 2016.

[29]   D. Ertzibengoa, S. Matthys, and L. Taerwe, "Bond behaviour of flat stainless steel rebars in concrete," *Mater. Struct.*, vol. 45, no. 11, pp. 1639–1653, 2012.

[30]   W. M. Thomas, D. Ball, R. Fenn, and R. Challis, "The Effect of Geometry on Reinforcement Anchorage Performance and Integrity," in *The Institute of Concrete Technology 43rd Annual Convention 2015 26th March 2015 Loughborough University, UK*, 2015, no. April.

MODELLING AND DYNAMIC ANALYSIS OF THREE-DIRECTION GRID PRESTRESSED RETICULATED MEGA-STRUCTURE

Wenbo Zhang[1], Fang Liu [2], Liangliang Zou[3] and Pei xiang Chen[2]

1. *Beijing Municipal Engineering Consulting Corporation, Beijing, China; WenboZhang @shu.edu.cn*
2. *Anhui Civil Airport Group Co., Anhui, China; 2608836030 @qq.com, chenpx2012 @163.com*
3. *Wenzhou Longwan Internation Airport, Zhejiang; China; 1070965597 @qq.com*

ABSTRACT

In this paper, the generation way of three-direction grid prestressed reticulated mega-structure is studied, and the three-direction grid prestressed reticulated mega-structure composite joint specific formation ideas are proposed. The important control parameters of three-direction grid prestressed reticulated mega-structure are determined, and the geometric modelling method of hexagon across the middle joint and octagon across the side joint is proposed. Coordinate formula of hexagonal and octagonal joints are derived to ensure reasonable grid arrangement and uniform stress distribution of the structure. Combined with the geometric parameters of the mega grid, a new method for creating the geometric model of three-direction grid prestressed mega reticulated structure is realized. The quadrangular pyramid space grid structure with the same length, span, rise and grid size and the three-direction grid prestressed grid structure are calculated, and the advantages of three-direction grid prestressed grid structure in dynamic performance are compared and analyzed.

KEYWORDS

Three-direction grid, Prestress, Giant grid, Geometric model

INTRODUCTION

With the development of economy and the improvement of human needs, people have higher requirements for spatial structure, especially the structural span. However, as the span increases, some problems within the space structure appear, such as the excessively small thickness-to-span ratio caused by the overall instability of the structure, excessive internal force of the component, and instability caused by the excessively long component. In recent years, the mega lattice structure system and the prestressed lattice structure system [4-6] proposed by He Yongjun and other scholars [1-3] can better improve the spanning capacity of the structure. Compared with ordinary grid structure, the material utilization rate of giant grid structure is higher, and the material used per unit building area is less, so the self-weight of the structure is relatively small. The stress of the structure is clear, although the stress of the member is relatively large, the phenomenon of excessive stress of a single member is effectively avoided and the deflection of the

----

structure is effectively reduced due to the existence of an assembly or a three-direction truss. However, the application of reticulated mega-structure in engineering has also some limitations. The stiffness of the reticulated mega-structure is usually smaller than that of the ordinary reticulated structure. In order to meet the design specifications, the reticulated mega-structure needs to be cambered, that is to form a reticulated mega structure with a certain rise to meet the structural stiffness requirements. The limitation of the giant network is more obvious in the case that the design is restricted by the height and the internal height is required, for example, in the design of the hangar roof structure, the height is restricted by the airport clearance, and directly adopting the giant reticulated shell structure as the hangar roof structure can cause the internal height of the hangar to be insufficient and influence the use function. In view of the above problems, it is particularly important to study a new type of large-span structure with small thickness and large stiffness.

Ding Leran [7] carried out the corresponding research on the giant grid suspen-dome structure with a span of 200m, and based on the analysis of static, stability and dynamic characteristics of the structure, the optimal range of geometric control parameters is determined. Hu Duo [8] carried out the corresponding research on the honeycomb grid spherical reticulated shell with a span of 100m, and comprehensively analyzed the geometric composition, internal force distribution law and main control parameters of the main structure, which effectively improved the theoretical guidance for the poor mechanical performance of the structure in practical engineering. Yao Li [9] made a systematic study on the super-long span Kiewitt reticulated mega-structure with the span of 800m, and put forward a more reasonable forming method for the mega-reticulated structure by using CAD three-direction modeling analysis. He Yongjun [10-12] studied the mechanical properties and related parameters of the main structure of the cylindrical intersecting three-direction truss system, and made a detailed analysis and description on the composition of the main structure, the selection of body parameters and supporting methods, as well as the sub-structure and its connection with the main structure. In this paper, the three-direction grid type prestressed reticulated mega-structure is based on the grid structure as the basic structure, combined with the idea of the mega-grid structure, that is to retain the member on the main force path, remove the member on the secondary force path. Besides, in order to meet the structural stiffness, prestressed cables replace the bottom chord of the mega-component in the main force direction. Finally, a three-direction grid type prestress mega-structure is formed. The Dynamic performance is the important content of the analysis on the mechanical performance of the prestressed three-direction grid mega-structure. In order to compare the advantages of the prestressed three-direction grid structure, the quadrilateral pyramid space grid structure and prestressed three-direction grid mega-structure with the same length, span, rise and grid size are calculated. From the structure of the dynamic performance of the comparative analysis.

Composition of mega-member and establishment of composite joint

Through the comprehensive consideration of the characteristics of several commonly used flat grid forms, the inverted pyramid truss is finally selected as the lattice mega component of the three-direction grid prestressed grid structure, and the inverted pyramid truss is specifically shown in Figure1.
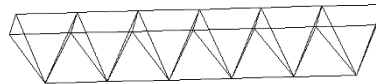

Fig. 1 – Inverted quadrangular pyramid truss

After the flat grid frame is evacuated, a three-direction grid type single-layer grid structure is formed, and the configuration is shown in Figure 2.
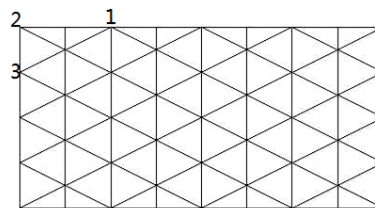

Fig. 2 – Evacuated Grid Structure

When a single bar is replaced by pyramid truss, the joint between mega components is complex. The joint of inverted pyramid truss structure is the key to form the geometric model of three-direction grid prestressed mega grid structure, which is called "composite joint" in this paper. Joints 1, 2 and 3 indicated in Figure 2 represent three types of connection forms respectively. Joint 1 with long direction indicates that five members are connected at the joint. Corner point 2 indicates that three members are connected at the joint. Joint 3 with cross direction indicates that four members are connected, indicating that the structure needs three different treatment methods to connect the inverted quadrangular pyramid trusses on the four edges. In order to make the modeling of the geometric model of the structure meet the connection of three different joints at the same time, eight groups of inverted quadrangular pyramid trusses are connected, and an inverted octagonal pyramid with an octagonal plane projection is formed at the cross connection. And that eight side on the upper part of the truss can simultaneously meet the form that the joints of the invert quadrangular pyramid truss are mutually crossed and connected in the three forms.

In addition to the four external giant components need to be connected to each other, the internal joints of the structure are connected to each other by six bars. Six groups of inverted quadrangular pyramid trusses are crosswise connected to form a composite joint with a hexagonal plane projection; Through the above treatment of the external and internal composite joints, a three-direction grid type prestressed mega-grid structure is finally formed as shown in Figure 3, wherein (A) is an axonometric view of the structure, and (B) is a plan view of the structure.
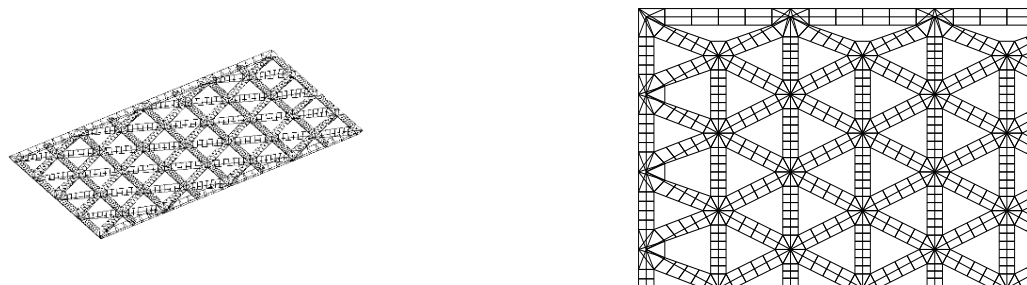
(A) Axonometric drawing of three-direction grid type prestressed giant grid structures


(B) Top view of prestressed mega-grid structure with three-direction grid

Fig. 3 – Schematic diagram of three-direction grid type prestressed mega-grid structures

METHOD FOR FORMING GEOMETRIC MODEL OF THREE-DIRECTION GRID PRESTRESSED RETICULATED MEGA-STRUCTURE

Formation of Composite Joint

The geometric model of three-direction grid prestressed reticulated mega-structure is essentially a flat plate-type space structure, so the establishment of the geometric model of the hexagonal mid-joint and the octagonal side joint is the key to generate the structural model. The above-mentioned "hexagon" refers to that projection of the inverted quadrangular pyramid truss in the interior of the structure on the intersect connecting plane, and the "octagon" refers to the projection of the inverted quadrangular pyramid truss on four out edges on the intersecting connecting plane. The specific connection mode is shown in Figure 4, wherein (A) is the connection mode of the internal inverted quadrangular pyramid;(B) is an inverted quadrangular pyramid connection with four outer edges.
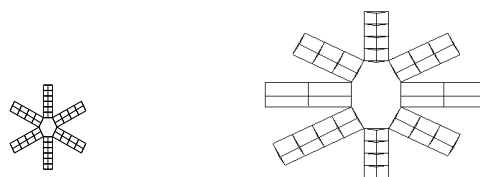

(A) Cross structure projected as hexagon (B) Cross structure projected as octagon

Fig. 4 – Hexagonal and Octagonal Connections

As shown in the figure above, both the internal and external connection modes of the cross connection part are hollowed out, which will cause uneven force on the bar and adversely affect the overall stiffness. And therefore that diagonal line of the upper polygons of the hollow structure need to be mutually crossed and connected; As the octagonal protruding structure part on four sides is easy to be stressed and concentrated, the part protruding out of the outer edge of the quadrangular pyramid is cut off. The corner points of the hexagon and the trimmed octagon are respectively connected with the corresponding joints of the three-direction grid type single-layer

grid structure to form partial web members of the three-direction grid type prestressed mega-grid structure. Finally, a composite joint is formed as shown in Figure 5.
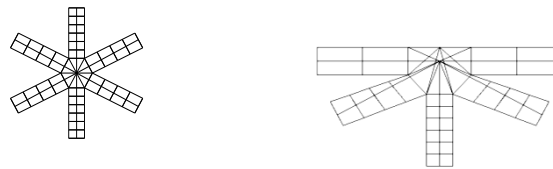

(A) Hexagonal internal connection (B) Octagonal internal connection

Fig. 5 – Composite joint in final form

Geometric parameter setting of mega-structure

According to the characteristics of the three-direction grid type prestress mega-grid structure, the geometric parameters of the mega-grid are set as shown in Figure 6, wherein Lx represents the length of the structural longitudinal mega-grid, Ly represents the length of the structural transversal mega-grid, and H represents the thickness of the structure; The number of long direction giant grids Nx, the number of span direction giant grids Ny, the number of long direction giant component interjoint grids N1, the numbers of span direction giant component interjoint grids N2, and the numbers of oblique direction giant component interjoint grids N3.
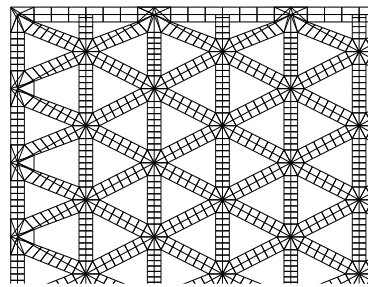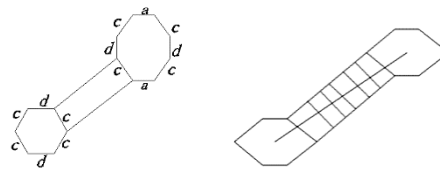

(A) Structural plan

(B) Structural elevation

Fig. 6 – Geometric parameters of structures

The projections of the midspan composite joint and the edge composite joint on the lower chord plane are hexagons and octagons respectively, and the hexagons and octagons are not necessarily regular polygons. The specific geometric parameters are shown in Figure 7 (a).

(a) Hexagonal and octagonal geometry (b) Non-uniform case of giant grid

Fig. 7 – Compound joints are not regular polygon

The single member of the three-direction grid single-layer reticulated structure is replaced by the inverted pyramid truss. In order to make the huge grid arrangement even, the overall structure stress reasonable, the member type reduces as far as possible, so the inverted quadrangular pyramid truss must be arranged reasonably. In the structure shown in Figure 8, the lines connecting the central point of the hexagon to the four corner points are equal, that is, the lengths of the four line segments are equal and are all e; The connecting lines of the central point of the hexagon and the remaining two corner points are equal, and the lengths of the two line segments are B; In order to ensure that the members are evenly distributed and properly stressed, l in the illustration must be perpendicular and bisect C.
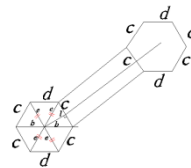

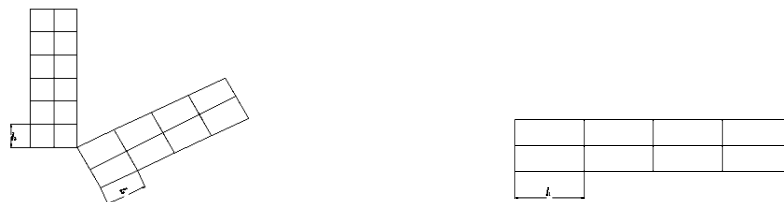*Fig. 8 – Diagram of the relationship between the hexagons*

To sum up, in order to reduce the structural mega grid to the form as shown in Figure 7 (b), and ensure uniform bar specification and uniform stress, the triangle divided by the hexagon must be a regular triangle, that is, b = e, so the hexagon of the projection of the mid-span composite joint in the lower chord plane must be a regular hexagon.

Similarly, the octagon with side spans is also designed as a regular octagon, and the side length of the octagon is also C. The number of the long direction giant component interjoint grids is N1, the number of the cross direction giant component interjoint grids is N2, and the number of the oblique direction giant component interjoint grids is N3, and the length of each corresponding small grid is respectively L1, L2 and L3, which are respectively expressed by formulas (1), (2) and (3). Figure 9 (a) Length L2 and L3 of that transversal and oblique small grids, wherein L3 is divide into two parts which are respectively positioned between two hexagons and between a hexagon and an octagon, and are respectively denote by L3 and L3; Figure 9 (b) is the length L1 of the lengthwise small mesh;

$$l_1 = \frac{L_x - \dfrac{c}{\tan 22.5^\circ}}{n_1} \cdot \qquad (1)$$

$$l_2 = \frac{L_y - \frac{\sqrt{3}}{2}c}{n_2} \tag{2}$$

$$\begin{cases} l_3^{'} = \dfrac{\sqrt{\dfrac{L_x^{\,2} + L_y^{\,2}}{2}} - \dfrac{\sqrt{3}}{2}c - \dfrac{c}{2\sin 22.5^\circ}}{n_3} \\[4ex] l_3 = \dfrac{\sqrt{\dfrac{L_x^{\,2} + L_y^{\,2}}{2}} - \sqrt{3}c}{n_3} \end{cases} \tag{3}$$

(a) Cross-direction and diagonal small grid length (b) Long-direction small grid length

Fig. 9 – Length of small grid

Structural Geometric Parameter Scheme

In order to accurately express the relationship between the coordinate value of each point and the length of the polygon, this paper establishes the local coordinate origin at the center point of the hexagon and octagon, and stipulates the serial number of the corner points of the hexagon and octagon as shown in Figure 10.
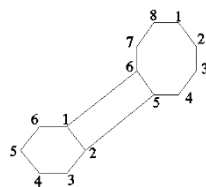

Fig. 10 – Sequence number of corner point of arbitrary polygon

According to the length of each side of the hexagon or the octagon, the coordinates of each corner point of the hexagon and the octagon in the local coordinate system can be expressed. The hexagon S and the octagon E can be expressed by the side length of the hexagon in local coordinates, and the coordinate formula of each corner point is (XSj, YSj), and the value range of J is 1-6; The side length of the octagon represents that the coordinate formula of each corner point is (XEk, YEk), and the value range of K is 1-8. The local coordinate formulas of the six corner points of the hexagon are shown in (4)- (9):

$$\begin{cases} X_{S1} = \dfrac{1}{2}c \\[2mm] Y_{S1} = \dfrac{\sqrt{3}}{2}c \end{cases} \tag{4}$$

$$\begin{cases} X_{S2} = c \\[2mm] Y_{S2} = 0 \end{cases} \tag{5}$$

$$\begin{cases} X_{S3} = \dfrac{\sqrt{3}}{2}c \\[2mm] Y_{S3} = -\dfrac{1}{2}c \end{cases} \tag{6}$$

$$\begin{cases} X_{S4} = -\dfrac{\sqrt{3}}{2}c \\[2mm] Y_{S4} = -\dfrac{1}{2}c \end{cases} \tag{7}$$

$$\begin{cases} X_{S5} = -c \\[2mm] Y_{S5} = 0 \end{cases} \tag{8}$$

$$\begin{cases} X_{S6} = \dfrac{1}{2}c \\[2mm] Y_{S6} = -\dfrac{\sqrt{3}}{2}c \end{cases} \tag{9}$$

The local coordinate formulas of the eight corner points of the octagon are shown in (10)-(17):

$$\begin{cases} X_{E1} = \dfrac{1}{2}c \\[2mm] Y_{E2} = \dfrac{c}{2\tan 22.5^\circ} \end{cases} \tag{10}$$

$$P = (N_1 + N_2)\cos\theta \tag{11}$$

$$\begin{cases} X_{E3} = \dfrac{c}{2\tan 22.5^\circ} \\[2mm] Y_{E3} = -\dfrac{c}{2} \end{cases} \tag{12}$$

$$
\begin{cases}
X_{E4} = \dfrac{1}{2}c \\[2ex]
Y_{E4} = -\dfrac{c}{2\tan 22.5^\circ}
\end{cases}
\tag{13}
$$

$$
\begin{cases}
X_{E5} = -\dfrac{1}{2}c \\[2ex]
Y_{E5} = -\dfrac{c}{2\tan 22.5^\circ}
\end{cases}
\tag{14}
$$

$$
\begin{cases}
X_{E6} = -\dfrac{c}{2\tan 22.5^\circ} \\[2ex]
Y_{E6} = -\dfrac{c}{2}
\end{cases}
\tag{15}
$$

$$
\begin{cases}
X_{E7} = -\dfrac{c}{2\tan 22.5^\circ} \\[2ex]
Y_{E7} = \dfrac{c}{2}
\end{cases}
\tag{16}
$$

$$
\begin{cases}
X_{E8} = -\dfrac{1}{2}c \\[2ex]
Y_{E8} = \dfrac{c}{2\tan 22.5^\circ}
\end{cases}
\tag{17}
$$

A hexagon on the upper chord of the mid-span joint is created according to the above method, and connected with the joint of the three-direction grid type single-layer grid structure to form a partial web member of the three-direction grid type prestressed giant grid structure. The schematic diagram is as shown in Figure 11, and the length is marked as L4. The length of L4 can be calculated by Formula (18):
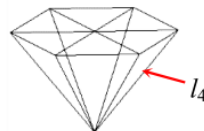

Fig. 11 – Connection between hexagon center and lower chord joints

$$
l_4 = \sqrt{\left(\frac{\sqrt{3}}{2}c\right)^2 + h^2}
\tag{18}
$$

According to the local coordinate formula of the octagon, mutually crossing and connection with the upper part of the inverted quadrangular pyramid truss structure on the outer edge, so that

----

the upper part of the structure forms four complete new out edges, namely the edge of the outermost edge of an upper chord of the whole structure, if it is external, cut it out.
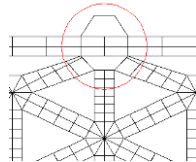

Fig. 12– Before octagon cutout

Each corner point of the polygon after cutting is respectively connected with the joint of the three-direction grid type single-layer grid structure to form the web member of the three-direction grid type prestressed giant grid structure, and the joint connection schematic diagram is shown in Figure 13 below.
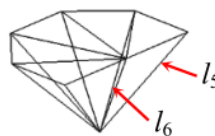

Fig. 13– Connection between octagon center and lower chord joints

The web member shown in the above figure is divided into two parts, one part is the corner point of the regular octagon connected with the three-direction grid type prestressed huge grid structure, and the length is marked as l5, the other part is the center point of the regular octagon connected with the joint of the three-direction grid type prestressed huge grid structure, and the length marked as l6 can be calculated by formula (19):

$$\begin{cases} l_5 = \dfrac{c}{2\sin 22.5^\circ} \\ l_6 = h \end{cases} \tag{19}$$

After the webs are formed, the center points of the hexagons and the octagons are connected with the corner points of the hexagons and the octagons to form partial top chords. Thus, a three-direction grid type prestressed mega-grid structure is finally formed.

ANALYSIS OF DYNAMIC BEHAVIOR OF PRESTRESSED MEGA-RETICULATED STRUCTURE WITH 3-D LATTICE

Selection of structural calculation model

Calculation Model of Three-direction Grid Prestressed Reticulated Mega-structure

Determination of basic geometry size: This paper refers to the geometry size design of 306m × 90m hangar roof structure of Capital Airport [48], the control parameter of three-direction grid prestressed reticulated megastructure is set as follows: length 300m, span 150m, structural

whole thickness 6m, structural megagrid number in long direction 4, structural megagrid number in span direction 4. The number of interjoint grids of long direction giant component is 10, and the number of interjoint grids of span direction giant component is 8. The number of interjoint grids of oblique giant components is 6. Replace the lower chords on the main diagonal and the middle span with prestressed cables, and finally form a three-direction grid type prestressed mega-grid structure as shown in Figure 14.
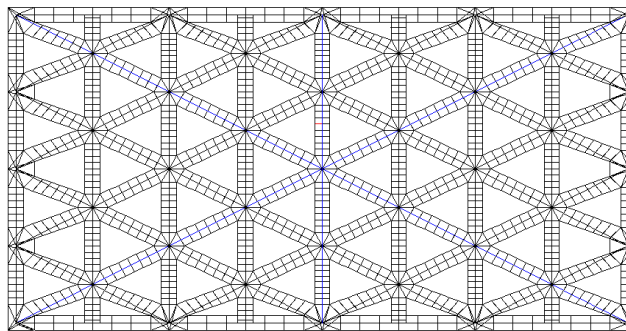

Fig. 14 – Arrangement position of prestressing cables

Orthogonal Pyramid Grid Structure

The modeling of square pyramid space truss structure can be obtained by inputting the corresponding parameters in MSTCAD software; The plane dimensions of square pyramid space grid structure are 300m in length direction, 150m in span direction, 31 grids in length direction, 19 grids in span direction and 6m in thickness. The load and constraint conditions are the same as those of the prestressed mega grid structure. The established model is shown in Figure 16 below:
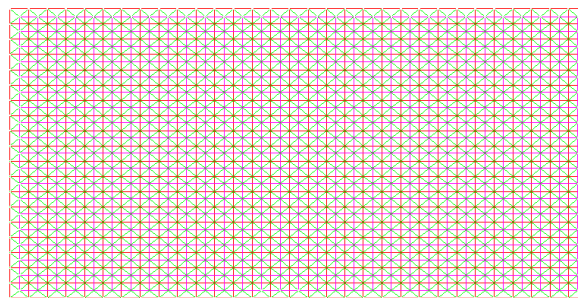

Fig. 15 – Orthogonal Pyramid Grid Structure

Analysis of natural vibration characteristics of three-direction grid prestressed reticulated mega-structure

The steel grade of the members is Q345, the nominal diameter of the prestressed cable is 300mm, and the basic level of the selected pretension is 23000kN. The modal analysis of the three-direction grid type prestressed huge grid structure model is carried out by using sap2000 software, and 1. 0 dead load + 0. 5 times live load is considered as the representative value of gravity load. In order to compare and analyze the dynamic characteristics of two kinds of space truss structures, the orthogonal square pyramid space truss in chapter 4 and chapter 3 are used to

----

compare and analyze the dynamic characteristics of the two kinds of space trusses. Table 1 is the first 30 natural frequencies of square pyramid space grid structure, and Table 2 is the first 30 natural frequencies of three-direction grid prestressed reticulated mega-structure.

Tab. 1 - The first 30 natural frequencies (Hz) of square pyramid space grid structures

Order Number	1	2	3	4	5	6	7	8	9	10
Natural Frequency	0.38	0.44	0.595	0.73	0.84	1.04	1.12	1.29	1.38	1.45
Order Number	11	12	13	14	15	16	17	18	19	20
Natural Frequency	8.45	8.86	9.12	9.65	11.45	12.04	12.48	12.56	12.7	12.79
Order Number	21	22	23	24	25	26	27	28	29	30
Natural Frequency	12.8	13.02	13.67	14.21	14.45	14.54	15.64	15.87	16.08	16.08

Tab. -: The first 30 natural frequencies (Hz) of three-direction grid prestressed reticulated mega-structure

Order Number	1	2	3	4	5	6	7	8	9	10
Natural Frequency	1.38	2.44	2.59	3.73	3.83	4.03	5.12	6.29	7.38	7.45
Order Number	11	12	13	14	15	16	17	18	19	20
Natural Frequency	8.54	8.64	8.67	8.69	9.71	11.72	11.78	11.80	12.87	12.89
Order Number	21	22	23	24	25	26	27	28	29	30
Natural Frequency	12.9	12.97	13.05	13.12	13.22	14.42	15.54	15.64	16.73	16.76

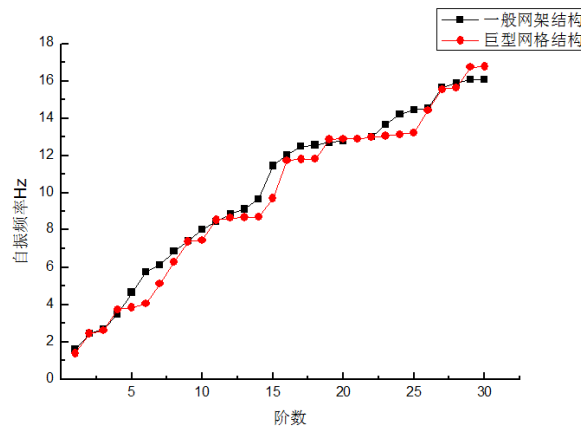

Fig. 16 – Comparison of the first 30 natural frequencies of the two structures

From Figure 16, it can be found that the natural frequency of the three-direction grid prestressed mega-grid structure is lower than that of the square pyramid grid structure, and its basic period is larger than that of the grid structure. The main reason is due to the three-direction grid type prestressed reticulated mega-structure caused by the intmemberuction of cable, with cable element as the tension element. It can also be concluded that the high order modes cannot be ignored in the dynamic response of the structure for the large span structure.

CONCLUSION

1. In this paper, the inverted pyramid truss is selected as the lattice mega-component of the three-direction grid prestressed reticulated mega-structure. By analyzing the connection form of the three-direction grid prestressed reticulated mega-structure, the specific ideas of "hexagon" and "octagon" cross connection composite joints are proposed, and the specific scheme of forming part of web members according to composite joints is proposed.

2. This paper determines the important control parameters of three-direction grid type prestressed reticulated mega-structure, and demonstrates the establishment of composite joints in the span and side composite joints, and finally chooses regular polygon to ensure that the mega-grid layout is uniform and the overall structure is reasonable.

3. According to the construction idea of three-direction grid type prestressed reticulated mega-structure, the hexagonal and octagonal joint coordinate schemes are deduced and formed, the geometric model establishment method of the hexagonal cross joint and the octagonal cross joint is proposed, and finally the specific scheme of three-direction grid type prestressed reticulated mega-structure geometric model construction is formed.

4. The quadrangular pyramid space grid structure with the same length, span, rise and grid size and the three-direction grid prestressed grid structure are calculated, and the

----

advantages of three-direction grid prestressed grid structure in dynamic performance are compared and analyzed.

REFERENCES

[1]   He Y., 2000. Shape analysis and mechanical model of reticulated mega-structure. In: Proceedings of the 9th Symposium on Spatial Structures, edited by China Civil Engineering Society, 6

[2]   He Y., 2001. Study on the Shape, Static and Stability of Reticulated Mega-structure. Master's thesis, Zhejiang University, Hangzhou

[3]   He Y., Li J., Zhou X., 2007. Composition, supporting method and mechanical model of spherical reticulated mega-structure. Journal of Hunan University (Natural Science Edition), vol 3: 11-14

[4]   Bai Z. X., Liu X. L., Li Y. S., 2001. A NewType of Spatial Structure－Beam String structure. Spatial Structures, vol. 7: 33-38

[5]   Zhang Y. G., 2000. Development of Cable-supported Structures in the Last Ten Years(1)-Concept of Cable-supported Strctures and Development of Plane Cable-supported Structures. Industrial Construction, vol. 2:105-113

[6]   Saitoh M., Okada A., 1999. The Role of String in Hy-brid String Structure. Engineering Structures, vol. 21: 756-769. https://doi.org/10.1016/S0141-0296(98)00029-7

[7]   Ding L. R., 2012. Analysis of static and dynamic characteristics of ribbed giant grid suspen-dome structure. Master's thesis, Xi'an University of Architecture and Technology, Xi'an

[8]   Hu D., 2015. Study on static and stability of honeycomb reticulated spherical huge reticulated shell. Master's thesis, Hunan University, Hunan.

[9]   Yao L., 2015. Study on static and stability of 800 m super-long Kiewitt reticulated mega-structure. Master's thesis, Harbin Institute of Technology, Harbin

[10]   He Y. J., Zhou X. H., 2007. Static properties and stability of cylindrical ILTDBS reticulated mega-structure with double-layer grid substructures. Journal of Constructional Steel Research, Vol. 63: 1580-1589. https://doi.org/10.1016/j.jcsr.2007.02.002

[11]   He Y. J., Zhou X. H., Xu L., 2009. Stability of a cylindrical ILTDBS reticulated mega-structure with single layer LICS substructures. Journal of Constructional Steel Research, Vol. 65: 159-168. https://doi.org/10.1016/j.jcsr.2008.05.013

[12]   He Y. J., Zhou X. H., Xu L., 2009. Formation and stability of a cylindrical ILTDBS Reticulated mega-structure braced with single-layer latticed membranous shell substructures. Thin-Walled Structures, Vol. 47: 537-546. https://doi.org/10.1016/j.tws.2008.10.001

MECHANICAL RESPONSE ANALYSIS AND TREATMENT MEASURES OF PARTITION WALL OF METRO STATION

LAI Jin-long [1], LIU Jin-liang [2,] AN Jian-yong [1] JIA Hang [1] and MA Jia [1]*

1. *China Construction Second Engineering Bureau Ltd, Huabei company, Beijing, 100160, China*
2. *Northeast Forestry University, School of civil engineering, Harbin, 150040, China; jinliangliu_2015@126.com*

ABSTRACT

In the process of metro station construction, the partition wall is usually used to prevent the displacement of the soil behind the wall to ensure the construction platform. This research aims to analyze the response of partition wall to keep the safety of the structure. The time-horizontal displacement and cracks of the partition wall are measured during the process of metro station construction. The finite element software FLAC 3D is used to simulate the response of partition wall, and the reasons of partition wall cracking and displacement are analyzed by finite element simulation and measurement data. The stiffness and self-stability of the partition wall in the station is powerful, the stress concentration appeared on the central area and caused cracks of the partition wall. Reducing the pressure exerted on the partition wall and shifting partial pressure exerted on the partition wall by the construction of the medium plate can solve the tress concentration problem. Through the data analysis of the strengthened partition wall, the reinforcement effect is good, ensuring the safety of the subsequent construction. The causes of partition wall cracking are found during process of metro station construction, and the solution proposed in this paper is effective. Engineers can refer to this paper to analyze the response of partition wall in the construction of similar structures, which can ensure construction safety and reduce construction cost.

KEYWORDS

Metro station, Partition wall, Force response analysis, FLAC 3D, Construction method

INTRODUCTION

Following unceasing economic development of world, the infrastructure facilities are being quickly built. In the process, metro has become the most important constituent of a city and the development mark, in addition, it has also become one of the important traffic tools for the resident. The construction of metro station often faces underground interleaved pipelines or pipe packs, for facilitating the construction of metro station, these pipelines or pipe packs need to be moved and restructured. However, a long move time will affect the construction period of metro station, therefore, for the avoidance of elongation of construction period, solution measures are necessary. The present usual measure is to divide one station into two parts for construction and two foundation pits are excavated for construction of main structure. In such case, partition facilities are necessary at the separation location for assuring the stability of foundation pit in the excavation process, therefore, it is quite necessary to carry out a force response analysis for the separation location of metro station.

On basis of the site environment of Chengdu metro station, XU utilized FLAC difference software to carry out a simulative calculation for the surrounding structure of station and the

Article no. 15

THE CIVIL ENGINEERING JOURNAL 1-2021
----

excavation of foundation pit, analyzed the reasonable insertion depth of the surrounding pile in the stratum of expansion soil and the changes of the increment of axial force of lateral bracing , the maximum pile movement and the displacement of pile end against expansion force, in addition, raised the measures for assuring the stability of surrounding structure [1]. ZHANG used FLAC 3D software to simulate the deformation of the surrounding structure of open-excavation metro station under force, carried out a comparison analysis for the calculation results and the site monitoring data and made the following conclusions: Following the increase of the diameter of the surrounding pile, the horizontal of pile body apparently reduces. However, overlarge diameter of surrounding pile is not apparently helpful for controlling the deformation of pile body [2]. For the special geological and geomorphic features in Nanning region, CHEN analyzed and investigated the deformation of various tiers of side slope and surrounding structure. The result shows that, if a bracing is used at pile top or not greatly affects the stability of pile, it is not suitable to apply cantilever pile as surrounding structure, due to the effect of the excavation of deep foundation pit, self-support structure, gravity stress and expansion properties of rock mass, horizontal deformation and vertical upheaval with different degrees appear on the top and face of various tiers of side slope [3]. A case study of interaction between a monitored deep excavation and existing buildings is presented by MOHAMED [4]. And the set of measurements obtained with different monitoring devices have been compared with the 3D numerical analysis using a finite difference code in which the dewatering is taken into account through an uncoupled flow-mechanical calculation. A good agreement is observed between the numerical results and the monitoring data. Short remarks regarding the prediction of the excavation behaviour by means of 2D compared to 3D numerical analysis results are briefly issued. An advanced finite element analysis model was developed to simulate the dynamic interactions among the soil, partition walls, and subway station by considering different connection modes for the diaphragm wall and sidewall and the effect of the initial static stress by ZHUANG [5]. The results show that the existence of diaphragm wall will strengthen the lateral stiffness and reduce the lateral deformation of underground subway station, however, in some cases, it is not entirely for preventing a seismic damage in the underground subway station. This paper presents a comparison between the diaphragm wall movements from FEM analysis predictions and field measurements for two projects by TEPARAKSA [6], the new Bank of Thailand head office and the Rosewood Hotel, which were constructed with different techniques. The predicted movement agreed well with the field measurements.

This paper took a three-floor metro station as the background and the surrounding structure of the station applied partition wall. The station passes electric power pipe rack, for avoiding the effect on construction period, the partition wall was built in the middle of station. In combination with actual engineering situations and monitoring data, the paper carried out a force response analysis for the partition wall in the construction. In addition, finite element software FLAC 3D [7,8] was used to simulate force response of partition wall. Then, the reasons of partition wall cracking and displacement are analyzed by finite element simulation and measurement data. Finally, the paper proposed corresponding solutions for the force status of the partition wall, which can provide a reference for the subsequent similar situations.

PROJECT DESCRIPTION

Main structure

The paper takes a three-floor station of a metro project as the background, the station was designed as three-story, one-island and one-side type, which can transfer train with the existing stations. The main structure of the station is 163.25m long, the standard segment is 31.35m wide, the island-type platform is 13m wide, the side-type platform is 4m wide, the standard segment is 26.85m deep and the end well is 29.39m deep. Furthermore, the partition wall is 31.35m long, 1m wide and 26.85m deep.

Enclosure structure

The enclosure structure of the station applied a system combining partition wall and internal bracing. Between the station and the existing stations, partition wall with 600 mm thick was applied, the enclosure structures in other segments applied partition wall with 1000 mm thick. I-steel connection with excellent watertight effect was used. The deformation of foundation pit and the environment protection level of the project were considered as level one. The total plane enclosure length of the partition walls was 395.874m, the standard length of wall segment was 6m (partially 5m), 69 segments were divided for constructed. The first and the fourth internal bracing applied reinforced concrete bracing, the second, the third, the fifth and the sixth internal bracing applied steel bracing.

Engineering background

Affected by the move & reconstruction construction period of electric power pipe rack, the partition wall used for the main foundation pit of the metro station was hard to be closed as scheduled, therefore, it was necessary to add underground continual partition wall at electric power pipe rack. The location of the partition wall is shown in the following Figure 1 and Figure 2. Concrete bracing and steel bracing were applied inside the station. In the east to the partition wall, partial structures had been done, only the first concrete bracing and the second steel bracing were left for construction in site. The first concrete bracing was 1.5m below ground, the second steel bracing was 6.5m below ground, the medium plate in the negative one floor was being constructed, the height was 9m below ground; due to electric power pipe rack, in the west to the partition wall, one segment of partition wall was respectively left for construction on the south and north side, therefore, the east and west side of the partition wall were constructed simultaneously. In the construction process of the partition wall west to the partition wall, channel-forming disturbance and running of large equipment brought large side pressure for the partition wall, caused such defects of the partition wall as cracking and deformation, which left large hidden safety hazards to the east structure.
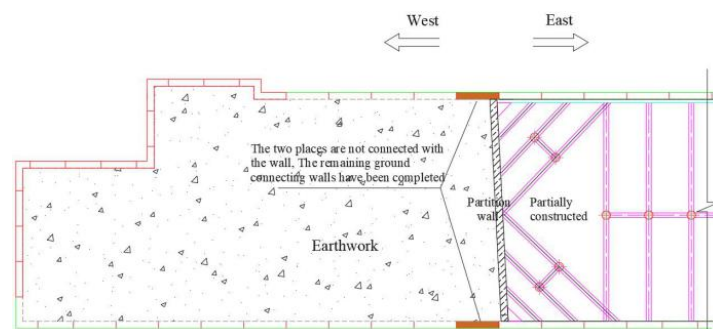

Fig. 1 - Position of underground continuous partition wall
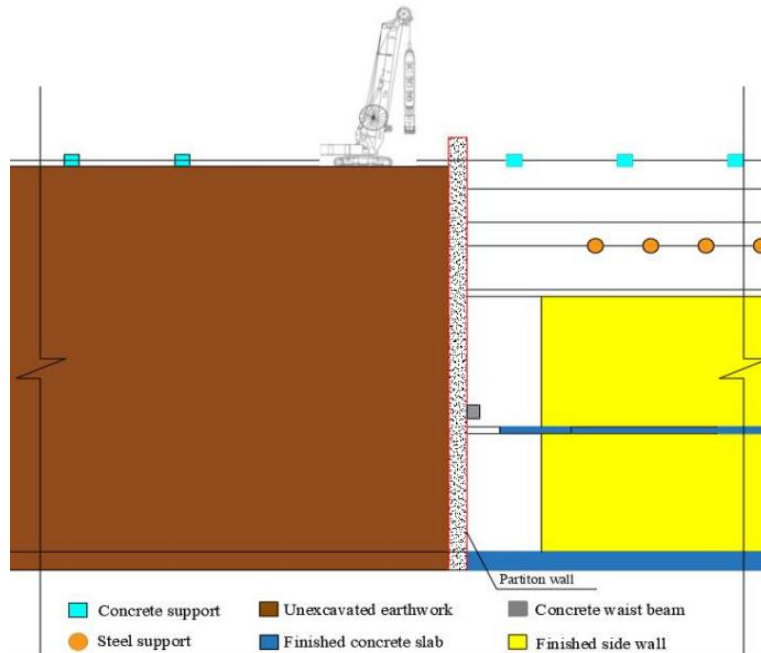
Fig. 2 - Longitudinal section of metro station

According to actual site progress, in the west to the underground continual partition wall, the remained partition wall was being constructed, the method of forming channel by hydraulic grab was applied. In the east to the underground continual partition wall, the reinforced bar used for the medium plate of negative one floor was being bound, within 10m below the first steel bracing, there was not a structure supporting to the partition wall. In the construction of the remained partition wall, apparent crack appeared in the partition wall, the sketch map on the location of crack is shown in Figure 3.
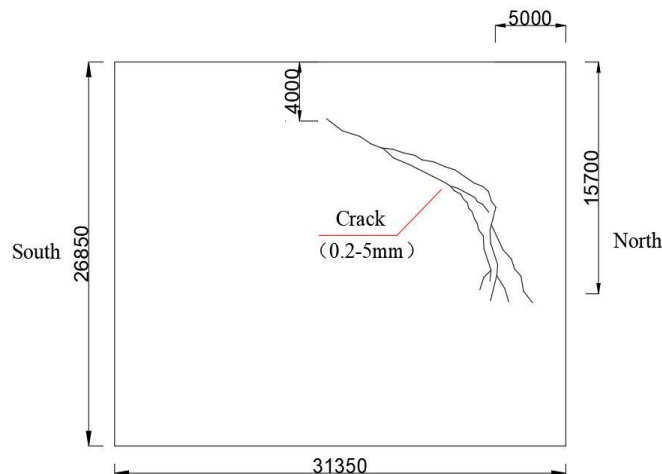

Fig. 3 - Position of crack on the partition wall

Figure 3 shows that the crack appeared at the location 5m to the north partition wall and 4~15.7m below ground. The following four main reasons were analyzed:

(1)   In the west to the partition wall, partition wall was being built, hydraulic grab channel-forming method was used, the disturbance caused by the slurry inside channel and hydraulic grab generated a large side pressure on the partition wall;

----

(2)   In the west to the partition wall, the secondary backfill of the old electric power pipe rack was not dense, slurry oozed and caused a large water pressure to the partition wall;

(3)   The use of such large machineries as hydraulic grab in the construction of partition wall generated a large eccentric pressure on the partition wall;

(4)   In the east to the partition wall and within the scope of 10m below the first steel bracing, there was not a structure, therefore, the lateral force at the partition wall was hard to effectively transmit to the main structure.

As mentioned above, the eccentric force undertaken by the partition wall within the scope exceeded the standard anti-crack value of wall, many cracks appeared [9,10]. Therefore, it is quite necessary to investigate the effect of the construction of the partition wall in the west to the partition wall on the partition wall.

PARTITION WALL MODEL

In order to further analyze the force at the partition wall, the paper utilized finite element software FLAC 3D for simulating the force at the partition wall, elastomer model was adopted. The concrete strength grade is C35, the volume modulus of material was $1.75×10^4$MPa, the shear modulus was $1.3125×10^4$MPa, the elasticity modulus was $3.15×10^4$MPa, the poisson ratio was 0.2, the constitutive relation adopted multilinear intensification model; the elasticity modulus of load-bearing reinforced bar used $2.05×10^5$MPa, the constitutive relation adopted bilinear isotropic intensification model. The model applied Kinematic Hardening Criterion and Mises Yield Criterion with isotropic intensification [11]. In the division of entity grid, hexahedron was applied. Between common reinforcement and concrete, node was used for coupling, the slippage between reinforcement and concrete was not considered. For the four corners at the bottom of the partition wall, XYZ direction was restrained; for the four corners at the top of the partition wall, XY direction was restrained. The division on model grid is shown in the following Figure 4.
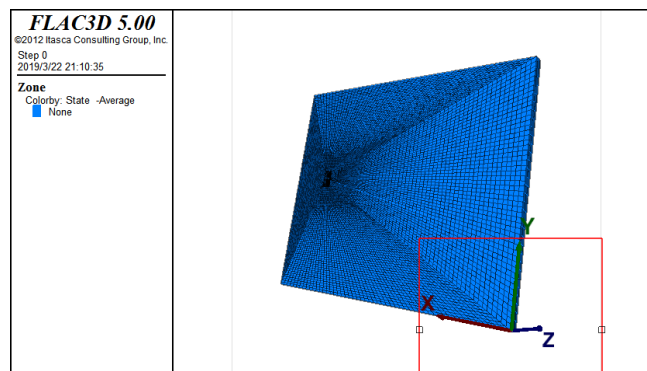

Fig. 4 - Partition wall model

ANALYSIS FOR MONITORING DATA AND MODEL

In case of a defect in construction site, it is quite important to seek for the reasons, effects and formulate the solutions. As mentioned previously, the cracking reasons of the partition wall in the metro station were introduced and a force model was established, in order to further analyze the effect of the crack on the station, the paper analyzed the monitoring data and the data calculated on basis of the model, defined the location with the largest force at the partition wall, analyzed its effect on the station, simultaneously, raised corresponding solutions for subsequent construction [12].

Analysis for monitoring data

Location of monitoring point

In consideration of risk, 14 monitoring points were arranged at the partition wall, the monitored data included horizontal displacement of wall(ZQT), surface settlement(DBC), groundwater level(DSW), supporting axial force(ZCL), vertical displacement of wall top(ZQC) and horizontal displacement of wall top(ZQS), etc. The locations of the monitoring points are shown in the following Figure 5.
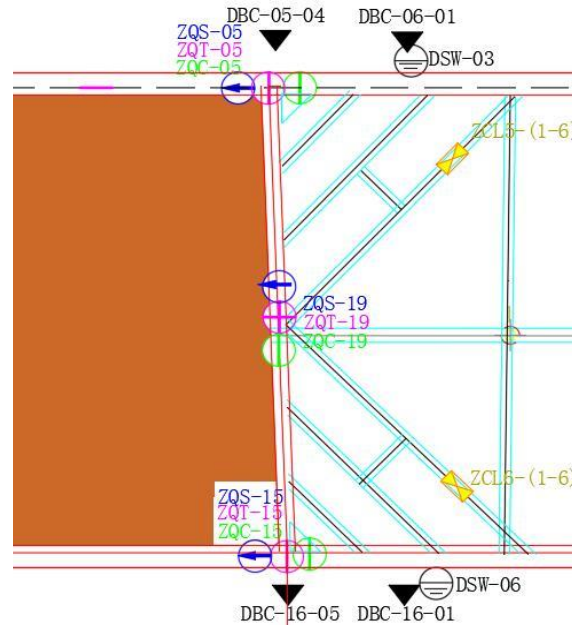

Fig. 5 - Position of monitoring points

Analysis for the data of the monitoring point

By analyzing, it is intuitively reflected that the data of all monitoring points are the horizontal displacement of the partition wall. Taking the monitoring point ZQT-19 as an example, these data were collected, the monitoring data half a month before and after a crack appeared in the partition wall were selected for drafting the curve of time-horizontal displacement on partition wall, as shown in Figure 6.
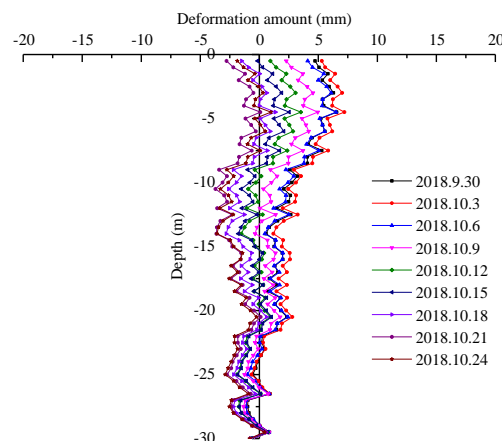

Fig. 6 - Curve of Time-Horizontal displacement on partition wall

By analyzing the curve of time-horizontal displacement on partition wall, the following conclusions may be made:

(1)   Following the continual increase of the burial depth of the partition wall, the deformation of the partition wall generated by external force becomes more and more small, main reasons: the bottom plate had been built, the partition wall had been linked with the bottom and inlaid into earth mass, therefore, the lower deformation is small.

(2)   The deformation of the underground continual partition wall is small, even at the time of cracking of the partition wall, the maximum deformation is only 5mm, this shows that the stiffness of the partition wall is large, the deformation caused by external force is small and the self-stability is powerful.

Model analysis

Through the above analysis on the monitored data, it is found that the stiffness of the underground continual partition wall is large and the self-stability is powerful. However, in the construction process of the adjacent partition wall west to the partition wall, crack appeared in the partition wall, this phenomenon shows that possible stress concentration occurred. Because the data could not be effectively monitored, finite element model was used to carry out a simulated force response analysis, seek for the most unfavourable force-bearing location, so as to raise corresponding solutions timely [13,14].

After a model was established, data analysis and calculation were carried out. After the displacement deformation attained by model calculation and the displacement deformation attained by monitoring were compared, as shown in Figure 7 and Table 1.
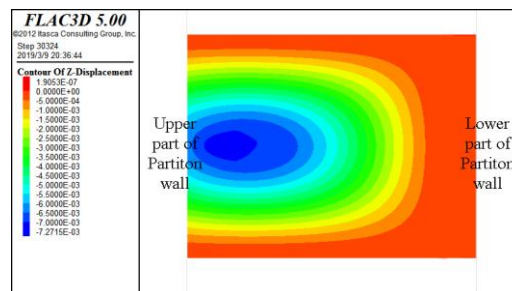

Fig. 7 - Cloud diagram of displacement deformation

Tab. 1 - Comparison between model data and monitoring data

Displacement deformation (mm)	Depth of foundation pit (m)						
	-1	-5	-10	-15	-20	-25	-30
monitoring data f_t	5.58	7.21	4.49	2.58	1.92	0.67	0.57
model data f	5.72	7.27	4.86	2.96	1.95	0.73	0.62
DR	2.51%	0.83%	8.24%	14.73%	1.56%	8.96%	8.77%

DR=difference ratio= (f - f_t)/ f_t

It is found that the error between both is smaller than 15%, the result shows that the model is correct. Subsequently, the model calculation results were used to output positive stress cloud picture in YY direction, as shown in Figure 8.
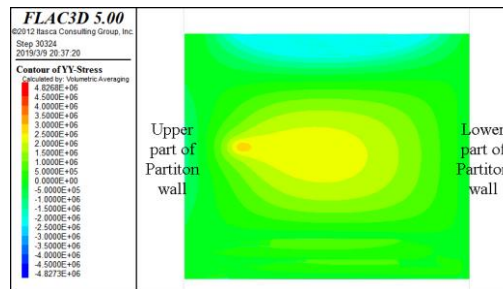
Fig. 8 - Cloud diagram of positive stress in YY direction

The following conclusions may be made after the cloud diagram of positive stress in YY direction is analyzed:

(1)   At the orange yellow location of the above figure, the partition wall cracks, it shows that the stress in the area is large and reaches 1.81MPa in the stress cloud picture. According to *Concrete Structure Design Specification GB 50010-2010*, the designed tensile strength of C35 concrete is 1.57MPa, the force borne by the concrete in the area is larger than the design strength, therefore, crack appeared on the surface of the partition wall.

(2)   For the blue area in the stress cloud picture, i.e. the area linking the partition wall and the north partition wall, the force is large and reaches 2.03MPa, the data shows that such area has overlarge force, it is possible that a large crack occurred, therefore, it is necessary to take timely measures for consolidating the partition wall for assuring the safety of subsequent construction.

TREATMENT MEASURES AND RESULTS

Treatment measures

Through the above calculation analysis on the monitored data of the partition wall and the finite element model, it was found that the stiffness of the partition wall is large and the self-stability is powerful. However, stress concentration appeared inside and caused crack of the partition wall in the stress concentration area. For assuring the safety of subsequent construction, the following measures were proposed:

(1)   When it was found that the partition wall cracked, the construction of the partition wall west to the partition wall was paused immediately, so as to avoid a larger impact force that might extend the cracks.

(2)   Because the medium plate in the negative second floor east to the partition wall was not directly built to the partition wall, steel bracing would be increased between the medium plate in the negative second floor and the partition wall, the interval is 2m, so as to assure that the pressure was transferred by the partition wall to the main structure;

(3)   Quickening the construction of the medium plate in the negative first floor until the partition wall, so as to bear partial pressure exerted to the partition wall.

Results

After the above treatment measures were taken to strengthen the partition wall. The model of partition wall was established again, and cloud diagram of positive stress was obtained, as shown in Figure 9.
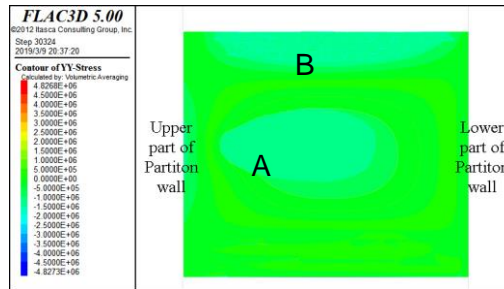
Fig. 9 - Cloud diagram of positive stress in YY direction after taking measures

The stress at the maximum stress point of the partition wall before and after reinforcement (i.e. A and B points in the figure above) were compared, and the data was shown in *Table* 2.

Tab.- 2 Stress comparison of A and B before and after reinforcement

Stress (MPa)	Before reinforcement	After reinforcement
A	1.81	0.56
B	2.03	0.69

The following conclusions can be obtained from the data analysis in the above table:

(1)   The stress at point A reached 1.81MPa before reinforcement, and the design strength of concrete has been exceeded and cracks have been produced. After reinforcement, the stress in this area was reduced to 0.56MPa. This shows that the cracks in this area have been effectively controlled and will not continue to expand, so subsequent construction can be carried out.

(2)   The stress at point B reached 2.03MPa before reinforcement, and it is connected by the ground connecting wall on the north side, so it cannot be observed directly. There may be large cracks in this area. After reinforcement, the stress in this area was reduced to 0.69MPa. This value is less than the design strength of concrete specified in the code, which indicates that the area has reached the safety index after reinforcement and can be used for subsequent construction tasks.

CONCLUSIONS

The paper took a three-floor station of a metro project as the background, in combination with the engineering practices that the partition wall to be used in the project cracked in the construction of other partition walls, analyzed the monitoring data on the partition wall, utilized the finite element software FLAC 3D for simulating the force at the partition wall, subsequently, proposed corresponding solutions on basis of the force borne by the partition wall, made the following conclusions:

(1)   The stiffness and self-stability of the partition wall in the station is powerful, the stress concentration appeared on the central area and caused cracks of the partition wall;

(2)   Reducing the pressure exerted on the partition wall and shifting partial pressure exerted on the partition wall by the construction of the medium plate can solve the stress concentration problem.

(3)   Through the data analysis of the strengthened partition wall, the reinforcement effect is good, ensuring the safety of the subsequent construction, and guiding the relevant construction work.

REFERENCES

[1]. XU Ren-zhong, YUAN Shun-de. (2016),"Analysis of stress and deformation in enclosure structure of metro foundation pit in expensive soil stratum", *Railway Engineering*, (02):84-87.

[2]. ZHANG Ming-ju, HE Huan, LI Chun-hui, et al. (2013),"Deformation and Force response analysis on Retaining Structure of an Open-excavated Subway Station by Monitoring and Numerical Simulation", *Journal of Beijing University of Technology*, 39(6):875-880.

[3]. CHEN Xin-nian, GUO Ying, HE Xiao-li, et al. (2014),"Analysis on the Deformation Laws of Deep Foundation Excavation of Subway Station in Soft Rock Area in Nanning", *Construction Technology*, 43(01):96-99+108.

[4]. MOHAMED Nabil Houhou, FABRICE Emeriault, ABDERAHIM Belounar, (2019),"Three-dimensional numerical back-analysis of a monitored deep excavation retained by strutted diaphragm walls", *Tunneling and Underground Space Technology*, (83), 153-164.

[5]. ZHUANG Hai-yang, YANG Jing, CHEN Su, et al. (2019),"Seismic performance of underground subway station structure considering connection modes and diaphragm wall", *Soil Dynamics and Earthquake Engineering*, (127), 105842.

[6]. TEPARAKSA Wanchai, TEPARAKSA Jirat, (2019),"Comparison of diaphragm wall movement prediction and field performance for different construction techniques", *Underground Space*, 4(3), 225-234.

[7]. GUO Ying. (2014), "The Study of Deformation Laws of Deep Foundation Pit and Its Design at a Metro Station in Xi'an", *Master thesis of Xi'an University of Science and Technology*, China.

[8]. XIAO Feng. (2014), "Three-dimensional force-deformation characteristics research of subway station with cover and excavation top down method construction process", *Master thesis of Beijing Jiaotong University*, China.

[9]. WEI Ran. (2014), "Study on the Deformation Law of Retaining Structure with Monitoring Data and Numerical Simulation", *Master thesis of Shijiazhuang Tiedao University*, China.

[10]. JIANG Kai. (2013), "Structure Force response analysis of Metro Station Built by Cover-excavation Method and Numerical Simulation Stud, *Master thesis of Beijing Jiaotong University*, China.

[11]. Mokhatar S N , Sonoda Y , Zuki S S M , et al. Simulation of Shear and Bending Cracking in RC Beam: Material Model and its Application to Impact[J]. IOP Conference Series Earth and Environmental Science, 2017, 140(1):012130.

[12]. WANG Jian-ning, MA Guo-wei, ZHUANG Hai-yang, et al. (2019)," Influence of diaphragm wall on seismic responses of large unequal-span subway station in liquefiable soils", *Tunneling and Underground Space Technology*, (91), 102988.

[13]. GUO Pan-pan, GONG Xiao-nan, WANG Yi-xian. (2019),"Displacement and force analyses of braced structure of deep excavation considering unsymmetrical surcharge effect, *Computers and Geotechnics*, (113), 103102.

[14]. ZHUANG Hai-yang, WANG Rui, SHI Pei-xin. (2019),"Seismic response and damage analysis of underground structures considering the effect of concrete diaphragm wall", *Soil Dynamics and Earthquake Engineering*, (116), 278-288.

DISPLACEMENTS OF SIDE WALLS WITH WALL-GIRTS IN INDUSTRIAL BUILDINGS UNDER VERTICAL SETTLEMENTS

Noemí M. Subelza[1], Verónica A. Pedrozo[1], Rossana C. Jaca[1] and Luis A. Godoy[2]

1. *Universidad Nacional del Comahe, Facultad de Ingeniería, Departmento Ingeniería Civil, Neuquén, Buenos Aires 1400, Argentina; sube_09@outlook.com, veropedrozo@gmail.com, rossana.jaca@fain.uncoma.edu.ar*
2. *Instituto de Estudios Avanzados en Ingeniería y Tecnología (IDIT), CONICET-Universidad Nacional de Córdoba, 5000 Córdoba, Argentina, luis.godoy@unc.edu.ar*

ABSTRACT

The localized settlement of columns in large metal industrial buildings induces out-of-plane displacements of side walls of the same order as the settlement, which may affect service conditions in the building. For a structural configuration formed by frames, side-walls and wall-girts, this work reports results from testing a small-scale model together with computational modeling of the full-scale structure. Dimensional analysis was used to scale the geometry and properties from full-scale to small-scale, leading to an overall scale factor of 1:15. Differential settlements having a controlled amplitude were imposed at the central column, and displacements were monitored using mechanical devices. The computational model employed shell elements for side-walls and wall-girts. Good agreement was found between tests and computer modeling. The results at the full-scale level, indicate that, for settlements likely to occur in granular soils, the associated lateral displacements exceed those allowed by current US regulations. Stiffening the structure was investigated by use of stiffer girts, as well as by reducing their spacing. The influence of frame height was also investigated. The overall conclusion is that out-of-plane displacements of side-walls may easily exceed allowable values unless they are specifically considered at a design stage.

KEYWORDS

Buckling, Finite elements, Settlement, Industrial buildings, Small-scale modeling, Wall-girts

INTRODUCTION

The effects due to localized settlements of part of the foundation in metal industrial buildings are not taken into account at a design stage; however, they frequently occur during the service life of a building. Such problems may become important when the building is constructed on compressible soils, in which the load-bearing capacity depends on soil type and moisture contents. Metal industrial buildings designed to process and store agricultural products are often built in zones with natural or artificial irrigation, in which the soil may lose part of its load-carrying capacity. Further, soil moisture may increase due to seasonal rains or due to accidents in an adjacent channel or piping system.

Light-weight industrial structures have low redundancy in their load-transfer mechanisms, so that differential settlements may cause changes in the way equilibrium is provided by the frame and roof system. Of special concern in this paper are settlements between adjacent columns or at the corners of a building.

Damage due to vertical settlements may affect the main resisting structure, secondary elements, and equipment protected by the construction, and their consequences are typically observed as out-of-plane displacements in the side walls. Such lateral displacements arise due to buckling of the side walls under imposed vertical displacements [1]. All this may weaken the overall structural strength and stiffness of the building; and may also affect the service conditions of the building, including the normal functioning of large sliding doors.

Only a small number of references have focused on this problem with reference to sustainability issues [2]. Effects of support settlements have been considered in metal cylindrical shells [3]. Buckling of storage tanks due to support settlements was studied by Godoy and Sosa [4], Zhao et al. [5], Gong et al. [6], Cao and Zhao [7] and Fan et al. [8]. Darmawan [9] reported severe damage induced by column settlement on a metal frame structure. The non-linear behavior of soil in a two-story frame building was studied by Agrawal and Hora [10]. All those results were based on computational modeling. Codes of practice, such as ASCE [11], specify limits to lateral displacements of the side walls in metal buildings in the order of H/400 to H/600, where H is the height of the building. Such limits were established based on wind pressures acting on the building and do not considerer either buckling or settlement of supports.

Previous works by the authors showed that the out-of-plane displacements in side walls due to vertical settlements are larger than allowed values when considering the main resisting structure but neglecting the contributions of secondary elements in side walls [1]. This paper aims to evaluate the influence of wall-girts as a strengthening aid in cases of localized support settlement in metal industrial buildings.

FULL-SCALE PROTOTYPE AND REDUCED-SCALE PHYSICAL MODEL

A physical model was built and tested in this research in order to obtain empirical evidence to validate computer models. A full-scale prototype was first defined and then a small-scale model was built using similitude theory (see, for example, [12]).

Full-scale prototype

With reference to Figure 1, the geometry of the prototype was characterized by height H, height of columns h, frame width B, and span between frames ℓ. The main resisting structure is formed by a set of steel frames, whereas secondary elements include wall panels which are strengthened by wall-girts and roof purlins.
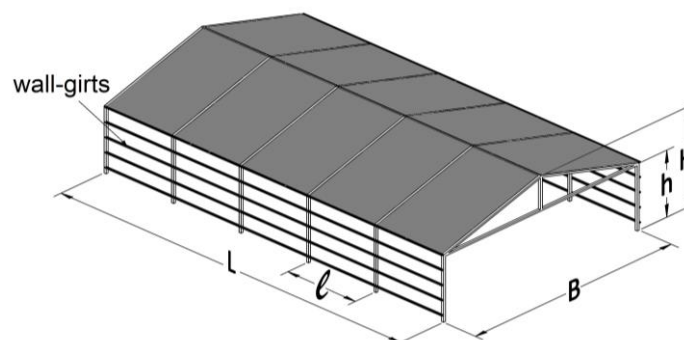

Fig. 1 – Geometry used to describe full-scale and small-scale model in this work.

Previous studies [1] showed that settlement of a single column may have severe consequences on the side walls that extend to the next frame in both directions, but do not extend further to other frames. For this reason, the fabricated model was limited to three frames, which includes the side walls with five wall-girts, whereas the computational model could use symmetry conditions and reduce the domain of interest to two frames, as shown in Figure 2.a. The initial case-study investigated had H = 6m, h = 4m, ℓ = 5m, and B = 15m. Separation between girts, shown in

Figure 2.a, was s = 0.90m. Such secondary elements are considered in this work to investigate their influence in reducing side displacements. The roof purlins and wall-girts were assumed as a C-shape cold-formed cross section with dimensions shown in Figure 2.b. The values of dimensions for the assumed prototype are given in the second column in Table 1.
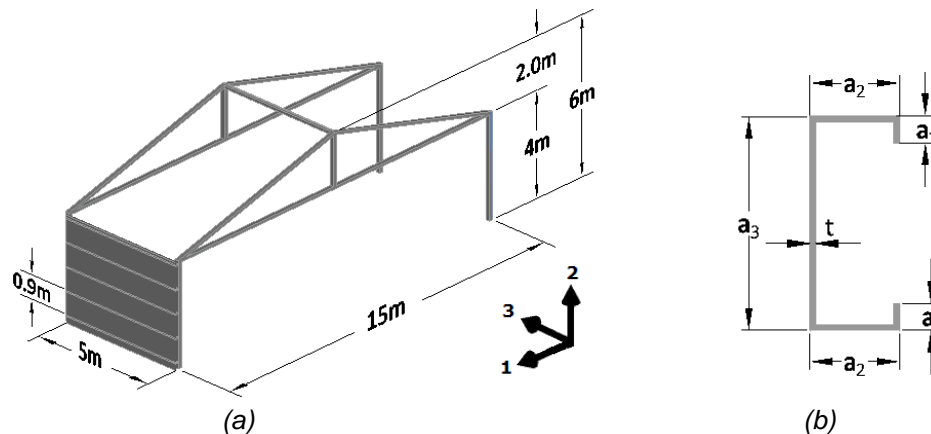

(a)   *(b)*

Fig. 2 – Geometric characteristics, (a) Symmetric geometry investigated by computational analysis in this work for the prototype, (b) Cross-sectional geometry of C-shape cold-formed wall-girts.

Tab. 1: Geometry of cross section of wall-girts (Figure 2.a). Values in [mm].

	Prototype	Small-scale model of prototype	Small-scale simplified model
a_1 [mm]	15	1	0
a_2 [mm]	50	3	2
a_3 [mm]	120	8	6
t [mm]	3.2	0.07	0.22

The side-walls in the prototype were initially assumed with a trapezoidal T1010 section. However, for both computational and experimental modeling, the cross section was substituted by another one with uniform thickness, in which the thickness was evaluated to have the same modulus of inertia as the trapezoidal section. This yields an equivalent thickness of side walls equal to t_{wall}=9.6mm. The modulus of elasticity of steel was assumed as E_p = 204GPa, with density ρ_p = 7850Kg/m^3.

Reduced-scale physical model

The full-scale building was modeled down to reduced-scale dimensions, and the resulting small-scale model was fabricated and tested during this research. Geometric similitude was used to scale the geometry, together with a similitude to represent the constitutive materials. The overall dimensions in Figure 2.a were scaled down to B_m = 1m, so that there is a scale factor in the geometry given by:

$$\alpha_A = \frac{B}{B_m} = 15 \tag{1}$$

This scale factor α_A was used to identify the geometry of the small-scale physical model, leading to model dimensions H_m = 400mm, h_m = 267mm, ℓ_m = 333mm, and s_m = 60mm. However, because of the considerable differences between the overall building dimensions and the side wall panels and wall-girts, different scale factors were used to identify the thicknesses, thus leading to a geometrically distorted model.

The adopted material for the main frame in the model is aluminum with a square cross-section having 12mm sides, with elastic properties are E = 70GPa, µ = 0.33. The side walls were made of acetate sheets with commercially available thickness t_m = 0.22mm. Mechanical properties for acetate were evaluated following ASTM D882-02 [13] and the values were E_m = 2294MPa (Young´s modulus) and μ_m = 0.4 (Poisson´s modulus), the density were also measured (ρ_m = 1320Kg/m³). The material scales for acetate are thus given by:

$$\theta = \frac{E_p}{E_m} = 89 \quad and \quad \gamma = \frac{F_p}{F_m} = \frac{\rho_p * (\ell * h * t)}{\rho_m * (\ell_m * h_m * t_m)} \quad with \quad \frac{\rho_p}{\rho_m} = 5.95 \tag{2}$$

where γ is the ratio between the weight of side wall panels (F_p for prototype and F_m for small-scale model). The scale factor for thicknesses is

$$\alpha_B = \frac{t}{t_m} = 43.6 \tag{3}$$

As required, the relation between θ, γ, and α satisfies the condition

$$\theta = \frac{\gamma}{\alpha_A * \alpha_B} \tag{4}$$

The third column in Table 1 (small-scale model of prototype) shows the cross section of a wall-girt under a scale factor 15 and 43.6 for thickness. However, such details could not be achieved in the small-scale model, with the consequence that a simplified section with dimensions shown in the fourth column of Table 1, based on an equivalence of the moment of inertia, were used.

(a)   *(b)*

Fig. 3 – Model testing at a 1:15 geometric scale: (a) General view of the three-frame configuration in the small-scale model; (b) Device used to impose vertical displacements at the central column.

The settlement was induced in the central column, as shown in Figure 3.b. The settlements of the column and the out-of-plane displacements were measured with 0.01mm precision. The relations between the imposed settlements in prototype and model are shown in Table 2. Limits in prototype settlement are usually given as 25mm in civil engineering structures (see, for example, [14] [15]).

Tab. 2: Applied settlements in prototype and model.

Settlement	Prototype	5	7	9	10	20	25
[mm]	Model	0.33	0.47	0.6	0.67	1.33	1.67

EXPERIMENTAL RESULTS FOR THE SMALL-SCALE PHYSICAL MODEL

Testing was carried out by imposing a vertical displacement at the central column, thus causing a relative displacement δ with respect to the side frames. To facilitate visualization of points on the side walls, a grid formed by 30 × 30 mm squares was drawn in the model. As a consequence of this vertical displacement, there are out-of-plane displacements w on the side walls, forming diagonal shear bands with alternate inwards and outwards displacements. These bands form a V-shape with a vertex at the joint between wall-girts and column, being symmetric with respect to the central column in which δ is imposed. The displacements in the model are scaled up to the prototype dimensions by use of the scale factor $\alpha_A = 15$, so that inwards and outwards displacements in the horizontal direction of the prototype can be plotted in Figure 4.
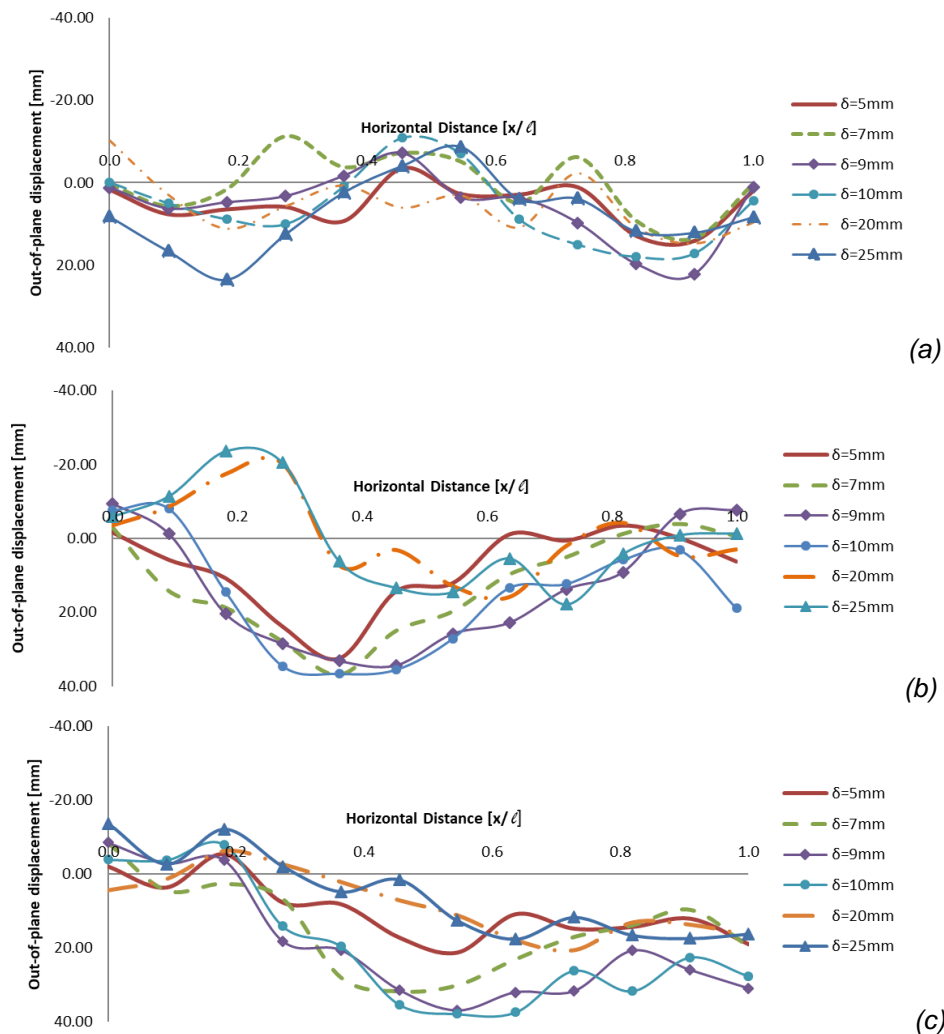

Fig. 4 – Out-of-plane displacements (w) due to vertical settlement 5mm < δ < 25mm. The horizontal axis spans from 0 at the central column to x/ℓ = 1 at the next column. (a) Variation at 0.90m (z/h=0.225) from bottom level; (b) at 2.25m (z/h=0.563) from bottom level; (c) at 3.15m (z/h=0.79) from bottom level.

The deflected shape is a function of settlement, with nonlinear changes in shape and amplitude. For example, for δ = 5mm there are outward displacements in Figure 4.b with a maximum of about w = 35mm; this increases to close to w = 50mm at δ = 10mm; but for larger settlements δ = 20mm and δ = 25mm the lateral displacement becomes inwards in the order of w = 25mm. On the other hand, the number of bands increases with increasing δ. A reduction in w is seen to occur near the columns and wall-girts, which induce a restraint to lateral deflections. This effect can also be

noticed in Figure 5, in which the vertical variation of displacements along the central column and at two intermediate positions, is shown, together with the location of the wall-girts in elevation.
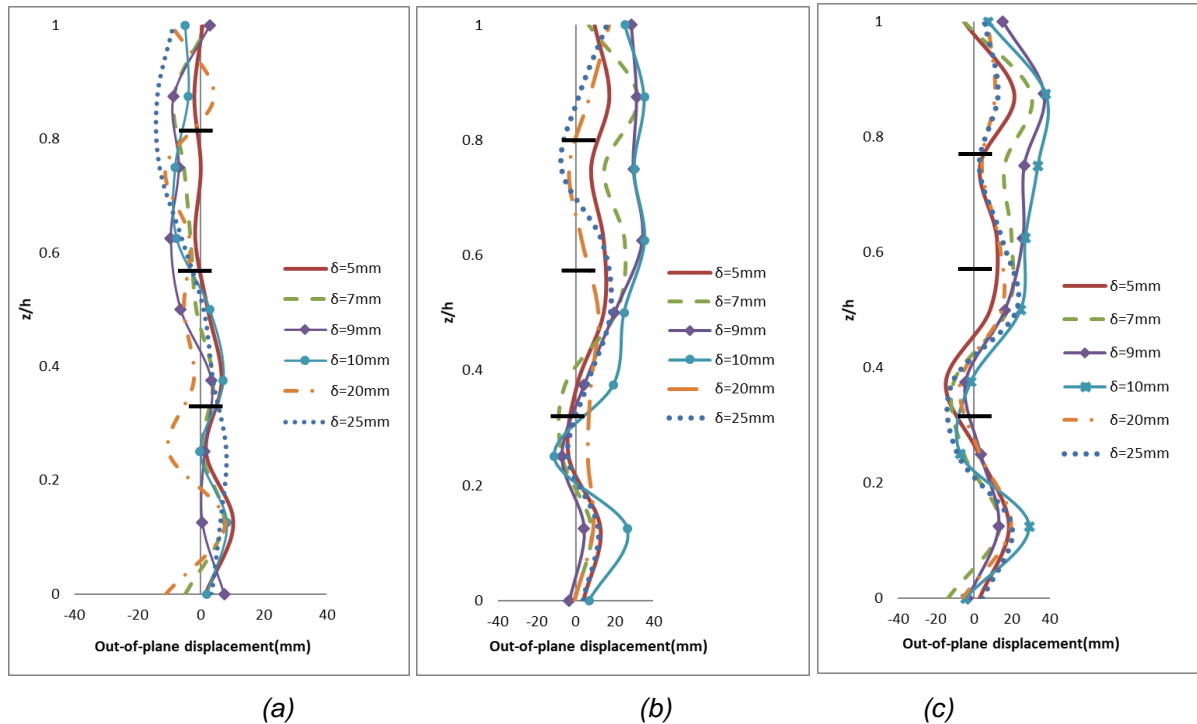

(a)   *(b)*   *(c)*

Fig. 5 – Out-of-plane displacements (w) due to vertical settlement 5mm < δ < 25mm. (a) Variation at the central column(x/l=0); (b) at 2.27m(x/l=0.45) from central column; (c) at 2.72 (x/l=0.54) from central column.

A summary of results is shown in Table 3, in which inward displacements (w) are identified with negative values; and outward displacements are positive values. The largest outward displacement occurs for δ = 10mm, whereas the largest inward displacement occurs for a low value δ = 5mm.

Tab. 3: Maximum and minimum lateral displacements, in [mm].

δ [mm]	5	7	9	10	20	25
Maximum [outward]	32.4	36.9	36.9	37.8	27.3	33.3
Minimum [inward]	-30.2	-29.1	-30.0	-29.3	-24.8	-25.7

Displacement maps are plotted in Figure 6. Wall-girts are also shown in the figures to facilitate visualization of restrains introduced by secondary elements. The general trend is the development of inclined bands, with an angle close to 45° for δ = 10mm, and the inclination reduces to about 32° for δ = 25mm. There is a clear incidence of wall-girts on displacements, not just by affecting their amplitude but also by modification of the shear bands. Previous computational models [1] showed continuous bands because wall-girts were not included in the model.
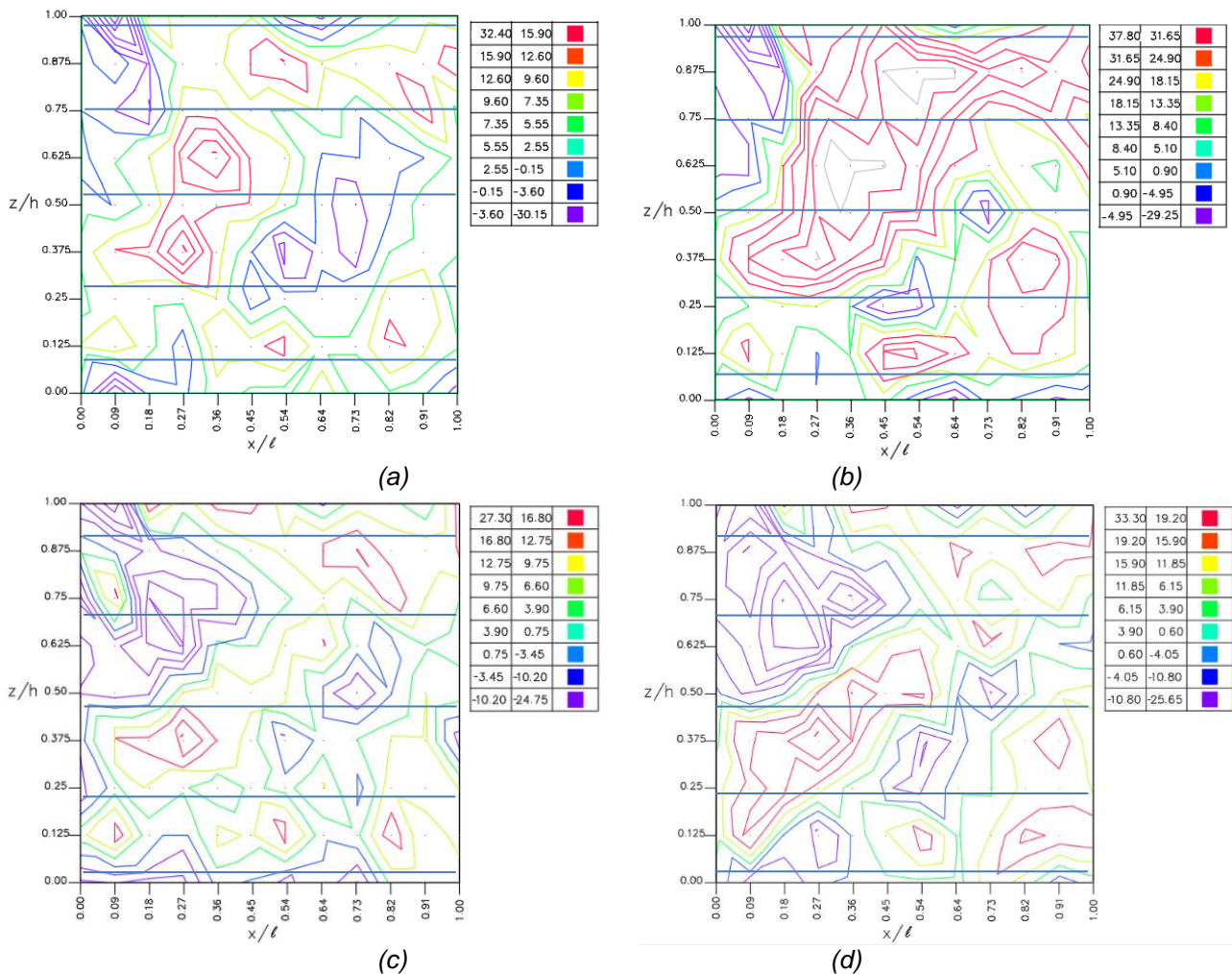
Fig. 6 – Maps of out-of-plane displacements for settlements (a) δ = 5mm; (b) δ = 10mm; (c) δ = 20mm; (d) δ = 25mm

FINITE ELEMENT MODEL AT FULL-SCALE

Configuration investigated

The prototype structure has been investigated using a finite element model [16]. The analysis requires modelling of the frame, wall-girts and side-walls, as shown in Figure 2.a. Structural symmetry was used to reduce the number of unknowns in the model. Rectangular shell elements (identified as S4R5 in ABAQUS) with five DOF per node and four nodes per element were employed. A finite element mesh with 32,000 elements was defined by means of convergence studies and has been used in the computations reported in the following sections. Wall-girts were modelled using shell elements and the assumed dimensions (120mm×50mm×15mm cross-section and 3.2mm thickness) are shown in Figure 2.b. The separation between girts was 0.90m, thus including five wall-girts in elevation.

Some details regarding modeling of joints need to be presented. (a) Girts are connected with columns by means of welds, which are represented in the model by joint elements identified as "Tie" elements. (b) Side panels are connected with girts by means of screws, and these are modeled by "Beam" joint elements, which restrain displacements and rotations. A total of 100 screws were used in the model, of which 20 were applied in each girt at a spacing of 260mm.

With reference to Figure 2.a, boundary conditions U1 = U2 = U3 = UR1 = UR3 = 0 are imposed at the base of columns that do not have settlement; conditions U1 = UR1 = UR3 = 0, and U2 = 25mm are imposed at the base of the column with settlement; condition U3 = UR1 = UR2 = 0 are used to represent symmetry on the central column; condition U1 = U2 = U3 = 0 is imposed at the joint between wall-girts and column; and conditions U1 = U2 = U3 = UR1 = UR2 = UR3 = 0 are imposed at the screw joints.

Computational results for the full-scale prototype

A geometrically non-linear static analysis was carried out to investigate the full-scale prototype shown in Figure 2.a. The assumed modulus of elasticity was E = 204GPa, with Poisson ratio μ = 0.3. The imposed vertical settlement was taken as δ = 5mm, 10mm, 20mm, and 25mm, to replicate the experiments. The dimensions of girts were considered as in Figure 2.b. To reduce computations, symmetry was used so that only the right-hand side panel is represented in the finite element discretization, as shown in Figure 2.a, and settlement is imposed on the column to the left of this figure.

Results for the case δ = 25mm are shown in Figure 7.a, leading to maximum out-of-plane displacements w = 25.7mm (inwards) and 33.3mm (outwards). The bands are seen to cross the lines of girts in this case, thus forming continuous diagonals. The values are compared with those measured in the tests (see Figure 6.d) and there are only 5% differences in maximum values, with some differences in the diagonal patterns. In the finite element model the displacements w affect the complete side-wall whereas they tend to be localized in the region where the settlement is imposed in the tests. The same number of shear bands occurs in both computational and physical models, with similar inclination.
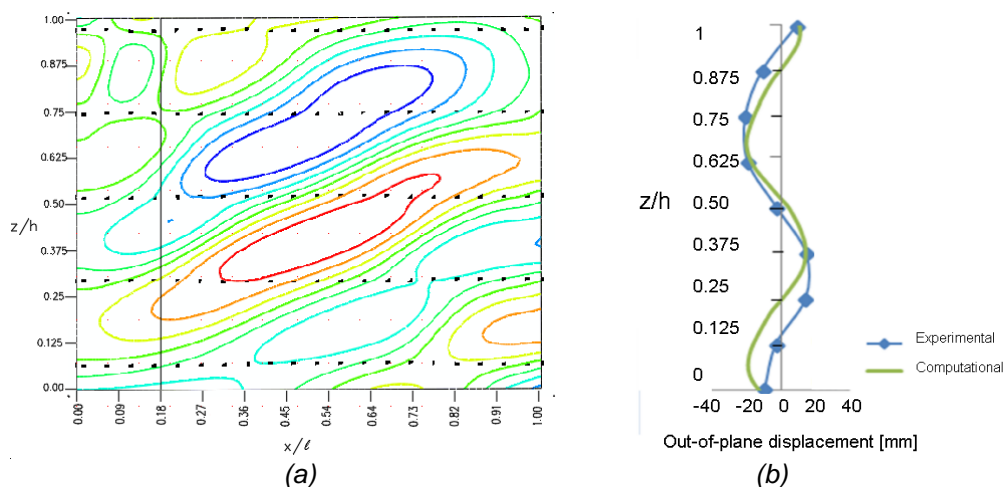

(a)   *(b)*

Fig. 7 – Computational results for δ = 25mm. (a) Map of out-of-plane displacements; (b) Out-of-plane displacements plotted in elevation z/h, at a distance x/l= 0.18 measured from the central column, and comparison with experiments.

A comparison of vertical variation of displacements is shown in Figure 7.b. The computational results seem to capture the main features of the behavior as detected in the physical model, and this provides confidence in pursuing a more thorough understanding of behavior based on computational modeling.

INFLUENCE OF PARAMETERS CONTROLLING THE RESPONSE

To understand the significance of the lateral displacements reported in the previous section, it is important to refer to what is acceptable in practice. ASCE [11] rules establish limits to out-of-plane deflections which range between H/400 and H/600; in the present case this means bounds between 15mm and 10mm. Such bounds are clearly exceeded by the values reported in the present

study. Thus, it would be desirable to understand what parameters may affect the response in order to reduce such lateral displacements.

Influence of strengthening the cross section of wall-girts

Computational modeling is used in this section to illustrate the influence of the stiffness of wall-girts on lateral deflections under a given settlement. In each case the separation between girts remains fixed at 0.90m, and the cross sections are modified as shown in Table 4. The thickness of the wall-girts is taken as t = 3.2mm, and the overall dimensions change from cases P1 to P7. The case already taken as case study in the previous section is P1. Although typical cross sections in practice range from P1 to P5, two stiffer cases, P6 and P7, were also investigated to understand what would it take to improve the behavior.

Tab. 4: Geometry of cross section of wall-girts considered in the analyses.
Variables a_1, a_2, a_3, t, are illustrated in Figure 2.b. Values in [mm].

	a_1	a_2	a_3	t
P1	15	50	120	3.2
P2	20	50	140	3.2
P3	20	60	160	3.2
P4	25	70	180	3.2
P5	25	70	200	3.2
P6	25	80	220	3.2
P7	20	80	240	3.2

Results are shown in Figure 8. The order of these figures corresponds to the order of girts in Table 4. In all cases considered in this section, a settlement δ = 25mm is imposed, and separation between girts is 0.90m. As expected, lateral displacements decrease with increasing stiffness of girts. For "weak" girts, the shear bands are continuous and affect the complete panel across girts. For "robust" girts the shear bands are interrupted and extreme values of w occur between girts.

In comparison with girt P1, the sections P2 and P3 cause a reduction of 19%, but more significant changes are found for P4 (30%) and P7 (52%) always measured with respect to P1. The w values for P7 are 22.2mm (outwards) and -21.4mm (inwards), which are about half of those computed for P1. A summary of results is shown in Table 5. Notice that acceptable values according to ASCE (H/400 or H/600) are not met in any case shown in Table 5.
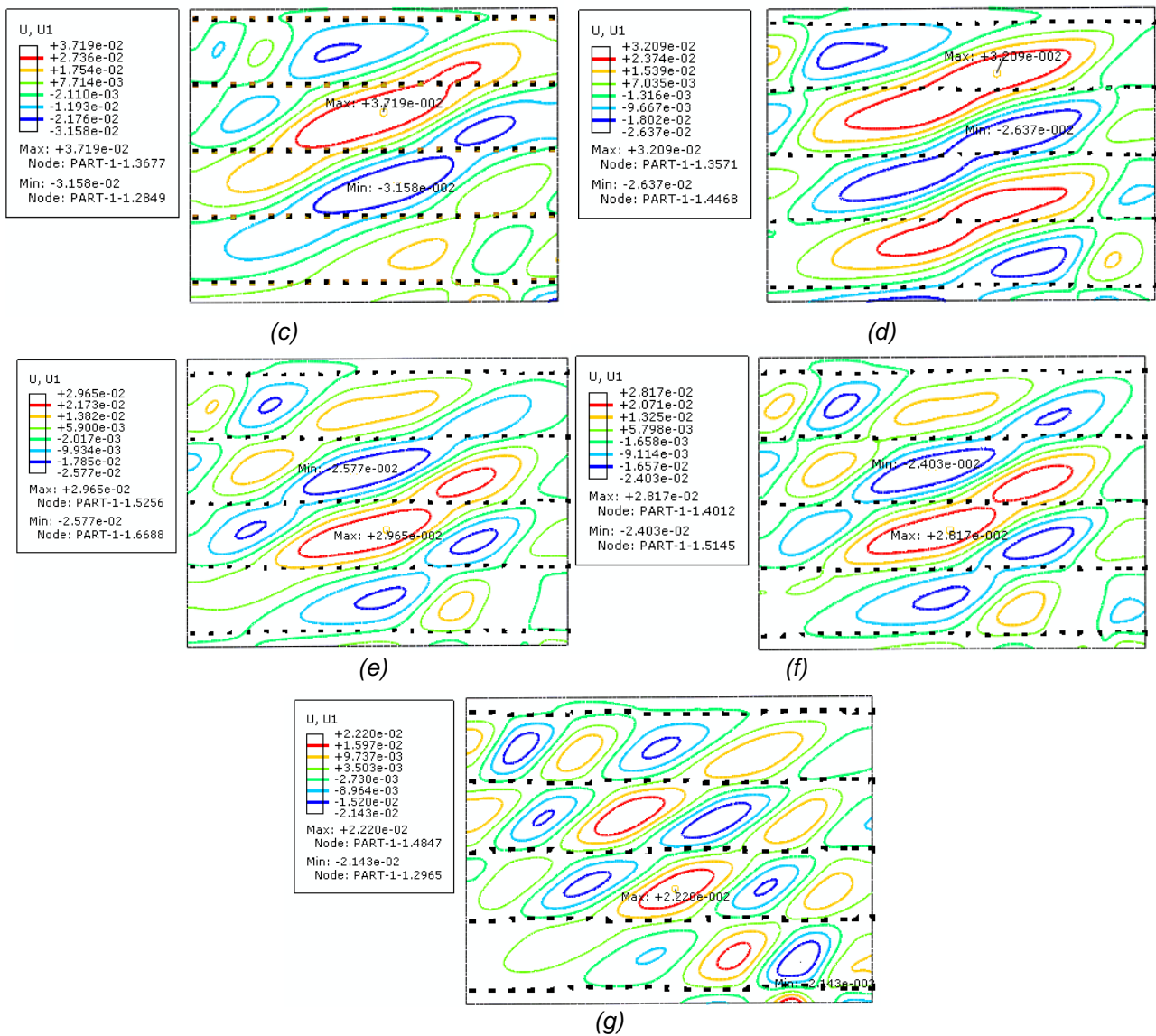

(a)	*(b)*

(c)

(d)

(e)

(f)

(g)
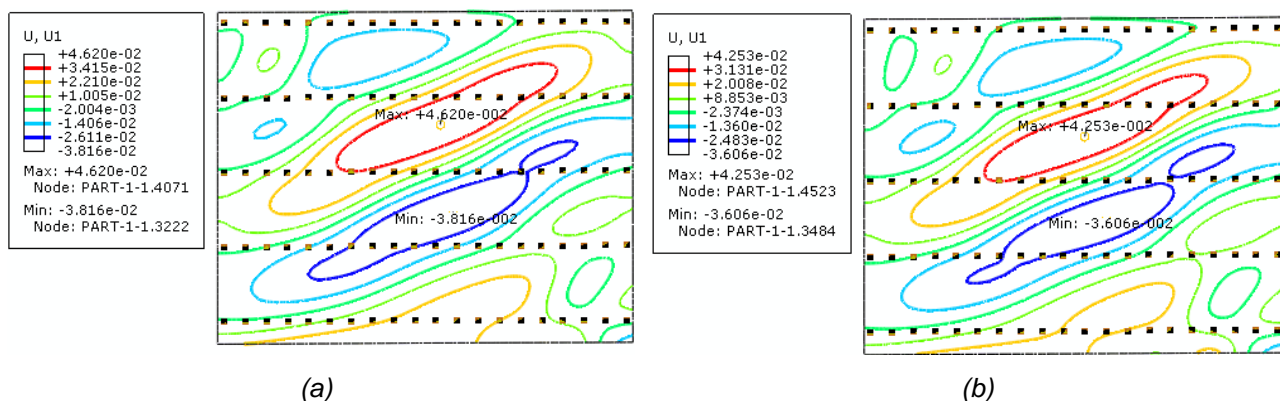
Fig. 8 – Out-of-plane displacements for various cross-sections of girts for δ = 25mm and s = 0.90m. (a) P1, (b) P2, (c) P3, (d) P4, (e) P5, (f) P6, (g) P7.

Tab. 5: Extreme out-of-plane displacements (outwards and inwards) for wall-girt sections of Table 4. Data: H = 6m; s = 0.9m; δ = 25mm.

Wall-girt cross-section	Displacement [mm]		Difference with respect to P1
P1	46.2	-38.1	
P2	42.5	-36.0	-8%
P3	37.2	-31.6	-19%
P4	32.1	-26.3	-30%
P5	29.6	-25.7	-36%
P6	28.2	-24.0	-39%
P7	22.2	-21.4	-52%

Influence of separation between wall-girts

To understand the influence of the separation between wall-girts, their values were reduced from 0.90m to 0.70m and 0.60m, as shown in Table 6. Changes are calculated by comparing the displacements for P1, P2, P3, P4, P5, P6, and P7 in this table with displacements for P1 in Table 5. Because there are positive and negative extreme values, the largest value is considered to compute changes.

Tab. 6: Influence of separation between wall-girts on lateral displacements,
for settlement δ = 25mm. Ridge height H = 6m.

Wall-girt cross-section	Number of wall-girt	Separation [m]	Displacement [mm]		Difference with respect to P1 in Table 3
P1	7	0.6	43.7	-35.2	-6%
P2	7	0.6	37.8	-22.4	-40%
P3	7	0.6	32.1	-23	-39%
P4	7	0.6	25.3	-19.4	-48%
P5	7	0.6	20.7	-16.1	-57%
P6	7	0.6	16.6	-13.8	-63%
P7	7	0.6	14.3	-12.7	-68%

For reasons of brevity, maps of lateral displacements are not shown here, but the number of bands increases for separation 0.60m, with an inclination of approximately 30°. There is an interruption of bands for P7 caused by the stiff girts. The practical case P5 with separation 0.60m shows a 57% reduction with respect to the reference case P1, but values still exceed those allowed by ASCE specifications.

Influence of ridge height

The influence of the ridge height H of the frame on the deflected pattern was next investigated under an imposed settlement δ = 25mm.

First, consider H = 10m. A summary of results is shown in Table 7 for girt separations in the range s = 0.90m to s = 0.50m, and for various cross-sections of girts. Changes in the last column were computed with respect to values for P1 in the first row.

Tab. 7: Out-of-plane displacements for a frame with H = 10m under
an imposed settlement δ = 25mm

Wall-girt cross-section	Separation (m)	Displacement [mm]		Difference with respect to P1
P1	0.9	43.84	-44.8	
P2	0.9	41.92	-35.9	-20%
P3	0.9	34.9	-31.1	-31%
P4	0.9	26.9	-25.3	-44%
P5	0.9	24.5	-27.1	-44%
P6	0.9	25.4	-22.2	-50%
P7	0.9	24.2	-23.4	-48%

P1	0.5	36.4	-30.5	-32%
P2	0.5	28.6	-24.5	-45%
P3	0.5	23.5	-20.6	-54%
P4	0.5	15.9	-15.2	-66%
P5	0.5	14.2	-11.9	-73%
P6	0.6	13.66	-13.7	-69%
P7	0.6	11.4	-13	-74%

Tab. 8: Out-of-plane displacements for a frame with H = 8m under an imposed settlement δ = 25mm.

Wall-girt cross-section	Separation (m)	Displacement [mm]		Difference with respect to P1
P1	0.7	37.12	-38.21	
P2	0.7	32.06	-32.58	-15%
P3	0.7	31.90	-27.03	-29%
P4	0.7	26.62	-24.66	-35%
P5	0.7	19.9	-16.3	-57%
P6	0.7	17.2	-15.9	-58%
P7	0.7	17.04	-14.79	-61%

Because of the increase H with respect to the previous results reported in this work for H = 6m, the allowable lateral displacements increase to H/400 = 25mm and H/600 = 17mm. For a spacing s = 0.90m, acceptable lateral displacements are reached for girts P4 to P7. Separations of s= 0.50m and s = 0.60m could be acceptable for all alternatives considered, except for P1.

Second, ridge height H = 8m was consider as an intermediate case, and results are shown in Table 8. The limit value for lateral displacements in this case is H/400 = 20mm; thus, wall-girts identified as P5, P6 and P7 with s = 0.70m yield satisfactory side displacements.

Wall-girt size and separation for buildings of different ridge height

Based on results of the finite element analyses, the range of wall-girt size and separation which lead to acceptable displacements in industrial buildings is shown in Figure 9. For ridge height equal to or larger than 6m, the displacements remain within acceptable values for wall-girts equal to or larger than P5 (200mm), with separations smaller than 0.6 m. For buildings with H ≥ 8m, displacements remain acceptable provided wall-girt size is at least P4 (180 mm) and separation is s ≤ 0.6m. Finally, admissible displacements in buildings with H ≥ 10m are achieved by using P4 or larger, with s ≤ 0.9m, or else P2 (140mm) with s ≤ 0.5m.
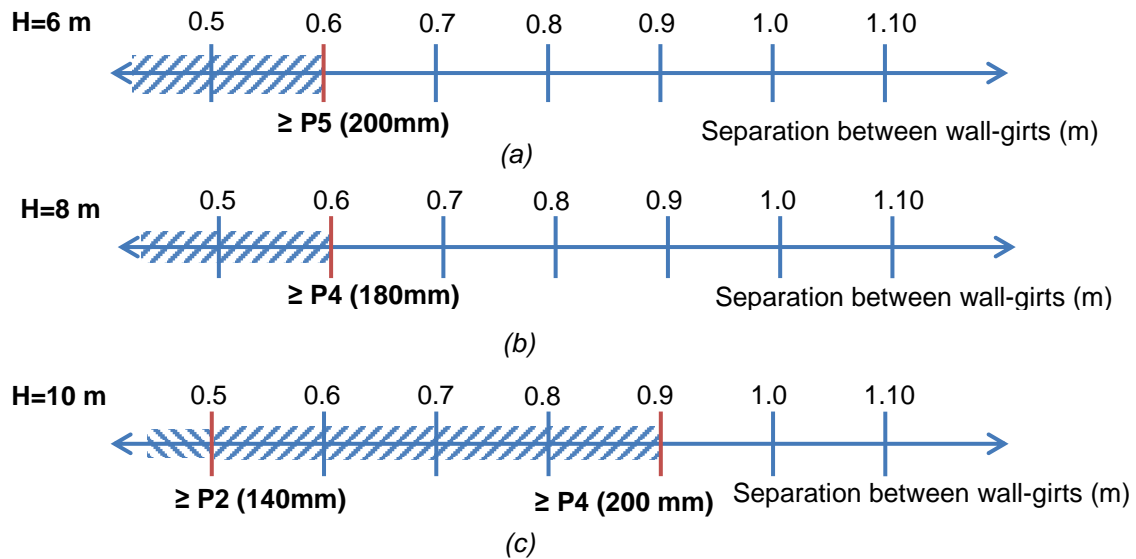
Fig. 9 – Wall-girt configuration for industrial buildings having different ridge height H. (a) H = 6m; (b) H = 8m; (c) H = 10m. Shaded separations are acceptable.

COMPARISON WITH OUT-OF-PLANE DISPLACEMENTS UNDER WIND LOADS

Wind loaded industrial buildings are investigated in this section in order to compare out-of-plane displacements with those derived from foundation settlements. For low rise buildings, i.e. H≤20m, ASCE [11] specifies the following expression for the pressure q_z on the windward walls:

$$q_z = 0.613 K_z \, K_{zt} \, K_d \, V^2$$

(5)

where V is the wind speed in [m/s], and q_z is evaluated in [N/m^2] at elevation z. K_{zt} is the topographic factor (with unit value for flat terrain); K_d refers to the direction of wind and a value $K_d = 0.85$ was adopted in this case; and K_z is the exposure factor, and $K_h = 0.9$ was adopted in this case. Wind speed V=48m/s was assumed as a reference value for the design of the industrial building. For a partially enclosed building and for the internal spans between columns, the internal pressure coefficient is (GCpi) =±0.55 whereas the external pressure coefficient is (GCpe) = 0.45.

The maximum displacements computed for the side walls for different locations in elevation are listed in Table 9, together with the limit displacements U_{limit} evaluated as H/400 according to ASCE provisions [11]. To perform calculations, the assumed stiffening was the weakest configuration investigated, i.e. P1 with separation s=0.90m.

Tab. 9: Comparison of out-of-plane displacements for wind and for support settlement, in [mm].

		H=6m	H=8m	H=10m
U_{limit}		15	20	25
U_{max} due to V=48m/s		**1.70**	**1.13**	**1.73**
U_{max} due to support settlement	δ = 3mm		1.58	1.05
	δ = 5mm	1.34	3.70	1.84
	δ = 7mm	1.48		2.89
	δ = 10mm	13.54	20.5	17.6
	δ = 15mm			23.06
	δ = 25mm	46.0	45.2	44.8

The resulting out of plane displacements for wind speed V=48m/s are lower than those specified by the design provisions, and are one order of magnitude lower than those obtained for a support settlement equal to δ = 25mm.

To identify the level of settlements that induce out-of-plane displacements of similar value to those due to wind, results for several values of δ are listed in Table 9. The out-of-plane displacements due to wind are similar to those computed for rather small settlements: δ = 7mm for H=6m, δ = 3mm for H=8m, δ = 5mm for H=10m.

Values of U_{limit} are also shown in Table 9, with the consequence that settlements up to δ = 10mm are acceptable in terms of design provisions. Notice that equivalent values under wind would require wind speed much higher than that adopted for the design of the building.

The first conclusion of this comparison is that the out-of-plane dispacements under a support settlement is dominant with respect to wind effects. A second conclusion is that whenever settlements of supports can occur, then some measures should be adopted to control their effects (i.e., following Item 1.3.3 Self-Straining Forces in Ref. [11]) because wind design does not cover this aspect of behavior of lateral walls in desing buildings. Possible remedial actions depend on their economic evaluation in each case, but may include strengthening the side walls by wall-girts, as described in this work; limiting the settlements by strengthening the soil or the foundation; and/or reducing the presence of water around the building.

CONCLUSIONS

Lateral displacements of side walls induced by a vertical settlement of a column were investigated in this work for metal industrial buildings. Two approaches were used in the research, one based on a physical small-scale model and another one based on a geometrically non-linear finite element model of the structure. The computational modeling was validated by comparison with the small-scale model tested. Finite element results included maps of lateral displacements for various wall-girt configurations for a given settlement at a column.

Based on the results, some conclusions may be drawn:
- The computational model discussed in this work adequately represents displacement levels obtained in the physical model. The maximum displacements tend to be located at the center between wall-girts.
- Because side-walls made with acetate are very flexible in the physical model, the deflected patterns tend to be interrupted at wall-girts, and there are some differences with patterns obtained in the finite element model, which tend to be continuous bands.
- Lateral displacements obtained in this work are considerably reduced (by approximately 50%) with respect to previous studies, in which the influence of wall-girts was not considered [1].
- Decreasing the separation between wall-girts and increasing their cross-section cause significant reductions in lateral displacements, and also change the deflected pattern by an interruption in shear bands as they cross the wall-girts.
- To satisfy limits to displacements established by current ASCE regulations, the wall-girt configurations are more stringent in shorter than in taller frames, as given by ridge height. Such limits in ASCE were established based on wind effects and do not take into account effects due to settlement or buckling.
- The out of plane displacements in side walls computed for small settlements (in the order of 5mm) are similar to those due to wind speed as used at the design stage.
- Special attention should be given to vertical support settlements larger than 10mm and they should be monitored during the service life of the structure. Remedial actions may include stiffening the lateral walls by means of wall-girts or improving the soil/foundation capacity.

ACKNOWLEDGEMENTS

REFERENCES

[1]   Fernández, S., Jaca, R.C., Godoy, L.A., 2015. Behavior of wall panels in industrial buildings caused by differential settlements. Structural Engineering and Mechanics, vol. 56 (3): 1-18, dx.doi.org/10.12989/sem.2015.56.3.443.

[2]   Švajlenka, J., Kozlovská, M., Pošiváková, T., 2018. Analysis of selected building constructions used in industrial construction in terms of sustainability benefits. Sustainability, vol. 10: 4394, doi:10.3390/su10124394.

[3]   Jonaidi, M., Ansourian, P., 1998. Harmonic settlement effects on uniform and tapered tank shells. Thin-Walled Structures, vol. 31: 237-255, doi.org/10.1016/S0263-8231(98)00007-X.

[4]   Godoy, L.A., Sosa, E.M., 2003). Localized support settlements of thin-walled storage tanks. Thin-Walled Structures, vol. 41: 941-955, doi.org/10.1016/S0263-8231(03)00043-0.

[5]   Zhao, Y., Cao, Q.S., Xie, X.Y., 2006. Floating roof steel tanks under harmonic settlement: FE parametric study and design criterion. Journal of Zhejiang University, Science A, vol. 7(3): 398-406, doi.org/10.1631/jzus.2006.A0398.

[6]   Gong, J., Cui, W., Zeng, S., 2012. Buckling analysis of large-scale oil tanks with a conical roof subjected to harmonic settlement. Thin-Walled Structures, vol. 52(7): 143-148, doi.org/10.1016/j.tws.2011.12.011.

[7]   Cao, Q.S., Zhao Y., 2010. Buckling strength of cylindrical steel tanks under harmonic settlement. Thin-Walled Structures, vol. 48(6): 391-400, doi.org/10.1016/j.tws.2010.01.011.

[8]   Fan, H., Chen, Z., Shen, J., Cheng, J., Chen, D., Jiao, P., 2016. Buckling of steel tanks under measured settlement based on Poisson curve prediction model. Thin-Walled Structures, vol. 106: 284-293, doi.org/10.1016/j.tws.2016.05.009.

[9]   Darmawan, M.S., 2009. A case-study of structural assessment of steel structure subjected to differential settlement of foundation. 1st Int. Conf. on Rehabilitation and Maintenance in Civil Engineering (Solo, Indonesia), 312-320.

[10]   Agrawal, R., Hora, M.S., 2010. Effect of differential settlements on nonlinear interaction behavior of plane frame-soil system. ARPN Journal of Engineering and Applied Sciences, vol. 5(7): 75-87.

[11]   ASCE STANDARD ASCE/SEI 7–10, 2010, Minimum Design Loads for Buildings and Other Structures, American Society of Civil Engineers, Reston, VA, USA.

[12]   Szirtes, T., 1998. Applied Dimensional Analysis and Modeling (McGraw Hill) 853 pp.

[13]   ASTM D882–02, 2002. Standard Test Method for Tensile Properties of Thin Plastic Sheeting. American Section of the International Association for Testing Materials, USA.

[14]   USACE EM 1110-1-1904, 1990. Settlement analysis (U.S. Army Corps of Engineers) 205 pp.

[15]   Bowles, J.E., 1988. Foundation Analysis and Design. 4th Edition (Ed. McGraw Hill Singapore) 1230pp.

[16]   ABAQUS, 2010. Abaqus Inc., Dassault Systèmes, Rhode Island, USA.

NUMERICAL INVESTIGATION OF GLASS-FIBER REINFORCED PLASTIC MORTAR PIPES CULVERT RESPONSE TO HEAVY TRUCK LOADS

Huawang Shi, Chencheng Gu,Chongchong Xue and Yancang Li

Hebei University of Engineering, School of Civil Engineering, Handan, Hebei 056038, China; stone21st@163.com

ABSTRACT

The main objective of this paper is to investigate the dynamic performance and behaviour of glass-fiber reinforced plastic (GRP) mortar pipes under heavy truck loads. According to the field conditions, a finite element dynamic analysis (FEDA) model of GRP pipe culverts was established. Modal analysis of the vibration system was carried out, and the main natural frequencies with 26.6Hz,32Hz,35.7Hz and corresponding mode shapes were obtained. On the basis of modal analysis, dynamic response of GRP pipe culverts under vehicle loads was simulated through random vibration. Based on the measured vibration velocity time histories, the modal and random vibration responses of the vibration system were analyzed. The results show that the spectral response value of pipeline to vehicle load decreases with the increase of buried depth. When the depth of GRP pipe culverts buried is greater than 0.8m, the influence of ground vehicle dynamic loads on the vibration of GRP pipe culverts cannot be taken into consideration. It can provide the basis for the design of GRP pipe culverts, especially under heavy loads.

KEYWORDS

GRP mortar pipe culvert, Finite element analysis, Dynamic response, Vibration properties

INTRODUCTION

Glass-fiber reinforced plastic (GRP) mortar pipe is a kind of new composite materials using resin as matrix material, glass fiber and its products as reinforced material, including quartz sand as filling material made of a certain process. In the 1970s, GRP mortar pipe was developed. As a new type of flexible pipe, it has been widely used in the world due to its good performance such as strong corrosion resistance, high strength, light weight, etc. After confirming that GRP mortar pipe is particularly suitable for underground pipeline, many countries began to apply GRP mortar pipe in municipal drainage and drainage, highway culvert and other fields [1,2].

In the 1960s and 1970s, numerous studies have been conducted on the interaction between pipeline and soil. In 1975, Newmark [3] presented the vibration of the buried pipe. He assumed that the pipe and the surrounding soil were a whole and moved together under the vibration load. According to R. A. Parmelee's study [4], the static Mindlin method was used to calculate the interaction between pipe and soil; T. Zhang et al. [5,6] collected and analyzed a large number of statistical data to find out the causes and solutions of damage and leakage, and then used the original parameter method of elastic semi-infinite plane foundation beam to verify the statistical results.

With the popularization and application of finite element mechanical analysis software, J. Lee [7] simulated the failure of GRP under internal pressure by using finite element analysis software. The results show that the finite element analysis software can be used for the failure

Article no. 17

THE CIVIL ENGINEERING JOURNAL 1-2021
----

analysis of GRP under lower internal pressure. In 1989, J. Jeyk [8] presented a finite element model of GRP mortar pipe by using the finite element analysis software. In this model, the problem of pipe soil contact is considered, and an example is analyzed with this model to summarize the causes of pipe failure. A numerical analysis model of GRP mortar pipe based on ABAQUS was established and its dynamic response under seismic load was investigated and the results are reported in the L. Xu, and Z.C. Ye [9]. Manko and Beben [11,12] measured the strain and vibration velocity of the steel bellows culvert under the dynamic load condition of passing through the vehicle at the speed of 10–70km/h. B. Flener and Karoumi [13] conducted an experimental study on culverts under railway dynamic load. The displacement and strain of the culvert are measured, and the dynamic amplification factor (DAF) is calculated.

At present, most of the dynamic response analysis of bridge and culvert structure is based on the method of field test, which is easily affected by various adverse factors such as cost and environment. In this paper, details including the dynamic response of the buried GRP mortar pipe by using the random vibration module based on the ANSYS Workbench finite element analysis software are discussed. First, the numerical analysis model of GRP mortar pipe is established by workbench, and the corresponding main natural frequencies and modes are obtained by modal analysis. Then the dynamic response of the buried pipe under different working conditions is simulated by the random vibration module. Finally, based on the field measurement data, the feasibility of using workbench random vibration module to analyze the frequency response of buried pipe is verified. It can provide the basis for the safety of engineering design under heavy load, and for the designers to determine the natural frequency and vibration mode of the buried pipe, so as to avoid resonance in the structural design of the buried pipe, and predict the vibration form of the buried pipe under different working conditions in the construction stage.

METHODS

Preparation method of ANSYS

According to the full-field test, the ANSYS finite element numerical model is used to simulate the stress state of pipe culvert. The model size is 10m × 6m × 6m (length × height × width). The length of pipe is 6 m with 1.5m diameter and 0.05m wall thickness [13,14]. The thickness of the pipe wall is much smaller than the pipe diameter, so shell element is used to simulate. The soil is analyzed by 3D solid element [15,16].

Boundary condition

After the numerical model is established, reasonable boundary conditions are applied. In the rectangular soil model, the horizontal displacement constraint is applied to the front and back facades, the horizontal displacement constraint is applied to both sides of the soil, and the full constraint is applied to the bottom.

Contraction between pipe and soil

The material characteristics of backfill and original soil are quite different. The soil is set as elastic system with two-layer: the upper layer is backfilling, and the lower layer is original soil. The vehicle load acts on the pipe indirectly through the soil. Therefore, it is necessary to consider the contact action between the pipe and the soil when establishing the finite element dynamic analysis model of the GRP mortar pipe culvert. In addition to transferring the pressure between the pipe and the soil, there are also friction and relative displacement between the pipe and the soil. In order to describe the nonlinear characteristics of the soil, the soil is set as the target surface, the pipeline as the contact surface, the contact surface between the pipe body and the backfill and the original soil is set as the friction surface, and the friction coefficient is set as 0.15; the contact surface between the backfill and the original soil is set as the bond contact; the model applies the gravity

acceleration perpendicular to the road surface as a whole (g=9.8m/s^2); and the soil constitutive model is the Drucker-Prager(D-P) nonlinear elastic model in finite element analysis. Due to considering the internal friction angle and cohesion of soil, the D-P constitutive model can reflect the nonlinear characteristics of soil.

Material property parameters

The influence of inertia force and damping should be considered in dynamic analysis under the condition of fast loading and impact. This topic analyzes the vibration load of the buried pipe when the vehicle passes through the road, so the influence of damping is ignored. The inertia of the structure should be considered in the dynamic response analysis. The mechanical parameters such as bulk density, modulus of elasticity and Poisson's ratio are given through experiments as shown in Table 1.

Tab. 1 - Material parameters.

Constituents	Unit weight ρ/（kg·m^{-3}）	Poisson's ratio	Modulus of elasticity E/MPa	Internal friction angle φ/°	Cohesion c/kPa	E^1 /MPa	$E^2=E^3$ /MPa	$G^{12}=G^{13}$ /MPa	G^{23} /MPa
Backfill	1940	0.3	32.4	26	20	—	—	—	—
Original soil	1820	0.3	50	35	60	—	—	—	—
Pipe culvert	1800	0.27	—	—	—	3210	8900	2800	1800

Note: E^1, E^2 and E^3 are the elastic modulus in X, Y and Z directions respectively, and G^{12}, G^{13} and G^{23} are shear modulus in X-Y, X-Z and Y-Z plane respectively.

RESULTS AND DISCUSSION

Field test

The total length of the selected road is 33.8km, and the whole line is second-lass highway. The GRP mortar pipes with diameter of DN1500 and wall thickness of 50mm are used as buried pipe culverts. In this test, the characteristic section of pipe culvert is selected as the test section, and the strain change rule of each test point of pipe culvert under different working conditions is tested by pasting strain gauge. In this experiment, the filling height of culvert top is 80cm and 100cm respectively, the weight of roller is 20t, the weight of truck is 40t and 60t respectively, the front and rear wheel axle of truck with speed of 30km/h is directly above the pipe axis, and the truck is in the middle line of road as shown in Figure1.
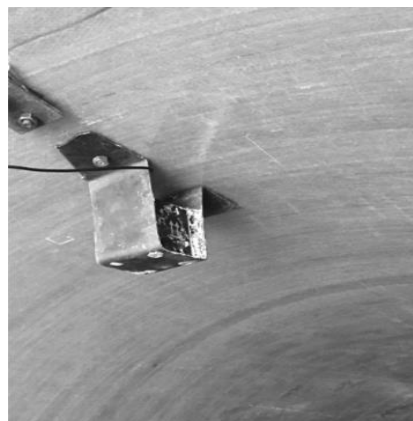

Fig.1 - Test vehicle   *Fig.2 - Speed sensor*

The Q9 wire at the other end of the speed sensor as shown in Figure 2 is connected to four channels of the TST5925EV wireless telemetry dynamic strain analysis system. The sampling frequency is set at 50Hz, and the instrument is continuously sampled for debugging. After all channels are connected correctly, data collection begins.

Test results

The working condition of the buried pipe test is shown in Table 2.

Tab. 2 - Working conditions

Vehicle weight	Height of fill	
	80cm	100cm
20t	Working condition 1#	Working condition 2#
40t	Working condition 3#	Working condition 4#
60t	Working condition 5#	Working condition 6#

Under working condition 1 (20t roller, filling height with 80cm), the vibration speed time history of the top and side of the GRP mortar pipe is as follows:
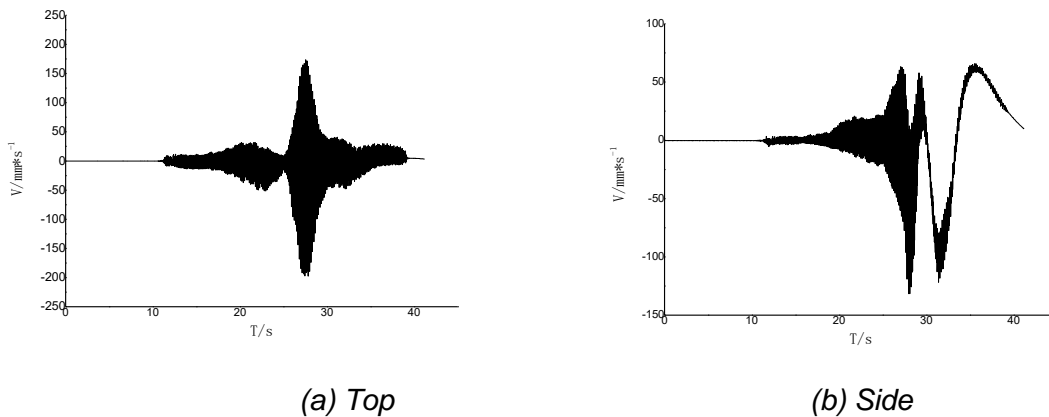

(a) Top   *(b) Side*
Fig.3 - Time history curve of vibration velocity under working condition 1

Under condition 2 (20t roller, filling height with 100cm), the vibration speed time history of pipe top and pipe side is as follows:
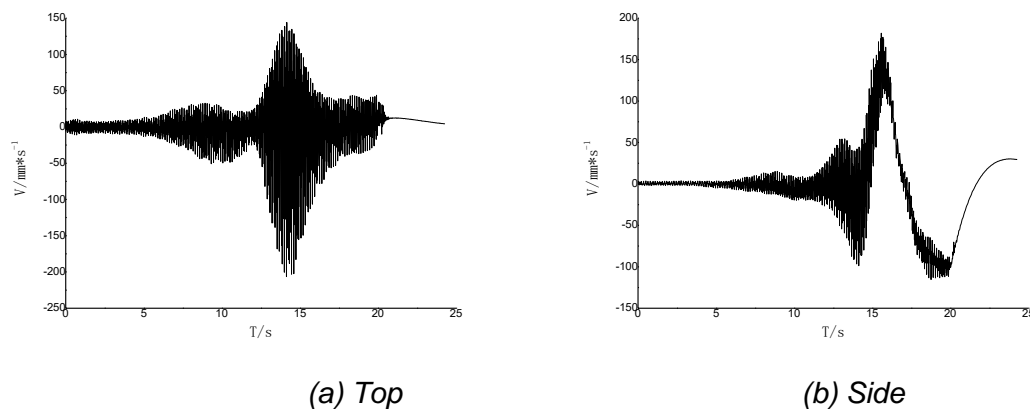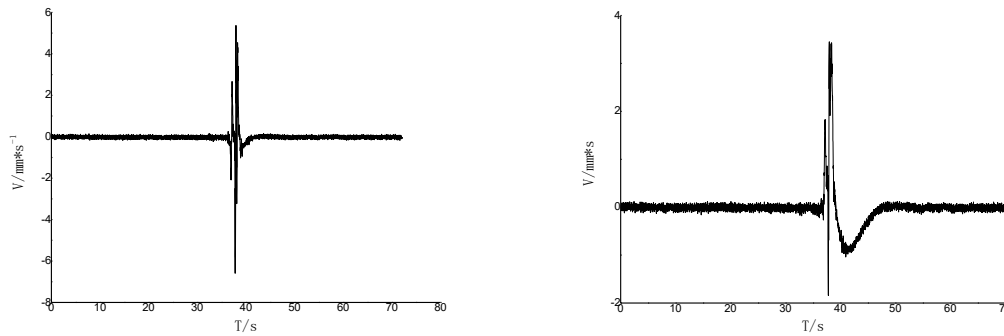

(a) Top   *(b) Side*
Fig.4 - Time history curve of vibration velocity under working condition 2

Under working condition 3 (40t truck, filling height with 80cm), the vibration speed time history of pipe top and pipe side is as follows:

(a) Top   *(b) Side*
Fig.5 - Time history curve of vibration velocity under working condition 3

Under working condition 4 (40t truck, filling height with100cm), the vibration speed time history of pipe top and pipe side is as follows:
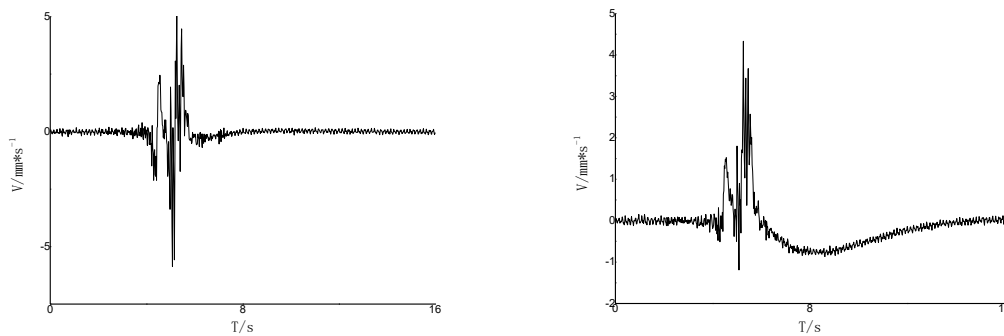

(a) Top   *(b) Side*
Fig.6 - Time history curve of vibration velocity under working condition 4

Under working condition 5 (60t truck, filling height with 80cm), the vibration speed time history of pipe top and pipe side is as follows:

(a) Top   *(b) Side*
Fig.7 - Time history curve of vibration velocity under working condition 5

Under working condition 6 (60t truck, filling height with 100cm), the vibration speed time history of pipe top and pipe side is as follows:
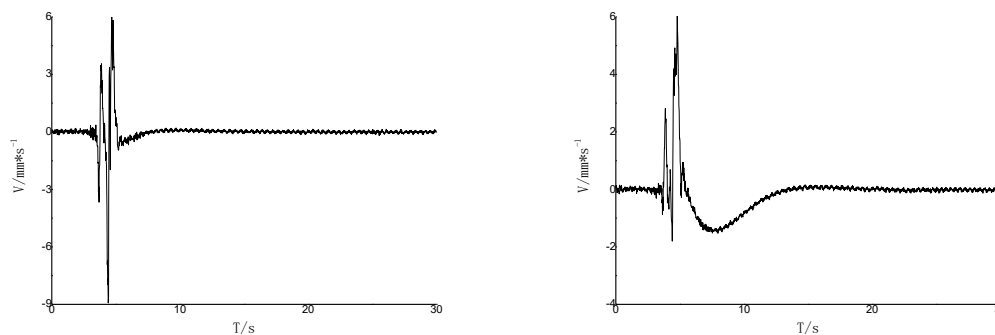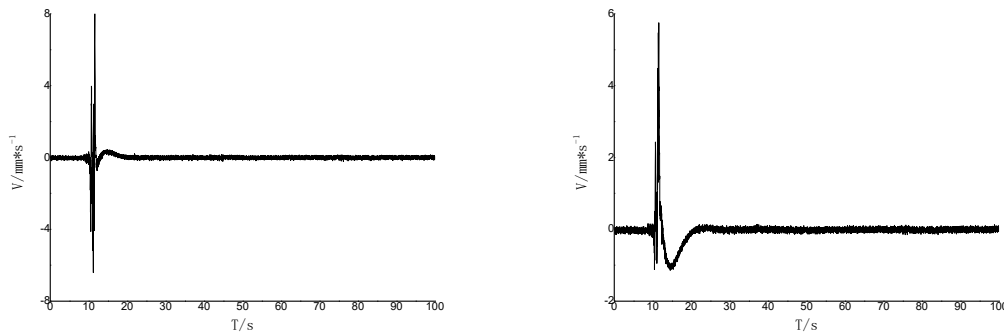

(a) Top   *(b) Side*
Fig.8 - Time history curve of vibration velocity under working condition 6

The fast Fourier transform (FFT) spectrum analysis of the vibration velocity data of the pipe crown and the pipe side under the action of 20T vibrating roller can obtain the spectrum characteristic curve of the pipe top and the pipe side, as shown in Figure 8. In the figure, the horizontal axis is the frequency (Hz), and the vertical axis is the vibration speed (mm/s).
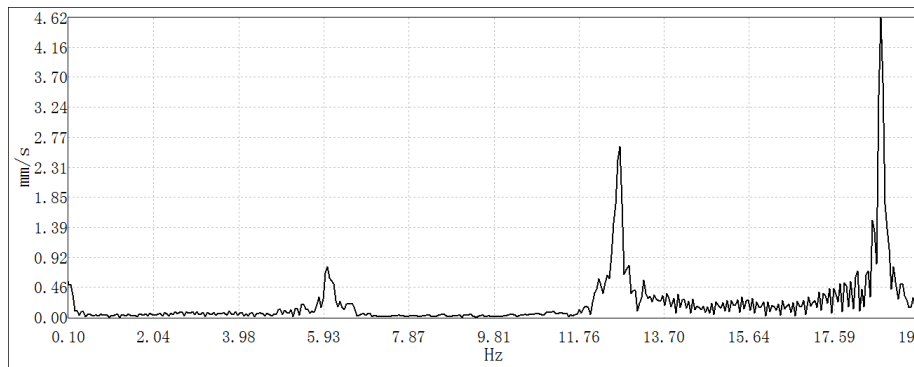
(a) V spectrum curve at the pipe crown
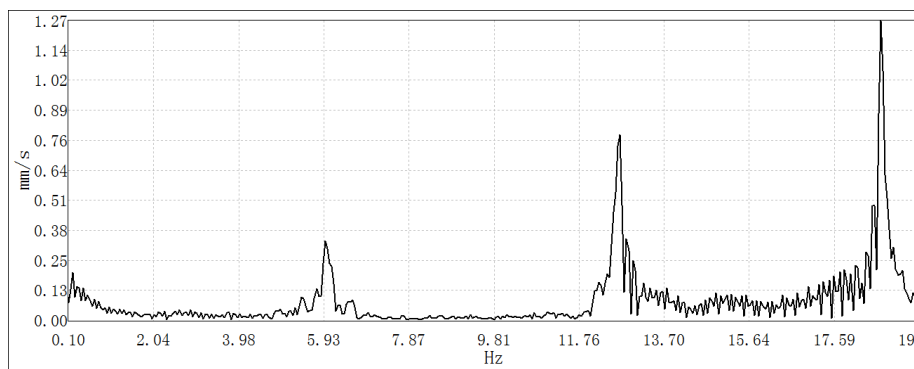
(b) H spectrum curve at the pipe spring line
Fig. 9 - Frequency spectrum of vibration velocity

The vibration speed data of the pipe crown and the pipe spring line are performed with FFT when the 40t heavy-duty engineering dumper is running, and the spectrum characteristic curve of the pipe top and the pipe side can be obtained, as shown in Figure 9. Where, (a) described the

vertical spectrum curve at the pipe crown, and (b) described the horizontal spectrum curve at the pipe spring line.

(a) V spectrum curve at the pipe crown

(b) H spectrum curve at the pipe spring line
Fig.10 - Frequency spectrum of vibration velocity

FFT transform the vibration speed data of the top and side of the pipe when the 60t heavy-duty engineering dumper is running, and the spectrum characteristic curve of the top and side of the pipe can be obtained, as shown in Figure 10. In the figure, the horizontal axis is the frequency (Hz), and the vertical axis is the vibration speed (mm/s).

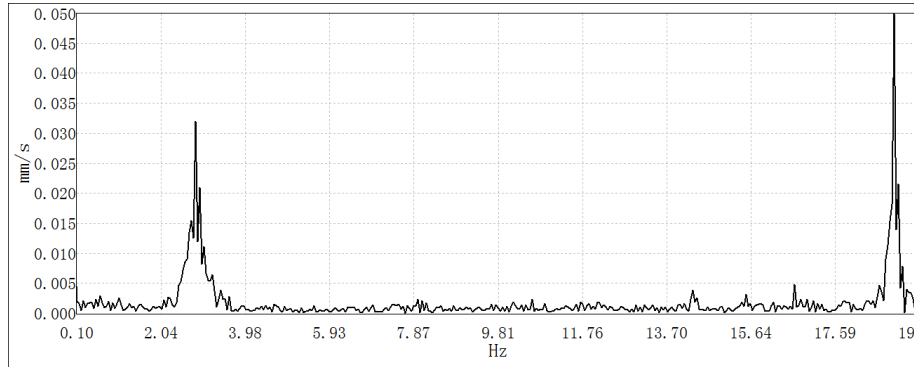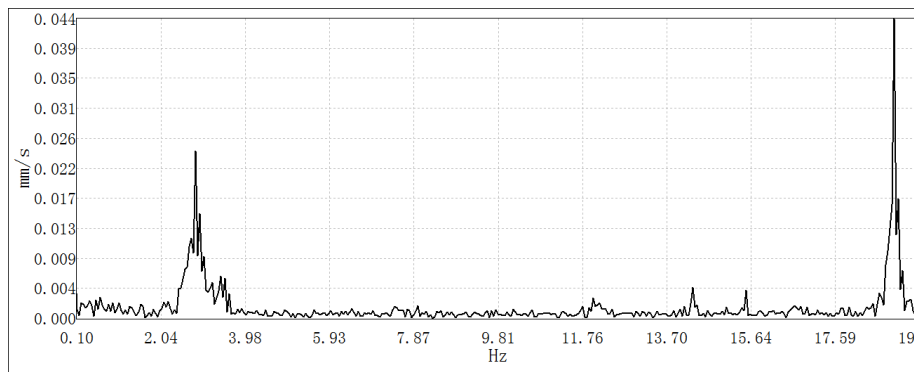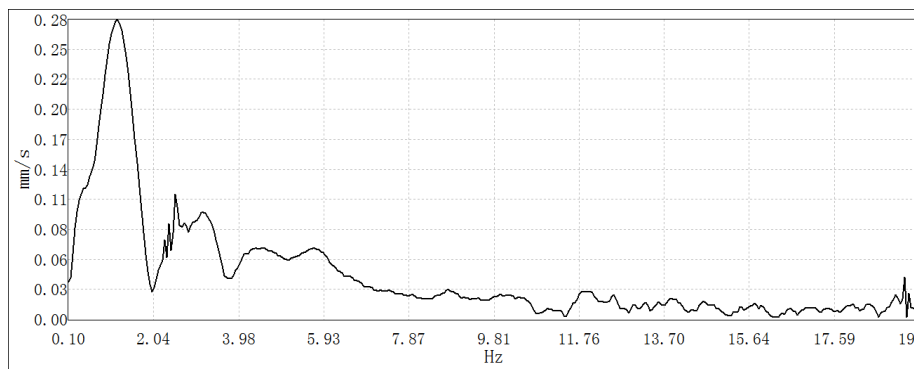*(a) V spectrum curve at the pipe crown*
Fig. 11 - Frequency spectrum of vibration velocity
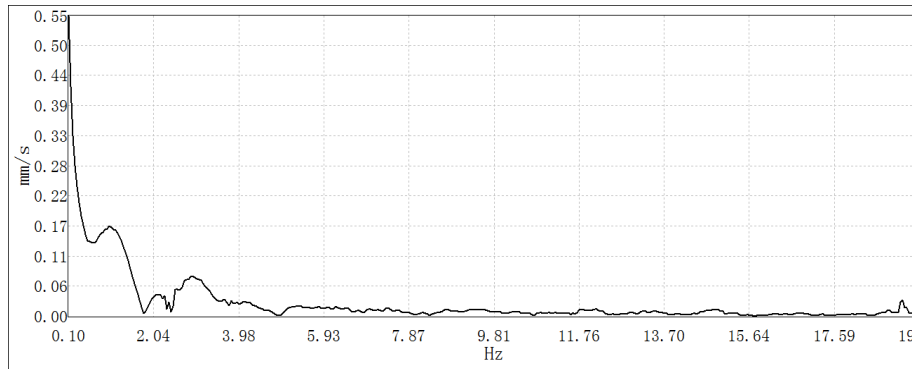
(b) H spectrum curve at the pipe spring line
Fig. 11 - Frequency spectrum of vibration velocity

As shown in Figures 3 to 11, when the 20t truck passes through the pipe culvert, the extreme value of the vibration velocity at the top of the pipe is obviously greater than that at the pipe side when the filling height is 80cm, but the extreme value of the vibration velocity at the pipe side is greater than that at the pipe top when the filling height is 100cm, which indicates that the filling height has a great influence on the vibration velocity at the pipe top. In other words, when the same weight vehicle passes through the pipe culvert, the higher the filling height is, the greater the consumption of vehicle vibration transmission to the pipe top is. Under condition 3 (truck 40t, filling height 80cm), the extreme value of vibration velocity at pipe top and pipe side has little difference, but the vibration response time at pipe side is significantly longer than that at pipe top; work condition 4, 5 and 6 are similar to this response.

Results of modal analysis

According to the results of modal analysis, the frequency and mode diagram of the first three main active modes are extracted. The first three natural frequencies are shown in Table 3. and Figure 12.

Tab. 3 - Natural frequency

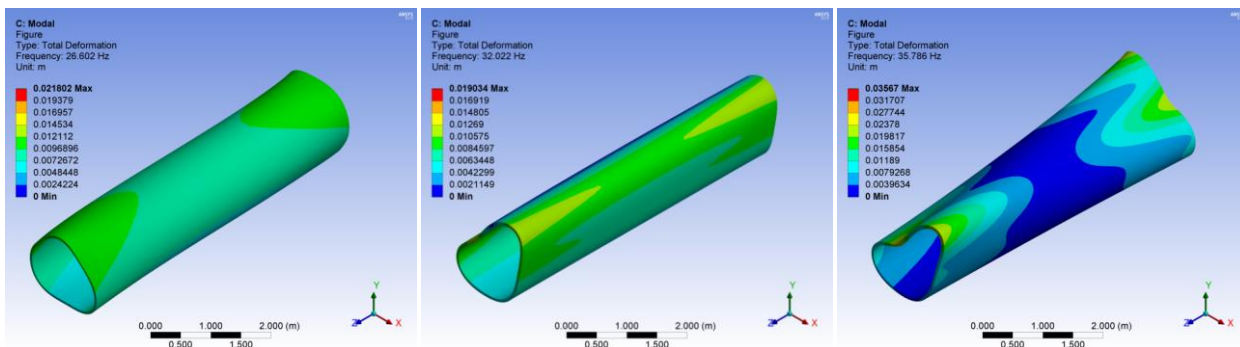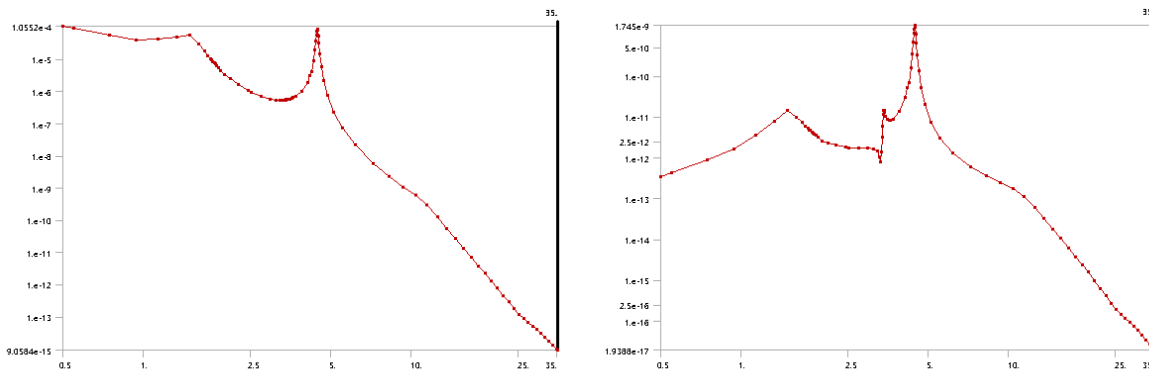| Order	100cm
1#	26.602Hz
2#	32.022Hz
3#	35.786Hz

Fig. 12- The first third mode diagram

In this paper, YES-DASP system is used to collect data, and GT-413 accelerometer is used as vibration sensor. The micro vibration speed signals of several common vehicles are collected. In the collected acceleration time history curve, select a representative section of load history curve a (T), and input the PSD spectrum value into the workbench. Using workbench, the models with buried depth of 50, 80 and 100 cm under different working conditions are established respectively. After the acceleration PSD spectrum is input, the corresponding degree of freedom constraints are applied in the X, Y and Z directions of the numerical model, and then the acceleration excitation in the Y direction is applied to each node of the whole model. In the analysis of calculation results, select representative points and draw their spectrum curve. In this paper, the top (V) point and the side (H) point are selected as examples, where H and V represent the horizontal and vertical directions respectively. Under the excitation of heavy-duty vehicle with vehicle weight of 40t and vehicle speed of 30km/h to the pavement with buried depth of 80cm, the corresponding frequency response curve of the measuring point is shown in Figure 13 – Figure 21. Where, the horizontal axis represents time(s), and the longitudinal axis represents the displacement(mm).

(a) V   *(b)H*

Fig.13 - Response curve of spectrum displacement under 50cm condition
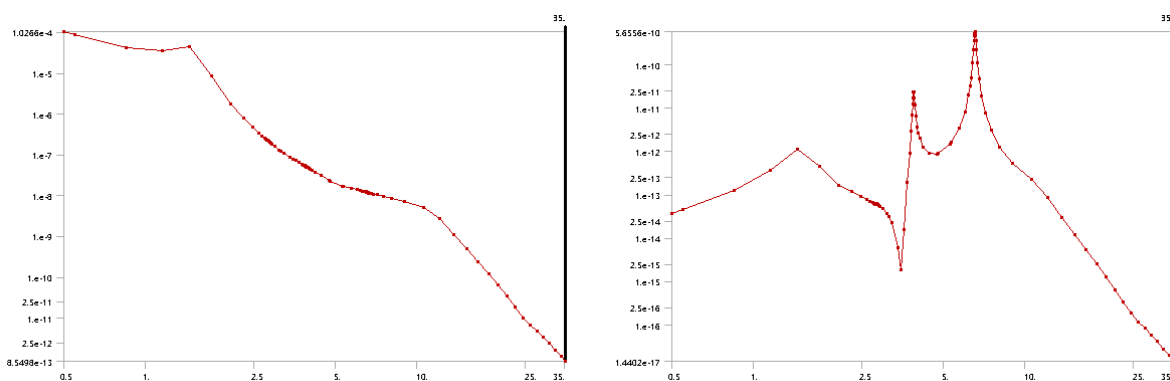
(a) V   *(b)H*

Fig.14 - Response curve of spectrum displacement under 80cm condition
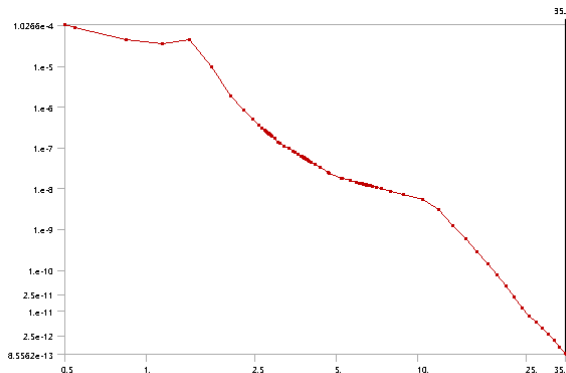
(a) V   *(b)H*

Fig.15 - Response curve of spectrum displacement under 100cm condition

The spectrum response curve of buried pipe under the excitation of vehicle type with vehicle weight of 60t and vehicle speed of 25m/s are as follow:

(a) V   *(b)H*

Fig.16 - Response curve of spectrum displacement of tube under 50cm condition

(a) V   *(b)H*

Fig.17 - Response curve of spectrum displacement under 80cm condition

(a) V   *(b)H*
Fig.18 - Response curve of spectrum displacement under 100cm condition

The spectrum response curve of buried pipe under the excitation of vehicle type with vehicle weight of 60t and vehicle speed of 20m/s are as follow:

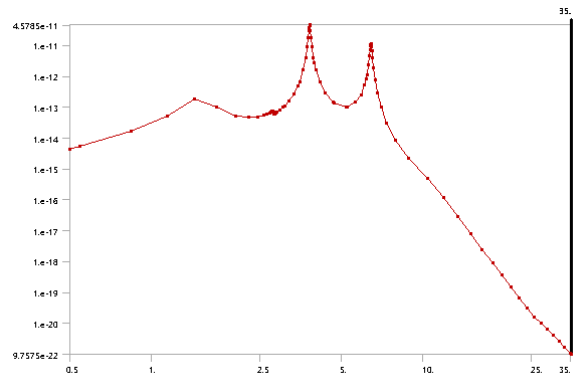*(a) V*   *(b)H*
Fig.19 - Response curve of spectrum displacement under 50cm condition
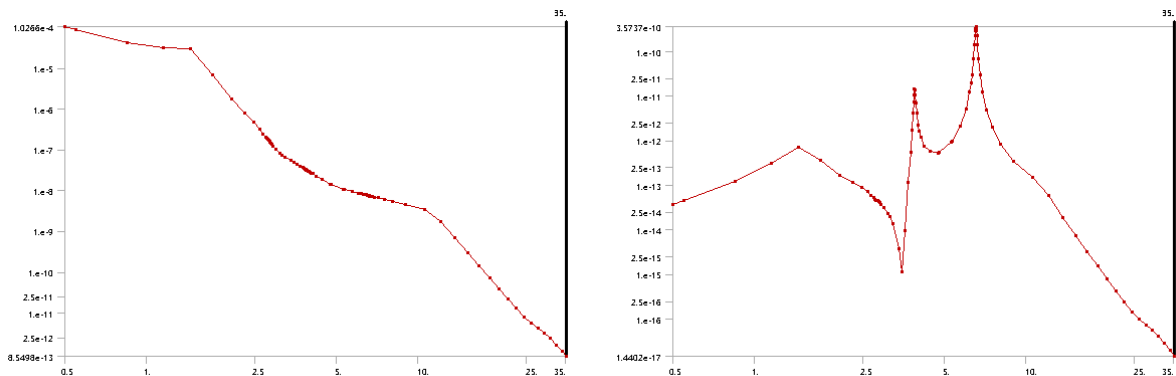
(a) V   *(b)H*
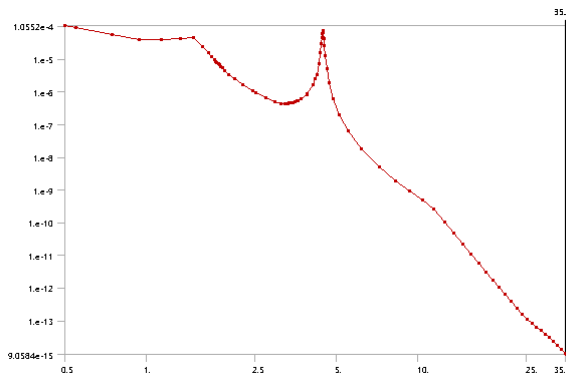*Fig.20 - Response curve of spectrum displacement under 80cm condition*
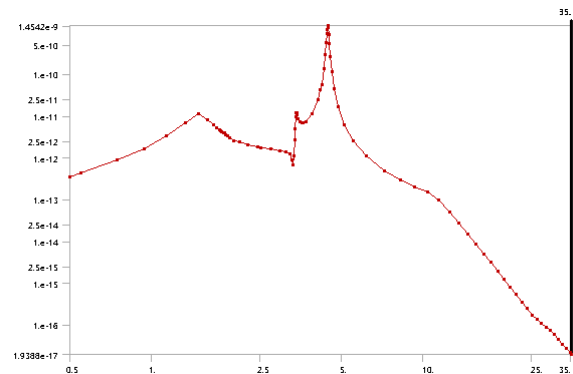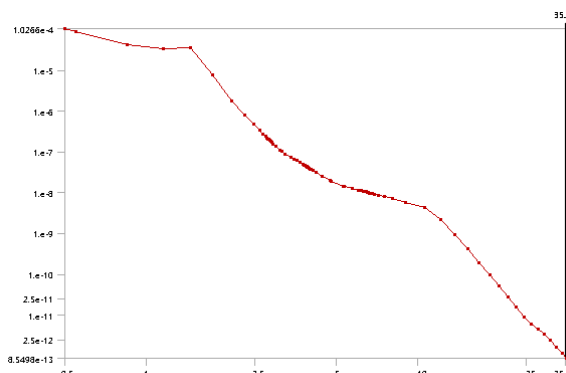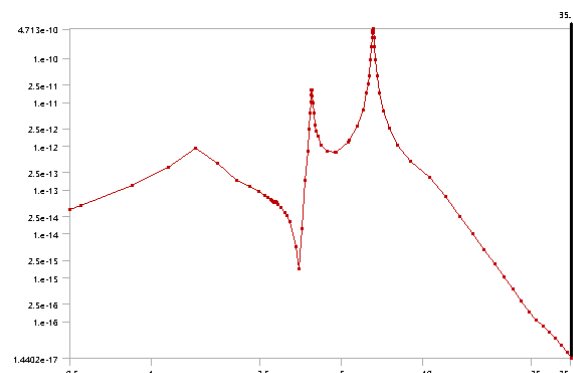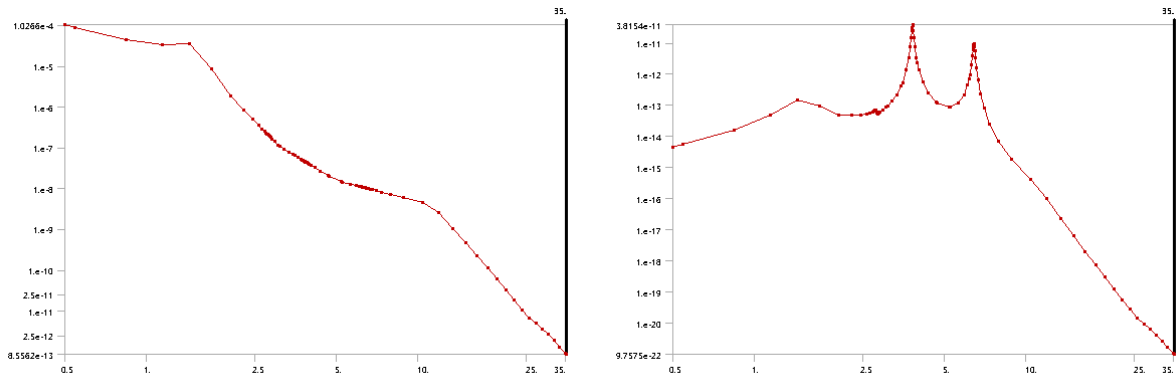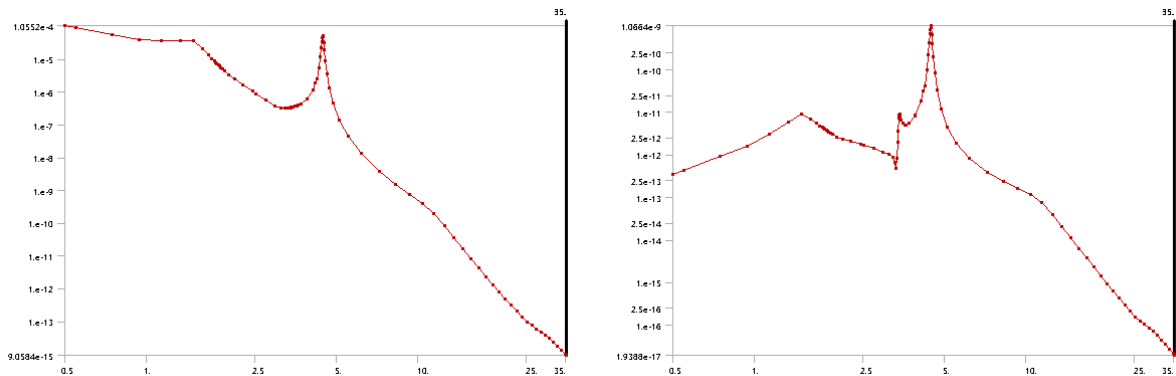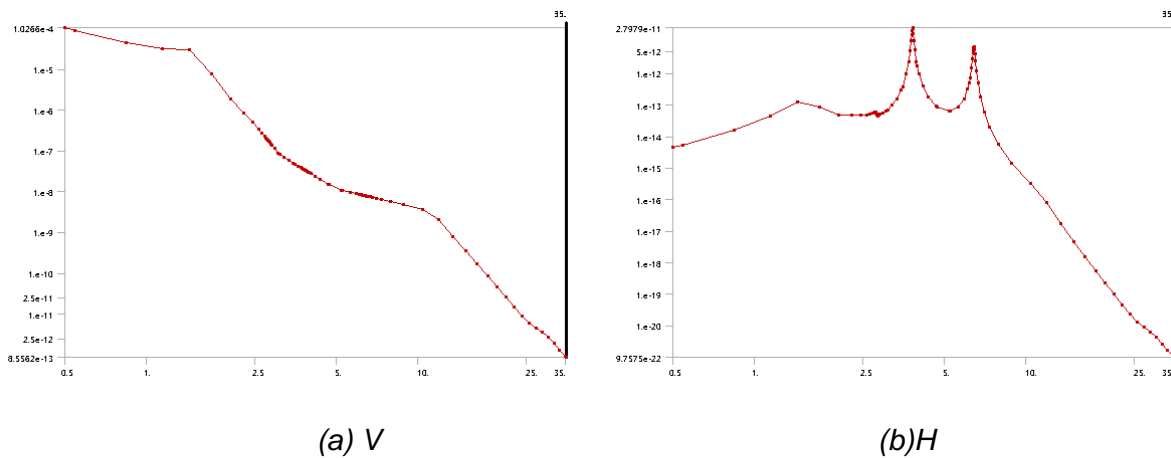
(a) V   *(b)H*
Fig.21 - Response curve of spectrum displacement under 100cm condition

Under the work condition of the burial depth with 50cm and the vehicle speed of 30m/s, the peak values of displacement frequency and acceleration frequency of the pipe top are the largest, which are respectively 1.0552e-4 (m²) / Hz and 5.2998 (m²/Hz); when the burial depth changes from 50cm to 80cm, the spectral response value of the pipe apex decreases accordingly When the buried depth changes from 50cm to 80cm, the peak value of the frequency at the pipe side will decrease more than that of the buried depth from 80cm to 100cm. The possible reason for this phenomenon is that with the increase of buried soil depth, the soil arching effect (uneven displacement or relative displacement between soil particles) of soil on the pipeline becomes more and more obvious, which changes the load diffusion angle; at the same time, it forms the supporting arch foot, which bears the automobile load together with the buried pipe [19,20,21]. For different buried depth, with the increase of vehicle speed, the peak value of displacement frequency and acceleration frequency corresponding to the pipe vertex and the pipe side point will also increase. As the vehicle speed increases, the vertical response of the vehicle becomes larger, and the increase of the vehicle speed makes the power spectral degree of the random dynamic load of the vehicle become larger, so does the dynamic response transmitted to the pipeline through the road. Table 4 shows the calculation results of pipe vertex and pipe side point under different working conditions.

Tab. 4 - The calculation results of spectrum response under different working conditions

Working condition		Peak value of displacement frequency (m²)/Hz		Peak acceleration frequency /(m/s²)²/Hz	
		Top(V)	Side(H)	Top (V)	Side (H)
30m/s	50cm	1.0552e-4	1.745e-9	5.2998	1.0697 e-3
	80 cm	1.0266e-4	5.66e-10	2.9801 e-1	1.5987 e-3
	100 cm	1.0266e-4	4.5785 e-11	2.8559 e-1	2.8863 e-5
25m/s	50cm	1.0552e-4	1.4542e-9	4.4165	8.9141 e-4
	80 cm	1.0266e-4	4.713e-10	2.4284 e-1	1.3322 e-3
	100 cm	1.0266e-4	3.8154 e-11	2.3386 e-1	2.4052 e-5
20m/s	50cm	1.0552e-4	1.0664e-9	3.2388	6.537 e-4
	80 cm	1.0266e-4	3.5737e-10	1.987 e-1	1.0102 e-3
	100 cm	1.0266e-4	2.7979 e-11	1.9226 e-1	1.8197 e-5

As shown in Table 4, under the condition of buried depth of 50cm, the peak value of vertical displacement frequency at the top of the pipe is mainly concentrated in three frequency segments of 0.5Hz, (1-1.5)Hz and (4-5)Hz, the maximum displacement frequency peak value is 1.0552e-4(m²)/Hz; under the condition of the buried depth of 80cm, the peak value of the vertical displacement frequency of the pipe top is mainly concentrated in two frequency segments of 0.8Hz and (1-1.5)Hz, the peak value of the maximum displacement frequency is 1.0266e-4(m²)/Hz; when the buried depth is 100cm, the peak value of the vertical displacement frequency of the pipe top is mainly 0.5Hz, the peak value of the maximum displacement frequency is 1.0266e-4(m²)/Hz. This shows that with the increase of the filling height, the distribution range of the peak frequency of the vertical displacement on the top of the pipe decreases, and the peak frequency of the maximum displacement also decreases. It is similar to the peak value of displacement frequency on the tube side. The peak value of acceleration frequency at the top of the pipe decreases with the increase of filling height, but the peak value of maximum acceleration frequency at the side of the pipe reaches the maximum value when the buried depth is 80 cm. In other words, the main factor influencing the apex value of culvert is the depth of fill, when it increases, causes the apex value to increase. Other important elements influencing the apex value are the vehicle speed. There is a positive correlation between the vehicle speed and the vibration response extreme of the pipe top and side.

CONCLUSIONS

In this paper, the dynamic response values of the glass sand pipe with buried depth of 80cm and 100cm under the weight of 20, 40 and 60 t truck are measured and analyzed through the field test. Then, according to the field situation, the finite element dynamic analysis model of GRP mortar pipe culvert is established by using the ANSYS Workbench finite element mechanical analysis program. The modal analysis of the buried GRP mortar pipe is carried out, and the main natural vibration frequency and the corresponding vibration mode diagram are obtained. On the basis of modal analysis, the dynamic response of GRP mortar pipe under different working conditions is studied by random vibration, and the following conclusions are obtained:

(1)   The error is less than 15% by comparing the simulation value with the test value under the same working condition. The feasibility of using workbench random vibration module to analyze the frequency response of buried pipe is verified.

(2)   The vehicle load is imposed as 20t, 40t and 60t respectively, the vibration frequency of the glass sand pipe with buried depth of 80 and 100cm is far less than the first three natural frequencies calculated by modal analysis. Therefore, when the filling height of the pipe culvert is 0.8m and 1m, the roller will not resonate and damage the buried pipe under strong earthquake. After the soil foundation is compacted, the traffic of the heavy material truck can be restored.

(3)   For the buried GRP mortar pipe under different working conditions, the frequency response of vertical vibration at the top of the pipe is generally greater than that of horizontal vibration

(4)   With the increase of the buried depth, the frequency response value of the pipeline to the vehicle load decreases. When the buried height of the GRP mortar pipe is greater than 0.8m, the soil arching effect becomes more and more obvious, and the impact of the ground vehicle dynamic load on the vibration of the buried pipe can be ignored. For different buried depth, with the increase of vehicle speed, the peak value of displacement frequency and acceleration frequency corresponding to the pipe vertex and the pipe side point will also increase.

(5)   A numerical model is established for the whole structure of the buried GRP mortar pipe with a buried depth of 50, 80 and 100 cm. The critical natural frequency is obtained by modal

analysis. Based on the measured micro vibration data of the site, the vibration response frequency range of the key points of the pipe is obtained by workbench random vibration simulation. After comparison, the vibration frequency does not intersect and resonance will not occur.

In summary, the results concluded in this paper show that the feasibility of using Workbench random vibration module to analyze the spectrum response of buried pipelines. It provides basis for safety degree of engineering design, especially for safety problems under heavy load, as well as construction and application of GRP mortar pipe culverts. The further research focuses on the mechanical analysis and life estimation of the buried GRP mortar pipe under the earthquake load. And further optimize the pipeline structure to realize the wide application of GRP mortar pipe in the field of bridge and culvert engineering.

ACKNOWLEDGEMENTS

REFERENCES

[1]	Specification for Fiberglass (Glass-Fiber-Reinforced Thermosetting-Resin) Pipe and Pipe Fittings, Adhesive Bonded Joint Type, for Aviation Jet Turbine Fuel Lines[S]. ASTM, 2003.
[2]	Test Methods for Constituent Content of Composite Materials[S]. ASTM, 2003.
[3]	Newmark N M, Hall W J. Pipeline design to resist large fault displacement [J]. Earthquake Engineering Res Inst, 1975,416- 425.
[4]	Parmelee R A, Ludtke C A. Seismic soil-structure interaction of buried pipelines [D]. Civil Engineering:Northwestern University, 1974.
[5]	Zhang Tuqiao, Shao Weiyun.Numerical analysis of buried pipe characteristics [J].Journal of Zhejiang University(Science), 2000, 1(2):144-147.
[6]	Zhang Tuqiao, Wu Xiaogang. A preliminary study on the longitudinal force analysis mode of pipelines under vertical loads [J]. Chinese municipal engineering,2001, 95(4):41-45.
[7]	J.Lee. Strength of filament wound GRP tubes with axisymmetric steps[J].composite, 1989 , 20 (3) :234-243.
[8]	Jeyapalan, J.K., et al .Analysis and design of RPM and other composite underground pipelines.Journal of Transportation Engineering,1990,115 (3):219-231.
[9]	Xu Lei, Ye Zhicai, Ren Qingwen. Dynamic response analysis of buried fiberglass reinforced plastic sand pipe under earthquake load [J]. Journal of disaster prevention and mitigation engineering, 2012, 32 (04): 468-474.
[10]	Manko Z, Beben D. Dynamic testing of a corrugated steel arch bridge. Can J Civ Eng 2008;35(3):246–57.
[11]	Beben D, Manko Z. Dynamic testing of a soil-steel bridge. Struct Eng Mech 2010;35(3):301–14..
[12]	Bayoglu Flener E, Karoumi R. Dynamic testing of a soil-steel composite railway bridge. Eng Struct 2009;31(12):2803–11.
[13]	Jeyapalan, J.K., et al .Analysis and design of RPM and other composite underground pipelines.Journal of Transportation Engineering,1990,115 (3):219-231.
[14]	Zhang Jiyuan, Wei Lianyu, Zhang Guopan, Chen Zhaonan, Zheng Yanjun. The flexure and deformation characteristics of buried FRP sand pipe in highway[J]. glass steel / composite material,2016 (10): 56-59.
[15]	Liu Baodong, Yin Hang, Feng Zhimao, Wang Quanlu. Stress analysis on the construction process of soil corrugated steel plate arch bridge based on the soil and steel joint action model[J]. Beijing Jiaotong University Journal,2009,33(04) : 66-68.

[16]   Li Mingyang, Chen Guohua. Finite element analysis of buried polyethylene gas pipeline under traffic load [J]. plastic industry.2009 (09) ,37(09) : 30-33..

[17]   Xu Jingjing. ANSYS 13.0 Workbench numerical simulation technology[M]. Beijing: China Water Conservancy and Hydropower Press, 2012.

[18]   Gao Guangyun, Nie Chunxiao, Li Shaoyi. Micro vibration test and numerical analysis of the electronics factory building [J]. Site Investigation Science and Technology,2011(03) :51-55.

[19]   Wu Yanling. Stress and deformation characteristics of highway steel corrugated pipe culvert and its application research [D]. Chang'an :Chang'an University,2012.

[20]   B.H.Kjartanson,GA.Heilers,R.A.Lohnes,F.W.Klaiber.Soil-Structure   Interaction   Analysis   of Longitudinal Uplift of Culverts[J].Journal of Geotechnical and Geoenvironmental Engineering, 1998, 124(2):128-139

[21]   Feng Li. Mechanical performance analysis of corrugated pipe culvert with soil interaction. [D]. Beijing:BeijingJiaotong University,2010.

REAL-TIME MONITORING DEFORMATION OF BUILDING USING PHOTOGRAPHY DYNAMIC MONITORING SYSTEM

Yongquan Ge[1], Chengxin Yu[2], Tonglong Zhao[1] and Xiaodong Liu[3]

1. *Shandong Jianzhu University, College of Surveying and Geo-Informatic, Fengming Road 1000, 250101 Jinan, Shandong, China; ge39953@163.com, zhaotongl@sdjzu.edu.cn*
2. *Shandong Jianzhu University, Business School, Fengming Road 1000, 250101 Jinan, Shandong, China; ycx1108@126.com (Corresponding author)*
3. *Shandong Jianzhu University, College of Continuing Education, Shandong Jianzhu University, Fengming Road 1000, 250101 Jinan, Shandong, China*

ABSTRACT

The spatial structure building is a type of building system; it is necessary to monitor deformation to determine its stability and robustness. Under the dynamic deformation of structures, it is challenging to determine appropriate zero image (the reference image) if we use the PST-IM-MP (photograph scale transformation-image matching-motion parallax) method to obtain the deformation of structures. This paper offers the Z-MP (zero-centered motion parallax) method to solve these problems and offers PDMS (Photography Dynamic Monitoring System) based on the digital photography system to monitor the dynamic deformation of the tennis stadium located in Jinan Olympic Sports Center. The results showed that the spatial structures of the tennis stadium were robust, and the deformations were elastic and within the permissible value. Compared with the PST-IM-MP method, the Z-MP method is more suitable for deformation monitoring structures under real-time deformation. This paper indicates PDMS has advantages of the simplicity of operations, automation, and the ability of non-contact dynamic deformation monitoring for multiple points in a short period. In the future, it will have broader application prospects.

KEYWORDS

Close-range photogrammetry, Dynamic deformation, The spatial structure, Z-MP (zero-centered motion parallax) method, PDMS (Photography Dynamic Monitoring System), Tennis stadium

INTRODUCTION

Over the last decade, space structures have evolved and found their usefulness in the modern world, since they are aesthetically appealing and architecturally flexible. They have lightweight profiles that reduce construction costs, stability, and strength, and cover large areas of uninterrupted spans [1]. The large-span spatial structure has been widely used in various large sports venues, theatres, exhibition centers, airport terminals, and various industrial plants. Such buildings are usually places where people gather, and large-scale activities occur, so the safety of the large-span spatial structures is particularly important.

Large-span spatial structures using a large number of new materials such as steel membranes, high strength steel bundles. However, corrosion of materials, uneven settlement of the aging foundation, and coupling effects of complex load fatigue, which will inevitably lead to damage accumulation and resistance attenuation of the structural system, and in extreme cases lead to catastrophic emergencies [2]. For example, the multifunctional stadium in Kuala Lumpur,

Malaysia collapsed caused design and construction quality in June 2009 [3]; overloading of the main roof structure caused the roof to collapse during the expansion of De Grolsch Veste FC Twente stadium in the Netherlands In July 2011 [4]; due to the accumulation of rain, the platform of the roof structure is thicker than the original design, and the greening vegetation laid by hall exceeds the load, finally leading to the city university of Hong Kong on the roof of the Chen dahe collapse in May 2016 [5]. The above examples show that although the spatial structure belongs to the statically indeterminate structure, the spatial force is relatively complex. When the damage occurs in the structure's critical parts, the whole structure may be destroyed quickly [6]. According to the collapse accident, the space structure will collapse in a few minutes, even seconds. Therefore, it is important to regularly monitor the deformation of large-span spatial structure and evaluate the structure's status timely.

There are various established methods used in experimental testing to conduct dynamic deformation monitoring. The conventional method used is the attachment of contact sensors such as strain gauges, accelerometers, and Fiber Bragg grating sensors on the structure [7, 8]. Among them, the fiber Bragg grating sensor abandons the traditional measurement method of the electrical signal. It adopts all-optical measurement, which has the advantages of substantial anti-electromagnetic interference, good anti-corrosion ability, excellent reliability, and long service life. However, this method can only obtain the 1-D deformation of specific points within a limited measurement range and cannot provide the overall deformation data of the structure [9]. The more sensors are used in theory, and the more accurate the obtained results will be. Therefore, it is necessary to reasonably allocate the number of installed sensors in the actual measurement. How to balance effectiveness and economy is a critical problem to be solved in the arrangement of measuring points of this method [10]. Undoubtedly, the problem increases the sensor layout time, and this method has many limitations of contact measurement. Relevant scholars have conducted extensive research on contactless deformation monitoring technology to solve the above problems and overcome these defects.

The optical technology as a non-contacting measurement technique has gained more attention in the last few decades, mainly because of its non-destructive imaging characteristics with high precision and sensitivity [11-13]. It has seen many advances in recent years that have manifested itself because of the exceptional advances in computer technology and camera sensors. Generally, the optical measurement techniques can be classified into two main categories: (a) approaches that use laser beams and (b) approaches that use white light. Laser surface scanners are based on laser beams, which move across the scanned surface and reflect to a light sensor [14]. The second class works by using white light and is called image-based systems. The photogrammetry technique falls into the second group and leverages rays of light that are reflected from a structure [9].

Some scholars have successfully applied photogrammetry technology to the deformation monitoring of engineering structures such as steel structures [15], bridges structures [16], regulating sluice structures [17], and shuttle steel shelves [18]. The DLT (direct linear transformation) method and the MP (motion parallax) method are two conventional methods used to obtain the deformation of the monitoring points. The DLT method is only suitable for a small range of measurements, and this method has high requirements for control points. The MP method is mainly used for obtaining the 2-D plane deformation and the relative variation of monitoring points. However, internal and external orientation elements are always changing during the measurement process. The IM-MP (image matching-motion parallax) method is used to correct the influence of this phenomenon on the measurement results and to improve the measurement accuracy, the PST-IM-MP (photograph scale transformation-image matching-motion parallax) method to solve the problem of the reference points and the monitoring points are not on the same plane [18]. However, since the algorithm is based on the comparison between the successive image and the zero image to obtain the deformation of monitoring points, the visualization results are not user-friendly. For the buildings that have been in dynamic deformation, we obtain $X - Z$

----

plane deformation by using the X and Z direction deformations is inappropriate. This paper proposed the Z-MP method will solve the above problems and conducted a monitoring dynamic deformation test on the tennis stadium of Jinan Olympic Sports Center in China. In this paper, the test results of the two methods were compared.

PHOTOGRAPHY DYNAMIC MONITORING SYSTEM

PDMS consists of two parts: information acquisition and information processing. The information acquisition consists of a digital camera, a distance finder and two tripods. The information processing is a computer with the photography dynamic monitoring software installed. The software can process images and output of deformation results. Figure 1 shows the view of PDMS. The view and parameters of the distance finder are shown in Figure 2 and Table 1, respectively.
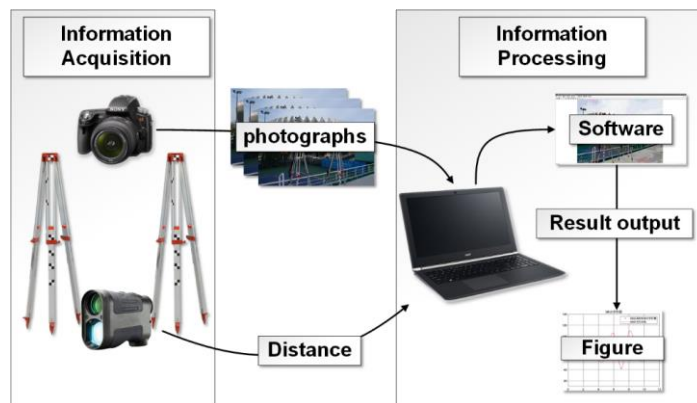
Fig. 1 – Photography dynamic monitoring system

Fig. 2 – Images of the distance finder

Tab.1 - Parameters of the distance finder

model	Bushnell PRIME 1200
range	7-1200Y
accuracy	±1Y

Camera and its distortion

In this paper, we used a Sony-α350. The view and parameters of the camera are shown in Figure 3 and Table 2, respectively.

Fig. 3 – Images of the Sony-α350 camera

Tab. 2 – Parameters of the Sony-α350 camera

Model ID	DSLR-A350
Image Sensor	CCD
Image Sensor Dimension	23.5×15.7mm
Image Dimension	4592×3056（14.0MP）
Lens Type	Minolta / Sony AF DT 18 - 70mm F3.5 - 5.6 (D)

Because the sensitive element of the non-metric digital camera used in this paper is CCD, the camera parameters are unknown and unstable, which leads to the instability of the imaging process, so there is a large lens distortion in the digital image. In order to reduce the interference caused by lens distortion, it is necessary to correct the lens distortion. The correction method used in this paper is a grid-based method [19]. Figure 4 (a) is the nine × nine grid used in this paper, which is printed on ISO-A0 matte paper. Figure 4 (b) is the analysis diagram of the distortion difference obtained after the analysis of the distortion difference of the grid. Through the analysis and comparison of several groups of distortion errors, the change rule of distortion difference is explored to correct the image distortion. The specific implementation process is as follows:

Step 1: fix the grid on the vertical plane, adjust the digital camera mode to "manual" to ensure constant exposure in the subsequent shooting process, and set it up at a specific distance S from the grid.

Step 2: control the digital camera to shoot the grid many times and record the distance at the same time;

Step 3: take the image with excellent image and the actual grid for careful comparison, through the observation of image feature points, analysis of the digital camera image distortion law;

Step 4: change the distance S before and after without changing the direction, repeat steps 2 and 3.

Step 5: obtain the mathematical relation of image distortion and complete the distortion correction.
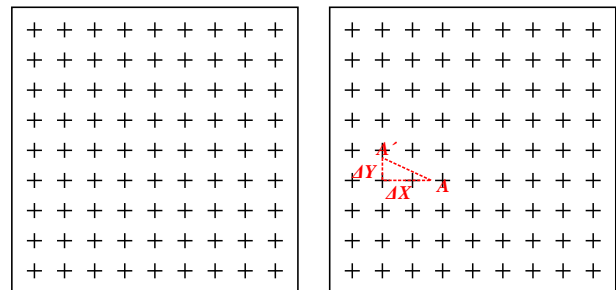
(a) 9*9 grid   *(b) Distortion analysis*
Fig. 4 – Camera calibration

Photography dynamic monitoring software

Figure 5 shows the software screenshot. The software can obtain the deformation value of multiple monitoring points through the PST-IM-MP method, the Z-MP method, and the MP method. It can also provide sufficient and reliable deformation data, finally forming user-friendly visualization results.

Fig. 5 – Photography dynamic deformation software

Import the data from the information acquisition part into the computer of the information processing part, and batch process the pictures: Import the images into software and carry out the unified preprocessing of the images as the case may be, such as cutting and drawing. Image processing operations such as binarization, sharpening, and improving contrast or clarity. Input scale deformation values, and then get the pixel position and pixel correction of monitoring points and reference points in the corresponding images, pixel displacement and all other images relative to the reference image the actual displacement of the monitoring point in mm.

The zero-centered motion parallax method

In Figure 6, suppose there are three planes, image plane, reference plane, and object plane. Image plane is the image of the camera, reference plane is formed by a pair of tripods, object plane is the side of the tennis stadium. And Figure 5 shows the number and distribution of points on a reference plane and a object plane. There are six control points distributed on the reference plane, namely C0-C6, twelve monitoring points on the object plane namely U0-U12. If monitoring point on the object plane is moved from A to B, its deformation Δx and Δz on the reference plane are:

$$\left. \begin{array}{l} \Delta x = \dfrac{y}{f}\Delta P_x \\[2mm] \Delta z = \dfrac{y}{f}\Delta P_z \end{array} \right\} \tag{1}$$

Where f is the principal distance of photo, where y is the distance of the image plane and the reference plane. ΔP_x and ΔP_z are the horizontal and vertical deformations of monitoring point on the image plane. Δx and Δz are the horizontal and vertical deformations of monitoring point on the reference plane.
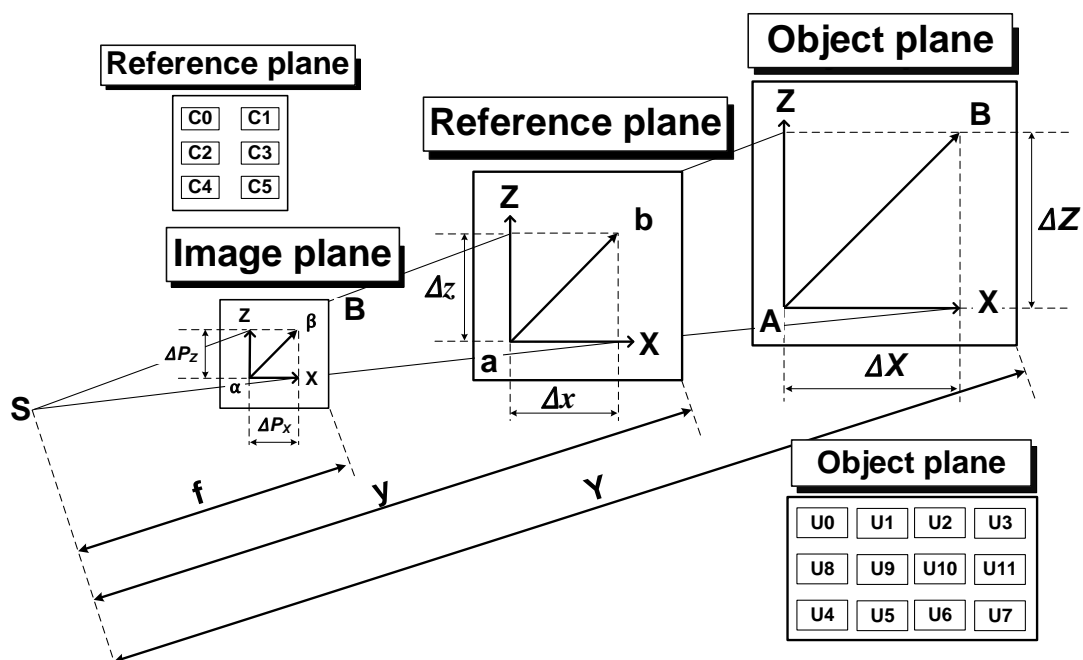

Fig. 6 – Principle of the Z-MP method

Correction of system errors in the Z-MP method on the reference plane

Strictly speaking, the photos before and after deformation are always taken under different elements of interior and exterior orientation, the interior orientation elements in a photo are the elements for restoring the shape of the photographic beam, the exterior orientation in a photo are the elements for determining the position and orientation of the photographic beam in the space coordinate system. In the test, we keep the camera as stable as possible and set the digital camera mode to ' manual '. Therefore, the error caused by the inconsistency of elements of interior and exterior orientation will have a slight impact on the monitoring results; we weaken the theoretical error to a certain extent by setting control points. To be exact, we weakened Δx_p^0; the specific process is as follows.

On the reference plane, if corresponding monitoring points in the zero image and successive image are (x_1, z_1) and (x_2, z_2), compared with the ideal image which without errors of camera external and internal parameters, systematic errors of corresponding monitoring point are (dx_1, dz_1) and (dx_2, dz_2), respectively. The equations can be expressed as Equation (2):

$$\left.\begin{array}{c} (x_2 - x_1) - (dx_2 - dx_1) - \Delta x = 0 \\ (z_2 - z_1) - (dz_2 - dz_1) - \Delta z = 0 \end{array}\right\} \tag{2}$$

If there are errors of camera external and internal parameters between the zero image and successive images, the control points located on the reference plane will generate parallax Δx_p and Δz_p as Equation (3):

$$\left.\begin{array}{c} \Delta x_p = (x_2 - x_1) = (dx_2 - dx_1) \\ \Delta z_p = (z_2 - z_1) = (dz_2 - dz_1) \end{array}\right\} \tag{3}$$

The parallax Δx_p and Δz_p of the control point must be caused by the errors of camera external and internal parameters in successive zero images, we take parallax Δx_p for example, it can be expressed as Equation (4), the detailed derivation process is shown in the reference[21]:

$$\Delta x_p = (x_2 - x_1) = (dx_2 - dx_1)$$

$$= -\left[\frac{f}{Y}dX_{S_2} + \frac{dY_{S_2}}{Y}x_2 + \left(f + \frac{x_2^2}{f}\right)d\varphi_2 + \frac{x_2 z_2}{f}d\omega_2 - z_2\,d\kappa_2 + \frac{x_2}{f}df_2 + dx_{0_2}\right]$$

$$+ \left[\frac{f}{Y}dX_{S_1} + \frac{dY_{S_1}}{Y}x_1 + \left(f + \frac{x_1^2}{f}\right)d\varphi_1 + \frac{x_1 z_1}{f}d\omega_1 - z_1\,d\kappa_1 + \frac{x_1}{f}df_1 + dx_{0_1}\right] \tag{4}$$

Where $\left(dX_{S_2}, dY_{S_2}, d\varphi_2, \cdots\right)$ and $\left(dX_{S_1}, dY_{S_1}, d\varphi_1, \cdots\right)$ are errors of zero image and successive images. From Equation (4), we notice $x_2 = x_1 + \Delta x_p$, assume the difference between the errors of zero image and successive images as Equation (5) shows:

$$\left.\begin{array}{c} \Delta X_S = dx_{S_2} - dx_{S_1} \\ \Delta Y_S = dY_{S_2} - dY_{S_1} \\ \Delta \varphi = d\varphi_2 - d\varphi_1 \\ \Delta \omega = d\omega_2 - dw_1 \\ \Delta k = dk_2 - dk_1 \\ \Delta f = df_2 - df_1 \\ \Delta x_0 = dx_{0_2} - dx_{0_1} \end{array}\right\} \tag{5}$$

Then, Equation (4) can be expressed as Equation (6):

$$\Delta x_s = -\frac{f}{Y}\Delta X_S - \frac{dY_S}{Y}x_1 - f\Delta\varphi - \frac{x_1^2}{f}\Delta\varphi - \frac{x_1 z_1}{f}\Delta\omega + z_1\Delta\kappa - \frac{\Delta f}{f}x_1 - \Delta x_0 - \Delta x_p\frac{dY_{S_2}}{Y} \tag{6}$$

$$- \Delta x_p\frac{2x_1}{f}d\varphi_2 - \frac{\Delta x_p z_1}{f}d\omega_2 - \frac{\Delta z_p x_1}{f}d\omega_2 + \Delta z_p\,d\kappa_2 - \Delta x_p\frac{df_2}{f}$$

After sorting out Equation (6), it can be expressed as Equation (7):

$$\Delta x_p = \Delta x_p^0 + \delta x_p$$

$$\Delta x_p^0 = \left[\left(-\frac{dY_S}{Y}-\frac{\Delta f}{f}\right)x_1 + z_1\Delta\kappa + \left(-\frac{f}{Y}\Delta X_S - f\Delta\varphi - \Delta x_0\right)\right] - \frac{x_1^2}{f}\Delta\varphi - \frac{x_1 z_1}{f}\Delta\omega$$

$$\delta x_p = -\left(\frac{\Delta x_p\, dY_{S_2}}{Y}\right) - \frac{2\Delta x_p x_1}{f}d\varphi_2 - \frac{\Delta x_p z_1}{f}d\omega_2 - \frac{\Delta z_p x_1}{f}d\omega_2 + \Delta z_p\, d\kappa_2 - \frac{df_2}{f}\Delta x_p$$

(7)

Because motion Δp_x^0 is caused by the change of camera external and internal parameters $(\Delta X_S, \Delta Z_S, \Delta\varphi, \Delta\omega, \Delta\kappa, \Delta f, \Delta x_0)$ in the successive and zero images, we can correct Δp_x^0 with a sufficient number of control points. Differently, motion δp_x is caused by the interaction of Δx_p, Δz_p, and camera external and internal parameters $(dZ_{S_2}, d\varphi_2, d\omega_2, d\kappa_2, df_2)$ in the successive image. However, Δx_p and Δz_p are different at each point, control points cannot be used to correct δx_p, so we only discuss Δx_p^0 as follows:

$$\Delta x_p^0 = \left(-\frac{\Delta Y_S}{Y}-\frac{\Delta f}{f}\right)x_1 + \Delta\kappa z_1 + \left(-\frac{f}{Y}\Delta X_S - f\Delta\varphi - \Delta x_0\right) - \frac{x_1^2}{f}\Delta\varphi - \frac{x_1 z_1}{f}\Delta\omega \qquad (8)$$

We can express Equation (8) as Equation (9):

$$\Delta x_p^0 = ax + bz + c + dx^2 + exz \qquad (9)$$

If there are more than five control points, each unknown coefficient (a, b, c, d, e) can be obtained according to their Δx_p^0. We assume the correction of Δx is v, so the error equation is:

$$v = ax + bz + c + dx^2 + exz - \Delta x \qquad (10)$$

For convenience, we selected the linear part of the Equation (10) for processing, as Equation (11) shows:

$$\left.\begin{array}{l} \Delta x_p^0 = ax + bz + c \\ \Delta z_p^0 = a'x + b'z + c' \end{array}\right\} \qquad (11)$$

In this case, we only need three or more reference points to obtain (a, b, c) and (a', b', c'). Take ΔP_x^0 as an example, when ΔP_x^0 contains only occasional errors, Equation (11) can express as Equation (12):

$$p_x' + V = ax' + bz' \qquad (12)$$

Where p_x' is the differential coefficient of ΔP_x^0. the error equation is:

$$V = ax' + bz' - p_x' \qquad (13)$$

The equation of the composition method is:

$$\left.\begin{array}{l} a\sum x'^2 + b\sum x'z' - \sum x'p_x' = 0 \\ a\sum x'z' + b\sum z'^2 - \sum z'p_x' = 0 \end{array}\right\} \qquad (14)$$

Calculate barycentric coordinates by control points on the reference plane.

$$\left.\begin{array}{l} x_s = x - \dfrac{\sum x}{n} \\ z_s = z - \dfrac{\sum z}{n} \end{array}\right\} \qquad (15)$$

Because coordinates of control points are barycentric coordinates, $\sum x_s \sum z_s = 0$ and the parallax coefficient in the X direction as Equation (16) shows:

$$\left.\begin{array}{l} a = \dfrac{\sum z_s'^2 \sum x_s'p_x' - \sum x_s'z_s' \sum z_s'p_x'}{\sum x_s'^2 \sum z_s'^2 - \sum x_s'z_s' \sum x_s'z_s'} \\[4mm] b = \dfrac{\sum x_s'^2 \sum z_s'p_x' - \sum x_s'z_s' \sum x_s'p_x'}{\sum x_s'^2 \sum z_s'^2 - \sum x_s'z_s' \sum x_s'z_s'} \end{array}\right\} \qquad (16)$$

Where $a = tan\,\varphi_x$ and $b = tan\,\omega_z$. Similarly, we can obtain the parallax coefficient a' and b' in the Z direction. Then, we can obtain Δx_p^0 and Δz_p^0. Finally, we figure out the value of Δx_p and Δz_p, as Equation (17) shows:

$$\Delta x_p \approx \Delta x_p^0 \approx ax + bz$$
$$\Delta z_p \approx \Delta z_p^0 \approx a'\,x + b'\,z$$

(17)

Obtain the deformation of monitoring points on the object plane

$$\left.\begin{aligned}\Delta X = \frac{Y}{y}\Delta x \\ \Delta Z = \frac{Y}{y}\Delta z\end{aligned}\right\}$$

(18)
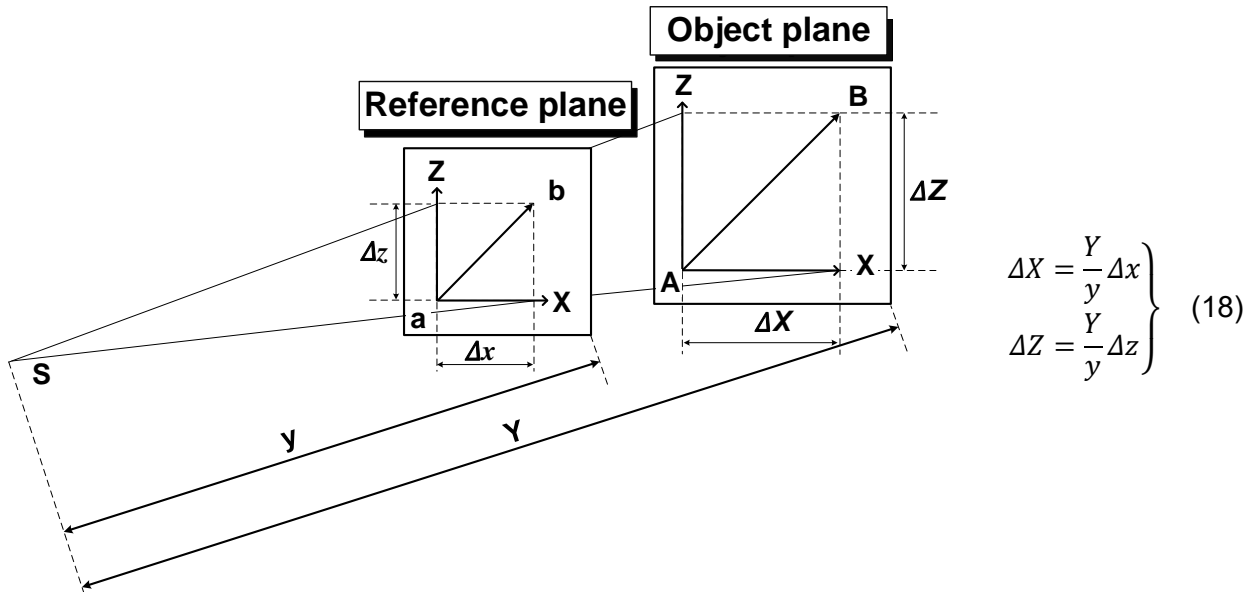
Fig. 7 – Principle of the PST-IM-MP method

Where ΔX and ΔZ are the horizontal and vertical initial deformations of the monitoring point on the object plane. Equation (18) is also the core of the PST-IM-MP method [18-20] (Zhang 2018).

Zero-centered motion parallax of monitoring points on the object plane

If the structure is in a state of elastic deformation, the deformation of the monitoring structure points in all directions repeatedly changes around their respective equilibrium positions. That is, the deformation of each point is independent. If we take the first image as the zero image (the reference image), the deformation of the monitoring points is obtained based on it, independence of monitoring points will be ignored. Although obtained by monitoring the relative deformation in X and Z direction is available. However, the visual result is not user-friendly. If we calculate the 2-D deformation value of monitoring points on the X-Z plane by using the data directly, it will exaggerate 2-D deformation value monitoring points in different degrees in the X-Z plane. In other words, for the structure is in a state of elastic deformation all the time, the result of the PST-IM-MP method obtained is incorrect. Therefore, it is necessary to select an independent reference position for each monitoring point and improve the PST-IM-MP method. That is, the deformation centralization:

$$\left.\begin{aligned}\Delta X' = \Delta X - \frac{\sum \Delta X}{n} \\ \Delta Z' = \Delta Z - \frac{\sum \Delta Z}{n}\end{aligned}\right\}$$

(19)

Where $\Delta X'$ and $\Delta Z'$ are the horizontal and vertical final deformations of monitoring point on the object plane. Because we obtained $\Delta X'$ and $\Delta Z'$ their mean are zero, named zero-centered.

BUILDING DEFORMATION MONITORING TESTS

Test process

The monitoring building tennis stadium is located in Jinan, Shandong Province. Tennis stadium has a building area of about 31400m². Reinforced concrete frame shear walls are used for the stands and functional rooms. The wall adopts the folded plate structure in the form of willow leaves, combined with the curtain wall steel columns of the building, to form a diamond lattice column. As Figure 8 shows, the valley depth of the folded plate structure of the outer wall is 3m and combined with the steel columns of the curtain wall to form diamond composite columns. The structure contributes to improving the stability of the folded plate structure out of plane. The height of the steel structure decreases from south to north, with the highest elevation is 31.3m, the lowest point is 21.3m, and the max span is 38.5m [22]. In the test, we used the PDMS to monitor the dynamic deformation of the southeast side of the tennis stadium.
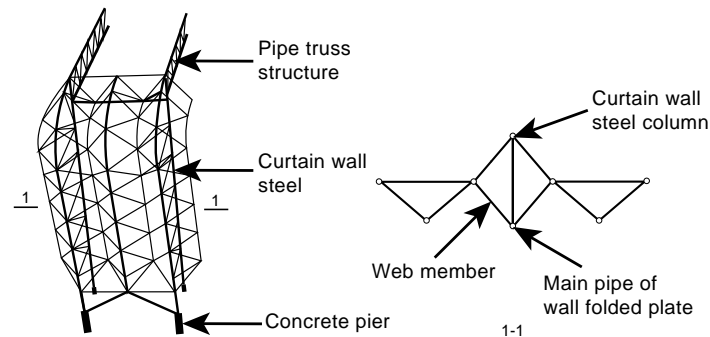
Fig. 8 – Layout of steel structure wall members

Figure 9 (a) shows we set up a camera at a suitable position on the test field, set up a reference plane by two tripods right in front of the camera. We selected 12 points as monitoring points, as Figure 9 (b) shows. Then, we control the camera to shoot them continuously with 12 times as a group, total four groups are shot. In the process, use rangefinder obtained the relative positions of camera and object plane, use steel ruler obtained the relative positions of camera and the reference plane, and the length of reference baselines. Figure 9 (b) shows the reference points and monitoring points used in this test.
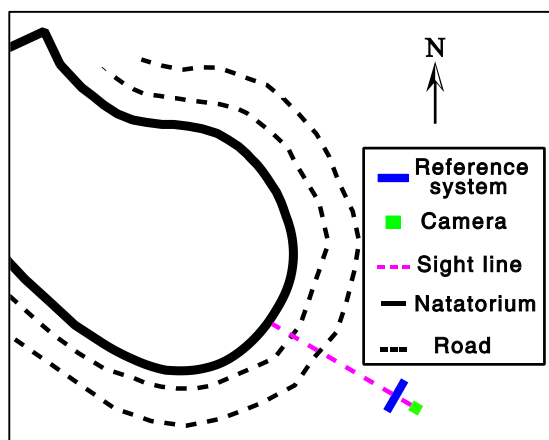
(a) Sketch Map
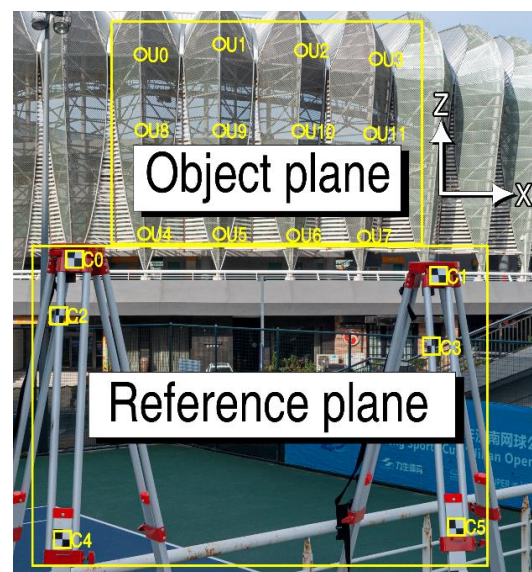
(b) Layout of points

Fig. 9 – Test field

Results and analysis

Use the PST-IM-MP method to obtain the deformation of the monitoring points U0-U11, and the deformations of these monitoring points in the X direction and the Z direction, as shown in Table 3 and 4. For the convenience of the display, only two decimal places were reserved here. Use the Z-MP method to obtain the deformation of monitoring points U0-U11, as shown in Table 5 and 6:

Tab. 3 – Deformation of U0–U11 in the X direction/mm

Time/s	U0$_X$	U1$_X$	U2$_X$	U3$_X$	U4$_X$	U5$_X$	U6$_X$	U7$_X$	U8$_X$	U9$_X$	U10$_X$	U11$_X$
0	12.91	6.58	-81.07	-3.89	59.20	53.59	48.06	42.97	15.13	9.34	3.56	39.24
1	46.45	46.95	-35.10	25.50	59.79	59.91	39.55	39.63	2.49	2.53	23.14	23.09
2	79.98	87.32	10.88	54.88	60.38	66.23	31.03	36.28	-10.16	-4.29	42.72	6.94
3	-30.66	-24.56	-58.96	-11.81	55.72	20.63	-14.55	-9.16	-28.78	-22.59	-16.48	-51.85
4	-9.59	-12.22	-56.18	-18.26	-13.41	24.88	-18.66	19.86	-11.20	-54.93	-57.68	-19.30
5	19.25	5.38	-47.24	-55.26	41.88	30.20	-22.19	8.10	-12.22	-24.13	-36.20	-6.03
6	72.85	30.15	-14.44	62.35	53.22	91.45	7.04	4.60	-17.22	20.77	17.95	15.14
7	-30.52	-72.78	-112.42	-68.06	-5.63	35.51	-5.28	-46.01	-102.04	-60.67	-60.44	-59.85
8	-34.57	-45.52	-94.23	-98.21	37.33	28.86	-61.28	12.80	-62.54	-30.21	-38.94	-46.36
9	14.37	-14.43	-82.59	-66.66	50.20	43.30	-24.86	30.21	-61.04	-27.20	-34.33	-20.11
10	63.31	16.67	-70.94	-35.11	63.07	57.73	11.57	47.61	-59.53	-24.19	-29.72	6.15

Tab. 4 – Deformation of U0–U11 in the Z direction/mm

Time/s	U0$_Z$	U1$_Z$	U2$_Z$	U3$_Z$	U4$_Z$	U5$_Z$	U6$_Z$	U7$_Z$	U8$_Z$	U9$_Z$	U10$_Z$	U11$_Z$
0	-62.69	22.39	107.28	-12.92	17.31	-20.69	23.11	66.67	-63.44	-19.50	24.43	27.16
1	-76.00	6.54	69.79	-50.19	18.92	-20.80	0.87	42.98	-70.56	-28.19	-6.41	-5.06
2	-89.31	-9.32	32.29	-87.46	20.52	-20.90	-21.38	19.28	-77.68	-36.87	-37.24	-37.27
3	-62.00	-60.59	-15.41	-90.86	-33.22	-71.36	-68.62	-24.98	-49.94	-5.72	-84.72	-81.66
4	-31.30	-73.01	-31.10	-69.46	-13.77	-54.47	-54.25	-54.00	-64.94	-23.55	-64.21	-22.75
5	-121.06	-117.43	-68.94	-99.20	-39.57	-74.94	-69.58	-23.50	-104.08	-57.01	-92.12	-86.33
6	-42.26	-1.71	39.63	-82.01	7.11	7.20	-33.70	-33.62	-38.73	-38.59	-38.49	2.65
7	-0.54	-83.38	40.18	-80.60	15.24	-25.69	-25.69	-25.65	-34.91	-34.75	-75.66	-34.44
8	-41.49	-83.30	40.14	-80.52	15.22	-25.67	-25.67	-25.63	-34.89	-34.72	-75.59	6.53
9	-34.68	-59.43	20.28	-61.30	28.44	-15.30	-38.59	-20.65	-45.87	-7.64	-71.94	7.62
10	-27.86	-35.56	0.41	-42.08	41.66	-4.92	-51.50	-15.66	-56.85	19.44	-68.29	8.71

Tab. 5 – Zero-centered deformation of U0–U11 in the X direction/mm

Time/s	U0$_X$	U1$_X$	U2$_X$	U3$_X$	U4$_X$	U5$_X$	U6$_X$	U7$_X$	U8$_X$	U9$_X$	U10$_X$	U11$_X$
0	-5.62	4.44	-22.68	15.61	17.22	7.02	48.93	25.98	46.69	28.94	20.51	46.69
1	27.92	44.81	23.29	45.00	17.81	13.34	40.42	22.64	34.04	22.12	40.09	14.48
2	61.46	85.18	69.27	74.38	18.40	19.66	31.90	19.29	21.40	15.31	59.67	-17.74
3	-49.19	-26.70	-0.57	7.69	13.74	-25.94	-13.68	-26.15	2.78	-2.99	0.47	-62.13
4	-28.12	-14.36	2.21	1.24	-55.39	-21.69	-17.79	2.87	20.36	-35.33	-40.73	-3.22
5	0.73	3.24	11.15	-35.76	-0.10	-16.37	-21.32	-8.89	19.34	-4.53	-19.25	-66.80
6	54.33	28.01	43.95	81.85	11.24	44.88	7.91	-12.39	14.34	40.37	34.90	22.18
7	-49.05	-74.92	-54.03	-48.56	-47.61	-11.06	-4.41	-63.00	-70.48	-41.07	-43.49	-14.91
8	-53.10	-47.66	-35.84	-78.71	-4.65	-17.71	-60.41	-4.19	-30.98	-10.61	-21.99	26.06
9	-4.16	-16.57	-24.20	-47.16	8.22	-3.28	-23.99	13.22	-29.48	-7.60	-17.38	27.15
10	44.79	14.53	-12.55	-15.61	21.09	11.16	12.44	30.62	-27.97	-4.59	-12.77	28.24

Tab. 6 – Zero-centered deformation of U0–U11 in the Z direction/mm

Time/s	U0$_Z$	U1$_Z$	U2$_Z$	U3$_Z$	U4$_Z$	U5$_Z$	U6$_Z$	U7$_Z$	U8$_Z$	U9$_Z$	U10$_Z$	U11$_Z$
0	-9.13	67.37	85.96	55.86	10.23	9.09	56.29	75.28	-5.09	4.78	78.09	46.69
1	-22.44	51.52	48.46	18.59	11.84	8.98	34.05	51.59	-12.21	-3.90	47.25	14.48
2	-35.75	35.66	10.97	-18.68	13.44	8.88	11.80	27.89	-19.33	-12.59	16.42	-17.74
3	-8.44	-15.61	-36.73	-22.08	-40.30	-41.58	-35.44	-16.37	8.41	18.56	-31.06	-62.13
4	22.26	-28.03	-52.42	-0.68	-20.85	-24.69	-21.07	-45.39	-6.59	0.73	-10.55	-3.22
5	-67.50	-72.45	-90.26	-30.42	-46.65	-45.16	-36.40	-14.89	-45.73	-32.73	-38.46	-66.80
6	11.30	43.27	18.31	-13.23	0.03	36.98	-0.52	-25.01	19.62	-14.31	15.17	22.18
7	53.02	-38.40	18.86	-11.82	8.16	4.09	7.49	-17.04	23.44	-10.47	-22.00	-14.91
8	12.07	-38.32	18.82	-11.74	8.14	4.11	7.51	-17.02	23.46	-10.44	-21.93	26.06
9	18.89	-14.45	-1.05	7.48	21.36	14.48	-5.40	-12.03	12.48	16.64	-18.28	27.15
10	25.70	9.42	-20.91	26.70	34.58	24.86	-18.32	-7.05	1.50	43.72	-14.63	28.24

Figures 10 (a)–(c) show the deformation curve of U0 - U11 point in X and Z direction generated by the PST-IM-MP method and the Z-MP method. The Z-MP method can shift the deformation curve to the X-axis without changing the relative deformation, and shape variable of the monitoring point fluctuates up and down around the X-axis. Figure 10 (d) shows the distribution of the data generated by the two algorithms. We can see that the Z–MP method not only facilitates the intra-group comparison of the monitoring points but also makes the deformation curve more reasonable and makes preparations for the next step to obtain the 2-D deformation of the monitoring points on the X-Z plane.
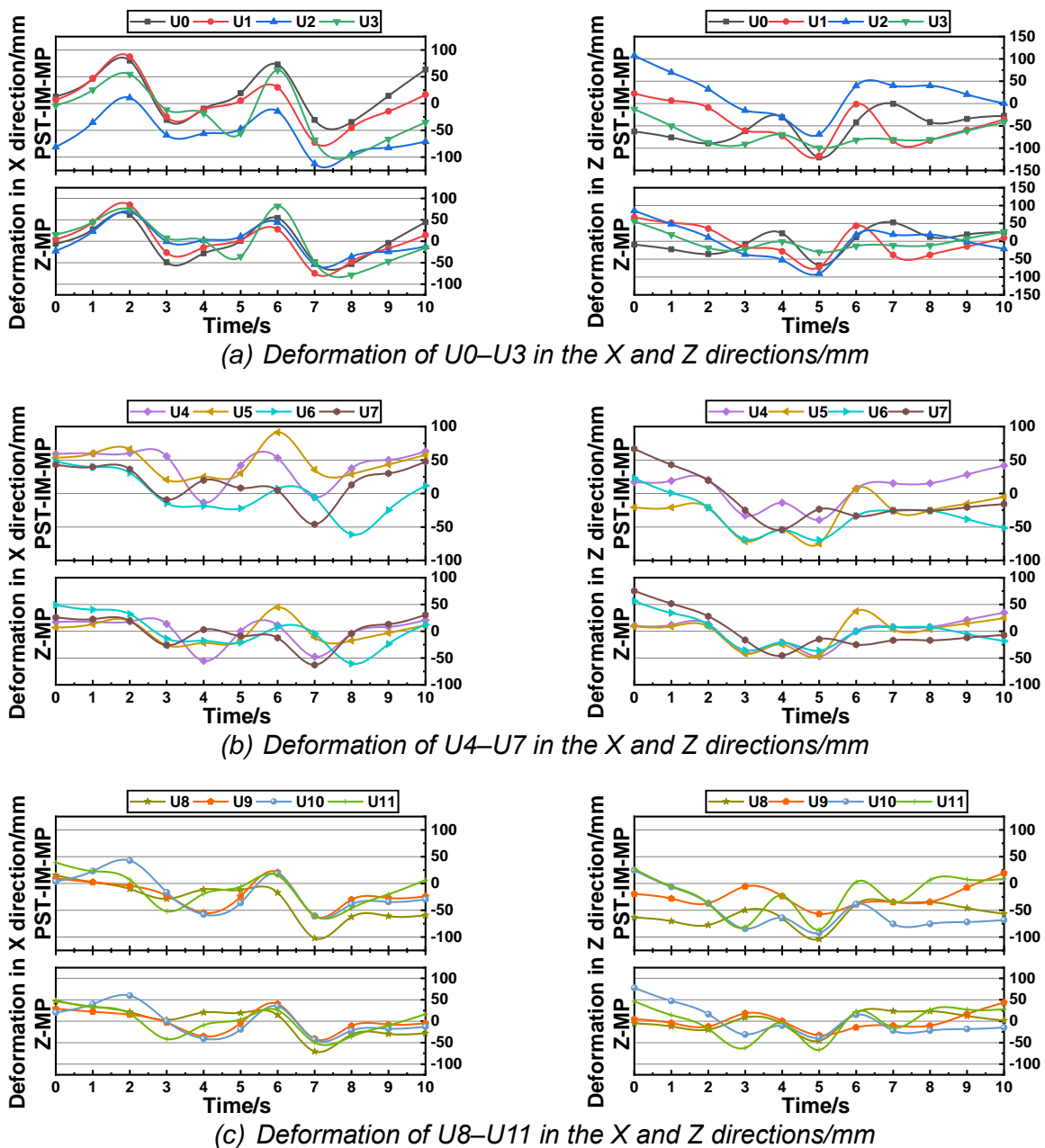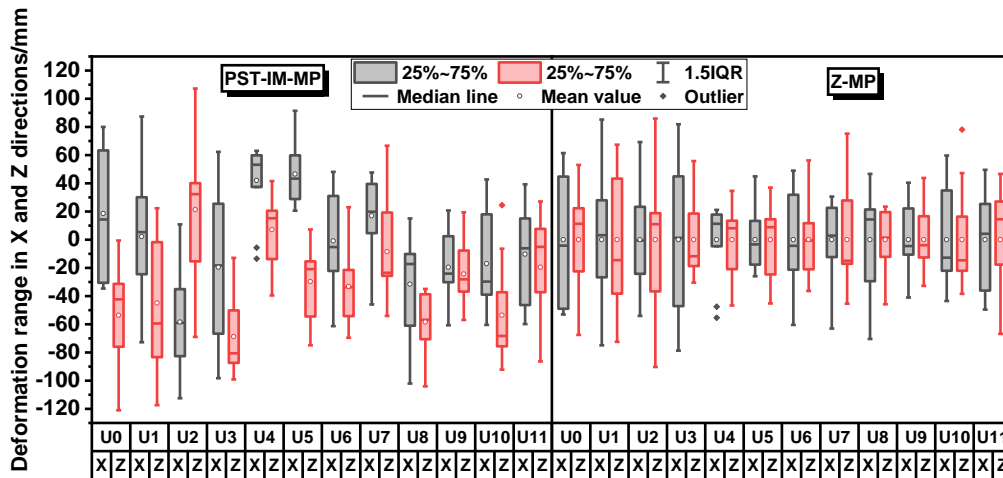

(a) Deformation of U0–U3 in the X and Z directions/mm

(b) Deformation of U4–U7 in the X and Z directions/mm

(c) Deformation of U8–U11 in the X and Z directions/mm

Fig. 10 – Deformation of U0–U11 in the X and Z directions/mm

(d) Deformation of U0–U11 in the X and Z directions/mm

Fig. 10 – Deformation of U0–U11 in the X and Z directions/mm

The deformations of each monitoring point by the PST-IM-MP method and the Z-MP method in the X direction and the Z direction are obtained as follows, the result as Table 7 and 8 shows.

$$Di'_{xz} = \sqrt{(\Delta X')^2 + (\Delta Z')^2} \tag{20}$$
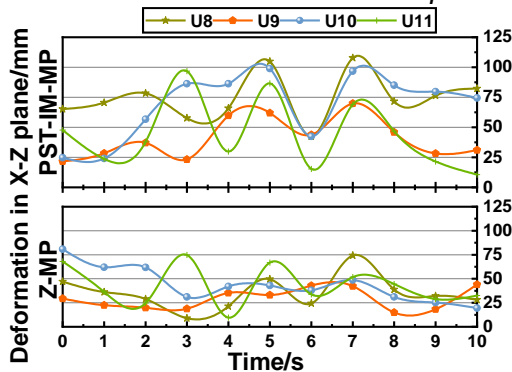
Tab. 7 – Deformation of U0–U11 in the X-Z plane/mm

Time/s	$D0_{xz}$	$D1_{xz}$	$D2_{xz}$	$D3_{xz}$	$D4_{xz}$	$D5_{xz}$	$D6_{xz}$	$D7_{xz}$	$D8_{xz}$	$D9_{xz}$	$D10_{xz}$	$D11_{xz}$
0	64.01	23.34	134.47	13.49	61.68	57.45	53.33	79.32	65.22	21.62	24.69	47.72
1	89.07	47.40	78.11	56.29	62.71	63.42	39.55	58.46	70.60	28.30	24.01	23.64
2	119.89	87.82	34.07	103.25	63.77	69.45	37.68	41.08	78.34	37.12	56.67	37.91
3	69.17	65.38	60.94	91.62	64.87	74.28	70.15	26.61	57.64	23.30	86.31	96.73
4	32.74	74.03	64.21	71.82	19.22	59.88	57.37	57.54	65.90	59.77	86.31	29.83
5	122.58	117.55	83.57	113.55	57.62	80.80	73.03	24.86	104.79	61.91	98.98	86.54
6	84.22	30.20	42.18	103.02	53.69	91.73	34.43	33.93	42.39	43.82	42.47	15.37
7	30.52	110.68	119.38	105.49	16.25	43.83	26.23	52.68	107.85	69.92	96.84	69.05
8	54.00	94.93	102.42	127.00	40.31	38.62	66.44	28.65	71.61	46.02	85.03	46.82
9	37.53	61.16	85.04	90.56	57.70	45.92	45.90	36.59	76.35	28.25	79.71	21.50
10	69.17	39.27	70.94	54.80	75.59	57.94	52.78	50.12	82.31	31.03	74.48	10.66

Tab. 8 – Zero-centered deformation of U0–U11 in the X-Z plane/mm

Time/s	$D0_{xz}$	$D1_{xz}$	$D2_{xz}$	$D3_{xz}$	$D4_{xz}$	$D5_{xz}$	$D6_{xz}$	$D7_{xz}$	$D8_{xz}$	$D9_{xz}$	$D10_{xz}$	$D11_{xz}$
0	10.72	67.52	88.90	58.00	20.03	11.48	74.58	79.64	46.96	29.33	80.74	68.05
1	35.82	68.28	53.77	48.69	21.39	16.08	52.84	56.34	36.16	22.46	61.97	36.36
2	71.10	92.34	70.13	76.69	22.79	21.57	34.01	33.92	28.83	19.82	61.88	24.71
3	49.90	30.93	36.74	23.38	42.58	49.01	37.99	30.85	8.86	18.80	31.07	74.76
4	35.86	31.49	52.47	1.42	59.18	32.87	27.57	45.48	21.39	35.34	42.08	9.59
5	67.50	72.52	90.95	46.94	46.65	48.04	42.18	17.34	49.65	33.04	43.01	66.93
6	55.49	51.55	47.61	82.92	11.24	58.15	7.93	27.91	24.30	42.83	38.05	33.73
7	72.23	84.19	57.23	49.97	48.30	11.79	8.69	65.26	74.28	42.39	48.74	51.78
8	54.45	61.15	40.48	79.58	9.38	18.18	60.88	17.52	38.87	14.89	31.06	44.52
9	19.34	21.98	24.22	47.75	22.89	14.85	24.59	17.87	32.01	18.30	25.23	28.88
10	51.64	17.32	24.39	30.93	40.51	27.25	22.14	31.42	28.01	43.96	19.42	32.67
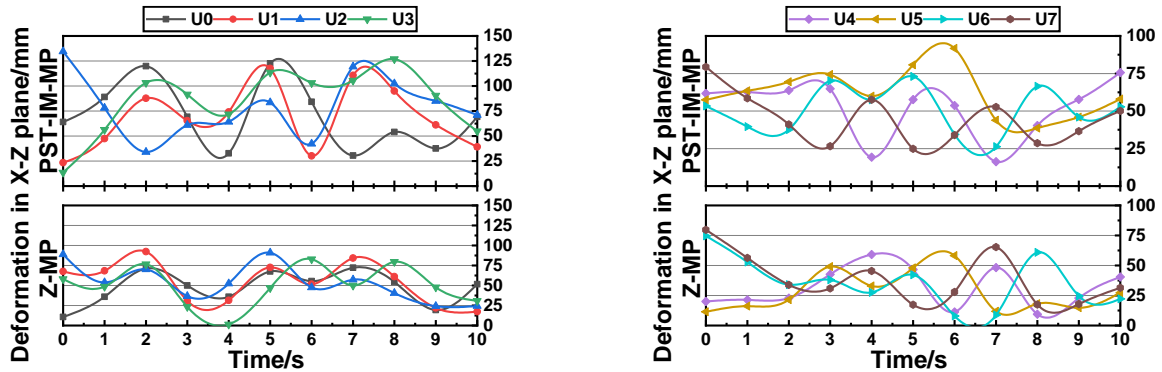
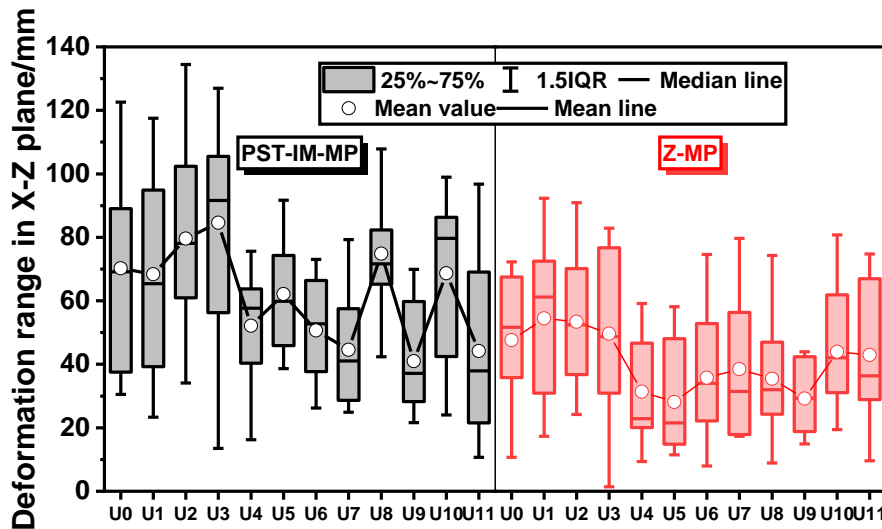

(a) Deformation of U0–U3 in the X-Z plane/mm

(b) Deformation of U4–U7 in the X-Z plane/mm

(c) Deformation of U8–U11 in the X-Z plane/mm

Figure 11 shows the deformation curve of each monitoring point on the X-Z plane by two methods. (a)–(c) show the difference of the deformation curve of each monitoring point generated by the PST-IM-MP method and the Z-MP method. The Z-MP method can reduce the situation in which deformation calculated by the PST-IM-MP method is exaggerated to varying degrees.

(d) Deformation of U0–U11 in the X-Z plane/mm

Fig. 11 – Deformation of U0–U11 in the X-Z plane/mm

The observation of three deformation curves generated by the Z-MP method shows that the three groups of points are undergoing elastic deformation, and the monitoring structure is in a stable equilibrium state. The observation of three deformation curves generated by the Z-MP method shows that the three groups of points are undergoing elastic deformation, and the monitoring structure is in a stable equilibrium state. If U0-U3, U4-U7, and U8-U11 group the data, they correspond to the upper, lower, and middle parts of the monitoring building. By comparing the deformation values of these three groups of points, it can be found that: U0-U3 group is the largest,

U8-U11 group is the second, and U4-U7 group is the smallest. Therefore, it can be determined: for the whole structure, the height of the monitoring structure is correlated positively with the deformation range on the whole. However, according to the analysis above, the deformation value and deformation interval of U9 point are the smallest, indicating that there may be abnormal deformation near U9 point, which hinders the normal elastic deformation of this point. If the deformation value and deformation interval of U1 and U3 are the largest, the nearby parts of these points are undergoing relatively large and rapid elastic deformation, prone to damage accumulation and resistance attenuation. Relevant safety maintenance personnel should find out the deformation's reasons and further refine the deformation observation of these parts to ensure the healthy and safe operation of tennis courts.

CONCLUSION

(1)   If the spatial structure in a state of elastic deformation, the deformation value using the PST-IM-MP method obtained is available. However, the deformation curve by using these data generated is not user-friendly. If we obtain the 2-D deformation value of monitoring points in the X-Z plane by directly using the data, it will exaggerate the 2-D deformation in the X-Z plane of points at different levels. This paper offered the Z-MP method to solve these problems effectively.

(2)   This paper proposed the PDMS to use for non-contact dynamic deformation monitoring of complex structures. Moreover, PDMS is robust, easy realizing, economical, and highly automatic, can apply to amounts of complex scenarios.

(3)   For the tennis stadium, the height of the monitoring structure is positively correlating with the deformation range.

(4)   According to the deformation monitoring, the maximum deflection of the monitoring points is 92.34mm, which conforms to the design standard [23]. The tennis stadium's spatial structure is safe on the whole, but there are still a few abnormal deformation values that need to be verified by relevant security personnel.

ACKNOWLEDGEMENTS

REFERENCES

[1]   Kabando E.K., Gong J., 2019. An overview of long-span spatial grid structures failure case studies. Asian Journal of Civil Engineering. Vol. 20. No. 8: 1137-1152. doi: 10.1007/s42107-019-00168-4

[2]   Dong S.L., Luo Y.Z., Zhao Y., 2005. Practical application and research advances of long-span space structures. SPATIAL STRUCTURES. Vol. 11. No. 4: 3-10. doi: 10.3969/j.issn.1006-6578.2005.04.001

[3]   Investigation C., 2009. On the roof collapse at Stadium Sultan Mizan Zainal Abidin: Final report on the roof collapse at Stadium Sultan Mizan Zainal Abidin, Terengganu, Malaysia.

[4]   Board D.S., 2012. Roof collapse during extension work at the stadium of FC Twente in Enshede Netherlands.

[5]   Department B., 2017. Final investigation report on the collapse of roof structure of Chan Tai Ho Multipurpose Hall of HU Fa Kuang Sports center of City University of Hong Kong at Chee Avenue, Kowloon

[6]   Luo Y.Z., Shen Y.B., Tong R.F., Wang X.B., 2009. Health Monitoring and Early Warning Health Monitoring and Early Warning Technology in Spatial Structure. CONSTRUCTION TECHNOLOGY. Vol. 38. No. 03: 4-8.

[7]   Sabamehr A., Lim C., Bagchi A., 2018. System identification and model updating of highway bridges

using ambient vibration tests. Journal of Civil Structural Health Monitoring. Vol. 8. No.755-771. doi: 10.1007/s13349-018-0304-5

[8] Doebling S.W., Farrar C.R., Prime M.B., Shevitz D.W., 1996. Damage Identification and Health Monitoring of Structural and Mechanical Systems from Changes in Their Vibration Characteristics: A Literature Review. Vol. doi: 10.2172/249299

[9] Goda I., L'Hostis G., Guerlain P., 2019. In-situ non-contact 3D optical deformation measurement of large capacity composite tank based on close-range photogrammetry. Optics and Lasers in Engineering. Vol. 119. No.37-55. doi: 10.1016/j.optlaseng.2019.02.006

[10] Zhou X., 2010. STRUCTURAL DESIGN AND HEALTH MONITORING OF JINAN OLYMPIC SPORTS CENTER. Engineering Mechanics. No. A02: 105-113.

[11] Xu J., Xi N., Zhang C., Zhao J.G., Gao B.T., Shi Q., 2011. Rapid 3D surface profile measurement of industrial parts using two-level structured light patterns. Optics and Lasers in Engineering. Vol. 49. No. 7: 907-914. doi: 10.1016/j.optlaseng.2011.02.010

[12] Xu X.Y., Yang H., Neumann I., 2018. Monotonic loads experiment for investigation of composite structure based on terrestrial laser scanner measurement. Composite Structures. Vol. 183. No.563-567. doi: 10.1016/j.compstruct.2017.07.001

[13] Cuypers W., Van Gestel N., Voet A., Kruth J.P., Mingneau J., Bleys P., 2009. Optical measurement techniques for mobile and large-scale dimensional metrology. Optics and Lasers in Engineering. Vol. 47. No. 3: 292-300. doi: https://doi.org/10.1016/j.optlaseng.2008.03.013

[14] Urbanová P., Hejna P., Jurda M., 2015. Testing photogrammetry-based techniques for three-dimensional surface documentation in forensic pathology. Forensic Science International. Vol. 250. No.77-86. doi: 10.1016/j.forsciint.2015.03.005

[15] Yu C.X., Song C.Z., Tong Y.B., Li X.L., Quan J., Xu F., 2001. Digital Photographic and Computer Technology in Real-time Monitored Structural Deformation. JOURNAL OF JINAN UNIVERSITY. Vol. 15. No. 3: 232-234. doi: 10.3969/j.issn.1671-3559.2001.03.014

[16] Chen M.Z., 2012. The Application and Comparison of Digital Ground Photogrammetry Technology for Bridge Safety Monitoring. Applied Mechanics and Materials. Vol. 170-173. No.2979-2986. doi: 10.4028/www.scientific.net/AMM.170-173.2979

[17] Zhang G.J., Yu C.X., Guo G.L., 2017. Application of digital close-range photogrammetry in the deformation observation of check gate. JOURNAL OF SHANDONG UNIVERSITY (ENGINEERING SCIENCE). Vol. 47. No. 06: 46-51.

[18] Yu C.X., Zhang G.J., Ding X.H., Zhao Y.Q., Guo G.L., 2019. MONITORING DYNAMIC DEFORMATION OF SHUTTLE STEEL SHELVES BY DIGITAL PHOTOGRAPHY. Civil Engineering Journal. Vol. 28. No. 2: 136-150. doi: 10.14311/CEJ.2019.02.0012

[19] Zhang G.J., Guo G.L., Yu C.X., Li L., Wang X., 2018. Monitoring Instantaneous Dynamic Displacements of Masonry Walls in Seismic Oscillation Outdoors by Monocular Digital Photography. Mathematical Problems in Engineering. Vol. 2018. 1-15. doi: 10.1155/2018/4316087

[20] Yu C.X., Zhang G.J., Ding X.H., Zhao Y.Q., Guo G.L., 2019. MONITORING DYNAMIC GLOBAL DEFLECTION OF A BRIDGE BY MONOCULAR DIGITAL PHOTOGRAPHY. Civil Engineering Journal. Vol. 27. No. 14: 168-182. doi: 10.14311/CEJ.2018.02.0014

[21] Wang P.J.，Xu Y.M.: photogrammetry. Wuhan university press: Wuhan (2016)

[22] Zhou Y., Fu X.Y., Yang X.B., 2008. Structural design of Tennis Gymnasium of Ji Nan Olympic Sports Center. SPATIALS TRUCTURES. Vol. 14. No. 04: 26-31.

[23] GB50017-2017, 2017. Steel structure design standard. China Standards Press.

[24] Feng W.H., 2002, Close Range Photogrammetry: Measuring an Object Shape and Motion State Imaging Method, section 8.5 (Wuhan University Press) 179 pp.

[25] Ge Y.Q., Yu C.X., Liu X.D.，Wang R.H., 2020. Monitoring dynamic deformation of communication tower using photography dynamic monitoring system. IOP Conference Series: Earth and Environmental Science. Vol. 558. No. 2: doi: 10.1088/1755-1315/558/2/022061

FLOW OVER BROAD-CRESTED WEIR WITH INFLOW BY APPROACH SHAFT – NUMERICAL MODEL

Jakub Major[1], Martin Orfánus[2] and Zbyněk Zachoval[3]

1. *AQUATIS a.s., Botanická 834/56, Brno, Czech Republic; jakub.major@aquatis.cz*
2. *Slovak University of Technology in Bratislava, Faculty of Civil Engineering, Department of Hydraulic Engineering, Bratislava, Slovakia; martin.orfanus@stuba.sk*
3. *Brno University of Technology, Faculty of Civil Engineering, Institute of Water structures, Brno, Czech Republic; zachoval.z@fce.vutbr.cz*

ABSTRACT

In the case of flow over rectangular broad-crested weir, where the inflow is realized by approach shaft, occurs influence of water surface level by approach flow velocity. The paper describes numerical model of flow including weir, approach and outlet shaft. Simulations of flow were created by 2D and 3D model with using three methods of turbulent modelling. In this paper a water surface level for each model setup is evaluated and then it is compared with measured values.

KEYWORDS

Approach shaft, Broad-crested weir, Free surface level, Numerical model

INTRODUCTION

In practice there are also used broad-crested weirs with approach shaft to determine the discharge, eventual to regulate the water surface level (laboratories, pond inlet structures, wastewater treatment plants, weirs of retention basins in sewer systems, etc.) (**Chyba! Nenalezen zdroj odkazů.**).

In the professional literature, the flow over the mentioned weir with the approach shaft is described in the publications **Chyba! Nenalezen zdroj odkazů.**, **Chyba! Nenalezen zdroj odkazů.** and **Chyba! Nenalezen zdroj odkazů.**, which are based on extensive experimental research. From the experimental research is known the water surface profile in the longitudinal plane of symmetry of the approach shaft and weir, as well as the pressure height on the approach shaft walls for the full range of geometric dimension ratios used in practice [2], [4]. The water surface level in the approach shaft and the velocity field in the wake area at the weir crest are known only for specific geometric and flow conditions [3], [4].

As the authors know, at present only models of overflow over broad-crested weir with vertical inflow are performed [5], [6], [7], [8] and [9], but none of the authors dealt with numerical modelling of overflow over broad-crested weir with approach shaft.

The aim of the research was creating a suitable numerical model for the most reliable description of the flow over rectangular broad-crested weir with inflow by approach shaft. Model was validated on the basis of measured water surface level profile. The results of the simulations could be used to supplement the measured data from experimental research.
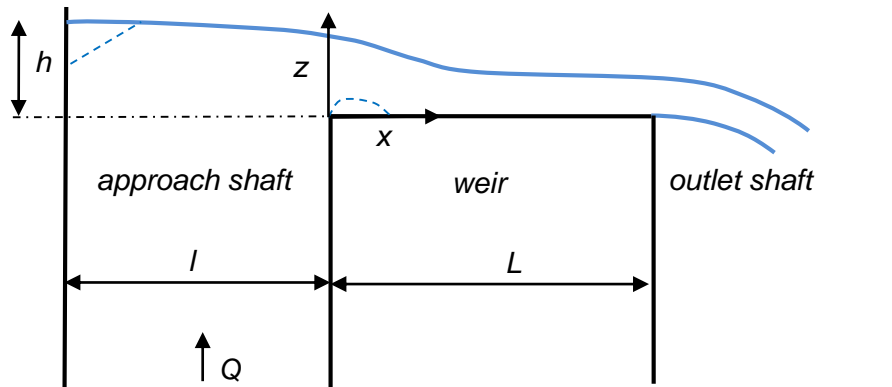
Fig. 1 – Scheme of flow over broad-crested weirs with approach shaft

WEIR GEOMETRY

The weir geometry, approach shaft and outlet shaft were created in the software FLOW-3D version 11.0.4 [10], in which calculations were also performed. Two concepts of model construction were used to evaluate their advantages and disadvantages. The 2D model used the concept of fixed blocks, which defined the space for flow by two blocks of the network (Figure 2, left). The width of the fixed blocks was 2 m, the width of the blocks of the computer network was the same as the width of the weir. There were three solid blocks. The first block (red in Figure 2) formed the opposite wall of the inlet shaft with respect to the weir. The second block (blue in Figure 2) formed a broad-crested weir, an adjacent wall of the inlet shaft and an adjacent wall of the outlet shaft. The third block (yellow in Figure 2) formed the opposite wall of the outlet shaft. Their mutual location was chosen so that the nodes of the network were in one case at the boundaries of the computational area and in the other case were not. The 3D model used the concept of five blocks of a network to define the space through which water can flow (Figure 2).

The weir had a length in the direction of flow $L = 0.650$ m. The side walls of the weir and the shaft were elevated 0.500 m above the crest of the weir. The weir, the approach shaft and the outlet shaft were same width $b = 0.500$ m. The length of the approach shaft was $l = 0.300$ m and its height was 4 m. In the case of a 3D model due to the reduction of the number of cells, the height was only 2 m. The length and height of the outlet shaft were the same as for the approach shaft. The overflow was free with a fully aerated nappe in the outlet shaft.

SIMULATIONS

To describe the water surface level a simulation using a 2D and 3D model for the head $h = 0.253$ m (measured 0.05 m from the shaft wall) at discharge 0.090 m³/s) was performed, therefore for a l/h ratio of approximately 1.2. Simulations were performed with RANS (Reynolds-averaged Navier-Stokes) turbulence models k-ω, k-ε and *LES* (Large eddy simulation). Information on individual turbulence models can be found in publications [10], [11] and [12], due to their scope and general knowledge they are not given here. Steady flow was solved with a free water surface, one incompressible fluid (water) with density 1000 kg/m³ and kinematic viscosity 0,001 m²/s. It was considered with a surface tension 0,073 N/m. The threshold deviation in the calculation was set to 2% [2].

The coordinate system has been chosen so that *x* coordinate defined the length of the shaft and crest of weir in the flow direction, the *y* coordinate defined the width of the shaft and the weir and the *z* direction the height of the shaft.

Boundary conditions of several types are described in Figure 2. The boundary condition at the inflow (bottom of the approach shaft) for 2D simulation was entered as the inflow velocity (V) corresponding to the specific discharge of the given state. The boundary condition at the inflow for the 3D simulation was entered as a pressure (P). The advantage of entering the velocity is the direct calculation, the disadvantage is relatively unstable solution. The advantage of entering the pressure is a stable solution, the disadvantage is the indirect (iterative) calculation. The wall boundary condition (W) with a hydraulically smooth surface was specified on all solid walls. The symmetric boundary condition (S) was specified at the junction of the network blocks. The free outflow (O) was entered at the outflow section of the outlet shaft and at the air boundaries (Figure 2). The initial condition was the hydrostatic pressure distribution along the height of the calculation space from the measured water level. The initial water level was entered as a horizontal level over the weir crest.
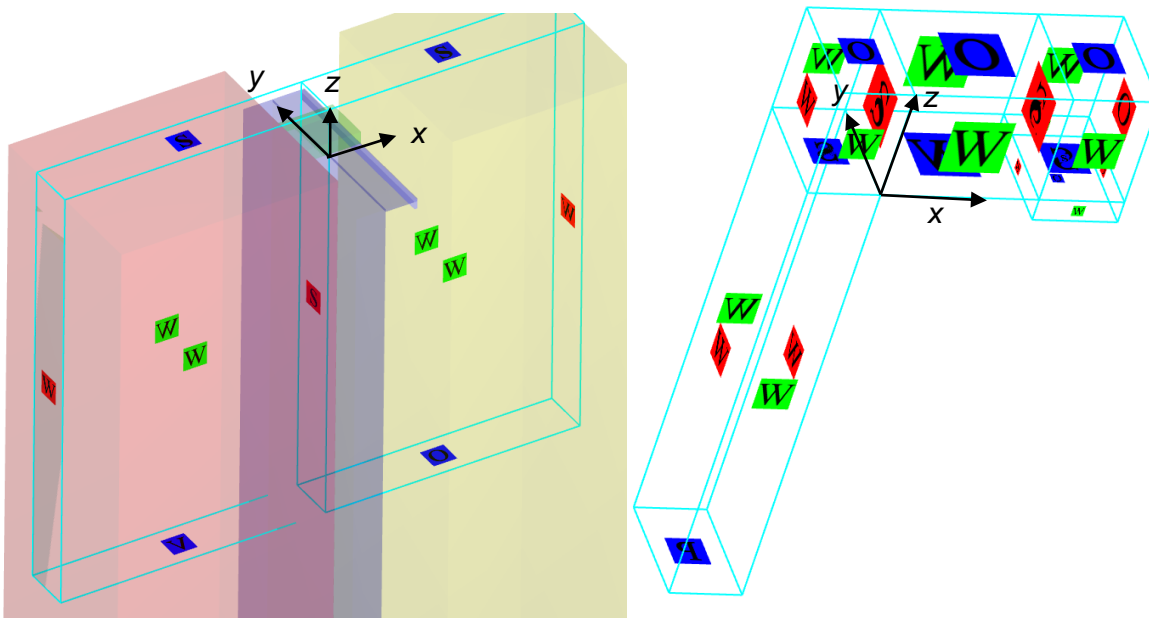

Fig. 2 – Scheme of calculation area and entering boundary conditions for 2D model (left) and for 3D model (right)

During the calculations, three analyses were performed to determine the minimum requirements for the models so that the results were conclusively and repeatable.

The first analysis concerned the influence of the position of the structured rectangular mesh against the solid walls, when it was shown that the mutual position influences the results. The effect on the water surface level was up to 0.004 m, the change was mainly reflected in the velocity field near the walls. For reasons of repeatability, a position was chosen where the nodes of the network corresponded to the surface of the solid wall.

The second analysis concerned the effect of cell size on the results. A 2D model with a $k\text{-}\omega$ turbulence model was used for the analysis. The length of the cell edges in the calculation area was gradually reduced until the water level did not change by more than 0.001 m. This state occurred at a cell size length (in the *x* and *z* direction) of 0.005 m in the whole calculation area. In the *y* direction, the size of the cells in the 3D model was set to 0.010 m over the whole width of the area. Guidelines for good mesh quality specified by FLOW-3D was satisfied. The maximum aspect

----

ratio within a single cell was less than 3, the maximum adjacent cell size ratio was less than 1.25, the maximum inter-block cell size ratio was less than 2, and mesh planes coincide in the boundaries.

The third analysis concerned the minimum required shaft height. A 2D model was used for the analysis, where the development of the velocity field and the influence of the shaft length on the water surface level were monitored. It turned out that the height of the approach shaft 2 m below the weir crest was sufficient due to achieve a constant velocity distribution along the shaft height. It was also determined that the height of the outlet shaft 0.100 m below the weir crest will suffice, when the position of the network boundary does not affect the water surface level above the weir.

The total number of cells in the 2D model was 183 911, of which 46 366 were active. In the 3D model, the total number of cells was 4 114 141, all cells were active. The stabilization time was determined based on the change in water surface level over time. The criterion was a change of water surface level smaller than 0.001 m during 10 s. Flow was stabilized in 20 s at the latest. A standard desktop computer was used for the calculations (Intel i7, 4 cores, 4,6 GHz, 8 GB RAM). The calculation time lasted in the case of a 2D model in the range of 3 to 4 hours, in the case of a 3D model 1 to 2 days, depending on the overflow height.

EVALUATION AND COMPARISON

Water levels in the longitudinal plane of symmetry for 2D and 3D models and water levels in the entire approach shaft were evaluated using RANS turbulence models k-ω, k-ε and the *LES* model. The evaluation was performed in MS Excel. The values were then compared with the measured values [3]. In summary, the experimental model has the length of the weir 0.650 m, widths of the weir as well as the shaft $b = 0.500$ m, and height of the shaft 4.02 m. Discharge was 0.090 m^3/s. The broad-crested weir and the right downstream wall of the weir were made from polymethyl methacrylate with a thickness of 0.010 m. The left downstream wall was made of waterproof plywood with a thickness of 0.021 m. Water surface was measured by the point gauge and discharge by the electromagnetic flowmeter. Free overflow was achieved. The space underneath the nappe was fully aerated.

Figure 3 shows measured and calculated (2D and 3D) water surface longitudinal profile (turbulence model k-ω). Figure 4 shows measured water surface longitudinal profile and calculated (3D model) by RANS turbulence models k-ω, k-ε and the *LES* model.

From the comparison of calculated and measured water surface profiles shown in Figure 3 and Figure 4 is visible the quantitative difference. All numerical models underestimate the water surface level. The difference between the calculated and measured values is up to −0,016 m. From Figure 3, the water surface profile in the 3D model is qualitatively similar to the measured. From the above, the flow simulation using a 3D model better captures measured water surface than using a 2D model, which is due to the inclusion of friction against the side walls in 3D model. From Figure 4 it is visible that the k-ω model describes water surface profile the most accurately.
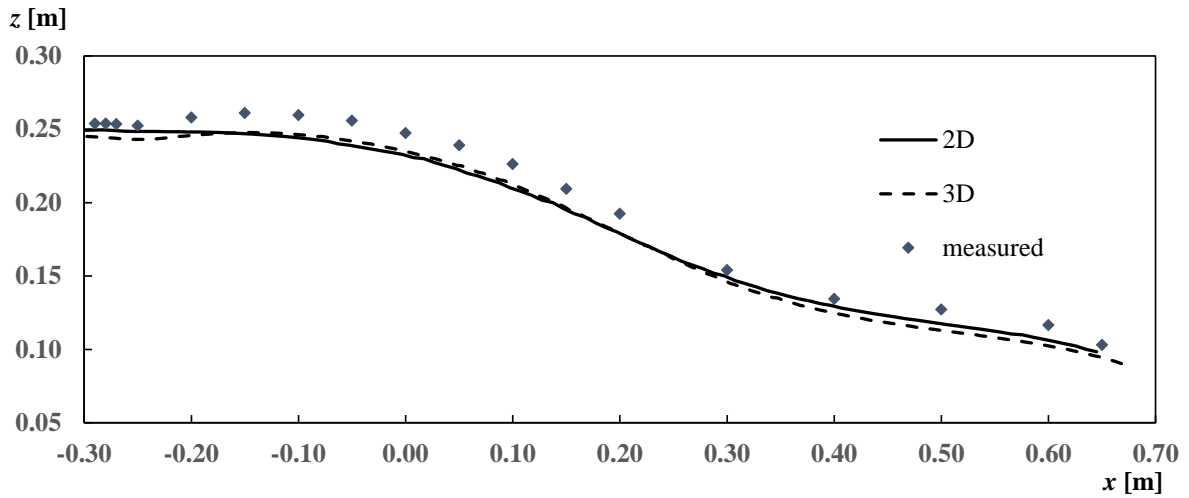
Fig. 3 – Longitudinal water surface profile, turbulence model k-ω, influence of model dimension
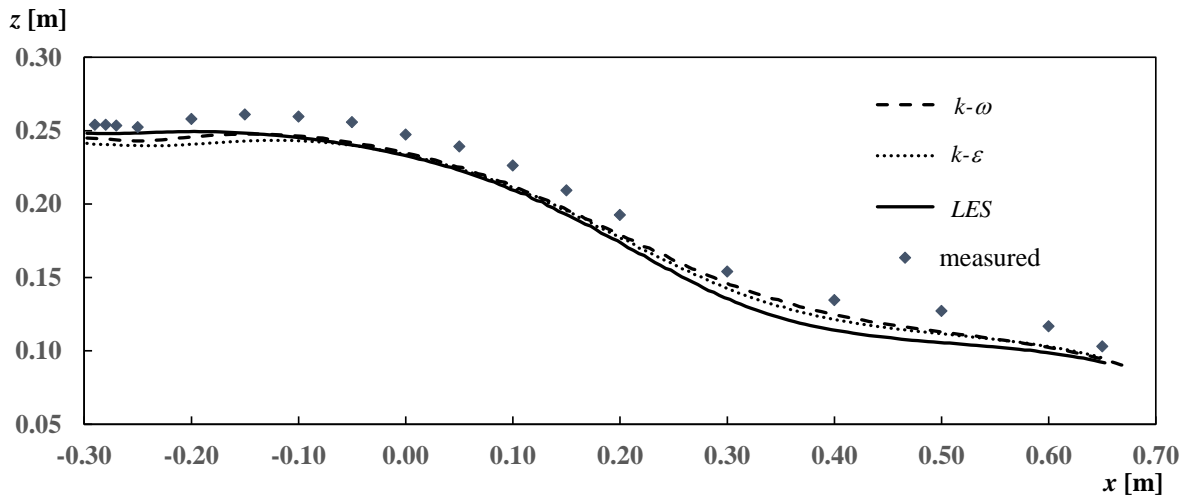

Fig. 4 – Longitudinal water surface profile, 3D model, influence of turbulence model

Figure 5 shows the relative error of the calculated water surface level profiles for the individual turbulence models, where h_M is measured water surface level and h_V is calculated for the individual models.

From Figure 5 it is visible that for $x < 0.15$ m the turbulence models show a relative error up to 10%, in the range $0.15 \leq x \leq 0.65$ up to 18 %.
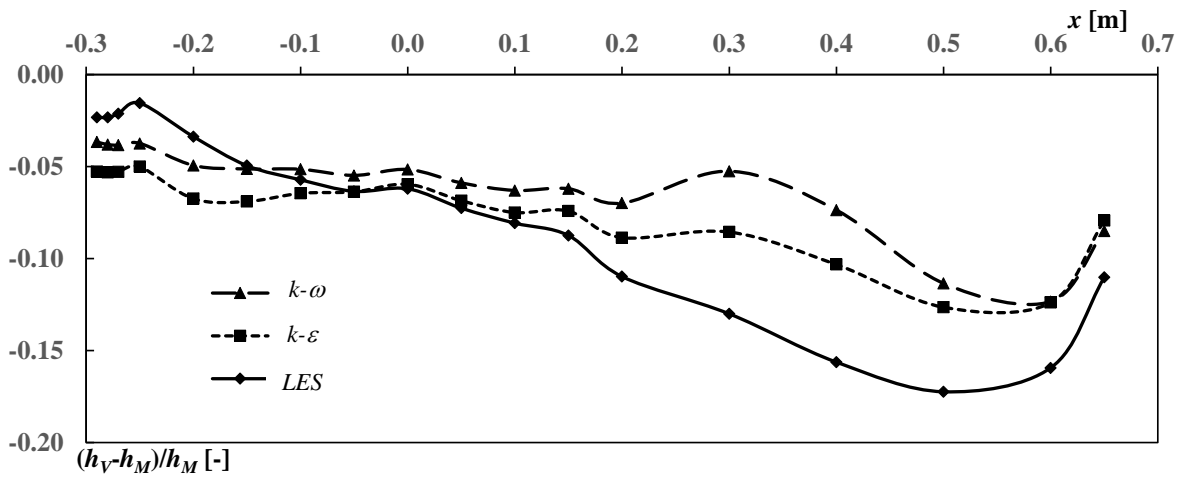
Article no. 19

THE CIVIL ENGINEERING JOURNAL 1-2021

Fig. 5 - Relative error of the calculated water surface profiles for individual models

The water surface levels in the whole approach shaft calculated by 2D and 3D model were evaluated in the program SMS 12.3. Figure 6 shows the isolines of the water surface level (relative to the weir crest level) calculated by 2D and 3D model using the $k\text{-}\omega$ model of turbulence and isolines from the measured values (linear interpolation on a triangular mesh) **Chyba! Nenalezen zdroj odkazů.**.
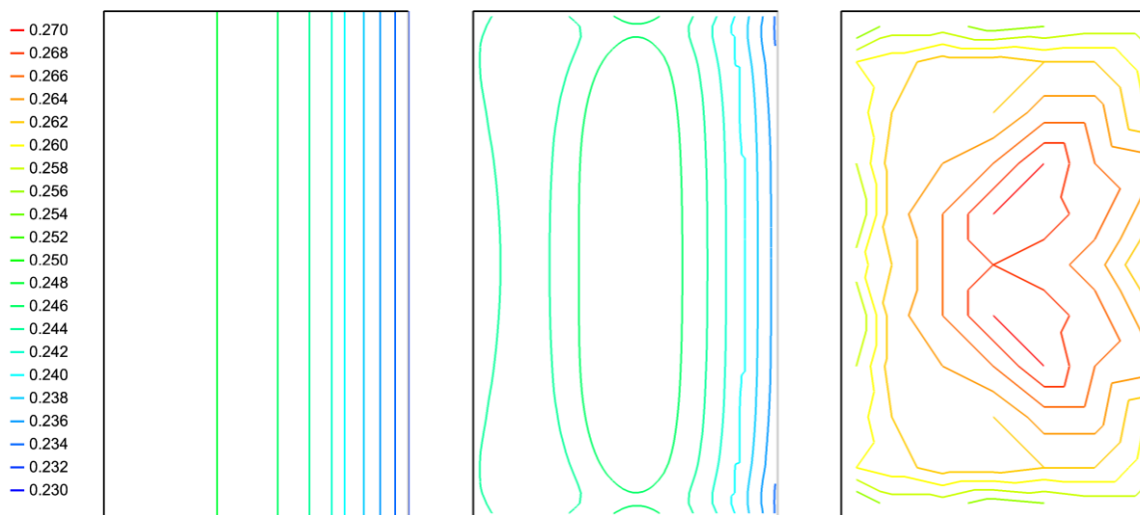

Fig. 6 - Water surface level above weir crest [m] in the approach shaft, left – 2D model, middle – 3D model and right – measured, the right boundary of the area defines the upstream edge of the weir crest
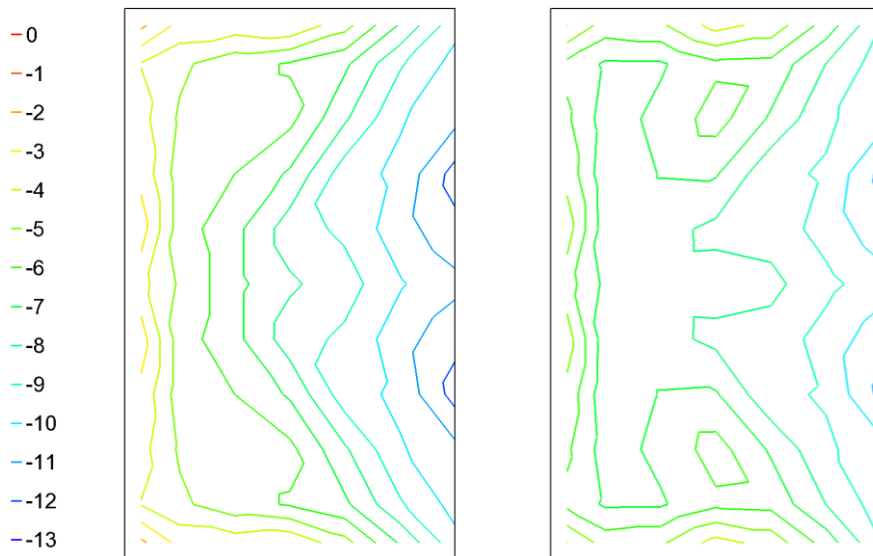
Fig. 7 – Deviation [%] of computed values of water surface level above the weir crest in the approach shaft from measured values, left – 2D model, right – 3D model, the right boundary of the area defines the upstream edge of the weir crest

In Figure 6 there are visible differences in the water surface levels of the calculated 2D and 3D models compared to the measured. In the Figure 7 there is visible the deviation of the computed values of the water surface level above the weir crest in the approach shaft from measured values.

In the case of 2D model, the water surface level is constant across the entire width of the inflow shaft. The water level does not correspond quantitatively and qualitatively to the measured water level. The given shape is similar to the conditions at lower overflow heights or large lengths of the approach shaft [2]. The difference between the calculated and measured water surface level is up to −0.033 m (deviation −12 %). The largest deviations are at the upstream edge of the weir crest.

In the case of 3D model, the results are quantitatively different, but qualitatively more similar to those measured. Near the approach shaft walls, the water surface level is lower, in the middle of the shaft it is higher. The difference is up to 0.006 m. The difference between the calculated and measured water surface level is up to −0.030 m (deviation −11 %). The largest deviations are at the upstream edge of the weir crest.

CONCLUSION

The numerical models in the case of flow over a broad-crested weir with approach shaft made it possible to determine the flow characteristics relatively quickly. The use of solid blocks in modelling allows for quick model creation, but at the cost of large number of inactive cells and frequent non-matching of the surface with the cell edges. Modelling without their use seems to be more suitable in terms of accuracy and complexity of calculation. It is necessary to observe a sufficient height of the approach and outlet shafts so that the influence of the input of boundary conditions, the size and position of the cells and sufficient simulation time to stabilize the flow do not show.

Qualitative agreement of the calculated water surface level profile by 2D and 3D models with RANS turbulence models *k-ω, k-ε* and *LES* model is relatively good, but quantitative agreement is insufficient. The water surface level calculated by numerical models in the section of the approach shaft and in the section of weir crest is significantly underestimated in the whole longitudinal plane of symmetry against to the measured. The relative error of the water surface level above the approach shaft is up to 10% and above the weir crest up to 18%. The RANS models calculate the water surface level profile more accurately than the LES model. Simulation using a 3D model gives a qualitatively better information about the water surface level in the approach shaft than the 2D model. The calculated water surface profiles using the RANS turbulence models *k-ω* and *k-ε* are very similar.

ACKGNOWLEDGEMENT

REFERENCES

[1]   Major J., 2020. Influence of inflow orientation on overflow characteristics over broad-crest (in Czech), Doctoral thesis, BUT, Brno.
[2]   Major, J., Zachoval, Z. Numerical model of flow over broad-crested-weir with inlet shaft (in Czech). Report of project ERASMUS+ č. 91/2017-2018, BUT, Brno, 2018.
[3]   Major, J., Zachoval, Z. Influence of inflow shaft geometry on capacity of broad-crested weir (in Czech). Report of project FAST-J-17-4577, BUT, Brno, 2018.
[4]   Major, J. Influence of the transverse dimension of the inlet shaft on overflow of broad-crested weir (in Czech). Czech Journal of Civil Engineering. 2018.
[5]   Afshar H., Hoseini S. H., 2013. Experimental and 3-D numerical simulation of flow over a rectangular broad-crested weir. International Journal of Engineering and Advanced Technology, 2(6), 214-219.
[6]   Hargreaves D. M., Morvan H. P., Wright N. G., 2007. Validation of the volume of fluid method for free surface calculation: The broad-crested weir. Engineering Applications of Computational Fluid Mechanics, 1(2), 136-146.
[7]   Kirkgoz M. S., Akoz M. S., Oner A. A., 2008. Experimental and theoretical analyses of two-dimensional flows upstream of broad-crested weirs. Canadian Journal of Civil Engineering, 35(9), 975-986.
[8]   Lu X., Zou Q., Reeve D., 2011. Numerical simulation of overflow at vertical weirs using a hybrid level set/VOF method. Advanced in Water Resources, 34(10), 1320-1334.
[9]   Sarker, M. A., Rhodes D. G., 2004. Calculation of free-surface profile over a rectangular broad-crested weir. Flow Measurement and Instrumentation, 15(4), 215-219, 2004.
[10]   FLOW 3D. User manual, Version 9.3. Flow Science, Inc., 2008.
[11]   MENTER, F. R. Improved Two Equation k-ω Turbulence Models for Aerodynamic Flows. Ames Research Center, Moffett Field, California, 1992.
[12]   URUBA, V. Turbulence. CTU in Prague, 2014.

THEORETICAL SOLUTION OF PILING COMPACTION AND THE INFLUENCE OF PILE-SOIL-BOUNDARY CURVE HYPOTHESIS

Zi-kun Gao

University of Lishui, Faculty of Civil Engineering Department, Li-shui Zhe-jiang 323000, China; gaozikun205@126.com

ABSTRACT

Research is ongoing to find theoretical solution to three-dimensional piling compaction. Considering the spacial-axis-symmetric characteristics, the boundary surface of pile-soil interaction is expressed by polynomials of different orders. First, the curve family parameter is introduced to construct the displacement and integral function. Then, the solution of pile-soil interaction is derived by combining the constitutive relation model of Duncan-Chang and the variational theory. Results of engineering computing show that the theoretical solution converges to the classical CEM and the limit equilibrium theory well at the corresponding computing area. Moreover, the effects of polynomial of different orders on the calculation results are not obvious. The conclusion in this paper can be used for reference in the derivation and application for other interaction of structure and soil problems.

KEYWORDS

Theoretical solution, Piling compaction, Boundary curve hypothesis, Variational method, Integral function

INTRODUCTION

For cavity expansion, a source-sink [1,2] method is proposed to solve the displacement field caused by pile-soil interaction. Displacement method [3,4]is also applied to solve the problem of cavity expansion in semi-infinite space. With the truth that the ground must be free or zero stress surface for semi-infinite space, the stress superposition [5] is adopted to correct the source-sink method. The above studies should have the following limitations:

(1)   Assumption of linear elasticity constitutive model of nonlinear material.

(2)   The superposition principle is used to solve the nonlinear displacement field.

METHODS

In this paper, three-dimensional piling compaction in half-space is researched to solve finite length pile-jacked problem. Firstly, quadratic and quartic polynomial functions are used to simulate the boundary curve respectively. Secondly, combining Duncan-Chang constitutive relation and variational theory, solution is derived for pile-soil interaction in semi-infinite space. Finally, the theoretical result is verified by analyzing the influence of initial boundary curve setting.

The computing workloads of functional integration under two kinds of boundary conditions are compared, and the influence of order of boundary curve on the calculation accuracy and convergence rate is also analyzed.

MATHEMATICAL MODELS

Pile-soil interaction is characterized by three-dimensional and strong nonlinearity. Based on the variational theory, the integral functional [6,7] is given as Equation (1).

When the displacement function satisfies all displacement constraints and Equation (1) takes the extreme value, u_i will be the theoretical displacement solutions.

$$\Pi = \iiint_V \left[A(\varepsilon_{ij}) - F_i u_i \right] \mathrm{d}V - \iint_{S_1} \bar{P}_i u_i \mathrm{d}S \tag{1}$$

In the above equation, F_i is the volume force, S_1 is the boundary of the known force, and $\bar{P}_i$ is the known force on the boundary; $A(\varepsilon_{ij})$ is the potential energy density.

The density of the pile-soil interaction can be given as Equation (2)

$$A(\varepsilon_{ij}) = \int_0^{\varepsilon_r} \sigma_r(\varepsilon_{ij}) \mathrm{d}\varepsilon_r + \int_0^{\varepsilon_\theta} \sigma_\theta(\varepsilon_{ij}) \mathrm{d}\varepsilon_\theta + \int_0^{\varepsilon_z} \sigma_z(\varepsilon_{ij}) \mathrm{d}\varepsilon_z + \int_0^{\gamma_{zr}} \tau_{zr}(\varepsilon_{ij}) \mathrm{d}\gamma_{zr} \tag{2}$$

where ε_{ij} refers to four strain components $\varepsilon_r, \varepsilon_\theta, \varepsilon_z, \gamma_{zr}$.

Displacement boundary condition is given as $u\big|_{g(z,r)=0} = \bar{u}(r,z)$.

where $\bar{u}(r,z)$ is the displacement value on the known displacement boundary, and $g(z,r)=0$ is the boundary curve equation of the known displacement expressed as Equation (3).

SETTING DISPLACEMENT FUNCTION

The interaction between pile and the soil around it in semi-infinite space can be regarded as a spatial axisymmetric problem. The mechanical components are independent of the coordinates θ and functions of the coordinates (r,z). The equation of boundary curve is given as Equation (3) and depicted in Figures 1-2.

Boundary curve of Equation (3) should satisfy, if $z=0$, $r=r_0$ and if $z=H$, $r=0$, where H is the pile length and r_0 is the radius of the pile hole at the ground surface.

$$g(z,r) = f(z,r,H) = 0 \tag{3}$$

In order to set the displacement function u_r, w to satisfy the known displacement boundary condition, the curve family parameter z_0 is introduced, as shown in Figures 1-2.

The equation of the curves family with z_0 is established as shown in Equation (4). The soil around the pile is covered by a series of curves with different values of z_0. When $z_0 \geq H$, Eq. (4) can cover any spatial point in the calculation range.

$$f(z,r,z_0) = 0 \tag{4}$$

Equation (4) satisfies $f(z,r,z_0)\big|_{z_0=H} = g(z,r) = 0$. $\partial f / \partial r\big|_{r=0, z \geq H} = 0$

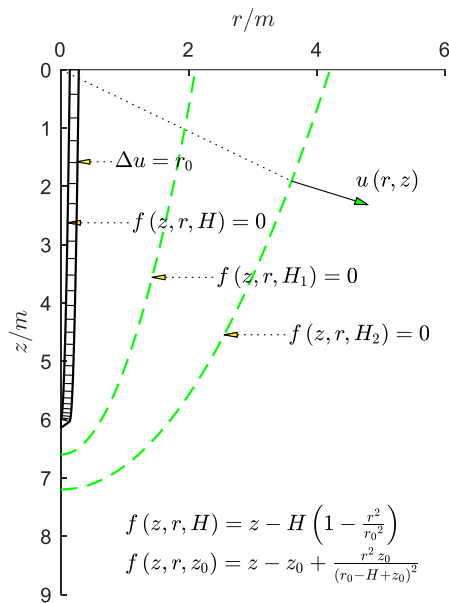

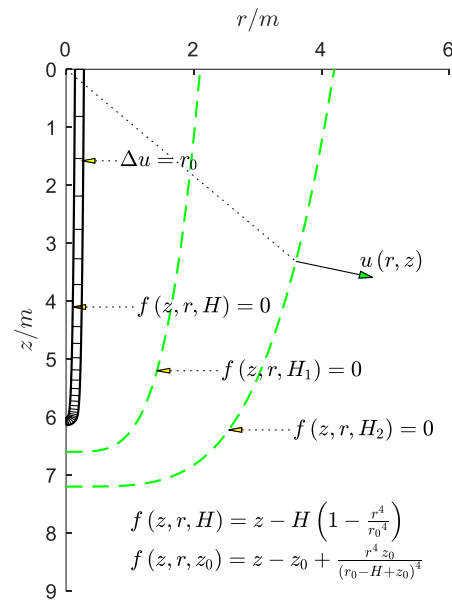*Fig. 1 - Quadratic polynomial piling compaction*   *Fig. 2 - Quartic polynomial piling compaction*

According to the above analysis, the displacement function is set as Equation (5)

$$u_r = u_{r0} + \sum_m A_m u_{rm}, w = w_0 + \sum_m B_m w_m \tag{5}$$

where $u_{r0} = u_0 M_0 \sin\alpha$, $w_0 = u_0 M_0 \cos\alpha$, $M_0 = r_0 / (z_0 - H + r_0)$, $u_{rm} = u_0 (M_0 \sin\alpha)(1 - H/z_0)^m$,
$w_m = u_0 (M_0 \cos\alpha)(1 - H/z_0)^m$, $m = 1,2,3,L$.

α is the angle between outward normal and coordinate line z for the points on the curve z_0.
$\cos\alpha, \sin\alpha$ can be expressed as Equation (6)

$$\cos\alpha = \frac{f_z}{\sqrt{f_z^2 + f_r^2}}, \sin\alpha = \frac{f_r}{\sqrt{f_z^2 + f_r^2}} \tag{6}$$

where $f_z = \dfrac{\partial f(z, r, z_0)}{\partial z}$, $f_r = \dfrac{\partial f(z, r, z_0)}{\partial r}$. A_m, B_m are $2m$ undetermined coefficients.

$z_0 = H$ represents the boundary curve of the hole wall. When $z_0 = H$, $1 - H/z_0 = 0$, the displacement function satisfies the boundary condition of the hole wall.

GEOMETRIC AND CONSTITUTIVE EQUATIONS

Since the parameters z_0 are introduced into the displacement function, the Strain-displacement relationship are given as Equation (7)

$$
\begin{cases}
\varepsilon_r = -\left(\dfrac{\partial u_r}{\partial r} + \dfrac{\partial u_r}{\partial z_0} \dfrac{\partial z_0}{\partial r} \right), \varepsilon_z = -\left(\dfrac{\partial w}{\partial z} + \dfrac{\partial w}{\partial z_0} \dfrac{\partial z_0}{\partial z} \right) \\[2ex]
\gamma_{zr} = \dfrac{\partial u_r}{\partial z} + \dfrac{\partial u_r}{\partial z_0} \dfrac{\partial z_0}{\partial z} + \dfrac{\partial w}{\partial r} + \dfrac{\partial w}{\partial z_0} \dfrac{\partial z_0}{\partial r}, \quad \varepsilon_\theta = -\dfrac{u_r}{r}
\end{cases}
\tag{7}
$$

where $\dfrac{\partial z_0}{\partial r} = -\dfrac{f_r(z,r,z_0)}{f_{z_0}(z,r,z_0)}$, $\dfrac{\partial z_0}{\partial z} = -\dfrac{f_z(z,r,z_0)}{f_{z_0}(z,r,z_0)}$, $f_{z0} = \dfrac{\partial f(z,r,z_0)}{\partial z_0}$.

Duncan-Chang model is adopted [8,9], as shown in Equation (8) and (9). The relationship curve between stress and primary strain of the constitutive model is shown in Figure 3.
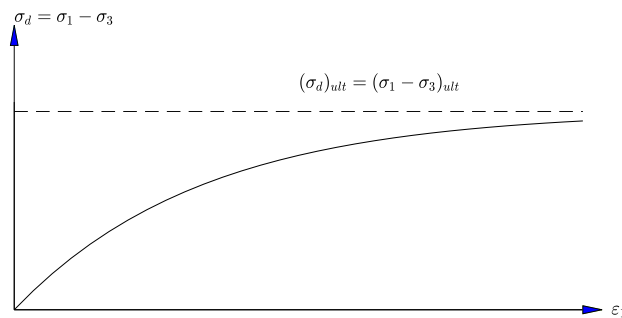

Fig. 3 - Duncan - Chang curve $\sigma_d \sim \varepsilon_1$

$$
\sigma_d = \varepsilon_1 \left/ \left[\frac{1}{E_i} + \frac{\varepsilon_1}{(\sigma_d)_f} R_f \right] \right.
\tag{8}
$$

Modulus of elasticity is given as

$$
E_i = K p_a \left(\sigma_3 / p_a \right)^n
\tag{9}
$$

where, $(\sigma_d)_f = (2c\cos\varphi + 2\sigma_3\sin\varphi)/(1-\sin\varphi)$ $R_f = (\sigma_d)_f / (\sigma_d)_{ult}$ is failure ratio. c,φ is cohesion and internal friction angle of the soil, p_a is the normal atmospheric pressure, σ_3 is pre-consolidation pressure, and K,n are the experimental constant.

Equation (8) can be used to derive nonlinear secant modulus by Equation (10)

$$E_{\text{sec}} = \frac{\sigma_d}{\varepsilon_1} = \frac{1}{\dfrac{1}{E_i} + \dfrac{\varepsilon_1}{(\sigma_d)_f} R_f} \tag{10}$$

where ε_1 is the first main strain [10], determined by Equation (11).

$$\frac{\varepsilon_1}{\varepsilon_3} = \frac{\varepsilon_r + \varepsilon_z}{2} \pm \sqrt{\frac{(\varepsilon_r - \varepsilon_z)^2}{4} + \frac{\gamma_{zr}^2}{4}} \tag{11}$$

The volume deformation modulus of Duncan-Chang model is expressed as Equation (12)

$$K_t = K_b p_a (\sigma_3 / p_a)^{m_0} \tag{12}$$

where, K_b, m_0 is the experimental constant.

POTENTIAL ENERGY DENSITY

The increment of stress components [11] can be expressed as Equation (13)

$$\begin{cases} \Delta\sigma_r = T_1\left[T_2\left(\varepsilon_r + \varepsilon_\theta + \varepsilon_z\right) + \varepsilon_r\right], \Delta\sigma_\theta = T_1\left[T_2\left(\varepsilon_r + \varepsilon_\theta + \varepsilon_z\right) + \varepsilon_\theta\right] \\ \Delta\sigma_z = T_1\left[T_2\left(\varepsilon_r + \varepsilon_\theta + \varepsilon_z\right) + \varepsilon_z\right], \Delta\tau_{zr} = T_1\gamma_{zr}/2 \end{cases} \tag{13}$$

where $T_1 = E_{\text{sec}}/(1+v_0)$, $T_2 = v_0/(1-2v_0)$,

$\varepsilon_r, \varepsilon_\theta, \varepsilon_z, \tau_{rz}$ is determined by Equation (7), v_0 is Poisson ratio. According to Equation (13), the total stress can be expressed as

$$\sigma_r = \Delta\sigma_r + \frac{v_0}{1-v_0}\gamma z, \ \sigma_\theta = \Delta\sigma_\theta + \frac{v_0}{1-v_0}\gamma z, \ \sigma_z = \Delta\sigma_z + \gamma z, \ \tau_{zr} = \Delta\tau_{zr}$$

where γ is the buoyant unit weight, γz is the consolidation stress. Therefore, the potential energy density can be expressed as:

$$A(\varepsilon_{ij}) = \int_0^{\Delta u}\left[\sigma_r\frac{\partial\varepsilon_r}{\partial u_0} + \sigma_\theta\frac{\partial\varepsilon_\theta}{\partial u_0} + \sigma_z\frac{\partial\varepsilon_z}{\partial u_0} + \tau_{zr}\frac{\partial\gamma_{zr}}{\partial u_0}\right]du_0$$

Since the curve parameter z_0 is introduced, the potential energy density can be written as Equation (14), which is a function of z, r, z_0 as

$$A(\varepsilon_{ij}) = \int_0^{\Delta u} D(z, r, z_0, u_0, \bar{A}, \bar{B})du_0 \tag{14}$$

where z, r, z_0 meet the constraint conditions of $f(z, r, z_0) = 0$, $\bar{A} = \{A_1, A_2, ..., A_m\}$, $\bar{B} = \{B_1, B_2, ..., B_m\}$, and

$$D(z,r,z_0,u_0,\bar{A},\bar{B}) = \sigma_r\left(\varepsilon_{ij}\right)\frac{\partial\varepsilon_r}{\partial u_0} + \sigma_\theta\left(\varepsilon_{ij}\right)\frac{\partial\varepsilon_\theta}{\partial u_0} + \sigma_z\left(\varepsilon_{ij}\right)\frac{\partial\varepsilon_z}{\partial u_0} + \tau_{zr}\left(\varepsilon_{ij}\right)\frac{\partial\gamma_{zr}}{\partial u_0}$$

FUNCTIONAL CONSTRUCTION AND COEFFICIENTS DETERMINATION

According to energy density of Equation (14), Equation (1) can be written as Equation (15)

$$\Pi = \iiint_V A\left(\varepsilon_{ij}\right)dV = 2\pi\iint_S\int_0^{\Delta u} D\left(z,r,z_0,u_0,\bar{A},\bar{B}\right)rdu_0dS \tag{15}$$

where: $A\left(\varepsilon_{ij}\right)$ is represented by Equation (14).

The coefficient $\bar{A}, \bar{B}$ can be solved by the extreme calculation of Equation (16), and the theoretical solution of displacement and stress field can be obtained then.

$$\frac{\partial\Pi}{\partial A_i} = 0, \qquad \frac{\partial\Pi}{\partial B_i} = 0 \tag{16}$$

PROJECT CASES

Equation (3) is set as the polynomial function as shown in Equation (17) - (18)

$$z = H\left(1 - r^2/r_0^2\right) \tag{17}$$

$$z = H\left(1 - r^4/r_0^4\right) \tag{18}$$

where H is the pile length, r_0 is the equivalent radius [12,13] of the pile hole on the ground surface. The equivalent condition of pile hole expansion is established as follows

$$\pi[\left(2r_0\right)^2 - r_0^2] = \pi R_0^2 \Rightarrow r_0 = R_0/\sqrt{3} = d/\left(2\sqrt{3}\right)$$

with regard to the pile of $H = 6\text{m}$, $d = 2R_0 = 0.5\text{m}$, $r_0 = d/\left(2\sqrt{3}\right) = 0.14\text{m}$.

Soil parameters are shown in Table 1. Considering the consolidation stress of shallow soil is small and it is relatively loose and has less influence on the calculation result, mean values of muddy clay and clay are calculated and we get $c = 14\text{kPa}, \varphi = 13.25^o$, where c, φ are consolidated undrained (CU) parameters.

The constitutive parameters of clay for example 4.1 and 4.2 are [9] $R_f = 0.8$, $K = 200$, $n = 0.5$, $K_b = 50$, $m_0 = 0.5$.

Tab. 1 - Soil parameters

Soil	Depth m	E_s MPa	v_0	γ KN/m³	c kP	φ
Silty clay	0 ~ 2	34	0.29	18.5	12	18.0°
Muddy clay	2 ~ 4	29	0.46	17.0	13	12.0°
clay	4~	32	0.42	17.5	15	14.5°

Example 1

Family curves can be written as Equation (19), as shown in Figure 1,

$$f\left(z, r, z_0\right) = z - z_0 + \frac{z_0 r^2}{\left(z_0 - H + r_0\right)^2} = 0 \tag{19}$$

when $z_0 = H$, $f\left(z, r, z_0\right) = z - H\left(1 - r^2 / r_0^2\right)$

Equation (20) are given for calculating the stress in the plastic and elastic zone around the pile by the cavity expansion method (CEM) [14,15].

Figure 4 shows a comparative analysis of the calculated results of Equation (20), numerical simulation results [16] and the theoretical solution derived in this paper based on Equation (19).

$$\Delta\sigma_r = 2c_u \ln\frac{R_p}{r} + c_u, \quad \Delta\sigma_z = 2c_u + \ln\frac{R_p}{r} \tag{20a}$$

$$\Delta\sigma_r = c_u \left(\frac{R_p}{r}\right)^2, \quad \Delta\sigma_z = 0 \tag{20b}$$

In the above equation, $R_p = R_0 \sqrt{E/\left[2(1+\mu)c_u\right]}$ is the radius of the plastic zone, c_u ($c_u \geq c$) is the index of unconsolidated undrained (UU), and this article takes $c_u = c$. R_0 is the radius of pile hole.

Equation (21) is given for calculating the stress in the r direction based on the limit equilibrium theory [17]. Figure 5 shows a comparative analysis of the lateral pressure results based on the limit equilibrium theory and the theoretical solution derived in this paper based on Equation (19).

$$\sigma_r = \gamma z \left[\tan^2\left(\frac{\pi}{4} + \frac{\varphi}{2}\right)\right] + 2c \tan\left(\frac{\pi}{4} + \frac{\varphi}{2}\right) \tag{21}$$

Figure 4 shows that calculated results of the theoretical solution are basically matching with those of the cavity expansion method at the zone located in the region of $r \geq 1d$ & $z \leq 6m$. Since the cavity expansion method (CEM) assumes that the expansion model satisfies the plane strain

condition, it is only suitable for solving the plane strain problem. For finite-length pile three-dimensional expansion, the region below or around the pile tip is obviously inconsistent with the assumption of the plane strain. Compared with the CEM results, the theoretical solution of this paper is more reasonable with the rapidly decreasing of radial pressure around or below the pile tip.

Figure 5 shows that the results of theoretical solution are basically matching with the results of limit equilibrium theory at plastic line located in the range of $0\text{m} \leq z \leq 6\text{m} \ \& \ \ r = 0.25\text{m}$. Compared with the limit equilibrium results, the theoretical solution of this paper is more reasonable, with the rapidly decreasing of radial pressure around or below the pile tip. In addition, because the limit equilibrium results are directly related to the volume-weight of the soil, the curve of passive earth pressure shown in Figure 5 has inflection points at the interface of the soil layer.

Figure 5 also shows that the results of theoretical solution are basically matching with the results of numerical simulation results at $r = 0.75\text{m}$.

Example 2

Family curves can be written as Equation (22), as shown in Figure 2

$$f\left(z, r, z_0\right) = z - z_0 + \frac{z_0 r^4}{\left(z_0 - H + r_0\right)^4} = 0 \tag{22}$$

when $z_0 = H$, $f\left(z, r, z_0\right) = z - H\left(1 - r^4 / r_0^4\right)$

Figures 6-7 can be obtained, in combination with the theoretical solution derived in this paper based on Equation (22), the results of numerical simulation results, CEM and limit equilibrium theory.

The stress regularities of distribution in Figures 6-7 are basically the same as those in Figures 4-5. They explain that the quadratic or quartic polynomial of the boundary curve has little effect on the calculation results, because the soil near the pile-soil interaction boundary has been in the plastic yield state already.

To sum up, with the increase of undetermined coefficients from 0 to 4, the additional stress generated by pile compaction rapidly converges to the reasonable value and polynomial with lower order can also be used to simulate the initial hole wall boundary to reduce the computational workload.
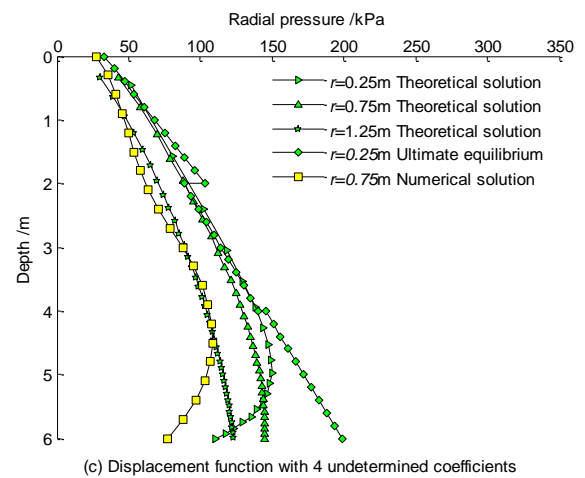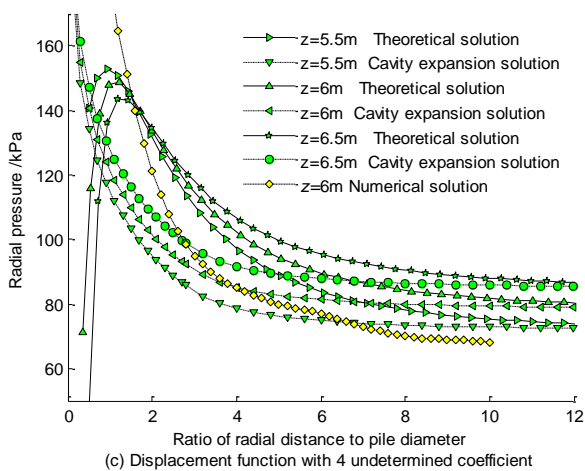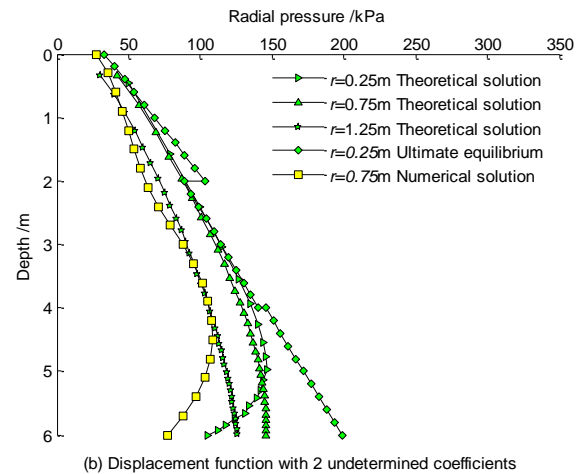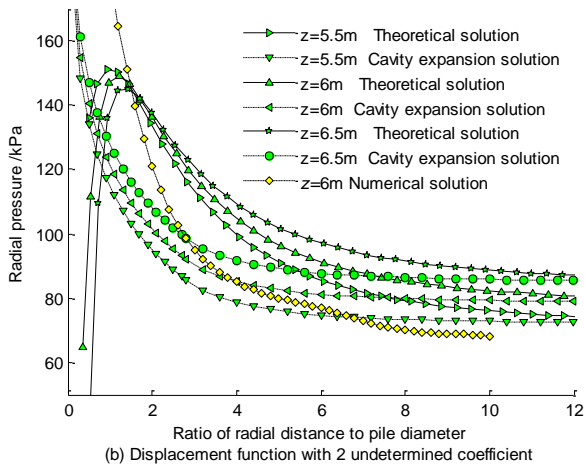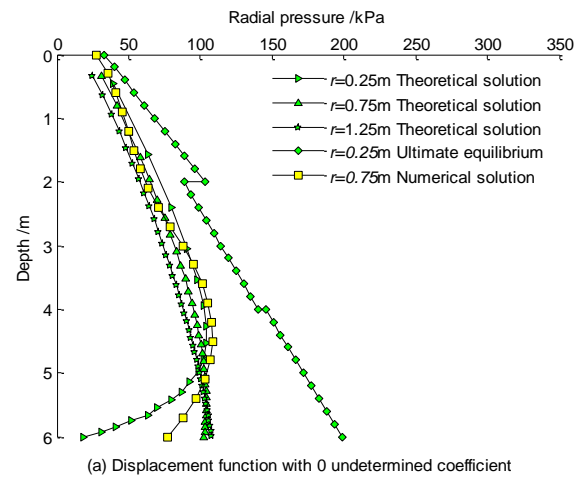
Fig. 4 - The radial pressure along radial direction

Fig. 5 - The radial pressure along depth

(a) Displacement function with 0 undetermined coefficient

(a) Displacement function with 0 undetermined coefficient

(b) Displacement function with 2 undetermined coefficient

(b) Displacement function with 2 undetermined coefficients

(c) Displacement function with 4 undetermined coefficient

(c) Displacement function with 4 undetermined coefficients

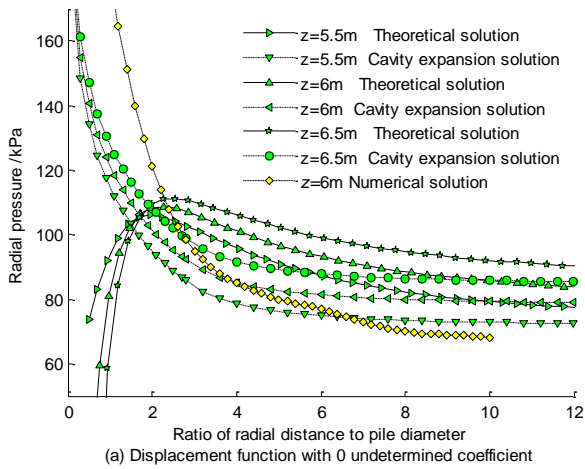*Fig. 6 - The radial pressure along radial direction*   *Fig. 7 - The radial pressure along depth*

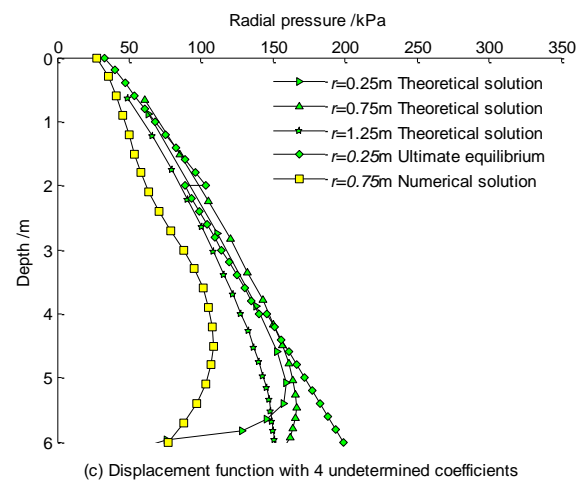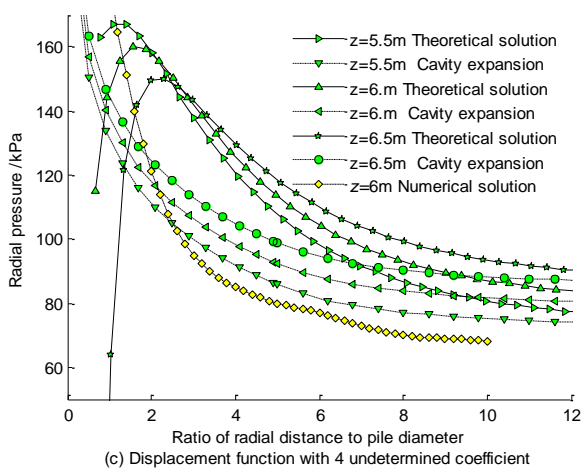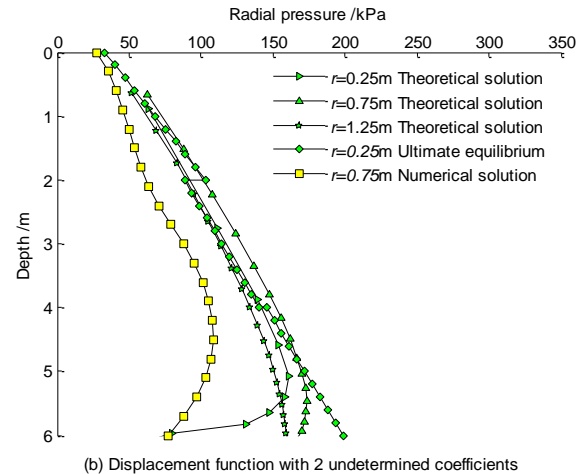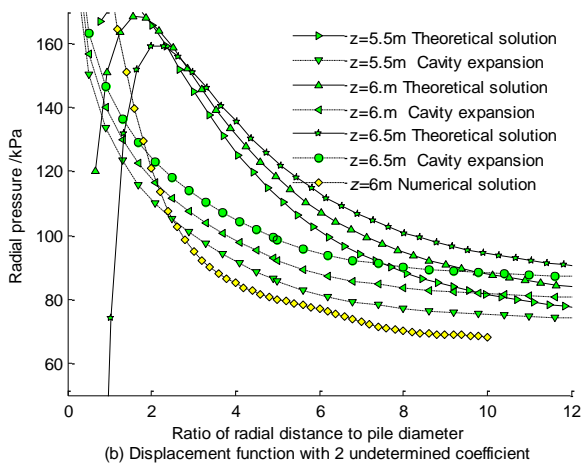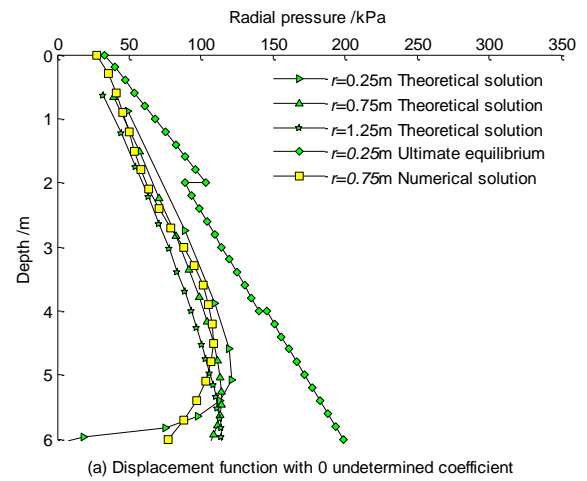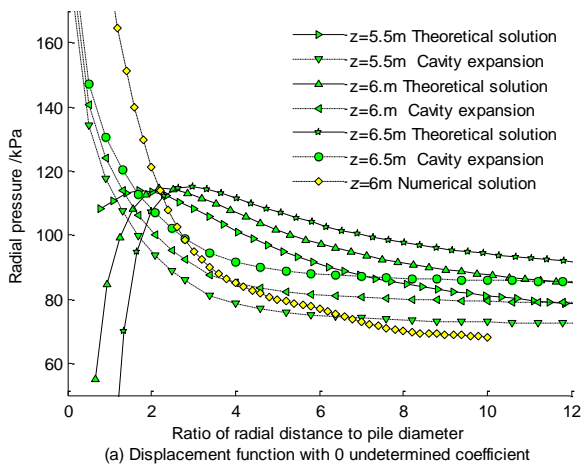### Example 3

The test site is located in a section of Taiwan high-speed railway project [18]. The precast concrete pile length is 34m, and diameter is 80 cm. The distribution of the test pile and measuring pipes are shown in Figure 8. Burial depth of survey tubes are 40m. The soil layers in the site are inter-bedded sandy soil and cohesive soil, and the critical values of sandy and clay are taken as parameters for calculating. Parameters of soil layer [9,18] are shown in Table 2. The equivalent pile-hole-expansion radius is $r_0 = 0.4/\sqrt{3} = 0.23\mathrm{m}$, and the normal displacement of the hole wall is $\Delta u = r_0 = 0.23\mathrm{m}$.
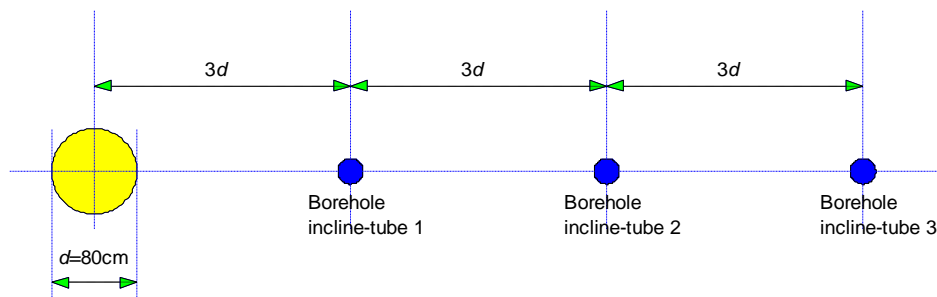

Fig.8 - Test pile and plane layout of incline-tubes

Tab. 2 - Geotechnical parameters of test site

Cohesion c/kPa	Friction Angle $\varphi/°$	Poisson's ratio v	Soil bulk density γ/kPa	Destructive ratio R_f	Constant K	Constant n
3	20	0.3	18	0.9	300	0.5

Displacement Equation (23~26) can be deduced based on Equation (16~17, 19), and Figure 9-10 can be obtained in combination with the theoretical solution derived in this paper and field test data in reference [18]. Figure 9 shows distribution-regularities comparison between theoretical computing radial displacement and the in-situ measured data at different penetration depth. Figure 10 shows comparison between theoretical displacement results and the in-situ measured data at different coordinate r. Figure 9 shows that for different penetration depth, the calculated value of displacement is basically agreement with the in-situ measured value, although the theoretical calculation cannot accurately reflect the characteristics due to injection interval. Figure 10 shows that for different radial coordinates, the calculated value is basically agreement with the measured value.

When Penetration depth: $H = 9\mathrm{m}$, displacement function due to pile compaction can be written as Equation (23)

$$\begin{cases} u_r = \Delta u \left(\dfrac{r_0}{z_0 - H + r_0} \sin \alpha \right) \left[1 - 1.0 \left(1 - \dfrac{H}{z_0} \right) \right] \\[4mm] w = \Delta u \left(\dfrac{r_0}{z_0 - H + r_0} \cos \alpha \right) \left[1 - 5.0 \left(1 - \dfrac{H}{z_0} \right) \right] \end{cases} \tag{23}$$

When Penetration depth: $H = 17\text{m}$, displacement function due to pile compaction can be written as Equation (24)

$$\begin{cases} u_r = \Delta u \left(\dfrac{r_0}{z_0 - H + r_0} \sin \alpha \right) \left[1 - 1.0 \left(1 - \dfrac{H}{z_0} \right) \right] \\[4mm] w = \Delta u \left(\dfrac{r_0}{z_0 - H + r_0} \cos \alpha \right) \left[1 - 1.7 \left(1 - \dfrac{H}{z_0} \right) \right] \end{cases} \tag{24}$$
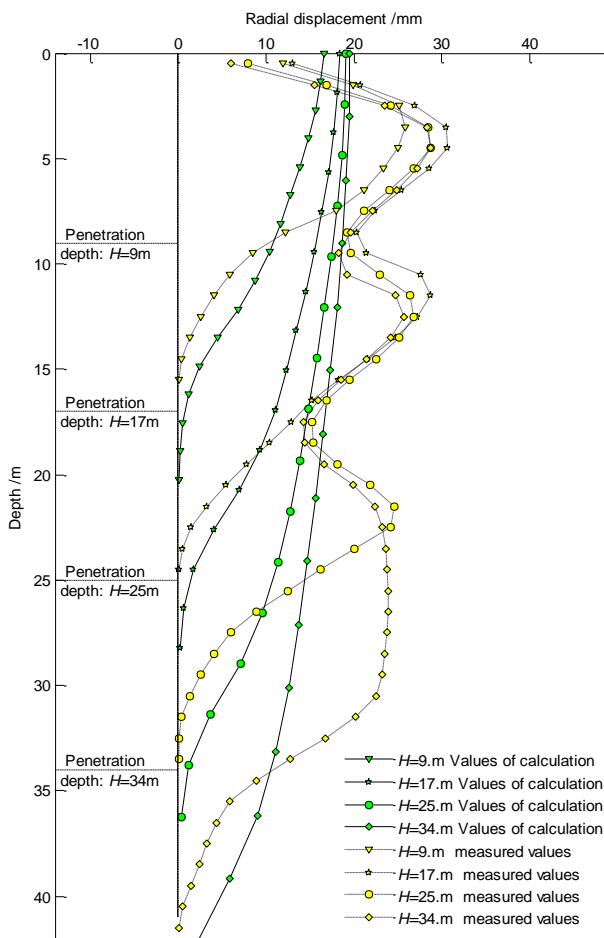

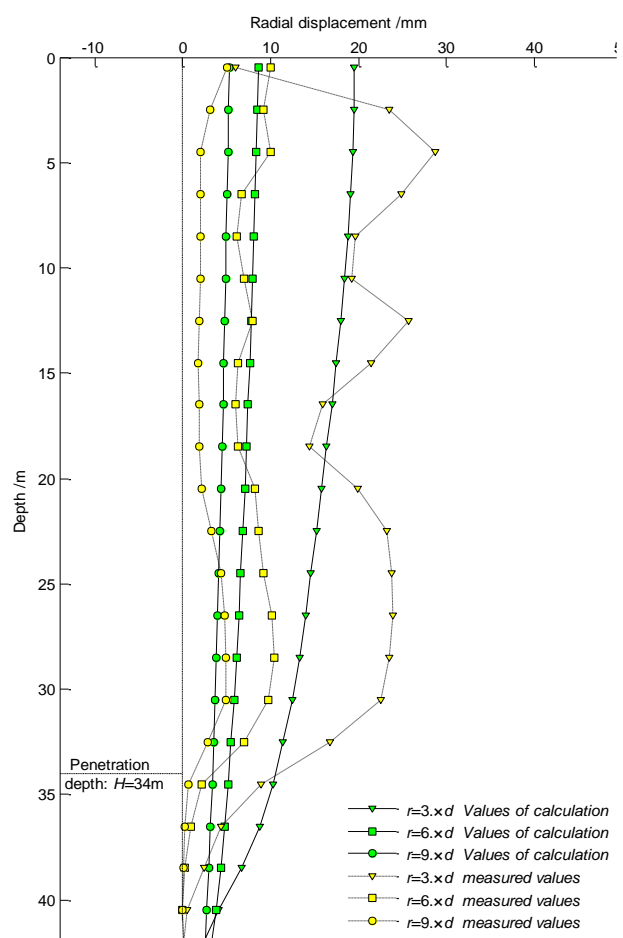Fig.9 - Displacement at different penetration depth   Fig.10 - Displacement at different r

When Penetration depth: $H = 25\text{m}$, displacement function due to pile compaction can be written as Equation (25)

$$\begin{cases} u_r = \Delta u \left(\dfrac{r_0}{z_0 - H + r_0} \sin \alpha \right) \left[1 - 1.0 \left(1 - \dfrac{H}{z_0} \right) \right] \\ w = \Delta u \left(\dfrac{r_0}{z_0 - H + r_0} \cos \alpha \right) \left[1 - 1.1 \left(1 - \dfrac{H}{z_0} \right) \right] \end{cases} \tag{25}$$

When Penetration depth: $H = 34\,\mathrm{m}$, displacement function due to pile compaction can be written as Equation (26)

$$\begin{cases} u_r = \Delta u \left(\dfrac{r_0}{z_0 - H + r_0} \sin \alpha \right) \left[1 - 1.0 \left(1 - \dfrac{H}{z_0} \right) \right] \\ w = \Delta u \left(\dfrac{r_0}{z_0 - H + r_0} \cos \alpha \right) \left[1 - 1.1 \left(1 - \dfrac{H}{z_0} \right) \right] \end{cases} \tag{26}$$

CONCLUSIONS

Theoretical solutions of the piling compaction are derived by combining the constitutive relation model of Duncan-Chang and the variational theory. Boundary surface could be expressed by polynomials of different orders for piling compaction, considering the characteristics of pile-soil interaction such as three-dimension and strong nonlinearity.

Computing of the project cases shows that the solutions of variational theory converges to results of cavity expansion and limit equilibrium theory well in the corresponding region. The influences of pile-soil boundary curve on the calculation accuracy and convergence rate are not obvious. Numerical and in-situ test results are also used to verify the reasonable and validity of the deduced theoretical solutions.

Researches in this paper show that the polynomial with lower order can be used to simulate the initial hole wall boundary to reduce the computational workload.

REFERENCES

[1]   Sagaseta. Analysis of undrained soil deformation due to ground loss[J]. Geotechnique,1987, 37(3): 301-320

[2]   Sagaseta. Prediction of Ground Movements Due to Pile- Driving in Clay [J]. Journal of Geotechnical and Geoenvironmental Engineering. 2001, 127(1): 55-66.

[3]   Luo Zhanyou. Study on compacting effects and construction measures of jacked pile [D]. Hangzhou: Zhejiang University, 2004. 19-21 (in Chinese)

[4]   Wang Pengcheng. Study on Cavities Expansion in Soils with Softening and Dilation and Analysis of Pile Driving Effects [D]. Hangzhou: Zhejiang Univ. 2005. 175-177 (in Chinese)

[5]   Zhu Ning. Theoretical Analysis of Soil Deformation Due to Pile Jacking [D]. Nanjing: Hohai Univ., 2005. 131-132. (in Chinese)

[6]   Niu Yangjun. Modernistic Variation Principle[M]. Beijing: Press of Beijing University of Technology, 1992 (in Chinese)

[7]   Wang Xucheng, Shao Min. Numerical method and basic theory of finite element method [M]. Beijing: Tsinghua University Press, 1997.

[8]   QIAN J H, YIN Z Z. Principle and calculation of geotechnical engineering[M].2nd ed. Beijing: China Water & Power Press,1996(in Chinese).

[9]   ZHENG Ying-ren, SHEN Zhu-jiang, GONG Xiao-nan. The principles of geotechnical plastic mechanics[M]. Beijing: China Architecture and Building Press, 2002: 180-183. (in Chinese))

[10]   GAO Zi-kun. Theoretical Analysis of Soil Squeezing Effect and Conslidation Characteristic Due to Pile Jacked [D]. Nanjing: Hohai Univ., 2007. 57-66. (in Chinese)

[11]   Xu Zhi-lun. Elastic mechanics[M]. 3rd ed. Beijing: Higher Education Press, 1984: 274-278. (in Chinese))

[12]   Carter, J.P., Randolph, M.F. and Wroth, C.P. (1979). Stress and pore pressure changes in clay during and after the expansion of cylindrical cavity. Int. J. for Num. and Analy. in Geomech. Vol.3, 1979.

[13]   RANDOLPH M F, CARTER J P, WROTH C P. Driven piles in clay - the effects of installation and subsequent consolidation[J]. Géotechnique, 1979, 29(4): 361-393.

[14]   Visic, A. C., Expansion of Cavity in Infinite Soil Mass, Jour. Soil Mech. Found. Div., A. S. C. E., 1972, 98(3), 265-289.

[15]   Atkinson, J. H. and Bransby P. L. The Mechanics of Soils[M].McGraw-Hill, England, 1978.

[16]   TANG Shi-dong, LI Yang. Analysis of a driven pile by ANSYS. Rock And Soil Mechanics [J]. Vol. 27 ，2006: 973～976.

[17]   Chen Xizhe. Soil mechanics and foundation [M]. Beijing: Tsinghua Press. 2004.

[18]   Jin-Hung Hwang, Neng Liang and Cheng-Hsing Chen. Ground Respond During Pile Driving. Journal of Geotechnical and Geoenvironmental Engineering. Nov., 2001: 939~948.

STABILITY ANALYSIS OF THE GRAVITY ANCHORAGE OF A SUSPENSION BRIDGE BASED ON LARGE-SCALE FIELD TESTS

Zhijun Zhou[1], Chaoran Chen[1], Longfei Wang[2], Yeqing Tian[1], Hongming Feng[1] and Kangchao Wang[1]

1. Chang'an University, School of Highway, Xi'an 710064, China; chenchaoran@chd.edu.cn,
2. Zhumadian Construction Survey & Design Institute Co.,Ltd., Zhumadian 463000 China; 454596968@qq.com

ABSTRACT

The stability of gravity anchorages is critical to the safe operation of suspension bridges. The purpose of this paper is to study the stability of a gravity anchorage under the tension of main cables. Large-scale load tests and direct shear tests under the nature state and the saturated state were carried out in the adit at the bottom of the gravity anchorage, because the bottom surface of the gravity anchorage is below the design water level of a reservoir to be built. Representative rock samples in the anchorage area were selected for indoor tests. The basic parameters of the rock mass and the characteristic value of subsoil bearing capacity were obtained based on the field and indoor tests results. The static theory was used to calculate the anti-sliding stability coefficient, anti-overturning stability coefficient and contact stress of the gravity anchorage. The finite element software was used to calculate the horizontal displacement, vertical settlement and contact stress of the gravity anchorage. The calculation results met the relevant requirements, and it can be considered that the gravity anchorage was stable under the tension of main cables. It would provide a reference for the stability study of the gravity anchorage of suspension bridges.

KEYWORDS

Suspension bridge, Gravity anchorage, Anti-sliding stability, Anti-overturning stability, Contact stress

INTRODUCTION

Suspension bridges have been widely used for its beautiful shape and huge span ability. With the progress of materials and construction technology, the span of suspension bridges is increasing. At present, suspension bridges have become one of the main options for long-span bridges. As the main load-bearing structure of suspension bridges, anchorages play a role of transferring the tension of main cables to the ground. Since the main cable tension is generally large, the anchorage is the key part to ensure the stability of the suspension bridge. Due to the strong adaptability to various geological conditions and simple force transmission mechanism, the gravity anchorage is currently used in most of the built suspension bridges [1]. The stability of the gravity anchorage is related to the safe use of the suspension bridge, and it is also one of the key issues in the design of the suspension bridge [2].

Before 1960s, the gravity anchorage of long-span suspension bridges was always set on hard ground such as rock, so as to prevent the anchorage from excessive displacement or instability. In the stability calculation, it is assumed that the anchorage will not noticeably slide, sink and rotate under load [3]. Since the Verrazano Bridge was built in the United States in 1964, gravity anchorages of the suspension bridge can be built on the soil ground, allowing sinking,

strictly restricting sliding, and minimizing the overturning angle [4,5]. Taylor proposed the concept and design idea of anchorages based on its own stability in 1982 and applied it to practical engineering [6]. Andersen et al. used the limit state formula based on the working principle to evaluate the structural safety of the gravity anchorage of the suspension bridge across the eastern channel of the Great Belt [7]. Carter introduced an innovative structural concept for the design of the gravity anchorage of the Izmit Bay Bridge in high seismic area [8].

Understanding the deformation law and failure mechanism of the gravity anchorage and ground is a prerequisite for evaluating its stability [9,10]. Yin et al. study the mechanical mechanisms and failure modes of the gravity anchorage and ground by using numerical simulation [11]. They believed that the joint deformation and bearing mechanisms of the gravity anchorage and ground are comprehensively performed by friction effect, clamping effect and backfilling effect. Soil creep has a long-term effect on the stability of gravity anchorages [12]. Notched sill effect, foundation pit support and foundation reinforcement are of great significance to improve the stability of gravity anchorages [13,14]. In addition, the surrounding soil has a significant effect on improving the stability of the gravity anchorage [15]. Guo et al. use FLAC 3D modeling technology to carry out detailed numerical simulation according to the construction steps of a gravity anchorage, and analyzed the stability of the anchorage [16]. Ya et al. analysis the stability of one gravity anchorage using standard methods, shear strength reduction methods and proportionally increasing main cable tension methods and obtained the anchorage stability coefficients corresponding to different calculation methods [17].

The previous researches mainly used model tests and numerical simulations and got many interesting conclusions. However, there are few large-scale field test studies on the stability of the gravity anchorage. This paper takes the gravity anchorage of the Hutiaoxia Jinsha River Bridge as the research object. The study carried out large-scale load tests and direct shear tests in the excavated adit at the bottom of the gravity anchorage and combined with the indoor test to obtain the rock mass parameters and the characteristic value of subsoil bearing capacity. The stability of the gravity anchorage is analyzed and calculated from three aspects of anti-sliding, anti-overturning and contact stress using static theory and numerical simulation.

PROJECT DESCRIPTION

Hutiaoxia Jinsha River Bridge is a key project of Lijiang-Shangri-la expressway. The bridge spans the deep valley of Jinsha River, with a maximum height of 630.2 m. The bridge area belongs to the structurally eroded high mountain canyon landform, with a ground elevation of 1800-5600 m, a relative height difference greater than 2000 m, and a natural cross slope of 30°-60°. The total length of the bridge is 1017 m, and the main bridge is a 766 m steel truss suspension bridge. The bridge's south bank (Lijiang bank) adopts the spread foundation gravity anchorage.

The terrain on the Lijiang bank of the bridge is wide and gentle, and the vegetation on the slope is relatively developed. The slope near the anchorage is about 33°. The dynamic metamorphism of the Lijiang bank is generally strong. Schistose basalt, cleaved slate, joints of carbon phyllite are well developed, and the rock is generally broken. The stability of shallow overburden and rock slope is generally poor. The topography and landform near the gravity anchorage are shown in Figure 1(a). The distribution of the main rock layers under the gravity anchor is shown in Figure 1(b). The design elevation of the bottom of the gravity anchorage is 1998 m. The design elevation of the water level of Hutiaoxia reservoir to be built is 2010 m. Obviously, the bottom of the gravity anchorage is 12 m below the design water level.
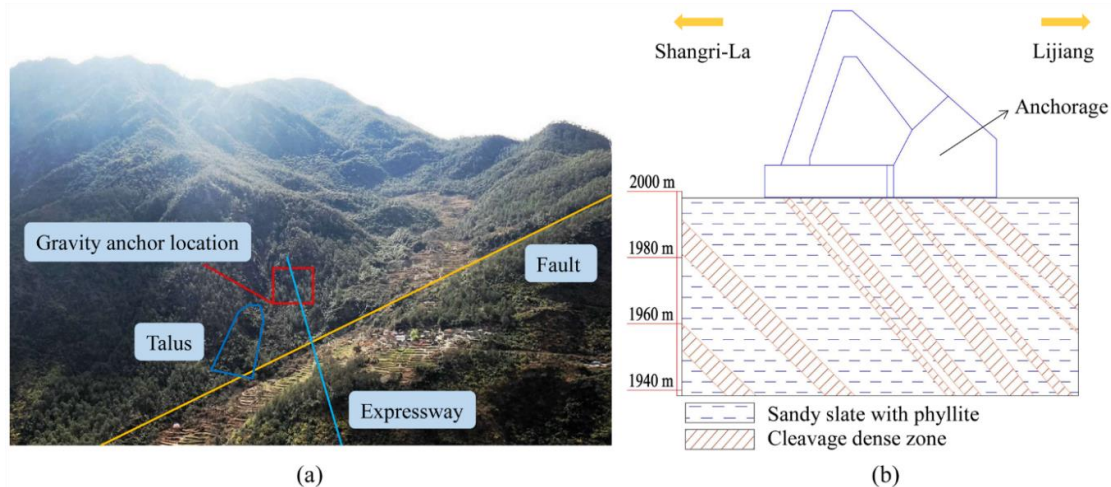
Fig. 1 - Basic information of the gravity anchorage, (a) Topography near the gravity anchor, (b) Distribution of main rock layers

The gravity anchorage adopts a frame structure. This frame type gravity anchorage effectively reduces its own gravity, reduces the stress on the ground, and reduces the amount of reinforced concrete. It has the advantages of time saving, labour saving, low cost, and beautiful appearance [18]. Therefore, most of the gravity anchorages adopt the triangular frame structure composed of a front anchor chamber, a buttress of splay saddle and anchor block.

The main structure of the gravity anchorage is shown in Figure 2(a). The gravity anchorage adopts the prestressed anchorage system, and the anchorage method adopts the front anchor type. The buttresses of splay saddle mainly bear the pressure transmitted by the saddle. The anchor block mainly bears the main cable tension transmitted by the prestressed anchorage system. The front anchor chamber is composed of side walls, roof and front walls to form a closed space, which protects the main cable strands. Because the anchor block and the side wall of the front anchor chamber mainly bear the main cable tension transmitted by the prestressed anchorage system, the concrete grade used is C40. The force of other parts of the gravity anchorage is transferred from the anchor block, and C30 concrete with lower strength grade is used.

The main dimensions of the gravity anchorage are shown in Figures 2(b) and 2(c). The total height of the gravity anchorage is 58 m, and the foundation height is 10 m. The bottom surface of gravity anchor foundation is 72 m long and 50 m wide. The design load of the main cable is 202201 kN/cable, and the horizontal incident angle of the main cable strand is 30°. The length of the main cable strand incident to the front anchor chamber is 38m, the anchorage length of the anchorage system is 20m, and the refraction angle of the main cable tension is 47°.
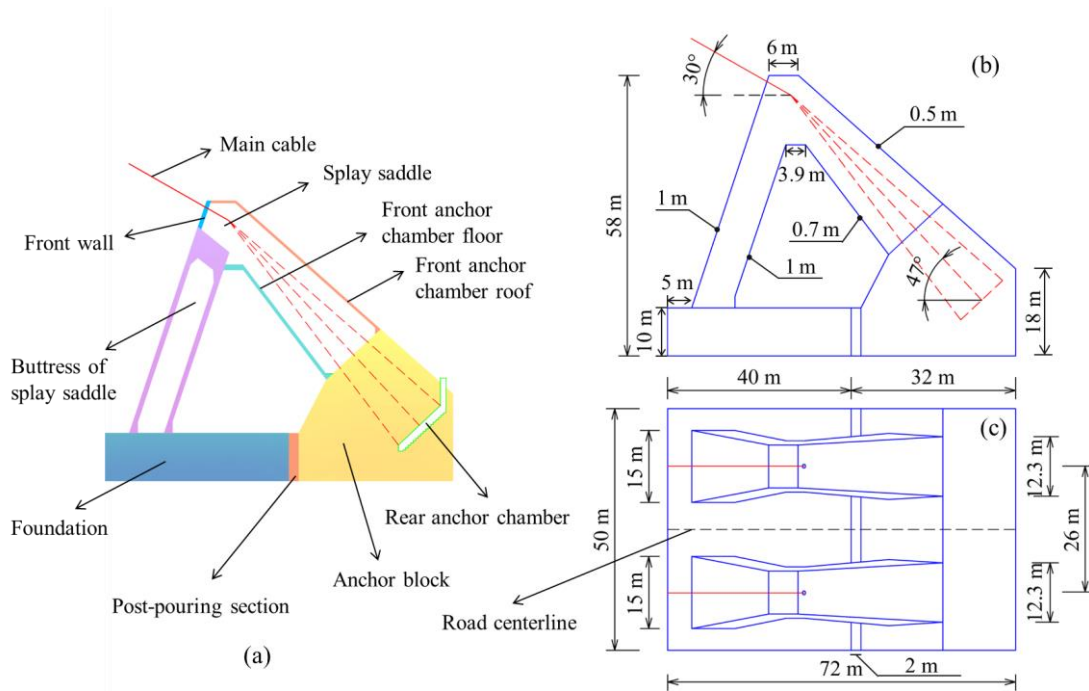
Fig. 2 - Composition and size of the gravity anchorage, (a) The main structure of the gravity anchorage, (b) Elevation of the gravity anchorage, (c) Top view of the gravity anchorage

LARGE-SCALE FIELD TEST

In order to understand the natural bearing capacity and saturated bearing capacity of the foundation under the gravity anchorage, the friction coefficient between the bottom surface of the gravity anchorage and the foundation, and the shear strength of the rock, a 50 m long adit was excavated at the bottom surface of the gravity anchorage, as shown in Figure 3(a).
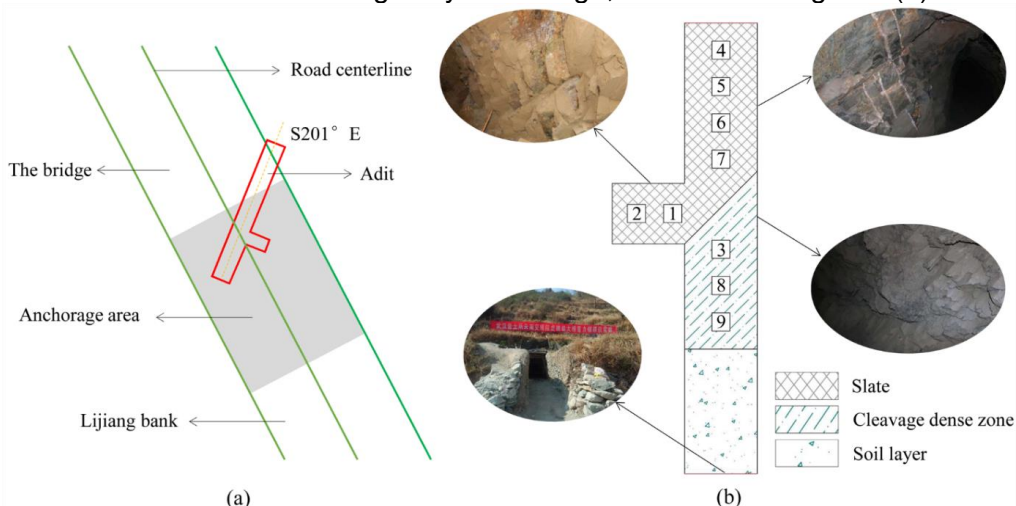
Fig. 3 - The adit location and test areas setting, (a) The adit location, (b) Test areas setting

The adit exploration reveals that the rock is a thin-thick slate, partly a cleavage dense zone, and the rock mass is relatively broken with thin phyllites. In view of the fact that the bottom of the anchorage is located 12 m below the water level of the reservoir to be built, combined with the geological conditions in the adit, a total of 9 test areas are set, as shown in Figure 3(b). Test area 1

is medium-thick layered slate. Test area 2 is thin-medium layered slate. The test areas 4, 5, 6, and 7 are thin-medium layered slate, which is intermediary weathered. The test areas 3, 8 and 9 are thin-layer slate mixed with thin-layer phyllite, which is relatively broken and is intermediary-strong weathered. Different test points were set in each test area, and the setting of test points is listed in Tables 1 and 2.

Tab. 1 - Test points of load test

Test types	Test point	Test content
Load test	1-LN	Load test in natural state
	1-LS	Load test in saturation
	2-LN	Load test in natural state
	2-LS	Load test in saturation
	3-LN	Load test in the natural state
	3-LS	Load test in saturation

Tab. 2 - Test points of direct shear test

Test types	Test point	Test content
Concrete-rock	4-SN	Shear test in natural state
	4-FN	Friction test in natural state
	4-FS	Friction test in saturation
	5-SS	Shear test in saturation
	5-FS	Friction test in saturation
	8-SS	Shear test in saturation
	8-FS	Friction test in saturation
Rock	6-SN	Shear test in natural state
	6-FN	Friction test in natural state
	7-SS	Shear test in saturation
	7-FS	Friction test in saturation
	9-SS	Shear test in saturation
	9-FS	Friction test in saturation

Load Test

Load tests were performed in representative and relatively weak positions in the adit. In order to compare the settlement deformation and consider the influence of changes of the water level, the tests were conducted in the natural state and saturated state. Load tests were carried out in accordance with the relevant specification [19]. The tests are shown in Figure 4.
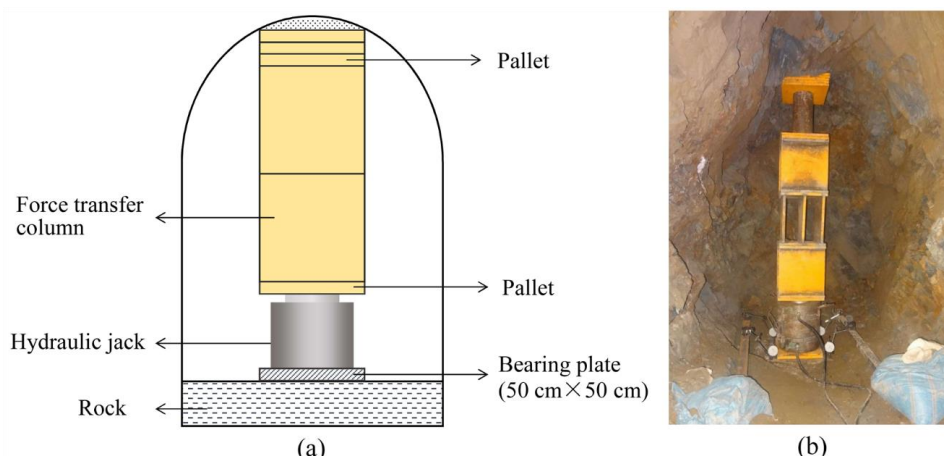

Fig. 4 - The load test, (a) Test schematic diagram, (b) Test photos

The deformation modulus of load test is calculated as follows:

$$E_0 = I_0(1-\mu^2)\frac{pd}{s} \tag{1}$$

where E_0 represents the deformation modulus of rock mass in MPa, I_0 represents the shape coefficient of the rigid bearing plate and the shape coefficient of the square bearing plate is 0.886, μ represents the Poisson's ratio of the rock mass, d is the diameter or side length of the bearing plate in m, p represents the pressure in the linear segment of the Load-Settlement curve in kPa, s is the settlement corresponding to p in mm.

The test curves are shown in Figure 5, and the test results are summarized in Table 3.
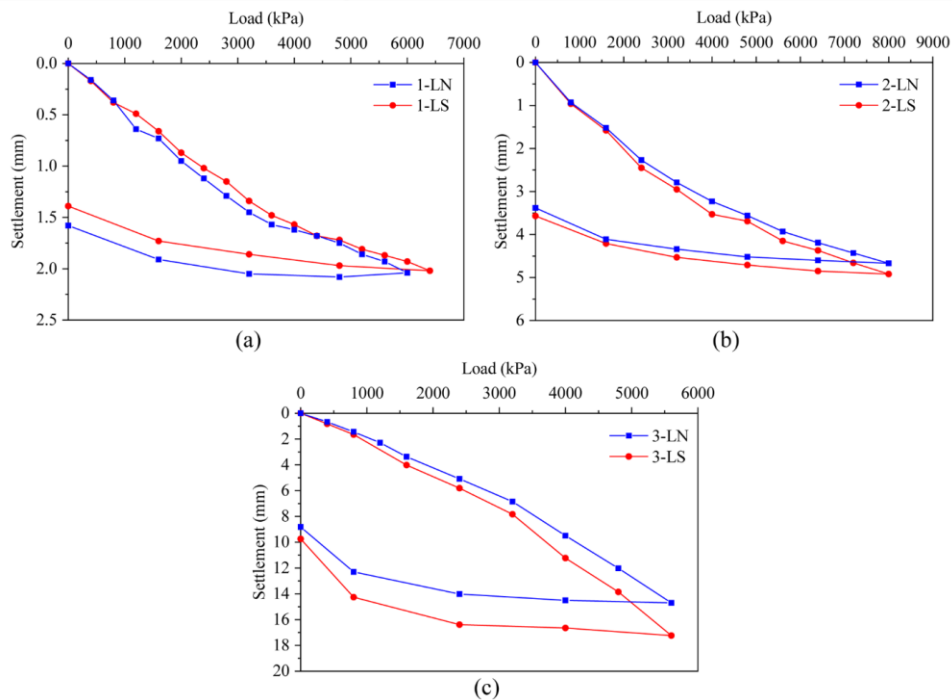
Fig. 5 - Load test curves, (a) Test curve of test area 1, (b) Test curve of test area 2, (c) Test curve of test area 3

Tab. 3 - Summary of load test results

Test point	Characteristic value of subsoil bearing capacity (kPa)	Deformation modulus		Residual deformation (mm)	Rock mass category
		0.8 MPa	3.2 MPa		
1-LN	>2213	923	916	1.58	Slate
1-LS	>2133	874	992	1.42	
2-LN	>2666	358	476	3.38	Slate
2-LS	>2666	346	450	3.57	
3-LN	>1866	231	194	8.82	Cleavage dense zone
3-LS	>1866	201	170	9.74	

The load test curves (Figure 5) are basically a linear segment with no inflection points and no obvious failure conditions. The characteristic value of the bearing capacity is obtained by dividing the maximum load by 3. In the natural state and the saturated state, the bearing capacity of the rock mass in the slate area is close, as shown in Figures 5(a) and 5(b). In the cleavage dense zone, the rock mass is broken, and the settlement deformation is larger than that in the slate area, and the settlement deformation in the saturated state is larger than that in the natural state, as shown in Figure 5 (c). It can be seen from Table 3 that the characteristic value of subsoil bearing capacity in slate area is not less than 2.133 MPa, and that in cleavage dense zone is not less than 1.866 MPa. The characteristic value of bearing capacity of rock mass of the anchorage is not less than 1.866 MPa. Under the design load (0.8 Mpa), the deformation modulus of the rock mass is 201~923 MPa. Considering that the bottom surface of the anchorage is 12m below the water level of the reservoir, the deformation modulus of the slate area in saturated state is 346 MPa, and that of the cleavage dense zone is 201MPa.

Direct Shear Test

The direct shear test is divided into a shear test and a friction test. The friction test is a direct shear test in which a sample continues to be sheared along the shear plane after the sample is cut. The direct shear test is carried out according to relevant specifications [20]. The direct shear tests are shown in Figure 6.
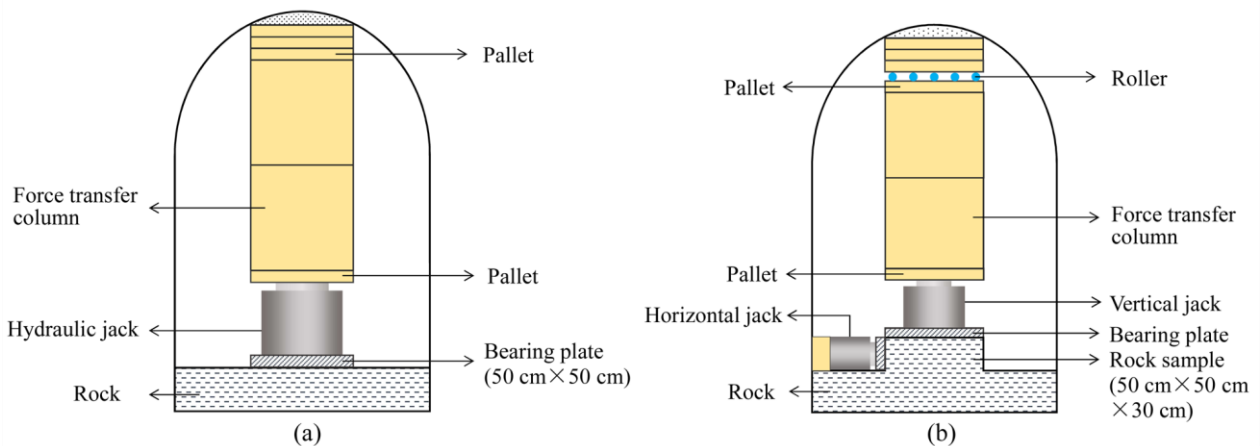
Fig. 6 - Direct shear tests, (a) The concrete-bedrock direct shear test, (b) The bedrock direct shear test

The normal pressure was applied to the sample, and the horizontal shear force was applied to the sample until it was destroyed after it was consolidated and stable. Recording the value of the shear force when the sample was destroyed and drawing the curve of shear stress τ and normal stress σ. The shear strength parameters of the rock mass can be obtained from the τ-σ curve.

The τ-σ curve follows Coulomb's law,

$$\tau = \sigma \tan \varphi + C \tag{2}$$

where τ is the shear stress acting on the shear plane in kPa, σ is the normal stress acting on the shear plane in kPa, C is the cohesion of the rock mass in kPa, φ is the internal friction angle of the rock mass in °, τ and σ can be calculated according to the following equations:

$$\sigma = \frac{P}{F} \tag{3}$$

$$\tau = \frac{Q}{F} \tag{4}$$

$$f = \tan \varphi \tag{5}$$

where P is the total normal load acting on the shear plane in kN, Q is the total shear load acting on the shear plane in kN, F is the area of the shear plane in m^2, f is the friction coefficient.

The maximum stable shear load obtained under each level of normal load was regressed to obtain the shear strength expression [21,22]. The concrete-bedrock direct shear test curves are shown in Figure 7, and the bedrock direct shear test curves are shown in Figure 8. The test results are summarized in Tables 4 and 5.
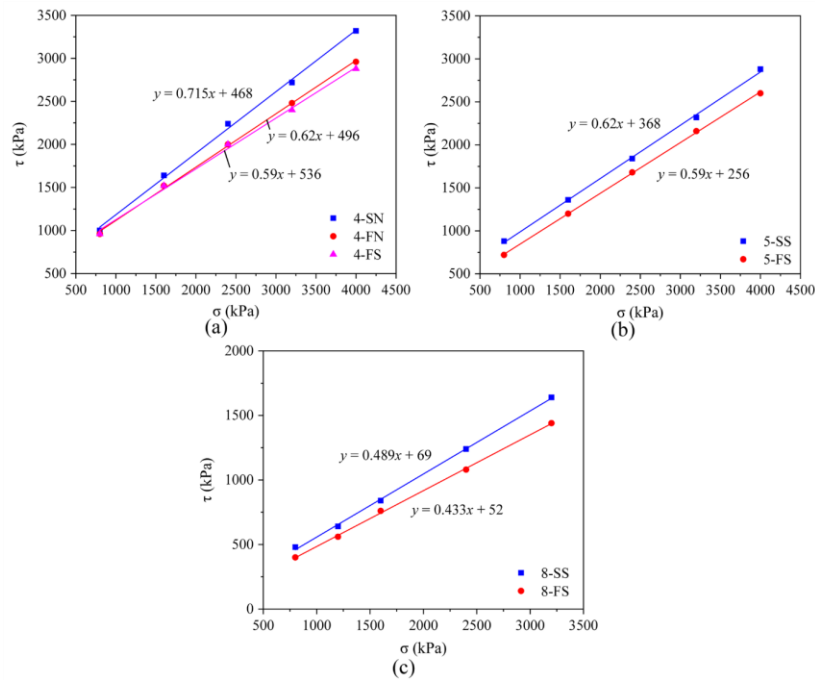

Fig. 7 - The concrete-bedrock direct shear test curves, (a) Test curve of test area 4, (b) Test curve of test area 5, (c) Test curve of test area 8
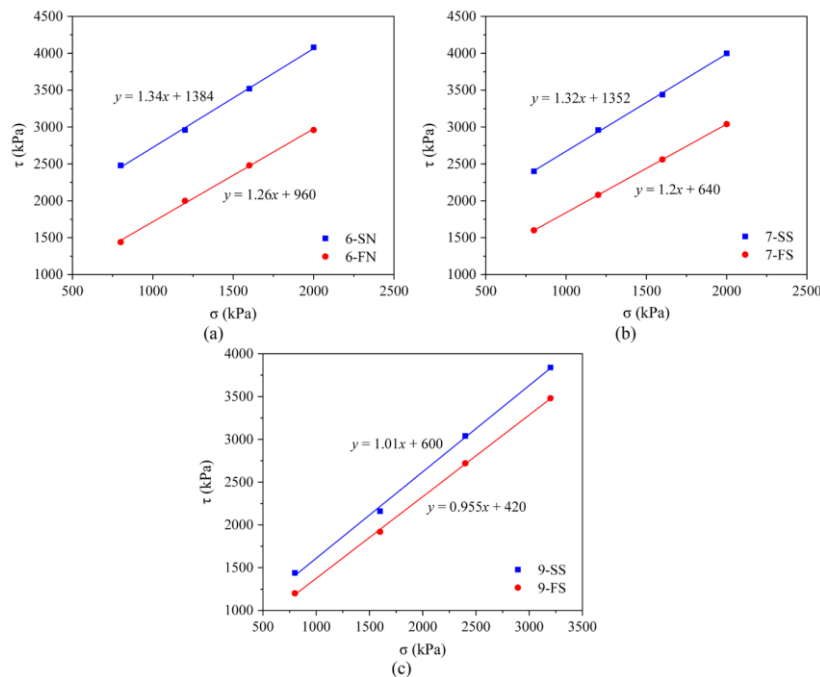

Fig. 8 - The bedrock direct shear test curves, (a) Test curve of test area 6, (b) Test curve of test area 7, (c) Test curve of test area 9

Tab. 4 - Summary of concrete-bedrock direct shear test results

Test point	Friction coefficient	Cohesion (kPa)	Rock mass category
4-SN	0.715	468	Slate
4-FN	0.62	496	
4-FS	0.59	536	
5-SS	0.62	368	
5-FS	0.59	256	
8-SS	0.489	69	Cleavage dense zone
8-FS	0.433	52	

Tab. 5 - Summary of bedrock direct shear test results

Test point	Friction coefficient	Cohesion (kPa)	Rock mass category
6-SN	1.34	1384	Slate
6-FN	1.26	960	
7-SS	1.32	1352	
7-FS	1.2	640	
9-SS	1.01	600	Cleavage dense zone
9-FS	0.955	420	

Some conclusions of the concrete-bedrock direct shear test can be obtained from Figure 7 and Table 4. The minimum friction coefficient of the test points in slate area is 0.59, which is about 26% higher than that in cleavage dense zone. The minimum cohesion of the test points in slate area is 256 kPa, which is about 5 times higher than that in cleavage dense zone. Compared with the saturated state and the natural state, the friction coefficient in the slate area decreases by about 5%, and the cohesion in the slate area increases by about 5%. The friction coefficient and cohesion of rock mass in slate area are very little affected by the water. The friction coefficient and cohesion of shear tests are larger than those of friction tests. The friction coefficients of test areas 4 and 5 are relatively small. It can be seen from the contact surface after shearing that there is residual slag on the contact surface. The friction coefficient and cohesion of the test area 8 are relatively low, because the rock mass in the cleavage dense zone is broken, and there is a lot of rock slag at the interface between the concrete and the rock mass.

Some conclusions of the bedrock direct shear test can be obtained from Figure 8 and Table 5. The minimum friction coefficient of test points in slate area is 1.2, which is about 25% higher than that in cleavage dense zone. The minimum cohesion of the test points in slate area is 640 kPa, which is about 50% higher than that in cleavage dense zone. Compared with the saturated state and the natural state, the friction coefficient of the slate area is reduced by about 4%, and the cohesion of the slate area is reduced by about 33%. The friction coefficient and cohesion in the test areas 6 and 7 are relatively high, mainly due to the steep slope of the slate layer, which intersects the shear plane at a large angle. The rock mass parameters of test area 9 are

significantly lower than those of test areas 6 and 7, mainly because the test area is in a dense cleavage and the rock mass is relatively broken.

Indoor Test

In order to accurately obtain the rock mass parameters of the gravity anchorage area, it is necessary to combine the results of field tests and indoor tests. In addition, the measured rock mass parameters also need to consider certain safety reserves. The sandy slate in the anchorage area was selected as the representative rock mass for indoor tests. The sandy slate samples are selected from weakly weathered rock layers, and there are weak layers in the interlayer structure surface, and the rock mass properties are relatively poor.

The physical and mechanical properties of the sandy slate can be obtained from indoor triaxial test, direct shear test and some basic density and water content tests. Based on the comprehensive analysis of indoor and outdoor test results, the density of the sandy slate is 2.4 g/cm³, the poisson ratio is 0.2, the internal friction angle is 26°, and cohesion is 640 kPa.

STATIC ANALYSIS

Simplified Force Model of the Gravity Anchorage

The simplified force model of the gravity anchorage is shown in Figure 9. The design load of the main cable of the gravity anchorage is 202201 kN/cable. In Figure 9, G_1 represents the weight of the pier of splay saddle, G_2 represents the weight of the foundation, G_3 represents the weight of the anchor block, G_4 represents the weight of the front anchor chamber, T_h is the horizontal component of the main cable tension, T_v is the vertical component of the main cable tension, F_r is the subgrade reaction, F_w represents the buoyancy of water, F_f represents the friction resistance and cohesion of bedrock. The forces on the anchorage are summarized in Table 6.
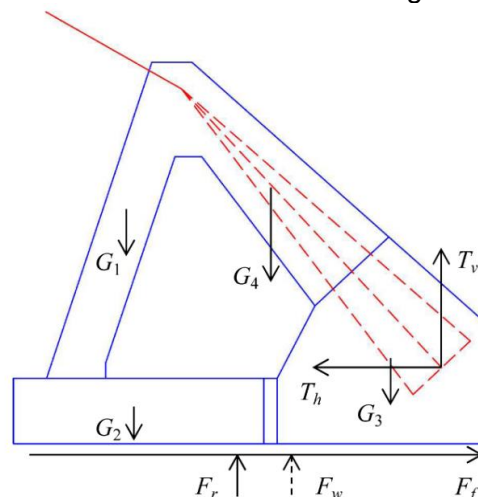

Fig. 9 - Force diagram of the gravity anchorage

Tab. 6 - Forces summary of the gravity anchorage

Force name	Force value (kN)	Arm of force to overturning axis[*] d_i (m)	Arm of force to center of gravity axis l_i (m)
G_1	0.804×10^5	23 (d_1)	11 (l_1)
G_2	5.055×10^5	20 (d_2)	16 (l_2)
G_3	8.99×10^5	56 (d_3)	21 (l_3)
G_4	1.98×10^5	38 (d_4)	4 (l_4)
F_w	0.36×10^5	36 (d_5)	0 (l_5)
T_h	2.758×10^5	12 (d_6)	12 (l_6)
T_v	2.958×10^5	62.5 (d_7)	28 (l_7)

[*] This paper takes the intersection of the bottom of the foundation and the front wall as the overturning axis.

Calculation of Anti-sliding Stability Coefficient

For the gravity anchorage with rigid enlarged foundation, the anti-sliding stability is generally calculated according to the rigid body model using the equilibrium condition. The gravity anchorage is simplified as a rigid body acting on a homogeneous ground, and only the frictional resistance between the anchorage and the ground is considered. The friction between the anchorage and the surrounding rock, as well as the rock mass resistance in the front side, are ignored as safety reserves.

The anti-sliding stability coefficient of the gravity anchor is calculated according to the following formula [19]:

$$K_a = \frac{\mu \sum P_i + \sum H_{ip}}{\sum H_{ia}} \tag{6}$$

where K_a represents the anti-sliding stability coefficient of the gravity anchorage, μ represents the friction coefficient between the bottom surface of the gravity anchorage and the ground, $\sum P_i$ is the sum of vertical forces in kN, $\sum H_{ip}$ is the sum of anti-sliding stability horizontal forces in kN, $\sum H_{ia}$ is the sum of sliding horizontal forces in kN. Substituting the relevant data into the above formula

$$K_a = \frac{\mu(G_1 + G_2 + G_3 + G_4 - F_w - T_v)}{T_h} = 2.12 > 2 \tag{7}$$

The calculated anti-sliding stability coefficient of the gravity anchorage is 2.12, which is larger than the value required by the code [23]. Therefore, the anti-sliding stability of the gravity anchorage under the tension of the main cable meets the requirement.

Calculation of Anti-overturning Stability Coefficient

The overturning mechanism of the gravity anchorage is that the anchorage will rotate with the increase of cable tension after the tension was transmitted by the cables. Moreover, the rotation direction is consistent with the cable tension direction. The rotation will eventually increase the stress in the front rock layer, and the rock layer at the posterior toe point will enter a plastic yield state, so that the ground under the anchorage will form a circular funnel-shaped sliding surface.

This paper takes the intersection of the bottom of the anchorage and the front wall as the overturning axis. The anti-overturning stability coefficient of the gravity anchorage is calculated by the following formula

----

$$K_0 = \frac{M_a}{M_c} = \frac{G_1 d_1 + G_2 d_2 + G_3 d_3 + G_4 d_4}{F_w d_5 + T_h d_6 + T_v d_7} = 3.02 > 2 \tag{8}$$

where K_0 is the anti-overturning stability coefficient of the gravity anchorage, M_a is the anti-overturning moment of force in kN·m, M_c is the overturning moment of force.

The calculated anti-overturning stability coefficient of the gravity anchor is 3.02, which is greater than the value required by the specification [23]. Therefore, the anti-overturning stability of the gravity anchorage meets the requirement.

Calculation of Subgrade Bearing Capacity

The calculation of subgrade bearing capacity requires that the contact stress does not exceed the characteristic value of subsoil bearing capacity of the bearing stratum. In the calculation, the effects of friction resistance and elastic resistance of the rock mass around the anchorage can be ignored [19].

The bearing capacity of the rock mass at the bottom of the anchorage is calculated as follows:

$$p_{\max} = \frac{N}{A} + \frac{M}{W} \leq \gamma_R f_a \tag{9}$$

where $p_{\max}$ represents the maximum compressive stress on the bottom surface of the anchorage in kPa, N represents the vertical force of the bottom surface of the foundation under the action combination in kN, A is the area of the bottom of the foundation and its value is 3600 m², M is the bending moment of the external force on the anchorage to the centre of gravity axis of the anchorage in kN·m, W represents the area resistance moment in the eccentric direction of the bottom surface of the anchorage and its value is 43200 m³, γ_R represents the resistance coefficient of bearing capacity of foundation soils and its value is 1.25, and f_a represents the characteristic value of subsoil bearing capacity which is 1866 kPa from the load tests.

When the effect of water buoyancy is not considered,

$$N = G_1 + G_2 + G_3 + G_4 - T_v = 1.387 \times 10^6 \, \text{kN} \tag{10}$$

$$W = G_1 l_1 + G_2 l_2 + T_h l_6 + T_v l_7 - G_3 l_3 - G_4 l_4 = 8.934 \times 10^5 \tag{11}$$

Substituting the relevant values into Equation (9),

$$p_{\max} = \frac{1.387 \times 10^6}{3600} + \frac{8.934 \times 10^5}{43200} = 405.96 \, \text{kPa} \leq \gamma_R f_a \tag{12}$$

When the effect of water buoyancy is considered,

$$N = G_1 + G_2 + G_3 + G_4 - T_v - F_w = 1.351 \times 10^6 \, \text{kN} \tag{13}$$

$$W = G_1 l_1 + G_2 l_2 + T_h l_6 + T_v l_7 - G_3 l_3 - G_4 l_4 = 8.934 \times 10^5 \tag{14}$$

Substituting the relevant values into Equation (9),

$$p_{\max} = \frac{1.351 \times 10^6}{3600} + \frac{8.934 \times 10^5}{43200} = 395.96 \, \text{kPa} \leq \gamma_R f_a \tag{15}$$

The calculated maximum contact stress on the bottom of the anchorage is 405.96 kPa, which is less than the characteristic value of subsoil bearing capacity. Therefore, the subgrade bearing capacity under the pulling force of the main cable meets the requirement.

NUMERICAL SIMULATION

The contact stress, anti-sliding stability coefficient and anti-overturning stability coefficient of the gravity anchorage can be obtained through static analysis, but the horizontal displacement and vertical settlement of the gravity anchorage under the pulling force of the main cable cannot be

obtained. Therefore, this paper also uses finite element software Abaqus to establish a three-dimensional model of the gravity anchorage, which is used to analyze the displacement of the gravity anchorage and the contact stress under the action of main cable tension. The purpose is to further verify the stability of the gravity anchorage using finite element method based on the static analysis.

Model Establishment

Three-dimensional finite element models of the gravity anchorage and the rock mass are established. The gravity anchorage adopts the isotropic linear elastic model, and the rock mass adopts the Mohr-Coulomb model. The foundation model is set to be 288 m long, 140 m wide and 80 m high, and an excavation with a length of 72 m, a width of 50 m and a depth of 10 m is cut in the middle of it. The mesh generation of the gravity anchorage and ground is shown in Figure 10.
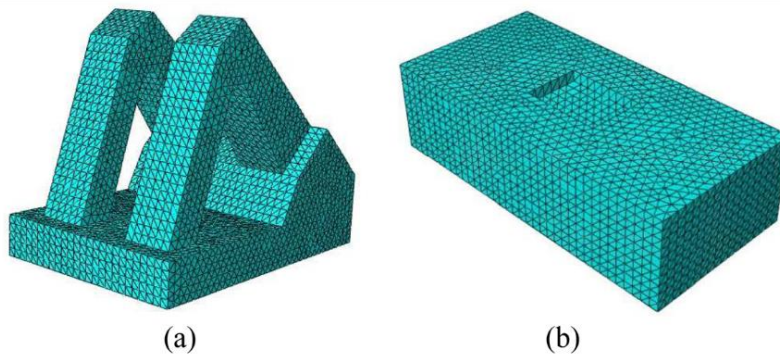

(a)   (b)

Fig. 10 - Model mesh generation, (a) Mesh generation of the gravity anchor, (b) Mesh generation of the ground

Calculation Results

Displacement Results

The gravity anchorage will be displaced horizontally under the action of the horizontal component of the main cable tension. Moreover, the oblique main cable tension will cause different settlements at the front and rear ends of the gravity anchorage, and further cause the anchorage to overturn. The horizontal sliding and the overall overturning are very detrimental to the stability of the gravity anchorage, so they must be limited in a certain range. The horizontal and vertical displacement of the gravity anchorage are shown in Figure 11.
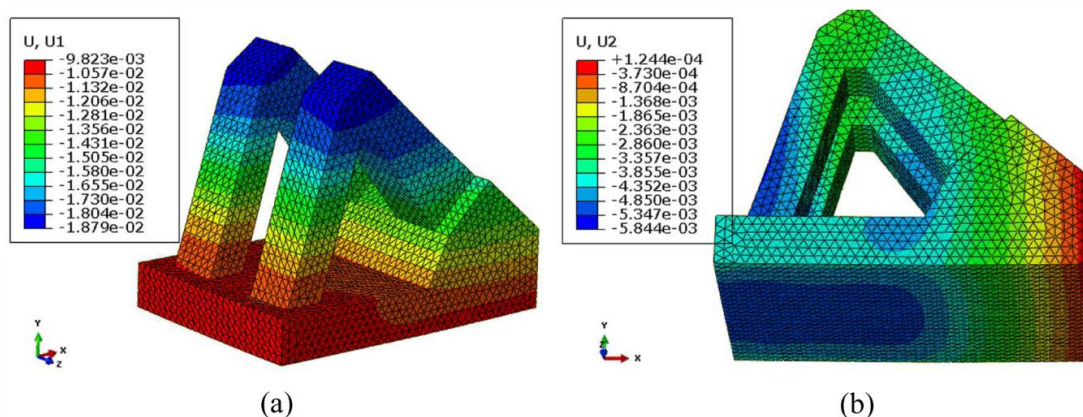

(a)   (b)

Fig. 11 - The horizontal and vertical displacements of the gravity anchorage (unit: m), (a) Horizontal displacement of the gravity anchorage, (b) Vertical displacement of the gravity anchorage

----

It can be seen from Figure 11(a) that the maximum horizontal displacement of the gravity anchorage is 18.79 mm, which occurs at the top of the side wall of the front anchor chamber. Moreover, the horizontal displacement gradually decreases from top to bottom. According to the Specification for Design of Highway Suspension Bridges [23], the allowable horizontal displacement of the gravity anchorage during the operation stage should not be greater than 0.0001 times of the main span. The calculated maximum value of 18.79 mm is smaller than the allowable value of 76.6 mm, so it meets the requirements.

As can be seen from Figure 11(b), the maximum settlement of the front end of the gravity anchorage is 5.84 mm, and the rear end is pulled up by 0.12 mm. The inclined tension of the main cable will cause the gravity anchorage to incline forward to a certain extent, resulting in uneven settlement at the front and rear ends. Therefore, the front end of the gravity anchorage may settle and the rear end may be pulled up. The specification requires that the vertical displacement of the gravity anchorage should not be greater than 0.0002 times of the main span. The calculated maximum value of 5.84 mm is less than 153.2 mm required by the specification. The overturning angle of the gravity anchor is 0.0047°, it is very small and almost negligible.

Stress Results

Because the weight of the gravity anchor is very large, it will cause very large stress on the ground. The contact stress obtained by finite element analysis is shown in Figure 12. It can be seen that the maximum compressive stress at the bottom of the anchorage is 497.6 kPa. This value is smaller than the characteristic value of subsoil bearing capacity (1866 kPa). Therefore, the contact stress under the action of the gravity anchorage meets the requirement.
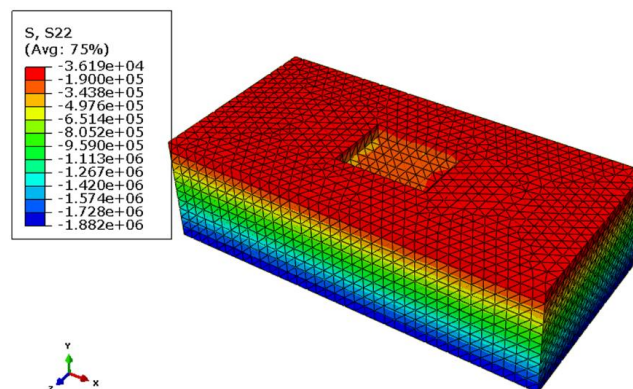

Fig. 12 - Ground stress (unit: Pa)

CONCLUSION

(1)   The basic physical parameters of the bedrock in the anchorage area can be obtained through field tests and indoor tests, including density, elastic modulus, cohesion, internal friction angle, and poisson ratio. In addition, the cohesion and friction coefficient of the contact surface between the bottom of the gravity anchorage and the bedrock, as well as the characteristic value of subsoil bearing capacity in the anchorage area are obtained. It can be concluded that the characteristic value of the subsoil bearing capacity is 1866 kPa. The deformation modulus of saturated rock mass is less than that of natural state, with a reduction of 10% ~ 20%.

(2)   The static method is used to analyze the stability of the gravity anchorage. Calculation results show that the anti-sliding stability coefficient is 2.12, the anti-overturning stability coefficient is 3.02, and the foundation stress is 405.96 kPa. The calculation results meet the relevant requirements. The anti-sliding, anti-overturning and subsoil bearing capacity of a gravity anchorage are three important aspects for checking its stability.

(3)   The stability of the gravity anchorage is analyzed by numerical simulation. The results show that the maximum horizontal displacement is 18.79 mm, the maximum vertical settlement is 5.84 mm, the maximum contact stress is 497.6 kPa, and the maximum overturning angle is 0.0047°. The calculation results meet the relevant requirements.

(4)   The gravity anchorage has a very large dead weight. In the calculation and analysis, the interaction between the bottom surface of the gravity anchorage and the ground is considered, and the shear failure of the deep rock mass is not considered. It is recommended that the shear failure of the gravity anchorage on the deep ground can be considered on the basis of meeting the stability requirements.

ACKNOWLEDGMENTS

REFERENCES

[1]   Zhang Q, Li Y, Yu M, Hu, H, Hu J, 2014. Study of the rock foundation stability of the Aizhai suspension bridge over a deep canyon area in China. Engineering Geology, 198(2015): 65–77. DOI: 10.1016/j.enggeo. 2015. 09. 012

[2]   Deng Y, Wang C, Shi Y, Liu R, 2012. Summary for Application of Super Gravity Anchorage. Highway Engineering, 37(06): 93-96.

[3]   Ge Y, Shao S, Pan H, Hu F, 2013. Deformation and safety analysis of Taizhou suspension bridge south - anchor foundation under surcharge. Science & Technology Review, 31(26): 35-39. DOI: 10.3981/j.issn.1000-7857.2013.26.004

[4]   Koji K, Fumio T, 2010. Several Geotechnical Design and Construction Issues with Akashi Strait Bridge. Soils and Foundations, 50(06): 829-845. DOI: 10.3208/sandf.50.829.

[5]   Koji M, Carlos A, Nuntikorn K, Wataru T, Kohei N, Eiji I, 2018. Performance Assessment Using Structural Analysis and Spatial Measurement of a Damaged Suspension Bridge: Case Study of Twantay Bridge, Myanmar. Journal of Bridge Engineering, 23(10): 1-14. DOI: 10.1061/(ASCE)BE.1943-5592.0001293

[6]   Taylor R J, 1982. Interaction of anchors with soil and anchor design. Naval Civil Engineering Lab, California, USA.

[7]   Andersen EY, Andreasen BS, Ostenfeld-Rosenthal P, 1992. Foundation reliability of anchor block for suspension bridge. In: Rackwitz R., Thoft-Christensen P. (eds) Reliability and Optimization of Structural Systems '91. Lecture Notes in Engineering, vol 76. Springer, Berlin, Heidelberg.

[8]   Carter M, 2012, Seismic Isolation of a Suspension Bridge Anchor Block. IABSE Congress Report, 18(12), 1235-1242.

[9]   Wu G, Zhang Y, Chen g, He S, 2013. Stress Analysis of Gravity Anchorage of Aizhai Bridge. Bridge Construction, 43(06): 40-44.

[10]   Xu S, Chen C, Zhu S, Xu F, li jie, Zhang Z, Xu T, Zhu L, 2020 Modeling Analysis of the Upper Limit Water Level Mechanism in the Upstream Reservoir of a Dam Embankment. Advances in Civil Engineering, 2020: 1-13. doi.org/10.1155/2020/8850681

[11]   Yin X, Yan F, Zhou L, Wang D, Deng Q, 2017. Joint bearing mechanism of structure and foundation for gravity anchor block of suspension bridge. Journal of Traffic and Transportation Engineering, 17(02): 1-11.

[12]   Chen T, Xiao S, Cheng Q, Zhou H, 2019. Long-term deformation and stability analysis of gravity anchorage slope on Kangding bank of Dadu River Bridge in Luding. Journal of Engineering Geology, 27(03): 632-639. DOI: 10.13544/ j.cnki.jeg.2018-253

[13]   Lai Y, Wu C, Zhang Z, 2010. Test and numerical analysis of effect of notched sill of gravity anchorage on soft rock ground of suspension bridge. Chinese Journal of Rock Mechanics and Engineering, 29(03): 593-602.

[14]   Xu T, Zhou Z, Yan R, Zhang Z, Zhu L, Chen C, Xu F, Liu T, 2020, Real-Time Monitoring Method for Layered Compaction Quality of Loess Subgrade Based on Hydraulic Compactor Reinforcement. Sensors, 20(15). DOI: 10.3390/s20154288

[15]   Luo X, 2011. Design of south anchorage foundation of Yingwuzhou Changjiang River Bridge in Wuhan. Bridge Construction, 2011(04): 05-09.

[16]   Guo S, Qi S, Li z, Ma J, Chai J, Zhai W, 2011. Stability Analysis of Anchorage for super suspension bridge over Longjiang River in Yunnan province. Journal of Engineering Geology, 19(6): 909-916.

[17]   Ya G, Han D, Shi H, Yang J, 2017. Study on the stability of gravity anchorage foundation of Nizhou Waterway Bridge of Second Humen Bridge. HIGHWAY, 62(04): 129-135.

[18]   Ma B, Ma X, Lu J, 2017. Design of anchorage and anchor system of Xiushan Bridge. Bridge Construction, 47(02): 89-94

[19]   CCCC HIGHWAY CONSULTANTS CO., LTD., 2019. Specifications for Design of Foundation of Highway Bridges and Culverts. China Communications Press Co., Ltd. Beijing, China, 73-75.

[20]   CHENDU ENGINEERING CORPORATION LIMITED, China Renewable Energy Engineering Institute, CHINA ELECTRICITY COUNCIL, 2013. Standard for test methods of engineering rock mass. China Planning Press. Beijing, China, 41-50.

[21]   Liu Y, Zhao M, Zheng S, 2011. Test study on the friction resistance of the north concrete anchor of Qingcaobei Yangtze River Bridge. JOURNAL OF CHONGQING JIAOTONG UNIVERSITY (NATURAL SCIENCE), 30(05): 911-915. DOI: 10. 3969/j. issn. 1674-0696. 2011. 05. 006

[22]   Ruan B, Xiao W, Yin H, 2011. Testing study on base resistance of the anchors at a suspension bridge. Journal of Railway Science and Engineering, 08(01): 59-62. DOI:10.19713/j.cnki.43-1423/u.2011.01.011

[23]   CCCC HIGHWAY CONSULTANTS CO., LTD., 2015. Specifications for Design of Highway Suspension Bridge. China Communications Press Co., Ltd. Beijing, China, 46-49.

ANALYZING THE EFFECT OF MICRO RUBBER, MICRO SIO₂, AND NANO SIO₂ IN MICROCRACKS IN SELF-CONSOLIDATING CONCRETE (SEM OBSERVATION)

Ehsan Adili[1], Moein Riginejad[2]

1. *Velayat University, Department of Civil Engineerning,Iranshahr, Iran; e.adili@velayat.ac.ir*
2. *Hatef University,Zahedan, Iran; rigimoein@gmail.com*

ABSTRACT

The present study is an attempt to analyze the effect of micro rubber waste in self-consolidating concrete (SCC) and to compare the concrete containing SCC with conventional additives such as micro SiO_2 and nano SiO_2. The use of rubber waste can be substantially important from the environmental point of view. Hence, concrete specimens containing 1, 3 and 5% micro rubber waste were made. Moreover, specimens containing 1, 3 and 5% nano SiO_2 and 4, 8 and 12% micro SiO_2 were prepared to compare their behaviour and microstructure with each other and with the witness specimens. The effect of the other parameters such as the specimen age and the w/c ratio on the microstructure of concrete containing rubber waste was also studied. Thereafter, the specimens were imaged using a scanning electron microscope (SEM) to observe and compare the microcracks in the concrete and secondary electron beam (SE) was used to obtain their images. The results of the microstructural consideration of different specimens showed that 1% of micro rubber waste can improve the behaviour of self-consolidating concrete, but the concrete microstructure strength and quality decline with an increase in its amount.

KEYWORDS

Self-consolidating concrete, Micro rubber waste, Microcrack, SEM

INTRODUCTION

Self-consolidating concrete (SCC) has been shown to achieve the fresh- and hardened-state requirements for modern concrete construction [1-4]. The American Concrete Institute (ACI) defines SCC as concrete that is highly flowable without segregation that can self-fill complicated or congested-reinforcing steel formwork with very little mechanical-forced consolidation [5].

The use of self-consolidating concrete is increasing due to its advantages including the lack of need for vibration and easy implementation. In the past decades, numerous researchers have extensively studied the behaviour of this type of concrete. Some researchers have tried to improve the behaviour of this type of concrete by adding additives. For instance, Makul [6] tried to analyze the behaviour of self-consolidating concrete by adding rice husk ash. The use of rice husk ash along with the presence of foundry sand waste increased the strength of self-consolidating concrete. The analysis of concrete microstructure has also garnered the attention of researchers in recent years. The microstructural condition of concrete reflects its technical properties such as compressive strength. The use of SEM images is one of the best methods of observing the microstructure of concrete. The images captured by this type of microscope can contribute to the highly precise examination of the details of concrete cracks and microstructure [7-10]. Safiuddin et al. [11] explored the mechanical properties and microstructure of carbon fiber reinforced self-

consolidating concrete. The important mechanical properties of this type of concrete including compressive strength, splitting tensile strength, modulus of rupture or flexural strength, and toughness were estimated. The addition of carbon fibers to self-consolidating concrete improved almost all of the aforementioned parameters. Afterward, the microstructure of the self-consolidating concrete specimens was examined using SEM images.

In this research, the overarching goal is to study the effect of using micro rubber waste powder in the production of self-consolidating concrete and analyze the behaviour of self-consolidating concrete containing micro rubber waste powder. The effect of using this material on the microstructure of self-consolidating concrete is also studied using SEM images. SE beams are used to capture the images and study the microstructure of the specimens. In addition, to compare the effects of the presence of micro rubber waste powder with conventional concrete additives such as micro SiO_2 and nano SiO_2, the self-consolidating concrete specimens were prepared with different percentages of these materials to compare their behaviour and microstructure conditions with the specimens containing micro rubber waste powder.

EXPERIMENTAL PROGRAM

Self-consolidating concrete is one of the most commonly used and beneficial types of concrete that does not require vibration for implementation and is easy to implement. The goal of this research is to study the effect of the presence of micro rubber waste in this type of concrete. This study is conducted based on the compressive strength of concrete as well as its microstructure. To analyze the behaviour and microstructure of self-consolidating concrete specimens containing micro SiO_2 waste and specimens containing micro SiO_2 and nano SiO_2, 15x15x15 cm cubic specimens were made. Besides, two specimen ages including 7 and 28 days were used to analyze the effect of improving the microstructure on time. Moreover, all of the self-consolidating concrete specimens were made with the 0.4 and 0.5 w/c ratios to study the effect of these parameters on the behaviour and microstructure of concrete. Type 2 cement produced by Sistan Cement Company was used to make the specimens. The chemical analysis of this cement product is presented in Table 1 and the results of its physical tests are presented in Table 2. The mix design of the witness self-consolidating concrete specimens is also shown in Table 3. Different additive percentages are used in different specimens.

Tab. 1- Cement chemical analysis (percent)

SiO_2	Al_2O_3	Fe_2O_3	CaO	MgO	SO_3	Na_2O	K_2O	L.O.I	I.R	C_3S	C_2S	C_3A	C_4AF	F.CaO
21.47	5.4	3.82	62.52	1.31	2.88	0.65	0.43	1.52	0.72	41.33	30.02	7.84	11.6	1.49

Tab. 2- Results of the physical tests on concrete

Blaine (cm^2/g)	Setting time (Min)		Autoclave Exp%	Comp. strength (kg/cm^2)			
	Initial	Final		2 Days	3 Days	7 Days	28 Days
3110	183	238	0.08	-	265	344	451

Tab. 3- Self-consolidating concrete mix design

Material	Quantity (kg/m^3)	Proportion
Cement	400	1
Fine aggregate	610	1.525
Coarse aggregate	1170	2.925
Water	200	0.5
Super plasticizer	10	2.5

Rubber segments were converted into rubber particles as shown in Figure 1 to obtain the micro rubber waste powder. Thereafter, they were turned into micro rubber waste powder using an ICAN ball mill, which is depicted in Figure 2. Figure 3 depicts the final micro rubber waste powder.

Fig. 1 – The initial rubber powder

Fig. 2- The ball mill used for the production of micro rubber

Fig. 3- Micro rubber waste powder

After making the specimens according to different mix designs, all the specimens containing micro SiO_2, nano SiO_2 and micro rubber waste were cured in water until they ruptured. Afterward, all specimens were broken with a digital jack at the same speed under equal conditions and their compressive strength was recorded. The location of the storage of specimens and the digital jack are shown in Figures 4 and 5, respectively.
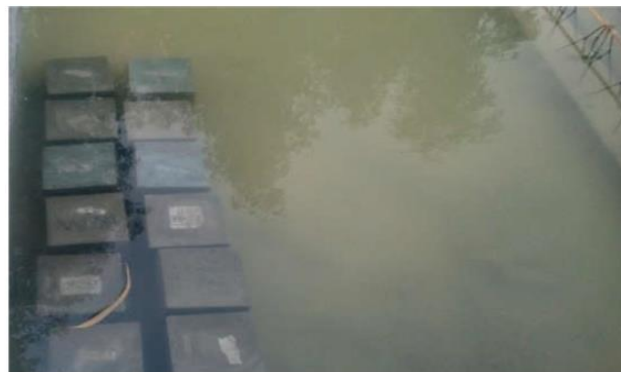

Fig. 4- Curing the specimens

Fig. 5- Testing the specimens' compressive strength

In this phase, the specimens were sent to the SEM laboratory of Sistan and Baluchestan University to study the microstructure of the specimens. The SEM device used is shown in Figure 6. Scanning electron microscopes basically operate different from optical microscopes. The microscope does not function based on the return of light. Rather, there is an electron gun at the top of the device that generates electrons at high voltage and shoots them at the specimen. The specimen surface is scanned by these electrons, and the electrons shot by the electron gun replace the electrons on the surface of the object. The electron shot by the surface of the object, which is known as a Secondary Electron (SE), hits the device detector and creates an image. Such a system is capable of providing highly accurate images of the specimen surface. The device is connected to a monitor that can display the SE images. The SE images are highly suitable for receiving the section roughness and showing the cracks and cavities.

Fig. 6 – The SEM device used for imaging

The use of the SEM device and production of appropriate images by this device depend on the qualification of the device operator because specialized operators can obtain better images than inexperienced operators. Before placing the specimens in the SEM, they have to be prepared. This process involves the dehydration of the specimens in vacuum, which is depicted in Figure 7. Thereafter, the specimens have to be covered in gold to be able to capture their images. The device that covers the specimens with gold is also shown in Figure 8. Figure 9 presents the dried specimens that are covered in gold and are ready to enter the SEM. The dimensions of these specimens are smaller than two centimeters. Basically, the specimens exceeding these dimensions cannot be placed in the device. The specimen preparation operations are highly precise and critical and take several hours. Precise preparation can significantly affect the results of imaging and the quality of the images.

Fig. 7 - Drying the specimens in vacuum

Fig. 8 – The machine that places gold covers on the specimens

Fig. 9 - Specimens ready for SEM imaging

Results and Discussion

The list of the specimens made and their compressive strength is presented in Table 4. A regards the names of the specimens in this table, the names of the witness specimens start with the letter W followed by their age and water to cement ratio. As for the other specimens, the first letter represents the additive (N = Nano SiO_2، M = Micro SiO_2 و MR = Micro Rubber) and the number after it is the percent of using the material. The numbers after S also show the age and the water to cement ratio, respectively.

Tab. 4- Specimens compressive strength

Specimen	Age (day)	W/C ratio	Nano SiO_2 (kg/m^3)	Micro SiO_2 (kg/m^3)	Micro Rubber (kg/m^3)	Compressive strength (MPa)
W74	7	0.4	———	———	———	24.5
W284	28	0.4	———	———	———	36.9
W75	7	0.5	———	———	———	21.3
W285	28	0.5	———	———	———	32.8
N1S74	7	0.4	1	———	———	21.4
N1S284	28	0.4	1	———	———	27.1
Specimen	Age (day)	W/C ratio	Nano SiO_2 (kg/m^3)	Micro SiO_2 (kg/m^3)	Micro Rubber (kg/m^3)	Compressive strength (MPa)
N3S74	7	0.4	3	———	———	28.0
N3S284	28	0.4	3	———	———	45.4
N5S74	7	0.4	5	———	———	25.3
N5S284	28	0.4	5	———	———	29.3
N1S75	7	0.5	1	———	———	17.9
N1S285	28	0.5	1	———	———	24.1
N3S75	7	0.5	3	———	———	24.3
N3S285	28	0.5	3	———	———	38.8

Specimen	Age (day)	W/C ratio	Nano SiO$_2$ (kg/m^3)	Micro SiO$_2$ (kg/m^3)	Micro Rubber (kg/m^3)	Compressive strength (MPa)
N5S75	7	0.5	5	——	——	19.5
N5S285	28	0.5	5	——	——	26.1
M4S74	7	0.4	——	4	——	43.0
M4S284	28	0.4	——	4	——	45.0
M8S74	7	0.4	——	8	——	50.6
M8S284	28	0.4	——	8	——	54.3
M12S74	7	0.4	——	12	——	48.3
M12S284	28	0.4	——	12	——	50.6
M4S75	7	0.5	——	4	——	34.1
M4S285	28	0.5	——	4	——	40.0
M8S75	7	0.5	——	8	——	36.3
M8S285	28	0.5	——	8	——	43.5
M12S75	7	0.5	——	12	——	29.6
M12S285	28	0.5	——	12	——	35.0
MR1S74	7	0.4	——	——	1	32.0
MR1S284	28	0.4	——	——	1	44.8
MR3S74	7	0.4	——	——	3	21.1
MR3S284	28	0.4	——	——	3	32.8
MR5S74	7	0.4	——	——	5	18.6
MR5S284	28	0.4	——	——	5	24.9

MR1S75	7	0.5	———	———	1	26.4
MR1S285	28	0.5	———	———	1	40.0
MR3S75	7	0.5	———	———	3	18.5
MR3S285	28	0.5	———	———	3	30.2
MR5S75	7	0.5	———	———	5	16
MR5S285	28	0.5	———	———	5	22.3

The diagram in Figure 10 shows the condition of the 7-day specimens with the 0.4 water to cement ratio. As seen, the specimens containing micro SiO_2 yielded the best results. Seemingly, at the early ages, the addition of 8 percent micro SiO_2 results in the highest strength level. Furthermore, the addition of a small amount of micro rubber, i.e. approximately 1 to 3 weight percent of cement, does not considerably affect the specimens' strength and their strength remains almost on the same level as the witness specimens. However, the specimen strength decreases with an increase in the micro rubber amount.
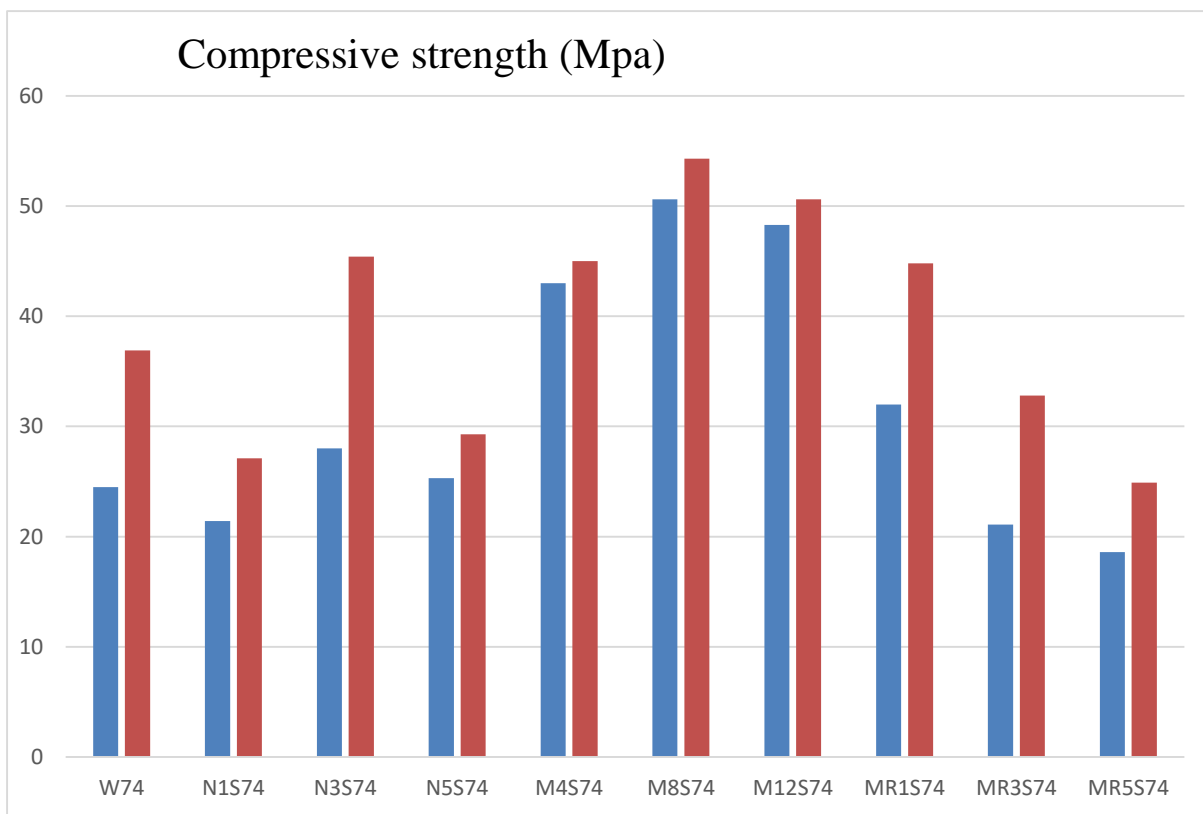

Fig. 10- The compressive strength of the specimens with the 0.4 water to cement ratio, the orange columns represent the same specimen at the age of 28 days.

Another finding is the rapid increase in the strength of the specimens containing micro SiO_2, which gained a large percent of their compressive strength at the age of 7 days. However, in the specimens containing micro rubber, there is a considerable difference between the 7-day and 28-day strength levels similar to the witness specimen.

A comparison of the microstructures of some of these specimens explains their macroscopic behaviour. In Figure 11, the microstructure of specimen W74 is presented. As seen, the microstructure of this specimen is completely disintegrated and porous with numerous cavities. Figure 12 shows the microstructure of the specimen containing micro SiO_2, which is more integrated and uniform with a stronger structure. This image clearly mirrors the effect of micro SiO_2 particles on the concrete integration.

Figure 14 indicates the compressive strength of the specimens with water to cement ratio of 0.5 at the ages of 7 and 28 days. Figures 15 and 16 also show the microstructure of the W75 and M8S74 specimens, respectively. As seen, the structure of the specimen containing micro SiO_2 is denser and more uniform, hence its higher strength. There are many more pores in the witness specimen. A comparison of both of these specimens with their similar specimens with a water to cement ratio of 0.4 reveals their weakness as well as their higher number of pores and lower strength. Considering the microstructure of the specimens containing micro rubber, which is shown in Figures 13 and 17, these microstructures are in a different condition. Although the porosity of the specimens containing micro rubber is lower and they have adequate integration, the mechanism of mixing with rubber is different in these specimens and the structure of CHs is also evidently different.
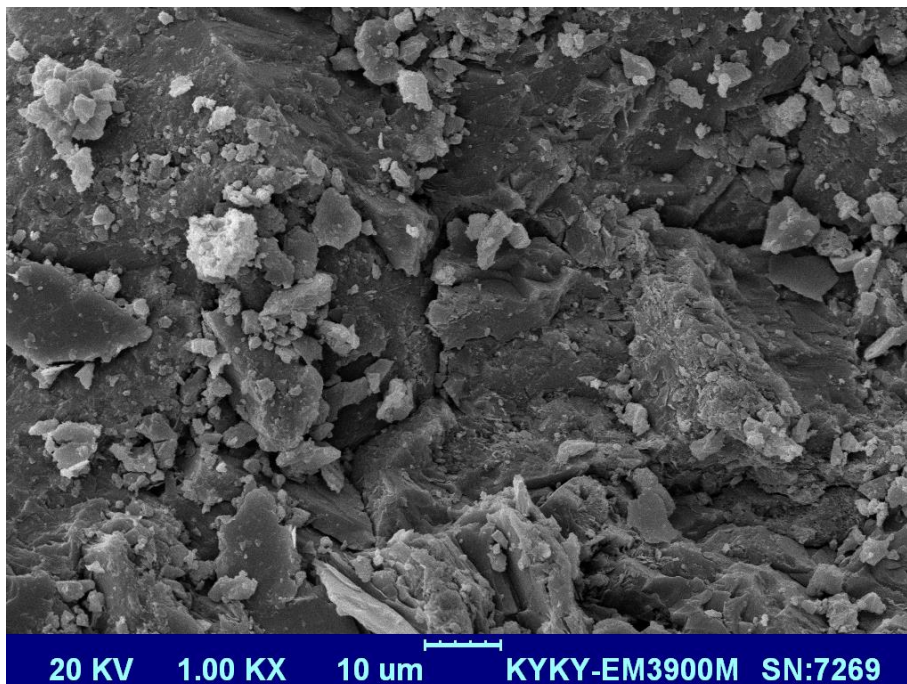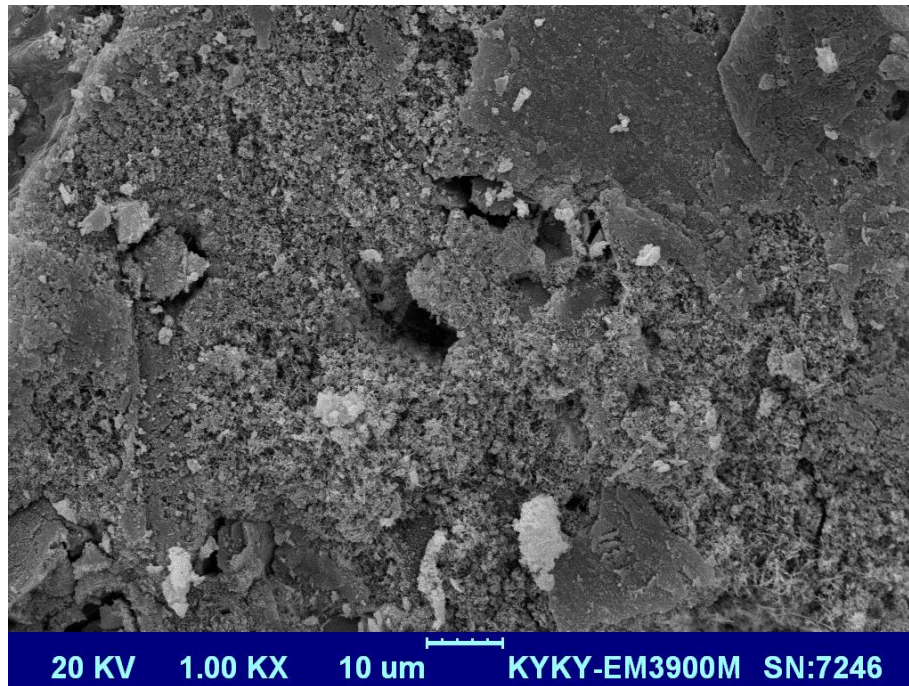

Fig. 11- The microstructure of the W74 specimen

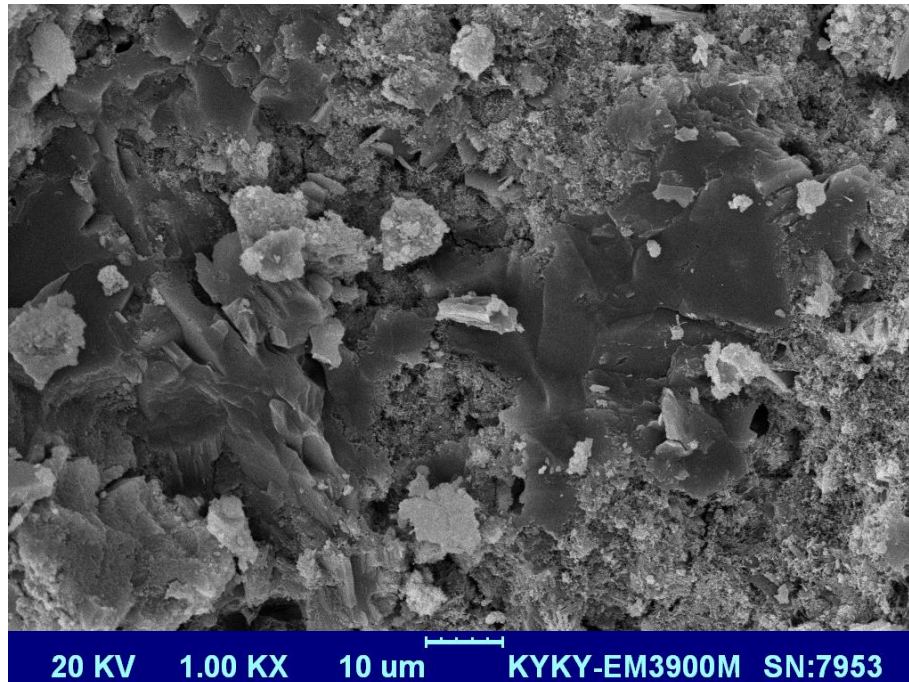*Fig. 12 - The microstructure of the M8S74 specimen*

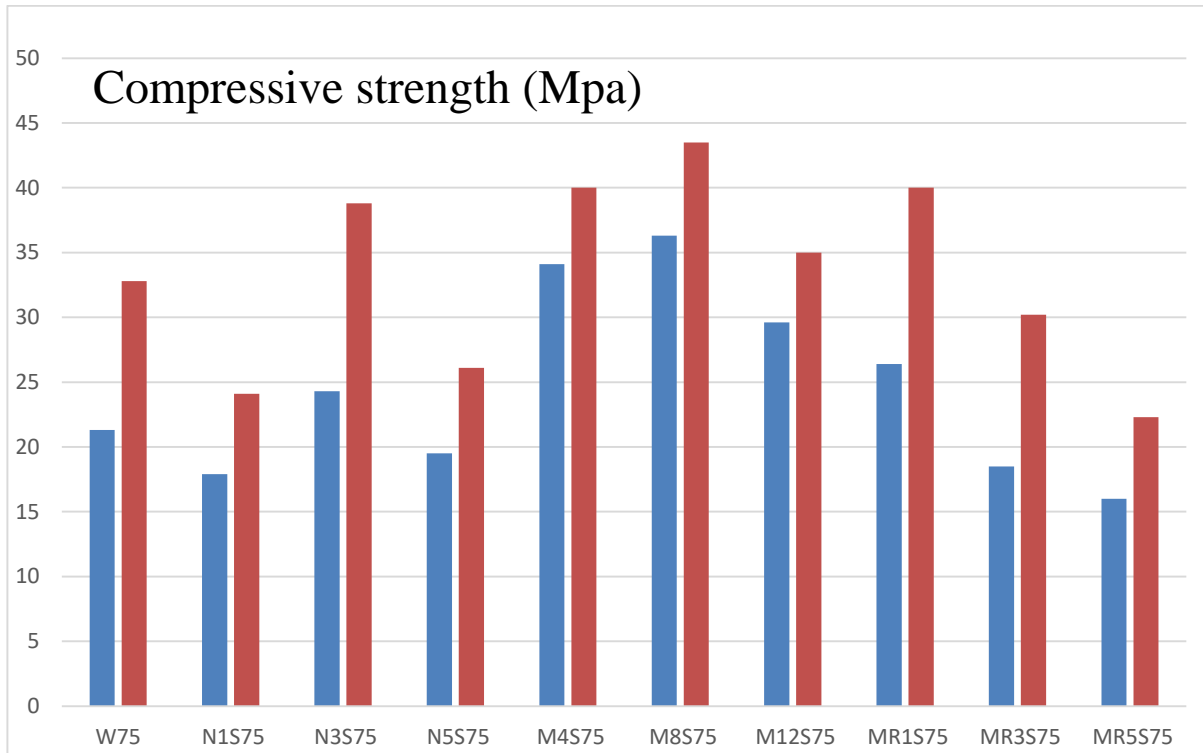*Fig. 13- The microstructure of the MR5S74 specimen*

Fig. 14 – The compressive strength of the specimens with a water to cement ratio of 0.5, the orange columns show the same specimen at the age of 28 days.
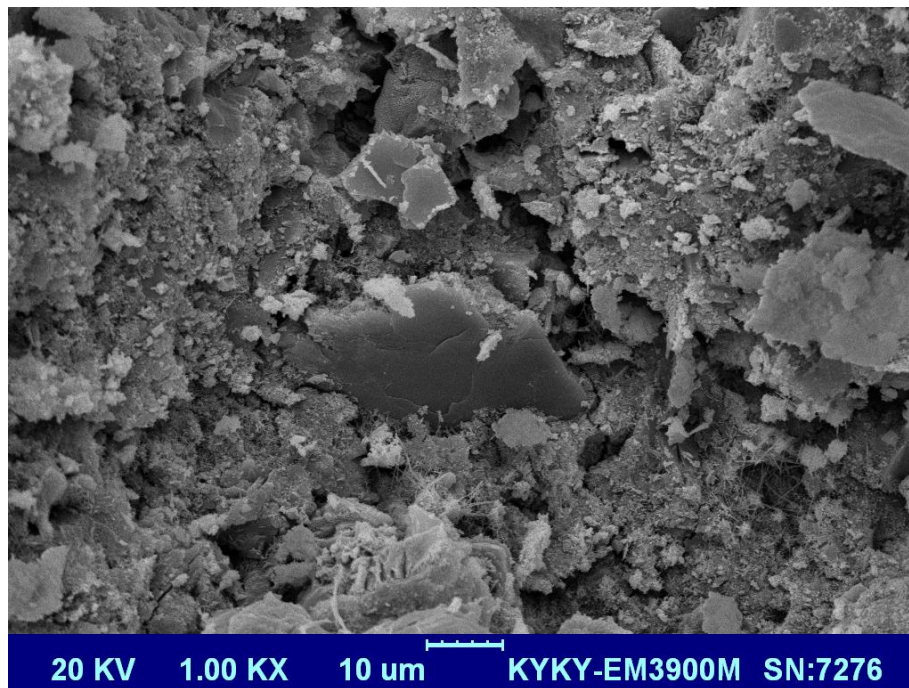

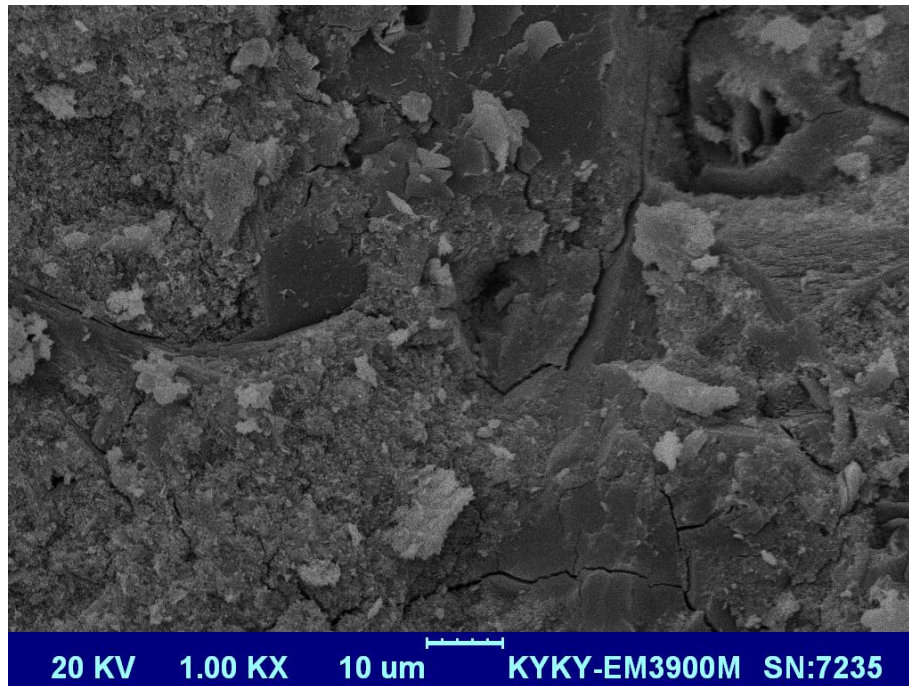*Fig. 15- The microstructure of the W75 specimen*

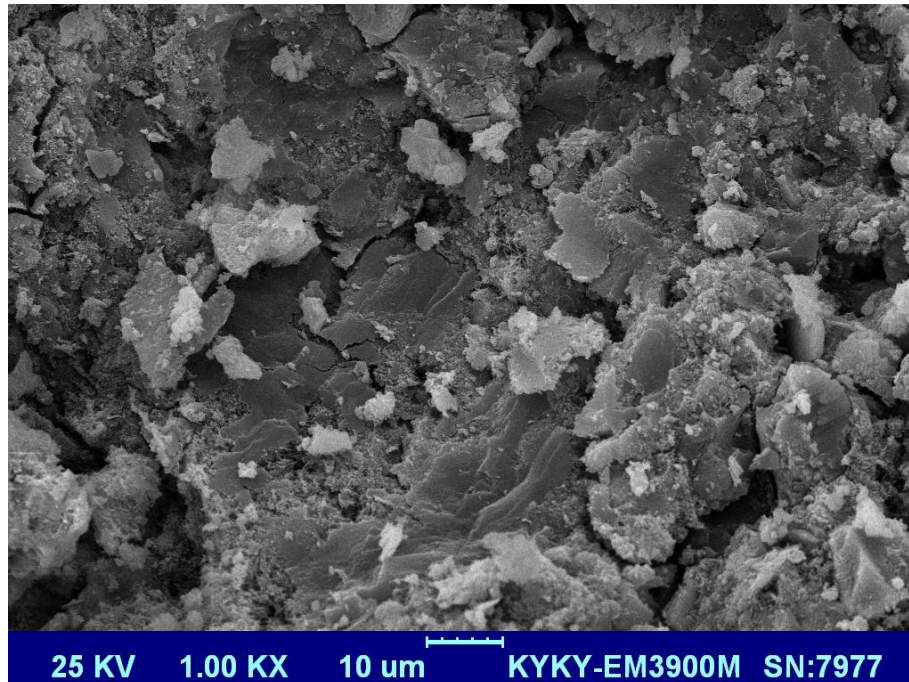*Fig. 16 – The microstructure of the M4S75 specimen*

Fig. 17 – The microstructure of the MR5S75 specimen

CONCLUSIONS

- The addition of 1 percent of micro rubber waste can increase compressive strength by approximately 20% as compared to the witness specimen. If the amount of micro rubber increases to 3 and 5%, the compressive strength of the self-consolidating concrete specimen decreases as compared to the witness specimen.
- In all specimens, the uniformity of the microstructures increases with a decrease in the water to cement ratio and an increase in the strength and the microstructure of the specimens containing micro SiO_2 is still better and more integrated than the witness specimen containing micro rubber. Seemingly, micro SiO_2 can hold different parts of concrete together like an adhesive and create a more integrated specimen.
- As the age of the specimens increases to 28 days, the specimen containing 1% of micro rubber waste still has a higher strength than the witness specimen. In addition, even the strength of the specimen containing 5% of micro rubber waste at this age is approximately equal to the strength of the witness specimen, which indicates the approximate amount of micro rubber waste that can be used in concrete.
- In the microstructure of specimens with a water to cement ratio of 0.5, there are cavities both in the witness specimen and the specimen containing micro rubber cavities. These cavities are relatively large and cause the porosity of concrete. However, after adding micro SiO_2, these cavities merge and technically fade away.
- Using micro rubber waste powder in SCC mixtures can be a considerable environmental protection. In fact, the natural materials of SCC can substitute by waste one. Furthermore, using low percent of rubber waste powder (1 percent) not only can improve SCC compressive strength, but also can reduce the cost of SCC providing. So low amounts of micro rubber waste powder can be used commonly in SCC mixtures.

REFERENCES

[1]	H. Okamura, M. Ouchi. "Self-consolidating concrete, Development, present use and future" 1st International RILEM Symposium on Self-Consolidating Concrete (1999).
[2]	H. Okamura, M. Ouchi. "Self-consolidating concrete" J. Adv. Concr. Technol., 1 (2003), pp. 5-15
[3]	H. Okamura, M. Ouchi. "Application of self-consolidating concrete in Japan" 3rd International RILEM Symposium on Self-Consolidating Concrete (2003).
[4]	M. Ouchi. "Self-compactability of fresh concrete" 1st International RILEM Symposium on Design, Performance and Use of Self-Consolidating Concrete (2005).
[5]	American Concrete Institute ACI 237R-07 Self-consolidating csoncrete ACI Manual of Concrete Practice, Part 1, Farmington Hills, Michigan (2007).
[6]	N. Makul. "Combined use of untreated-waste rice husk ash and foundry sand waste in high-performance self-consolidating concrete". Results in Materials. 1 (2019) 10014.
[7]	Adili, E; Sohrabi, M. R; Nehi, H. M "Prediction of microcracks in concrete using fuzzy systems" journal of intelligent & fuzzy system. Vol 27. No 3. pp 1161-1168, 2014.
[8]	Diamond, S. and Huang, J. "The ITZ in concrete- a different view based on image analysis and SEM observation" Cement and Concrete Composites. 23 (2001) 179-188.
[9]	Feiteira, J; Tsangouri, E; Gruyaert, E; Lors, C; Louis, G and Debelie, N "Monitoring crack movement in polymer-based self-healing concrete through digital image correlation, acoustic emission analysis and SEM in-situ loading" *Materials & Design*, Vol 115, 5 February 2017, Pages 238-246.
[10]	A. Santamaría , A. Orbe, M.M. Losañez, M. Skaf, V. Ortega-Lopez, Javier J. González. "Self-compacting concrete incorporating electric arc-furnace steelmaking slag as aggregate". Materials and Design 115 (2017) 179–193.
[11]	Md. Safiuddin, M. Yakhlaf and K.A Soudki. "Key mechanical properties and microstructure of carbon fibre reinforced self-consolidating concrete". Construction and Building Materials. Vol 164. 2018. PP 477-488.

STUDY ON PERMEABILITY AND ELECTRICAL RESISTIVITY OF RED CLAY CONTAMINATED BY CU²⁺

Rulong Ban[1,2] Xuejun Chen[1,2] Yu Song[1,2] Pengyan Bi[1,2] Xin Yang[1,2] and Xiaochen Zhang[1,2]

1. *College of Civil and Architectural Engineering, Guilin University of technology, Guilin541004, China 1023095210@qq.com*
2. *Guangxi Key Laboratory of Mechanics and Geotechnical Engineering, Guilin541004, China*

ABSTRACT

In order to study the permeability characteristics of heavy metal ions contaminated red clay and explore the rapid detection of permeability of heavy metal contaminated red clay. Through variable-head permeability test and electrical resistivity test (different voltages and methods), the effects of Cu^{2+} concentration and initial water content on hydraulic conductivity characteristic and resistivity of contaminated red clay was systematically investigated. The relationship between permeability characteristic and electrical resistivity was further explored by taking Cu^{2+} concentration and moisture content as the intermediate variable. The obtained results indicate that the different voltage has no obvious effect on the resistivity of the samples. The four-phase electrode method is more accurate than the two-phase electrode method. With increasing Cu^{2+} concentrations the hydraulic conductivity of specimens increases, however the permeability coefficient of contaminated soil decreases with increasing initial water content. In the resistivity test, with increasing of Cu^{2+} concentrations and water content, the resistivity of samples presented a downward trend, which is decreased sharply at first and then tended to be gentle. The relationship between hydraulic conductivity and resistivity of contaminated soil showed a good fitting curve no matter in different Cu^{2+} concentration or in different water content, but the fitting curves of them presented opposite trend.

KEYWORDS

Red clay, Moisture content, Cu^{2+}pollution, Hydraulic conductivity, Resistivity

INTRODUCTION

Red clay is a kind of high plastic clay with special engineering mechanical characteristics formed by weathering of carbonate rock [1]. The rapid development of industry and agriculture has also brought about serious pollution problems. About 90% of the polluted soil is related to heavy metals. Copper ion is a common environmental pollution, which has the characteristics of high accumulation, easy migration and persistence[2-3].Therefore, it is necessary to study the permeability characteristics of heavy metal contaminated soil in order to effectively prevent and control the pollution of soil and groundwater in polluted areas, and to improve the strength of foundation soil and the actual construction quality.

At present, scholars have carried out some related research on the permeability of contaminated soil. According to the variable-head test, the permeability of clay decreases after being polluted by domestic waste, and the hydraulic conductivity increases gradually with the increase of contaminated depth [4]. By studying the influence of acid rain on the properties of red clay, it is found that the smaller pH value of acid rain, the greater influence on permeability and the

----

permeability coefficient decreased with the increase of acid concentrations[5-6].The results show that the higher the concentration of heavy metal ions, the higher the hydraulic conductivity of contaminated soil[7-9].It is found that alkali and zinc pollution has great influence on the permeability of soil, and it is related to the infiltration time[10].The influence of heavy metal pollution on soil microstructure and permeability was studied through laboratory tests[11-12].It is found that the concentration of Ca^{2+} has a great influence on the permeability of bentonite sand mixture[13].For the above traditional experimental methods, although the exact test results can be obtained, it is expensive and time-consuming. As an important branch of geophysical methods, resistivity has been widely used in geotechnical engineering research because of its continuous, rapid and non-destructive characteristics [14]. The relationship between resistivity and permeability coefficient has been studied by scholars. Through the test of cement mixed soft clay and resistivity, the permeability of resistivity reaction is in good agreement with that of consolidation test[15].In order to understand the ability of rock to allow fluid to pass through, the resistivity and permeability characteristics are simulated to better understand the relationship between fractured rock and them[16].Taking structure factor and porosity as intermediate variables, calculate the relationship between permeability coefficient and resistivity of sand , and the feasibility of the formula is verified by experiments[17].At present, there are relatively few researches on the relationship between soil permeability and electrical resistivity, and the relationship between resistivity and other parameters is still in the initial stage, especially the research on the permeability and resistivity of heavy metal contaminated red clay is even less. Therefore, it is worth studying how to quickly detect its hydraulic conductivity.

Taking Guilin Red Clay as the research object, the influence of pollutant concentration and water content on the permeability and resistivity of contaminated soil was studied through the variable-head test and electrical resistivity test, respectively. The relationship between resistivity and hydraulic conductivity is further discussed through Cu^{2+} concentration and different water content as intermediate variables. It is expected that this investigation will give a certain reference value for the engineering applications of contaminated soil.

METHODS

Materials

The red clay used in the test was collected from a construction site in Yanshan Town, Guilin City, China at a depth of approximately 3m. It was a residual layer of Upper Pleistocene series (Q_3^{e1}), which was brownish red and was not polluted by Cu^{2+}. After sampling, the red clay was first air-dry under the ambient condition, then ground and sieved to pass a 2 mm sieve [18]. Basic physical indexes of soil are summarized in Table 1. The liquid limit and plastic index of the natural res clay are 45.64% and 33.8%, respectively. The maximum dry density and optimum moisture content of red clay obtained from the standard proctor compaction test were 1.536g•cm^{-3} and 30%, respectively. In this experiment, the Cu^{2+} contaminated solution is a $CuSO_4$ solution prepared by $CuSO_4 \cdot 5H_2O$ crystal (analytical pure) and deionized water.

Tab. 1 - Basic physical properties of red clay

Parameter	Value
Liquid limit w_L（%）	45.64
Plastic limit w_P（%）	33.18
Plasticity index I_P	12.46
Optimum moisture content (%)	30.00
Maximum dry density(g•cm^{-3})	1.536
Specific gravity G_s	2.70

Specimen preparation

The Cu^{2+} concentrations and initial water content were selected 0g/L, 0.5g/L, 1g/L, 5g/L, 10g/L (according to the regional pollution assessment report) and 20%, 25%, 30%, 35%, respectively. When studying the effect of Cu^{2+} concentrations, the initial water content was fixed at optimum moisture content 30%. When studying the influence of initial water content, the Cu^{2+} concentrations was fixed at 0.5g/L.

The air-dry and sieves soil was first mixed with a predetermined amount of heavy metal solution to reach the desired water content. After mixing, the wet contaminated red clay mixtures were stored in a sealed plastic bag and placed in the standard curing chamber (temperature of 23℃, humidity≥90%) for at least 24h for homogenization. Then, the homogenous contaminated soil were placed into a cylindrical steel mold, and compacted by using a hydraulic jack to achieve the same dry density 1.45 g•cm^{-3}, which was controlled at 95% of the maximum dry density, because the sample could be consistently made and smoothy demolded. According to the Standard for Soil Test Method [19], the samples used for hydraulic conductivity test shall have a specified size(61.8mm×40mm) and prepared 5 parallel samples for each initial parameters. Specimens of permeability test were placed into vacuum saturation device, vacuum for 2 h and then deionized water was pumped into the device to cover samples for 12 h in order to samples saturated. According to previous studies[14,25] the specimens used for electrical resistivity test shall use improved Miller Soil Box(5cm×15cm) to test and prepared 3 parallel samples for each initial parameters, thereafter, the samples of electrical resistivity test were sealed in the plastic bags.

Test methods

Hydraulic conductivity test

Permeability test was performed according to JTG2007[18], the laboratory test on hydraulic conductivity usually includes the constant-head and variable-head permeability test, which are applied for highly hydraulic conductivity coarse soil and low-permeability fine soil, respectively. The permeability test of red clay was suitable for the variable-head method as shown in Figure1. Samples are recorded water level height difference and falling time, respectively, and measured water temperature at the same time. The permeability coefficient can be calculated by the following equation:

$$k = \left[2.3 \frac{a \cdot L}{A(t_2 - t_1)} log \frac{H_1}{H_2}\right] \cdot \eta \tag{1}$$

Where k is the permeability coefficient (cm/s); a is the cross-sectional area(cm^2) of glass tube; L is the heigh(cm) of specimen; t_1 and t_2 are the beginning time and ending time, respectively; H_1 and H_2 are beginning water head and ending water head, respectively; η is coefficient of viscosity under different temperature. According to the Standard for Soil Test Method [19], the data collected is based on the average of the 24 times measurement of permeability coefficient.

Fig.1 - TST-55 Osmometer

Electrical resistivity test

At present, the resistivity tests on soil usually include two-phase electrode and four-phase electrode method, two-phase and four-phase method interaction was adopted in this study by using the VC4091C LCR precision digital bridge (0.0001Ω～99.999MΩ) and set parameters as low-frequency and AC. The current frequency in this paper is based on the 50Hz adopted by most scholars in China [20-21]. The resistivity of soil was calculated by following equation:

$$\rho = \frac{V \cdot A}{I \cdot L} \tag{2}$$

where V is the measured voltage; A is area(cm2) of specimen; I is the measured current; L is the length between copper bars. The overall schematic diagram is shown in Figure 2(a) and the overall test diagram is shown in Figure 2(b).
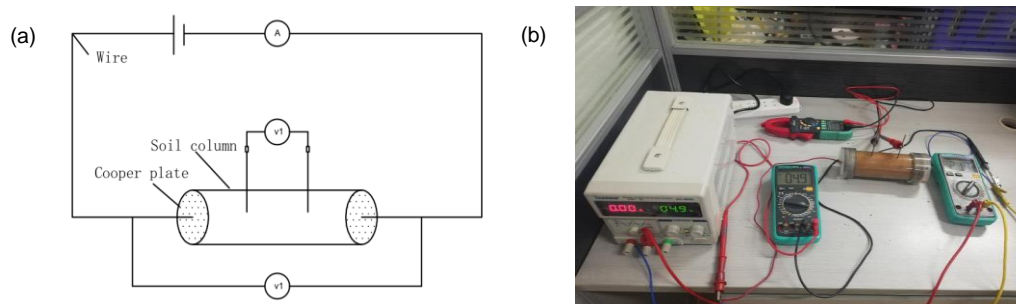

Fig.2 (a)- Schematic diagram for resistivity test; (b)The chart of overall test

ANALYSIS OF THE RESULTS AND DISCUSSION

Influence of Cu^{2+} concentration on permeability of red clay

According to the recorded data, the excessive variation of permeability coefficient is removed, and then the corresponding permeability coefficient is obtained by averaging it, and the change diagram of Cu^{2+} concentration and permeability coefficient is drawn. As shown in Figure 3 it can be seen that the permeability coefficient of red clay ranges from 3.54×10^{-6} cm/s to 42.25×10^{-}

6 cm/s, and increases with the increase of Cu^{2+} concentration. When the concentration is greater than 0.5g/L, the permeability coefficient changes more obviously with the increase of Cu^{2+} concentration. When the copper ion concentration is greater than 5g/L, the permeability coefficient increases slowly. Analyze the reasons: red clay is a special soil, and its engineering characteristics are inseparable from the cementation between soil particles [22]. Due to the complex physical and chemical reaction between Cu^{2+} and red clay soil particles, the chemical composition has changed[23].When the Cu^{2+} concentration is small, a small amount of Cu^{2+} will be hydrolyzed, and a small amount of $Cu(OH)_2$ colloid will be produced. However, the acidity of the solution is too weak to react with the cementation material between the soil particles to form a small amount of Fe^{2+}, Fe^{3+}, Al^{3+}, etc. , which results in less erosion of clay mineral flakes and micro crystalline free iron oxide "coating", and the cementation between particle cluster is not significantly weaken. Although the number of small soil particles increased during this process, the large clusters of particles did not decrease significantly. Therefore, when the concentration of Cu^{2+} is 0.5g/L, the permeability coefficient of red clay is not significantly increased compared with that of uncontaminated soil. With the increase of Cu^{2+} content, the acidity of the solution becomes stronger, which will obviously dissolve the crystalline free iron oxide and other cementing substances between the particles, the cementation between the soil particles will weaken, and the diffusion double layer will also become thinner, the repulsive force among soil particles is weakened, and small particles will agglomerate to cause the pore size to change from tiny pores to small pores, mesopores or even large pores, and then the effective pore transportation channel of the soil will be enlarged. Therefore, when the concentration of Cu^{2+} is greater than 1g/L, the permeability coefficient of red clay increases obviously, and the higher the concentration of polluted liquid, the higher the permeability coefficient.
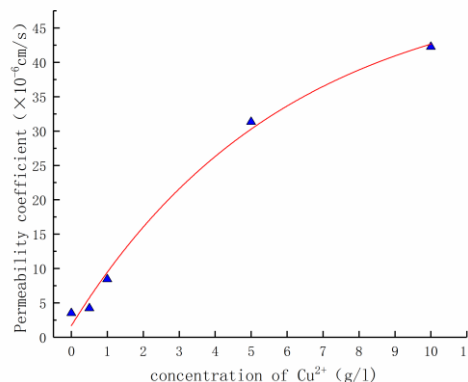

Fig.3 - Relation curve between permeability coefficient of red clay and Cu^{2+} concentration

Influence of moisture content on permeability of red clay

The concentration of contaminated solution is 0.5g/L, and the water content is 20%, 25%, 30% and 35% respectively, the variation law of permeability coefficient of soil sample is shown in Figure 4 It can be seen from Figure 4 that the permeability coefficient of the soil sample decreases with the increase of moisture content. The main reasons are as follows: The binding materials in red clay are mainly Fe_2O_3, Al_2O_3, etc. under dry conditions, the free ferric oxide between soil particles is mostly in the form of crystalline ferric oxide [24]. When the water content is low, the water molecules in the red clay are adsorbed by the clay minerals to form a strong bound water film, at this time, the bound water film is relatively weak, and the repulsion force between soil particles decreases, resulting in the combination of small particles to form a relatively stable particle structure, which makes the pores in the soil tend to widen and the effective transport pore channels enlarge. Hence, when the water content is low, the permeability coefficient of the sample

----

is larger; When the water content increases to 30%, due to the electric double layer structure of red clay has strong water absorption, with the increase of water molecules, the thin strong bound water film changes into the thick weak bound water film, and the crystal ferric oxide gradually changes into amorphous ferric oxide, so the attraction between soil particles is weakened, and the structure of particle group cannot be formed, and the soil sample pores are reduced, so in this stage, the permeability coefficient decreases rapidly; When the water content is as high as 35%, due to the further increase of water molecules, the large pores between the soil particles have been gradually filled with water molecules, and the gravitational force between particles is further reduced, moreover, because the low concentration of Cu^{2+} makes the soil produce a bit of small particles, the pores can be effectively filled in the process of soil sample preparation. Therefore, when the optimal water content is exceeded, the permeability coefficient of soil will further decrease. And the permeability of red clay is mainly affected by water content when Cu^{2+} concentration is low.
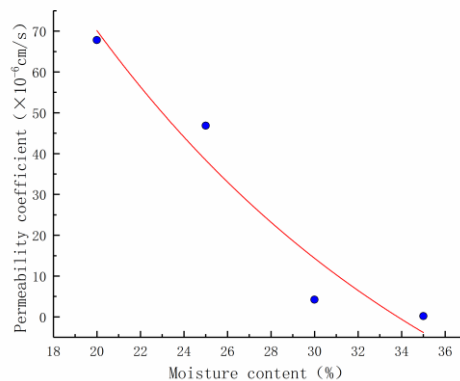

Fig.4 - Relationship curve between moisture content and permeability

Relationship between Cu^{2+} concentration and resistivity

According to the resistance change value measured under different voltage and formula $\rho = R\dfrac{S}{L}$, the change diagram of Cu^{2+} concentration resistivity is obtained. In the formula: R is the measured resistance of the soil sample; S is the cross-sectional area of the soil sample; L is the distance between the two electrodes. As shown in Figure 5, ρ2 and ρ4 represent two-phase resistivity and four-phase resistivity respectively. It can be seen that the change of voltage has no obvious effect on the resistivity, no matter the two-phase electrode method or the four-phase electrode method, the relationship between the resistivity and Cu^{2+} concentration of contaminated red clay presents an exponential function relationship. With the increase of Cu^{2+} concentration, the resistivity ρ2 and ρ4 decrease rapidly, then gradually slow down, and finally tend to be stable. The reasons for the above rules are as follows: Because the soil is prepared with the optimal water content, the pore water connectivity between the red clay particles has reached a good state, so the conduction path is mainly between the pore liquid when the soil is electrified[25].After the red clay is contaminated, Cu^{2+} is more active in the pore fluid, under the action of the clay mineral flakes (kaolinite) with strong electrostatic attraction, it will be preferentially adsorbed to the fixed layer, and the conductivity of the fixed layer is much greater than The conductivity of the diffusion layer, so when the Cu^{2+} concentration is less than 5g/L, the resistivity of the soil can be rapidly reduced; With the increase of Cu^{2+} concentration more than 5g/L, the adsorption sites on the surface of clay minerals gradually reach saturation state. Then the surplus Cu^{2+} flows into the diffusion layer, which will produce complex physical and chemical reactions with various Cementitious substance between soil particles, and produce free Fe^{2+}, Fe^{3+}, Al^{3+}, etc. plasma, the

Article no. 23

THE CIVIL ENGINEERING JOURNAL 1-2021
----

increase of the number of ions in the pore liquid leads to the increase of the current between the soil and the further decrease of the resistivity. However, the conductivity of the diffusion layer is far less than that of the fixed layer, so the decline of the resistivity becomes slower; When the concentration of Cu^{2+} reaches 10g/L, the dissolution and loss of crystalline free iron oxide and other cementation materials among the particles are enhanced, the cementation between soil particles is weakened, and the pores between particles increase, resulting in the increase of inter particle spacing, the decrease of contact area and the decrease of current flow rate. Therefore, when the concentration of Cu^{2+} is further increased, the resistivity gradually tends to be flat.
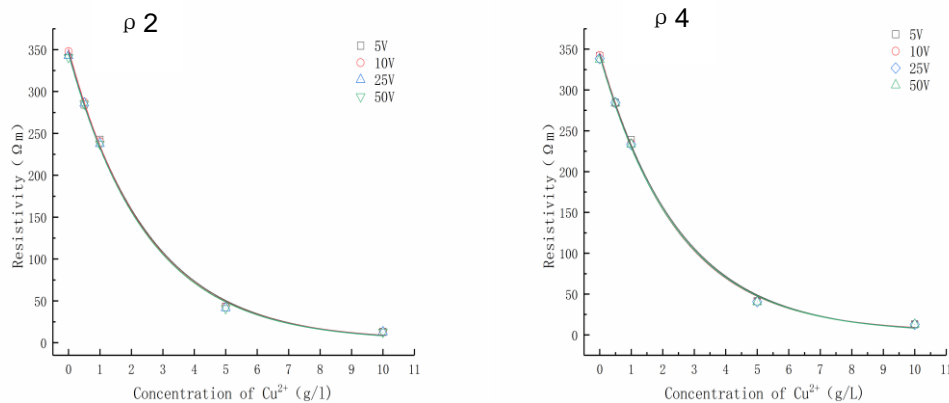

Fig.5 - Relation curves between Cu^{2+} concentration and resistivity

Relationship between moisture content and resistivity

Test the relationship between moisture content and resistivity under the condition of changing the voltage, and the data obtained is plotted as shown in Figure 6. It can be seen from the figure that the relationship between moisture content and resistivity and the relationship between Cu^{2+} concentration and resistivity show similar trends, showing a negative exponential correlation. Under different voltage, the resistivity corresponding to different water content has little difference. Under the voltage of 5V for analysis, the range of resistivity measured by two-phase electrode method and four-phase electrode method is 548.41~267.12Ωm and 462.5~262.48Ωm, respectively. It can be seen that the data measured by the four-phase electrode method is smaller than that by the two-phase electrode method when the water content is low. When the water content increases, the measurement results of the two methods are similar. The main reason is: when the water content is low, the conductive path is through the contact between soil particles, and a small amount of water and clay minerals to form a strong binding water film, because the water film is thin, the soil particles attract each other, and the water film contacts with each other, at the same time, the pore fluid increases correspondingly, which enhances the connectivity and further improves the soil conductivity. Therefore, the increase of a small amount of water will significantly increase the conductivity of the sample; When the water content continues to increase to 30%, the strong bound water film begins to change into the weak bound water film and free water, and the pore between particles is filled by water, at this time, the conductive path begins to change to pore water and water-soil contact, the connectivity continues to increase, and the resistivity decreases; Continue to increase the water to a moisture content of 35%, the pores between the soil particles in the sample are basically filled with water. the main conduction path is pore water, at this time, the improvement of conductivity is weak, so the increasing trend of resistivity slows down. The results of the two-phase electrode method test are affected by the contact resistance, and the lower the moisture content, the greater the contact resistance; after the moisture content increases, the sample is in good contact with the electrode sheet, and the contact resistance is very weak, so the test results of the two methods are similar[26].
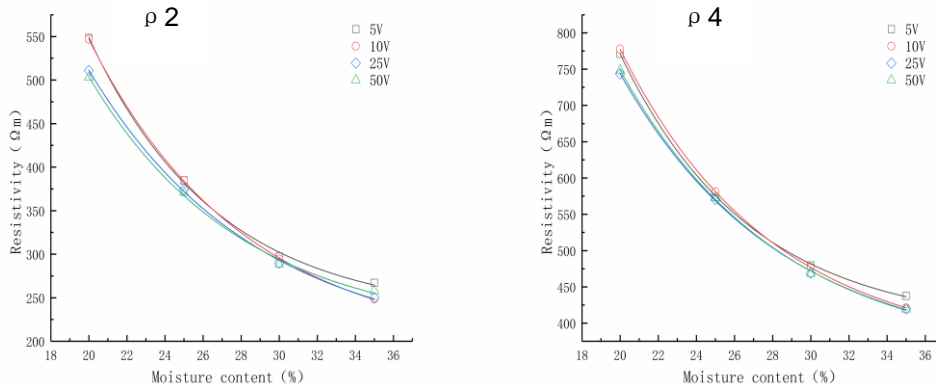

Fig.6 - Relation curves between moisture content and resistivity

Relationship between resistivity and permeability coefficient

Permeability coefficient reflects the difficulty of water flowing in soil pores, which is one of the important basic parameters of soil. Resistivity is one of the inherent physical properties of soil. Both of them are inherent parameters of soil, so the internal relationship between the two parameters is discussed. Now, taking Cu^{2+} concentration and water content as intermediate variables, the measured permeability coefficient of contaminated soil is correlated with the relative resistivity of contaminated soil, and find the relationship between the permeability coefficient and electrical property index of contaminated red clay under different Cu^{2+} concentration and water content. Figure 7 shows the relationship between permeability and resistivity of red clay polluted by different Cu^{2+} concentration; Figure 8 shows the relationship between permeability coefficient and resistivity of red clay under different moisture content.
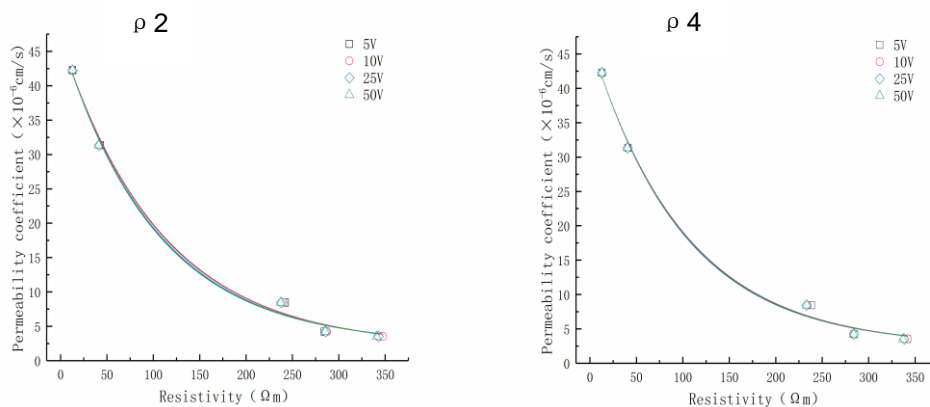

Fig.7 - Relation curves between permeability and resistivity under different Cu^{2+} concentrations
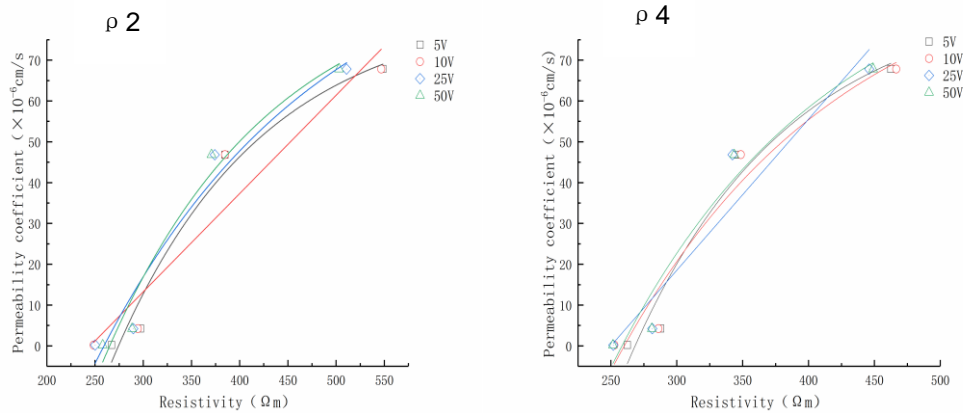
Fig.8 - Relation curves between permeability and resistivity under different moisture content

It can be seen from Figure 7 that the permeability coefficient under different voltage and different Cu^{2+} concentration has a good exponential function relationship with the resistivity measured by the two-phase electrode method and the four-phase electrode method. The permeability coefficient decreases with the increase of the resistivity. The fitting formula is shown in Table 2. Figure 8 shows the relationship between the permeability coefficient under different voltages and different water content conditions and the resistivity changes measured by the two electrode methods, both showing a better fitting curve, and the greater the resistivity, the permeability coefficient increases. The fitting formula is shown in Table 3.

Tab. 2 - Relations between permeability and resistivity under different Cu^{2+} concentrations

Electrode method	Voltage （V）	Fitting formula	R^2
ρ2	5	k=44.76×exp(-ρ2/108.66)+1.99	0.99623
	10	k=44.72×exp(-ρ2/107.26)+2.12	0.99649
	25	k=44.61×exp(-ρ2/103.97)+2.30	0.99628
	50	k=44.57×exp(-ρ2/102.09)+2.42	0.99606
ρ4	5	k=44.55×exp(-ρ4/102.01)+2.44	0.9959
	10	k=44.63×exp(-ρ4/101.31)+2.42	0.99629
	25	k=44.61×exp(-ρ4/100.75)+2.43	0.99629
	50	k=44.58×exp(-ρ4/99.73)+2.50	0.99611

Tab.3 - Relations between permeability and resistivity under different moisture content

Electrode method	Voltage （V）	Fitting formula	R^2
ρ2	5	k=-495.0×exp(-ρ2/153.56)+82.93	0.97221
	10	k=1.12×exp(-ρ2/-4.67)-1.12	0.92174
	25	k=-332.79×exp(-ρ2/229.03)+104.04	0.95988
	50	k=-431.16×exp(-ρ2/172.01)+92.25	0.97122
ρ4	5	k=-818.59×exp(-ρ4/119.17)+86.11	0.96034
	10	k=-456.44×exp(-ρ4/169.9)+98.73	0.94924
	25	k=1.12×exp(-ρ4/-3.04)+-1.12	0.92724
	50	k=-491.9×exp(-ρ4/162.64)+100.44	0.95878

In the formula: k is the permeability coefficient; ρ2 is the resistivity obtained by the two-phase electrode method; ρ4 is the resistivity obtained by the four-phase electrode method. The correlation coefficients R^2 are all above 0.9, and the correlation degree is high. It can be proved that the combination of permeability coefficient and resistivity is feasible to evaluate the permeability of heavy metal contaminated red clay. The resistivity method combined with the above formula can quickly detect the permeability coefficient under different water content and different concentration of pollution ions, which provides a convenient method for the construction and treatment of actual contaminated sites.

CONCLUSION

1. When measuring resistivity with different electrode methods, the two-phase electrode method will be disturbed by the contact resistance compared with the four-phase electrode method. Therefore, in order to avoid modifying the resistivity value, the four-phase electrode method should be selected for measurement. Under the action of different voltages, the measured resistivity does not change obviously, so the voltage does not affect the value of resistivity.

2. With the increase of Cu^{2+} concentration, the permeability coefficient of red clay also increases, and the curve fitting is better; Under the condition of different water content, the permeability coefficient of soil presents the opposite trend to that under the action of ion concentration, and the permeability coefficient decreases with the increase of water content. When it is less than the optimal water content, the downward trend is obvious, and when it is greater than the optimal water content, the decline tends to be flat.

3. The resistivity curves corresponding to different Cu^{2+} concentration and water content show negative exponential correlation, which first decreases sharply with the increase of variables, gradually slows down, and finally tends to be stable.

4. The permeability coefficient of red clay has good fitting in the curves of Cu^{2+} concentration and resistivity, the curves of water content and resistivity, but their change trend is opposite. Under different Cu^{2+} concentrations, the permeability coefficient decreases with the increase of resistivity; In the case of different water content, the permeability coefficient increases with the increase of resistivity.

ACKNOWLEDGEMENTS

REFERENCES

[1] Chen X J, Xie T, Song Y, Yu Y.2015.Experimental study on soil tectonics characteristics of red clay in Guilin [J] Subgrade Engineering ,(04):72-75.

[2] Zhao J Y, Li Y, Li S S. 2013.Zhang S. Polluted soil remediation technology and industry status in China [J] China Environmental Protection Industry, (03):53-57.

[3] Dou X K. 2017.Contamination and Harm of Copper [J] Science, Technology and Economics Guide ,(08):126

[4] Wang Y, Cao L W, Wen W F, Huo P. 2014.Microstructure and Permeability of domestic waste contaminated clays [J] Hydrogeological & Engineering Geology ,41(02):138-142.

[5] Xiao G Y, Chen X J, Wei C F, Huang X, Chen L. 2016.Mechanism of permeability and control of compaction for red clay under the influence of acid rain [J] Chinese Journal of Rock Mechanics and Engineering ,35(S1):3283-3290.

[6]   Liu H, He J T, Zhao X, Wang T X, Guo C Y.2020.Experimental study on the evolution rules of micro-permeability characteristics acid-contaminated undisturbed loess [J] Rock and Soil Mechanics ,41(03):765-772.

[7]   Zhang Z H, Li H Y, Chen J Y, Lei Y.2016.Permeability of saturated clay eroded by mixed heavy metal ions [J] Rock and Soil Mechanics ,37(09):2467-2476.

[8]   Li K, Zhang D W, Cao Z G.2019.Effect of carbonation on permeability characteristics of cement-stabilized/solidfied lead-contaminated soil [J] Chinese Journal of Geotechnical Engineering ,41(S2):117-120.

[9]   Taheri, S. and T. Ebadi, et al. 2018. Predicting variations in the permeability and strength parameters of a sand-bentonite mixture (SBM) contaminated simultaneously with lead (II) and diesel. Applied Clay Science 157: 102-110.

[10]   Wang W J, Chen Y, Jiang J L, Cai G C.2020.Experimental Study on compression and infiltration characteristics of silt clay contaminated by alkaline and zinc [J] Geotechnical investigation&surveying,48(02):6-12.

[11]   Nayak S,Sunil B M, Shrihari S.2007.Hydralic and compaction characteristics of leach ate-contaminated lateritic soil [J]. Engineering Geology, 94(3-4): 134-144.

[12]   Serranti S,Bonifazi G.2012.Pollution level detection in dump clay liners by hyperspeetral imaging [J]. International Journal of Environment and Waste Management, 10(2-3): 163-176.

[13]   Xu, S. and M. Bian, et al. 2018.Effects of calcium concentration and differential settlement on permeability characteristics of bentonite-sand mixtures. Applied Clay Science 153: 16-22.

[14]   Chu Y, Liu S Y, Cai G J, Bian H L.2015.An experimental study of physical and electrical characteristics of zinc contaminated silty soil [J] Rock and Soil Mechanics ,36(10):2862-2868.

[15]   Khin.M.M.Latt, P.H. Giao. 2017. Prediction of permeability of cement-admixed soft clay using resistivity and time-domain IP measurements. Journal of Applied Geophysics 137: 92-103.

[16]   Alison Kirkby, Graham Heinson. 2016. Three-dimensional resistor network modeling of the resistivityand permeability of fractured rocks. Journal of Geophysical Research:Solid Earth 122(4):2653-2669

[17]   Peng C, Wang B H, Yuan Z H et al.2018. Investigation on permeability of sands based on electrical resistivity. Journal of Jiangsu University of Science and Technology 32(06): 891-897

[18]   JTG E40 (2007) Test methods of soils for highway engineering. Industrial Standard of People's Republic of China, Ministry of communications, PRC

[19]   Nanjing Hydraulic Research Institute.2019 Standard for soil test method(GB/T 5023-2019) [S]. Beijing: China Planning Press

[20]   Liu G H, Wang Z Y, Huang J P.2004.Research on electrical resistivity feature of soil and it's application [J] Chinese Journal of Geotechnical Engineering ,(01):83-87.

[21]   Liu S Y, Cha F S, Yu X J.2006.Laboratory measurement techniques of the electrical resistivity of soils [J] Journal of Engineering Geology ,(02):216-222.

[22]   Song Y and Yang Y et al.2015.Characteristics and deformation mechanism of microstructure for red clay.[J] Journal of Geological Hazards and Environmental Protection ,26(03):73-76.

[23]   Chen X J, Chen Y C, Song Y, Li J M, Yu S Z, Chen L J.2019.Analysis on variation of physical-mechanical properties of red clay contaminated by Cu^{2+}[J] Journal of Engineering Geology ,27(05):1010-1018.

[24]   Chen H B, Chen X J,Qi Y L et al.2019. Effects of dry density and moisture content on shear strength parameters of remolded red clay soil ［J］. Journal of Engineering Geology，27(5): 1035－1040

[25]   Chen Y C, Huang X, Chen X J, Zhang X C, Ban R L.2020.Study on relationship between shear strength and electrical resistivity of Cu~(2) contaminated red clay [J/OL] Journal of Yangtze River Scientific Institute,1-13.

[26]   Chen Y C, Song Y, Chen X J et al. 2020. Resistivity characteristics of red clay contaminated by Cu [2+] [J] Rock and Soil Mechanics, 2020(S2): 1-10

--

EVALUATION OF THE EFFECT OF EXTERNAL PRESTRESSED STEEL STRANDS ON CABLE-STAYED BRIDGES BASED ON FINITE ELEMENT ANALYSIS AND STATIC TEST

Chunwei Li, Haitao Yu, Dongzhe Jia and Quansheng Sun

Northeast Forestry University, Department of Civil Engineering, 26 Hexing road, Harbin, PR China; Quansheng Sun;hrbsqs @126.com.

ABSTRACT

This article relies on the reinforcement project of the Mulinghe cable-stayed bridge to explore the changes in the mechanical properties of the reinforced concrete cable-stayed bridge before and after reinforcement. The bridge has large cable spacing, large internal force of a single cable, and the main beam is mainly Reinforced Concrete. Therefore, structural calculation, disease analysis, and damage state simulation are carried out. Afterwards, the bridge's commonly used reinforcement methods were compared, and suitable reinforcement schemes were selected. After the reinforcement, the field test was carried out on the cable-stayed bridge, the main beam deflection, the strain of the main beam and the main tower, and the increase in the cable force of the cable-stayed were analyzed. The results show that external prestressed reinforcement is the best way, which can significantly reduce the vertical displacement of the main beam and the horizontal displacement of the main tower, and also improve the stress on the upper and lower edges of the main beam. After the external prestressed reinforcement, the ratio of the observed value to the observed value in the filed load test of the cable-stayed bridge's decreased significantly. It is up to 31% increase in bending capacity of main beams and up to 24% increase in stiffness. This article is instructive for the reinforcement of the early-built sparse-cable reinforced concrete cable-stayed bridge, while also expanding the scope of implementation of external prestressed reinforcement technology.

KEYWORDS

INTRODUCTION

The increase in traffic density and vehicle load are unavoidably damaged and aging, resulting in a considerable part of the in-service bridges with early construction time, especially cable-stayed bridges, can no longer meet the current safety and durability requirements. If these conditions are not controlled and strengthened, it will further seriously affect the safe use of the bridge. Therefore, considering the structural safety and economic benefits of the cable-stayed bridge, timely and effective maintenance and reinforcement work has become an important research topic in front of the majority of researchers.

Chen Hao [1] took a prestressed concrete cable-stayed bridge with a span of (38.5+71+38.5) m as the research object, analyzed the damage of the superstructure of the cable-stayed bridge and established a finite element model, which was strengthened by section and adjusted by cable force. In the reinforcement method, the tension and compression stresses of the main beam and the tower are reduced, and the reinforcement effect is obvious. Pan Zhulan et al [2] conducted a cable

replacement study for cable-stayed bridges based on disease detection. After the cable replacement of the full bridge was completed, a filed load test way was designed. The results show that the strength and rigidity of the bridge have been significantly improved. Lei Jinsheng et al [3] analyzed the cable force adjustment of 15 pairs of stay cables in the main technical steps. The study shows that the process of cable replacement and reinforcement has a great influence on the stress of the main beam of the bridge and the cable force of the linear and diagonal cables. After the reinforcement, the safety performance of the bridge structure meets the design requirements. Zou Zexi [4] used cross-section reinforcement and cable force adjustment to strengthen a PC cable-stayed bridge. Through the finite element simulation of the cable-stayed bridge damage and reinforcement construction phase, the main girder alignment reached the expected goal after reinforcement and maintenance, and the cable force tended to be more uniform. J. Guo [5] applied the simulated annealing algorithm and the B-spline curve interpolation method to the cable force optimization of a three-span curved cable-stayed bridge. The cable force after the cable force adjustment was further optimized, and through the filed load test the effectiveness of this method is verified. Wu Zhongxin [6] used the comparison and mutual verification of the two finite element calculation software for the Tianjin Yonghe Bridge cable replacement project to monitor the parameters of the main beam linear and cable force during the cable replacement process and change the cable. The influence matrix method is used to optimize the cable force after cable replacement so that the reinforced cable-stayed bridge can reach the original design state. Qiao Changjiang [7] proposed the reinforcement way of the main beams with carbon fiber cloth and steel plates and replacement of stay cables based on the disease inspection, and focused on the cable replacement technology of the cable-stayed bridge. The geometry of the bridge changed slightly after changing the cable, and the stress state of the tower-beam consolidation is improved.

At present, domestic and foreign researchers on the reinforcement of cable-stayed bridges mainly focuses on the replacement of cable-stayed cables and the adjustment of cable strength. However, for the cable-stayed bridges built early in China, due to the large spacing of the cables, the large internal force of the single cable, and the main beam being mainly bent, In the general cable adjustment and cable replacement way, a backup cable must be set to prevent the stress of the main beam from exceeding the limit during the cable replacement process and causing cracks. During the reinforcement process, the stress on the main tower of the original bridge must be strictly monitored and strengthened, and the local compressive stress in the rear main beam span has not increased significantly. In the face of the general cable adjustment and cable replacement method, the construction process is complicated and the reinforcement effect is not good, it is more necessary to find a reinforcement method with good reinforcement effect and convenient construction without cable replacement. In this paper, taking a cable-stayed bridge in China as the research background, analysed of the bearing capacity of the cable-stayed bridge before and after reinforcement, and the filed load test is carried out to evaluated the bearing capacity of the cable-stayed bridge. This paper provides technical data for the subsequent operation, detection and maintenance of this bridge, provides references for the same type of construction methods, and improves the bridge reinforcement theory.

BACKGROUND

The cable-stayed bridge studied in this paper is a reinforced concrete T-beam cable-stayed bridge across Muling River in the eastern part of Heilongjiang Province. The bridge structure is a tower-pier consolidation and tower-beam separation system. The twin towers are 14 meters high, the bridge has a total length of 106.4 m, the span combination is 28 m+50.4 m+28 m, and the full bridge width is 9 m. The upper structure is reinforced concrete T beam, each bridge tower is provided with 4 pairs of stay cables, and 16 pairs of stay cables are arranged on the upstream and downstream sides, and the anchor spacing on the main beam is 5.6 m. The lower structure is a

gravity bridge abutment, and the tower foundation uses a caisson foundation. The bridge panoramic photo is shown in Figure 1. The bridge was completed in October 1995, with a design load rating of car-20 and trailer-100.

Fig. 1 - Elevation drawing of the cable-stayed bridge

During the 25 years of operation, there are multiple vertical cracks in the main beam web of each hole due to environmental effects and increasing vehicle load. The width of the crack is between 0.13 ~ 0.5 mm, which exceeds the specified limit, there are more cracks in the mid-span area, and the main beam is severely deflected; The top and bottom beams have long longitudinal cracks, and the crack width is between 0.1 ~ 0.4 mm, which exceeds the specified limit, and the cracks are irregularly distributed; The protective tube at the anchor end of the stay cables were damaged and the anchors were corroded. The apparent typical diseases are shown in Figure 2. Based on pathogen analysis, the reinforcement way proposed in this article.

T beam reinforcement: one longitudinal external prestressed beam is set on each side of each T beam, the steel beam is made of three high-strength low-relaxation steel strands of Φ15.24 mm, the standard strength is f_{pk} = 1860 MPa, and the elastic modulus is E_p = 1.95×10^5 MPa, the tensile control force of a single steel strand is 168.05 kN, and the tensile control stress of the prestressed steel strand is 1209 MPa. The external prestressed steel beams are tensioned at both ends, using OVM15-3 anchors, which are respectively bent and anchored at the corresponding webs at both ends of the T beam.

Cross beam reinforcement: the cross beam between the side beam and the middle beam is pasted with N1 steel plate with a size of 1500×300×10 mm, the beams between the middle beams are pasted with N2 steel plates and the size is 2400×300×10 mm to strengthen the shear strength and suppress the crack development. The size of the N3 steel plate pasted at the bottom of each beam is 8400×400×10 mm in order to increase the bending resistance of the bottom plate. N1 and N2 steel plates are fixed with 10.9 grade φ22 high strength bolts, and N3 steel plates are fixed with M12 high strength bolts. In order to ensure the bonding quality, the steel plate should also be scrubbed with gasoline to completely remove floating dust and oil stains, and then the steel plate should be pasted with an adhesive and fixed with high-strength bolts. Finally, in order to prevent the corrosion of the steel plate and delay the aging of the adhesive, the surface of the pasted steel plate should be sealed, waterproofed and rust-proofed after removing the surface oil stains and rust. The main beam and cross beam reinforcement are shown in Figure 3.
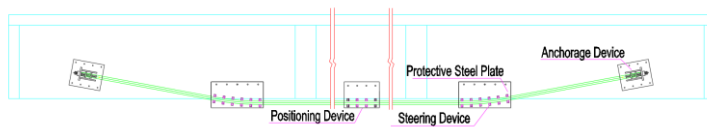
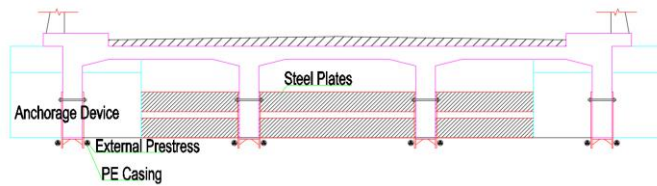Vertical cracks in main span   Vertical cracks in side span   Broken protective tube

Fig. 2 - Apparent disease of cable-stayed bridge

(a) External prestress layout of main beam

(b) Photo of external beam reinforcement of main beam

(c) Paste drawing of cross beam steel plate

(d) Photo of steel plate pasted to cross beam

(e) Photo of the strengthened structure

Fig. 3 - Reinforcement drawing of main beam and cross beam

METHODS

Comparison of reinforcement design schemes based on finite element analysis

A total of five reinforcement ways, including external prestress reinforcement of the main girder by changing the parameter values and optimization and adjustment of the cable tension of the stay cables are proposed according to the analysis of the bridge disease on site. The reinforcement ways are shown in Table. 1. MIDAS / CIVIL was used to establish a finite element model considering disease damage simulation and theoretical calculation of five reinforcement ways. The model

building process is divided into damage simulation stage and structural reinforcement simulation stage. Both the main beam and the main tower are simulated using plane beam elements, and the setting of the cross-sectional dimensions is consistent with the actual situation. Each cable adopts a truss unit with only a tensile structure and is divided into one unit. The whole bridge finite element model of the cable-stayed bridge includes 607 main beam elements and 128 main tower elements, and there are 32 tension-only truss (cable-stayed cable) units with a total of 800 nodes.

Damage simulation (the stiffness of the main beam section is reduced by 20%, the shrinkage and creep coefficient is changed by 50%, the environmental humidity is simulated, the cable tension is reduced by 3%, and the cable damage is simulated) and reinforcement simulation (external restraint of main beam, steel plate pasted on beam, cable adjustment of stay cables) is carried out in the finite element model. Reinforcement simulation is to simulate the external beam of the main beam, the steel plate pasted to the beam, and the cable adjustment of the stay cable. The external beam is simulated by using the steel beam type as "external" and the friction coefficient and deviation coefficient of the pipeline are "0", the steel plate reinforcement is simulated by the method of converting the elastic modulus of the beam, the aim is to find the most reasonable line shape and internal force state of the cable-stayed bridge for cable force optimization. The model of the cable-stayed bridge after reinforcement is shown in Figure 4.

Tab. 1-   Reinforcement way based on disease analysis

| Type of reinforcement	Way number	Reinforcement way
External prestress	Way1	Both sides of the main beam are reinforced with a bundle of Φ15.24 mm prestressed steel beams, the tensile control stress is 651 MPa, which is 35 % of the standard strength. Maintenance of the cable stay at the anchor end of the stay cable and the rust removal of the anchor.
	Way2	Both sides of the main beam are reinforced with a bundle of Φ15.24 mm prestressed steel beams, the tensile control stress is 930 MPa, which is 50 % of the standard strength. Maintenance of the cable stay at the anchor end of the stay cable and the rust removal of the anchor.
	Way3	Both sides of the main beam are reinforced with a bundle of Φ15.24 mm prestressed steel beams, the tensile control stress is 1209 MPa, which is 65 % of the standard strength. Maintenance of the cable stay at the anchor end of the stay cable and the rust removal of the anchor.
cable force optimization	Way4	Change the stay cable from long to short.
	Way5	Change the stay cable from short to long.
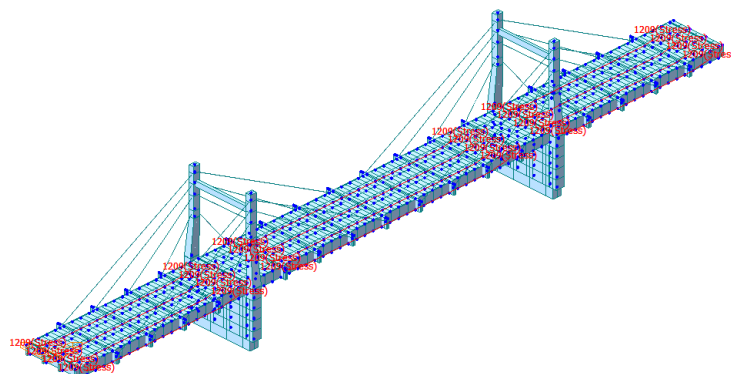
Fig. 4 - Finite element model of reinforced cable-stayed bridge

Static test to verify the actual reinforcement effect

The cable-stayed bridge sets 3 test sections according to the calculation results of the model: A-A section, B-B section, and C-C section. In order to prevent the damage caused by excessive transient load applied during the static behavior test of the cable-stayed bridge, and at the same time, it can intuitively and deeply understand the change trend of the main beam and cable-stayed structure of the cable-stayed bridge with the load, this static filed load test adopts 2-level loading mode, and the test cross-section is shown in Figure 5. The test content is shown in Table 2.
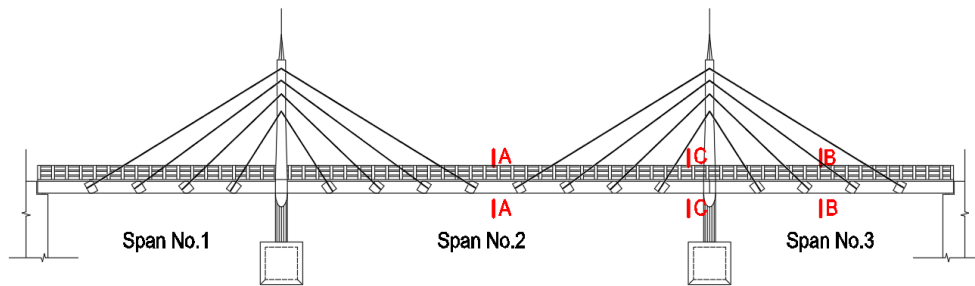

Fig. 5 - Schematic diagram of test section

Tab. 2 -Test items of each section

Static load conditions	Test section	Test items	Test contents
1	A-A	Maximum positive bending moment of the (2#spans)	Deflection, strain, tower deflection, cable force increment
2	C-C	Maximum negative bending moment of the 2# Pier top section	Strain
3	B-B	Maximum positive bending moment of the side span (3#spans)	Deflection, strain, tower deflection, cable force increment

Measuring point arrangement: The vertical displacement measuring points of 2# span and 3# span are arranged at the bottom section of the mid-span beam, the strain measuring points of 2# span and 3# are arranged at the mid-span section, and the negative bending moment measuring points of the 2# pier fulcrum point, the cross section of the main beam on the right is evenly arranged, the strain measurement points of the cable tower are arranged at the root section of the 2# cable tower, and the offset measurement points of the cable tower are arranged at the top section of the tower, the arrangement of measuring points is shown in Figure 6.
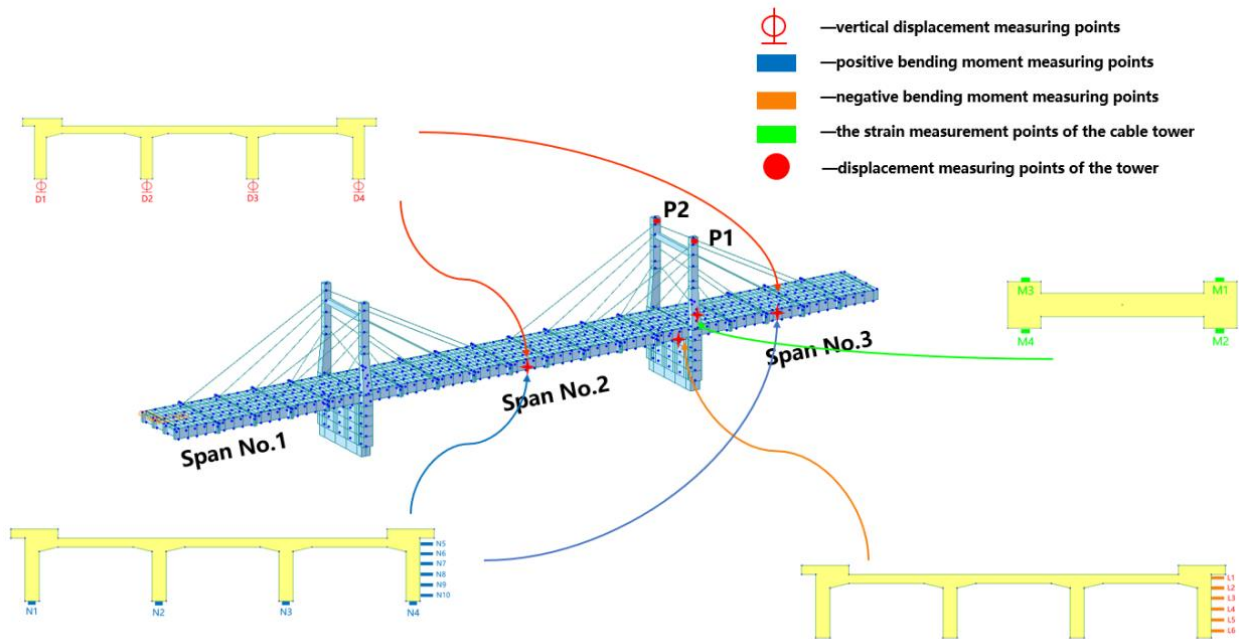

Fig. 6 - Layout of measuring points

In this static filed load test, four 300kN three-axle trucks were selected, the test loads before reinforcement were 303.6kN, 306.0kN, 300.2kN, and 302.8kN, and the test loads after reinforcement were 301.8kN, 302.4kN, 301.2kN, and 303.8kN. The on-site loading situation is shown in Figure 7. Table 3 shows the static filed load test efficiency.


Fig. 7 - On-site loading situation

Tab. 3 - static filed load test efficiency

| Static load conditions	Test items	Design bending moment（kN m）	Loading bending moment（kN m）	static filed load test efficiency
1	A-A section Partial load	3246.1	3278.6	1.01
2	B-B section Partial load	-2214.8	-2259.1	1.02
3	C-C section Partial load	3096.7	3003.8	0.97

RESULTS

### Reinforcement effect based on finite element analysis

Aiming at the above five kinds of reinforcement schemes, theoretical analysis, data comparison and scheme comparison are carried out under the basic load combination specified in the document "Code for Design of Highway Reinforced Concrete and Prestressed Concrete Bridges and Culverts". In consideration of the displacement of the main beam, the main tower deflection, the cable force of the stay cable, the stress on the upper and lower edges of the main beam, and finally determine two different types of reinforcement schemes represented by Way 3 and Way 4, the changes of the stress characteristics of the bridge before and after the two ways are strengthened are shown in Figure 8.
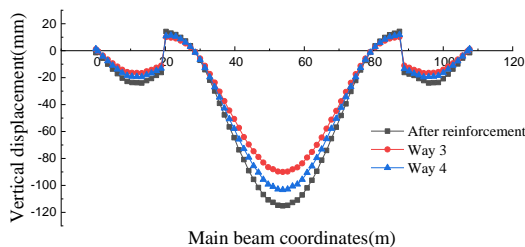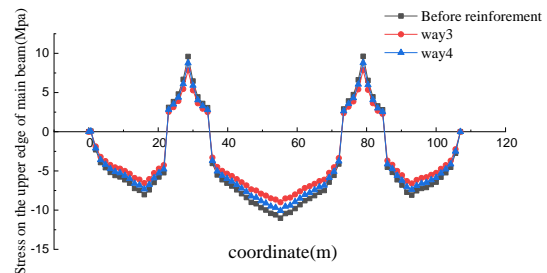

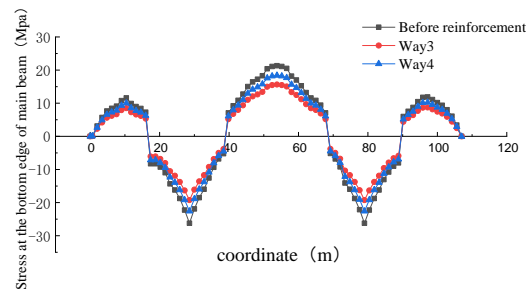
(a) Vertical displacement comparison of main beam
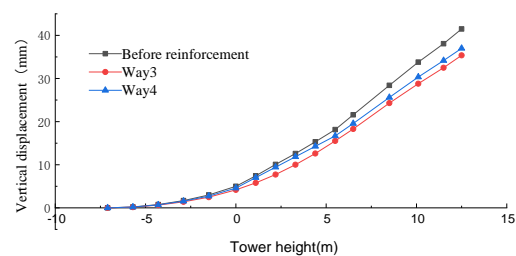
(b) Horizontal displacement comparison of main tower
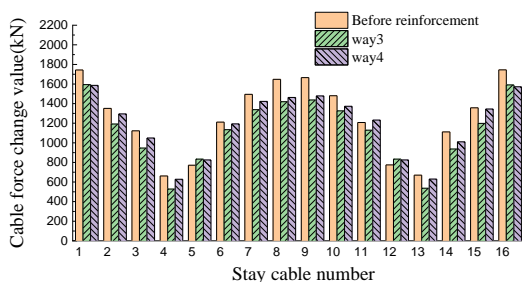
(c) Cable force comparison of stay cable

(d) Comparison of stress on the upper edge of main beam

(e) Stress comparison of the lower edge of the main beam

Fig. 8 - Comparison of reinforcement effects of two ways

The above two reinforcement schemes will reduce the vertical displacement of the main beam of the cable-stayed bridge, the horizontal displacement of the main tower and cable force of the cable stay, and the stress on the upper and lower edges of the main beam. In the deflection analysis, the reinforcement effect of Way 3 is more significant, after reinforcement, the maximum vertical displacement of the mid-span main beam is reduced by 11.49 % compared with Way 4, and the maximum vertical displacement of the side-span main beam is reduced by 11.89 %. The effect of Way 3 on the deflection of the main tower is more significant, after the reinforcement of Way 3, the maximum horizontal displacement of the main tower is reduced by 3.89 % compared with Way 4. In the cable force analysis, the reinforcement effect of Way 3 and Way 4 is close, after reinforcement, the cable force values of 2# ~ 4#, 6# ~ 11#, 13# ~ 15# in the cable stay are lower than those in Way 4, 1# , 5#, 12#, 16# cable stay cable strength value has been improved compared with the Way 4. In the stress analysis, the reinforcement effect of Way 3 is more significant, after the reinforcement of Way 3, the maximum stress of the upper edge of the mid-span main beam is reduced by 9.7 % more than that of Way 4, and the maximum stress of the upper edge of the side span main beam is reduced by 9.71 %, the maximum stress of the lower edge of the beam is reduced by 12.8 % more than that of Way 4, and the maximum stress of the lower edge of the main beam of the side span is reduced by 12.83 %.

In summary, the final reinforcement way adopted for the cable-stayed bridge is Way 3, which can significantly reduce the vertical displacement of the main beam and the horizontal displacement of the main tower. It also has an improvement effect on the stress of the upper and lower edges of the main beam and can meet the highway-II vehicle load Usage requirements.

Reinforcement effect static on load test analysis

Analysis of the vertical displacement of the main beam before and after reinforcement

The vertical displacement of the structure is a parameter that can reflect the structural stiffness macroscopically and is an important control index of the static test. This main beam vertical displacement measurement uses a dial indicator and a magnetic table base for detection. Table 4 is the comparison of vertical displacement before and after reinforcement of 2# span and 3# span under partial load.

*Tab. 4 - Comparison of vertical displacement before and after reinforcement*

conditions	point number	Test value before reinforcement				Test value after reinforcement				Promotion	
		Level 1 loading measured value	Level 2 loading measured value (a)	Theoretical value (b)	Measured value/theoretical value (c)	Level 1 loading measured value	Level 2 loading measured value (d)	Theoretical value (e)	Measured value/theoretical value (f)	Bearing capacity Promotion （e-d）/e-（b-a）/b	（c-f）/c
1	D1	22.64	39.09	32.79	1.19	13.99	24.48	27.83	0.88	0.31	0.26
	D2	25.46	43.78	36.05	1.21	15.56	27.96	31.57	0.89	0.33	0.27
	D3	28.26	48.46	42.45	1.14	16.66	30.12	34.47	0.87	0.27	0.23
	D4	30.26	51.79	45.02	1.15	18.19	32.14	37.28	0.86	0.29	0.25
3	D1	8.06	16.48	14.81	1.11	4.06	10.13	11.19	0.91	0.21	0.19
	D2	9.36	19.52	16.89	1.16	5.29	12.51	13.65	0.92	0.24	0.21
	D3	10.39	21.82	18.63	1.17	6.48	14.19	15.12	0.94	0.23	0.20
	D4	11.27	23.06	19.97	1.15	6.93	15.40	16.49	0.93	0.22	0.19

Under the condition 1, the ratio of the measured value and the theoretical value of the vertical displacement loading at the measuring point is 0.86~0.89, with an average of 0.875; Under the condition 3, the ratio of the measured value of the vertical displacement of the measuring point to the theoretical value is 0.91~0.94, with an average of 0.925;

After the reinforcement of the main beam under the load of each working condition, the measured vertical displacement values of each measurement point are less than the theoretical value, and the stiffness of the bridge after reinforcement is satisfied, and the ratio between the measured value and the theoretical value of the main span loading is increased by 27%, and the bearing capacity is increased by 33%. The ratio between the measured value of the side span and the theoretical value can be increased by up to 20%, and the bearing capacity can be increased by up to 24%. The results show that the external prestressed reinforcement method significantly reduces the vertical displacement of the main beam and effectively improves the load-bearing capacity and stiffness of the cable-stayed bridge.

Analysis of strain of main beam before and after reinforcement

Strain is also an important data that intuitively reflects the stress on the bridge. A comprehensive tester is connected to the pre-embedded concrete strain gauge to detect strain. The strain comparison of the main components before and after reinforcement is shown in Figures 9-11

--
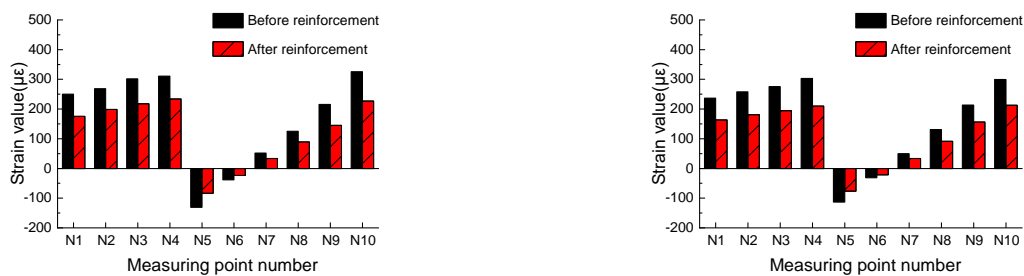
Strain comparison of 2# span main beam
before and after reinforcement(με)

Strain comparison of 3# span main beam
before and after reinforcement(με)

Fig. 9 - Comparison of the measured strain values before and after the reinforcement of
the main beam

The ratio of the measured value and the theoretical value of the Level 2 loading of the main span strain measurement point is 0.85~0.96, with an average of 0.91; The side span ratio is 0.84~0.92, the average is 0.880.

It can be seen from Figure 9 that after reinforcement, the measured strain value at each measuring point is less than the theoretical calculation value under each condition, the strength of the bridge after reinforcement is satisfied. After the main span is strengthened, the ratio between the measured value and the theoretical value is increased by up to 34%, and the load capacity is increased by up to 28%; After the reinforcement of the side span, the ratio between the measured value and the theoretical value is up to 26%, and the bearing capacity is up to 31%, indicating that the external prestressed reinforcement has a significant improvement effect on the stress level of the main beam.
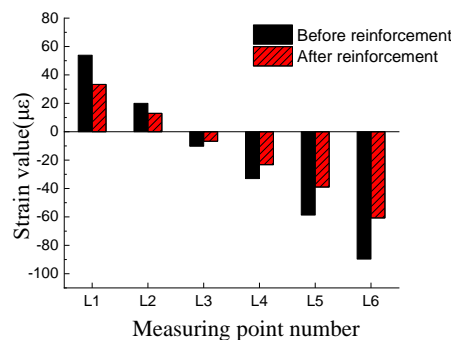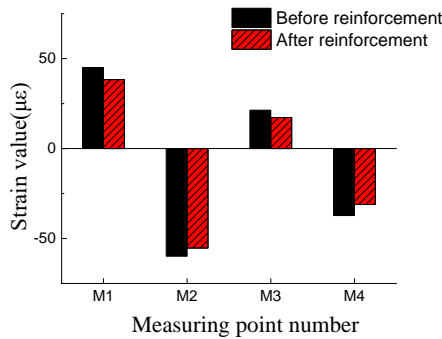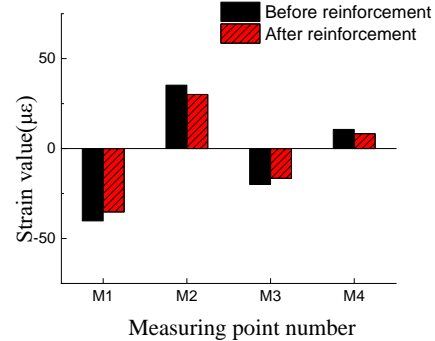

Fig. 10 - Comparison of strain of partial load on the top of 2# pier before and after reinforcement

The ratio of the measured and theoretical values of the strain on the top of the pier under the test load is 0.41~0.54, with an average of 0.475; It can be seen from Figure 10 that the measured strain value is less than the theoretical value under the load of each condition after reinforcement, and the strength of the bridge after reinforcement meets the design requirements. After reinforcement, the ratio between the measured value and the theoretical value of the 2 level loading is up to 32%, and the load capacity is up to 25%, indicating that the external prestressed reinforcement significantly increased the stress of the main beam.

Comparison of measured strain of cable tower before and after reinforcement of 2# spans

Comparison of measured strain of cable tower before and after reinforcement of 3# spans

Fig. 11 - Comparison of measured strains of cable tower before and after reinforcement

The ratio of the measured and theoretical values of the cable tower strain under level 1 loading is 0.41~0.54, with an average of 0.475; The ratio of the measured and theoretical values of the strain under level 3 loading is 0.69~0.77, with an average of 0.73.

After reinforcement, the ratio between the measured value and the theoretical value of the level 2 loading is up to 10%, and the load capacity is up to 8%, indicating that the external prestressed reinforcement significantly increased the stress of the cable tower.

Offset analysis of main tower before and after reinforcement

Set a measuring point on the top and bottom of the D-D section of the top of the tower, and use a prism-free total station to test the deflection of the top of the tower after the static conditions are fully loaded and stable. Table 5 shows the detection offset results of the main tower, the positive values in the table represent the northwest direction, and the negative values represent the southeast direction.

Tab. 5- Comparison of measured offset of main tower before and after reinforcement(mm)

conditions	point number	Test value before reinforcement				Test value after reinforcement				Promotion	
		Level 1 loading measured value	Level 2 loading measured value (a)	Theoreti cal value (b)	Measured value/the oretical value (c)	Level 1 loading measured value	Level 2 loading measured value (d)	Theore tical value (e)	Measured value/theo retical value (f)	Bearing capacity Promotion（e-d）/e-（b-a）/b	（c-f）/c
1	P1	5.1	9.4	11.49	0.82	3.9	7.3	10.18	0.72	0.10	0.12
	P2	6.7	12.3	15.36	0.80	5.5	10.2	13.69	0.75	0.06	0.07
3	P1	-2.5	-4.9	-6.27	0.78	-2.1	-4.0	-5.52	0.72	0.06	0.07
	P2	-3.7	-7.2	-8.97	0.80	-2.8	-5.5	-7.84	0.70	0.10	0.13


It can be seen from Table 5 that under eccentric loading, the measured value of the main tower's deflection is smaller than the theoretical value, and the main tower's deflection trend is consistent. After reinforcement, the ratio between the measured value and the theoretical value is increased by 13%, and the load capacity is increased by up to 10%, indicating that the stiffness of the main tower of the cable-stayed bridge after reinforcement is qualified.

Incremental analysis of cable force before and after reinforcement

The cable force test is carried out using a cable force tester, the measured and calculated cable force increment of the typical cable near the test cross-section are shown in Figure 12.
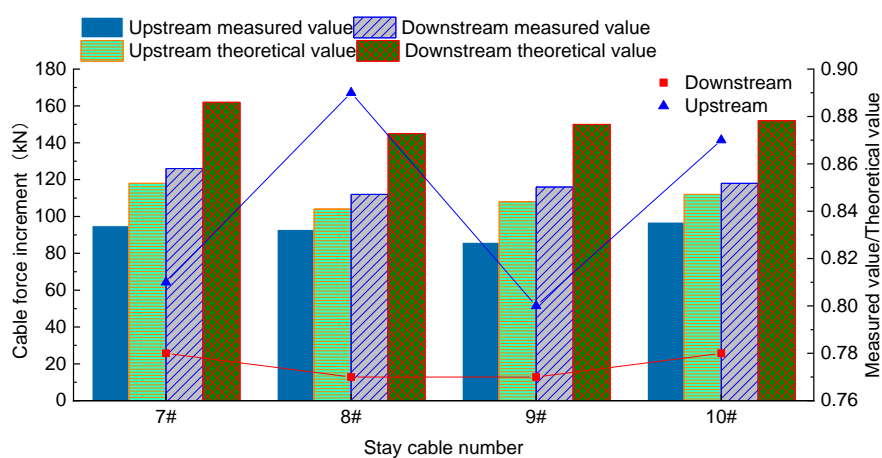
Condition1: Change of cable force before and after reinforcement
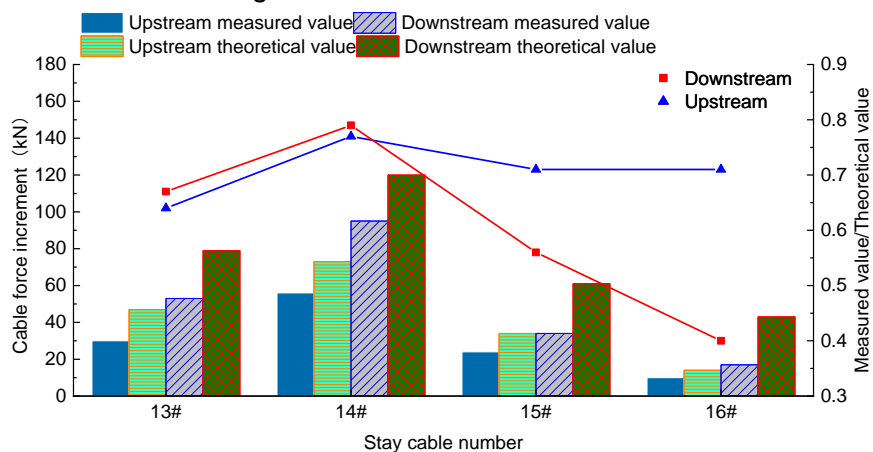
Condition3: Change of cable force before and after reinforcement
Fig. 12 - Change of cable force before and after reinforcement

The ratio of the measured and calculated values of each typical cable force of the cable-stayed bridge is 0.40 to 0.89, and the trend of the measured cable force and the calculated cable force is generally consistent. But the ratio of the measured value to the calculated value of the stay cable is generally low. The analysis shows that the stay cable is a parallel steel wire with a sheath outside the cable. At the same time, the sag effect of the stay cable has an influence on the determination of the cable force value.

The cable force increases of the cable stay on the upstream side of the cable-stayed bridge is significantly smaller than the cable force increases of the cable stay on the downstream side. The

asymmetry amplitude of the cable force increment ranges from 17% to 43%, maximum asymmetry amplitude is in condition 3.

CONCLUSION

(1)   External prestressed reinforcement technology can greatly increase the bending capacity of the main beam, reduce the main tensile stress, and increase the safety reserve of compressive stress.

(2)   The maximum vertical displacement of the main beam of Way 3 is 11.49%~11.89% lower than that of Way 4; the maximum horizontal displacement of the main tower of Way 3 is 3.89% lower than that of Way 4; the maximum stress of the upper edge of the main beam of Way 3 is lower than that of the Way 4 decreased by 9.70% to 9.71%; the maximum stress of the lower edge of the main beam of Way 3 was reduced by 12.80% to 12.83% more than Way 4; the reinforcement effect of Way 3 and Way 4 in the cable force analysis was close. The final reinforcement way adopted for the cable-stayed bridge is Way 3, which can significantly reduce the vertical displacement of the main beam and the horizontal displacement of the main tower, and also improve the stress on the upper and lower edges of the main beam.

(3)   Based on the comparison of the static filed load test data of the actual bridge before and after the reinforcement of the cable-stayed bridge, the measured strain and displacement of the main beam main tower are less than the calculated value after the reinforcement, and the change trend of the measured cable force is consistent with the calculated cable force. The application of external prestressed reinforcement technology to the cable-stayed bridge can significantly improve the strength, stiffness and safety reserve of the structure, and the bearing capacity of the bridge has improved significantly.

REFERENCES

[1]   Chen hao,2015.Calculation and analysis of prestressed concrete cable-stayed bridge and its reinforcement scheme.Southwest Jiaotong University.
[2]   Pan Zhulan,Zhao Changjun,Lou liang,2011. Design and Construction of Cable Replacement of Zhangzhen Cable-stayed Bridge.Highway, vol. 08 : 89-92.
[3]   Lei Jinsheng,Wang Yongfei,Dai Xiaodong,2010. Maintenance and reinforcement design of the main bridge of Changsha Yinpenling Xiangjiang River Bridge. Highway Engineering, vol. 35(04):97-99+115.
[4]   Zhou Zexi,Chen Yunhai,2014. Analysis of the whole process control of cable-stayed bridge construction, maintenance and reinforcement. Journal of Highway and Transportation Research and Development, vol. 31(04):100-105.
[5]   J. Guo, Wancheng Yun,2019.Cable force optimization of a curved cable-stayed bridge with combined simulated annealing method and cubic B-Spline interpolation curves.Engineering Structures, vol.201:109813.
[6]   Wu Zhongxin,Sheng Haijun,2013. Construction monitoring technology for reinforcement and reconstruction of cable-stayed bridge. Highway, vol.01:100-103.
[7]   Qiao Changjiang,2010. Research on Cable Replacement Technology of Prestressed Concrete Cable-stayed Bridge. Huazhong University of Science and Technology.
[8]   Liu Huichao, 2015. Research on Strengthening Technology of Prestressed Concrete Continuous Beam Bridge. Chang'an University.
[9]   Jia Libo, 2012. Analysis of Active Reinforcement Methods of Prestressed Concrete Monolithic Box Girder Bridges with Small and Medium Spans. Chang'an University.
[10]   Song Guangjun,Hua Longhai,2014. Analysis of Cracks in Diaphragm of Steel Box Girder of a Cable-stayed Bridge and Research on Reinforcement.Bridge Construction, vol. 44(04):107-111.
[11]   Niu Bin,1999. Analysis of Bending Performance of External Prestressed Concrete Beam. China Civil Engineering Journal, vol. 04:3-5

--

[12]   Liu Hang,Gao Huizong,Yang Xuezhong et al,2012. Post-tensioned external prestress reinforcement technology and its engineering application. Architecture Technology, vol. 43(01):49-52.

[13]   Angel C. Aparicio, Gonzalo Ramos, Juan R. Casas,2002.Testing of externally prestressed concrete beams, Engineering Structures , vol.24:73-84.

[14]   Ghallab A H , Khafaga M A , Farouk M F ,et al, 2013. Shear behavior of concrete beams externally prestressed with Parafil ropes. Ain Shams Engineering Journal, vol.4(01):1-16.

[15]   Tiejiong,Loua,Sergio,M.R.Lopes,2012.Numerical analysis of behaviour of concrete beams with external FRP tendons.Construction and Building Materials, vol.35:970-978.

[16]   Dong Bin, 2009. Experimental Study on Strengthening of Concrete Beams with External Prestress Considering the Influence of Secondary Axial Force. Tianjin University.

[17]   Qu Dechao, 2013. Research on Strengthening of External Prestress of Reinforced Concrete Continuous Curved Beam Bridge. Harbin Institute of Technology.

[18]   Lv Liang,Jia Yi,Ji Yuntao,2019. Evaluation of Bearing Capacity of Double-Tower Partial Cable-stayed Bridge Based on Load Test. Journal of Architecture and Civil Engineering, vol.36(03):101-109.

[19]   Liu Yongjian,Yang Jian,Liang Peng et al,2009. Load test of cable-stayed bridge without backstay leaning tower. Journal of Chang'an University（Natural Science Edition）, vol.29(05):59-63.

[20]   Alemdar Bayratar,Temel Turker,et al,2017.Static and dynamic field load testing of the long span Nissibi cable-stayed bridge. Soil Dynamics and Earthquake Engineering, vol.94:136-157.

[21]   Dall'Asta A , Ragni L , Zona A, 2007 . Simplified Method for Failure Analysis of Concrete Beams Prestressed with External Tendons. Journal of Structural Engineering, vol.133:121-131.

[22]   Richard Andrew Barnes, Geoffrey Charles Mays,2006. Strengthening of reinforced concrete beams in shear by the use of externally bonded steel plates: Part 1- Experimental programme. Construction and building materials, vol.20: 396-402.

[23]   Bimal Babu Adhikary, Hiroshi Mutsuyoshi,2006. Shear strengthening of RC beams with web-bonded continuous steel plates, Construction and Building Materials, vol.20:296-307.

[24]   Zhang D, Ueda T, Furuuchi H, 2012. Concrete cover separation failure of overlay-strengthened reinforced concrete beams. Construction & Building Materials, vol.26(01):735-745.

[25]   Liu Chuanle,Zhang Guogang,2018. Static load test study on a super long-span suspension bridge spanning cable crane. Journal of China and Foreign Highway , vol.38(05):105-108.

[26]   Liu Kai,Pei Bingzhi,Zhang Menzhe et al,2019. Research on Reasonable Distribution of Girder Section Rigidity and Bearing Capacity in the Region Around Steel-Concrete Joint Section of Hybrid Girder Cable-stayed Bridge. Journal of China and Foreign Highway, vol.39(06):66-72.

BEARING CAPACITY OF SINGLE-ANGLE COMPRESSION MEMBER: EXPERIMENTAL AND NUMERICAL INVESTIGATION

Javad Majrouhi Sardroud and Mohammad Hossein Zaghian

Islamic Azad University, Central Tehran Branch, Faculty of Technology and Engineering, Civil Engineering, Tehran, Iran; j.majrouhi@iauctb.ac.ir, moh.zaghian.eng@iauctb.ac.ir

ABSTRACT

This study was conducted to investigate the load-bearing capacity of a single angle column under various loading conditions to determine the loading condition offering the highest load-bearing capacity. In all cases, the load is transferred through one leg (or two legs) of the angle which has a smaller cross-sectional area compared to the total area of the angle profile. The main objective of this study is to develop almost all of the possible support conditions for the single angle section and carry out laboratory tests on the chosen specimens to determine the most suitable one. Also, there are some finite element investigations done using ABAQUS software to find out the maximum forces in which all the elements of the structures remain their linear behavior and the stress spots concentration. Based on the obtained results, it is possible to increase the axial critical load of a single angle by using the connections at the main axis of the section.

KEYWORDS

Bearing capacity, Buckling, Compression angle, Single angle, Stability, Optimization, FEM

INTRODUCTION

Single angle section (SAS) is one of the first structural shapes and is commonly used as a traditional structural member, for instance it can be utilized as a member of steel bridges, radio towers, and Trusses [1]. This section is usually available with an association of two equal legs and it is the shape of the section that makes it unique because of the easy manufacturing and transportation [2]. Single angle is preferred by construction engineers, because its two perpendicular legs provide a superior way of connection with other structural members. However, SAS formed members are found to be difficult shapes, analytically, as they are difficult to apply force (and moment) on them [1]. The points mentioned above, have motivated researchers to conduct a great number of studies.

Regarding economic aspects of the plan, in steel profiles made as thin walls (like angle profile), buckling is one of the most important problems which can occur [3]. Buckling appears in two forms (i.e., partial and overall), both forms are related to loading conditions and to the geometry of the member.

LITERATURE REVIEW

Botelho *et al* (2021) [2] have focused on the torsional buckling behavior of starred angle rolled sections under compression. They found out that compared to their experimental and numerical results, Eurocode 3 prediction, presents more significant discrepancies. Veerendra

Kumar Shukla *et al* (2021) [5] have provided a new insight on Analysis of a Cruciform-Leg Transmission Line Tower. Their paper gives some suggestions for angle connection. Sayed (2020) [6] numerically investigated single-angle steel member under tension load with damage in the unconnected leg and he found out that the damage ratio can affect the stress distribution and load capacity. Fábio Paiva and Rui C. Barros (2020) [7] developed a numerical analysis of the buckling resistance of a single angle in OPENSEES. The study contains hysteretic behavior of angle profile under cyclic loads. Xiaonong Guo *et al* (2020) [8] presented an investigation about the mechanical behavior of in-service axial compression angle steel members. They concluded that the influence of initial load on ultimate bearing capacity of steel members can be ignored when the initial stress is less than $0.4f_y$. Masoud Mirtaheri et al (2019) [9] carried out an experimental research to investigate the role of a new connection in steel structures and they found out that the resistance of connections in steel structures plays an important role in decreasing the damage from the progressive collapse. Tong and Guo (2018) [10] investigated the elastic buckling and hysteretic behavior of steel angles. They suggested ratios to prevent local buckling failure. Li Tian *et al.* (2018) [11] carried out a study about single-angle compression members, and according to their test results, a model was developed to determine the effective slenderness ratios of single-angle members with both legs bolted at the end. Markus Kettler et al. (2017) [12] tested 300 steel angles in compression and also conducted some numerical investigations. They concluded that the end support of the gusset plate plays an important part in the compression Member (angle) capacity. Amit Jain and his colleagues (2014) [1] studied the lateral-torsional buckling of laterally unsupported single angle sections loaded along a geometric axis and simulated this buckling using the ABAQUS software. For this purpose, they placed an equal leg angle in four different modes under the bending moment. The results of this research showed that IS800-2007 does not provide sufficient instructions for single angle's modelling. Giuseppe Brando *et al.* (2013) [13], used the finite element method (FEM) to determine the critical load of perforated single angle, the result showed that having less than 9% holes affects the critical load. Ruhi Aydin *et al* (2011) [14] found out that it would be useful to set a limiting value for the second order when a design code is used. Liu and Hui (2010) [15] applied a FEM analysis in steel single angle beam-columns and recognized a significant non-compliance between "AISIC-2005" and the performed FEM analysis. Also, he and his colleagues (2008) [16], test 28 single angles and their conclusion was: "AISC Specification 2005 equations intended for doubly symmetric sections provide improved capacity estimates of eccentrically loaded single angles failing by flexural–torsional buckling".

THE FINITE ELEMENT METHOD IN SHELLS

The Finite Element Method (FEM) has been widely used to solve different kinds of engineering problems for years. This method is recognized as a reliable method to analyze civil engineering complications in spite of some unsolved issues [17]. In the FEM modelling, the structure is fractionalized into a limited number of elements (usually in rectangular or triangle shapes) which are connected to each other in the knots and borders between the supposed elements so that the balance and conformity in every knot and the direction of the borders between elements can be satisfied [18].

THE COMPRESSION TEST ON THE SINGLE ANGLE PROFIL

This study presents the buckling and single angle load-carrying capacity under the effect of compression load from a new aspect. Angles usually are loaded in the form of a plate coupling to a flange. In this study, for finding a better way of loading angles, some states of the case were

studied to enhance the safety factor and determine the best outcome for various experimental and numerical methods. All the tests were conducted in a material laboratory.

The technical characteristics of used steel and the geometric features of the profile

In this modelling, construction steel (St-37) was used. The modulus of it, yield point, and Poisson's ratio were assumed to be 201035.5 MPa, 230.8 MPa, and 0.3, respectively. There is an information about the used angle profile in Figure 1 and Table 1.
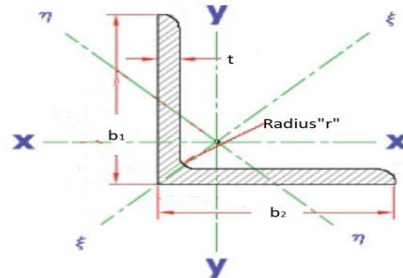

Fig. 1 – Axes are mentioned in Table 1

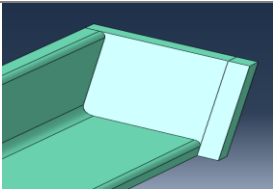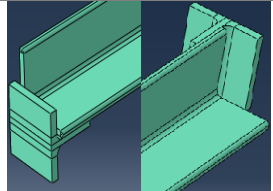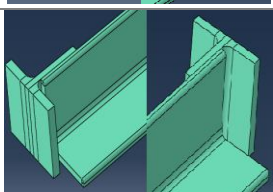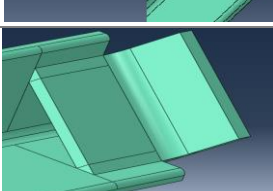*Tab. 1 - Some of the Specifications used single angel*
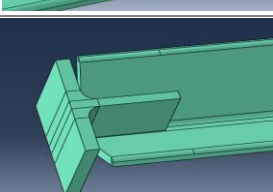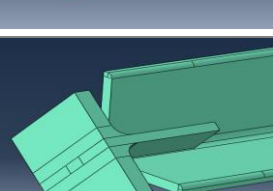
Mechanical Properties ST-37	F_y=230.8 MPa	G=7732.1 MPa	E=201035.5 MPa	υ=0.3
Specifications Section (Figure1)	b_1=40 mm	b_2=40 mm	t=4 mm	A=308 mm²
The radius of gyration (Figure1)	r_ζ=15.2 mm	r_η=7.8 mm	r_x=12.1 mm	r_y= 12.1 mm
Second Moment of Area (Figure1)	I_ζ=7.09 mm⁴	I_η=1.86 mm⁴	I_x=4.48 mm⁴	I_y= 4.48 mm⁴

Preparing the samples of the test

Six samples, each 1m long, were cut. Except for one sample (sample No.1), the rest were loaded while the T shaped pieces were connected to them. Also, to transfer the load in five samples, some T-shaped samples were prepared and welded to the end of angles with an E60 electrode on specific spots.

To make the geometry of the models, instead of a gusset plate, a T-bar web was used in the simulations and tests. The T-bar web and flange acted as the gusset plate and the loading plate, respectively. In all models, a 40*40*4 angle (length=1000mm) was used. On both ends of this angle, two halves of an IPE 80 T-bars (length = 40mm) were installed; however, in one model (sample No.1), only two gusset plates were installed. Each model represented a different case of the angle to the T-bar joint. Table 2 gives the 3D representation, name, and description of each model.

Article no. 25

THE CIVIL ENGINEERING JOURNAL 1-2021

Tab. 2 - The geometry of the models

Code of Model	3D View	Description
No.1		- Basic model - Contains no T-bat - Single angle with two 40 mm × 46 mm steel plates attached
No.2		- The T-bar sides are connected to the horizontal and vertical flanges of the angle respectively. - The T-bars are placed at the outer surface of the - The Connecting dimensions (welding) is (2.3 mm × 2.3 mm × 40 mm)
No.3		- The T-bar webs are connected to a single flange of the angle. - The T-bars are fixed at the outer part of the angle - The Connecting dimensions (welding) is (2.3 mm × 2.3 mm × 40 mm)
No.4		- The T-bar flange edges were mitered at 45°. - The T-bars were placed inside the angle in such a way that the webs would make 45° angles with the respective angle flanges.
No.5		- Each T-bar is placed at the intersection of the angle flanges. - The angle between the T-bar web and each flange is 45°. - The centers of gravity of the T-bars are aligned with that of the angle
No.6		- Each T-bar is placed at the intersection of the angle flanges. - The angle between the T-bar web and each flange is 45°. - Center of the area of the T-bar web section lies at the intersection of the angle flange axes

Experimental plan

The apparatus used for conducting the tests was the 500 KN AMSLER, which was able to measure the deformation. The accuracy of this machine is 0.005 mm. Also, two codes were used [19] [20]in this study and according to these codes, the rate of stressing was considered 110 Mpa/min. The temperature of the laboratory was approximately 26°C during the testing processes. Figure 2 shows model No.5 under testing process and all samples after mechanical tests.
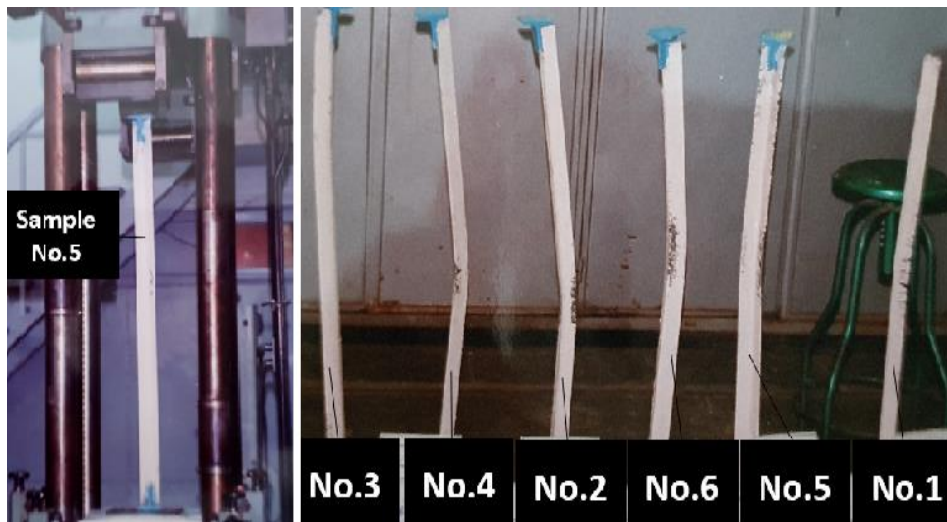
Fig. 2 - model No.5 under loading process and all samples after mechanical tests

The experiment was conducted as follows: First, the sample was set between two jaws of the apparatus and, after setting the two layers of sponge on both ends between the samples and the jaws of the apparatus, a small load was applied, and the sample was fixed by a balancer in a vertical mode. Afterwards, the load was applied gradually, the ultimate bearing capacity was measured, and the force diagram was plotted. The changes in the length were recorded using the apparatus. All six samples were set under compressive forces. The diagram of sample No.5 is depicted in Figure 3 as a sample. Also, in Figure 4, there are two views of sample No.2 under the loading process.
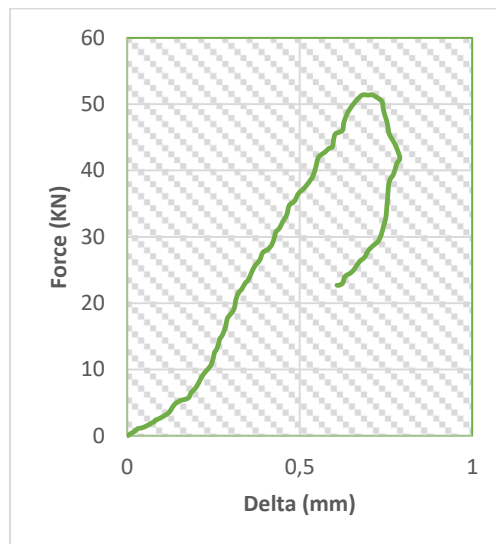

Fig. 3 – Force-Delta Diagram of sample No.5

Fig. 4 – Two views of sample No.2 under the loading process

The Result of compression test

The ultimate capacity of a single angle profile was measured in all loading modes. Sample No.1 had the highest load capacity. The loading capacity of Sample No.5 is lower than sample No.1 by 6.2%. Sample No.4 had the lowest load capacity (26.38 KN). The loading capacities of sample No.2 and sample No.3 are 38.15 KN and 35.21 KN, respectively. The summary of these tests is presented in Figure 5.

In terms of buckling, under compression forces, steel members can experience five types of buckling: Local Buckling, Distortional Buckling, Overall Flexural Buckling, Overall Torsional Buckling, and Overall Flexural-Torsional Buckling [21]. In all of the samples in this study, Overall Flexural Buckling occurred.
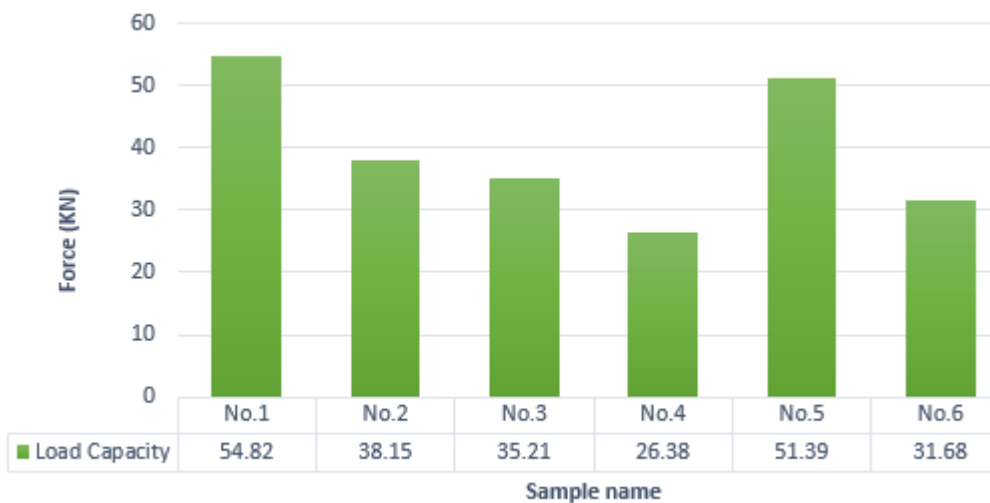

	No.1	No.2	No.3	No.4	No.5	No.6
Load Capacity	54.82	38.15	35.21	26.38	51.39	31.68

Fig. 5 – The load capacity for the samples (experimental)

NUMERICAL MODELLING

This section examines 6 cases of angle to gusset plate joint. The computer modelling was done using ABAQUS software. The purpose of this section is to find out the maximum force in which all elements of the structure remain their linear behavior. In other words, the maximum force in which the cases behave absolutely linear and none of the elements reach to yield strength. Figure 6 shows the simulation of model No.4 and its different parts.
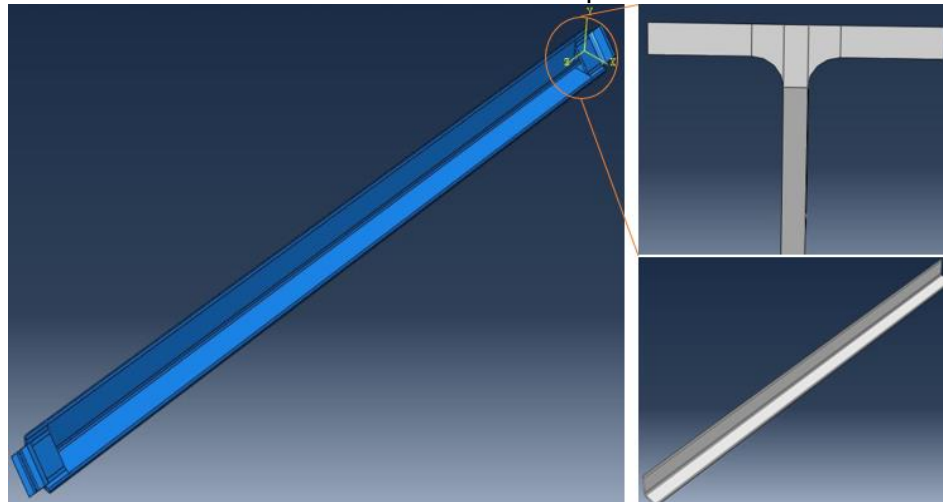

Fig. 6–the simulation of model No.4 (assembled and different parts)

Type of analysis

In this study the method used for analysis was the general nonlinear static analysis method which ignores the inertial effects and time-dependent behaviors of the material. These two assumptions are also set forth in construction design codes. The main reason for selecting this method for the analysis is to establish a condition that is as close as possible to the construction code requirements. In the analysis method, the materials were assumed to be solid and homogeneous with 3D stresses and strains.

The variables used for modelling were:

Independent variables: forces applying on the structure and the techniques used for connecting the angles and the T-bars (tees)

Dependent variables: the maximum force which none of the elements failed in it.

Research constants: angle and T-bar sizes, section materials, a method of analysis, loading type and duration, boundary conditions, and type of the supports used.

Connections

A constraint called "tie" was used for joining the T-bars to the angle. This constraint, which is used frequently in the modelling of civil engineering problems, can combine two surfaces with different meshing by making all the six degrees of freedom (DOFs) in one surface dependent to the other surface [22].

Applied loads and supports

To apply loads on the simulation models, loading components of the laboratory jack was used. In general, laboratory jacks have one movable jaw and one fixed jaw. The load is applied from the movable jaw of the jack to the test specimen and, at the same time, the fixed jaw of the jack develops a reaction to this load along the line of action of the applied force. Also, upon applying compression to the specimen by the jack, a friction connection is developed between the

jack jaw and the parts of the specimen that are in contact with the jaw. This friction would prevent the contact surface on the specimen from moving along any direction but the loading direction.

In this apparatus, the load is applied to the surface of one of the T-bars. Therefore, the outer surface of a T-bar was selected and the compression load was applied to the same surface (as in the case of the movable jaw). Figure 7 shows the place of the applied load.
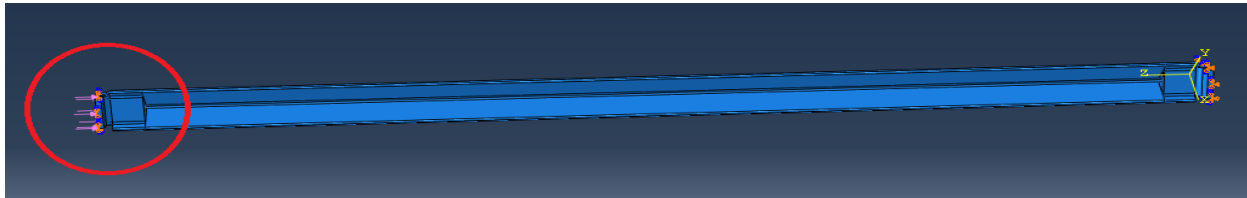

Fig. 7– Point of action of the applied load

On the opposite side, deflection along the z-axis -which is the line that the force is applied to- on the outer surface of the T-bar is prevented. Figure 8 shows the support oriented along the z-axis.
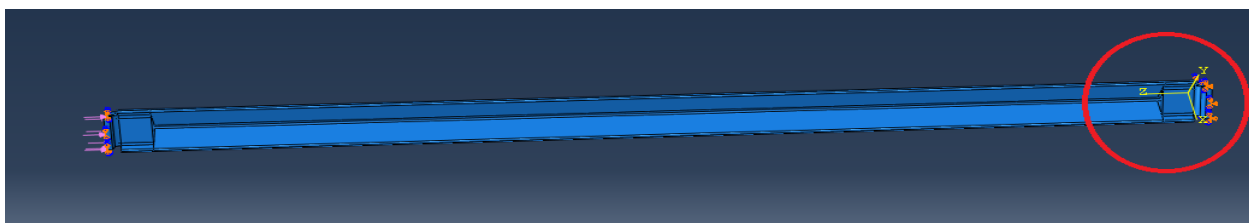

Fig. 8 – Support oriented along the line of action of the applied load

To examine the effect of the friction joint referred to above on the outer surface of the flanges at the end of T-bars, displacement was prevented along the x and y-axes. As shown in Figure 9, this support is defined at both ends of the models.
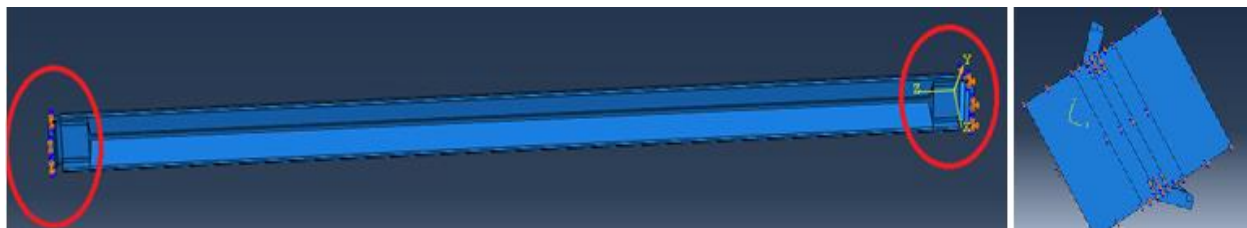
Fig. 9 – Supports oriented concerning x and y directions

In other words, both ends were fully restrained (translations and rotations) except the axial translation of the load-applying end [23]. This method of applying load and defining boundary conditions is conventional in many numerical investigations. For example, Poursharifi et al. (2020) [24]and El-Kholy et al. (2019) [23] used this method in their numerical studies.

Since the applied force was the most important independent variable in each model, to achieve the objective of the present study, the value of the distributed compressive load applied to the flange surface of one T-bar was changed, followed by observing and analyzing the corresponding models and their outputs. Loading was started at 20 N/mm^2 and was decreased by 0.25 N/mm^2 in each analysis. Besides, the maximum amount of load in which the stress of all of the elements of the model remained below the yield strength by applying it, was measured and

recorded. It has to be noted that this is a comparative study and the results are approximated. Table 3 illustrates the brief information related to numerical modelling.

Tab. 3 - Brief of input in numerical software

Modeling Space:	3D, deformable	Young's Modulus:	201035.5 Mpa
Base Feature:	Solid, Homogeneous	Poisson's Ratio:	0.3
Method of Analysis:	Nonlinear	Mass Density:	7850 Kg/m3
Type of Analysis:	Static, General	Yield Point:	230.8 MPa
Type of Element Analysis:	Standard,3D Stress	Number of steps:	2 (initial and step1)
Job Type:	Full Analysis	Independency:	Dependent
Load Distribution:	Uniform	Type Boundary Condition:	Displacement/Rotation
Load Type:	Pressure	Large Displacements:	Considered
Material Behavior:	Isotropic	Type of Connection:	Tie

Validation of results

Experimental results of sample No.5 (the most optimized model) are used to verify the efficiency of the FEM model. To verify, the experimental type of the force-displacement curve of sample No.5 is compared to the computer-based type of it. Figure 10 includes both curves. However, in the numerical investigation the maximum force applied to the models is just over 9.81 KN, the greatest force applied on sample No.5 for verification is 19.61 KN (to ensure the accuracy of modelling). This method of validation is conventional in steel study. For example, FENG Ningning et al (2018) [25]compared finite element analysis results with experimental data in their study to verify their FEM modelling.
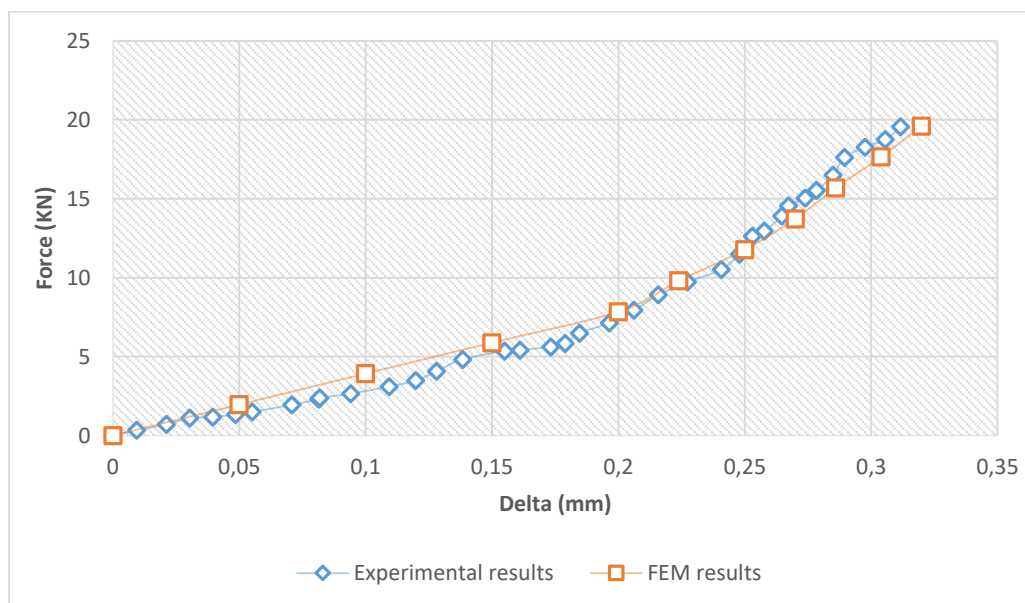
Fig. 10– Comparison of results

Results of computer modelling

The results of the computer simulation are given in Figure 11. The force mentioned in the figure is the force under which none of the elements reached yield strength. The figure also presents the distribution of the applied forces on the T-bar flange surface. Model No.3 requires the lowest force for its first element shows plastic behavior but sample No.5 requires the highest force. Analysis of the models in ABAQUS was continued until the element started behaving plastically.

Sample name	No.1	No.2	No.3	No.4	No.5	No.6
■ Maximum Force in which All Elements Behave Linearly	8.57	5.41	4.51	6.32	8.57	9.92
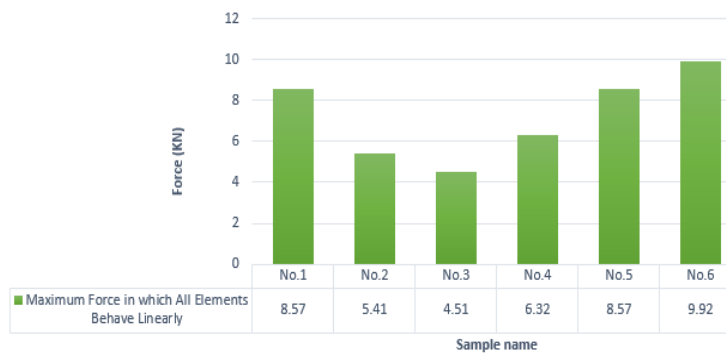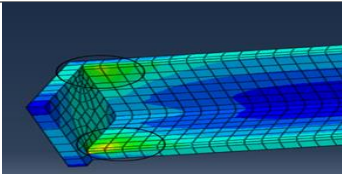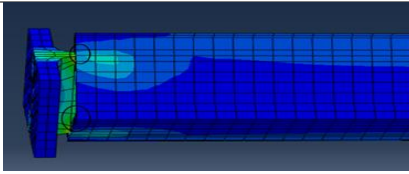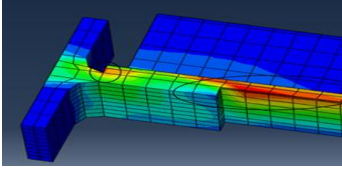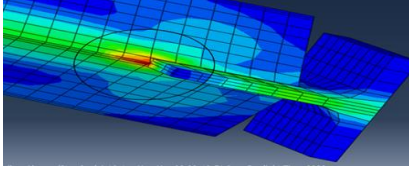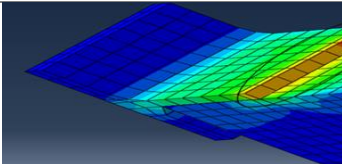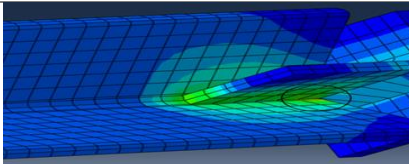
Fig. 11 – Modelling results

Also, Table 4 illustrates the stress concentration spots in all of the samples. This may help engineers who want to use one of the mentioned models to recognize the critical regions. As can be seen in Table 4, in all samples, stress concentrations occurred from about the T-bar profiles.

Tab. 4 - The places of stress concentrations

Code of Model	Stress distribution	Code of Model	Stress distribution
No.1		No.4	
No.2		No.5	
No.3		No.6	

Each sample experiences three stages during the loading process from applying load to buckling. In the first stage, all elements of the sample behave linearly until an element starts to behave plastically. In the second stage, the stiffness of the element decreases and as a general rule, the force distributes among the elements based on their stiffness (the more stiffness, the more stress). This causes more elements to show plastic behavior. The last stage is buckling. By comparing the experimental results with the numerical results, it is realized how much of the plastic potential of a sample was used before buckling. In other words, if "the maximum force in which all elements behave linearly" of a sample is much lower than the "Bearing capacity", the sample is more efficient economically because it uses more plastic potential. The summary of experimental and computer-based modelling is shown in Table 5.

Tab. 5 - The summary of results

sample name	Bearing capacity (experimental) (column 2)	maximum force in which all elements behave linearly (FEM) (column 3)	Differences between column 2 and 3	the ratio of column 3 to column 2
No.1	54.82 (KN)	8.57 (KN)	46.25 (KN)	15.64%
No.2	38.15 (KN)	5.41 (KN)	32.73 (KN)	14.19%
No.3	35.21 (KN)	4.51 (KN)	30.69 (KN)	12.81%
No.4	26.38 (KN)	6.32 (KN)	20.06 (KN)	23.94%
No.5	51.39 (KN)	8.57 (KN)	42.82 (KN)	16.68%
No.6	31.68 (KN)	9.92 (KN)	21.75 (KN)	31.33%

CONCLUSION

Plenty of studies have been conducted about single angle. This fact can demonstrate the importance of angle profile in construction industry and researchers' appetite to know about the behavior of the profile. This study focuses on an omitted area: The position of gusset plate. The aim of this paper was to find a practical and innovative manner to increase the baring capacity of single angle compressing member without increasing the weight of the member by concentrating on joining area. However, further studies in different single angle boundary condition are necessary. Gaining profound insight into seismic and static behavior of this profile not only can be beneficial economically, but also can provide an opportunity for engineers to design high-performance structures.

It is conventional to connect gusset plates to the flanges of the single angle (like sample No.2 and sample No.3), especially in steel structure braces. However, according to this study, it is recommended to install gusset plates on single angle like model No.5. In other words, if the angle between the gusset plates and each of the flanges of the single angle is 45° and the gravity center of the gusset plate is alleged with that of the single angle, the optimal joint will be provided. Figure 12 illustrates the optimum connection. The specific results are mentioned as follows.
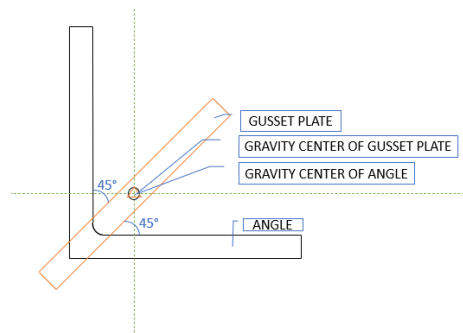

Fig. 12– The schematic illustrator picture of optimal installation according to this study

In the present study, laboratory tests were conducted to determine the highest load-bearing capacity of a single angle column with using various loading conditions on one or two legs. It is concluded that the highest compressive strength is related to model 1, while the lowest compressive strength is related to model No.4. Besides, by comparing the experimental and FEM results, it can be stated that the angel which its first element enters the plastic area with less power, will not necessarily fail with less power. Regarding the point that gusset plates are placed orthogonal to the section, the most useful and optimized model will be model No .5.

The load-bearing capacity of sample No .1 is the highest, and all samples were failed because of buckling. Consequently, it can be said that gusset plate installation, which is inevitable in particular for braces and members of a truss, can contribute to a reduction of critical buckling force.

Samples No .4 and No .6 had the worst performances not only because they had the lowest load-bearing capacity but also because the ratio of maximum force in which all elements behave linearly to load-bearing capacity was high (23.94% and 31.33%, respectively). It implies that the larger proportion of the plastic capacity of the samples were not used before buckling.

Table 3 demonstrates the critical regions of all samples under loading which can be beneficial for anyone who wants to use the mentioned methods of installation of a gusset plate to a single angle. In Sample No.5 stress concentration occurred at the end of the gusset plate (web of T-bar).

REFERENCES

[1]   Jain, A., Rai, D.C., 2014. Lateral-torsional buckling of laterally unsupported single angle sections. Journal of Constructional Steel Research, vol. 102: 178–189. DOI: http://dx.doi.org/10.1016/j.jcsr.2014.06.013.

[2]   Botelho. I. et al., 2021. Starred rolled stainless steel angle sections under compression: An experimental and numerical investigation. Thin-Walled Structures, vol. 158, pp. 1-17 DOI: https://10.1016/j.jcsr.2012.10.009

[3]   Simonian, V., Majrouhi Sardroud, J., 1997. Investigation into the stability of single angle. Journal of Faculty of Engineering, vol. 18: 29-46.

[4]   Hussain, A., Liu, Y.P., Chan, S.L., 2018. Finite Element Modeling and Design of Single Angle Member Under Bi-axial Bending Structures, vol. 16: 373-389. DOI: https://doi.org/10.1016/j.istruc.2018.11.001.

[5]   Shukla. K. et al., 2021. Failure Analysis of a Cruciform-Leg Transmission Line Tower. International Journal of Steel Structures, vol. 17, pp. 1127-1141. DOI: https://doi.org/10.1007/s13296-021-00454-5

[6]   Sayed, A.M., 2020. Numerical analysis of single-angle steel member under tension load with damage in the unconnected leg. Structures, vol. 25, 920-929. DOI: https://doi.org/10.1016/j.istruc.2020.04.001.

[7]   Paiva, F., Barros, R.C., 2020. PARAMETRIC STUDY OF THE BUCKLING RESISTANCE OF A

SINGLE ANGLE IN OPENSEES, vol. 16: 373-389. Porto.

[8]   Guo, X., et al., 2020. Mechanical behavior of in-service axial compression angle steel members strengthened by welding. Journal of Building Engineering, vol. 32, pp. 1-16. DOI: https://doi.org/10.1016/j.jobe.2020.101736

[9]   Mirtaheri, M., et al., 2019. Numerical investigations on elastic buckling and hysteretic behavior of steel angles assembled buckling-restrained braces. Structural Engineering and Mechanics, vol. 70(4): 381-394. DOI: https://doi.org/10.12989/sem.2019.70.4.381

[10]   Tong, J., Guo, Y., 2018. Mitigation of progressive collapse in steel structures using a new passive connection. Journal of Constructional Steel Research, vol. 144: 21-39. DOI: https://doi.org/10.12989/sem.2019.70.4.381

[11]   Tian, L., et al., 2018. Single-Angle Compression Members with Both Legs Bolted at the Ends: Design Implications from an Experimental Study. Journal of Structural Engineering, vol. 144(9): 381-394. DOI: https://doi.org/10.1061/(ASCE)ST.1943-541X.0002158

[12]   Kettler, M., Taras , A.,Unterweger, H., 2017.Member capacity of bolted steel angles in compression – Influence of realistic end supports.Journal of Constructional Steel Research, vol. 130: 22-35. DOI:http://dx.doi.org/10.1016/j.jcsr.2016.11.021.

[13]   Brando, G.,De Mattei, G., 2013. Buckling resistance of perforated steel angle members. Journal of Constructional Steel Research, vol. 81: 52-61. DOI: https://doi.org/10.1016/j.jcsr.2012.10.009.

[14]   Aydin, R.,et al., 2011. Experimental and code based study of beam–column behaviour of equal leg single-angles. Journal of Constructional Steel Research, vol. 67(5): 780-789. DOI: https://doi.org/ 10.1016/j.jcsr.2010.12.016.

[15]   Liu, Y. Hui, L., 2010. Finite element study of steel single angle beam_columns. Engineering Structure, vol. 32(8): 2087-2095. DOI: https://doi.org/10.1016/j.engstruct.2010.03.009.

[16]   Liu, Y., Hui, L.,2008. Experimental study of beam–column behaviour of steel single angle Journal of Constructional Steel Researc, vol. 64(5): 505-514.

[17]   P.-S. Lee, H.-C. Noh., C.-K. Choi, "Geometry-dependent MITC method for a 2-node iso-beam element," Structural Engineering and Mechanics, vol. 29, no. 2, pp. 203-221, 30 May 2008. DOI: 10.12989/sem.2008.29.2.203.

[18]   J. Reddy, An Introduction to the Finite Element Method. Inc. USA: McGraw-Hill Book Company, 1993.

[19]   ASTM A370.,2010. Standard Methods and definitions for Mechanical Testing of Steel Products. American Society for Testing and Materials; West Conshohocken, Pennsylvania, United States.

[20]   AISC ,2000. Load and Resistance Factor Design Specification for Single-Angle Members. American Institute of Steel Construction, Inc; Chicago, United States.

[21]   Anbarasu, M., Bharath Kumar, S., Sukumar, S., 2013. Study on the effect of ties in the intermediate length Cold Formed Steel (CFS) columns. Structural Engineering and Mechanics, vol. 46(3): 323-335. DOI:http://dx.doi.org/10.12989/sem.2013.46.3.323

[22]   Zaghian M. H., majrouhi sardrod j., 2015. Investigation into the Behavior of Comparison Single Angle Subject to Various Loading Condition Using Computer-Base Modelling. International Congress on Civil Engineering ,Architecture &Urban development. Tehran, desember.

[23]   El-Kholy, A.M., et al.,2019. Finite element simulation for steel tubular members strengthened with FRP under compression. Structural Engineering and Mechanics, vol. 72(5): 569-583. DOI: https://doi.org/10.12989/sem.2019.72.5.569.

[24]   Poursharifi, M., et al., 2020. Introducing a new all steel accordion force limiting device for space structures", Structural Engineering and Mechanics, vol. 74(1): 69-82. DOI: https://doi.org/10.12989/sem.2020.74.1.069.

[25]   F. Ningning, et al., 2018. THE EFFECT OF AXIAL COMPRESSION RATIO ON SEISMIC BEHAVIOR OF INFILLED REINFORCED CONCRETE FRAMES WITH PROFILED STEEL SHEET BRACING. THE CIVIL ENGINEERING JOURNAL, vol. 2018: 439-449. DOI: https://doi.org/10.14311/CEJ.2018.03.0035

BUCKLING DELAMINATION IN COMPRESSED NO-TENSION HOMOGENEOUS BRITTLE BEAM-COLUMNS REINFORCED WITH FRP

Francesco Marchione

Università Politecnica delle Marche, Dipartimento di Ingegneria Civile, Edile e Architettura (DICEA), Ancona, via Brecce Bianche 60131, Italy, f.marchione @pm.univpm.it

ABSTRACT

The main issue of this paper is the instability of no-tension structural members reinforced with FRP. This study concerns the instability of FRP reinforcement. The primary buckling problem of a compressed element involves the division of the deflected section into a compressed and a tensioned zone. In particular, in the case of a compressed slender element reinforced on both tense and compressed side FRP delamination phaenomenon could occur on the latter. This entails the loss of the reinforcement effectiveness in the compressed area for nominal load values much lower than material effective strength. Therefore, structural elements or portions thereof which absorb axial components in the direction of the reinforcement may exhibit relatively modest performance with respect to the unreinforced configuration. By employing a no-tension material linear in compression, an analytical solution for FRP buckling delamination length is provided. The main objective of this paper is to provide a simplified tool which allows to evaluate the critical load of the reinforced beam-column and to predict the tension at which delamination and the loss of effectiveness of reinforcement in the compressed area could occur.

KEYWORDS

Buckling analysis, FRP delamination, Compressed beam-columns, Composite beam-column, buckling composite delamination, FRP reinforced beam-columns

INTRODUCTION

Nowadays the use of FRP reinforcements for the consolidation of existing structures is becoming increasingly popular in the field of civil engineering [1], [2] thanks to their flexibility, ease, and speed of installation. They also have a high strength-to-weight ratio and add practically no mass to the structure [3], [4].

The use of FRP reinforcements allows providing the masonry panel with adequate tensile strength for stresses both bending in or out of the plane and shear in the plane [5] – [8].

However, it is observed that a structural element subject to seismic action undergoes the cyclic action of external forces. If we consider some common techniques of reinforcement (e.g. shear reinforcement of masonry panels, bending reinforcements of reinforced concrete beam-columns) it could be observed how these reinforcements are subjected to alternate cycles of tensile and compressive forces.

The case of axially loaded beam-columns is the simplest of the phenomena of elastic equilibrium instability, or of the balance between internal tensions and external forces. This case, studied by Euler in the mid-1700s, remained for over a century almost without any practical interest,

since the construction techniques and materials used at the time were guarantors against any possibility of failure or instability phenomena.

The instability phenomena could occur in all types of structures except those subject to tension. Therefore, it can occur in elements subject to compression, flexion, torsion, shear, and in compound stress states. The instability occurs in a sudden and unpredictable way, without the possibility of reinforcing or decreasing loads.

However, the problem of instability entails very serious analytical difficulties, so recourse to calculation procedures that provide approximate solutions to the problem. Numerous studies analysed the problem; Aboudi, Gilat [9] studied the analogy between the equations for the analysis of instability in elastic structures and the equations of the wave propagation motion. Employing this analogy, the exact and approximate instability stress of continuous fiber composite laminated materials are established. With a certain variation of variables in these dispersion relations, the instability corresponding to the stresses can be determined.

Further studies concerned the problem of the instability of composite beam-columns and panels: Marouene et al. [10] analysed the instability behaviour of composite panels with variable stiffness, produced by the automated fiber positioning process (AFP). To minimize the occurrence of intrinsic defects such as gaps and overlaps, the so-called tow-drop method was used. It has been established that the tow-drop method has significantly improved the structural performance in terms of pre-buckling stiffness and the tensile strength, obviously keeping the geometric disturbances minimal.

Athhan [11] conducted studies on composite beams, observing the effects of load sequences, fiber orientation angles, boundary conditions and delamination modes on the critical loads of laminated beams. The results show that a reduction in critical loads occurs when the length of the delamination increases. In numerical analysis, the appropriate buckling load values of the laminated beams are obtained using a reduced elastic modulus for the contact elements in the region where delamination is induced. Cappello, Tumino [12] studied the buckling behaviour of flat laminates in composite material characterized by the presence of multiple delamination, subject to axial compression loads. The FEM method was used, conducting a both linear and non-linear analysis. The non-linear analysis considers large displacements and a contact constraint between the edges to prevent their interpenetration. The results were compared with those of analytical theories and with other numerical and experimental results found in the literature. It has been found that both the length and the positioning of the delamination and the packaging sequence of the laminae influence the critical load of the laminate.

Despite this, all the studies carried out to consider the problem of delamination because of the propagation of a detachment already present on the structural support.

Since FRP strips reinforcements are scarcely resistant to compression, attention is focused on this weakness. Slender beam-columns in no-tension homogeneous material and subjected to compression are considered, both in normal and FRP reinforced configurations. The global instability of the analysed model may occur accompanied by local instability of the reinforcement in the compressed area. This can lead to a considerable reduction in stiffness and to the loss of reinforcement effectiveness [13]. The choice of a non-tensile structural element simulates the behaviour of the most widespread materials in historic buildings such as masonry. For example, the vulnerability of masonry panels to out-of-plane stress often requires the application of reinforcement. A modern approach is represented by fiber-reinforced plastic composite materials (FRP).

This reinforcement provides the surfaces of the existing panel with the capacity to withstand tensile stress and, as a result, increases the panel's resistance to out-of-plane bending. The cyclicality and uncertainty of seismic action, the tension-free nature of masonry require the application of the reinforcement on both sided of the panel [14], [15]. The problem of buckling delamination becomes even more critical in cases where external composite strips are applied to both sides of the wall. An explanatory application is illustrated in Figure 1.
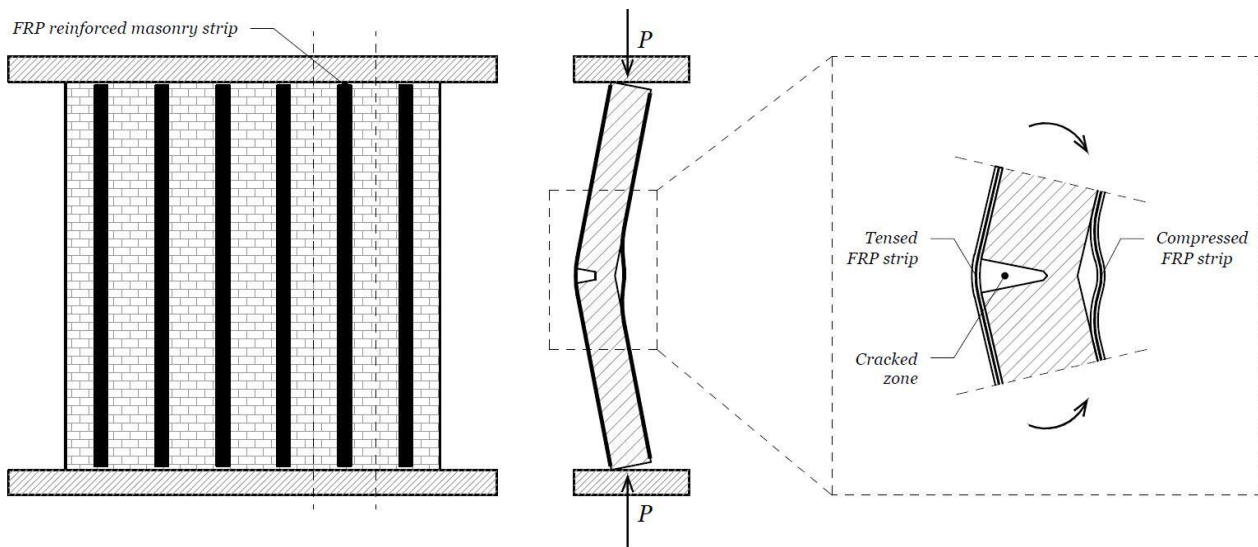
Fig. 1 - FRP strengthened masonry panel (example) and debonding mechanisms

Under the out-of-plane deflection of the reinforced panel (Figure 1), one layer of FRP is subjected to tension, but the other is subjected to compression. Under these conditions, the two reinforcement layers are subjected to tension and compression, respectively. At the same time, the increase in axial tension in the compressed FRP tape can also trigger a delamination process tension.

The problem of interfacial deboning is a fundamental problem in the structural performance of almost any type of composite or layered structure [16].

The present work aims to study the behaviour of a slender structural element subjected to axial loads, and to highlight the different behaviour of the reinforcements when they are stretched or compressed. The main objective is to provide a simplified method to predict delamination or loss of effectiveness of the reinforcement in the compressed region.

Analysing the state of art, this paper:
- Provides an analytical closed-form expression for the buckling delamination length;
- Validate the prediction of critical load for a prismatic compressed beam-column.

BUCKLING ANALYSIS

In this phase the general method of calculating the critical load for a beam-column hinged at the ends is illustrated; then the case of a beam-column composed of no-tension and brittle material (e.g. stone, marble) with eccentric load, which better approximates the common real cases, is analysed. Finally, the reinforcement layers are analysed.

A compressed beam-column with no-tension constitutive model may experience three stress regimes:
i. every cross-section is compressed;
ii. every cross-section is partially damaged;
iii. the beam-column is compressed at the ends and cracked in its remaining parts.
In this study, the iii) phase is considered.

Buckling analysis of a no-tensile structural element

A beam-column element subject to axial compression could fail either by buckling or by reaching the maximum compression stress. The prediction of the critical load value obtained with the Euler formula (1), is valid only for very long and thin beam-columns without geometric imperfections

----

$$P_e = \frac{\pi^2 EI}{l^2} \tag{1}$$

A solution that well approximates the real case was provided by Yokel [17]. This model provides an approximate solution of the critical load for compressed prismatic elements made of materials with no tensile strength. Refer to the beam-column in a state of post-buckling equilibrium represented in Fig. 2 with compression load applied with eccentricity $t/6 \le e < t/2$.

Fig. 2 - Cracked compressed beam-column with eccentric load
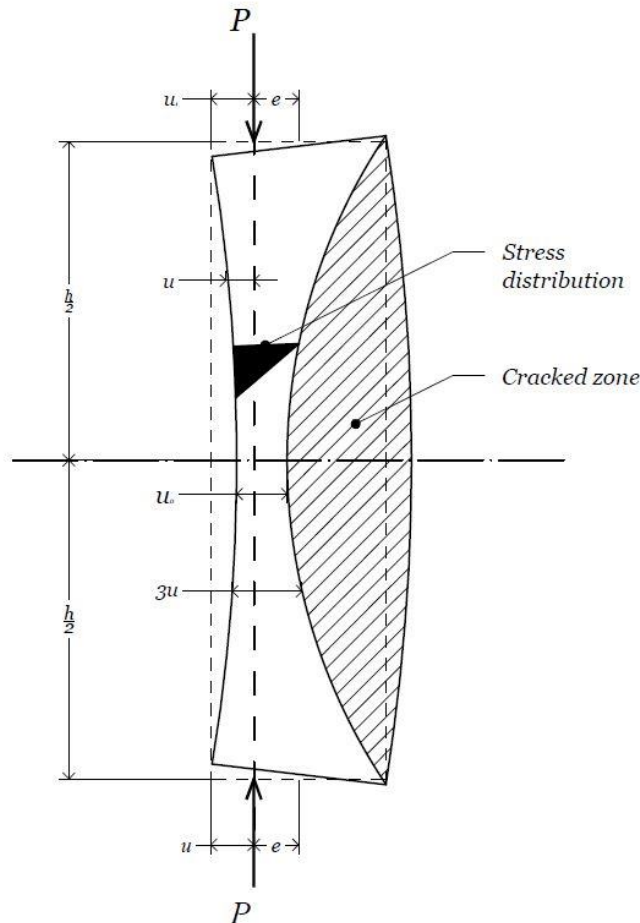
The dotted area represents the compressed area; the triangular shaded area represents the trend of the compression tensions in a generic section; u represents the distance between the compressed edge of the beam-column and the load application line. The maximum value of u (u1) is at the beam-column top, while the minimum value (u0) is in the middle, as shown in Figure 2.

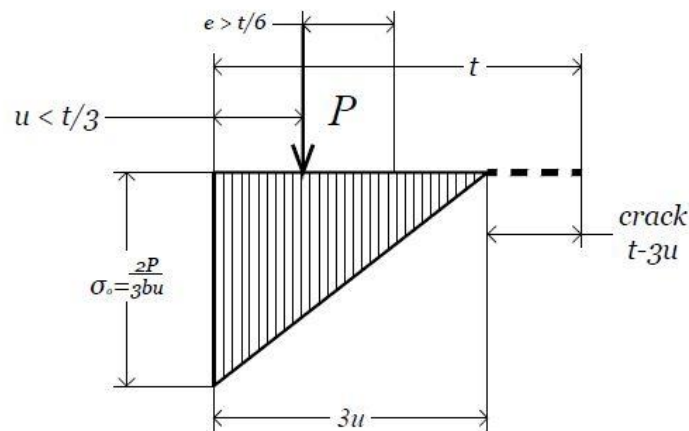

Fig. 3 - Stress distribution in the middle section

The maximum value of the compression tension could be expressed as follows:

$$\sigma_{max} = \frac{2P}{3bu_0} \tag{2}$$

The value of the equivalent critical load is determined:

$$P_{ec} = \frac{9}{4}\frac{Ebu_1{}^3}{h^2} \tag{3}$$

Yokel [17] determined with good approximation the critic load value:

$$P_{cr} = 0.285\,P_{ec} \tag{4}$$

That is:

$$P_{cr} = 0.64125\,\frac{Ebu_1{}^3}{h^2} \tag{5}$$

The critical load value could be also approximated to:

$$P_{cr} = 8\pi^2\left(\frac{1}{2}-\frac{e}{t}\right)^3\frac{EI_0}{h^2} \tag{6}$$

Where I_0 represent the moment of inertia of non-cracked sections.
For $e = 0$, Equation 6 is the Euler formula.

Analytical model of FRP reinforced beam-column

The assumption that the material is elastic in compression and without any resistance in tension is postulated. A slender element is considered with a constant rectangular section and reinforced on the major faces with FRP strips applied longitudinally to the support, Figure 3. As mentioned above, the instability of the support leads to distinguish a compressed and a tensed area.

Therefore, the reinforcement applied to the tensed area follows the deformation of the substrate. The reinforcement in the compressed area could be subject to delamination phenomena due to the high stress [7] that occurs at the interface of the two materials, which can lead to the propagation of micro-cracks present or to the formation of new ones.

Pre-buckling phase

In the loading phase before the critical load value, the beam-column only bears axial compression stresses (i) phase. The compression stress is given by the area density of the load on the overall section. Previous studies [18] illustrated how the behaviour of the instability of thin layers (e.g. FRP reinforcements) depends on the stiffness of the substrate and of the reinforcement itself.

Buckling phase – FRP stability contribution

The beneficial contribution to the stability of the beam-column given by the reinforcement in the tensed area can be investigated using the elastic model of the beam-column on the Winkler elastic soil [19]. The conditions of instability of a beam-column of finite length with hinged ends (Figure 3) can be expressed by the following:
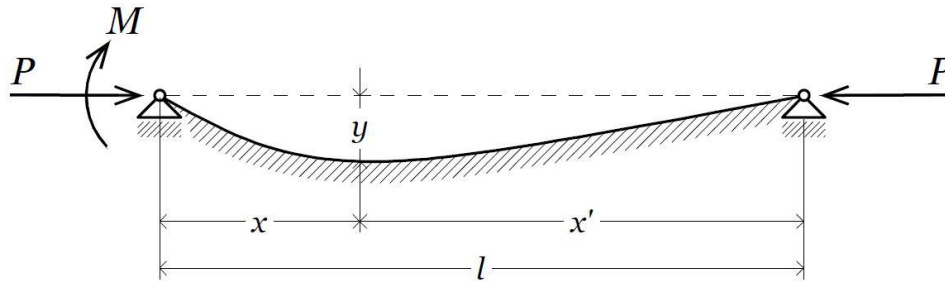

Fig. 2 - Static diagram of hinged beam-column on elastic soil

The + or - sign in the denominator correspond to a symmetrical or asymmetrical inflection respectively. When no moments are applied to the ends, the beam-column can have a deflection of finite value only if Equation 7 is cancelled.

This can only happen if $\alpha\beta = 0$, which provides the value of the critical load as a solution:

$$P_{cr} = 2\sqrt{kEI} \tag{8}$$

Equivalent to the critical load for a beam-column of infinite length.

Since this condition does not consider the finite length of the beam-column, it can be stated that it is not the complete solution; therefore, other possibilities must be considered.

From the same denominator another condition is obtained:

$$\cosh \beta l \pm \cos \alpha l = 0 \tag{9}$$

Since $\cosh \beta l > 1$ e $\cos \alpha l < 1$, this equation cannot be satisfied by real values of α e β, where:

$$\alpha = \sqrt{\sqrt{\frac{k}{4EI}} + \frac{P}{4EI}} \; ; \quad \beta = \sqrt{\sqrt{\frac{k}{4EI}} - \frac{P}{4EI}} \tag{10}$$

It should therefore be noted that the value of the critical load due to the instability of a hinged beam-column must be sought if $P_{cr} > 2\sqrt{kEI}$.

Considering thus:

$$\beta = i\,\overline{\beta}$$

where:

$$\overline{\beta} = \sqrt{\frac{P}{4EI} - \sqrt{\frac{k}{4EI}}}$$

With these substitutions the following equation is obtained:

$$\cosh \overline{\beta} l \pm \cos \alpha l = 0$$

Which is satisfied by the following:

$$(\alpha - \overline{\beta})l = n\pi$$

For odd values of n there is a positive sign in the penultimate equation; for even values, there is a negative sign. Substituting in the last one the expressions for α and β, we obtain the following formula for the critical load:

$$P_{cr} = n^2 \frac{\pi^2 EI}{l^2} + \frac{1}{n^2} \frac{kl^2}{\pi^2} \qquad (11)$$

Since in the specific case the first buckling mode is investigated, by setting $n = 1$ the value of the critical load is obtained:

$$P_{cr} = \frac{\pi^2 EI}{l^2} + \frac{kl^2}{\pi^2} = P_{cr,E} + \frac{kl^2}{\pi^2} \qquad (12)$$

k represents the FRP stiffness constant.

FRP reinforcement provides a beneficial effect to buckling, as the critical load value is increased by the quantity proportional to the characteristic constant of the reinforcement and to the length of the same.

Considering Equations 5 and 12, the reinforced beam-column governing equation is obtained:

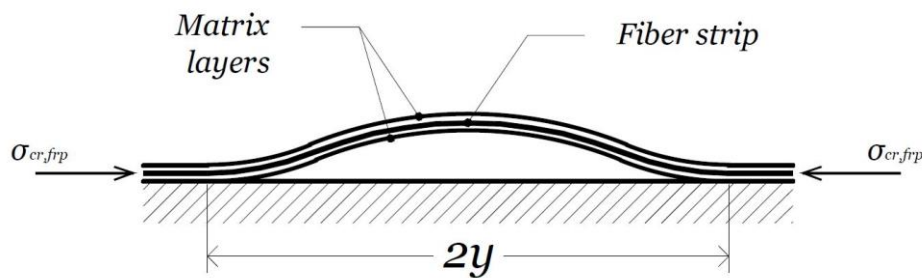$$P_{cr} = 0.64125 \frac{Ebu_1{}^3}{h^2} + \frac{kl^2}{\pi^2} \qquad (13)$$

Fig. 3 - FRP buckling on compressed face

Buckling phase – FRP buckling delamination

As reported in previous works [13], in the case of a soft substrate, the phenomenon of wrinkling occurs in the external film; in the case of a rigid substrate, the substrate is delaminated (Figure 5). This phenomenon does not depend on the substrate, but only on the reinforcement and on the dimensions of the initial delamination [13].

In case of high compression stresses, reinforcement delamination could occur without the presence of cracks or initial cracks. The instability of a thin laminate could be solved as a classic problem of buckling a strip with clamped ends. The following critical stress is therefore obtained [13]:

$$\sigma_{cr} = \frac{\pi^2 E_{frp}}{3(1 - v^2)} \left(\frac{t_{frp}}{2y}\right)^2 \qquad (14)$$

Where E is the Young's modulus and v is the Poisson's modulus, t is the thickness of the reinforcement layer and l is the delamination length. The deflection due to buckling is given by [13]:

$$w = \frac{1}{2} w_0 (1 + \cos \frac{2\pi x}{l}) \qquad (15)$$

Where w_0 is the maximum deflection, l is the delamination length. From the expression of the generic deflection and through geometric considerations, the expression of the maximum deflection is obtained [13]:

$$w_0^2 = \frac{4}{\pi^2} \varepsilon_c l^2 \qquad (16)$$

In the reinforced beam-column model, it is possible to consider - for the sake of simplicity - a linear distribution of the cracked areas according to the height previously illustrated in Fig.1.

In the model of the reinforced beam-column, a linear distribution (Fig. 3) of the cracked sections can be considered for simplification as the height varies since $l \gg t$.

The linear stress distribution leads to define the equation of the neutral axis in this way:

$$x(y) = \frac{2\,y\,(t-3u)}{h} + 3u \tag{17}$$

with $3u < x < t$

The compression stress in the beam-column at a generic height y is given by the following:

$$\sigma(y) = \frac{2\,P}{x(y)\,b} \tag{18}$$

or:

$$2\,P = \sigma(y) \cdot x(y) \cdot b \tag{19}$$

As the compression stress is equal to the critical stress, the reinforcement is delaminated. By equating equations (14,17,19), it is possible to find the delamination position.

Supposing $u_1 = t/3$, the following is obtained:

$$2\,P_{cr} = \frac{\pi^2 E_{frp}}{3(1-v^2)}\left(\frac{t_{frp}}{2y}\right)^2 \frac{2y\,(t_{beam}-3u)+3uh}{h}\,b \tag{20}$$

or:

$$P_{cr} = \frac{1}{24}\frac{\pi^2}{(1-v^2)}E_{frp}\frac{t_{frp}^{\,2}}{y^2}\frac{2y\,(t_{beam}-3u)+3uh}{h}\,b \tag{21}$$

or:

$$y^2 \cdot P_{cr} = A\,\alpha\,\beta\,(2yt_{beam}-6uy+3uh) \tag{22}$$

from which:

$$y^2\,P_{cr} - y(2\gamma t_{beam}-6u\gamma) - 3uh\gamma = 0 \tag{23}$$

where:

$$A = \frac{1}{24}\frac{\pi^2}{(1-v^2)};$$
$$\alpha = \frac{b}{h};$$
$$\beta = E_{frp}\,t_{frp}^{\,2};$$
$$\gamma = A\,\alpha\,\beta \tag{24.i}$$

Thus, the delamination half-length is:

$$y = \frac{(2\gamma t_{beam}-6u\gamma) \pm \sqrt{(2\gamma t_{beam}-6u\gamma)^2 + 12\,P_{cr}u\,\gamma\,h}}{2\,P_{cr}} \tag{25}$$

CASE STUDY

The aim of this study is to provide a simplified method to predict delamination or loss of effectiveness of the reinforcement itself during the buckling phenomenon.

In this section, a numerical application is illustrated. The case of the beam-column with hinged ends and reinforced on both the major faces with FRP – as in the formulation of the problem – is considered.

In analogy with the experimental campaign carried out in [20], the same brittle homogeneous beam-column and FRPs reinforcements are considered. Poisson ratio is set 0.37 for all reinforcement considered, as in its typical values. Materials mechanical and geometrical parameters are summarized in Table 1. Marble beam-column analysed in [20] are depicted in Fig. 6. Specimens with SRP/BFRP strips on both side surfaces - dimensions 300 mm x 28 mm - were subjected to compression until the reinforced SRP/FRP strips on the compressed side of the specimen were delaminated. For both types of reinforcement, the marble surfaces were treated with a primer and

----

then a two-component epoxy adhesive was used as a fibre matrix to ensure the adhesion to the substrate.

The test setup used during the tests included: cell loading to measure compressive load, P; three LVDTs to record lateral deflections; one LVDT to measure vertical displacements; two strain gauges (E1-E2) in the middle of the specimen span on the lateral surface to measure the deformation of SRP/BFRP strips under compression.

Tab. 1 - Mechanical parameters

MARBLE				SRP*				BFRP*			
$t_{beam-column}$ (mm)	$b_{beam-column}$ (mm)	$h_{beam-column}$ (mm)	$E_{beam-column}$ (kN/mm^2)	t_{frp} (mm)	b_{frp} (mm)	h_{frp} (mm)	E_{frp} (kN/mm^2)	t_{frp} (mm)	b_{frp} (mm)	h_{frp} (mm)	E_{frp} (kN/mm^2)
6	28	300	68.90	0.48	28	300	118*	0.14	28	300	100*

*Provided by manufacturers.

Table 2 summarizes experimental results by compression tests on column specimens obtained by [20].
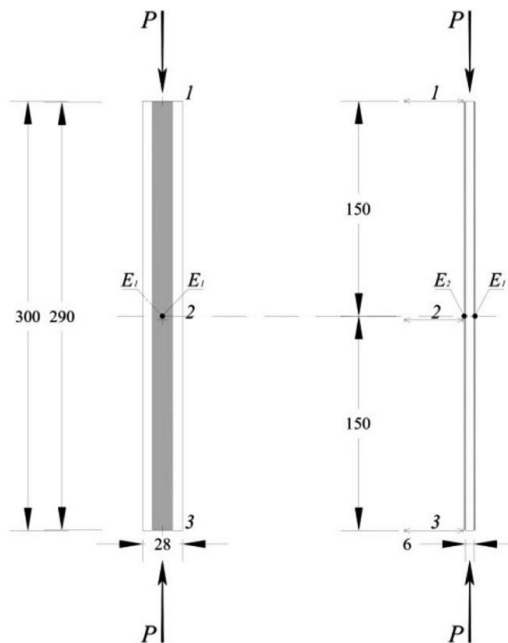

Fig. 4 - Specimens with SRP/BFRP strips under compression

Tab. 2 - Experimental results on beam-column specimens

SPECIMEN	TYPE OF STRENGTHENING	EXP. BUCKLING LOAD (mean value)
UMC	-	4.56 kN
RMC 2	SRP	6.99 kN
RMC 3-4	BFRP	5.53 kN

Once the mechanical and geometrical parameters of the reinforcement and critical load for reinforced beam-column configuration are known, it is possible to determine the experimental stiffness constant value from Equation 24 (Table 3).

Tab. 3 - Stiffness constant calculation

TYPE OF STRENGTHENING	k (N/mm^3)
SRP	0.7544
BFRP	0.5944

Once all parameters all well-defined, it is possible to determine the delamination length which occur in the FRP reinforcement layer as the critical stress is achieved. These lengths are 10.65 mm and 35.29 mm for BFRP and SRP reinforced beam-columns, respectively.

Obviously, the delamination lengths increase as the axial load increases until the specimen failure, as reported in [20]. This paper aims to determine the delamination length in the FRP reinforcement layer at the exact moment when the beam-column undergoes buckling.

NUMERICAL APPLICATIONS

In this section, a numerical application is illustrated. The case of the hinged beam-column and reinforced on both the major faces with FRP – as in the formulation of the problem – is considered.

Different beam-column lengths are considered, from 200 to 425 mm. The beam-column is assumed made of marble material of fixed dimensions (Table 4).

Tab. 4 - Mechanical parameters for numerical application

$t_{beam-column}$ (mm)	t_{frp} (mm)	$b_{beam-column}$ (mm)	$h_{beam-column}$ (mm)	$E_{beam-column}$ (kN/mm^2)	E_{frp} (kN/mm^2)	v (-)	u (mm)
6	0.14 or 0.48	28	from 200 to 425	68.90	100 or 118	0.37	2

Once the mechanical and geometrical parameters of the reinforcement type are known, it is possible to determine the value of the critical stress and delamination, as illustrated in Table 5.

Tab. 5 - BFRP reinforcement parameter calculation

h (mm)	α (-)	β (-)	γ (mm)	$\sigma_{cr,frp}$ (N/mm²)	y/h (-)
200	0.14	1.96	0.13	31.62	0.0769
225	0.14	1.96	0.13	34.33	0.0656
250	0.12	1.96	0.12	42.02	0.0533
275	0.11	1.96	0.10	50.71	0.0441
300	0.10	1.96	0.10	60.35	0.0371
325	0.09	1.96	0.09	70.93	0.0316
350	0.09	1.96	0.08	82.44	0.0272
375	0.08	1.96	0.07	94.88	0.0237
400	0.07	1.96	0.07	108.23	0.0208
425	0.07	1.96	0.07	122.49	0.0184

Table 6 shows the parameters obtained for SRP reinforced beam-columns.

Tab. 6 - SRP reinforcement parameter calculation

h (mm)	α (-)	β (-)	γ (mm)	$\sigma_{cr,frp}$ (N/mm²)	y/h (-)
200	0.14	27,19	1,81	39,35	0,2566
225	0.14	27.19	1.81	43.02	0.2181
250	0.12	27.19	1.61	52.89	0.1771
275	0.11	27.19	1.45	63.98	0.1463
300	0.10	27.19	1.32	76.28	0.1229
325	0.09	27.19	1.21	89.76	0.1045
350	0.09	27.19	1.12	104.41	0.0900
375	0.08	27.19	1.04	120.23	0.0783
400	0.07	27.19	0.97	137.20	0.0687
425	0.07	27.19	0.91	155.32	0.0608

It is noted that the critical stress required to start the delamination decreases as the length of the beam-column increases. The graph in Figure 5 shows the trend of the delamination length percentage on total length with respect to the variation of the beam-column and reinforcement length.
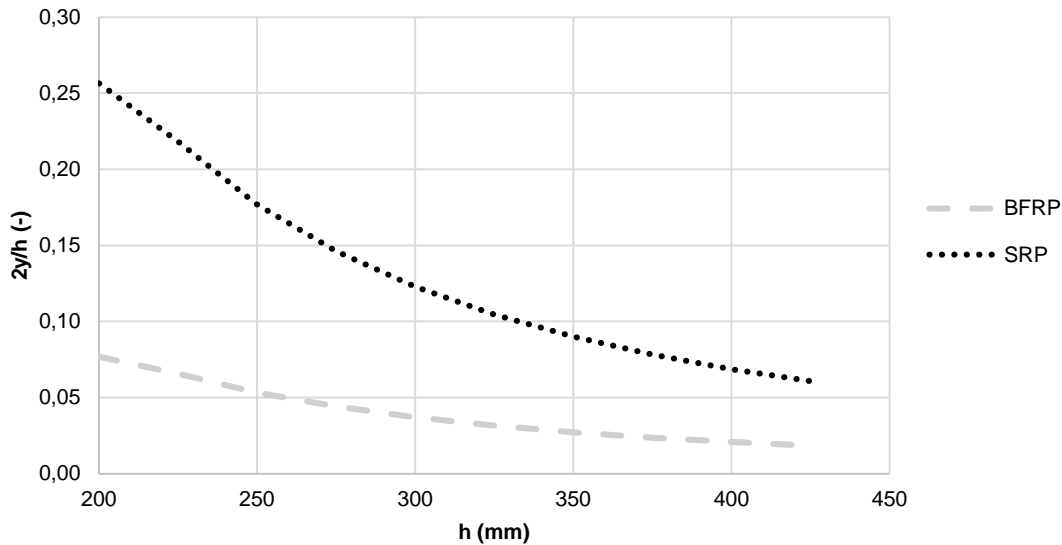
Article no. 26

THE CIVIL ENGINEERING JOURNAL 1-2021

Figure 5 - Delamination percentage on total beam-column length

CONCLUSIONS

Since FRP strips reinforcements are scarcely resistant to compression, the present paper focuses its attention on this characteristic. Slender beam-columns in homogeneous linear brittle no-tension material and subjected to compression, both normal and FRP-reinforced conditions are considered. The problem of the stability of a no-tensile structural element and reinforced with FRP is analytically analysed, according to the elastic theory. The aim of this work is to highlight the different behaviour of reinforcements when they are tense or compressed, and to provide a simplified method to predict detachment or loss of effectiveness of the reinforcement itself. In particular, the reinforcement layer applied in the tense face of the specimens showed a stability contribution, while the one applied in the opposite side underwent buckling delamination. If the geometric and mechanical parameters of materials are known, it is possible to estimate the critical load of the entire beam-column. It is therefore possible to establish the delamination length of the compressed reinforcement at the critical load and therefore of the critical tension.

The results obtained make it possible to estimate the contribution to stability resulting from the use of FRP reinforcements. The study presented analyses the contribution of BFRP and SRP reinforcements. It is observed that increasing the height of the structural element considered, the percentage of delamination on the total length of the reinforcement decreases according to a non-linear trend. In the case of the BFRP reinforcement, the critical tension necessary to trigger delamination - for a 400 mm high column - triples its value with respect to the same 200 mm high structural element. The same phenomenon could be observed for SRP reinforcement.

The results obtained by means of hypotheses and simplified theories make it possible to estimate the value of the critical load at which delamination of the compressed reinforcement occurs, which loses its effectiveness for low load values. A further result is consequently that of providing a method for estimating the critical load of the reinforced beam-column, developing a useful, practical, and rapid instrument in the design phase.

REFERENCES

[1]   T. C. Triantafillou, "Strengthening of Historic Structures with Advanced Composites: A Review," in *Recent Advances in Composite Materials*, Dordrecht: Springer Netherlands, 2003, pp. 337–344.

[2]   T. C. Triantafillou, "Composites: a new possibility for the shear strengthening of concrete, masonry and wood," *Compos. Sci. Technol.*, vol. 58, no. 8, pp. 1285–1295, Aug. 1998.

[3]   C. Faella, E. Martinelli, G. Camorani, M. A. Aiello, F. Micelli, and E. Nigro, "Masonry columns confined by composite materials: Design formulae," *Compos. Part B Eng.*, vol. 42, no. 4, pp. 705–716, Jun. 2011.

[4]   C. Faella *et al.*, "Masonry columns confined by composite materials: Experimental investigation," *Compos. Part B Eng.*, vol. 42, no. 4, pp. 692–704, Jun. 2011.

[5]   L. Ascione, L. Feo, and F. Fraternali, "Load carrying capacity of 2D FRP/strengthened masonry structures," *Compos. Part B Eng.*, vol. 36, no. 8, pp. 619–626, Dec. 2005.

[6]   M. Corradi, A. Borri, and A. Vignoli, "Strengthening techniques tested on masonry structures struck by the Umbria–Marche earthquake of 1997–1998," *Constr. Build. Mater.*, vol. 16, no. 4, pp. 229–239, Jun. 2002.

[7]   M. R. Valluzzi, D. Tinazzi, and C. Modena, "Shear behavior of masonry panels strengthened by FRP laminates," *Constr. Build. Mater.*, vol. 16, no. 7, pp. 409–416, 2002.

[8]   D. Bruno and F. Greco, "An asymptotic analysis of delamination buckling and growth in layered plates," *Int. J. Solids Struct.*, vol. 37, no. 43, pp. 6239–6276, Oct. 2000.

[9]   J. Aboudi and R. Gilat, "Buckling analysis of fibers in composite materials by wave propagation analogy," *Int. J. Solids Struct.*, vol. 43, no. 17, pp. 5168–5181, Aug. 2006.

[10]   A. Marouene, R. Boukhili, J. Chen, and A. Yousefpour, "Buckling behavior of variable-stiffness composite laminates manufactured by the tow-drop method," *Compos. Struct.*, vol. 139, pp. 243–253, Apr. 2016.

[11]   G. Atlihan, "Buckling analysis of delaminated composite beams," *Indian J. Eng. Mater. Sci.*, vol. 20, no. 4, pp. 276–282, 2013.

[12]   D. Tumino, F. Cappello, and D. Rocco, "3D Buckling Analysis of Multidelaminated Composite Specimens," *Sci. Eng. Compos. Mater.*, vol. 14, no. 3, Jan. 2007.

[13]   L. M. Kachanov, "Delamination Buckling," 1988, pp. 19–56.

[14]   A. Gawandi, L. A. Carlsson, T. A. Bogetti, and J. W. Gillespie, "Mechanics of discontinuous ceramic tile core sandwich structure: Influence of thermal and interlaminar stresses," *Compos. Struct.*, vol. 92, no. 1, pp. 164–172, Jan. 2010.

[15]   O. Rabinovitch and E. Hamed, "Bending Behavior of Sandwich Panels with a 'Soft' Core and Embedded Rigid Inserts," in *Sandwich Structures 7: Advancing with Sandwich Structures and Materials*, Berlin/Heidelberg: Springer-Verlag, pp. 261–270.

[16]   J. W. Hutchinson and Z. Suo, "Mixed Mode Cracking in Layered Materials," 1991, pp. 63–191.

[17]   F. Y. Yokel, "Stability and capacity of members with no tensile strength," *ASCE J. Struct. Div.*, vol. 97, pp. 1913–1926, 1971.

[18]   H. Mei, R. Huang, J. Y. Chung, C. M. Stafford, and H.-H. Yu, "Buckling modes of elastic thin films on elastic substrates," *Appl. Phys. Lett.*, vol. 90, no. 15, p. 151902, Apr. 2007.

[19]   M. Hetényi, *Beams on Elastic Foundation: Theory with Applications in the Fields of Civil and Mechanical Engineering*. Ann Arbor: University of Michigan Press, 1946.

[20]   R. Capozucca, E. Magagnini, and M. V. Vecchietti, "Delamination Buckling of FRP: Experimental Tests and Theoretical Model," 2020, pp. 753–766.

STRUCTURAL CARTOGRAPHIC ANALYSIS OF A THEMATIC ATLAS WORK: EXAMPLE OF THE CZECH HISTORICAL ATLAS

Tomáš Janata, Petra Jílková and Jan Daniel Bláha

Czech Technical University in Prague, Faculty of Civil Engineering, Department of Geomatics, Thákurova 7, Praha 6, Czechia; tomas.janata@fsv.cvut.cz; petra.jilkova@fsv.cvut.cz; jd@jackdaniel.cz

ABSTRACT

The article introduces the Czech historiographical work called the Czech Historical Atlas and presents its analysis in terms of its concept, structure and technical layout. The primary focus is on the atlas content and its subdivision into thematic and logical sections or the semiological structure of the used space. Last but not least, the cartographic and technical aspects of the atlas format are also analysed, including, for example, the analysis of used scales or cartographic projections. The findings are presented through a series of visuals and interpreted in the context of the thematic concept of the atlas. The authors' aim is to present the currently not much addressed structural analysis of a cartographic atlas, which allows revealing the potential for the innovation of an original cartographic work.

KEYWORDS

Historiography, atlas cartography, Czech Historical Atlas, cartographic semiology

INTRODUCTION

The Czech Historical Atlas (hereinafter also CHA, [1]) is one of the new works of Czech historiography, aiming at least partially at presenting a complex overview of a selected segment of the Czech history, both in terms of the time frame (20th century) or the spatial or material scope. The atlas has come out after approximately five years of work as another achievement of a team of historians, cultural geographers and cartographers. It builds on the cooperation among the team members, who joined efforts in the preparation of the Academic Atlas of Czech History (hereinafter also AACH, [2] – for more information cf. [3]), which, in many respects, can be considered as a predecessor of CHA. Therefore, in this study, the Czech Historical Atlas will be, to some extent, compared with AACH, particularly with its last chapter devoted to modern history.

From the very beginning, the Czech Historical Atlas was conceived completely differently than the Academic Atlas of Czech History. While cartographers had not been invited to the design and the initial phase of the AACH preparation and development, and thus the map section of the work was only created in a more advanced phase of work on the atlas, during the design of CHA, the cartographic team had prepared a set of recommendations at the very start of work on the atlas, and these recommendations were consulted with historians as the guarantors of the atlas content part. Based on these recommendations, a set of technical designs, models and graphic styles was created to be subsequently applied in the development of the atlas.

At the start of work on the atlas, thematic sections were discussed and identified to be further divided into chapters. Based on the graphic layout, this structure was fitted with individual text fields, maps, images, reproductions and other content components. The aim was to achieve a higher level of internal balance and consistency than was the case of AACH. From the very beginning, the authors, i.e. historians and geographers, were acquainted with the limited space for the textual and

pictorial part, and especially the part for thematic maps. Thanks to this step, the maps could be prepared conceptually from the beginning eliminating thus the need for their repeated reworking and modifications due to the limited space available.

OBJECTIVES

The objective of the analysis presented in this article is to provide a basis for further comparative analyses of atlas works, particularly those with a similar thematic focus. Another authors' objective is to reveal, on the one hand, undesirable disproportions in the methods of presenting the topic, and, on the other hand, the unused potential for further innovations of the atlas, which could find its application in future editions of the atlas.

Unfortunately, structural analyses of cartographic atlases are not common at present, although they can reveal valuable knowledge not only for the readers, but also for the authors of these works themselves. Instead, numerous current analyses are more guided by the effort to assess the quality (i.e. negative vs. positive aspects of the work) for the purposes of the peer-review process, or for an easier choice between two similar products (with an exception of, e.g., a review in [4], which evaluates the atlas as a whole in a relatively thorough way and goes into deeper comparisons). Other analyses are more focused on the analysis of the mathematical fundamentals of maps, addressing either the distortion of old maps or the cartographic projections available ([5]).

Such analyses, however, usually lack sufficient in-depth exposure to identify further possibilities for the innovation of the cartographic work (for future publications of the work, for further cooperation of cartographers with experts in the thematic content, etc.). It is structural analysis that can help to reveal, among other things, the relationship between the thematic focus of maps in the atlas and the degree of its complexity, as well as the depth of the concept of the work (appropriate diversity of scales, used methods of thematic cartography, etc.). The results of such an analysis in particular lead the authors to questions like: Has the potential of cartographic representation of the thematic content been used effectively? Was the effort of the experts specializing in the thematic content of maps to include in it as many known objects and phenomena as possible adequate or over the top?

A relatively crucial step is also the visualization of the results of the analysis allowing a simple synthesis with a subsequent comparison. In addition to commonly used visualization concepts of similar data (e.g. [6]), the authors built on their previous experience in this type of analysis.

Atlas Concept

Unlike AACH, whose topics offer an overview of periods from prehistory to the beginning of the 21st century, CHA is exclusively devoted to selected 20th-century chapters considered as periods of great social changes (not only) in Central Europe. Thus, it extensively develops the topics treated in AACH only in the last chapter dedicated to modern history, or introduces completely new topics. With a view to the chronological and thematic continuity of both atlases works, individual parts of the analysis will compare the CHA content and structure mainly with the AACH last Chapter V. The comparison with AACH as a whole does not seem to be very useful due to the different scope, focus and concept of both works (see Table 1).

In contrast to most historiographical works, which typically respect the chronological subdivision of the thematic content, CHA applies a relatively non-traditional form of a thematic subdivision placing the content of depicted topics in factual and social contexts.

Tab. 1 Comparison of CHA and AACH by scope. Source: authors.

	CHA	AACH	AACH (Chap. V)
number of pages	297	587	89
number of maps	96	365	73
dimensions	234 × 326 × 28 mm	308 × 427 × 60 mm	—
weight	970 g	5020 g	—
volume	2136 cm^3	7891 cm^3	—

If we consider the time aspect as a kind of horizontal scaling of reality, we cannot neglect the very significant vertical aspect that puts the atlas content in a factual, social context and, unlike the majority of historiographical works respecting primarily the chronological, horizontal plane, represents a non-traditional form of thematic division.

CHA divides the events of the 20th century into three vertical pillars (thematic sections), called Space, Time and Society. Although the meaning of the pillars is largely clear from the terms used, they are not discrete areas trying to separate mutually interconnected historical events. On the contrary, the topics overlap and the overall attempt is to present history not as an all-encompassing list of individual chronologically consecutive events, but rather as a selection of thematically interesting and cartographically not very often presented areas, which, however, must be categorized and subdivided to be more reader-oriented.
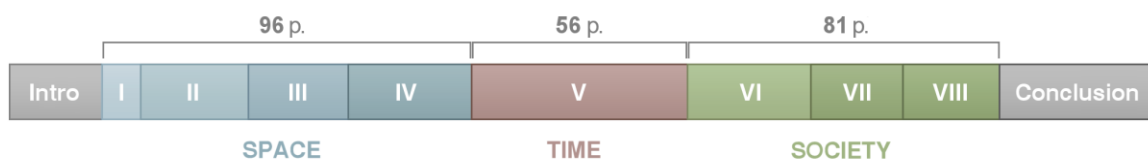

Fig. 1 – Atlas subdivision into individual sections and chapters. Source: authors.

The first third of the work covers the chapters of the section devoted to Space (Chapters I – IV, occupying a total of 96 pages, or 87 pages of actual content, respectively; presenting a total of 42 maps), which mostly describe the territorial delimitation and integration of the Czech Lands (Czechoslovak Republic/Czech Republic) into Central European and international structures in individual phases of the 20th-century historical development, the division of the territory in relation to the economic or political development, together with political and administrative maps, as well as socio-economic themes on the stage of changes in space. Related to them is a small part of the section devoted to changes in the landscape as such and its utilization.

The shorter middle passage, Time (single Chapter V, a total of 56 pages; presenting 29 maps), focuses on military and political topics. This chapter, for the most part, is cartographically more demanding for processing and the cartographic concept. Topographic data appear in contrast

to extensive historical descriptions of the respective events, the data are non-uniformly distributed and frequent changes in historical development must be reflected. This brings the necessity of selecting the topics with regard to the final processing.

The final section, Society (Chapters VI – VIII covering a total of 81 pages, or 76 pages of actual content, respectively; presenting 25 maps), addresses social issues like migration and population transfers, general demographic issues (national or religious structure, education, etc.) or diplomacy and Czech footprints around the world.

Structural Analysis in Terms of Thematic Content

This part of structural analysis evaluates the atlas work in terms of the thematic focus of maps. For the purposes of the analysis, individual maps were typologically divided into seven thematic categories identified by the authors. In the classification, the authors drew upon previous studies (e.g. [3, 7]) and upon other general categorizations of maps with a thematic content (see [8]), among other things, with respect to the comparability with the previous AACH. The aim of this analysis was to assess the typology of maps, particularly in connection with their inclusion in the thematically defined sections of the atlas (see the CHA concept). The chart in Figure 2 shows the proportion of maps with a specific thematic focus in the whole atlas and within individual sections. In the case of polythematic maps (about 22% of all the maps, see Figure 3), where the map could not be unambiguously classified in one single category only, all topics were identified and the inclusion in the respective category was expressed by a quotient denoting the representation of the given topic in the map (e.g. in the case of three topics uniformly represented within one map, each of them was expressed by one third).
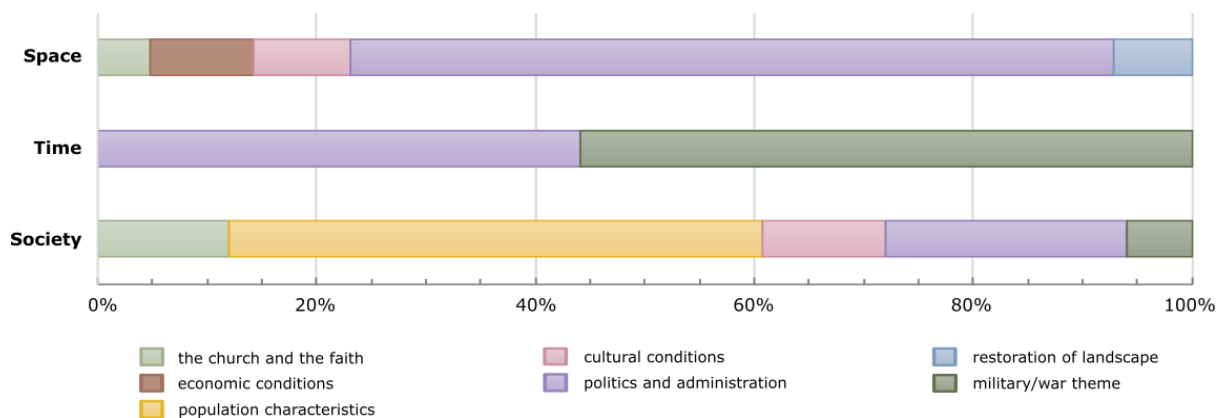

Fig. 2 – *Structure of the thematic focus of maps in individual sections of the atlas. Source: authors.*

The degree of the polythematic focus of maps differs significantly within individual sections of the atlas. The thematically very narrowly defined atlas section (nearly 97% of monothematic maps) is the section of "Time" devoted to selected chapters from military and political history. Thus, most maps with *military/war themes* can be found in this section, representing mainly the issues of prisoner-of-war camps during the First World War or the events of the Second World War. Most polythematic maps can be found in the section of "Society", where up to 52% of maps illustrate more than one topic.

MT monothematic maps
PT polythematic maps
2T polythematic maps (two topics)
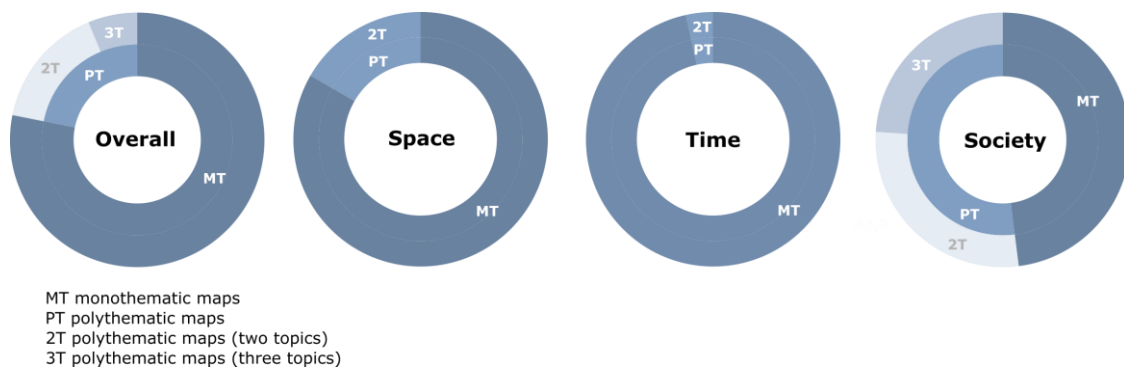3T polythematic maps (three topics)

Fig. 3 – The degree of polythematicity of maps in particular sections of the atlas. Source: authors.

The least elaborated thematic category is *landscape and space reconstruction*, to which mere 3.1% of all maps are devoted (see Figure 4), and these maps are only included in the "Space" section, in the chapter reflecting changes in the landscape due to political and economic changes. This result clearly shows the concept of the atlas as a work that puts more emphasis on the social component of historical events rather than their impacts on shaping the landscape. The same unambiguous classification applies to the maps of *economic conditions* or *population characteristics* where the maps illustrating the topics of industry and trade or the utilization of water resources were included in the thematic category of *economic conditions* by the authors, and the maps of the national structure, migration, etc. were put in the category of *population characteristics*. Unlike landscape reconstruction, however, these thematic categories very often appear in connection with other thematic categories (e.g. cultural or political situation).

The maps of *population characteristics* can only be found in the "Society" section, where they account for almost half of all maps. The population topic most frequently occurs in connection with *political topics* in the chapters addressing forced population transfers during the Second World War. In addition to migration processes (natural or forced), the maps of the national or religious structure of the population were also included in population characteristics. The "Space" section, in turn, is dominated (70% of all maps) by an extensive category of *politics and administration*, which includes maps describing the political and territorial structure, election results, course of a revolution or diplomatic relations. While nearly half of the maps in CHA (49.6%) focus on the issues of the political and territorial structure, only 20% of maps elaborate this topic in AACH. On the contrary, the chapter in AACH devoted to modern history is more oriented towards the economic situation, which is the most addressed topic in this atlas (26.3% of maps), or the topic of landscape and space reconstruction (12.5% of maps).
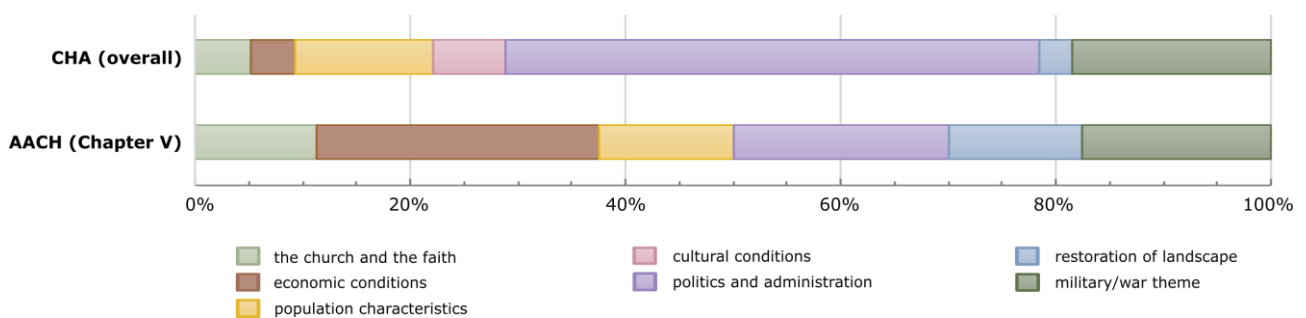

Fig. 4 – Comparison of thematic focus of maps within CHA and AACH. Source: authors.

Structural Analysis in Terms of Meta-Cartographic Semiotics

Another approach used by the authors is the analysis of the atlas in terms of meta-cartographic semiotics (see [9]), i.e. analysis of the proportion of visuals, maps and texts within the atlas and its sections, based on the graphic layout of individual pages. This analysis primarily covers the assessment of the mutual balance of the textual (texts accompanying individual topics of the atlas) and visual components of the atlas, including, in addition to a separate semiological category of *map*, also the representation of categories of *graph, photograph* and *map reproduction*. Map reproductions are classified as a separate category with regard to the thematic focus of the atlas. This part of the analysis can be compared with AACH. In principle, this analysis is based on the authors' experience gained from the analysis of textbooks [10, 11], but also from other studies [12, 13].

The analysis investigated the spatial proportions of the above semiological categories – maps, texts (tables are part of the text category due to their small number), visuals (graphs, photographs, map reproductions), as well as empty (unused) space (blank pages, etc.). For the purposes of a more accurate analysis, each page was divided into halves, thirds and quarters. This choice was based on the setting pattern of pages (two columns and, in many places, the space is divided into thirds with the ratio of the text to the remaining part of - one to two or two to one).

In terms of the overall concept of the atlas (for more detail see Figure 5), maps take up less than one third of the page area of the map and texts more than one third (including tables). These two basic categories represent more than 60% of the atlas structure leaving thus a relatively large space for further visual accompanying material, which can be expected considering the encyclopaedic nature of the publication. About one sixth (17%) of the volume is occupied by photographs, and about half of this percentage (8%) by map reproductions. The absolutely marginal part are graphs, and a relatively surprising finding is that there is approximately one tenth of the space without any use, which is largely due to relatively strict setting patterns.
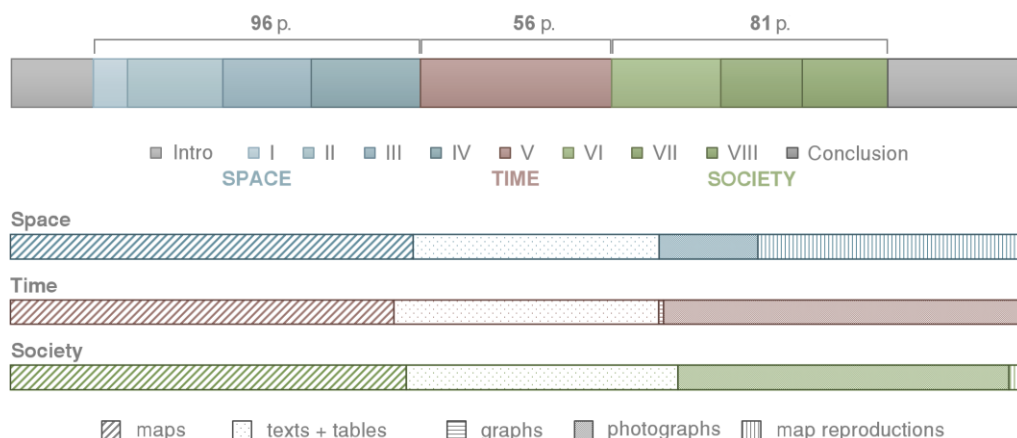

Fig. 5 – Structure of atlas sections in terms of the number of pages and proportions of individual content components

So much for the general concept of the atlas as a whole; more interesting figures can be obtained from a more detailed analysis of its individual sections. It is obvious that all the three sections contain a similar percentage of the cartographic or textual content within their defined share in the atlas, identically around two-fifths and one-quarter in the order they appear in the atlas. The remaining 35% of the space in the section of Time and Society is mostly devoted to photographs – map reproductions only represent a marginal item accounting for up to 2%, and graphs in the section of Time for up to 0.5%. The section of Space, however, is laid out in a completely different way; map reproductions represent an important source of its content comparable in scope to the textual

component. Here, the display of period maps complements particularly the topics devoted to the development of the administrative division and the development of the Central European space as such.

The above mentioned only applies to the three main chapters with cartographic contents. The sections of Introduction and Conclusion contain practically only text (with a small percentage of map reproductions), and, therefore, they are not included in the comparison in the bottom part of Figure 5.

Comparing the lexical aspects with AACH Chapter V, reflecting the period of the 20th century, we find the greatest similarity with the section of Society. To be specific, in AACH, pictures and reproductions occupy about one third of the space, while texts account for one quarter and maps for the remaining ca two fifths. This subdivision is similar to the last section of CHA and may reflect the openness of the last AACH chapter to social issues like leisure, nature conservation, elections, etc., as AACH as a whole differs from its Chapter V quite significantly. However, the differences in the content distribution within CHA are not so obvious to be able to draw deeper conclusions from the analysis on this topic.

CARTOGRAPHIC ANALYSIS OF THE ATLAS

Complexity of the Map Content

In the first part of cartographic analysis, individual maps of the atlas were assessed in terms of their *content complexity*. The analysis of the thematic content of maps was mostly based on a study [14]. The whole atlas is clearly dominated by analytical maps (61.5%), whereas synthetic maps were not identified in the atlas at all (see Figure 6). The complexity of the map content varies considerably across individual sections of the atlas, which is mainly due to their different thematic focus (see Figure 2). In the section of "Space" addressing in its chapters the *delimitation of borders* or *territorial changes*, analytical maps were mostly identified (73.8%). Within this section, the close connection of the content complexity with the typology of maps can be very well presented (see structural analysis in terms of thematic content), which reflects the diversity of approaches on the part of different experts (cf. historians' and geographers' approaches) to the presented topics. Analytical maps dominate particularly in the first three chapters of the section (87.5%) devoted mostly to administration and politics (91.5%), which were prepared with the participation of historians. The only exception is Chapter IV addressing the issues of landscape changes, where, on the contrary, 70% of complex maps can be identified. Typologically, maps with socially oriented topics (landscape reconstruction and economic or cultural conditions) completely dominate here, elaborated with the participation of experts from the field of social and historical geography.

Likewise, more than 75% of analytical maps can be found in the section of "Time" (see Figure 6). Compared to the previous section, however, there are many more so-called polycomplex maps, i.e. maps containing in addition to the representation of a larger number of phenomena also links among them (17.2%), even though this section is devoted to purely historical topics (administration and politics or military/war themes – see Figure 2). This fact testifies, above all, to the historians' efforts to achieve the maximally detailed and "content-complete" cartographic representation of the respective topic, which, unfortunately, not always allows a sufficient degree of cartographic generalization. An example of such a polycomplex map is e.g. the liberation of Czechoslovakia in 1945 (Chapter V.4). The "Society" section is completely different in terms of the map content complexity, as complex maps (76%) absolutely predominate there. The interconnection with the thematic focus was manifested here as well, because this section is also significantly dominated by maps devoted to social topics like migration and population transfers or general demographic issues (national and religious structure, education, etc.) (see Figure 2).
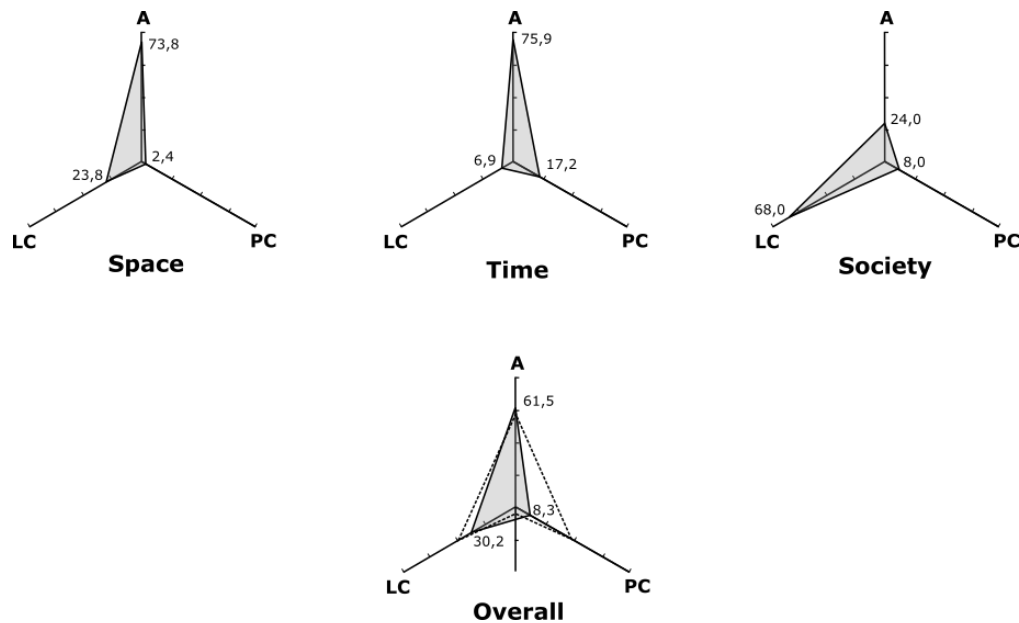

Fig. 6 – Percentage of the representation of analytical (A), less complex (MK) and polycomplex (PK) maps in the atlas. Source: authors.

For comparison, the previous graph also shows the result of the analysis of AACH Chapter V, where analytical maps also predominate (57.5%), like in CHA. Unlike CHA, however, at least a few synthetic maps (3.8%) can be found there.

Scale Series of Maps in the Atlas

In the next part of cartographic analysis, the design of scale series in the atlas was assessed (see Figure 7). A total of 25 different scales were identified in the atlas, of which 18 different scales were only used for 22 maps. Although the scale of these maps differs only minimally in many cases and the enlargement of the area to the nearest used scale would not cause the collision of the map content with the map frame, the adopted solution is certainly a justifiable step in most cases considering the territorial and content diversity of these maps. The illustrated topic is often related to areas situated outside the present-day territory of the Czech Republic or the territory of inter-war or post-war Czechoslovakia (e.g. on maps of Czech settlements in the Banat region or prisoner-of-war camps in selected European countries or the Asian part of Russia) and thus the difference in scale does not interfere with potential comparability in terms of spatial and temporal relationships. For other maps, specific scales are deliberately chosen (this mainly applies to large-scale maps) due to non-uniform coverage of the territory by the thematic content to display details of the area of interest (e.g. in maps of US troops advance in Western Bohemia or February Communist Takeover of 25 February 1948 in Prague).

The greatest *variability of map scales* was identified in the section of "Time" (a total of 13 scales were used for only 18 maps, i.e. 62% of maps in the whole section), which de facto demonstrates the diverse spatial scope of the section devoted to military and political topics related mostly to the areas of interest of inter-war and post-war Czechoslovakia (Prague, Western Bohemia, Slovakia) or Europe (France, Italy, Asian part of Russia, etc.). As the cartographers themselves commented in the introduction to the atlas, this section in particular was hard to grasp in terms of cartographic representation (Semotanová et al., 2019).
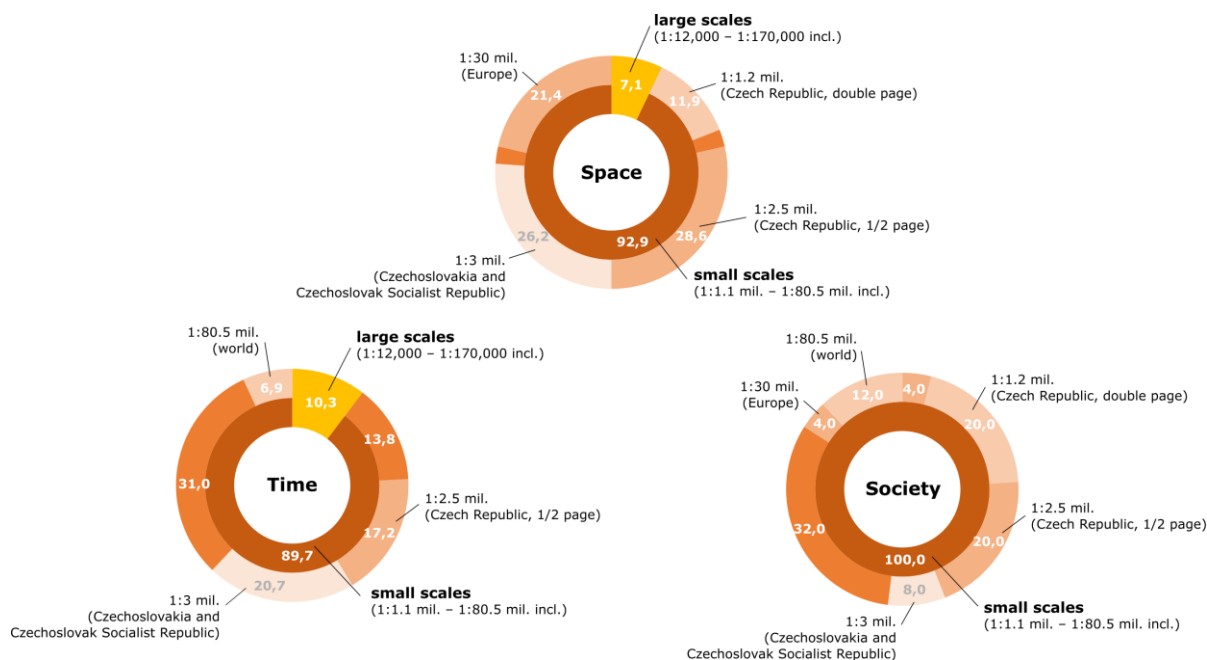

Fig. 7 – Representation of individual scales in the atlas and its sections. Source: authors.

The above-mentioned scale diversity can be offset by the fact that only six scales were used for almost three quarters of maps in the atlas. The scale series has been integrated mainly for maps of the territory of the present-day Czech Republic, interwar and post-war Czechoslovakia, which represent more than half of the maps in the atlas allowing the atlas reader to visually compare the spatial and temporal relationships within one topic, but also between topics.

In terms of the scale series, the least variable section seems to be "Space", where the cartographers only managed with eight scales (for 88% of the maps in this section and, moreover, only four scales were used). This follows mainly from the content of the section; whose individual chapters mostly monitor the territorial development of the chosen topic. An interesting fact is also the use of two scales to display different topics on the territory of the Czech Republic (a total of one third of maps) in connection with the map complexity and typology. The 1: 2.5 million scale is used mainly in simple analytical maps (almost three quarters of maps at this scale) depicting predominantly the topic of administration and politics (two thirds of maps at this scale). On the contrary, the maps of the territory of the Czech Republic at twice the scale (1: 1.2 mil.) are mostly less complex (90% of maps at this scale) and are primarily used to illustrate social topics dealing with population characteristics (national or religious structure) or cultural issues (spa treatment, tourism or conservation of natural and cultural heritage).

Like in AACH, small-scale maps absolutely predominate in CHA (93.8%), whereas medium-scale maps do not appear in CHA at all (see Figure 8). A significant difference can also be found in the use of the basic scale for depicting the territory of today's Czech Republic and the former territory of the Czechoslovak Republic and the Czechoslovak Socialist Republic, which primarily results from the different format and composition of the atlas.
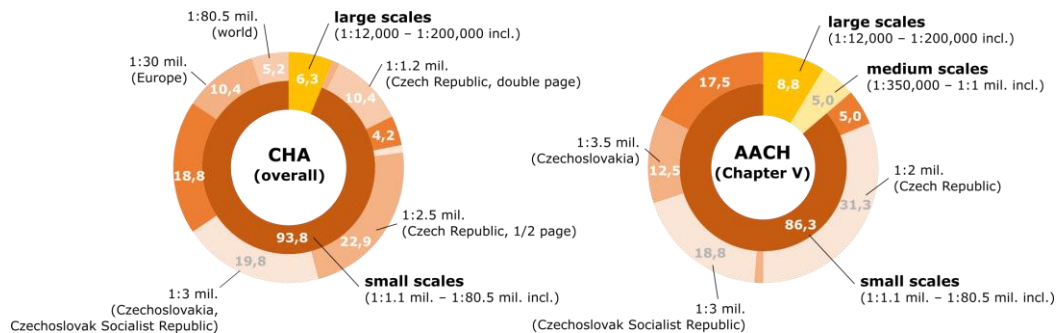

Fig. 8 – Comparison of scale numbers used within CHA and AACH. Source: authors.

Map Design and Composition

Unlike AACH, the uniformity of style was achieved. This is mainly due to the fact that the cartographic part of the team had been involved in the activities on the atlas from the beginning of preparatory work, thanks to which they had significantly corrected the requirements for the spatial representation of phenomena on the part of experts in the thematic content (both historians and geographers) so that they would be consistent with the rules of creating an atlas cartographic work. In addition to the above scale series, considerable attention was given to the *preparation of spatial data sets* during the preparatory phase of creating maps for individual sections of the atlas. The cartographers' objective was to have data available for different scales, i.e. data with an optimum degree of cartographic generalization.

An extensive debate of both cartographers and, partially, geographers and historians, took place over the *cartographic projections* used and their unification within the whole atlas to achieve both suitability for individual territories and not a very wide range of different projections that would impair comparability. For all maps (except for world maps using the Robinson pseudo-cylindrical compensating projection), the Albers equal area conic projection was used as the initial cartographic projection, in four variants with a specific setting of the central meridian position and undistorted parallels respecting the character of the displayed area. Compared to AACH, where a uniform projection was used for most maps regardless of the size of the territory (Czech Republic vs. Central Europe, Europe as a whole), this is again a significant step forward and a proof of a conceptual cartographic design of the atlas.

An equally complex debate focused on the setting pattern of individual pages, i.e. the location and graphic layout of map legends, the number and size of map fields and the general aesthetic appearance, function, clarity and other attributes enhancing the usability of the atlas. Legends and scales are already placed inside the map frame or in its immediate vicinity, a unified look of graphic scales, map legends have been ensured, and the concept of the symbol map legend has been very successfully processed to show the development of the results of parliamentary elections or the religious structure allowing comparisons between individual maps and periods.

CONCLUSION

The article assesses and analyses the Czech Historical Atlas, particularly with regard to its typology and internal structure. The logic of the sections as a vertical counterweight to the horizontal concept of the chronology of the chapters indicates the suitability of the chosen approach, especially in terms of the prevailing map typology and the principal topics. The results of the structural analysis of the thematic focus of maps further indicate the suitability of the subdivision of the atlas into individual sections, and the maps are thematically very well classified.

The classification of topics and their composition into individual units within the atlas is in contrast to the Academic Atlas of Czech History, where the classification was, with some exceptions, chronological and without further ambitions to unite topics into related sections. The advantage of

----

this approach, which fully respects the time aspect, is primarily in the clarity and easy orientation in discrete topics that reflect the standard orientation towards data and timelines. However, there is a disadvantage of mixing thematically different maps and separating visually thematically related maps and chapters that are often very similarly cartographically processed, making it difficult for the reader to perceive history as mutually connected and complex facts (and not as isolated events) and compare these related topics.

The thematic structure of maps reflects the participation of historians and geographers in the creation of the atlas. Overall, the atlas is dominated by classical history themes (military affairs, politics/administration, genesis of space – about 70% of maps) over social themes (civic society, migration, education, tourism, etc.), which fall under the domain of social and historical geographers in terms of authorship. The difference in the approach of historians and geographers to the presented topics is also clear from the results of the cartographic analysis of the atlas, which imply a close connection between the complexity of the content and the typology of maps.

It certainly cannot be claimed that the content of the atlas as a medium is exploited to the full – for example, the map complexity analysis shows a not very high proportion of complex maps in some chapters, which, however, is not a state deviating in any way from the general historiographic cartographic production. Given the complexity of some of the topics themselves, truly synthetic maps could pose problems in the identification of the message contained in the maps. The opposite problem, i.e. excessive filling of maps with symbols (and information in general), does not occur either. At least not to the extent that accompanied some of the economic themes treated in its predecessor, AACH.

The cartographic qualities of the atlas make it a balanced whole benefiting from a reasonably coupled set of technical elements, such as cartographic projections, scales, but also e.g. the map key style, legends and other elements. Any potential unfulfilled expectations on the part its readers and a higher degree of user ergonomics can be compensated by the electronic version, which is being launched to the public at the time of publishing this article.

ACKNOWLEDGEMENTS

REFERENCES

[1]   Semotanová, E., Zudová-Lešková, Z., Močičková, J., Cajthaml, J., Seemann, P., & Bláha, J. D. et al. 2019. *Český historický atlas: kapitoly z dějin 20. století*. Praha: Historický ústav.

[2]   Semotanová, E., & Cajthaml, J. 2014. *Akademický atlas českých dějin*. Praha: Academia.

[3]   Bláha, J. D., & Kučera, Z. 2014. E. Semotanová, J. Cajthaml a kol.: Akademický atlas českých dějin. *Informace ČGS*, 33(2): 36–46. Available from: https://geography.cz/publikace/informace-cgs/ /informace-cgs-201433-2/

[4]   Český historický atlas. Internetový literární časopis iLiteratura.cz [online]. 2020, 29-03-2020, 18.(1), 1 [cit. 2021-01-25]. ISSN ISSN 1214-309X. Available from: http://www.iliteratura.cz/Clanek/42803/ /semotanova-eva-et-al-cesky-historicky-atlas

[5]   Jenny, B., & Hurni, L. 2011. Studying cartographic heritage: Analysis and visualization of geometric distortions. *Computer & Graphics*, 35(2): 402–411. ISSN 0097-8493.

[6]   Chen, C., Härdle, W., & Unwin, A. (eds.) 2008. *Handbook of Data Visualization*. Springer, Berlin, 936 p. ISBN 978-3-540-33036-3.

[7]   Bláha, J. D., & Močičková, J. 2018. The research-analytic part of preparation of a cartographic work: a case study of an analysis of historical atlases as the basis for creating the Czech Historical Atlas. *AUC Geographica*, 53(1): 58–69. ISSN 0300-5402.

[8]   Slocum, T., Robert B. MacMaster, F. Kessler and H. Howard. Thematic cartography and geovisualization, 3rd Edition. (2008).

[9]   Wolodtschenko, A. 2010. Atlaskartosemiotik: neue Möglichkeiten und Lösungen. *Meta-carto-semiotics. Journal for Theoretical Cartography*, 3: 1–10.

[10]   Trahorsch, P., & Bláha, J. D. 2019. Visual representation of the curriculum in Geography textbooks: Quantification of visuals in educational medium analysis. *IARTEM e-Journal*, 11(2): 1–20.

[11]   Trahorsch, P., Bláha, J. D., & Chytrý, V. 2019. Comparative Analysis of the Quality of Visuals in Geography Textbooks for ISCED 1 and ISCED 2 Levels of Education. *Review of International Geographical Education Online*, 9(2): 264–283. ISSN 2146-0353.

[12]   Houghton, H. A., & Willows, D. M. (eds.) 1987. *The psychology of illustration: instructional issues*. New York: Springer.

[13]   Metallinos, N., Muffoletto, R., Petterson, R., Shaw, J., & Takakuwa, Y. 1990. The use of verbovisual information in textbooks – a cross-cultural experience. Londýn: University of London.

[14]   Pravda, J. 2002. Analytické a syntetické mapy v klasifikácii máp. *Geografický časopis*, 54(4): 367–380.